

Habilitační práce – Habilitation Thesis



České
vysoké
učení technické
v Praze

F4

Fakulta jaderná a fyzikálně inženýrská
Katedra matematiky

Pokročilé metody pro matematické modelování dvoufázového proudění a transportu v porézním prostředí

**Advanced methods for mathematical modeling of
two-phase flow and transport in porous media**

Radek Fučík

Abstrakt

Matematické modelování komplexních dynamických procesů v porézním prostředí vyžaduje pokročilé metody pro řešení příslušného systému diferenciálních rovnic. V předložené práci jsou představeny metody pro řešení modelu dvoufázového filtračního proudění v obecné dimenzi, modelu dvoufázového kompozičního proudění s přestupem hmoty mezi fázemi v porézním prostředí obecné dimenze a modelu elektro-chemické interakce v porézním prostředí lithiového-iontového elektrického článku. Použité matematické metody jsou založené buď na analytickém, nebo numerickém přístupu.

V prvním případě se jedná o transformaci parciálních nebo obyčejných diferenciálních rovnic na jednu obyčejnou diferenciální rovnici, která je dále převedena na integrální rovnici. Výsledná integrální rovnice je poté řešena iteračně pomocí numerické aproximace integrálu. Tento přístup je použit pro získání semi-analytického řešení úlohy dvoufázového proudění v porézním prostředí obecné dimenze a pro řešení elektro-chemické interakce v lithiovém-iontovém elektrickém článku.

Ve druhém případě je uvažován systém parciálních diferenciálních rovnic s obecnými koeficienty, pro který je použita diskretizace pomocí smíšené hybridní metody konečných prvků. Tato diskretizace je modifikována tak, aby bylo možné řešit i degenerující úlohy dvoufázového kompozičního proudění v porézním prostředí. Výsledný numerický řešič **NumDwarf** lze výhodně masivně paralelizovat pro počítání na grafických akcelerátorech (GPU) nebo na výpočetních klastrech CPU. V práci je uveden přehled konkrétních úloh, které byly a v současné době jsou řešeny pomocí řešiče **NumDwarf**.

Abstract

Mathematical modeling of complex dynamic processes in porous media requires advanced methods for solving a corresponding system of differential equations. The presented work presents methods for solving the two-phase flow model in multi-dimensional porous media, the two-phase compositional flow model with mass transfer between phases in a porous medium of general dimension, and the electrochemical interaction model in the porous environment of a lithium-ion electric cell. The mathematical methods used are based on either an analytical or a numerical approach.

The first case involves the transformation of partial or ordinary differential equations into a single ordinary differential equation, which is further transformed into an integral equation. The resulting integral equation is then solved iteratively using a numerical approximation of the integral. This approach is used to obtain a semi-analytical solution of the two-phase flow problem in a porous medium of a general dimension to solve the electrochemical interaction in a lithium-ion cell.

In the second case, a system of partial differential equations with general coefficients is considered, for which discretization using a mixed finite element hybrid method is used. This discretization is modified so that it is possible to solve degenerative problems of two-phase compositional flow in a porous medium. The resulting numerical solver **NumDwarf** can be advantageously massively parallelized for computing on graphics accelerators (GPUs) or CPU computational clusters. The thesis provides an overview of specific tasks that have been solved using the **NumDwarf** solver.

Obsah

1 Předmluva	1
2 Matematické modelování proudění, transportu a přestupu veličin v porézním prostředí	3
2.1 Dvoufázové proudění v porézním prostředí	3
2.2 Transport rozpuštěných látek v porézním prostředí	8
2.3 Transport iontů a elektrického náboje v Li-ion článku	11
3 Přesná řešení úlohy dvoufázového proudění s kapilaritou v obecné dimenzi	15
3.1 Formulace úlohy	15
3.2 Transformace na ODR	17
3.3 Integrované řešení ODR	19
3.4 Výsledky a aplikace	23
3.5 Shrnutí autorova přínosu	24
4 Numerické řešení metodou smíšených hybridních konečných prvků	25
4.1 Formulace obecné úlohy	26
4.2 Diskretizace	27
4.3 Diskretizace PDR	29
4.4 Bilance toku na hranách	30
4.5 Výpočetní algoritmus	31
4.6 Výsledky a aplikace	31
4.7 Shrnutí autorova přínosu	34
5 Integrované řešení elektrochemických interakcí v Li-ion článku	35
5.1 Formulace úlohy	35
5.2 Odvození integrované rovnice	36
5.3 Iterační schéma pro řešení integrované rovnice	37
5.4 Výsledky a aplikace	37
5.5 Shrnutí autorova přínosu	38
6 Shrnutí vědecko-pedagogického přínosu autora k dané problematice	39
6.1 Shrnutí příspěvků autora k dané problematice	39

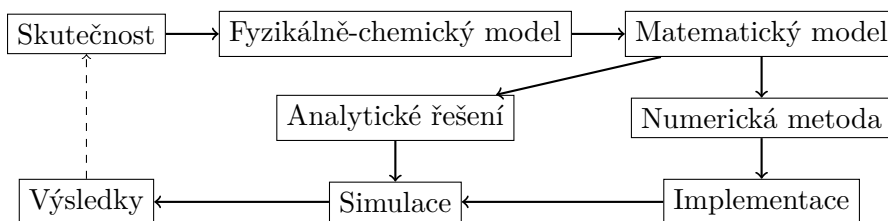
6.2 Stručný přehled přiložených článků	40
6.3 Vedení a spolupráce se studenty	43
6.4 Současný výzkum a mezinárodní spolupráce	43
6.5 Budoucí výzkum	44
Bibliografie	45
Přílohy	51
P.1 Článek v Advances in Water Resources	51
P.2 Článek v Computer Physics Communications	58
P.3 Článek v Groundwater	102
P.4 Článek v Journal of Computational Physics	117
P.5 Článek v International Journal of Heat and Mass Transfer	141
P.6 Článek v Mathematical Problems in Engineering	155
P.7 Kapitola v Handbook of Chemical Mass Transport in Environment	168
P.8 Kapitola v Pore Scale Phenomena: Frontiers in Energy and Environment	208

Kapitola 1

Předmluva

Předkládaná práce shrnuje hlavní výsledky autora v oblasti výzkumu pokročilých metod matematického modelování dynamických procesů v porézním prostředí. Jak je znázorněno na Obrázku 1.1, tato oblast má interdisciplinární povahu. Výchozím bodem jsou fyzikální, chemické nebo biologické poznatky o přírodě, které jsou popsány pomocí matematických rovnic vycházejících ze základních zákonů a principů. Tyto rovnice jsou dále analyzovány a pro jejich řešení je navržena vhodná analytická nebo numerická metoda. V případě numerického modelu je tento dále řešen pomocí vhodné počítačové implementace, kde je kladen důraz na její efektivitu s ohledem na moderní paralelní výpočetní možnosti, jako jsou rozsáhlé výpočetní klastry nebo počítání na grafických akcelerátorech.

Tematicky zapadá předložená práce do náplně oboru Matematického inženýrství, který je tradičním oborem Katedry matematiky Fakulty jaderné a fyzikálně inženýrské Českého vysokého učení technického v Praze.



Obrázek 1.1: Schéma ilustrující proces matematického modelování přírodního nebo průmyslového jevu se zpětnou vazbou z výsledků matematického modelování, např. při řízení technologických procesů v průmyslu.

Matematické modelování komplexních dynamických procesů v porézním prostředí je důležitým nástrojem ve vývoji a výzkumu v mnoha oborech lidské činnosti, jako například v ekologii (v problematice ochrany zdrojů pitné podzemní vody), ropném průmyslu (simulace ropných rezervoárů), v lékařství (perfuze cév nebo myokardu) nebo v automobilovém průmyslu (studium stárnutí lithiových-iontových elektrických článků) [1, 2, 3, 4, 5, 6].

Tato práce se zabývá pokročilými analytickými a numerickými metodami

Kapitola 2

Matematické modelování proudění, transportu a přestupu veličin v porézním prostředí

2.1 Dvoufázové proudění v porézním prostředí

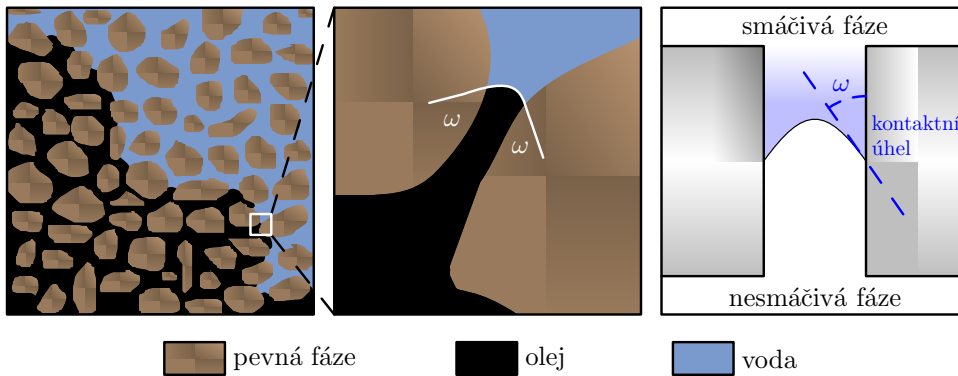
V této kapitole jsou shrnuty základy matematicko-fyzikálního popisu dvoufázového proudění v porézním prostředí, které vychází především z [1, 3, 7, 8]. Nechť porézní prostředí vyplňuje oblast $\Omega \subseteq \mathbb{R}^d$, kde d značí dimenzi prostoru, $d = 1, 2, 3$.

Porézní prostředí

Porézním prostředím lze chápat materiál složený z pevné fáze a volného, vzájemně propojeného prostoru (póry). V nejobecnějším smyslu lze téměř každý materiál považovat za porézní, pokud uvnitř obsahuje prázdný prostor. Velikost (měřítko) a morfologie je klíčem k pochopení procesů v porézním prostředí. Proto jsou na geometrii a rozměry porézního média kladeny následující předpoklady [3]:

- A. Pórový prostor je propojen (jinak by nemohla tekutina proudit).
- B. Rozměry prázdného prostoru musí být dostatečně velké ve srovnání s rozměry molekul tekutiny, přičemž pevná fáze může být považována za hypotetické kontinuum.
- C. Rozměry prostoru pórů musí být dostatečně malé, aby tok tekutiny byl řízen adhezivními silami na rozhraní kapaliny a pevné látky a soudržnými silami na rozhraní dvou kapalin ve vícefázových systémech.

Při modelování toku v porézním prostředí je důležité brát v úvahu různá měřítka. Obrázek 2.1 zobrazuje různá zvětšení porézního prostředí od makroskopické po mikroskopickou škálu.



Obrázek 2.1: Ilustrace různých měřítek v porézním médiu (první dva obrázky zleva) a reprezentace kontaktního úhlu na rozhraní tekutin a pevné fáze.

Rovnice dynamiky tekutin musí být doplněny okrajovými a počátečními podmínkami. Ovšem kvůli složité a komplexní geometrii porézního prostředí nelze okrajové podmínky na rozhraní pevné fáze a volného prostředí v mikroskopickém měřítku předepsat. Za účelem vývoje matematického modelu se proto používá koncepce porézního média jako kontinua v makroskopickém měřítku.

V každém bodě kontinua v makroskopickém popisu je uvažována střední hodnota veličin přes reprezentativní elementární objem (REV). Bear a Verruijt [1] definují REV jako objem, který je dostatečně velký na to, aby statisticky odhadl všechny relevantní parametry konfigurace prázdného prostoru, a zároveň dostatečně malý, aby ho šlo považovat za zanedbatelnou část celkového objemu z makroskopického pohledu. Pokud takový REV nelze najít, nelze dané prostředí považovat za kontinuum.

■ Porozita

Pomocí zvoleného REV se definuje porozita ϕ [-] jako poměr objemu volného prostoru porézního prostředí k celému objemu REV:

$$\phi(\vec{x}_0) = \frac{1}{|\text{REV}|} \int_{\text{REV}} \gamma(\vec{x}) d\vec{x}, \quad (2.1)$$

kde $\vec{x}_0 \in \text{REV} \subset \Omega$, $|\text{REV}|$ je objem REV a γ označuje charakteristickou funkci volného prostoru uvnitř porézního prostředí, která je pro každé $\vec{x} \in \text{REV}$ zavedená jako

$$\gamma(\vec{x}) = \begin{cases} 1 & \text{pokud } \vec{x} \text{ náleží volnému prostoru,} \\ 0 & \text{pokud } \vec{x} \text{ náleží pevné fázi.} \end{cases} \quad (2.2)$$

Porozita je charakteristická vlastnost porézního prostředí a lze ji určit experimentálně [1].

V obecném případě se může porozita měnit v čase, např. v důsledku deformace porézního prostředí. V této práci vystačíme s předpokladem konstantní porozity, což znamená, že porézní prostředí je rigidní.

■ Fáze

Fáze je chemicky homogenní část systému, která je od ostatních takových částí oddělena určitou fyzickou hranicí a je charakterizovaná dynamickou viskozitou μ [Pa s], objemovou hmotnostní hustotou ρ [kg m⁻³], případně dalšími veličinami. Nutnost určité fyzické hranice mezi dvěma nebo více fázemi znamená, že ve vícefázovém systému nemůže být přítomna více než jedna plynná fáze, protože plyny jsou vždy plně mísitelné.

Ve většině případů je v porézních prostředích předmětem zkoumání proudění vody a dalších fází, jako je olej, chlorované uhlovodíky, CO₂ nebo vzduch. Obecně se pro kapaliny nemísitelné s vodou používá zkratka NAPL (z angl. Non-Aqueous Phase Liquid). Tyto kapaliny jsou dále děleny na husté (DNAPL), resp. lehké (LNAPL) s vyšší, resp. nižší hustotou než voda.

Podle kontaktního úhlu rozhraní mezi tekutými fázemi u pevné stěny (viz ω na Obrázku 2.1) rozlišujeme smáčivou (přísluší k ostrému úhlu) a nesmáčivou (přísluší k tupému úhlu) fázi. Tato práce se mimo jiné zabývá dynamikou dvou nemísivých tekutin voda-NAPL, přičemž voda je vždy smáčivá a označována indexem w (z angl. wetting). Druhá, nesmáčivá fáze je pak značena indexem n (z angl. non-wetting). Systémy se dvěma tekutými fázemi se nazývají dvofázové, tj. pevná fáze, která je v porézním prostředí vždy přítomna, se do označení nezahrnuje.

■ Saturace

V mikroskopickém měřítku náleží každý bod REV buď pevné, nebo právě jedné tekuté fázi $\alpha \in \{w, n\}$. Pomocí charakteristické funkce γ_α tekuté fáze α , definované v čase t pro každý bod $\vec{x} \in \Omega$ vztahem

$$\gamma_\alpha(t, \vec{x}) = \begin{cases} 1 & \text{pokud } \vec{x} \text{ náleží fázi } \alpha \text{ v čase } t, \\ 0 & \text{jinak,} \end{cases} \quad (2.3)$$

lze zavést saturaci S_α [-] fáze α :

$$S_\alpha(t, \vec{x}_0) = \frac{\int_{\text{REV}} \gamma_\alpha(t, \vec{x}) d\vec{x}}{\int_{\text{REV}} \gamma(t, \vec{x}) d\vec{x}}, \quad (2.4)$$

kde $\vec{x}_0 \in \text{REV} \subset \Omega$.

Z definice (2.4) plyne, že saturace fáze α je bezrozměrná veličina s hodnotami mezi 0 a 1, přičemž v případě uvažovaného dvofázového systému platí

$$S_w + S_n = 1. \quad (2.5)$$

Je dobře známo, že jednotlivé fáze nelze zcela mechanicky vytlačit z porézního prostředí, např. [9, 10]. Proto se pro každou fázi $\alpha \in \{w, n\}$ zavádí reziduální (zbytková) saturace $S_{r,\alpha}$ vyjadřující takové minimální nasycení, které se v porézním médiu udrží vlivem adheze vůči pevné matici.

K popisu zbylé, mechanicky vytlačitelné části dané fáze α se používá efektivní saturace $S_{e,\alpha}$ [–]:

$$S_{e,\alpha} = \frac{S_\alpha - S_{r,\alpha}}{1 - \sum_{\beta} S_{r,\beta}}, \quad (2.6)$$

kteřá, stejně jako saturace S_α , nabývá hodnot mezi 0 a 1, a pro níž platí

$$S_{e,w} + S_{e,n} = 1. \quad (2.7)$$

■ Řídící rovnice proudění

Dynamiku fáze α řídí zákon zachování hmoty ve tvaru [1, 3, 7]

$$\frac{\partial(\phi \varrho_\alpha S_\alpha)}{\partial t} + \nabla \cdot (\varrho_\alpha \vec{v}_\alpha) = \varrho_\alpha F_\alpha, \quad (2.8)$$

kde filtrační rychlost \vec{v}_α je dána Darcyho zákonem

$$\vec{v}_\alpha = -\lambda_\alpha \mathbf{K}(\nabla p_\alpha - \varrho_\alpha \vec{g}), \quad (2.9)$$

kde \vec{g} [m s⁻²] je vektor gravitačního zrychlení, \mathbf{K} [m²] je tenzor vnitřní propustnosti porézního prostředí, p_α [Pa] je tlak, λ_α [Pa⁻¹s⁻¹] je mobilita a F_α [kg m⁻³s⁻¹] je zdrojový člen fáze α .

Darcyho zákon je důsledkem zákona zachování hybnosti, přičemž v případě dvoufázového (a obecně vícefázového) proudění se v porézním prostředí zanedbává výměna hybnosti mezi fázemi.

Mobilita fáze α označuje

$$\lambda_\alpha = \frac{k_{r,\alpha}}{\mu_\alpha}, \quad (2.10)$$

kde $k_{r,\alpha}$ je relativní propustnost fáze α , která vyjadřuje snížení hydraulické propustnosti porézního prostředí v důsledku přítomnosti fáze α a nabývá hodnot mezi 0 a 1.

Kapilární jevy na pórové, mikroskopické úrovni způsobí skok mezi fázovými tlaky na makroskopické úrovni. Tento skok se nazývá kapilární tlak, značí se p_c [Pa] a je definován vztahem

$$p_c = p_n - p_w. \quad (2.11)$$

■ Empirické modely pro kapilární tlak

V případě dvoufázového proudění se dá experimentálně změřit závislost $p_c = p_c(S_{e,w})$ pro $S_{e,w} \in (0, 1)$, přičemž z matematického pohledu lze o této

závislosti předpokládat, že p_c je ostře klesající a spojitě diferencovatelná na $(0, 1)$ a $\lim_{S_{e,w} \rightarrow 1^-} p_c(S_{e,w}) \geq 0$, [11].

Pro empirické zjištění závislosti $p_c = p_c(S_{w,e})$ pro dané porézní prostředí a systém smáčivá-nesmáčivá fáze se nejčastěji používají následující dva modely.

První model byl navržen Brooksem a Coreym [12] ve tvaru

$$S_{e,w}(p_c) = \left(\frac{p_c}{p_d}\right)^\lambda \quad \text{pro } p_c \geq p_d, \quad (2.12)$$

kde $\lambda [-]$ odpovídá míře variability velikosti zrn v porézním prostředí a p_d [Pa] se nazývá vstupním tlakem a vyjadřuje minimální kapilární tlak, který je nutný překonat k vytlačení smáčivé fáze v maximální saturaci z největšího póru.

Za předpokladu invertovatelnosti závislosti $S_{e,w}(p_c)$ lze vyjádřit Brooksův a Coreyův model pro p_c ve tvaru

$$p_c(S_w) = p_d S_{e,w}^{-\frac{1}{\lambda}} \quad \text{pro } S_{e,w} \in (0, 1]. \quad (2.13)$$

Druhý model byl navržen van Genuchtenem [13] ve tvaru

$$S_{e,w}(p_c) = [1 + (\alpha p_c)^n]^m \quad \text{pro } p_c \geq 0, \quad (2.14)$$

kde α [Pa⁻¹], m a n jsou empiricky určené parametry, přičemž m a n charakterizují pórovou strukturu porézního prostředí a někdy se mezi nimi používá vztah

$$m = 1 - \frac{1}{n}. \quad (2.15)$$

Inverzí (2.14) se odvodí vztah pro $p_c = p_c(S_{e,w})$ ve tvaru

$$p_c(S_w) = \frac{1}{\alpha} \left(S_{e,w}^{-\frac{1}{m}} - 1 \right)^{\frac{1}{n}} \quad \text{pro } S_{e,w} \in (0, 1]. \quad (2.16)$$

Parametry těchto modelů se určují experimentálně nejprve při primárním odvodnění plně nasyceného vzorku porézního prostředí (primary drainage), poté jsou měřeny parametry druhotného (sekundárního) zavodnění (secondary imbibition). Výsledné křivky, jejichž příklady jsou ukázány na Obrázku 2.3, představují horní a dolní mez kapilárního tlaku, který se může v závislosti na historii dynamiky systému v daném bodě pro danou saturaci nacházet. Taková situace se označuje jako hystereze kapilárního tlaku [1, 2]. Pro jednoduchost se v této práci bude uvažovat buď proces primárního odvodnění, nebo druhotného zavodnění.

Empirické modely pro relativní propustnost

Na základě zvoleného modelu pro kapilární tlak lze odvodit model pro relativní propustnosti smáčivé a nesmáčivé fáze pomocí vztahů [7]:

$$k_{r,w}(S_{e,w}) = S_{e,w}^A \left(\frac{\int_0^{S_{e,w}} [p_c(\xi)]^{-B} d\xi}{\int_0^1 [p_c(\xi)]^{-B} d\xi} \right)^C, \quad (2.17a)$$

$$k_{r,n}(S_{e,w}) = (1 - S_{e,w})^A \left(\frac{\int_0^{S_{e,w}} [p_c(\xi)]^{-B} d\xi}{\int_0^1 [p_c(\xi)]^{-B} d\xi} \right)^C, \quad (2.17b)$$

kde A , B a C jsou parametry. Nejčastěji se používají dva modely.

První, Burdinův model [14, 15] volí $A = B = 2$ a $C = 1$ a v propojení s Brooksovým a Coreyho modelem pro p_c má tvar

$$k_{r,w}(S_w) = S_{e,w}^{3+\frac{2}{\lambda}}, \quad (2.18a)$$

$$k_{r,n}(S_w) = (1 - S_{e,w})^2 (1 - S_{e,w}^{1+\frac{2}{\lambda}}). \quad (2.18b)$$

Druhý, Mualemův model [16] volí $A = \frac{1}{2}$, $B = 1$ a $C = 2$ a v propojení s van Genuchtenovým modelem pro p_c má tvar:

$$k_{r,w}(S_w) = S_{e,w}^{\frac{1}{2}} \left(1 - (1 - S_{e,w}^{\frac{1}{m}})^m \right)^2, \quad (2.19a)$$

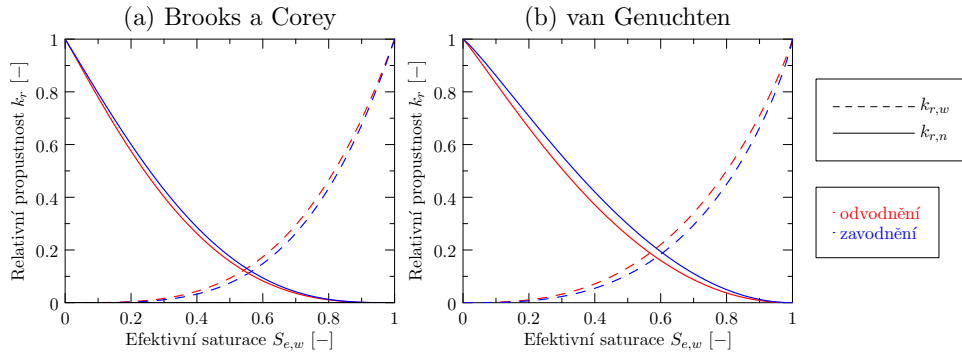
$$k_{r,n}(S_w) = (1 - S_{e,w})^{\frac{1}{3}} (1 - S_{e,w}^{\frac{1}{m}})^{2m}. \quad (2.19b)$$

Pro jednoduchost se použití Burdiného, resp. Mualemova modelu nazývá podle příslušného modelu pro kapilární tlak, tj. Brooksův a Coreyho, resp. van Genuchtenův model.

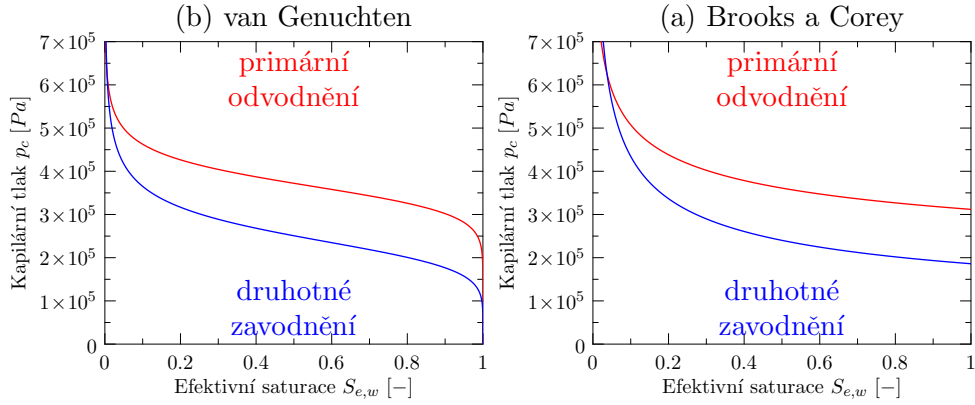
V Obrázku 2.2 jsou zobrazeny křivky relativní propustnosti získané experimentálně pro jeden vzorek písku.

2.2 Transport rozpuštěných látek v porézním prostředí

V porézním prostředí se jednotlivé tekuté fáze mohou skládat z jedné nebo více chemických komponent (složek). Matematicko-fyzikální popis dynamiky proudění, transportu a přestupu hmoty vychází z formulace zákona zachování hmoty každé takové komponenty (označené v této kapitole indexem κ) v dané fázi (značené indexem α) [17, 18]. V této kapitole budou pro obecnou fázi s indexem α a její komponentu s indexem κ popsány řídicí transportní rovnice.



Obrázek 2.2: Ilustrace typického průběhu křivek relativních propustností pro jeden vzorek písku s použitím Brooksova a Coreyho, resp. van Genuchtenova modelu. Data byla poskytnuta spolupracujícím pracovištěm CESEP, Colorado School of Mines.



Obrázek 2.3: Ilustrace typické závislosti kapilárního tlaku na efektivní smáčivé saturaci pro model podle (a) Brookse a Coreyho a (b) van Genuchtena, změřené experimentálně pro primární zavodnění a následné odvodnění. Data byla poskytnuta spolupracujícím pracovištěm CESEP, Colorado School of Mines.

Řídící transportní rovnice

Rovnice kontinuity pro komponentu κ ve fázi α lze zapsat ve tvaru

$$\frac{\partial(\phi S_\alpha \rho_\alpha X_{\kappa,\alpha})}{\partial t} + \nabla \cdot (\rho_\alpha X_{\kappa,\alpha} \vec{v}_\alpha + \vec{j}_{\kappa,\alpha}) = F_{\kappa,\alpha}, \quad (2.20)$$

kde $X_{\kappa,\alpha}$ [-] je hmotnostní zlomek komponenty κ ve fázi α , $F_{\kappa,\alpha}$ [$\text{kg m}^{-3} \text{s}^{-1}$] je zdrojový člen a $\vec{j}_{\kappa,\alpha}$ označuje difuzní tok, pro který se používá první Fickův zákon ve tvaru

$$\vec{j}_{\kappa,\alpha} = -\mathbf{D}_{\kappa,\alpha} \nabla(\rho_\alpha x_{\kappa,\alpha}), \quad (2.21)$$

P.7 [str. 168], P.4 [str. 117], P.3 [str. 102]). Tok mezi fázemi je poté zahrnut do zdrojových členů $F_{\kappa,\alpha}$ a $F_{\kappa,\beta}$ [25], přičemž platí bilanční rovnice

$$Q_{\kappa,\alpha\rightarrow\beta} + Q_{\kappa,\beta\rightarrow\alpha} = 0. \quad (2.26)$$

2.3 Transport iontů a elektrického náboje v Li-ion článku

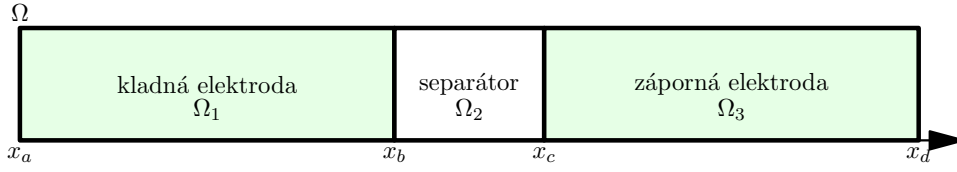
V případě matematického popisu a modelování životnosti elektrických bateriových článků je jedním ze základních procesů elektrochemická interakce a transport iontů a elektrického náboje v porézním prostředí obou elektrod a separátoru. V této kapitole je předmětem zkoumání lithiový-iontový elektrický článek (zkráceně Li-ion článek), pro který je stručně shrnut matematický model těchto procesů v jednorozměrné geometrii vycházející z [5, 6, 26, 27, 28] a [29] (Příloha P.6 [str. 155]).

Cílem matematického modelování je určit vnější i vnitřní napětí článku při dodávání nebo odebírání proudu o dané intenzitě, a to vše v závislosti na chemickém stavu článku, který je popsán rozložením koncentrace lithiových iontů v pevné fázi elektrod a gelovitém elektrolytu. Předepsaný proud je udáván v podobě proudové hustoty na jednotku plochy I_{app} [A m^{-2}] a je přiveden na jednu z elektrod, přičemž $I_{\text{app}} > 0$ odpovídá režimu nabíjení a $I_{\text{app}} < 0$ režimu vybíjení. Pomocí soustavy transportních rovnic v porézním prostředí pro lithiové ionty a elektrický náboj (níže popsané rovnicemi (2.27a), (2.28), (2.30) a (2.31)), ve kterých I_{app} je předepsán jako toková (Neumannova) okrajová podmínka, vznikne odezva článku v podobě výsledného napětí mezi oběma elektrodami.

V 1D je Li-ion článek reprezentován intervalem $\Omega = [x_a, x_d]$, viz Obrázek 2.4, který je rozdělen na tři části $\Omega = \Omega_1 \cup \Omega_2 \cup \Omega_3$, kde $\Omega_1 = [x_a, x_b]$, $\Omega_2 = [x_b, x_c]$ a $\Omega_3 = [x_c, x_d]$ jsou po řadě kladná elektroda, separátor a záporná elektroda. Elektrody i separátor se skládají z pevného, porézního materiálu a v dalším jsou veličiny příslušné k této pevné fázi značeny indexem s (z angl. solid phase). Uvnitř porézního prostředí se v celé oblasti Ω nachází elektrolyt, jehož příslušné veličiny jsou v dalším značeny indexem e . Veličiny příslušné k jednotlivým podintervalům Ω_i jsou dále indexovány příslušným číslem $i = 1, 2, 3$.

Hodnoty všech veličin jsou obecně závislé na prostorové souřadnici $x \in \Omega$ a na čase $t \in \mathcal{J} = (0, t_f)$, kde t_f označuje předem zvolený konečný čas.

V Li-ion článku jsou lithiové ionty Li^+ v rámci elektrochemických procesů uvolňovány z porézního materiálu jedné elektrody (deinterkalace), transportovány difuzí elektrolytem přes separátor, až jsou nakonec sloučeny s porézním materiálem druhé elektrody (interkalace).



Obrázek 2.4: Jednorozměrná aproximace lithiového-iontového elektrického článku.

Řídící transportní rovnice lithiových iontů v elektrolytu

Podle [6] lze řídicí difuzní rovnice pro lithiové ionty Li^+ v elektrolytu zapsat pro každé $i = 1, 2, 3$ ve tvaru

$$\phi_i \frac{\partial c_{e,i}}{\partial t} = \frac{\partial}{\partial x} \left(D_e \tau_i \frac{\partial c_{e,i}}{\partial x} \right) + (1 - t_+^0) a_i j_i \quad \text{v } \Omega_i \times \mathcal{J}, \quad (2.27a)$$

kde $c_{e,i}$ [mol m^{-3}] je molární koncentrace Li^+ v elektrolytu, ϕ_i [–] je porozita, D_e [$\text{m}^2 \text{s}^{-1}$] je difuzní koeficient lithiových iontů v elektrolytu, τ [–] je tortuozita porézního prostředí (charakterizující zvlněnost či zakroucenost porézního prostoru), t_+^0 [1] je transferenční číslo Li^+ , a_i [m^{-1}] je povrch porézní elektrody na jednotku objemu a j_i [$\text{mol m}^{-2} \text{s}^{-1}$] je tok iontů z vnitřního povrchu elektrody do elektrolytu vztážený k jednotce plochy. V případě separátoru je tok nulový, proto $j_2 = 0$.

Rovnice (2.27a) v jednotlivých částech článku jsou mezi sebou propojeny okrajovými podmínkami popisujícími jednak spojitost koncentrace, resp. difuzních toků mezi elektrodami a separátorem:

$$c_{e,2}|_{x=x_b} = c_{e,1}|_{x=x_b} \quad \text{a} \quad c_{e,3}|_{x=x_c} = c_{e,2}|_{x=x_c}, \quad (2.27b)$$

resp.

$$D_e \tau_2 \frac{\partial c_{e,2}}{\partial x} \Big|_{x=x_b+} = D_e \tau_1 \frac{\partial c_{e,1}}{\partial x} \Big|_{x=x_b-}, \quad (2.27c)$$

$$D_e \tau_3 \frac{\partial c_{e,3}}{\partial x} \Big|_{x=x_c+} = D_e \tau_2 \frac{\partial c_{e,2}}{\partial x} \Big|_{x=x_c-}, \quad (2.27d)$$

a nulový tok Li^+ skrz vnější hranici článku:

$$\frac{\partial c_{e,1}}{\partial x} \Big|_{x=x_a+} = \frac{\partial c_{e,3}}{\partial x} \Big|_{x=x_d-} = 0. \quad (2.27e)$$

V čase $t = 0$ je potom předepsána počáteční podmínka pro koncentraci ve tvaru

$$c_{e,i}|_{t=0} = c_{e,i}^0, \quad \text{v } \Omega_i, \quad \forall i \in \{1, 2, 3\}. \quad (2.27f)$$

V pevné fázi porézních elektrod dochází k ukládání (interkalaci) a uvolňování (deinterkalaci) Li^+ , přičemž jejich množství na povrchu elektrod popisují koncentrace $c_{s,i}$ [mol m^{-3}], $i = 1, 3$. Zároveň se symbolem $c_{s,max,i}$, $i = 1, 3$,

označuje maximální možná (saturovaná) koncentrace, kterou mohou lithiové ionty na povrchu elektrody nabývat.

Dynamiku difuzních procesů lithiových iontů uvnitř pevné fáze porézních elektrod lze dále modelovat například tak, že se pevná fáze aproximuje souborem kuliček, přičemž na každou z nich se aplikuje druhý Fickův zákon ve sférických souřadnicích, viz [6, 29, 30].

■ Butlerova-Volmerova reakční kinetika

V každém bodě a časovém okamžiku popsané rovnice udávají chemický stav článku pomocí hodnot koncentrací $c_{e,i}$ v elektrolytu a $c_{s,i}$ v elektrodách, $i = 1, 3$. Toky j_1 a j_3 jsou zodpovědné nejen za přestup aktivní hmoty (iontů) mezi elektrodami a elektrolytem, ale zároveň popisují klíčové elektrochemické interakce, které pak udávají výsledné napětí článku. Podle Butlerovy-Volmerovy reakční kinetiky [6, 31, 32, 33] lze tyto toky pro $i = 1, 3$ vyjádřit ve tvaru

$$j_i = \delta_i \left[\exp\left(\frac{\alpha_{a,i}F}{RT}\eta_i\right) - \exp\left(-\frac{\alpha_{c,i}F}{RT}\eta_i\right) \right] \quad (2.28a)$$

s

$$\delta_i = K_i \sqrt{(c_{s,max,i} - c_{s,i})c_{s,i}c_{e,i}}, \quad (2.28b)$$

kde F [C mol⁻¹] je Faradayova konstanta, R [J mol⁻¹K⁻¹] je univerzální plynová konstanta, T [K] je teplota, K_i [mol^{-1/2}m^{5/2}s⁻¹] je reakční koeficient, $\alpha_{a,i}$ [1], resp. $\alpha_{c,i}$ [1] jsou koeficienty přestupu elektrochemické reakce na anodě, resp. katodě a η_i [V] je interkalační potenciál definovaný vztahem

$$\eta_i = \varphi_{s,i} - \varphi_{e,i} - U_i, \quad (2.29)$$

kde $\varphi_{s,i}$ [V], resp. $\varphi_{e,i}$ [V] jsou elektrické potenciály v elektrodách, resp. v elektrolytu a U_i [V] je napětí otevřeného obvodu (bez zatížení).

■ Rovnice pro výpočet elektrického potenciálu

Podle Ohmova zákona [6] lze rovnice zákona zachování elektrického náboje v porézních elektrodách, resp. elektrolytu v $\Omega_i \times \mathcal{J}$ zapsat ve tvaru

$$\sigma_i^{\text{eff}} \frac{\partial^2 \varphi_{s,i}}{\partial x^2} = a_i F j_i \quad \text{pro } i = 1, 3, \quad (2.30)$$

resp.

$$\frac{\partial}{\partial x} \left(\kappa_i^{\text{eff}} \frac{\partial \varphi_{e,i}}{\partial x} \right) = -a_i F j_i + \frac{2RT}{F} (1 - t_+^0) \frac{\partial}{\partial x} \left(\kappa_i^{\text{eff}} \frac{\partial \ln c_{e,i}}{\partial x} \right) \quad \text{pro } i = 1, 2, 3, \quad (2.31)$$

kde σ_i^{eff} [S m⁻¹] je efektivní elektronická vodivost v porézním prostředí a κ_i^{eff} [S m⁻¹] je efektivní iontová vodivost elektrolytu.

V každém časovém okamžiku lze rovnice (2.31), resp. (2.30) interpretovat jako systém obyčejných diferenciálních rovnic druhého řádu, které je nutné doplnit o následující okrajové podmínky pro $\varphi_{s,i}$:

$$-\sigma_1^{\text{eff}} \left. \frac{\partial \varphi_{s,1}}{\partial x} \right|_{x=x_a+} = I_{\text{app}}, \quad (2.32a)$$

$$-\sigma_1^{\text{eff}} \left. \frac{\partial \varphi_{s,1}}{\partial x} \right|_{x=x_b-} = 0, \quad (2.32b)$$

$$-\sigma_3^{\text{eff}} \left. \frac{\partial \varphi_{s,3}}{\partial x} \right|_{x=x_c+} = 0, \quad (2.32c)$$

$$-\sigma_3^{\text{eff}} \left. \frac{\partial \varphi_{s,3}}{\partial x} \right|_{x=x_d-} = I_{\text{app}}, \quad (2.32d)$$

$$\varphi_{s,3}|_{x=x_d} = 0, \quad (2.32e)$$

resp. pro $\varphi_{e,i}$:

$$-\kappa_1^{\text{eff}} \left. \frac{\partial \varphi_{e,1}}{\partial x} \right|_{x=x_a+} = 0, \quad (2.33a)$$

$$-\kappa_1^{\text{eff}} \left. \frac{\partial \varphi_{e,1}}{\partial x} \right|_{x=x_b-} = -\kappa_2^{\text{eff}} \left. \frac{\partial \varphi_{e,2}}{\partial x} \right|_{x=x_b+}, \quad (2.33b)$$

$$-\kappa_2^{\text{eff}} \left. \frac{\partial \varphi_{e,2}}{\partial x} \right|_{x=x_c-} = -\kappa_3^{\text{eff}} \left. \frac{\partial \varphi_{e,3}}{\partial x} \right|_{x=x_c+}, \quad (2.33c)$$

$$-\kappa_3^{\text{eff}} \left. \frac{\partial \varphi_{e,3}}{\partial x} \right|_{x=x_d-} = 0, \quad (2.33d)$$

$$\varphi_{e,1}|_{x=x_b} = \varphi_{e,2}|_{x=x_b}, \quad (2.33e)$$

$$\varphi_{e,2}|_{x=x_c} = \varphi_{e,3}|_{x=x_c}. \quad (2.33f)$$

■ Výpočet napětí článku

V daném časovém okamžiku je při znalosti I_{app} a chemického stavu článku (tj. prostorového rozložení koncentrace lithiových iontů $c_{s,i}$ pro $i = 1, 3$ a $c_{e,i}$ pro $i = 1, 2, 3$) možné vyřešit soustavu obyčejných diferenciálních rovnic (2.30) a (2.31), jak je ukázáno v [29] a v Kapitole 5. Výstupem řešení těchto rovnic jsou nejen toky j_1 a j_3 , které vystupují ve zdrojových členech transportních rovnic pro lithiové ionty (2.27a), ale též hodnoty potenciálů η_1 a η_3 , z nichž se určí hodnota $\varphi_{s,1}|_{x=x_a}$ jako výsledné napětí článku. Detaily výpočtu jsou uvedeny v Kapitole 5.

Kapitola 3

Přesná řešení úlohy dvoufázového proudění s kapilaritou v obecné dimenzi

Za předpokladu nestlačitelného dvoufázového proudění v rigidním, homogenním a izotropním porézním prostředí bez zdrojů a gravitace lze v obecném prostoru \mathbb{R}^d , $d \in \mathbb{N}$, formulovat úlohu tak, že pro ni existuje přesné, semi-analytické řešení. Tato úloha se nazývá McWhorterova a Sunadova úloha [34, 35, 36, 37, 38].

Úloha představuje situaci, kdy je jedna z fází vtlačena v počátku souřadné soustavy do oblasti vyplněné druhou fází (s jistou saturací), přičemž se předpokládá, že výsledný profil saturace bude symetrický okolo bodu vtlačení umístěného v počátku soustavy souřadnic. V této práci budeme pro jednoduchost uvažovat pouze případ vtlačení smáčivé fáze (se saturací $S_w = S_0$) do oblasti naplněné fází nesmáčivou (se saturací $S_w = S_i < S_0$). Odvození přesného řešení pro opačnou situaci je analogické [34, 36].

Principem odvození přesného řešení je transformace parciální diferenciální rovnice dvoufázového proudění na obyčejnou diferenciální rovnici (ODR), která je následně převedena na rovnici integrální. Pro řešení integrální rovnice je pak použita numerická iterační metoda, proto se výsledné řešení nazývá semi-analytické.

3.1 Formulace úlohy

Za výše uvedených předpokladů se rovnice kontinuity (2.8) pro fázi $\alpha \in \{w, n\}$ zjednoduší na

$$\phi \frac{\partial S_\alpha}{\partial t} + \nabla \cdot \vec{v}_\alpha = 0, \quad (3.1a)$$

kde Darcyho rychlost fáze α je dána vztahem

$$\vec{v}_\alpha = -\lambda_\alpha K \nabla p_\alpha, \quad (3.1b)$$

kde K [m^2] označuje izotropní (skalární) vnitřní propustnost porézního prostředí.

■ Formulace v kartézských souřadnicích

Zavedením celkové rychlosti $\vec{v}_T = \vec{v}_w + \vec{v}_n$ a použitím definice kapilárního tlaku (2.11) lze rovnice (3.1b) pro $\alpha = w$ a $\alpha = n$ zkombinovat a vyjádřit tak Darcyho rychlost smáčivé fáze ve tvaru

$$\vec{v}_w = f(S_w)\vec{v}_T - D(S_w)\nabla S_w, \quad (3.2)$$

kde $f[-]$ je frakční funkce smáčivé fáze

$$f(S_w) = \frac{\lambda_w(S_w)}{\lambda_w(S_w) + \lambda_n(S_w)} \quad (3.3)$$

a $D [\text{m}^2\text{s}^{-1}]$ je funkce zahrnující jevy kapilární difuze

$$D(S_w) = -K \frac{\lambda_w(S_w)\lambda_n(S_w)}{\lambda_w(S_w) + \lambda_n(S_w)} \frac{dp_c}{dS_w}(S_w). \quad (3.4)$$

Rovnice kontinuity (3.1a) pro obě fáze lze s využitím zavedeného značení přeformulovat na soustavu rovnic

$$\nabla \cdot \vec{v}_T = 0, \quad (3.5a)$$

$$\phi \frac{\partial S_w}{\partial t} + \nabla \cdot (f(S_w)\vec{v}_T - D(S_w)\nabla S_w) = 0, \quad (3.5b)$$

pro neznámé funkce $S_w = S_w(t, \vec{x})$ a $\vec{v}_T = \vec{v}_T(t, \vec{x})$, $\forall t > 0$, $\forall \vec{x} \in \mathbb{R}^d$.

■ Formulace ve sférických souřadnicích

Předpoklad symetrie hledaného přesného řešení vzhledem k počátku umožňuje převést soustavu rovnic (3.5) z kartézských souřadnic do sférických souřadnic v \mathbb{R}^d , tj. předpokládají se funkční závislosti $\vec{v}_T = \vec{v}_T(t, r)$ a $S_w = S_w(t, r)$, kde $r [\text{m}]$ označuje (nezápornou) radiální souřadnici.

Rovnici (3.5a) splňuje

$$\vec{v}_T(t, r) = \frac{Q_0(t)}{\gamma_d r^{d-1}} \vec{t}, \quad (3.6)$$

kde $Q_0 [\text{m}^d\text{s}^{-1}]$ je obecně časově závislý objemový tok a \vec{t} je jednotkový vektor v kladné směru radiální souřadnice. V rovnici (3.6) ještě vystupuje $\gamma_d [\text{m}^{d-1}]$, což je povrch jednotkové koule v \mathbb{R}^d daný vztahem

$$\gamma_d = \frac{d\pi^{\frac{d}{2}}}{\Gamma\left(\frac{d}{2} + 1\right)}, \quad (3.7)$$

kde Γ označuje gama funkci.

Zavedením bezrozměrné funkce $F = F(t, r)$ vztahem

$$F = F_w - \frac{\gamma_d r^{d-1}}{(1 - f(S_i))Q_0} D \frac{\partial S_w}{\partial r}, \quad (3.8)$$

kde $F_w [-]$ označuje normalizovanou frakční funkci smáčivé fáze

$$F_w(S_w) = \frac{f(S_w) - f(S_i)}{1 - f(S_i)}, \quad (3.9)$$

lze rovnici (3.5b) pro všechna $r > 0$ a $t > 0$ převést do tvaru

$$\gamma_d r^{d-1} \phi \frac{\partial S_w(t, r)}{\partial t} + (1 - f(S_i)) Q_0(t) \frac{\partial F(t, r)}{\partial r} = 0. \quad (3.10)$$

■ Počáteční a okrajové podmínky

Rovnice (3.10) je doplněna následujícími počátečními a okrajovými podmínkami pro funkci $S_w = S_w(t, r)$

$$S_w(0, r) = S_i, \quad \forall r > 0, \quad (3.11a)$$

$$S_w(t, 0) = S_0, \quad \forall t > 0, \quad (3.11b)$$

$$\lim_{r \rightarrow +\infty} S_w(t, r) = S_i, \quad \forall t > 0, \quad (3.11c)$$

které pro $S_0 > S_i$ vyjadřují bodové vtlačení smáčivé fáze v počátku souřadného systému.

V [38] je podrobně popsáno, že funkce $F = F(t, r)$ splňuje okrajové podmínky

$$F(t, 0) = 1, \quad \forall t > 0, \quad (3.12a)$$

$$\lim_{r \rightarrow +\infty} F(t, r) = 0, \quad \forall t > 0. \quad (3.12b)$$

První podmínka (3.12a) souvisí s rovností celkového toku a toku smáčivé fáze v počátku souřadného systému. Podmínka (3.12b) platí při splnění dodatečného předpokladu

$$\lim_{r \rightarrow +\infty} r^{d-1} \frac{\partial S_w}{\partial r}(t, r) = 0, \quad \forall t > 0. \quad (3.13)$$

■ 3.2 Transformace na ODR

■ Substitute

Pokud vstupní tok Q_0 splňuje časovou závislost

$$Q_0(t) = At^{\frac{d-2}{2}}, \quad (3.14)$$

kde $A [\text{m}^d \text{s}^{-\frac{d}{2}}]$ je konstanta, lze ukázat, že F je funkcí pouze saturace, tj. $F = F(S_w)$, [38] a pomocí podobnostní substitute

$$S_w(t, r) = S_w(\lambda), \quad (3.15)$$

kde

$$\lambda = rt^{-\frac{1}{2}}, \quad (3.16)$$

lze redukovat parciální diferenciální rovnici (3.10) na ODR druhého řádu pro neznámou funkci $F = F(S_w)$. Tato rovnice je ve tvaru

$$F''(S_w) [F'(S_w)]^{\frac{2}{d}-2} = -A^{-\frac{2}{d}} \frac{C_d D(S_w)}{F(S_w) - F_w(S_w)}, \quad \forall S_w \in [S_i, S_0], \quad (3.17)$$

kde

$$C_d = d \left(\frac{\gamma_d}{1 - f(S_i)} \right)^{\frac{2}{d}} \left(\frac{\phi}{2} \right)^{\frac{2}{d}-1}, \quad (3.18)$$

přičemž výsledné řešení $S_w = S_w(t, r)$ se pro všechna $t > 0$ a $r > 0$ získá z implicitní rovnice

$$r^d t^{-\frac{d}{2}} = \frac{2A(1 - f(S_i))}{\gamma_d \phi} F'(S_w(t, r)). \quad (3.19)$$

Okrajové podmínky

V důsledku transformačního vztahu (3.16) plynou z počáteční a okrajových podmínek (3.11) a (3.12) následující okrajové podmínky pro F

$$\lim_{S_w \rightarrow S_i^+} F(S_w) = 0, \quad (3.20a)$$

$$F(S_0) = 1. \quad (3.20b)$$

Navíc platí následující okrajové podmínky i pro F' :

$$F'(S_i^+) := \lim_{S_w \rightarrow S_i^+} F'(S_w) = \lambda_*^d \frac{\gamma_d \phi}{2A(1 - f(S_i))}, \quad (3.21a)$$

$$F'(S_0) = 0, \quad (3.21b)$$

kde λ_* označuje limitu inverzního vztahu $\lambda = \lambda(S_w)$

$$\lim_{S_w \rightarrow S_i^+} \lambda(S_w) = \lambda_* \quad (3.22)$$

o které lze dokázat, že je konečná, viz [38].

Přestože by se mohlo zdát, že úloha (3.17) má o dvě okrajové podmínky více, než je pro ODR druhého řádu přípustné z hlediska existence řešení, není tomu tak. Vztah (3.21a) nelze považovat za okrajovou podmínku, protože pouze přiřazuje význam neznámé hodnoty λ_* k limitní hodnotě $F'(S_i^+)$. Druhá podmínka (3.21b) má přímý dopad na možnost volby buď parametru A , nebo vstupní saturace S_0 v závislosti na d , jak bude ukázáno v další kapitole.

3.3 Integrální řešení ODR

V původních článcích McWhortera a Sunady [34, 35] byl pro $d = 1$ a $d = 2$ navržen způsob řešení rovnice (3.17) pomocí jejího převodu na integrální rovnici, která je posléze řešena iteračně a pomocí numerické aproximace integrálů. V článku [38] (Příloha P.1 [str.51]) byl autorem této práce navržen způsob získání řešení (3.17) i pro $d \geq 3$. Všechny výsledné integrální rovnice a iterační schémata k jejich řešení jsou shrnuty v následujících sekcích. Integrální rovnice, ekvivalentní rovnici (3.17), se odvodí z (3.17) dvojnásobnou postupnou integrací a použitím okrajových podmínek (3.20) a (3.21b).

Řešení pro $d = 1$

Věta 3.1. Pro $d = 1$ je řešení úlohy (3.17) s okrajovými podmínkami (3.20) a při splnění podmínky (3.21b) ekvivalentní řešení integrální rovnice

$$F(S_w) = 1 - \frac{\int_{S_w}^{S_0} \frac{(\beta - S_w)D(\beta)}{F(\beta) - F_w(\beta)} d\beta}{\int_{S_i}^{S_0} \frac{(\beta - S_i)D(\beta)}{F(\beta) - F_w(\beta)} d\beta}, \quad (3.23)$$

pokud platí vztah mezi A a S_0 ve tvaru

$$A^2 = C_1 \int_{S_i}^{S_0} \frac{(\beta - S_i)D(\beta)}{F(\beta) - F_w(\beta)} d\beta. \quad (3.24)$$

Důkaz. Integrací (3.17) od S_w do S_0 a použitím podmínky (3.21b) vznikne vztah pro F' ve tvaru

$$F'(S_w) = A^{-2} C_1 \int_{S_w}^{S_0} \frac{D(\beta)}{F(\beta) - F_w(\beta)} d\beta, \quad \forall S_w \in (S_i, S_0). \quad (3.25a)$$

Další integrací (3.25) od S_w do S_0 a použitím podmínky (3.20b) vznikne

$$1 - F(S_w) = A^{-2} C_1 \int_{S_w}^{S_0} \int_{\eta}^{S_0} \frac{D(\beta)}{F(\beta) - F_w(\beta)} d\beta d\eta, \quad \forall S_w \in (S_i, S_0). \quad (3.25b)$$

Integrál na pravé straně (3.25b) se pomocí integrace per partes převede na [34]

$$1 - F(S_w) = A^{-2} C_1 \int_{S_w}^{S_0} \frac{(\beta - S_w)D(\beta)}{F(\beta) - F_w(\beta)} d\beta, \quad \forall S_w \in (S_i, S_0). \quad (3.25c)$$

Limitním přechodem $S_w \rightarrow S_i^+$ v (3.25c) a použitím podmínky (3.20a) dostaneme požadovaný vztah mezi A a S_0 daný rovnicí (3.24).

Posledním krokem je dosazení vztahu (3.24) pro A^2 do (3.25c), čímž vznikne (3.23). \square

Derivace rovnice (3.23) podle S_w umožní explicitně vyjádřit F' :

$$F'(S_w) = \frac{S_0 \int_{S_i}^{S_0} \frac{D(\beta)}{F(\beta) - F_w(\beta)} d\beta}{S_w \int_{S_i}^{S_0} \frac{(\beta - S_i) D(\beta)}{F(\beta) - F_w(\beta)} d\beta}, \quad \forall S_w \in (S_i, S_0). \quad (3.26)$$

Integrální rovnici (3.23) lze vyřešit iteračně pomocí numerické integrace ve tvaru navrženém v [34]:

$$F_{k+1}(S_w) = 1 - \frac{S_0 \int_{S_i}^{S_0} \frac{(\beta - S_w) D(\beta)}{F_k(\beta) - F_w(\beta)} d\beta}{S_w \int_{S_i}^{S_0} \frac{(S_i - S_w) D(\beta)}{F_k(\beta) - F_w(\beta)} d\beta}, \quad (3.27)$$

kde F_k značí k -tou iteraci F , přičemž $F_0 \equiv 1$ je doporučená počáteční hodnota. Iterační schéma (3.27) je konvergentní, pouze pokud je vstupní saturace S_0 dostatečně daleko od maximální smáčivé saturace $S_w^{max} := 1 - S_{n,r}$ [36, 38, 34, 35]. Pokud $S_0 \rightarrow S_w^{max}$, pak dochází v původně navrženém iteračním schématu k významnému nárůstu iterací, až k divergenci.

V článku [36] byly autorem této práce navrženy dvě různé modifikace iteračního schématu (varianty A a B), které umožňují získat řešení pro podstatně vyšší hodnoty S_0 . Obě varianty modifikované iterační metody jsou založené na substituci

$$G(S_w) = \frac{D(S_w)}{F(S_w) - F_w(S_w)}, \quad (3.28)$$

přičemž varianty A, resp. B jsou ve tvaru

$$G_{k+1}(S_w) = D(S_w) + G_k(S_w) \left(F_w(S_w) + \frac{S_0 \int_{S_i}^{S_0} (\beta - S_w) G_k(\beta) d\beta}{S_w \int_{S_i}^{S_0} (\beta - S_i) G_k(\beta) d\beta} \right), \quad (3.29)$$

resp.

$$G_{k+1}(S_w) = [D(S_w) + G_k(S_w) F_w(S_w)] \left(1 - \frac{S_0 \int_{S_i}^{S_0} (\beta - S_w) G_k(\beta) d\beta}{S_w \int_{S_i}^{S_0} (\beta - S_i) G_k(\beta) d\beta} \right)^{-1}, \quad (3.30)$$

s doporučenou počáteční hodnotou $G_0 \equiv 0$ [36].

Iterační schémata jsou zastavena, pokud je velikost rozdílu po sobě jdoucích iterací menší než předem stanovená mez.

Analýzu této problematiky lze nalézt i v pozdějším článku [39], kde je rovnice (3.17) řešena pomocí spektrálních metod.

■ Řešení pro $d = 2$

Věta 3.2. Pro $d = 2$ je řešení úlohy (3.17) s okrajovými podmínkami (3.20) a při splnění podmínky (3.21b) ekvivalentní řešení integrální rovnice

$$F(S_w) = \frac{\int_{S_i}^{S_w} \exp\left(-\frac{C_2}{A} \int_{S_i}^{\beta} \frac{D(\eta)}{F(\eta) - F_w(\eta)} d\eta\right) d\beta}{\int_{S_i}^{S_0} \exp\left(-\frac{C_2}{A} \int_{S_i}^{\beta} \frac{D(\eta)}{F(\eta) - F_w(\eta)} d\eta\right) d\beta}, \quad \forall S_w \in (S_i, S_0), \quad (3.31)$$

pokud $S_0 = S_w^{max}$.

Důkaz. Integrací (3.17) od S_i do S_w vznikne

$$F'(S_w) = F'(S_i^+) \exp\left(-\frac{C_2}{A} \int_{S_i}^{S_w} \frac{D(\eta)}{F(\eta) - F_w(\eta)} d\eta\right), \quad \forall S_w \in (S_i, S_0), \quad (3.32a)$$

kde $F'(S_i^+) := \lim_{S_w \rightarrow S_i^+} F'(S_w)$ je zatím neznámá, ale konečná hodnota odpovídající λ_* z podmínky (3.21a). Podmínka (3.21b) je splněna jen tehdy, pokud je integrál na pravé straně rovnice (3.32a) nekonečný při $S_w \rightarrow S_0^-$. Vzhledem k omezenosti funkce $D = D(S_w)$ to znamená, že musí platit

$$0 = \lim_{S_w \rightarrow S_0^-} F(S_w) - F_w(S_0) = 1 - F_w(S_0), \quad (3.32b)$$

tj. $F_w(S_0) = 1$, což je podle definice F_w v rovnici (3.9) a frakční funkce f v rovnici (3.3) splněno právě tehdy, když $S_0 = S_w^{max}$.

Další integrací rovnice (3.32a) od S_i do S_w a při použití okrajové podmínky (3.20a) vznikne

$$F(S_w) = F'(S_i^+) \int_{S_i}^{S_w} \exp\left(-\frac{C_2}{A} \int_{S_i}^{\beta} \frac{D(\eta)}{F(\eta) - F_w(\eta)} d\eta\right) d\beta, \quad \forall S_w \in (S_i, S_0). \quad (3.32c)$$

Z rovnice (3.32c) je zřejmé, že k splnění poslední okrajové podmínky (3.20b) musí $F'(S_i^+)$ splňovat

$$F'(S_i^+) = \left[\int_{S_i}^{S_0} \exp\left(-\frac{C_2}{A} \int_{S_i}^{\beta} \frac{D(\eta)}{F(\eta) - F_w(\eta)} d\eta\right) d\beta \right]^{-1}, \quad (3.32d)$$

odkud již v kombinaci s (3.32c) plyne tvrzení (3.31). □

Derivace rovnice (3.31) podle S_w umožní explicitně vyjádřit F' :

$$F'(S_w) = \frac{\exp\left(-\frac{C_2}{A} \int_{S_i}^{S_w} \frac{D(\eta)}{F(\eta) - F_w(\eta)} d\eta\right)}{\int_{S_i}^{S_0} \exp\left(-\frac{C_2}{A} \int_{S_i}^{\beta} \frac{D(\eta)}{F(\eta) - F_w(\eta)} d\eta\right) d\beta}. \quad (3.33)$$

Řešení integrální rovnice (3.31), navržené v [34], je opět založené na iteračním schématu a numerické aproximaci integrálů ve tvaru

$$F_{k+1}(S_w) = \frac{\int_{S_i}^{S_w} \exp\left(-\frac{C_2}{A} \int_{S_i}^{\beta} \frac{D(\eta)}{F_k(\eta) - F_w(\eta)} d\eta\right) d\beta}{\int_{S_i}^{S_0} \exp\left(-\frac{C_2}{A} \int_{S_i}^{\beta} \frac{D(\eta)}{F_k(\eta) - F_w(\eta)} d\eta\right) d\beta}, \quad (3.34)$$

přičemž $F_0 \equiv 1$ je doporučená počáteční hodnota. Iterační schéma je zastaveno, pokud je velikost rozdílů po sobě jdoucích iterací menší než předem stanovená mez.

■ Řešení pro $d \geq 3$

Věta 3.3. Pokud $S_0 = S_w^{max}$, je řešení úlohy (3.17) pro $d \geq 3$ s okrajovými podmínkami (3.20) a při splnění podmínky (3.21b) ekvivalentní řešení integrální rovnice

$$F(S_w) = \int_{S_i}^{S_w} \left[\left(F'(S_i^+)\right)^{\frac{2-d}{d}} + \frac{d-2}{d} C_d A^{-\frac{2}{d}} \int_{S_i}^{\beta} \frac{D(\eta)}{F(\eta) - F_w(\eta)} d\eta \right]^{\frac{d}{2-d}} d\beta, \quad (3.35)$$

kde $F'(S_i^+)$ splňuje

$$1 = \int_{S_i}^{S_0} \left[\left(F'(S_i^+)\right)^{\frac{2-d}{d}} + \frac{d-2}{d} C_d A^{-\frac{2}{d}} \int_{S_i}^{\beta} \frac{D(\eta)}{F(\eta) - F_w(\eta)} d\eta \right]^{\frac{d}{2-d}} d\beta. \quad (3.36)$$

Důkaz. Integrací (3.17) od S_i do S_w vznikne

$$F'(S_w) = \left[\left(F'(S_i^+)\right)^{\frac{2-d}{d}} + \frac{d-2}{d} C_d A^{-\frac{2}{d}} \int_{S_i}^{S_w} \frac{D(\eta)}{F(\eta) - F_w(\eta)} d\eta \right]^{\frac{d}{2-d}}, \quad (3.37)$$

$\forall S_w \in (S_i, S_0)$, kde $F'(S_i^+)$ je zatím neznámá, ale konečná hodnota z podmínky (3.21a). Dále se postupuje analogicky jako v důkazu Věty 3.2, tj.

podmínka (3.21b) je splněna jen tehdy, pokud je integrál na pravé straně rovnice (3.37) nekonečný při $S_w \rightarrow S_0^-$, odkud plyne nutnost $S_0 = S_w^{max}$.

Další integrací (3.37) od S_i do S_w při použití okrajové podmínky (3.20a) rovnou vznikne rovnice (3.35), přičemž je zřejmé, že poslední okrajová podmínka (3.20b) je splněna právě tehdy, když $F'(S_i^+)$ splňuje rovnici (3.36). \square

Autorem této práce bylo v [38] navrženo nejen odvození obecné ODR (3.17) a ekvivalentní integrální rovnice ve Větě 3.3, ale též iterační způsob řešení této integrální rovnice (3.35) při splnění požadované vazby (3.36) ve tvaru

$$F_{k+1}^{(B)}(S_w) = \min \left\{ \int_{S_i}^{S_w} \left[B^{\frac{2-d}{d}} + \frac{d-2}{d} C_d A^{-\frac{2}{d}} \int_{S_i}^{\beta} \frac{D(\eta) d\eta}{F_k^{(B)}(\eta) - F_w(\eta)} \right]^{\frac{d}{2-d}} d\beta; 1 \right\}, \quad (3.38)$$

kde parametr $B \in \mathbb{R}$ zastupuje neznámou hodnotu $F'(S_i^+)$ a $F_k^{(B)}$ je k -tá iterace aproximace funkce F při dané hodnotě B . Jako počáteční hodnotu je doporučeno zvolit $F_0^{(B)} \equiv 1$ pro každé $B \in \mathbb{R}$.

Samotný algoritmus výpočtu je navržen tak, že pro dané B je iterační schéma (3.38) zastaveno po $k^{(B)}$ krocích, pokud je velikost rozdílu po sobě jdoucích iterací menší než předem stanovená mez.

Dále je zaveden funkcionál

$$\mathcal{H}_B(\xi) := 1 - \int_{S_i}^{S_0} \left[B^{\frac{2-d}{d}} + \frac{d-2}{d} C_d A^{-\frac{2}{d}} \int_{S_i}^{\beta} \frac{D(\eta)}{\xi(\eta) - F_w(\eta)} d\eta \right]^{\frac{d}{2-d}} d\beta, \quad (3.39)$$

jehož nulová hodnota pro nějaké B a $\xi \equiv F^{(B)}$ odpovídá splnění podmínky (3.36). Výsledná hodnota funkcionálu \mathcal{H}_B je pro dané B a $F_{k^{(B)}}^{(B)}$ označena $H(B) := \mathcal{H}_B(F_{k^{(B)}}^{(B)})$. Numerické simulace v článku [38] naznačují, že funkce $H = H(B)$ je monotonní a má právě jeden kořen B^* , který odpovídá hledané hodnotě $F'(S_i^+)$, tj. B^* splňuje rovnici

$$B^* = \left(F^{(B^*)} \right)'(S_i^+). \quad (3.40)$$

3.4 Výsledky a aplikace

Pro $d = 1$ jsou numerické řešiče pro původní schéma a obě varianty modifikovaného iteračního schématu volně k dispozici v podobě webové aplikace na webové stránce autora <http://mmg.fjfi.cvut.cz/~fucik/mcwhorter>.

V článku [37] bylo navíc autorem ukázáno, že dvě jednorozměrná přesná řešení se dají použít k odvození přesného řešení pro úlohu dvoufázového proudění v porézním prostředí s materiálovou nespojitostí. Numerický řešič pro tuto úlohu autor taktéž implementoval v podobě volně dostupné webové aplikace na webové stránce <http://mmg.fjfi.cvut.cz/~fucik/exacthetero>.

Nakonec i numerická řešení iteračních schémat (3.34) pro $d = 2$ a (3.38) pro $d \geq 3$ jsou ve formě webové aplikace volně k dispozici na webové stránce autora <http://mmg.fjfi.cvut.cz/~fucik/exact>.

Ukázky přesných řešení jsou uvedeny v [38] (Příloha P.1 [str. 51]). Přesná řešení byla použita k testování implementace numerických metod například v [40] (Příloha P.2 [str. 58]) nebo též v publikaci [41] odeslané k recenzi do Computer Physics Communications v únoru 2021.

3.5 Shrnutí autorova přínosu

Autorův přínos v této kapitole lze shrnout v těchto bodech:

- Formulace úlohy (3.1) ve zobecněných sférických souřadnicích v \mathbb{R}^d , $d \in \mathbb{N}$ ve tvaru (3.10).
- Vyjasnění konečnosti limity (3.22).
- Odvození přesného řešení pro $d \geq 3$ jako řešení integrální rovnice.
- Návrh iteračních numerických metod pro řešení integrálních rovnic
 - pro $d = 1$ v [36, 37],
 - pro $d \geq 3$ v [38].
- Odvození přesného řešení pro úlohu dvoufázového proudění v porézním prostředí s materiálovou nespojitostí v [37].
- Implementace iteračních řešičů integrálních rovnic ve formě webových aplikací volně dostupných vědecké komunitě na webových stránkách autora:
 - pro $d = 1$ na adrese <http://mmg.fjfi.cvut.cz/~fucik/mcwhorter>,
 - pro $d \geq 2$ na adrese <http://mmg.fjfi.cvut.cz/~fucik/exact>,
 - pro jednorozměrnou úlohu v porézním prostředí s materiálovou nespojitostí na adrese <http://mmg.fjfi.cvut.cz/~fucik/exacthetero>.

Kapitola 4

Numerické řešení metodou smíšených hybridních konečných prvků

Řešení úloh dvoufázového proudění v porézním prostředí s transportem rozpuštěných látek vyžaduje netriviálních matematických postupů, protože se jedná o úlohy s obecně nelineárními koeficienty a někdy i s degenerující difuzí například v případech, kdy se z dvoufázového systému stane lokálně systém jednofázový. Ve vzácných případech formulací úloh lze nalézt analytické nebo semi-analytické řešení takových úloh, viz například semi-analytická řešení popsaná v Kapitole 3.

V obecném případě vzniká potřeba nalézt robustní a efektivní numerickou metodu, která by se dala aplikovat na kompletní systém dvoufázových rovnic s transportem rozpuštěných látek, případně s přestupem hmoty mezi fázemi. V současné době je k dispozici nesčetné množství softwarových balíků pro numerickou simulaci těchto úloh založených na metodách konečných diferencí, konečných objemů nebo konečných prvků, jako například DUNE [42], TOUGH2 [43] nebo COMSOL Multiphysics, které však mají svá omezení použitelnosti.

V této kapitole bude popsán autorem navržený numerický řešič NumDwarf, který je založen na numerické smíšené hybridní metodě konečných prvků (MHFEM, z angl. Mixed-Hybrid Finite Element Method) a je navržen pro řešení obecného systému časově proměnného systému parciálních diferenciálních rovnic (PDR) s obecnými koeficienty v 1D, 2D a 3D. Konkrétní úlohy dvoufázového nebo dvoufázového kompozičního proudění v porézním prostředí se potom formulují jen pomocí volby koeficientů a okrajových podmínek. Název NumDwarf je složen z jednotlivých symbolů, které označují volitelné koeficienty v obecném systému parciálních diferenciálních rovnic, viz rovnice (4.1) níže.

Mezi hlavní přednosti navrženého řešiče NumDwarf patří schopnost simulovat již zmíněné degenerované dvoufázové úlohy, nízká numerická difuze v MHFEM [44, 45, 46] v aproximaci advekce a možnost efektivní paralelizace na výpočetních klastrech CPU nebo GPU.

Stěžejní publikace [40] popisující numerický řešič NumDwarf je uvedena včetně doplňujících materiálů v Příloze P.2 [str. 58]. V současné době existují

celkem tři implementace numerického řešiče NumDwarf:

- První byla implementována autorem této práce v C++ pro počítání na jednom výpočetním uzlu nebo vícejádrovém PC (pomocí OpenMP). Pro řešení soustavy lineárních rovnic s řídkou maticí byly použity knihovny UMFPACK [47] (přímý řešič) a PETSc [48] nebo TNL [49] (iterační řešiče). Účelem této varianty bylo především ověření konceptu numerického schématu pro simulaci úloh s degenerujícím dvoufázovým prouděním v porézním prostředí a úloh s transportem rozpuštěných látek. Poprvé byla tato metoda použita v článku [24], viz Příloha P.3 [str. 102].
- Druhá implementace je určena pro paralelní počítání na výpočetních klastrech CPU a využívá metod rozkladu oblasti (domain decomposition) a MPI. Byla implementována pod autorovým vedením diplomantem (a později doktorandem) J. Solovským v C++ [50, 51, 41]. Tato implementace byla použita v článkách [23, 52], první z nich viz Příloha P.4 [str. 117].
- Třetí implementace je masivně paralelní pro počítání na GPU, přičemž kompletní výpočetní kód běží na GPU, tj. neprovádí se řádově pomalejší kopírování dat mezi pamětí GPU a pamětí počítače. Byla implementována pod autorovým vedením diplomantem (a později doktorandem) J. Klinkovským v C++ a CUDA v rámci numerické knihovny Template numerical library (TNL), která vzniká na KM FJFI ČVUT v Praze pod vedením T. Oberhubera, <http://www.tnl-project.org> [53, 49]. V současné době je v přípravě publikace popisující propojení MHFEM a mřížkové Boltzmannovy metody a jejich kompletní implementaci na GPU.

4.1 Formulace obecné úlohy

Systém PDR je uvažován ve tvaru rovnic s obecnými koeficienty $N_{i,j}$, \vec{u} , m_i , $\mathbf{D}_{i,j}$, \vec{w}_i , $\vec{a}_{i,j}$, $r_{i,j}$ a f_i , $i, j \in \hat{n}$, $\hat{n} := \{1, 2, \dots, n\}$:

$$\sum_{j=1}^n N_{i,j} \frac{\partial Z_j}{\partial t} + \sum_{j=1}^n \vec{u}_{i,j} \cdot \nabla Z_j + \nabla \cdot \left[m_i \left(- \sum_{j=1}^n \mathbf{D}_{i,j} \nabla Z_j + \vec{w}_i \right) + \sum_{j=1}^n Z_j \vec{a}_{i,j} \right] + \sum_{j=1}^n r_{i,j} Z_j = f_i, \quad (4.1)$$

pro neznámé funkce Z_1, Z_2, \dots, Z_n , které závisí na čase $t \in [0, T]$ a prostorové souřadnici $\vec{x} \in \Omega \subset \mathbb{R}^d$, kde T označuje konečný čas simulace, Ω je polygonální oblast a d je dimenze prostoru. Předpokladem je, že funkce $Z_j(t, \vec{x})$ jsou alespoň spojitě diferencovatelné vzhledem k času a slabě diferencovatelné vzhledem k prostorové souřadnici \vec{x} v Ω . Význam koeficientů v (4.1) je detailně popsán v [40].

Podle potřeb řešené úlohy jsou rovnice (4.1) doplněny počátečními, resp. okrajovými podmínkami, viz [40, 23], které lze obecně zapsat

$$Z_j(0, \vec{x}) = Z_j^{ini}(\vec{x}), \quad \forall \vec{x} \in \Omega, \quad j \in \hat{n}, \quad (4.2a)$$

resp.

$$Z_j = Z_j^D, \quad \forall \vec{x} \in \Gamma_{Z_j} \subset \partial\Omega, \quad j \in \hat{n}, \quad (4.2b)$$

$$\vec{q}_i \cdot \vec{n} = q_i^N, \quad \forall \vec{x} \in \Gamma_{\vec{q}_i} \subset \partial\Omega, \quad i \in \hat{n}, \quad (4.2c)$$

$\forall t \in (0, T)$, kde symbol \vec{q}_i označuje konzervativní tok

$$\vec{q}_i = m_i \left(- \sum_{j=1}^n \mathbf{D}_{i,j} \nabla Z_j + \vec{w}_i \right). \quad (4.3)$$

Matematický tvar toku zavedený rovnicí (4.3) je autorem navržen tak, aby umožnil simulaci úloh (nejen) dvoufázového proudění s degenerující difuzí, kdy difuzní koeficient se blíží k nule při lokálním přechodu z dvoufázového do jednofázového proudění (případ mizející fáze), viz například difuzní koeficient daný rovnicí (3.4). V těchto případech lze difuzní koeficient zapsat ve tvaru $m \mathbf{D}_{i,j}$, kde m je koeficient zahrnující mobilitu dané fáze (který nabývá kladných i nulových hodnot) a na část nenulovou (odraženou od nuly nějakou kladnou konstantou), která odpovídá řádu velikosti difuze.

4.2 Diskretizace

Oblast $\Omega \subset \mathbb{R}^d$ je diskretizována pomocí konečně prvkové sítě $\mathcal{K}_h \subset \mathbb{R}^d$, která se skládá z úseček v \mathbb{R}^1 , trojúhelníků nebo obdélníků v \mathbb{R}^2 a čtyřstěnů nebo kvádrů v \mathbb{R}^3 . Symbol $h > 0$ označuje velikost dané sítě a jedná se o průměr největší z koulí opsaných prvkům z \mathcal{K}_h . Předpokládá se, že síť \mathcal{K}_h je konformní (tj. průnikem dvou prvků je buď společná stěna, společná hrana, společný vrchol, nebo prázdná množina). Symboly \mathcal{V}_h , resp. \mathcal{E}_h označují množinu všech vrcholů, resp. hran sítě \mathcal{K}_h , přičemž \mathcal{E}_h^{int} , resp. \mathcal{E}_h^{ext} jsou podmnožiny \mathcal{E}_h obsahující vnitřní, resp. vnější (hraniční) hrany. Množina všech hran prvku $K \in \mathcal{K}_h$ je označena symbolem \mathcal{E}_K . Index i bude v dalším vždy odpovídat i -té rovnici nebo proměnné Z_i pro $i \in \hat{n}$.

Z hlediska časové diskretizace je časový interval $[0, T]$ rozdělen diskretními body $0 = t_0 < t_1 < \dots < t_M = T$, přičemž diskretní časový interval je $\Delta t_k = t_{k+1} - t_k$. V dalším je exponent k použit k označení hodnoty na časové hladině t_k , např. $Z_{j,K}^k$ je diskretní hodnota funkce Z_j na elementu K v čase t_k .

Diskretizace vektorových veličin

V rovnici (4.1) je dále možné označit tok bez mobility (nebo též rychlost) symbolem \vec{v}_i jako

$$\vec{v}_i = - \sum_{j=1}^n \mathbf{D}_{i,j} \nabla Z_j + \vec{w}_i, \quad (4.4)$$

tudíž $\vec{q}_i = m_i \vec{v}_i$.

Při diskretizaci vektorů \vec{v}_i a \vec{q}_i se vychází z předpokladu, že oba patří do funkčního prostoru $\mathbf{H}(\text{div}, \Omega)$. Potom na každém prvku $K \in \mathcal{K}_h$ je uvažována diskretizace \vec{v}_i v Raviartově–Thomasově–Nédélecově prostoru nejnižšího řádu $\mathbf{RTN}_0(K) \subset \mathbf{H}(\text{div}, K)$ [40, 54, 55] ve tvaru

$$v_{i,K,E}^k = \sum_{j \in \sigma_{i,K}} \left(b_{i,j,K,E} Z_{j,K}^k - \sum_{F \in \mathcal{E}_K} b_{i,j,K,E,F} Z_{j,F}^k \right) + w_{i,K,E}^k, \quad (4.5)$$

$\forall k \in \mathbb{N}$, $\forall E \in \mathcal{E}_K$, $\forall K \in \mathcal{K}_h$, kde $v_{i,K,E}^k$, resp. $w_{i,K,E}^k$ označují koeficienty projekce \vec{v}_i , resp. \vec{w}_i do $\mathbf{RTN}_0(K)$ v čase t_k , $b_{i,j,K,E,F}$ a $b_{i,j,K,E}$ jsou koeficienty vztahované ke geometrii daného prvku a difuznímu koeficientu (viz jejich definice v [40]) a $\sigma_{i,K} \subseteq \hat{n}$ je množina všech indexů j , pro které je $\mathbf{D}_{i,j}$ nenulový na $K \in \mathcal{K}_h$.

Diskretizace skalárních veličin

Hodnota skalární neznámé funkce Z_j je na každém prvku $K \in \mathcal{K}_h$ aproximována konstantní hodnotou $Z_{j,K}$, kterou lze interpretovat buď jako střední hodnotu funkce Z_j na prvku K z metody konečných objemů, nebo jako výsledek projekce funkce Z_j do prostoru po částech konstantních funkcí z nespojitě Galerkinovy metody konečných prvků. Druhý přístup je bližší označení MHFEM, tj. jedná se míšení dvou různých konečně-prvkových aproximací vektorových a skalárních veličin.

Časová derivace funkce Z_j v (4.1) je na elementu $K \in \mathcal{K}_h$ v čase t_k nahrazena diferencí

$$\frac{dZ_{j,K}}{dt} \approx \frac{Z_{j,K}^{k+1} - Z_{j,K}^k}{\Delta t_k}, \quad (4.6)$$

4.3 Diskretizace PDR

Pomocí zavedených diskretizací lze i -tou PDR (4.1) zapsat v čase t_k na prvku $K \in \mathcal{K}_h$ ve tvaru

$$\begin{aligned} & \frac{|K|_d}{\Delta t_k} \sum_{j=1}^n N_{i,j,K} (Z_{j,K}^{k+1} - Z_{j,K}^k) + \sum_{j=1}^n \sum_{E \in \mathcal{E}_K} Z_{i,j,E}^{k,upw} (a_{i,j,K,E} + u_{i,j,K,E}) \\ & + \sum_{E \in \mathcal{E}_K} m_{i,E}^{k,upw} v_{i,K,E}^{k+1} + \sum_{j=1}^n \left(r_{i,j,K} |K|_d - \sum_{E \in \mathcal{E}_K} u_{i,j,K,E} \right) Z_{j,K}^{k+1} = |K|_d f_{i,K}, \end{aligned} \quad (4.7)$$

kde dolní indexy K , resp. E označují střední hodnotu příslušné veličiny přes prvek K , resp. hranu $E \in \mathcal{E}_K$. Hodnoty $Z_{j,E}^{k+1}$ představují stopy Z_j příslušné hraně $E \in \mathcal{E}_K$, přičemž díky předpokladu spojitosti Z_j v Ω se vynechává index K , protože je tato hodnota společná sousedícím prvkům. Symboly $u_{i,j,K,E}$ a $a_{i,j,K,E}$ označují koeficienty projekce vektorových koeficientů $\vec{u}_{i,j}$ a $\vec{a}_{i,j}$ do báze prostoru $\mathbf{RTN}_0(K)$. Hodnoty $m_{i,E}^{k,upw}$ a $Z_{i,j,E}^{k,upw}$ jsou určeny pomocí upwindové stabilizace na základě hodnot toků z předchozí časové vrstvy, detaily viz [40] (Příloha P.2 [str. 58]).

Lokální soustava rovnic pro $Z_{j,K}^{k+1}$

Dosazením výrazu pro $v_{i,K,E}^{k+1}$ z (4.5) do (4.7) vznikne lineární soustava rovnic pro $Z_{j,K}^{k+1}$, kterou lze maticově reprezentovat ve tvaru

$$\vec{Z}_K^{k+1} = \sum_{F \in \mathcal{E}_K} \mathbf{Q}_K^{-1} \mathbf{R}_{K,F} \vec{Z}_F^{k+1} + \mathbf{Q}_K^{-1} \vec{R}_K, \quad (4.8)$$

kde \vec{Z}_K^{k+1} je vektor tvořený neznámými $Z_{j,K}^{k+1}$, $j = 1, \dots, n$. Prvky matic \mathbf{Q}_K a $\mathbf{R}_{K,F}$ jsou dány vztahy

$$\{\mathbf{Q}_K\}_{i,j} = \frac{|K|_d}{\Delta t_k} N_{i,j,K} - \sum_{E \in \mathcal{E}_K} u_{i,j,K,E} + \sum_{E \in \mathcal{E}_K} m_{i,E}^{k,upw} b_{i,j,K,E} + |K|_d r_{i,j,K}, \quad (4.9a)$$

$$\{\mathbf{R}_{K,F}\}_{i,j} = \sum_{E \in \mathcal{E}_K} m_{i,E}^{k,upw} b_{i,j,K,E,F}, \quad (4.9b)$$

a složky vektoru \vec{R}_K jsou

$$\begin{aligned} \{\vec{R}_K\}_i &= |K|_d f_{i,K} + \frac{|K|_d}{\Delta t_k} \sum_{j=1}^n N_{i,j,K} Z_{j,K}^k - \sum_{E \in \mathcal{E}_K} m_{i,E}^{k,upw} w_{i,K,E} \\ & - \sum_{j=1}^n \sum_{E \in \mathcal{E}_K} Z_{i,j,E}^{k,upw} (a_{i,j,K,E} + u_{i,j,K,E}). \end{aligned} \quad (4.9c)$$

Z rovnice (4.8) plyne, že koeficienty v obecném systému PDR (4.1) musí být předepsány tak, aby matice \mathbf{Q}_K byla nesingulární [40].

4.4 Bilance toku na hranách

Bilance normálové složky toku \vec{q} na vnitřních hranách $E \in \mathcal{E}_h^{int}$ lze za předpokladu nulových zdrojů na hraně E zapsat v diskrétní podobě

$$\sum_{\ell=1}^2 m_{i,K_\ell,E}^k \left[\sum_{j \in \sigma_{i,K_\ell}} \left(b_{i,j,K,E} Z_{j,K_\ell}^{k+1} - \sum_{F \in \mathcal{E}_{K_\ell}} b_{i,j,K_\ell,E,F} Z_{j,F}^{k+1} \right) + w_{i,K_\ell,E} \right] = 0. \quad (4.10)$$

Pokud je ovšem alespoň jedna z hodnot $m_{i,K_\ell,E}$ nulová, systém lineárních rovnic (4.10) se stane singulárním. Jelikož se jedná o bilanci numerického toku přes hranu E , byla autorem této práce navržena regularizace rovnic (4.10) zavedením upwindové stabilizace tak, že obě hodnoty $m_{i,K_\ell,E}$ jsou nahrazeny jednou hodnotou $m_{i,E}^{k,upw}$ na dané hraně E .

V případě $m_{i,E}^{k,upw} > 0$ lze tuto hodnotu z (4.10) vydělit, čímž vznikne

$$\sum_{\ell=1}^2 \left[\sum_{j \in \sigma_{i,K_\ell}} \left(b_{i,j,K_\ell,E} Z_{j,K_\ell}^{k+1} - \sum_{F \in \mathcal{E}_{K_\ell}} b_{i,j,K_\ell,E,F} Z_{j,F}^{k+1} \right) + w_{i,K_\ell,E} \right] = 0. \quad (4.11)$$

Pokud $m_{i,E}^{k,upw} = 0$, je bilanční podmínka (4.10) triviálně splněna pro libovolné hodnoty $v_{i,K_\ell,E}^k$. Odtud plyne, že výsledek není poškozen předepsáním dodatečné podmínky (4.11), která slouží čistě pro regularizaci výsledné lineární soustavy.

Poznamenejme, že uvedený postup regularizace je výhodný i pro případy mizející fáze, kdy hodnoty koeficientu $m_{i,E}^{k,upw}$ jsou sice kladná, ale velmi malá čísla.

Globální soustava rovnic pro $Z_{j,E}^{k+1}$

Rovnice (4.8) umožňuje eliminovat $Z_{j,K}^k$ z (4.5), čímž z (4.11) vznikne soustava lineárních rovnic pouze pro stopy $Z_{j,E}^{k+1}$, $\forall E \in \mathcal{E}_h^{int}$. Pro hrany $E \in \mathcal{E}_h^{ext}$ ležící na hranici oblasti $\partial\Omega$ se hodnoty $Z_{j,E}$ předepisují podle příslušných okrajových podmínek (4.2b), detaily viz [40] (Příloha P.2 [str. 58]).

Výslednou (globální) soustavu lineárních rovnic pro $Z_{j,E}^{k+1}$ lze zapsat v maticovém tvaru

$$\mathbf{M}\vec{Z}^{k+1} = \vec{b}, \quad (4.12)$$

kde $\vec{Z}^{k+1} = \left\{ Z_F^{k+1} \right\}_{F \in \mathcal{E}_h} = \left\{ \left\{ Z_{j,F}^{k+1} \right\}_{j=1}^n \right\}_{F \in \mathcal{E}_h}$ je vektor $n \times n_{\mathcal{E}}$ neznámých, kde $n_{\mathcal{E}}$ označuje počet hran v \mathcal{E}_h . Matice $\mathbf{M} \in \mathbb{R}^{n \times n_{\mathcal{E}}, n \times n_{\mathcal{E}}}$ je řídká, nesingu-

lární a je pozitivně definitní, pokud i matice tenzorů $\{\mathbf{D}_{i,j}\}_{i,j=1}^n$ je pozitivně definitní [40].

V každém časovém kroku t_k je soustava (4.12) jedinou soustavou, kterou je nutné vyřešit. Na základě vypočítaných hodnot $\vec{Z}^{k+1} = \mathbf{M}^{-1}\vec{b}$ se z (4.8) spočítají hodnoty na prvcích $Z_{j,K}^{k+1}$, $\forall K \in \mathcal{K}_h$, čímž se uzavře jedna časová iterace $t_k \rightarrow t_{k+1}$.

4.5 Výpočetní algoritmus

Výpočetní algoritmus lze shrnout v následujících krocích:

1. Polož $k = 0$ a použij (4.2a) k inicializaci $Z_{j,K}^0$, $\forall K \in \mathcal{K}_h$ a $\forall j \in \hat{n}$.
2. Opakuj následující kroky, dokud není dosaženo konečného času T :
 - a. Spočítej $N_{i,j,K}$, $u_{i,j,K,E}$, $m_{i,K}$, $w_{i,K,E}$, $a_{i,j,K,E}$, $r_{i,j,K}$, $f_{i,K}$, $\forall i, j \in \hat{n}$, $\forall K \in \mathcal{K}_h$ a $\forall E \in \mathcal{E}_K$.
 - b. Spočítej koeficienty dané upwindovou stabilizací $m_{i,E}^{upw}$ a $Z_{i,j,E}^{upw}$, $\forall E \in \mathcal{E}_h$ a $\forall i, j \in \hat{n}$.
 - c. Spočítej koeficienty $\mathbf{b}_{i,j,K}$, $\forall K \in \mathcal{K}_h$ a $\forall i, j \in \hat{n}$.
 - d. Na základě hodnot $Z_{j,K}^k$ z předchozí časové vrstvy t_k použij (4.9) k výpočtu \mathbf{Q}_K , $\mathbf{R}_{K,F}$, \vec{R}_K , $\mathbf{Q}_K^{-1}\mathbf{R}_{K,F}$ a $\mathbf{Q}_K^{-1}\vec{R}_K$, které jsou potřeba v (4.8), $\forall K \in \mathcal{K}_h$ a $\forall F \in \mathcal{E}_K$.
 - e. Sestav \mathbf{M} a \vec{b} v (4.12) pomocí (4.11) a okrajových podmínek (4.2b).
 - f. Vyřeš řídký systém lineárních rovnic (4.12) k výpočtu $Z_{j,E}^{k+1}$, $\forall E \in \mathcal{E}_h$ a $\forall j \in \hat{n}$.
 - g. Spočítej $Z_{j,K}^{k+1}$ pomocí (4.8), $\forall K \in \mathcal{K}_h$ a $\forall j \in \hat{n}$.
 - h. Polož $t_{k+1} = t_k + \Delta t_k$ a $k := k + 1$.

4.6 Výsledky a aplikace

Numerický řešič NumDwarf byl použit k řešení řady úloh jednofázového a dvoufázového kompozičního proudění v porézním prostředí.

Publikované výsledky

- První publikace [44, 45] využívaly v té době teprve vyvíjený výpočetní kód založený na MHFEM a zabývaly se především otázkou správné simulace podmínek na materiálových rozhraních v porézním prostředí.

- Posledním matematickým modelem využívajícím **NumDwarf** je model perfuze myokardu, který je vyvíjen studentem J. Kovářem pod autorovým vedením ve spolupráci s IKEM Praha (J. Tintěra) a R. Chabiniokem (INRIA Paris-Saclay, King's College London, UTSW Medical Center Dallas a FJFI ČVUT v Praze). První výsledky jsou shrnuty v článku [59] podaném k recenzi do impaktovaného časopisu *Japan Journal of Industrial and Applied Mathematics* v březnu 2021.

Kapitola 5

Integrální řešení elektrochemických interakcí v Li-Ion článku

5.1 Formulace úlohy

Při modelování elektrochemických procesů v Lithiovém-iontovém elektrickém článku je základem řešení elektrochemických interakcí reprezentovaných toky j_1 a j_3 . V každém čase t jsou tyto toky řešením soustavy dvou diferenciálních rovnic (2.30) a (2.31), spolu s nelineární algebraickou vazbou (2.28a) pro neznámé veličiny $\phi_{e,i}$, $\phi_{s,i}$, η_i , a j_i , $i \in \{1, 3\}$ a při respektování okrajových podmínek uvedených v Kapitole 2.3.

Autorovi této práce se podařilo ukázat, že systém těchto rovnic lze převést na soustavu dvou obyčejných diferenciálních rovnic (ODR) pro η_i a J_i , kde J_i je definována jako

$$J_i(x) = \int_{x_{\ell,i}}^x j_i(\xi) d\xi, \quad \forall x \in [x_{\ell,i}, x_{r,i}], \quad i \in \{1, 3\}, \quad (5.1)$$

kde $x_{\ell,i}$, resp. $x_{r,i}$ označují levou, resp. pravou souřadnici hranice Ω_i . Odvození těchto rovnic je detailně popsáno v [29] (Příloha P.6 [str. 155]).

Výsledné ODR lze zapsat ve tvaru ODR s obecnými koeficienty

$$\eta'(x) = \alpha(x)J(x) + \beta(x), \quad (5.2a)$$

$$J'(x) = \mathfrak{B}(\eta(x), x), \quad (5.2b)$$

kde

$$\mathfrak{B}(\eta(x), x) = \delta(x) (\exp(\alpha_a \gamma(x) \eta(x)) - \exp(-\alpha_c \gamma(x) \eta(x))), \quad (5.2c)$$

$\forall x \in (x_l, x_r)$ s následujícími okrajovými podmínkami:

$$J(x_l) = 0, \quad (5.2d)$$

$$J(x_r) = \varepsilon, \quad (5.2e)$$

přičemž se na každé podoblasti Ω_i s indexem $i = 1$ nebo $i = 3$ používá: $x_l = x_{l,i}$, $x_r = x_{r,i}$, $\alpha_a = \alpha_{a,i}$, $\alpha_c = \alpha_{c,i}$, $\delta = \delta_i$ ze vztahu (2.28b) a koeficienty $\alpha = \alpha_i$, $\beta = \beta_i$ a $\varepsilon = \varepsilon_i$ jsou dány vztahy:

$$\begin{aligned}\alpha_1 &= a_1 F \frac{\sigma_1 + \kappa_1^{\text{eff}}}{\sigma_1 \kappa_1^{\text{eff}}}, & \alpha_3 &= a_3 F \frac{\sigma_3 + \kappa_3^{\text{eff}}}{\sigma_3 \kappa_3^{\text{eff}}}, \\ \beta_1 &= -\frac{I_{\text{app}}}{\sigma_1} - \frac{2RT}{F} (1 - t_+^0) \frac{c'_{e,1}}{c_{e,1}} - U'_1, & \beta_3 &= \frac{I_{\text{app}}}{\kappa_3^{\text{eff}}} - \frac{2RT}{F} (1 - t_+^0) \frac{c'_{e,3}}{c_{e,3}} - U'_3, \\ \gamma_1 &= \frac{F}{RT}, & \gamma_3 &= \frac{F}{RT}, \\ \varepsilon_1 &= \frac{I_{\text{app}}}{a_1 F}, & \varepsilon_3 &= -\frac{I_{\text{app}}}{a_3 F}.\end{aligned}$$

5.2 Odvození integrální rovnice

Autorem této práce bylo dále zjištěno, že soustavu dvou ODR s obecnými koeficienty je možné převést na integrální rovnici, kterou lze posléze vyřešit iteračně pomocí numerické aproximace integrálů (podobně jako v Kapitole 3 [29] (viz Příloha P.6 [str. 155])).

Integrací rovnic (5.2) od x_l do $x \in [x_l, x_r]$ vznikne

$$\eta(x) = \lambda + \int_{x_l}^x \alpha(\zeta) J(\zeta) + \beta(\zeta) d\zeta, \quad (5.3a)$$

$$J(x) = \int_{x_l}^x \mathfrak{B}(\eta(\zeta), \zeta) d\zeta, \quad (5.3b)$$

přičemž okrajová podmínka (5.2d) je zahrnutá v (5.3b) a $\lambda = \eta(x_l)$ označuje neznámou integrační konstantu v (5.3a).

Kombinací rovnic (5.3a) a (5.3b) lze získat dvě různé integrální rovnice

$$\eta(x) = \lambda + \int_{x_l}^x \alpha(\zeta) \int_{x_l}^{\zeta} \mathfrak{B}(\eta(\xi), \xi) d\xi + \beta(\zeta) d\zeta, \quad (5.4)$$

resp.

$$J(x) = \int_{x_l}^x \mathfrak{B} \left(\lambda + \int_{x_l}^{\zeta} \alpha(\xi) J(\xi) + \beta(\xi) d\xi, \zeta \right) d\zeta, \quad (5.5)$$

přičemž každá z nich obsahuje pouze jednu neznámou funkci η , resp. J .

Jak je ukázáno v [29] (Příloha P.6 [str. 155]), lze hodnotu konstanty λ určit pomocí (5.5) a okrajové podmínky (5.2e) jako řešení nelineární rovnice

$$\varepsilon = \exp(\gamma \alpha_a \lambda) I_a - \exp(-\gamma \alpha_c \lambda) I_c, \quad (5.6)$$

kde I_a a I_c označují

$$I_a = \int_{x_l}^{x_r} \delta(\zeta) \exp \left(\alpha_a \gamma \int_{x_l}^{\zeta} \alpha(\xi) J(\xi) + \beta(\xi) d\xi \right) d\zeta, \quad (5.7a)$$

$$I_c = \int_{x_l}^{x_r} \delta(\zeta) \exp \left(-\alpha_c \gamma \int_{x_l}^{\zeta} \alpha(\xi) J(\xi) + \beta(\xi) d\xi \right) d\zeta. \quad (5.7b)$$

Pokud $\alpha_a = \alpha_c$, lze rovnici (5.6) vyřešit analyticky jako

$$\lambda = \frac{1}{\gamma} \ln \left(\frac{\varepsilon + \sqrt{\varepsilon^2 + 4I_a I_c}}{2I_a} \right). \quad (5.8)$$

5.3 Iterační schéma pro řešení integrální rovnice

Integrální rovnici (5.5) lze řešit iteračně pomocí rovnice

$$\tilde{J}_{n+1}(x) = \int_{x_l}^x \mathfrak{B} \left(\lambda_n + \int_{x_l}^{\zeta} \alpha(\xi) J_n(\xi) + \beta(\xi) d\xi, \zeta \right) d\zeta, \quad (5.9)$$

$$J_{n+1}(x) = (1 - \omega) J_n(x) + \omega \tilde{J}_{n+1}(x), \quad (5.10)$$

kde λ_n je řešení rovnice (5.6), které je nutné v každé iteraci vypočítat na základě známé aproximace J_n , $n = 0, 1, 2, \dots$, a $\omega \in (0, 1]$ je relaxační parametr iteračního schématu sloužící k zajištění konvergence [29].

Jako počáteční iterace v (5.5) je voleno $J_0 \equiv 0$. Iterační proces je zastaven, pokud norma \tilde{J}_{n+1} je menší než předem zvolená mezní hodnota ϑ .

5.4 Výsledky a aplikace

Iterační schéma slouží k výpočtu proudů a napětí uvnitř elektrického článku na základě jeho elektrochemického stavu (hodnoty koncentrací lithiových iontů a předepsaného proudu I_{app}). V rámci komplexního, časově proměnného modelu stárnutí Li-ion článku se pak toto schéma použije v každém časovém kroku, viz [29] (Příloha P.6 [str. 155]).

V rámci výzkumného projektu TAČR č. TA04021244 (Dynamické řízení lithium-iontových baterií v systémech hybridních elektrických pohonů) bylo iterační integrální schéma použito jako základní prvek složitějšího matematického modelu, který simuloval dynamiku stárnutí Li-Ion článku, viz technické zprávy [60, 61, 62].

5.5 Shrnutí autorova přínosu

Autorův přínos v této kapitole by se dal shrnout v těchto bodech:

- Transformace systému rovnic popisujících dynamiku elektrochemických procesů na soustavu dvou obyčejných diferenciálních rovnic (5.2).
- Odvození integrální rovnice (5.5) ze soustavy dvou obyčejných diferenciálních rovnic popsané v kapitole 5.2.
- Návrh numerického iteračního schématu pro řešení integrální rovnice (5.5).
- Implementace v C++ a testování numerického iteračního řešiče.

Kapitola 6

Shrnutí vědecko-pedagogického přínosu autora k dané problematice

6.1 Shrnutí příspěvků autora k dané problematice

Z výše uvedeného přehledu úloh a přiložených publikací plyne, že autor ve svém dosavadním vědecko-pedagogickém působení dosáhl řady původních výsledků, mezi které patří:

- nalezení přesného, semi-analytického řešení pro speciální formulaci dvoufázového proudění v porézním prostředí pro dimenzi $d \geq 3$, včetně implementace algoritmu pro jeho nalezení a volné zpřístupnění tohoto algoritmu vědecké komunitě prostřednictvím autorových webových stránek,
- návrh, odvození, implementace a testování numerického řešiče `NumDwarf` pro řešení systému parciálních diferenciálních rovnic s obecnými koeficienty a zapojení studentů bakalářského, magisterského a doktorského studia KM FJFI ČVUT v Praze pod autorovým vedením při jeho vývoji pro masivně paralelní implementaci na grafických akcelerátorech a paralelní implementaci pro výpočetní klastry,
- řada aplikací numerického řešiče `NumDwarf` pro řešení konkrétních úloh z ekologických, průmyslových nebo medicínských oblastí a zapojení studentů bakalářského, magisterského a doktorského studia KM FJFI ČVUT v Praze pod autorovým vedením do řešení těchto úloh,
- analýza úlohy modelu elektrochemické interakce v lithiovém-iontovém elektrickém článku a návrh, odvození a implementace semi-analytického řešení tohoto modelu.

6.2 Stručný přehled přiložených článků

Přílohou práce je následujících šest impaktovaných článků a dvě kapitoly v knihách.

Publikace P.1 na str. 51: článek v *Advances in Water Resources*, 2016

Radek Fučík, Tissa H. Illangasekare a Michal Beneš: *Multidimensional self-similar analytical solutions of two-phase flow in porous media*, *Advances in Water Resources*, 90:51–56, 2016.

V článku je představeno přesné řešení speciální úlohy dvoufázového proudění v porézním prostředí v obecné dimenzi a způsob jeho získání pomocí numerického řešení integrální rovnice.

Pro $d = 1$ jsou numerické řešiče pro původní schéma a obě varianty modifikovaného iteračního schématu volně k dispozici v podobě webové aplikace na webové stránce autora <http://mmg.fjfi.cvut.cz/~fucik/mcwhorter>.

Numerické řešení iteračních schémat (3.34) pro $d = 2$ a (3.38) pro $d \geq 3$ jsou ve formě webové aplikace volně k dispozici na webové stránce autora <http://mmg.fjfi.cvut.cz/~fucik/exact>.

Obsah článku a autorův přínos je shrnut v Kapitole 3.

Publikace P.2 na str. 58: článek v *Computer Physics Communications*, 2019

Radek Fučík, Jakub Klinkovský, Jakub Solovský, Tomáš Oberhuber a Jiří Mikyška: *Multidimensional mixed-hybrid finite element method for compositional two-phase flow in heterogeneous porous media and its parallel implementation on GPU*, *Computer Physics Communications*, 238:165–180, 2019.

Jedná se o stěžejní článek popisující řešič NumDwarf a jeho masivně paralelní implementaci na GPU. V článku je mimo jiné použito přesného řešení z Publikace P.1 [str. 51] k ověření konvergence numerické metody. Článek a autorův přínos v něm je shrnut v Kapitole 4. Součástí Publikace P.2 je i doplňující příloha (Supplementary material), kde jsou ukázky řešení testovacích úloh a tabulky s experimentálním řádem konvergence.

■ **Publikace P.3 na str. 102:**
článek v Groundwater, 2015

Benjamin G. Petri, Radek Fučík, Tissa H. Illangasekare, Kathleen M. Smits, John A. Christ, Toshihiro Sakaki a Carolyn C. Sauck: *Effect of NAPL source morphology on mass transfer in the vadose zone*, Groundwater, 53(5):685–698, 2015.

Článek se zabývá rozpouštěním těžkého NAPL do proudící vody, přičemž je zkoumána dynamika tohoto rozpouštění. Experimentální část článku, která se opírá o laboratorní experimenty v CESEP, Colorado School of Mines, Golden, Colorado, USA, je doplněna o výsledky numerické simulace získané metodou smíšených hybridních prvků.

■ **Publikace P.4 na str. 117:**
článek v Journal of Computational Physics, 2020

Jakub Solovský, Radek Fučík, Michael R. Plampin, Tissa H Illangasekare a Jiří Mikyška: *Dimensional effects of inter-phase mass transfer on attenuation of structurally trapped gaseous carbon dioxide in shallow aquifers*, Journal of Computational Physics, 405:109178, 2020.

V článku je zkoumán vývin a zpětné rozpouštění CO₂ ve vodní fázi v poréz- ním prostředí. Na základě experimentálních dat (CESEP, Colorado School of Mines, Colorado, USA) je diskutováno použití kinetického (nerovnovážného) přístupu pro modelování přestupu hmoty mezi fázemi, přičemž je zohledněno, zda se jedná typově o jednorozměrné, nebo dvourozměrné proudění. Numerické simulace byly provedeny pomocí řešiče NumDwarf (viz Publikace P.2 [str. 58]).

■ **Publikace P.5 na str. 141:**
článek v International Journal of Heat and Mass Transfer, 2020

Tomáš Smejkal, Jiří Mikyška a Radek Fučík: Numerical modelling of adsorption and desorption of water vapor in zeolite 13X using a two-temperature model and mixed-hybrid finite element method numerical solver. *International Journal of Heat and Mass Transfer*, 148:119050, 2020.

V článku je zkoumán termo-chemický model ukládání energie skrz adsorbce a desorbce vodních par v zeolitu 13X. Diskuze v článku se opírá o výsledky matematického modelu, který je řešen pomocí řešiče NumDwarf (viz Publikace P.2 [str. 58]).

■ **Publikace P.6 na str. 155:**
článek v *Mathematical Problems in Engineering*, 2018

Michal Beneš, Radek Fučík, Vladimír Havlena, Vladimír Klement, Miroslav Kolář, Ondřej Polívka, Jakub Solovský a Pavel Strachota: *An Efficient and Robust Numerical Solution of the Full-Order Multiscale Model of Lithium-Ion Battery*, *Mathematical Problems in Engineering*, ID3530975, 2018.

V článku je představen jednorozměrný matematický model lithiového-iontového elektrického článku a pomocí numerických simulací zkoumán proces jeho stárnutí. Základní součástí numerického řešení je semi-analytické řešení elektrochemické interakce, které je shrnuto v Kapitole 5.

■ **Publikace P.7 na str. 168:**
kapitola v *Handbook of Chemical Mass Transport in the Environment*, 2010

Tissa H. Illangasekare, Christophe C. Frippiat a Radek Fučík: *Dispersion and mass transfer coefficients in groundwater of near-surface geologic formations*, kapitola v: *Handbook of Chemical Mass Transport in the Environment*, strany 418–456. CRC Press, 2010.

Jedná se o kapitolu v knize, ve které je rozebírána problematika přestupu hmoty v porézním prostředí a přehled kinetických modelů rozpouštění NAPL do vodní fáze.

■ **Publikace P.8 na str. 208:**
kapitola v *Pore Scale Phenomena: Frontiers in Energy and Environment*, 2015

Tissa H. Illangasekare, Kathleen M. Smits, Radek Fučík a Hossein Darvazani: *From pore to the field: Upscaling challenges and opportunities in hydrogeological and land-atmospheric systems*, kapitola v: *Pore Scale Phenomena: Frontiers in Energy and Environment*, strany 163–202. World Scientific, 2015.

Jedná se o kapitolu v knize, ve které je diskutována problematika zvětšování měřítko (upscaling) při popisu proudění, transportu rozpuštěných látek a přestupu hmoty v porézním prostředí.

6.3 Vedení a spolupráce se studenty

Autorova vědecká činnost je úzce spjata především s jeho pedagogickou činností v oboru Matematického inženýrství na Katedře matematiky FJFI ČVUT v Praze v tom smyslu, že každá oblast, kterou se zabývá, je zároveň přirozeným předmětem širšího vzdělávání a výchovy mladých vědeckých pracovníků v rámci bakalářského, magisterského a doktorského studia. Proto většina uvedených impaktovaných publikací vznikla ve spoluautorství se studenty, většinou na základě výsledků dosažených v jejich bakalářské či diplomové práci nebo v rámci jejich doktorského studia.

Přehled konkrétních v minulosti a v současnosti studovaných témat ve spolupráci se studenty je uveden v Kapitole 4.6.

6.4 Současný výzkum a mezinárodní spolupráce

V současné době neustále sílí potřeba výsledků matematického modelování v oblastech uvedených v této práci ve spojení s výrazným vývojem masivně paralelních výpočetních prostředků (zejména klastrů grafických akceleratorů). To umožňuje uvažovat o vývoji komplexnějších modelů, které rozšíří stávající matematické modely o další procesy (např. závislost veličin na teplotě, přesnější termodynamický popis roztoků a plyných směsí apod.).

Výsledky prezentované v této práci částečně vznikly díky úzké spolupráci Katedry matematiky FJFI ČVUT v Praze se zahraničním pracovištěm Center for Experimental Study of Subsurface Environmental Processes (CESEP), Colorado School of Mines, Golden, CO, USA (prof. T. H. Illangasekare) a relativně nově navázané spolupráci s U.S. Geological Survey, Eastern Energy Resources Science Center, Reston, VA, USA (M. R. Plampin) a U. S. Army Engineer Research and Development Center, Geotechnical and Structures Laboratory, Vicksburg, MS, USA (A. Trautz).

V případě teprve vznikajících výsledků v oblasti medicínských aplikací je navázána úzká spolupráce s Institutem klinické a experimentální medicíny v Praze (J. Tintěra) a R. Chabiniokem (UTSW Medical Center Dallas, TX, USA a FJFI ČVUT v Praze).

Z řady domácích a mezinárodních projektů, na kterých se autor podílel buď jako člen řešitelského týmu nebo hlavní řešitel, jsou relevantní z hlediska předložené práce tyto:

- Development and Validation of Porous Media Flow and Transport Models for Subsurface Environmental Application, projekt MŠMT Kontakt ME878, 2006-2009, hlavní řešitel M. Beneš.
- Numerical Methods for Multiphase Flow and Transport in Subsurface Environmental Applications, projekt MŠMT Kontakt ME10009, 2010-2012, hlavní řešitel M. Beneš.



Bibliografie

1. BEAR, J.; VERRUIJT, A. *Modeling Groundwater Flow and Pollution*. Dordrecht: D. Reidel, Holland, 1990.
2. HELMIG, R.; HUBER, R. Comparison of Galerkin-type Discretization Techniques for Two-Phase Flow in Heterogeneous Porous Media. *Advances in Water Resources*. 1998, vol. 21, no. 8, s. 697–711.
3. BASTIAN, P. Numerical Computation of Multiphase Flows in Porous Media. *Habilitation Thesis, Kiel university*. 1999.
4. COOKSON, A. N.; LEE, J.; MICHLER, C.; CHABINIOK, R.; HYDE, E.; NORDSLETTEN, D.; SMITH, N. A spatially-distributed computational model to quantify behaviour of contrast agents in MR perfusion imaging. *Medical image analysis*. 2014, vol. 18, no. 7, s. 1200–1216.
5. SUBRAMANIAN, V. R.; DIWAKAR, V. D.; TAPRIYAL, D. Efficient macro-micro scale coupled modeling of batteries. *J. Electrochem. Soc.* 2005, vol. 152, no. 10, A2002–A2008.
6. DAO, T.-S.; VYASARAYANI, C. P.; MCPHEE, J. Simplification and order reduction of lithium-ion battery model based on porous-electrode theory. *J. Power Sources*. 2012, vol. 198, s. 329–337.
7. HELMIG, R. *Multiphase Flow and Transport Processes in the Subsurface: A Contribution to the Modeling of Hydrosystems*. Berlin: Springer Verlag, 1997.
8. ILLANGASEKARE, T. H.; SMITS, K. M.; FUČÍK, R.; DAVARZANI, H. From Pore to the Field: Upscaling Challenges and Opportunities in Hydrogeological and Land–Atmospheric Systems. In: *Pore Scale Phenomena: Frontiers in Energy and Environment*. World Scientific, 2015, s. 163–202.
9. HELMIG, R.; WEISS, A.; WOHLMUTH, B. I. Dynamic Capillary Effects in Heterogeneous Porous Media. *Computational Geosciences*. 2007, vol. 11, no. 3, s. 261–274.
10. BEAR, J. *Modeling phenomena of flow and transport in porous media*. Springer, 2018.

24. PETRI, B. G.; FUČÍK, R.; ILLANGASEKARE, T. H.; SMITS, K. M.; CHRIST, J. A.; SAKAKI, T.; SAUCK, C. C. Effect of NAPL source morphology on mass transfer in the vadose zone. *Groundwater*. 2015, vol. 53, no. 5, s. 685–698.
25. NIESSNER, J.; HASSANIZADEH, S. M. Modeling kinetic interphase mass transfer for two-phase flow in porous media including fluid–fluid interfacial area. *Transport in Porous Media*. 2009, vol. 80, no. 2, s. 329.
26. DOYLE, M.; FULLER, T. F.; NEWMAN, J. Modeling of galvanostatic charge and discharge of the lithium/polymer/insertion cell. *J. Electrochem. Soc.* 1993, vol. 140, no. 6, s. 1526–1533.
27. NEWMAN, J.; TIEDEMANN, W. Porous-electrode theory with battery applications. *AIChE J.* 1975, vol. 21, no. 1, s. 25–41. ISSN 1547-5905. Dostupné z DOI: 10.1002/aic.690210103.
28. SUBRAMANIAN, V. R.; BOOVARAGAVAN, V.; VINTEN, D. D. Toward Real-Time Simulation of Physics Based Lithium-Ion Battery Models. *Electrochem. Solid-State Lett.* 2007, vol. 10, no. 11, A255–A260.
29. BENEŠ, M.; FUČÍK, R.; HAVLENA, V.; KLEMENT, V.; KOLÁŘ, M.; POLÍVKA, O.; SOLOVSKÝ, J.; STRACHOTA, P. An Efficient and Robust Numerical Solution of the Full-Order Multiscale Model of Lithium-Ion Battery. *Mathematical Problems in Engineering*. 2018, vol. ID3530975.
30. CAI, L.; WHITE, R. E. Mathematical modeling of a lithium ion battery with thermal effects in COMSOL Inc Multiphysics (MP) software. *J. Power Sources*. 2011, vol. 196, no. 14, s. 5985–5989.
31. NEWMAN, J.; THOMAS-ALYEA, K. E. *Electrochemical Systems*. Wiley Interscience, 2004.
32. RAMADASS, P.; HARAN, B.; GOMADAM, P. M.; WHITE, R.; POPOV, B. N. Development of First Principles Capacity Fade Model for Li-Ion Cells. *J. Electrochem. Soc.* 2004, vol. 151, A196–A203.
33. RAMADASS, P.; HARAN, B.; WHITE, R.; POPOV, B. N. Mathematical modeling of the capacity fade of Li-ion cells. *J. Power Sources*. 2003, vol. 123, s. 230–240.
34. MCWHORTER, D. B.; SUNADA, D. K. Exact Integral Solutions for Two-Phase Flow. *Water Resources Research*. 1990, vol. 26, no. 3, s. 399–413.
35. MCWHORTER, D. B.; SUNADA, D. K. Reply to "Comment on 'Exact integral solutions for two-phase flow'" by Z.-X. Chen, G. S. Bodvarsson, and P. A. Witherspoon. *Water Resources Research*. 1992, vol. 28, no. 5, s. 1479–1479.

47. DAVIS, T. A. A Column Pre-Ordering Strategy for the Unsymmetric-Pattern Multifrontal Method. *ACM Transactions on Mathematical Software*. 2004, vol. 30, no. 2, s. 165–195.
48. BALAY, S.; GROPP, W. D.; MCINNES, L. C.; SMITH, B. F. Efficient Management of Parallelism in Object Oriented Numerical Software Libraries. In: ARGE, E.; BRUASET, A. M.; LANGTANGEN, H. P. (eds.). *Modern Software Tools in Scientific Computing*. Birkhäuser Press, 1997, s. 163–202.
49. OBERHUBER, T.; KLINKOVSKÝ, J.; FUČÍK, R. TNL: Numerical library for modern parallel architectures. *Acta Polytechnica*. 2021, vol. 61, no. SI, s. 122–134.
50. SOLOVSKÝ, J. *Matematické modelování dvoufázového vícesložkového proudění v porézním prostředí v problematice ochrany životního prostředí*. 2016-06. Dipl. pr. FNSPE CTU in Prague.
51. SOLOVSKÝ, J.; FUČÍK, R. A Parallel Mixed-Hybrid Finite Element Method for Two Phase Flow Problems in Porous Media Using MPI. *Computer Methods in Materials Science*. 2017, vol. 17, s. 84–93.
52. SOLOVSKÝ, J.; FUČÍK, R. Mass Lumping for MHFEM in Two Phase Flow Problems in Porous Media. In: RADU, F. A.; KUMAR, K.; BERRE, I.; NORDBOTTEN, J. M.; POP, I. S. (eds.). *Numerical Mathematics and Advanced Applications ENUMATH 2017*. Springer International Publishing, 2019, s. 635–643. ISBN 978-3-319-96415-7.
53. KLINKOVSKÝ, J. *Mathematical modelling of two-phase compositional flow in porous media*. 2017-06. Dipl. pr. FNSPE CTU in Prague.
54. BREZZI, F.; FORTIN, M. *Mixed and hybrid finite element methods*. Springer Science & Business Media, 2012.
55. RAVIART, P.-A.; THOMAS, J.-M. A mixed finite element method for 2-nd order elliptic problems. In: *Mathematical aspects of finite element methods*. Springer, 1977, s. 292–315.
56. FUČÍK, R.; SOLOVSKÝ, J.; PLAMPIN, M. R.; WU, H.; MIKYŠKA, J.; ILLANGASEKARE, T. I. H. Computational Methodology to Analyze the Effect of Mass Transfer Rate on Attenuation of Leaked Carbon Dioxide in Shallow Aquifers. *Acta Polytechnica*. 2021, vol. 61, no. SI, s. 77–88.
57. SMEJKAL, T.; MIKYŠKA, J.; FUČÍK, R. Numerical modelling of adsorption and desorption of water vapor in zeolite 13X using a two-temperature model and mixed-hybrid finite element method numerical solver. *International Journal of Heat and Mass Transfer*. 2020, vol. 148, s. 119050.



Přílohy



P.1 Článek v *Advances in Water Resources*

Radek Fučík, Tissa H. Illangasekare a Michal Beneš: *Multidimensional self-similar analytical solutions of two-phase flow in porous media*, *Advances in Water Resources*, 90:51–56, 2016.



Contents lists available at ScienceDirect

Advances in Water Resources

journal homepage: www.elsevier.com/locate/advwatres

Multidimensional self-similar analytical solutions of two-phase flow in porous media

Radek Fučík^{a,*}, Tissa H. Illangasekare^b, Michal Beneš^a^aDepartment of Mathematics, Faculty of Nuclear Sciences and Physical Engineering, Czech Technical University in Prague, Trojanova 13, 120 00 Prague, Czech Republic^bCenter for Experimental Study of Subsurface Environmental Processes, Colorado School of Mines, 1500 Illinois St. Golden, CO 80401, United States

ARTICLE INFO

Article history:
 Received 10 February 2016
 Revised 13 February 2016
 Accepted 14 February 2016
 Available online 20 February 2016

Keywords:
 Self-similar solution
 Benchmark
 Two-phase flow

ABSTRACT

In general, analytical solutions serve a useful purpose to obtain better insights and to verify numerical codes. For flow of two incompressible and immiscible phases in homogeneous porous media without gravity, one such method that neglects capillary pressure in the solution was first developed by Buckley and Leverett (1942). Subsequently, McWhorter and Sunada (1990) derived an exact solution for the one and two dimensional cases that factored in capillary effects. This solution used a similarity transform that allowed to reduce the governing equations into a single ordinary differential equation (ODE) that can be further integrated into an equivalent integral equation. We present a revision to McWhorter and Sunada solution by extending the self-similar solution into a general multidimensional space. Inspired by the derivation proposed by McWhorter and Sunada (1990), we integrate the resulting ODE in the third and higher dimensions into a new integral equation that can be subsequently solved iteratively by means of numerical integration. We developed implementations of the iterative schemes for one- and higher dimensional cases that can be accessed online on the authors' website.

© 2016 Elsevier Ltd. All rights reserved.

1. Introduction

Development of complex mathematical models of two-phase flow in porous media such as those described by Fučík and Mikyška [9,10] and Petri et al. [17] often requires versatile benchmark solutions that allow to verify numerical convergence and estimate the accuracy of the numerical method. A simplification of the domain geometry, system properties or parameters, and boundary conditions allows to derive exact (analytical or semi-analytical) solutions for the displacement of two incompressible and immiscible phases within a homogeneous or a layered heterogeneous porous medium [4,5,12]. These exact solutions not only serve as benchmark solutions, but also as effective tools to study fundamental displacement processes. A number of researchers have investigated exact solutions for cases where the gravity and/or capillarity are neglected and the exact solution of the governing equations is obtained in a form of a traveling wave such as the well-known Buckley and Leverett one dimensional analytical solution [2], generalization of the Buckley and Leverett so-

lution by van Duijn et al. [6], or the relatively recent approach presented by Mathias et al. [14].

When the capillary effects are important, the exact solution can be found in the form of a self-similar solution as shown by Chen [3], McWhorter and Sunada [15], Sander et al. [19], Fučík et al. [11], Bjørnarå and Mathias [1] for a homogeneous porous medium and by van Duijn et al. [4], van Duijn and de Neef [5], Fučík et al. [12] for a porous medium with a single material discontinuity. For a particular functional choice of the capillary diffusion coefficient that allows to reduce the system of governing equations to the first integral, a d -dimensional exact solution can be obtained as reported previously by Sander et al. [18] and Weeks et al. [21].

This paper focuses on the self-similar solution in a homogeneous porous medium without gravity that was originally published by McWhorter and Sunada [15] and generalize its derivation to a d -dimensional space where $d \in \mathbb{N}$. This includes the self-similar solution for $d = 3$ that to the best of our knowledge has not been published in the literature and will have important practical applications in the analysis of three-dimensional numerical schemes such as convergence verification and/or estimation of the order of convergence. Even though this solution assumes the zero gravity condition that may not be realistic in three-dimensional groundwater flow, a practical application that is of relevance is in

* Corresponding author. Tel.: +420 224 358 540.
 E-mail address: fucik@fjfi.cvut.cz (R. Fučík).

flow simulations in space. Such an application for plant irrigation in micro-gravity was discussed by Scovazzo et al. [20].

Note that in the one dimensional case, unidirectional or counter-current flows can be considered [11,12,15], but in two and higher dimensional spaces, the self-similar solution can be derived for the unidirectional displacement only [3,15]. The main idea behind the derivation of the self-similar solution is to use a *similarity substitution* to transform the governing two-phase flow equations into a single ordinary differential equation (ODE) in the d -dimensional spherical coordinates. The resulting ODE is either solved directly as proposed by Bjørnarå and Mathias [1] for $d = 1$, or transformed into an equivalent integral equation that can be solved iteratively by means of numerical integration [15] for $d = 1, 2$. We show that the derivation of the self-similar solution can be done in a general way regardless of the choice of $d \in \mathbb{N}$. For $d \geq 3$, we transform the resulting ODE into a new, general integral equation for which we propose a fast and efficient iterative solution.

The paper is organized in the following way. First, we briefly present the mathematical model and describe its transformation into the multidimensional spherical coordinates. In Section 3, we discuss the similarity transform of the governing equations into a single ODE and we highlight the important mathematical aspects of the transform that have been omitted previously in the literature but are essential in the further derivation of the self-similar solution. Then in Section 4, we present the integral approach of solving the ODE for a general dimension $d \geq 3$. In the final section, we present several typical self-similar solutions and discuss the applicability of the computational method with respect to the magnitude of the injection rate and the initial saturation.

2. Governing equations

2.1. Two-phase flow equations

We consider incompressible and immiscible flow of two phases in a homogeneous and rigid porous medium without gravity in a d -dimensional space \mathbb{R}^d , $d \in \mathbb{N}$. The wetting and non-wetting phases are indexed by w and n , respectively.

The continuity equation for the phase $\alpha \in \{w, n\}$ is given by

$$\phi \frac{\partial S_\alpha}{\partial t} + \nabla \cdot \vec{v}_\alpha = 0, \quad (1)$$

where $\phi [-]$ is the porosity, $S_\alpha [-]$ is the α -phase volumetric saturation, and $\vec{v}_\alpha [LT^{-1}]$ is the Darcy velocity of the phase α given by

$$\vec{v}_\alpha = -\frac{k_{r,\alpha}}{\mu_\alpha} k \nabla p_\alpha, \quad (2)$$

where $k [L^2]$ is the intrinsic permeability and $k_{r,\alpha} [-]$, $\mu_\alpha [ML^{-1}T^{-1}]$, and $p_\alpha [ML^{-1}T^{-2}]$ are the relative permeability, dynamic viscosity, and pressure of the phase α , respectively. By definition, $S_w + S_n = 1$.

The Eqs. (1) and (2) can be combined to express the wetting phase velocity as

$$\vec{v}_w = f(S_w) \vec{v}_T - D(S_w) \nabla S_w, \quad (3)$$

where $\vec{v}_T [LT^{-1}]$ denotes the total velocity defined by $\vec{v}_T = \vec{v}_w + \vec{v}_n$, $f [-]$ is the wetting-phase fractional flow function defined by

$$f(S_w) = \frac{\frac{k_{r,w}(S_w)}{\mu_w}}{\frac{k_{r,w}(S_w)}{\mu_w} + \frac{k_{r,n}(S_w)}{\mu_n}}, \quad (4)$$

and $D [L^2T^{-1}]$ is the capillary diffusion function given by

$$D(S_w) = -k \frac{\frac{k_{r,w}(S_w)}{\mu_w} \frac{k_{r,n}(S_w)}{\mu_n}}{\frac{k_{r,w}(S_w)}{\mu_w} + \frac{k_{r,n}(S_w)}{\mu_n}} p'_c(S_w), \quad (5)$$

where $p_c [ML^{-1}T^{-2}]$ is the capillary pressure defined by $p_c = p_n - p_w$ and p'_c denotes its first derivative with respect to S_w . In this work, we consider the following empirical models for the S_w -dependent functions

$$k_{r,w}(S_w) = S_e^{\frac{1}{2}} \left(1 - \left(1 - S_e^{\frac{1}{m}} \right)^m \right)^2, \\ k_{r,n}(S_w) = (1 - S_e)^{\frac{1}{2}} \left(1 - S_e^{\frac{1}{m}} \right)^{2m}, \quad (6a)$$

[16] and

$$p_c(S_w) = P_0 \left(S_e^{\frac{1}{m}} - 1 \right)^{1-m} \quad (6b)$$

[13]. In Eqs. (6), $m [-]$ and $P_0 [Pa]$ are the fitting parameters and $S_e [-]$ denotes the effective wetting phase saturation defined by

$$S_e = \frac{S_w - S_{w,r}}{1 - S_{w,r} - S_{n,r}}, \quad (7)$$

where $S_{\alpha,r} [-]$ denotes the residual saturation of the phase α .

Further, the continuity Eq. (1) for both phases can be transformed into

$$\nabla \cdot \vec{v}_T = 0, \quad (8a)$$

$$\phi \frac{\partial S_w}{\partial t} + \nabla \cdot (f(S_w) \vec{v}_T - D(S_w) \nabla S_w) = 0, \quad (8b)$$

where the unknown functions are the wetting phase saturation $S_w = S_w(t, \vec{x})$ and the total velocity $\vec{v}_T = \vec{v}_T(t, \vec{x})$ for all $t > 0$ and $\vec{x} \in \mathbb{R}^d$. The boundary and initial conditions will be discussed in Section 2.3.

2.2. Multidimensional spherical transform

A general multidimensional self-similar solution of the governing Eq. (8) can be obtained in the radial phase displacement flow where the wetting phase is injected through a point source placed at the origin of coordinates. Note that the complementary problem where the non-wetting phase is injected and displaces the wetting phase is described by an equation similar to Eq. (8) but with different coefficients as shown by McWhorter and Sunada [15] or Fučík et al. [11]. The derivation of the corresponding self-similar solution is analogous to the one given here.

Assuming $\vec{v}_T = \vec{v}_T(t, r)$ and $S_w = S_w(t, r)$ exhibit spherical symmetry in \mathbb{R}^d , where $r [L]$ denotes the non-negative radial coordinate, Eq. (8a) is resolved by

$$\vec{v}_T(t, r) = \frac{Q_0(t)}{\gamma_d r^{d-1}} \vec{e}, \quad (9)$$

where $Q_0 [L^d T^{-1}]$ denotes the time-dependent volumetric injection rate, \vec{e} is the unit vector in the spherical coordinates pointing in the positive radial direction, and

$$\gamma_d = \frac{d\pi^{\frac{d}{2}}}{\Gamma\left(\frac{d}{2} + 1\right)}, \quad (10)$$

where Γ is the Γ -function, denotes the surface area of the d -dimensional unit sphere.

As in [15], Eq. (8b) is then transformed into

$$\gamma_d r^{d-1} \phi \frac{\partial S_w}{\partial t} + (1 - f(S_i)) Q_0 \frac{\partial F}{\partial r} = 0, \quad (11)$$

where $S_i [-]$ denotes the initial saturation. The function $F = F(t, r) [-]$ is expressed as

$$F = \frac{Q_0 - f(S_i)}{1 - f(S_i)}, \quad (12)$$

with the wetting-phase volumetric flow rate $Q_w = Q_w(t, r) [L^d T^{-1}]$ defined by

$$Q_w = fQ_0 - \gamma_d r^{d-1} D \frac{\partial S_w}{\partial r}. \quad (13)$$

The volumetric flow rate $Q_w(t, r)$ for each $r > 0$ describes the overall volumetric flux of the wetting phase through the surface of a d -dimensional sphere $B(\vec{0}, r)$ centered around the origin with radius r . Hence, Q_w is related to the phase radial velocity $v_w = v_w(t, r)$ for spherical symmetry as

$$Q_w(t, r) = \gamma_d r^{d-1} v_w(t, r). \quad (14)$$

Eq. (12) can be combined with Eq (13) to obtain

$$F = F_w - \frac{\gamma_d r^{d-1}}{(1-f(S_i))Q_0} D \frac{\partial S_w}{\partial r}, \quad (15)$$

where $F_w[-]$ denotes the normalized wetting-phase fractional flow function

$$F_w(S_w) = \frac{f(S_w) - f(S_i)}{1 - f(S_i)} \quad (16)$$

as in Fučík et al. [11].

2.3. Initial and boundary conditions

Eq. (11) is endowed with the boundary and initial conditions for the unknown functions $S_w = S_w(t, r)$ and $v_T = v_T(t, r)$. According to the formulation by McWhorter and Sunada [15], the following boundary and initial conditions are considered for S_w :

$$S_w(t, 0) = S_0, \quad \forall t > 0, \quad (17a)$$

$$\lim_{r \rightarrow +\infty} S_w(t, r) = S_i, \quad \forall t > 0, \quad (17b)$$

$$S_w(0, r) = S_i, \quad \forall r > 0, \quad (17c)$$

where $S_i < S_0$ because of the wetting fluid being injected into a domain with lower water saturation.

Since we assume that the unidirectional displacement occurs in the radial direction only, the total velocity $v_T(t, r)$ is equal to the wetting phase velocity $v_w(t, r)$ at the inlet $r = 0$ and, therefore, it has to be compatible with the expression for the total velocity \bar{v}_T that is given by Eq. (9) for $r > 0$. If $d > 1$, however, $v_T(t, r)$ is unbounded as $r \rightarrow 0^+$ and therefore the injection velocity of the wetting phase cannot be prescribed at $r = 0$. Instead, for $d = 2$, McWhorter and Sunada [15] propose to formulate the boundary conditions for Q_w and Q_T as

$$Q_w(t, 0) = Q_T(t, 0) = Q_0(t), \quad (18)$$

for all $t > 0$. We extend applicability of this condition for all $d \in \mathbb{N}$.

In order to derive a self-similar solution in the sense of McWhorter and Sunada [15], the following boundary conditions are imposed on the function F :

$$F(t, 0) = 1, \quad \forall t > 0, \quad (19a)$$

$$\lim_{r \rightarrow +\infty} F(t, r) = 0, \quad \forall t > 0. \quad (19b)$$

First condition (19a) is a straightforward combination of Eq. (18) and the definition of F given by Eq. (12). In order to obtain zero value of F at $r \rightarrow +\infty$ in Eq. (19b), we need to assume that, for all $t > 0$,

$$\lim_{r \rightarrow +\infty} r^{d-1} \frac{\partial S_w}{\partial r}(t, r) = 0. \quad (20)$$

The physical meaning of Eq. (19b) is that the propagation of the injected fluid has finite velocity and the total volume of the injected fluid is contained inside a d -dimensional sphere of a finite radius.

3. Reduction to an ordinary differential equation

3.1. Similarity transform

The similarity substitution $S_w(t, r) = S_w(\lambda)$, where

$$\lambda = rt^{-\frac{1}{d}}, \quad (21)$$

allows to express the function F in terms of S_w only, and to transform the partial differential equation (11) into a second order ordinary differential equation for F . As in Weeks et al. [21], the similarity transform is possible if and only if the volumetric injection rate has the specific form

$$Q_0(t) = At^{\frac{d-2}{2}}, \quad (22)$$

where $A [L^d T^{-\frac{d}{2}}]$ denotes the volumetric injection rate constant.

We use Eq. (21) to transform F given by Eq. (15) into

$$F(S_w) = F_w(S_w) - \frac{\gamma_d}{A(1-f(S_i))} D(S_w) \frac{\lambda(S_w)^{d-1}}{\lambda'(S_w)}, \quad (23)$$

and the governing Eq. (11) into

$$\lambda(S_w)^d = \frac{2A(1-f(S_i))}{\gamma_d \phi} F'(S_w), \quad (24)$$

where λ' and F' denotes the first derivative of λ and F , respectively. For a known function F , the saturation $S_w = S_w(t, r)$ is implicitly expressed by Eq. (24) as

$$r^d t^{-\frac{d}{2}} = \frac{2A(1-f(S_i))}{\gamma_d \phi} F'(S_w(t, r)), \quad (25)$$

for all $t > 0$ and $r > 0$.

We differentiate Eq. (24) and combine the result with Eq. (23) to eliminate λ and its derivative λ' to obtain the following second order ODE for F :

$$F''(F)^{\frac{2}{d}-2} = -A^{-\frac{2}{d}} \frac{C_d D}{F - F_w}, \quad (26)$$

where

$$C_d = d \left(\frac{\gamma_d}{1-f(S_i)} \right)^{\frac{2}{d}} \left(\frac{\phi}{2} \right)^{\frac{2}{d}-1}. \quad (27)$$

3.2. Boundary conditions

At $r = 0$, $S_w = S_0$ as a result of Eq. (17a) and the boundary value for λ follows from (21) as

$$\lambda(S_0) = 0. \quad (28)$$

It is important to note that the transform $S_w(t, r) = S_w(\lambda)$ is invertible to $\lambda = \lambda(S_w)$ only if $S_i < S_w \leq S_0$ because for a given time $t > 0$, $S_w(t, r) = S_i$ for all $r \geq r_*(t)$ where $r_*[L]$ denotes the position of the head of the saturation profile. McWhorter and Sunada [15] state that $S_w = S_i$ when $\lambda \rightarrow +\infty$. This can, however, lead to a misinterpretation that $\lambda(S_w)$ tends to infinity as $S_w \rightarrow S_i^+$. In fact, the relationship $\lambda \leftrightarrow S_w$ is not unique for all $\lambda \in [0, +\infty)$ but only for $\lambda \in [0, \lambda_*]$, where λ_* denotes the upper bound given by

$$\lim_{S_w \rightarrow S_i^+} \lambda(S_w) = \lambda_* \quad (29)$$

as illustrated in Fig. 1. Consequently, we can compute the position of the head of the solution as $r_*(t) = \lambda_* \sqrt{t}$ for all $t > 0$.

The boundary conditions described by Eq. (19) are transformed by Eq. (21) into

$$\lim_{S_w \rightarrow S_i^+} F(S_w) = 0, \quad (30a)$$

$$F(S_0) = 1. \quad (30b)$$

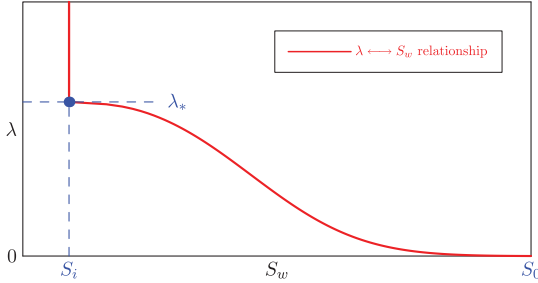


Fig. 1. Illustration of the typical $\lambda \leftrightarrow S_w$ relationship that is not uniquely invertible for $S_w = S_i$.

Eqs. (24),(28) and (29) allow to express the boundary conditions for the derivative of F in the form

$$F'(S_i^+) := \lim_{S_w \rightarrow S_i^+} F'(S_w) = \lambda_*^d \frac{\gamma_d \phi}{2A(1 - f(S_i))}, \quad (31a)$$

$$F'(S_0) = 0. \quad (31b)$$

Evaluating Eq. (23) at $S_w = S_0$ and using $F(S_0) = 1$ and $\lambda(S_0) = 0$ reveals that for $d = 1$, A is related to S_0 as

$$A = -\frac{\gamma_d}{1 - f(S_i)} \frac{D(S_0)}{1 - F_w(S_0)} \frac{1}{\lambda'(S_0)}. \quad (32)$$

For $d > 1$, however, A does not depend on S_0 and Eq. (23), evaluated at $S_w = S_0$, reduces into

$$1 = F_w(S_0). \quad (33)$$

This relation holds if and only if $S_0 = S_w^m$, where S_w^m denotes the maximal wetting phase saturation for which $f(S_w^m) = 1$.

In the next section, we will show that the second order ODE in Eq. (26) can be integrated twice to obtain an equivalent integral equation for F that can be solved iteratively by means of numerical integration.

4. Integral solution of ODE

As pointed out by McWhorter and Sunada [15] who in their work discussed the cases $d = 1$ and $d = 2$, ODE (26) can be integrated twice to obtain an integral equation for the unknown function F that can be solved iteratively by using numerical integration. Note that in the one-dimensional case, the resulting iterative scheme converges fast for S_0 lower than the maximal saturation $S_w^m = 1 - S_{n,r}$. However, the number of iterations increase considerably as $S_0 \rightarrow S_w^m$. The numerical algorithm can even cease to converge. Fučík et al. [11] proposed to overcome such numerical difficulties for S_0 close to S_w^m by transforming the integral equation into two variants of modified integral equations. The authors show that both these variants can be used to obtain the numerical solution for a larger extent of values of S_0 close to S_w^m than the original iteration scheme by McWhorter and Sunada [15]. The online implementation of the numerical solver capable of solving the original and modified integral equations mentioned above can be accessed on the website in Fučík [7].

For $d \geq 3$, we propose to integrate ODE (26) from S_i to S_w and after algebraic manipulations, we obtain the following expression of F'

$$F'(S_w) = \left[(F'(S_i^+))^{2-d} + \frac{d-2}{d} C_d A^{-\frac{2}{d}} \int_{S_i}^{S_w} \frac{D(\eta)}{F(\eta) - F_w(\eta)} d\eta \right]^{\frac{d}{2-d}}, \quad (34)$$

for all $S_w \in [S_i, S_0]$. In Eq. (34), it is important to emphasize that the limit $F'(S_i^+)$ given by Eq. (31a) is finite as discussed in Section 3.2, c.f. Eq. (29). Similar to the case $d = 2$ discussed by McWhorter and Sunada [15], Eq. (34) is consistent with $F'(S_0) = 0$ given by Eq. (31b) if and only if the integral

$$\int_{S_i}^{S_0} \frac{D(\eta)}{F(\eta) - F_w(\eta)} d\eta \quad (35)$$

is divergent.

Further integration of Eq. (34) allows to obtain the following integral equation for F

$$F(S_w) = \int_{S_i}^{S_w} \left[(F'(S_i^+))^{2-d} + \frac{d-2}{d} C_d A^{-\frac{2}{d}} \int_{S_i}^{\beta} \frac{D(\eta)}{F(\eta) - F_w(\eta)} d\eta \right]^{\frac{d}{2-d}} d\beta, \quad (36)$$

where the boundary condition given by Eq. (30a) has been already used. Evaluating Eq. (36) at $S_w = S_0$ and using the remaining condition (30b), we obtain an implicit equation for $F'(S_i^+)$

$$1 = \int_{S_i}^{S_0} \left[(F'(S_i^+))^{2-d} + \frac{d-2}{d} C_d A^{-\frac{2}{d}} \int_{S_i}^{\beta} \frac{D(\eta)}{F(\eta) - F_w(\eta)} d\eta \right]^{\frac{d}{2-d}} d\beta. \quad (37)$$

Due to the implicit form of Eq. (37) with respect to the value of $F'(S_i^+)$, the solution of the integral equation (36) is not straightforward as for $d = 1$ or $d = 2$.

Eq. (36) can be solved iteratively and by means of numerical integration in the form

$$F_{k+1}^{(B)}(S_w) = \min \left\{ \int_{S_i}^{S_w} \left[B^{\frac{2-d}{d}} + \frac{d-2}{d} C_d A^{-\frac{2}{d}} \times \int_{S_i}^{\beta} \frac{D(\eta)}{F_k^{(B)}(\eta) - F_w(\eta)} d\eta \right]^{\frac{d}{2-d}} d\beta; 1 \right\}, \quad (38)$$

with $F_0^{(B)} \equiv 1$ as the initial guess, where $F_k^{(B)}$ denotes the k th iteration of F and B approximates the value of $F'(S_i^+)$. For a given B , the iterative process is terminated when the difference between the successive values of the functional \mathcal{H} that represents the constraint given by Eq. (37)

$$\mathcal{H}(F_k^{(B)}, B) := 1 - \int_{S_i}^{S_0} \left[B^{\frac{2-d}{d}} + \frac{d-2}{d} C_d A^{-\frac{2}{d}} \times \int_{S_i}^{\beta} \frac{D(\eta)}{F_k^{(B)}(\eta) - F_w(\eta)} d\eta \right]^{\frac{d}{2-d}} d\beta \quad (39)$$

is sufficiently small. For simplicity, we denote by $H(B)$ the value of $\mathcal{H}(F_\ell^{(B)}, B)$, where the index ℓ denotes the final iteration of the iterative process. Altogether, solving Eq. (36) with the constraint given by Eq. (37) is equivalent to finding $F'(S_i^+)$ such that $H(F'(S_i^+)) = 0$.

Our numerical experiments show that the behavior of $H = H(B)$ is monotone with respect to B as illustrated in Fig. 2. Therefore, the bisection method can be used to compute the root of H .

5. Computational examples

In this section, we show examples of the solutions computed using the integral iterative scheme given by Eq. (38) with the emphasis on novelty of the presented approach for $d = 3$ and discuss the admissible range for the input injection parameter A . Additionally, we show how the initial wetting phase saturation affects the saturation redistribution profiles.

All results are computed using the following setting of the material and fluid properties: $\phi = 0.4$, $k = 10^{-10} \text{ m}^2$, $m = \frac{1}{2}$, $P_0 = 1000 \text{ Pa}$, $\mu_w = 0.001 \text{ kg m}^{-1} \text{ s}^{-1}$, and $\mu_n = 0.0009 \text{ kg m}^{-1} \text{ s}^{-1}$.

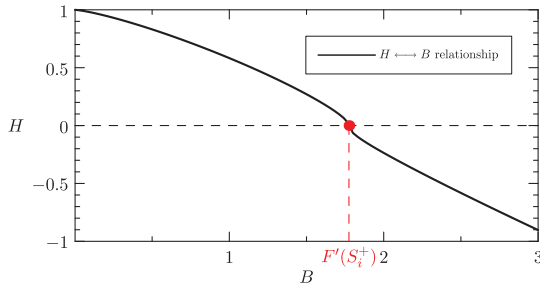


Fig. 2. Illustration of the $H \leftrightarrow B$ relationship for the simulation parameters given in Section 5, $d = 3$, $A = 10^{-6} [m^3s^{-3/2}]$.

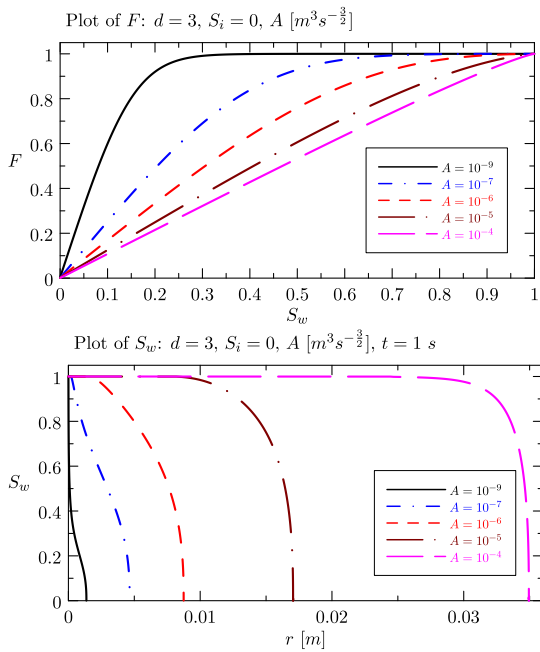


Fig. 3. Example of the functions F and the saturation profiles S_w evaluated at $t = 1$ for $S_i = 0$ and various choices of the injection rate constant A in the three-dimensional space, $d = 3$.

Although an arbitrary value of A can be chosen for $d \geq 2$ in theory (c.f. Section 3.2), our numerical experiments indicate that the solution can be computed for a bounded range of A , depending on the dimension d considered. As shown in Fig. 3, larger values of A correspond to flow situations where the advection produced by the large injection rate dominates over the capillary diffusion and the solution profile resembles the traveling wave solution similar to the one dimensional case, where the self-similar solution approaches the Buckley and Leverett analytical solution (where capillary diffusion is neglected) as $S_0 \rightarrow S_w^m$ as reported by McWhorter and Sunada [15], Fučík et al. [11], or Bjørnarå and Mathias [1].

On the other hand, under lower injection rates, A corresponds to slower propagation of the wetting phase front and as $A \rightarrow 0$, the function F approaches a step function as illustrated in Fig. 4 where the horizontal axis corresponds to $\log(S_w)$.

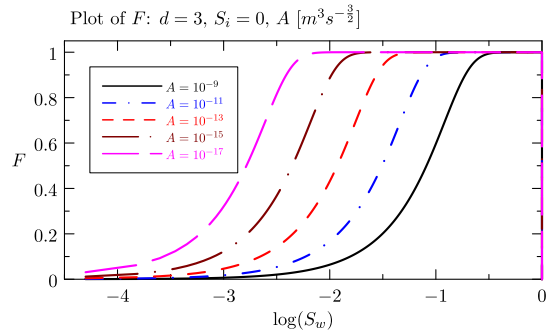


Fig. 4. Illustration of the evolution of the function F as $A \rightarrow 0^+$ for $d = 3$ shown using the decadic logarithmic scale for the horizontal axis.

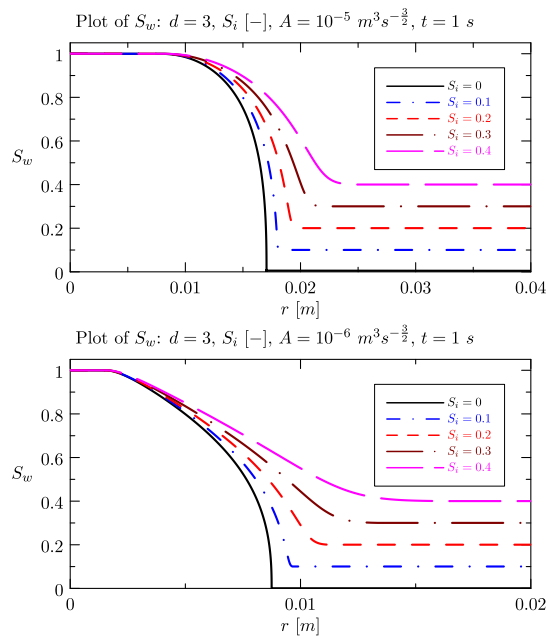


Fig. 5. Comparison of the saturation profiles S_w evaluated at $t = 1$ for various choices of the injection rate parameter A and initial water saturation S_i in the three-dimensional space, $d = 3$.

In Fig. 5, the effect of the initial saturation on the solution profiles at $t = 1$ is shown for various choices of the injection rate parameter A . As expected, the initial presence of the wetting phase facilitates the propagation of the front with respect to the case with $S_i = 0$. Note that similar saturation profiles as in Figs. 3 and 5 were shown by Weeks et al. [21] using their exact solution for a particular functional choice of the capillary diffusion function. Similar behavior can be shown for solution profiles in higher dimensional spaces $d \geq 4$ although the physical meaning of such solutions is disputable.

In order to facilitate computation of the self-similar solutions discussed in this paper, we developed an online implementation of the integral solution of ODE (26) that includes the iterative scheme

proposed by McWhorter and Sunada [15] for $d = 2$ and the one given by Eq. (38) for $d \geq 3$, c.f. [8].

6. Conclusion

We discussed the higher dimensional generalization of the self-similar (or semi-analytical) solution originally proposed by McWhorter and Sunada [15] that can be obtained for a unidirectional displacement of two immiscible and incompressible phases without gravity. Regardless the dimension d considered, we showed that a particular similarity transform can be used to reduce the system of the governing partial differential equations into a single ordinary differential equation (ODE). Similar to McWhorter and Sunada [15], we transformed the resulting ODE for $d \geq 3$ into the equivalent integral equation and proposed a numerical algorithm for obtaining its solution.

We developed online implementations of the computational algorithms that can be accessed on the website in Fučík [7] for $d = 1$ and Fučík [8] for $d \geq 2$.

Acknowledgments

The work reported in this paper was supported by the Czech Ministry of Education, Youth and Sports through the project Kontakt II LH14003: *Development and Validation of Porous Media Fluid Dynamics and Phase Transitions Models for Subsurface Environmental Application*. This project is a collaboration with the Center for Experimental Study for Subsurface Environmental Processes at the Colorado School of Mines. We gratefully acknowledge professors David B. McWhorter and Daniel K. Sunada at Colorado State University as their original paper provided the foundation for this work. The second author got introduced to the basics of groundwater through a class taught by Prof. McWhorter when he was a graduate student. The mentorship of both professors McWhorter and Sunada is gratefully acknowledged.

References

- [1] Bjørnård TI, Mathias SA. A pseudospectral approach to the McWhorter and Sunada equation for two-phase flow in porous media with capillary pressure. *Comput Geosci* 2013;17(6):889–97.
- [2] Buckley SE, Leverett M, et al. Mechanism of fluid displacement in sands. *Trans AIME* 1942;146(01):107–16.
- [3] Chen Z. Some invariant solutions to two-phase fluid displacement problems including capillary effect. *SPE Reserv Eng* 1988;3(2).
- [4] van Duijn C, Molenaar J, de Neef M. The effect of capillary forces on immiscible two-phase flow in heterogeneous porous media. *Transp Porous Media* 1995;21(1):71–93.
- [5] van Duijn C, de Neef M. Similarity solution for capillary redistribution of two phases in a porous medium with a single discontinuity. *Adv Water Resour* 1998;21:451–61.
- [6] van Duijn C, Peletier L, Pop IS. A new class of entropy solutions of the Buckley–Leverett equation. *SIAM J Math Anal* 2007;39(2):507–36.
- [7] Fučík R. Online implementation of the McWhorter and Sunada exact solution in 1D; 2016. URL: <http://mmg.fjfi.cvut.cz/~fucik/exact1d>.
- [8] Fučík R. Online implementation of the multidimensional exact solution of two-phase flow in porous media; 2016. URL: <http://mmg.fjfi.cvut.cz/~fucik/exact>.
- [9] Fučík R, Mikyška J. Discontinuous Galerkin and mixed-hybrid finite element approach to two-phase flow in heterogeneous porous media with different capillary pressures. *Proc Comput Sci* 2011;4:908–17.
- [10] Fučík R, Mikyška J. Mixed-hybrid finite element method for modelling two-phase flow in porous media. *J Math Ind* 2011;3:9–19.
- [11] Fučík R, Mikyška J, Beneš M, Illangasekare TH. An improved semi-analytical solution for verification of numerical models of two-phase flow in porous media. *Vadose Zone J* 2007;6(1):93–104.
- [12] Fučík R, Mikyška J, Beneš M, Illangasekare TH. Semianalytical solution for two-phase flow in porous media with a discontinuity. *Vadose Zone J* 2008;7(3):1001–7.
- [13] van Genuchten MT. A closed-form equation for predicting the hydraulic conductivity of unsaturated soils. *Soil Sci Soc Am J* 1980;44:892–8.
- [14] Mathias SA, Gluyas JG, González Martínez de Miguel GJ, Hosseini SA. Role of partial miscibility on pressure buildup due to constant rate injection of CO₂ into closed and open brine aquifers. *Water Resour Res* 2011;47(12):1–11.
- [15] McWhorter DB, Sunada DK. Exact integral solutions for two-phase flow. *Water Resour Res* 1990;26(3):399–413.
- [16] Muallem Y. A new model for predicting the hydraulic conductivity of unsaturated porous media. *Water Resour Res* 1975;12(3):513–22.
- [17] Petri BG, Fučík R, Illangasekare TH, Smits KM, Christ JA, Sakaki T, et al. Effect of NAPL source morphology on mass transfer in the vadose zone. *Groundwater* 2015;53(5):685–98.
- [18] Sander G, Norbury J, Weeks S. An exact solution to the nonlinear diffusion–convection equation for two-phase flow. *Quarterly J Mech Appl Math* 1993;46(4):709–27.
- [19] Sander G, Parlange J-Y, Lisle I, Weeks S. Exact solutions to radially symmetric two-phase flow for an arbitrary diffusivity. *Adv Water Resour* 2005;28(10):1112–21.
- [20] Scovazzo P, Illangasekare TH, Hoehn A, Todd P. Modeling of two-phase flow in membranes and porous media in microgravity as applied to plant irrigation in space. *Water Resour Res* 2001;37(5):1231–43.
- [21] Weeks S, Sander G, Parlange J-Y. n-dimensional first integral and similarity solutions for two-phase flow. *ANZIAM J* 2003;44(03):365–80.

■ P.2 Článek v *Computer Physics Communications*

Radek Fučík, Jakub Klinkovský, Jakub Solovský, Tomáš Oberhuber a Jiří Mikyška: *Multidimensional mixed-hybrid finite element method for compositional two-phase flow in heterogeneous porous media and its parallel implementation on GPU*, *Computer Physics Communications*, 238:165–180, 2019.

Contents lists available at [ScienceDirect](https://www.sciencedirect.com)

Computer Physics Communications

journal homepage: www.elsevier.com/locate/cpc

Multidimensional mixed–hybrid finite element method for compositional two–phase flow in heterogeneous porous media and its parallel implementation on GPU



Radek Fučík*, Jakub Klinkovský, Jakub Solovský, Tomáš Oberhuber, Jiří Mikyška

Faculty of Nuclear Sciences and Physical Engineering, Czech Technical University in Prague, Trojanova 13, 120 00 Prague, Czech Republic

ARTICLE INFO

Article history:

Received 10 March 2017

Received in revised form 5 December 2018

Accepted 7 December 2018

Available online 15 December 2018

Keywords:

Mixed–hybrid finite element method

Parallel implementation on GPU

47.56.+r

47.11.fg

ABSTRACT

A general multidimensional numerical scheme, primarily designed to simulate two-phase compositional flow in porous media, is presented with serial and parallel implementations suitable for solving problems with degenerate (capillary) diffusion or capillary barrier effect in heterogeneous porous materials. The numerical scheme is based on the mixed–hybrid finite element method with the semi-implicit approach for the time discretization in order to obtain a system of linear equations in each time step. The scheme is implemented in serial for CPU and in parallel for CPU and GPU using TNL that provides an efficient abstraction layer for accessing various parallel hardware architectures. In order to demonstrate the applicability of the numerical scheme, a numerical analysis is presented for problems of two-phase flow in 1D, 2D, and 3D for which exact (semi-analytical) solutions are known and a series of benchmark problems for two-phase flow in heterogeneous porous media is discussed to show correct simulation of the capillary barrier effect. The efficiency and accuracy of the implementations on CPU and GPU are discussed. Moreover, we construct an analytical solution and use it to demonstrate convergence of the numerical scheme for two-phase compositional flow problems in porous media.

© 2018 Elsevier B.V. All rights reserved.

1. Introduction

Numerous general-purpose or custom-designed computational tools are available for solving systems of partial differential equations originating from mathematical modeling of various industrial, biological, or environmental problems. In particular, for multiphase compositional flows in porous media, computational software such as DUNE [1], TOUGH2 [2], or COMSOL Multiphysics that are used in practical applications take limited or no advantage of using parallel computation on graphical processing units (GPUs).

Based on the mixed–hybrid finite element method (MHFEM) [3–5], we have developed a numerical scheme capable of solving general systems of non-stationary partial differential equations (PDEs) in 1D, 2D, or 3D and we propose a modification that allows to consider problems with vanishing or degenerate diffusion. The ability to handle degenerating diffusive fluxes is important, for instance, in dealing with near-saturated regions in two-phase flow in porous medium.

The numerical scheme is implemented using the Template numerical library (TNL) that is being developed at the FNSPE, CTU in

Prague [6].¹ TNL provides all requisite algorithms and data structures such as structured or unstructured meshes, vectors, sparse matrices, or linear solvers that have unified interface and allows to implement numerical schemes independently of the architecture: CPU or GPU via CUDA.

The system of PDEs is considered in the general coefficient form as

$$\sum_{j=1}^n N_{i,j} \frac{\partial Z_j}{\partial t} + \sum_{j=1}^n \mathbf{u}_{i,j} \cdot \nabla Z_j + \nabla \cdot \left[m_i \left(- \sum_{j=1}^n \mathbf{D}_{i,j} \nabla Z_j + \mathbf{w}_i \right) + \sum_{j=1}^n Z_j \mathbf{a}_{i,j} \right] + \sum_{j=1}^n r_{i,j} Z_j = f_i, \quad (1)$$

where the unknown vector function $\mathbf{Z} = [Z_1, \dots, Z_n]^T$ depends on time $t \in [0, T]$ and position vector $\mathbf{x} \in \Omega \subset \mathbb{R}^d$, where T denotes the final simulation time, Ω is a polygonal domain, and d is the spatial dimension. Based on the letters denoting the coefficients in (1), we refer to the computational method presented in this paper as NumDwarf.

* Correspondence to: Katedra matematiky, FJFI CVUT v Praze, Trojanova 13, 120 00 Praha 2, Czech Republic.

E-mail address: fucik@fjfi.cvut.cz (R. Fučík).

<https://doi.org/10.1016/j.cpc.2018.12.004>

0010-4655/© 2018 Elsevier B.V. All rights reserved.

¹ <http://www.tnl-project.org>.

System of Eqs. (1) is supplemented by the initial condition

$$Z_j(0, \mathbf{x}) = Z_j^{ini}(\mathbf{x}), \quad \forall \mathbf{x} \in \Omega, \quad j = 1, \dots, n, \quad (2a)$$

and boundary conditions for all $t \in (0, T)$,

$$Z_j = Z_j^D, \quad \forall \mathbf{x} \in \Gamma_{Z_j} \subset \partial\Omega, \quad j = 1, \dots, n, \quad (2b)$$

$$\mathbf{q}_i \cdot \mathbf{n} = q_i^N, \quad \forall \mathbf{x} \in \Gamma_{q_i} \subset \partial\Omega, \quad i = 1, \dots, n, \quad (2c)$$

where by \mathbf{q}_i , we denote the conservative flux

$$\mathbf{q}_i = m_i \left(- \sum_{j=1}^n \mathbf{D}_{i,j} \nabla Z_j + \mathbf{w}_i \right). \quad (3)$$

In general, the coefficients in Eq. (1) are functions of t , \mathbf{x} , and \mathbf{Z} . Their meaning can be described as follows: $\mathbf{N} = \{N_{i,j}\}_{i,j=1}^n$ is the damping matrix, $\mathbf{u} = \{\mathbf{u}_{i,j}\}_{i,j=1}^n$ describes the convection in the non-conservative form, $\mathbf{m} = \{m_i\}_{i=1}^n$ is the vector of the mobility coefficients of the conservative fluxes given by Eq. (3) assumed to be non-negative, $\mathbf{D} = \{\mathbf{D}_{i,j}\}_{i,j=1}^n$ is the matrix of diffusion tensors, $\mathbf{w} = \{\mathbf{w}_i\}_{i=1}^n$ is the vector representing external conservative forces, $\mathbf{a} = \{\mathbf{a}_{i,j}\}_{i,j=1}^n$ describes the convection in the conservative form, $\mathbf{r} = \{r_{i,j}\}_{i,j=1}^n$ is the matrix of reaction terms, and $\mathbf{f} = \{f_i\}_{i=1}^n$ is the vector of the source/sink terms.

Although NumDwarf has been primarily developed for two-phase compositional flows in porous media that include capillarity, gravity, and heterogeneous porous materials, its applicability may be extended to other systems of partial differential equations simply by specifying the coefficients in (1).

In this paper, we describe derivation and main features of the numerical scheme, both serial and parallel implementations, and present a numerical analysis of the method using available benchmark problems. The paper is organized as follows. First, we present a detailed derivation of the proposed numerical scheme based on the semi-implicit time discretization variant of the MHFEM and describe the computational algorithm and its implementation. Then, we present results of the numerical analysis for two-phase flow and two-phase compositional flow benchmark problems in Sections 3 and 4, respectively. Finally, we summarize the paper in the last section.

2. Mixed-hybrid finite element method

We use the mixed-hybrid finite element method to solve the system of general coefficient form partial differential equations given by Eq. (1). The unknown functions $Z_j(t, \mathbf{x})$ are assumed continuously differentiable with respect to time t and weakly differentiable with respect to spatial coordinate vector \mathbf{x} in Ω .

We consider a spatial discretization \mathcal{K}_h of $\Omega \subset \mathbb{R}^d$ consisting of segments in \mathbb{R}^1 , triangles or rectangles in \mathbb{R}^2 , and tetrahedra or cuboids in \mathbb{R}^3 where $h > 0$ is the mesh size defined as largest ball diameter circumscribed around elements in \mathcal{K}_h . We assume that the mesh is conforming. We denote by \mathcal{V}_h the set of all vertices of \mathcal{K}_h , by \mathcal{E}_h the set of all sides of \mathcal{K}_h , and by \mathcal{E}_h^{int} and \mathcal{E}_h^{ext} the set of interior and exterior sides of \mathcal{K}_h , respectively. By \mathcal{E}_K , we denote the set of all sides of an element $K \in \mathcal{K}_h$. In the following subsections, we will always use index $i = 1, \dots, n$ that corresponds to the i th equation of Eq. (1).

2.1. Velocity approximation

In Eq. (1), we define the velocity v_i by

$$v_i = - \sum_{j=1}^n \mathbf{D}_{i,j} \nabla Z_j + \mathbf{w}_i \quad (4)$$

and thus the conservative flux defined by Eq. (3) is related to v_i by $\mathbf{q}_i = m_i v_i$. We assume that both the conservative velocity

and flux \mathbf{q}_i belong to the functional space $\mathbf{H}(\text{div}, \Omega)$. On each element $K \in \mathcal{K}_h$, we shall approximate v_i and \mathbf{q}_i in the lowest order Raviart–Thomas–Nédélec space $\mathbf{RTN}_0(K) \subset \mathbf{H}(\text{div}, K)$, [7,8]. The basis functions $\omega_{K,E} \in \mathbf{RTN}_0(K)$ are chosen such that $\forall E, F \in \mathcal{E}_K$

$$\omega_{K,E} \cdot \mathbf{n}_{K,F} = \delta_{EF} \frac{1}{|E|^{d-1}}, \quad \nabla \cdot \omega_{K,E} = \frac{1}{|K|^d}, \quad (5)$$

where $d = 1, 2, 3$, $\mathbf{n}_{K,E}$ is the outward unit normal to side $E \in \mathcal{E}_K$ with respect to element K , δ_{EF} is the Kronecker symbol, and $|\cdot|_s$ is the s -dimensional Lebesgue's measure, $s = 0, 1, 2, 3$ and $|\cdot|_0 \equiv 1$. The approximated velocity v_i and flux \mathbf{q}_i are given in the basis of $\mathbf{RTN}_0(K)$ as

$$v_i = \sum_{E \in \mathcal{E}_K} v_{i,K,E} \omega_{K,E}, \quad \mathbf{q}_i = \sum_{E \in \mathcal{E}_K} q_{i,K,E} \omega_{K,E}, \quad (6)$$

where $v_{i,K,E}$ and $q_{i,K,E}$ are the velocity and flux across the side $E \in \mathcal{E}_K$ in the outward direction with respect to K , respectively. Since $\mathbf{q}_i = m_i v_i$, we approximate the flux across the side E by

$$q_{i,K,E} = m_{i,K,E} v_{i,K,E}, \quad (7)$$

where $m_{i,K,E}$ is the mean value of the mobility m_i over the side $E \in \mathcal{E}_K$.

In order to express $v_{i,K,E}$ in terms of the unknown variables $Z_{j,K}$ and $Z_{j,F}$, we define partial velocities $v_{i,j}$ by $v_{i,j} = -\mathbf{D}_{i,j} \nabla Z_j$ and assume that $v_{i,j}$ belongs to $\mathbf{H}(\text{div}, \Omega)$ where its approximation in the basis of $\mathbf{RTN}_0(K)$ for all $K \in \mathcal{K}_h$ can be written as

$$v_{i,j} = \sum_{E \in \mathcal{E}_K} v_{i,j,K,E} \omega_{K,E} = -\mathbf{D}_{i,j} \nabla Z_j. \quad (8)$$

We assume that the tensor $\mathbf{D}_{i,j}$ is either zero or positive definite. In the first case, the zero tensor $\mathbf{D}_{i,j}$ implies that $v_{i,j} = \mathbf{0}$ and its projection into $\mathbf{RTN}_0(K)$ is trivial. If the tensor $\mathbf{D}_{i,j}$ is positive definite, we can multiply Eq. (8) by its inversion and project the resulting ∇Z_j into $\mathbf{RTN}_0(K)$ to obtain for all $F \in \mathcal{E}_K$

$$Z_{j,K} - Z_{j,F} = \sum_{E \in \mathcal{E}_K} v_{i,j,K,E} \mathbf{B}_{i,j,K,E,F}, \quad (9)$$

where the coefficients

$$\mathbf{B}_{i,j,K,E,F} = \int_K \omega_{K,E}^T \mathbf{D}_{i,j}^{-1} \omega_{K,F} d\mathbf{x} \quad (10)$$

form a local, positive definite matrix $\mathbf{B}_{i,j,K}$ and by $\mathbf{b}_{i,j,K} = \{b_{i,j,K}\}_{E,F \in \mathcal{E}_K}$, we denote its inversion, i.e., $\mathbf{b}_{i,j,K} = \mathbf{B}_{i,j,K}^{-1}$. The system of linear equations given by Eq. (9) for $v_{i,j,K,E}$ is solved locally (per element $K \in \mathcal{K}_h$) and its solution allows to express the components of $v_{i,j}$ in $\mathbf{RTN}_0(K)$ as

$$v_{i,j,K,E} = b_{i,j,K,E} Z_{j,K} - \sum_{F \in \mathcal{E}_K} b_{i,j,K,E,F} Z_{j,F}, \quad (11)$$

where $b_{i,j,K,E} = \sum_{F \in \mathcal{E}_K} \mathbf{B}_{i,j,K,E,F}$.

As a result, Eq. (11) is used to express $v_{i,K,E}$ in terms of $Z_{j,K}$ and $Z_{j,F}$ as

$$v_{i,K,E} = \sum_{j \in \sigma_{i,K}} \left(b_{i,j,K,E} Z_{j,K} - \sum_{F \in \mathcal{E}_K} b_{i,j,K,E,F} Z_{j,F} \right) + w_{i,K,E}, \quad (12)$$

where $w_{i,K,E}$ denote the coefficients of the projection of \mathbf{w}_i into $\mathbf{RTN}_0(K)$ and by $\sigma_{i,K} \subseteq \{1, \dots, n\}$, we denote the set of all indices j for which $\mathbf{D}_{i,j}$ is non-zero (i.e., positive definite) on element $K \in \mathcal{K}_h$, $i = 1, \dots, n$.

As shown later in Section 3.2, a mass-lumping technique based on [9] needs to be employed to stabilize the numerical scheme.

2.2. Discrete spatial and temporal approximation

We use the finite volume approach in order to discretize the i th Eq. (1). As a result, we obtain a system of ordinary differential equations (ODEs) for the averages of Z_j over K denoted by

$$Z_{j,K} = Z_{j,K}(t) = \frac{1}{|K|_d} \int_K Z_j(t, \mathbf{x}) d\mathbf{x}, \quad j = 1, \dots, n. \quad (13)$$

First, we integrate Eq. (1) over a finite volume $K \in \mathcal{K}_h$ and use Green's formula together with the discretization of the phase velocities defined by Eq. (6) and the properties of the $\mathbf{RTN}_0(K)$ basis functions given by Eq. (5). The resulting system of ODEs is further discretized in time using

$$\frac{dZ_{j,K}}{dt} \approx \frac{Z_{j,K}^{k+1} - Z_{j,K}^k}{\Delta t_k}, \quad (14)$$

where $\Delta t_k = t_{k+1} - t_k$ and $0 < t_k < t_{k+1}$, $k \in \mathbb{N}$, are the discrete time levels. By a superscript k , we denote the value of a function evaluated at time $t = t_k$, i.e., $Z_{j,K}^k = Z_{j,K}(t_k)$. Consequently, the i th Eq. (1) is discretized in time ($k \in \mathbb{N}$) and space ($K \in \mathcal{K}_h$) as

$$\begin{aligned} & \frac{|K|_d}{\Delta t_k} \sum_{j=1}^n N_{i,j,K} (Z_{j,K}^{k+1} - Z_{j,K}^k) + \sum_{j=1}^n \sum_{E \in \mathcal{E}_K} Z_{j,j,E}^{k,upw} (a_{i,j,K,E} + u_{i,j,K,E}) \\ & + \sum_{E \in \mathcal{E}_K} m_{i,E}^{k,upw} v_{i,K,E} + \sum_{j=1}^n \left(r_{i,j,K} |K|_d - \sum_{E \in \mathcal{E}_K} u_{i,j,K,E} \right) Z_{j,K}^{k+1} \\ & = |K|_d f_{i,K}, \end{aligned} \quad (15)$$

where the subscripts K and E denote the mean value of a variable over the finite volume K and side $E \in \mathcal{E}_K$, respectively. By $Z_{j,E}^{k+1}$, we denote the average of Z_j over side E evaluated at time $t = t_{k+1}$ where we drop the element index K due to the assumption of Z_j being continuous in Ω . The symbols $u_{i,j,K,E}$ and $a_{i,j,K,E}$ denote the coefficients in the basis of $\mathbf{RTN}_0(K)$ of the projection of $\mathbf{u}_{i,j}$ and $\mathbf{a}_{i,j}$ into $\mathbf{RTN}_0(K)$, respectively. In Eq. (15), all coefficients are evaluated at the previous time level t_k or by using the initial condition given by Eq. (2a) at the beginning of the simulation. This includes the upwinded variables $m_{i,E}^{k,upw}$ and $Z_{j,E}^{k,upw}$ defined by

$$m_{i,E}^{k,upw} = \begin{cases} m_{i,K_1}^k & \text{if } v_{i,K_1,E}^k > 0, \\ m_{i,K_2}^k & \text{if } v_{i,K_2,E}^k > 0, \\ 0 & \text{otherwise,} \end{cases} \quad (16a)$$

$$Z_{j,E}^{k,upw} = \begin{cases} Z_{j,K_1}^k & \text{if } a_{i,j,K_1,E} + u_{i,j,K_1,E} > 0, \\ Z_{j,K_2}^k & \text{if } a_{i,j,K_2,E} + u_{i,j,K_2,E} > 0, \\ 0 & \text{otherwise,} \end{cases} \quad (16b)$$

for all interior sides $E \in \mathcal{E}_h^{int}$ such that $E \in \mathcal{E}_{K_1} \cap \mathcal{E}_{K_2}$ and

$$m_{i,E}^{k,upw} = \begin{cases} m_{i,K_1}^k & \text{if } v_{i,K_1,E}^k \geq 0, \\ m_{i,E}^D(t_k) & \text{otherwise,} \end{cases} \quad (16c)$$

$$Z_{j,E}^{k,upw} = \begin{cases} Z_{j,K_1}^k & \text{if } a_{i,j,K_1,E} + u_{i,j,K_1,E} \geq 0, \\ Z_{j,E}^D(t_k) & \text{otherwise,} \end{cases} \quad (16d)$$

for all external sides $E \in \mathcal{E}_h^{ext}$ and $E \in \mathcal{E}_{K_1}$, where $m_{i,E}^D$ and $Z_{j,E}^D$ denote the mean value of the Dirichlet boundary condition for m_i and Z_j over E , respectively, and K_1 and K_2 are the neighboring elements of side E . The upwind technique is used in Eq. (15) to stabilize the numerical approximation of the advection terms [10]. Note that the convection coefficients $\mathbf{a}_{i,j}$ and $\mathbf{u}_{i,j}$ are assumed continuous across side E , i.e.,

$$u_{i,j,K_1,E} + u_{i,j,K_2,E} = 0, \quad a_{i,j,K_1,E} + a_{i,j,K_2,E} = 0, \quad (17)$$

$\forall E \in \mathcal{E}_h^{int} \cap \mathcal{E}_{K_1} \cap \mathcal{E}_{K_2}$. If a negative Neumann boundary condition is prescribed at $E \in \mathcal{E}_h^{ext}$ for $q_{i,K,E} = q_{i,K,E}^N$, a non-zero value of $m_{i,E}^{k,upw}$ (usually unity) must be supplemented.

Following Eq. (12), the velocities $v_{i,K_\ell,E}^k$ in Eq. (16) are considered as

$$v_{i,K_\ell,E}^k = \sum_{j \in \sigma_{i,K_\ell}} \left(b_{i,j,K_\ell,E} Z_{j,K_\ell}^k - \sum_{F \in \mathcal{E}_{K_\ell}} b_{i,j,K_\ell,E,F} Z_{j,F}^k \right) + w_{i,K_\ell,E}, \quad (18)$$

where the coefficients $b_{i,j,K_\ell,E}$, $b_{i,j,K_\ell,E,F}$ and $w_{i,K_\ell,E}$ are evaluated at time t_{k-1} . This will be the basis for the balance equation discussed later in this section which will ensure that the upwind direction is selected based on conservative quantity.

Eq. (15) describes a system of $n \times n_{\mathcal{K}}$ equations for $n \times (n_{\mathcal{K}} + n_{\mathcal{E}})$ unknowns $Z_{j,K}^{k+1}$ and $Z_{j,E}^{k+1}$, where $n_{\mathcal{K}}$ and $n_{\mathcal{E}}$ denote the number of elements and sides in \mathcal{K}_h , respectively. The system of Eqs. (15) is closed by adding $n \times n_{\mathcal{E}}$ equations that represent the balance of the normal components of the conservative fluxes $q_{i,K,E}$ across internal sides $E \in \mathcal{E}_h^{int}$.

Assuming no mass is produced or lost at a common side E of two neighboring elements K_1 and K_2 , the balance of the normal components of \mathbf{q}_i can be written by virtue of Eqs. (7) and (11) as

$$\sum_{\ell=1}^2 m_{i,K_\ell,E}^k \left[\sum_{j \in \sigma_{i,K_\ell}} \left(b_{i,j,K_\ell,E} Z_{j,K_\ell}^{k+1} - \sum_{F \in \mathcal{E}_{K_\ell}} b_{i,j,K_\ell,E,F} Z_{j,F}^{k+1} \right) + w_{i,K_\ell,E} \right] = 0. \quad (19)$$

Eq. (19) can, however, degenerate when one of the terms $m_{i,K_\ell,E}$ (or both) vanishes as, for instance, it is the case for multi-phase flow in porous media. Inspired by the ideas in [3,5], we propose to employ the unique upwinded variable $m_{i,E}^{k,upw}$ at side E instead of $m_{i,K_\ell,E}^k$ in Eq. (19), i.e., $m_{i,E}^{k,upw} = m_{i,K_\ell,E}^k$, $\ell = 1, 2$, allowing us to cancel $m_{i,E}^{k,upw}$ in Eq. (19) if $m_{i,E}^{k,upw} > 0$. Vanishing mobility $m_{i,E}^{k,upw} = 0$ implies that $q_{i,K_\ell,E} = 0$ at side E , $\ell = 1, 2$, thus yielding the value of $Z_{j,F}^{k+1}$ undefined and the resulting system of linear equations singular. To overcome this difficulty, we impose balancing $v_{i,K,E}$ instead of $q_{i,K,E}$ across side E in the form

$$\sum_{\ell=1}^2 \left[\sum_{j \in \sigma_{i,K_\ell}} \left(b_{i,j,K_\ell,E} Z_{j,K_\ell}^{k+1} - \sum_{F \in \mathcal{E}_{K_\ell}} b_{i,j,K_\ell,E,F} Z_{j,F}^{k+1} \right) + w_{i,K_\ell,E} \right] = 0, \quad (20)$$

for all values of $m_{i,E}^k$, i.e., even if the upwinded mobility term is zero. Later in Sections 3 and 4, we demonstrate that this approach works in terms of numerical convergence and accuracy for the selected benchmark problems and computational examples.

2.3. Local system of equations for cell-averages

The combination of the discretized equation (15) and the expression for the conservative velocities given by Eq. (12) allows to express the vector \mathbf{Z}_K^{k+1} containing the cell-averaged unknowns $Z_{j,K}^{k+1}$, $j = 1, \dots, n$, for all $K \in \mathcal{K}_h$, in the matrix form

$$\mathbf{Z}_K^{k+1} = \sum_{F \in \mathcal{E}_K} \mathbf{Q}_K^{-1} \mathbf{R}_{K,F} \mathbf{Z}_F^{k+1} + \mathbf{Q}_K^{-1} \mathbf{R}_K, \quad (21)$$

where the entries of the matrices \mathbf{Q}_K and $\mathbf{R}_{K,F}$ are given by

$$\{\mathbf{Q}_K\}_{ij} = \frac{|K|_d}{\Delta t_k} N_{i,j,K} - \sum_{E \in \mathcal{E}_K} u_{i,j,K,E} + \sum_{E \in \mathcal{E}_K} m_{i,E}^{k,upw} b_{i,j,K,E} + |K|_d r_{i,j,K}, \quad (22a)$$

$$\{\mathbf{R}_{K,F}\}_{ij} = \sum_{E \in \mathcal{E}_K} m_{i,E}^{k,upw} b_{i,j,K,E,F}, \quad (22b)$$

and the components of the vector \mathbf{R}_K are given by

$$\begin{aligned} \{\mathbf{R}_K\}_i = & |K|df_{i,K} + \frac{|K|d}{\Delta t_k} \sum_{j=1}^n N_{i,j,K} Z_{j,K}^k - \sum_{E \in \mathcal{E}_K} m_{i,E}^{k,upw} w_{i,K,E} \\ & - \sum_{j=1}^n \sum_{E \in \mathcal{E}_K} Z_{i,j,E}^{k,upw} (a_{i,j,K,E} + u_{i,j,K,E}). \end{aligned} \quad (22c)$$

As follows from Eq. (21), the coefficients in Eq. (1) must be given such that the matrix \mathbf{Q}_K is non-singular.

2.4. System of equations for side-averages

Using Eq. (21), the cell-averaged variables $Z_{j,K}^{k+1}$ are algebraically eliminated in Eq. (20) and we complete the system by including the boundary conditions (2b). As a result, we obtain a global system of linear equations for the unknown side-averaged variables $Z_{j,F}^{k+1}$ for all $F \in \mathcal{E}_h^{int}$ that can be represented in the matrix form as

$$\mathbf{M}\mathbf{Z}^{k+1} = \mathbf{b}, \quad (23)$$

where $\mathbf{Z}^{k+1} = \{Z_F^{k+1}\}_{F \in \mathcal{E}_h} = \{Z_{j,F}^{k+1}\}_{j=1}^n \}_{F \in \mathcal{E}_h}$ is the vector of $n \times n_E$ unknowns. As follows from Eq. (20) and the definition of the coefficients $b_{i,K,E,F}$, the non-singularity of the sparse matrix \mathbf{M} is determined by the choice of coefficients in Eq. (1). In particular, \mathbf{M} is positive definite if the matrix of tensors $\{\mathbf{D}_{ij}\}_{i,j=1}^n$ is positive definite. Note that Eq. (23) is the only global linear system (of $n \times n_E$ equations) that needs to be solved in order to proceed from t_k to the next time level t_{k+1} . Based on the computed $\mathbf{Z}^{k+1} = \mathbf{M}^{-1}\mathbf{b}$, we use Eq. (21) to compute $Z_{j,K}^{k+1}$ which completes the time step $t_k \rightarrow t_{k+1}$.

2.5. Barrier condition implementation

In applications such as two-phase flow in a porous medium with material discontinuities, a zero flux condition for one of the equations in Eq. (1) are required at some interior sides, typically placed at material interfaces. When this is the case, instead of balancing the velocities from K_1 and K_2 in Eq. (20), we consider the following zero flux condition

$$\sum_{j=1}^n \left(b_{i,j,K,E} Z_{j,K}^{k+1} - \sum_{F \in \mathcal{E}_K} b_{i,j,K,E,F} Z_{j,F}^{k+1} \right) + w_{i,K,E} = 0, \quad (24)$$

where K denotes the element from which the zero flux condition is required. The application of the barrier condition given by Eq. (24) is further discussed in Section 3.2.

2.6. Computational algorithm

The computational algorithm of the numerical solution can be summarized in the following order:

1. Set $k = 0$ and use Eq. (2a) to initialize $Z_{j,K}^0$ for all $K \in \mathcal{K}_h$ and $j = 1, \dots, n$.
2. Repeat the following steps until the final time of the simulation is reached.
 - (a) Update the discrete coefficients $N_{i,j,K}$, $u_{i,j,K,E}$, $m_{i,K}$, $w_{i,K,E}$, $a_{i,j,K,E}$, $r_{i,j,K}$, $f_{i,K}$ for all $i, j = 1, \dots, n$, $K \in \mathcal{K}_h$ and $E \in \mathcal{E}_K$.
 - (b) Update the coefficients of upwinded variables $m_{i,E}^{upw}$ and $Z_{i,j,E}^{upw}$ according to Eq. (16) for all $E \in \mathcal{E}_h$ and $i, j = 1, \dots, n$.
 - (c) Compute the mesh-dependent coefficients of matrices $\mathbf{b}_{i,j,K}$ for all $K \in \mathcal{K}_h$ and $i, j = 1, \dots, n$.

- (d) Based on $Z_{j,K}^k$ from the previous time t_k , use Eq. (22) to compute the coefficients of matrices \mathbf{Q}_K , $\mathbf{R}_{K,F}$ and vectors \mathbf{R}_K and compute the inverses $\mathbf{Q}_K^{-1}\mathbf{R}_{K,F}$, $\mathbf{Q}_K^{-1}\mathbf{R}_K$ needed in Eq. (21) for all $K \in \mathcal{K}_h$ and $F \in \mathcal{E}_K$.
- (e) Assemble \mathbf{M} and \mathbf{b} in Eq. (23) using Eq. (20) and boundary conditions (2b).
- (f) Solve the linear system given by Eq. (23) to obtain $Z_{j,E}^{k+1}$, $E \in \mathcal{E}_h$ and $j = 1, \dots, n$.
- (g) Compute $Z_{j,K}^{k+1}$ using Eq. (21) for all $K \in \mathcal{K}_h$ and $j = 1, \dots, n$.
- (h) Set $t_{k+1} = t_k + \Delta t_k$ and set $k := k + 1$.

For simplicity, we assume that the temporal discretization of the numerical scheme is given by the set $\{t_k\}$. However, an adaptive time stepping strategy can be implemented for each particular application of the numerical scheme. Here, for the sake of brevity, we use constant time stepping strategy only.

2.7. Implementation on CPU

On CPU, the resolution of many local linear systems in Eq. (22) (per elements $K \in \mathcal{K}_h$) is done using the LAPACK package [11] or using a custom implementation of the LU decomposition. The global sparse linear system in Eq. (23) is resolved with either direct solvers from UMFPACK [12] or iterative solvers from TNL where common iterative methods such as (restarted) GMRES or BiCGStab with Jacobi or ILU preconditioners are implemented. In TNL, a parallel implementation of GMRES is also available for multicore CPUs using OpenMP.

2.8. Parallel implementation on GPU

All steps of the computational algorithm summarized in Section 2.6 can be implemented entirely on GPU. The steps 2b, 2a, 2c and 2g of the computational algorithm involve local computations on element $K \in \mathcal{K}_h$ that are independent of data stored in other elements in \mathcal{K}_h and thus their implementation on GPU is straightforward: we map one CUDA thread either to each element $K \in \mathcal{K}_h$ (steps 2a, 2c, and 2g) or side $E \in \mathcal{E}_h$ (step 2b). All supporting algorithms and data structures, including unstructured meshes [13], are implemented in TNL.

In step 2d, the local matrices \mathbf{Q}_K are usually small ($n \times n$) and they can be discarded after the evaluation of $\mathbf{Q}_K^{-1}\mathbf{R}_{K,F}$ and $\mathbf{Q}_K^{-1}\mathbf{R}_K$. Hence, we map one CUDA thread per element $K \in \mathcal{K}_h$, allocate the matrices in the fast on-chip shared memory and write only the results $\mathbf{Q}_K^{-1}\mathbf{R}_{K,F}$ and $\mathbf{Q}_K^{-1}\mathbf{R}_K$ into the much slower global memory. The inversions are resolved using the LU factorization of the matrix \mathbf{Q}_K .

Regarding the assembly of the global sparse matrix in step 2e, the choice of MHFEM is advantageous for the GPU architecture because degrees of freedom are associated with mesh sides $E \in \mathcal{E}_h$ rather than vertices $V \in \mathcal{V}_h$ as is the case of the standard finite element method (FEM) with Lagrangian elements. Hence, the MHFEM assembly involves accessing at most two neighboring elements per row, which significantly reduces the number of conflicts between elements contributing to the same non-zero matrix elements. Note that several approaches for assembling FEM on GPU were investigated in [14–17], but only some of them are applicable to MHFEM. Most importantly, the element data computed in step 2d are used to construct the global sparse matrix and then reused in step 2g, so the *Local* and *Shared* approaches from [14], which discard the element data after the matrix assembly, would cause significant computational redundancy. Of the remaining approaches, we have implemented a *row-by-row* assembly which avoids conflicts between elements and provides more work per thread compared to the *non-zero* approach from [14].

Another advantage of MHFEM is that if the mesh consists of the same type of elements, the resulting linear system has the same number of non-zero matrix elements in each row (except for the rows associated with the domain boundaries). This is advantageous for GPUs because it avoids insertion of padding zeros to the sparse matrix storage format as well as divergent threads during the sparse matrix–vector multiplication. The sparse matrix is represented in the Sliced ELLPACK (SELLPACK) format [18], whose GPU-optimized implementation is available in TNL.

The resolution of the linear system in step 2f is the computationally most demanding part of the algorithm. The system is solved using the (restarted) GMRES(s) method [19,20] which can be implemented efficiently on GPU by replacing the traditional modified Gram–Schmidt procedure with Householder transformations and using the compact WY representation (CWY) [21] to express the products of Householder transformations in terms of dense matrix multiplications. Similar technique was proposed in [22] and tested in [23,24]. In order to reduce the number of iterations needed for the GMRES method, we use the Jacobi (diagonal) preconditioner and the adaptive strategy for the selection of the restarting parameter proposed in [25].

3. Two-phase flow in porous media

We use the numerical scheme presented above to solve the two-phase flow equations in porous media. First, in order to investigate the convergence, accuracy, and efficiency of the numerical scheme implementation, we perform a numerical analysis using exact (semi-analytical) solutions available for two-phase flow in homogeneous porous medium for 1D, 2D, and 3D. Then, we use two benchmark problems for flow across material discontinuities in heterogeneous porous media to demonstrate the need of using the mass-lumping technique discussed in Section 2.1 as well as the barrier condition discussed in Section 2.5.

We set $n = 2$ for the number of equations in Eq. (1) and use the vector \mathbf{Z} to represent the primary unknown variables $\mathbf{Z} = (p_w, p_n)^T$. The non-zero coefficients in (1) describing the incompressible and immiscible two-phase in isotropic porous medium are evaluated as follows:

$$\mathbf{N} = \begin{pmatrix} -\phi \frac{\partial S_w}{\partial p_c} & \phi \frac{\partial S_w}{\partial p_c} \\ \phi \frac{\partial S_w}{\partial p_c} & -\phi \frac{\partial S_w}{\partial p_c} \end{pmatrix}, \quad (25a)$$

$$\mathbf{m} = \begin{pmatrix} \frac{\lambda_w}{\lambda_t} & \frac{\lambda_n}{\lambda_t} \\ \frac{\lambda_t}{\lambda_t} & \frac{\lambda_t}{\lambda_t} \end{pmatrix}^T, \quad (25b)$$

$$\mathbf{D} = \begin{pmatrix} \lambda_t \mathbf{KI} & \mathbf{0} \\ \mathbf{0} & \lambda_t \mathbf{KI} \end{pmatrix}, \quad (25c)$$

$$\mathbf{w} = (\lambda_t \rho_w \mathbf{Kg}, \quad \lambda_t \rho_n \mathbf{Kg})^T, \quad (25d)$$

where ϕ [1] is the porosity, K [L^2] is the intrinsic permeability, \mathbf{g} [LT^{-2}] is the gravitational acceleration vector. The symbols ρ_α [ML^{-3}], S_α [1], λ_α [$ML^{-1}T^{-1}$], and p_α [$ML^{-1}T^{-2}$] stand for the α -phase density, volumetric saturation, mobility, and pressure, respectively, where $\alpha \in \{w, n\}$. The α -phase mobility is defined as $\lambda_\alpha = k_{r,\alpha}/\mu_\alpha$, where $k_{r,\alpha}$ [1] is the relative permeability and μ_α [$ML^{-1}T^{-1}$] is the dynamic viscosity of the phase α .

The relative permeability functions $k_{r,w}$ and $k_{r,n}$ are assumed to be nonlinear functions of the wetting phase saturation S_w and the empirical models by Burdine [26] and Mualem [27] are employed, cf. Eqs. (C.3) and (C.4), respectively. The wetting phase saturation S_w is related to the difference between the phase pressures, defined as the capillary pressure $p_c = p_n - p_w$, as $S_w = S_w(p_c)$ and the Brooks and Corey (B&C) [28] and van Genuchten (vG) [29] empirical models are employed, cf. Eqs. (C.1) and (C.2), respectively. In

Eq. (25), $\lambda_t = \lambda_w + \lambda_n$ denotes the total mobility. Additionally, by

$$\mathbf{v}_\alpha = -\lambda_\alpha K (\nabla p_\alpha - \rho_\alpha \mathbf{g}), \quad (26)$$

we denote the α -phase Darcy velocity, $\alpha \in \{w, n\}$.

3.1. Numerical analysis: flow in homogeneous porous medium without gravity

For homogeneous porous media with neglected gravitational effects, exact (semi-analytical) solutions can be derived that include effects of both diffusion and advection. For one- and two-dimensional cases, these are the well known semi-analytical solutions by McWhorter and Sunada [30,31]. Recently, the work of the first author showed that the semi-analytical solution can be obtained also for the three-dimensional case [32]. In 2D and 3D, the exact solutions are derived for radially symmetric problems with a point injection source placed at the origin of the coordinate system.

By means of the L_p norms of the error of the numerical solution denoted by E_{h,S_n} and the experimental order of convergence $eoc_{S_n,p}$ (for $p = 1, 2$) evaluated at the final time of the simulation T , we investigate the accuracy and convergence of the numerical scheme in all dimensions $d = 1, 2, 3$. Definitions of E_{h,S_n} and $eoc_{S_n,p}$ are given in Appendix A. For the numerical analysis presented in this section, we employ the non-wetting saturation S_n for which the semi-analytical solution is known.

The setup of the computational domain is depicted in Fig. 1. To optimize computational resources, we take advantage of the radial symmetry of the exact solution [32] and consider a quarter and an eighth of the computational domain instead of the full geometry in 2D and 3D, respectively. For 1D, 2D, and 3D cases, we use the same material denoted as Sand A (see Table C.8) and fluid properties of water and DNAPL₂ (see Table C.7). Since both B&C and vG empirical properties are available for Sand A based on [33], we compare results for both of these models in the numerical analysis.

At $t = 0$, the saturation of water in the computational domain is $S_w^{\text{ini}} = 0.95$ and through a point source placed at the origin $\mathbf{x} = \mathbf{0}$, the injection of the non-wetting phase begins. Based on [32], the volumetric rate of DNAPL₂ injected through the point source, denoted by Q_0 [$L^d T^{-1}$], is given by

$$Q_0 = Q_0(t) = A_d t^{\frac{d-2}{2}}, \quad (27)$$

where A_d [$L^d T^{-\frac{d}{2}}$] denotes the volumetric injection rate parameter. The values of A_d , the final simulation time T , and the domain dimensions are selected such that for both B&C and vG models, the non-wetting phase saturation profile does not reach the neighborhood of the boundaries that approximate boundaries placed in infinity (see Fig. 1). We consider the dimensions of the computational domain as shown in Fig. 1, we fix $T = 20\,000$ s, and we select the following values of A_d : $A_1 = 3 \cdot 10^{-4} \text{ ms}^{-\frac{1}{2}}$, $A_2 = 10^{-5} \text{ m}^2 \text{ s}^{-1}$, and $A_3 = 10^{-7} \text{ m}^3 \text{ s}^{-\frac{3}{2}}$. In 1D, A_1 is related to the inlet boundary saturation S_w^0 as described in [30,31], here, $S_w^0 = 0.378$ for the B&C and $S_w^0 = 0.427$ for the vG models, respectively.

As follows from the derivation of the numerical scheme, the point source boundary condition at the origin cannot be treated directly by the numerical scheme but it has to be approximated by all elements adjacent to the origin $\mathbf{x} = \mathbf{0}$ as shown in Fig. 2 where the injection part of the domain boundary $\Gamma = \partial\Omega$ is denoted by Γ_{in} . At Γ_{in} , we prescribe a zero Neumann boundary condition for the wetting phase velocity and a non-zero Neumann boundary condition for the non-wetting phase velocity \mathbf{v}_n such that

$$\int_{\Gamma_{\text{in}}} \mathbf{v}_n \cdot \mathbf{n} = -Q_0(t), \quad \forall t \in [0, T]. \quad (28)$$

The remaining boundary conditions are shown in Fig. 1.

In Table 1, we show results of the numerical analysis for segments, rectangles, triangles, cuboids, and tetrahedrons, respectively, for both B&C and vG models. For each case, a series of

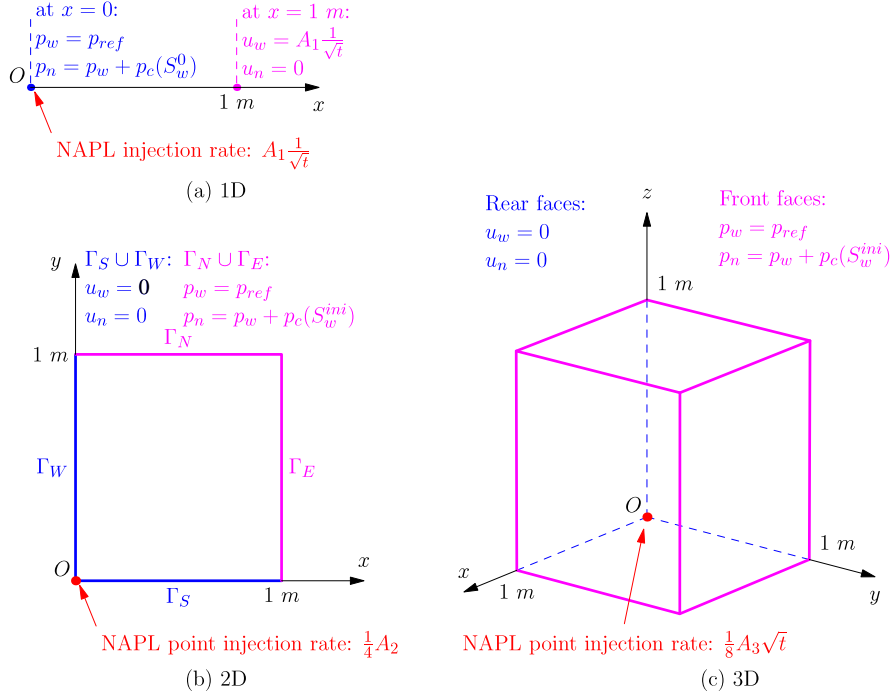


Fig. 1. Setup of the computational domain with boundary conditions for (a) 1D, (b) 2D, and (c) 3D cases, respectively.

Table 1
Results of the numerical analysis using the L_1 and L_2 norms of E_{h,S_n} .

Id.	Brooks & Corey				van Genuchten			
	$\ E_{h,S_n}\ _1$	$eoc_{S_n,1}$	$\ E_{h,S_n}\ _2$	$eoc_{S_n,2}$	$\ E_{h,S_n}\ _1$	$eoc_{S_n,1}$	$\ E_{h,S_n}\ _2$	$eoc_{S_n,2}$
1D ₁	$6.04 \cdot 10^{-3}$	0.94	$1.56 \cdot 10^{-2}$	0.61	$3.45 \cdot 10^{-3}$	1.21	$5.06 \cdot 10^{-3}$	1.26
1D ₂	$3.14 \cdot 10^{-3}$	0.91	$1.02 \cdot 10^{-2}$	0.70	$1.49 \cdot 10^{-3}$	1.04	$2.11 \cdot 10^{-3}$	1.02
1D ₃	$1.67 \cdot 10^{-3}$	0.92	$6.28 \cdot 10^{-3}$	0.72	$7.24 \cdot 10^{-4}$	1.01	$1.04 \cdot 10^{-3}$	1.01
1D ₄	$8.83 \cdot 10^{-4}$	0.92	$3.80 \cdot 10^{-3}$	0.69	$3.59 \cdot 10^{-4}$	1.00	$5.17 \cdot 10^{-4}$	1.01
1D ₅	$4.67 \cdot 10^{-4}$	0.95	$2.35 \cdot 10^{-3}$	0.84	$1.79 \cdot 10^{-4}$	0.98	$2.57 \cdot 10^{-4}$	0.96
1D ₆	$2.42 \cdot 10^{-4}$	0.96	$1.31 \cdot 10^{-3}$	0.89	$9.06 \cdot 10^{-5}$	0.91	$1.32 \cdot 10^{-4}$	0.80
1D ₇	$1.24 \cdot 10^{-4}$		$7.05 \cdot 10^{-4}$		$4.83 \cdot 10^{-5}$		$7.56 \cdot 10^{-5}$	
2D ₁ [□]	$1.52 \cdot 10^{-2}$	0.80	$3.26 \cdot 10^{-2}$	0.65	$1.41 \cdot 10^{-2}$	0.84	$2.17 \cdot 10^{-2}$	0.81
2D ₂ [□]	$8.75 \cdot 10^{-3}$	0.82	$2.08 \cdot 10^{-2}$	0.62	$7.88 \cdot 10^{-3}$	0.87	$1.24 \cdot 10^{-2}$	0.86
2D ₃ [□]	$4.97 \cdot 10^{-3}$	0.85	$1.35 \cdot 10^{-2}$	0.60	$4.31 \cdot 10^{-3}$	0.88	$6.83 \cdot 10^{-3}$	0.88
2D ₄ [□]	$2.76 \cdot 10^{-3}$	0.87	$8.93 \cdot 10^{-3}$	0.63	$2.34 \cdot 10^{-3}$	0.86	$3.72 \cdot 10^{-3}$	0.85
2D ₅ [□]	$1.51 \cdot 10^{-3}$		$5.79 \cdot 10^{-3}$		$1.29 \cdot 10^{-3}$		$2.06 \cdot 10^{-3}$	
2D ₁ [△]	$1.45 \cdot 10^{-2}$	0.92	$3.17 \cdot 10^{-2}$	0.78	$1.42 \cdot 10^{-2}$	0.98	$2.12 \cdot 10^{-2}$	0.94
2D ₂ [△]	$7.94 \cdot 10^{-3}$	0.78	$1.91 \cdot 10^{-2}$	0.60	$7.51 \cdot 10^{-3}$	0.86	$1.15 \cdot 10^{-2}$	0.84
2D ₃ [△]	$4.40 \cdot 10^{-3}$	0.95	$1.21 \cdot 10^{-2}$	0.69	$3.93 \cdot 10^{-3}$	1.05	$6.11 \cdot 10^{-3}$	1.03
2D ₄ [△]	$2.41 \cdot 10^{-3}$	0.85	$7.84 \cdot 10^{-3}$	0.66	$2.03 \cdot 10^{-3}$	0.90	$3.19 \cdot 10^{-3}$	0.89
2D ₅ [△]	$1.30 \cdot 10^{-3}$		$4.85 \cdot 10^{-3}$		$1.06 \cdot 10^{-3}$		$1.68 \cdot 10^{-3}$	
3D ₁ [□]	$8.28 \cdot 10^{-3}$	0.83	$2.59 \cdot 10^{-2}$	0.70	$8.15 \cdot 10^{-3}$	0.88	$1.64 \cdot 10^{-2}$	0.86
3D ₂ [□]	$4.67 \cdot 10^{-3}$	0.84	$1.59 \cdot 10^{-2}$	0.69	$4.42 \cdot 10^{-3}$	0.90	$9.06 \cdot 10^{-3}$	0.89
3D ₃ [□]	$2.60 \cdot 10^{-3}$	0.86	$9.87 \cdot 10^{-3}$	0.69	$2.36 \cdot 10^{-3}$	0.93	$4.90 \cdot 10^{-3}$	0.92
3D ₄ [□]	$1.44 \cdot 10^{-3}$		$6.12 \cdot 10^{-3}$		$1.24 \cdot 10^{-3}$		$2.58 \cdot 10^{-3}$	
3D ₁ [△]	$1.12 \cdot 10^{-2}$	0.69	$3.38 \cdot 10^{-2}$	0.60	$1.21 \cdot 10^{-2}$	0.77	$2.43 \cdot 10^{-2}$	0.73
3D ₂ [△]	$7.82 \cdot 10^{-3}$	0.84	$2.47 \cdot 10^{-2}$	0.72	$8.13 \cdot 10^{-3}$	0.93	$1.66 \cdot 10^{-2}$	0.90
3D ₃ [△]	$4.35 \cdot 10^{-3}$	1.03	$1.49 \cdot 10^{-2}$	0.92	$4.25 \cdot 10^{-3}$	1.14	$8.84 \cdot 10^{-3}$	1.12
3D ₄ [△]	$2.37 \cdot 10^{-3}$	0.82	$8.63 \cdot 10^{-3}$	0.79	$2.17 \cdot 10^{-3}$	1.04	$4.56 \cdot 10^{-3}$	1.02
3D ₅ [△]	$1.41 \cdot 10^{-3}$		$5.23 \cdot 10^{-3}$		$1.12 \cdot 10^{-3}$		$2.39 \cdot 10^{-3}$	

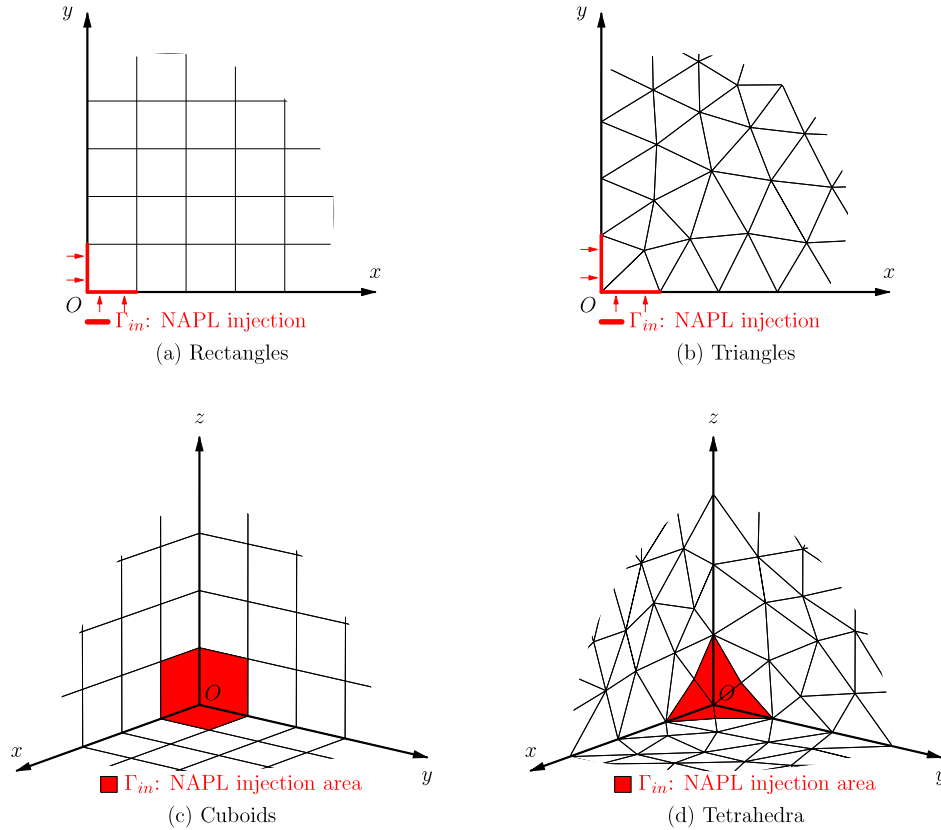


Fig. 2. Approximation of the point injection boundary condition at $x = 0$ for (a) rectangles, (b) triangles, (c) cuboids, and (d) tetrahedra elements, respectively.

meshes was generated such that the mesh size parameter h is consecutively reduced approximately by the factor of 2. The computed experimental orders of convergence indicate that the numerical scheme converges with the first order of accuracy in all dimensions. As listed in the tables, different strategies for the choice of the constant time step τ had to be used in 1D, 2D, and 3D to ensure the numerical convergence.

The computational times CT [s], multicore CPU efficiency Eff [1], and GPU speed-up GSp [1] in [Tables 2](#) and [3](#) demonstrate the advantages of the parallel implementation of the MHFEM numerical scheme on GPU. Additionally, we show the performance of two GMRES(s) variants: using the modified Gram–Schmidt procedure with re-orthogonalization (MGSR) or using the compact WY representation (CWY) as discussed in [Section 2.8](#). The computational analysis was performed on 2D rectangular and triangular meshes and 3D cuboidal and tetrahedral meshes using the B&C model for which the results of the numerical analysis are given in [Table 1](#). For the comparison, we used Nvidia Tesla K40 GPU (with 2880 cores, 12 GB GDDR5 global memory) and Intel Core i7-5820K CPU (with 6 cores and 12 threads). In order to obtain distortionless CPU computational times, the Intel Turbo Boost Technology was disabled on the CPU during computations. The efficiency index Eff quantifies the parallel scalability of the numerical scheme on multicore CPU using OpenMP with ℓ -threads as

$$Eff = \frac{CT \text{ for 1 thread}}{\ell \times (CT \text{ for } \ell \text{ threads})}. \quad (29)$$

The GPU speed-up GSp is the ratio between the CPU and GPU computational times.

The CWY variant of GMRES is substantially faster than MGSR on GPU as shown in [Tables 2](#) and [3](#). When compared to the single-threaded CPU, the GPU speed-up GSp for grids rises above 20 or 24 and above 5 or 7 for the six-threaded CPU for finer meshes in 2D or 3D, respectively. The speed-ups for unstructured meshes in [Tables 2b](#) and [3b](#) are slightly lower compared to structured grids in [Tables 2a](#) and [3a](#).

Additionally in [Appendix D](#), we illustrate the computational accuracy and performance of the proposed MHFEM approach in comparison with the fully time-implicit box method implemented using the DuMu^x project [\[34\]](#).

3.2. Flow in heterogeneous porous media

In heterogeneous porous media, mathematical modeling of two-phase flow across sharp material discontinuities requires a careful treatment that includes the capillary barrier effect (or the extended capillary pressure condition) at material interfaces as reported by [\[35,36\]](#). In brief, the capillary barrier condition describes a phenomenon where the non-wetting phase cannot penetrate into a finer material until its capillary pressure reaches the entry capillary pressure of the finer material.

We use two benchmark problems in 1D (denoted as BP_1) and 2D (denoted as BP_2) from [\[35,37\]](#) that consider a gravity induced

Table 2

Comparison of the computational time *CT*, multicore CPU efficiency index *Eff*, and GPU speed-up *GSp* of the numerical scheme solver in 2D using the problem described in Section 3.1.

(a) 2D grids														
	Id.	GPU		CPU										
		<i>CT</i>		1 thread			2 threads			4 threads			6 threads	
				<i>CT</i>	<i>GSp</i>	<i>CT</i>	<i>Eff</i>	<i>GSp</i>	<i>CT</i>	<i>Eff</i>	<i>GSp</i>	<i>CT</i>	<i>Eff</i>	<i>GSp</i>
MGSR	2D ₁ [□]	5.1		0.6	0.12	0.7	0.45	0.13	0.8	0.19	0.15	0.9	0.11	0.17
	2D ₂ [□]	28.1		11.5	0.41	7.9	0.72	0.28	6.4	0.45	0.23	6.8	0.28	0.24
	2D ₃ [□]	117.1		173.6	1.48	95.9	0.91	0.82	61.2	0.71	0.52	52.8	0.55	0.45
	2D ₄ [□]	740		4024	5.43	2154	0.93	2.91	1192	0.84	1.61	942	0.71	1.27
	2D ₅ [□]	8237		82324	9.99	47982	0.86	5.82	26919	0.76	3.27	19916	0.69	2.42
CWY	2D ₁ [□]	1.5		0.7	0.45	0.4	0.79	0.28	0.3	0.52	0.22	0.3	0.41	0.18
	2D ₂ [□]	11.0		13.2	1.20	7.6	0.87	0.69	4.8	0.68	0.44	4.0	0.55	0.37
	2D ₃ [□]	46.3		197.0	4.25	107.5	0.92	2.32	65.7	0.75	1.42	52.6	0.62	1.14
	2D ₄ [□]	380		4326	11.38	2361	0.92	6.21	1448	0.75	3.81	1196	0.60	3.15
	2D ₅ [□]	4450		91166	20.49	49004	0.93	11.01	29182	0.78	6.56	24684	0.62	5.55
(b) 2D unstructured meshes														
	Id.	GPU		CPU										
		<i>CT</i>		1 thread			2 threads			4 threads			6 threads	
				<i>CT</i>	<i>GSp</i>	<i>CT</i>	<i>Eff</i>	<i>GSp</i>	<i>CT</i>	<i>Eff</i>	<i>GSp</i>	<i>CT</i>	<i>Eff</i>	<i>GSp</i>
MGSR	2D ₁ [△]	4.7		0.3	0.07	0.5	0.33	0.11	0.5	0.18	0.10	0.6	0.09	0.13
	2D ₂ [△]	22.4		5.0	0.22	3.9	0.65	0.17	3.1	0.40	0.14	3.6	0.23	0.16
	2D ₃ [△]	120.0		98.5	0.82	59.5	0.83	0.50	38.3	0.64	0.32	35.7	0.46	0.30
	2D ₄ [△]	778		2383	3.06	1299	0.92	1.67	701	0.85	0.90	574	0.69	0.74
	2D ₅ [△]	7388		45953	6.22	25512	0.90	3.45	14603	0.79	1.98	11976	0.64	1.62
CWY	2D ₁ [△]	1.5		0.4	0.27	0.3	0.60	0.22	0.2	0.45	0.15	0.2	0.32	0.14
	2D ₂ [△]	8.9		6.2	0.70	3.7	0.84	0.42	2.3	0.66	0.26	2.0	0.52	0.23
	2D ₃ [△]	51.1		122.0	2.39	67.7	0.90	1.32	40.3	0.76	0.79	32.5	0.63	0.64
	2D ₄ [△]	396		2696	6.80	1481	0.91	3.74	855	0.79	2.16	672	0.67	1.70
	2D ₅ [△]	4008		57404	14.32	32101	0.89	8.01	18814	0.76	4.69	16414	0.58	4.09

Table 3

Comparison of the computational time *CT*, multicore CPU efficiency index *Eff*, and GPU speed-up *GSp* of the numerical scheme solver in 3D using the problem described in Section 3.1.

(a) 3D grids														
	Id.	GPU		CPU										
		<i>CT</i>		1 thread			2 threads			4 threads			6 threads	
				<i>CT</i>	<i>GSp</i>	<i>CT</i>	<i>Eff</i>	<i>GSp</i>	<i>CT</i>	<i>Eff</i>	<i>GSp</i>	<i>CT</i>	<i>Eff</i>	<i>GSp</i>
MGSR	3D ₁ [□]	5.9		13.8	2.34	7.2	0.96	1.22	4.3	0.80	0.73	3.4	0.67	0.58
	3D ₂ [□]	55.7		524.6	9.42	304.7	0.86	5.47	173.7	0.76	3.12	128.2	0.68	2.30
	3D ₃ [□]	1234		21129	17.12	12771	0.83	10.35	7317	0.72	5.93	6242	0.56	5.06
	3D ₄ [□]	44798				(not computed on 1, 2 and 4 threads)						272104		6.07
CWY	3D ₁ [□]	2.1		15.2	7.30	8.0	0.96	3.82	4.4	0.86	2.13	3.4	0.75	1.62
	3D ₂ [□]	30.8		564.3	18.33	319.5	0.88	10.38	186.7	0.76	6.07	150.3	0.63	4.88
	3D ₃ [□]	828		20570	24.84	12406	0.83	14.98	7093	0.73	8.57	5534	0.62	6.68
	3D ₄ [□]	31806				(not computed on 1, 2 and 4 threads)						234066		7.36
(b) 3D unstructured meshes														
	Id.	GPU		CPU										
		<i>CT</i>		1 thread			2 threads			4 threads			6 threads	
				<i>CT</i>	<i>GSp</i>	<i>CT</i>	<i>Eff</i>	<i>GSp</i>	<i>CT</i>	<i>Eff</i>	<i>GSp</i>	<i>CT</i>	<i>Eff</i>	<i>GSp</i>
MGSR	3D ₁ [△]	3.8		1.7	0.44	1.2	0.71	0.31	0.8	0.53	0.21	0.8	0.33	0.22
	3D ₂ [△]	6.1		7.2	1.19	4.3	0.84	0.70	2.6	0.70	0.43	2.3	0.53	0.37
	3D ₃ [△]	45.3		274.5	6.06	152.6	0.90	3.37	87.5	0.78	1.93	72.4	0.63	1.60
	3D ₄ [△]	873		11270	12.91	6228	0.90	7.13	3415	0.83	3.91	3188	0.59	3.65
	3D ₅ [△]	55880				(not computed on 1, 2 and 4 threads)						298810		5.35
CWY	3D ₁ [△]	1.4		2.0	1.48	1.2	0.85	0.88	0.7	0.68	0.54	0.6	0.54	0.46
	3D ₂ [△]	2.6		8.7	3.30	4.9	0.89	1.85	2.9	0.75	1.10	2.3	0.64	0.86
	3D ₃ [△]	23.9		330.9	13.87	184.8	0.90	7.75	107.9	0.77	4.53	93.4	0.59	3.92
	3D ₄ [△]	566		12070	21.32	6506	0.93	11.49	3771	0.80	6.66	3306	0.61	5.84
	3D ₅ [△]	37695				(not computed on 1, 2 and 4 threads)						201786		5.35

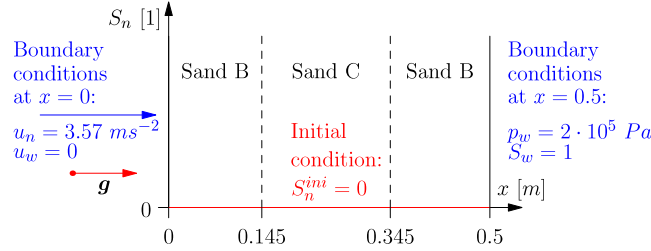


Fig. 3. Setup and the boundary and initial conditions of the benchmark problem BP₁ in 1D based on [35].

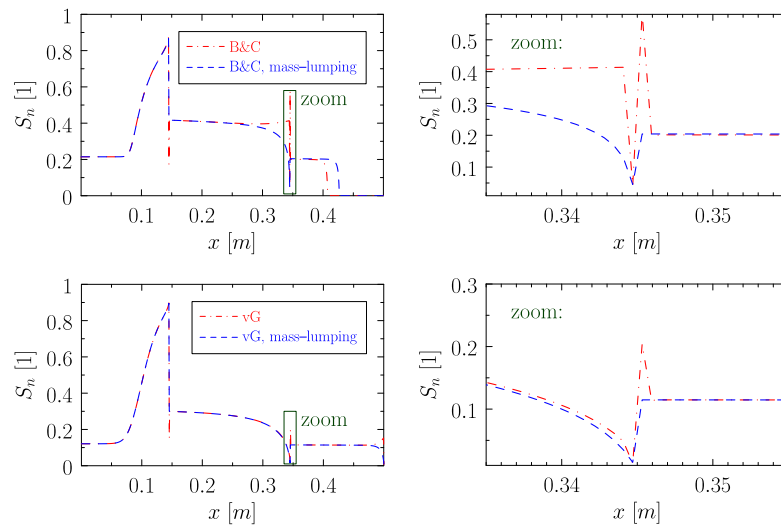


Fig. 4. Example behavior of the numerical solution across material discontinuities when the mass-lumping technique is or is not employed for the barrier effect benchmark problem in 1D. Top and bottom figures correspond to the B&C and vG models, respectively.

imbibition of a dense non-aqueous phase liquid (DNAPL) into a fully water saturated domain. We demonstrate how the numerical solution behaves at material discontinuities with and without using (a) the mass lumping technique (in BP₁) and (b) the capillary barrier condition (in BP₂) described in Sections 2.1 and 2.5, respectively.

The setup together with the boundary and initial conditions of the first benchmark problem BP₁ are shown in Fig. 3 with the material properties given in Table C.8. The fluid properties used in BP₁ are given in Table C.7: the wetting and non-wetting phases are water and DNAPL₁, respectively. The gravity acts along the x -axis. At material discontinuities placed at $x = 0.145$ m and $x = 0.345$ m, the spatial profile of S_n exhibits a jump across the interfaces as shown in Fig. 4 where the numerical solutions for both B&C and vG models are shown at $t = 1650$ s. When the mass-lumping technique is employed, the numerical solution of S_n matches the results in [35], pages 286 and 289. Without this technique, the saturation profiles are approximated incorrectly especially at the material interface at $x = 0.345$ m where the non-wetting fluid flows from the finer to the coarser material. In higher dimensions, we have observed the same behavior and a mass-lumping technique based on [9] needs to be employed.

The second benchmark problem BP₂ consists of a 2D computational domain illustrated in Fig. 5 with the boundary conditions for

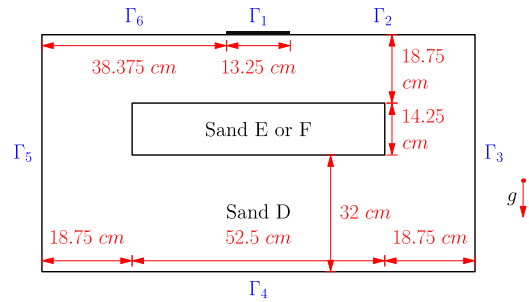


Fig. 5. Setup of the benchmark problem BP₂ based on [37].

all $t \in [0, T]$:

$$\mathbf{v}_n \cdot \mathbf{n} = -5.13 \cdot 10^{-5} \text{ m s}^{-1} \quad \text{and} \quad \mathbf{v}_w \cdot \mathbf{n} = 0 \quad \text{on } \Gamma_1, \quad (30a)$$

$$p_w = 10^5 \text{ Pa} \quad \text{and} \quad S_w = 1 \quad \text{on } \Gamma_3 \cup \Gamma_5, \quad (30b)$$

$$\mathbf{v}_n \cdot \mathbf{n} = 0 \quad \text{and} \quad \mathbf{v}_w \cdot \mathbf{n} = 0 \quad \text{on } \Gamma_2 \cup \Gamma_4 \cup \Gamma_6, \quad (30c)$$

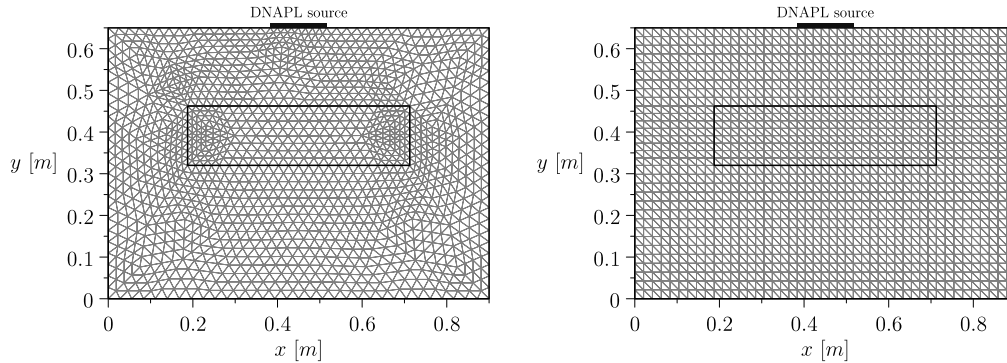


Fig. 6. Illustration of the unstructured (a) and structured (b) meshes in 2D consisting of 2880 elements used in the benchmark problem BP₂.

and the initial condition: $S_w(0, \mathbf{x}) = 1$ for all $\mathbf{x} \in \Omega$. The material properties of sands D, E, and F are given in Table C.8. The fluids used in the simulations are water and DNAPL₂ with the parameters given in Table C.7. The gravity acts in the negative direction of the y-axis. The purpose of BP₂ is to investigate whether the barrier effect has been simulated properly. Based on the material properties of the buried lens consisting of either coarser sand E or finer sand F, the non-wetting phase infiltrates into or pools around the lens, respectively. In [5], a similar approach to solving the two-phase flow equations in heterogeneous porous media using an implicit pressure-explicit saturation (IMPES) variant of the MHFEM was presented. The authors concluded that the numerical scheme is able to handle flows across material interfaces without any explicit implementation of the extended capillary pressure condition. For some particular (structured) meshes, we found that this is not the case when the barrier effect occurs.

In Figs. 7 and 8, we show a series of numerical solutions of S_n at $t = 4500$ s for both unstructured (left columns) and structured (right columns) meshes where the first two rows of figures demonstrate numerical convergence using a coarser and a finer mesh and the last row contains results computed using the barrier condition. In Fig. 6, we show two examples of unstructured (a) and structured (b) meshes that both consist of 2880 elements.

For the coarser lens (sand E), the numerical results in Fig. 7a–d using the unstructured and structured meshes are comparable with the results in [37], page 211. Therefore, it may seem that no explicit implementation of the barrier condition is required in accordance with the findings by [5]. For the finer lens (sand F), however, the numerical solution is strongly mesh-dependent as shown in Fig. 8b and d, where the majority of the non-wetting phase is deflected side-wise following the orientation of the structured mesh. As shown in Fig. 8d, such apparently incorrect solution converges numerically as the mesh is further refined indicating that the non-symmetry of the solution is not caused by coarseness of the mesh. For unstructured meshes, such as the one shown in Fig. 6a, the non-uniformity of elements suffices to produce symmetrical pooling of the non-wetting phase at material interfaces, thus supporting the observations by [5] again.

When employing the barrier condition described in Section 2.5, the numerical solutions on both structured and unstructured meshes preserve their symmetry and are comparable with the

results published in [37], page 211. Furthermore, the solutions for the coarser lens (sand E) show better symmetry when the barrier condition is used in Fig. 7g compared to the case in Fig. 7d, where no attention is paid to the fluid behavior across material interfaces. This is because a pooling (i.e., the barrier effect) occurs for a short period of time that affects the final symmetry of the solution before the non-wetting fluid penetrates into the coarser lens.

Consequently, we recommend using the mass-lumping technique as well as the implementation of the (capillary) barrier condition in order to obtain reliable numerical results.

4. Compositional two-phase flow in porous media

In order to demonstrate the applicability of the presented method, we construct an analytical solution for a transport equation for mass fraction $X = X(t, \mathbf{x})$ coupled with the two-phase flow problem in \mathbb{R}^d described in Section 3.1 in the form

$$\phi \frac{\partial X}{\partial t} + \nabla \cdot (X \mathbf{v}_t - D_X \nabla X) + r_X X = 0, \quad (31)$$

where \mathbf{v}_t [LT^{-1}] is the total velocity defined as the sum of the Darcy's phase velocities given by Eq. (26), i.e. $\mathbf{v}_t = \mathbf{v}_w + \mathbf{v}_n$, and X [1] is the mass fraction of some chemical compound dissolved in both phases under the assumption of local equilibrium. Derivation of Eq. (31) is summarized in Appendix B.

4.1. Analytical solution

Eq. (31) is considered as another equation added to the system of two-phase flow equations discussed in porous media in Section 3 in the same domain, shown in Fig. 1, and radial symmetry as the semi-analytical solution by [32] in the general dimension $d = 1, 2, 3$. The analytical solution of (31) is assumed in the radial coordinates as

$$X(t, \rho) = X_0 \exp(-B_X \rho^2 e^{-A_X t}), \quad (32)$$

where $\rho = \|\mathbf{x}\|_2$ is the radius, X_0 [1] is the injection mass fraction at the origin $\mathbf{x} = \mathbf{0}$, and A_X [T^{-1}] and B_X [L^{-2}] are positive coefficients.

The analytical function given by Eq. (32) resolves Eq. (31), if the reaction term r_X is given in the radial coordinates as

$$r_X(t, \rho) = -B_X (\phi \rho^2 A_X + 2D_X d - 2\rho v_t(t, \rho) - 4D_X \rho^2 B_X e^{-A_X t}) e^{-A_X t}, \quad (33)$$

where $v_t(t, \rho)$ is the radial component of the total velocity \mathbf{v}_t .

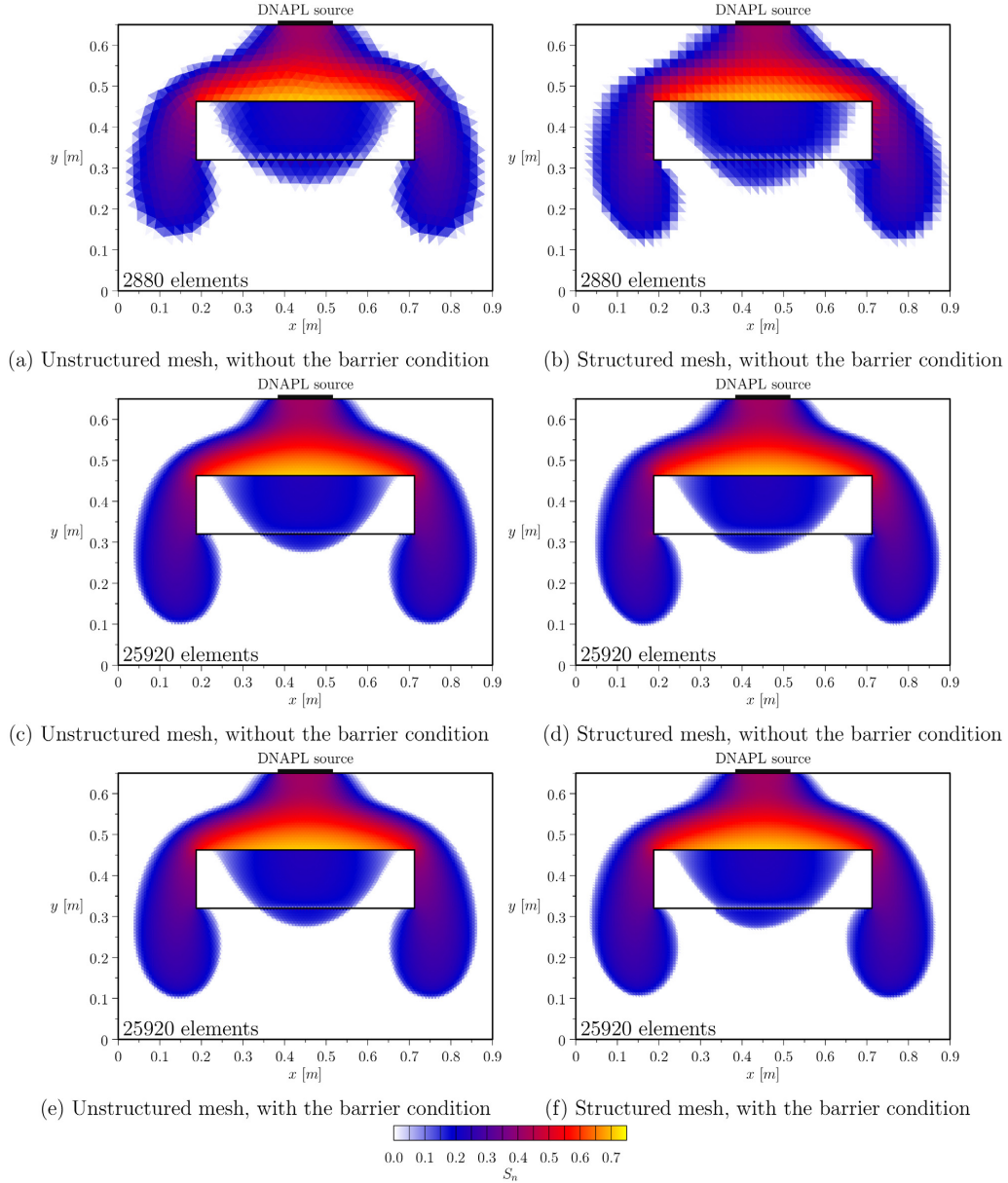


Fig. 7. Spatial distribution of the non-wetting phase saturation S_n at $t = 4500$ s for and various meshes with (left) and without (right) using the barrier condition. The lens consists of the coarser sand E.

Eq. (31) and the analytical solution in Eq. (32) allow to use vanishing or zero diffusion coefficient D_X . Hence, the problem is suitable for benchmarking numerical schemes for both diffusion-advection and pure advection cases. In order to simulate the vanishing diffusion case using the presented MHFEM numerical scheme, we split the diffusion coefficient D_X into two parts as $D_X = m_X D_0$, where $D_0 > 0$ is a constant diffusion coefficient

and $m_X \geq 0$ is a mobility coefficient that can be set small for the vanishing diffusion case or even to zero for the pure advection case.

4.2. Conservative and non-conservative formulations

The transport equation given by Eq. (31) together with the two-phase flow equations can be represented by the coefficients in

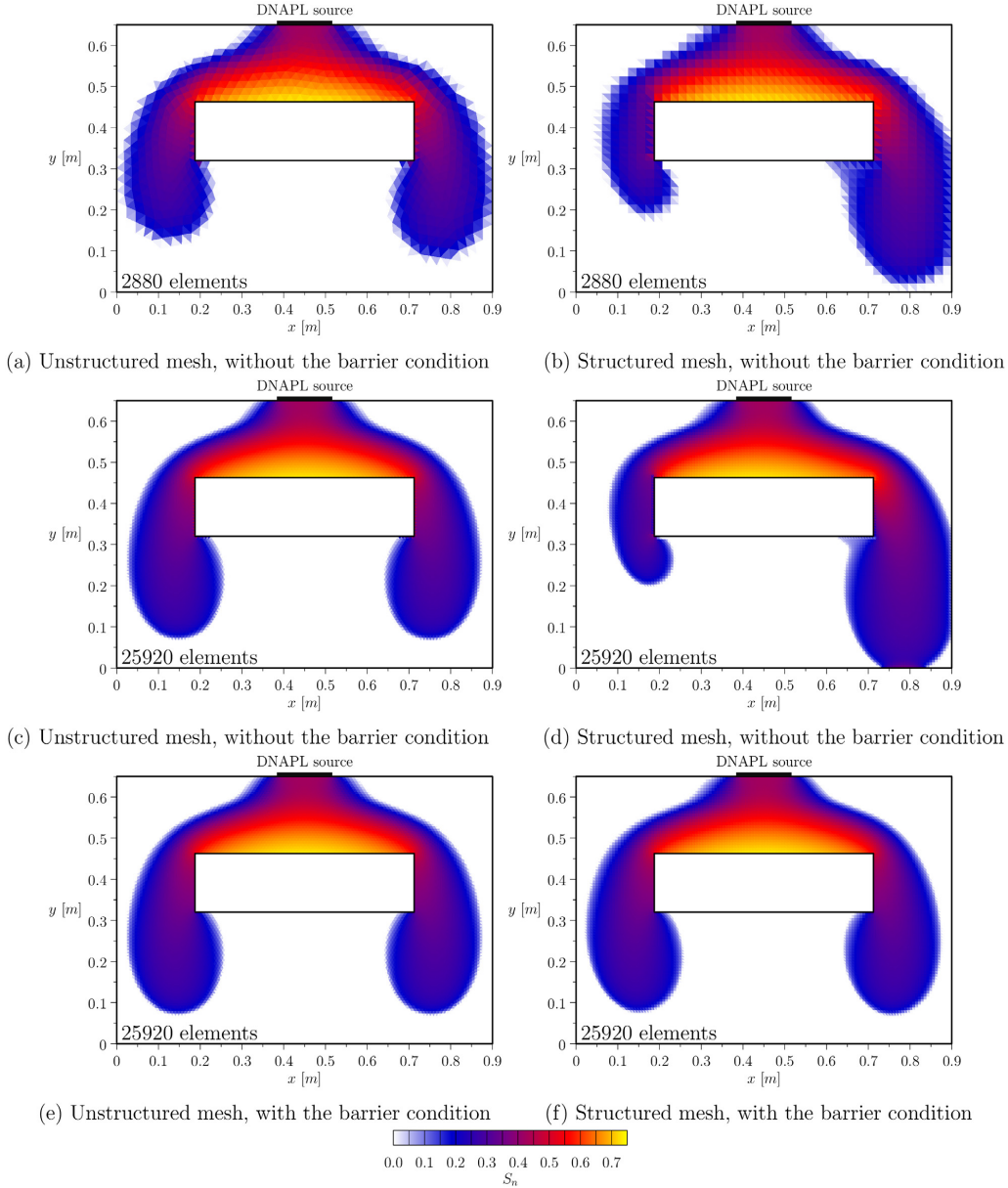


Fig. 8. Spatial distribution of the non-wetting phase saturation S_n at $t = 4500$ s for and various meshes with (left) and without (right) using the barrier condition. The lens consists of the finer sand F.

Eq. (1) using either a conservative (C) or a non-conservative form (NC). The conservative form is directly given by Eq. (31) while the non-conservative form results from the combination of Eq. (31) with the two-phase flow continuity equations as follows:

$$\phi \frac{\partial X}{\partial t} + \mathbf{v}_t \cdot \nabla X - \nabla \cdot (D_X \nabla X) + r_X X = 0. \quad (34)$$

For both (C) and (NC) variants, we set $n = 3$, $\mathbf{Z} = (p_w, p_n, X)^T$, and the coefficients in (1) as

$$\mathbf{N} = \begin{pmatrix} -\phi \frac{\partial S_w}{\partial p_c} & \phi \frac{\partial S_w}{\partial p_c} & 0 \\ \phi \frac{\partial S_w}{\partial p_c} & -\phi \frac{\partial S_w}{\partial p_c} & 0 \\ 0 & 0 & \phi \end{pmatrix}, \quad \mathbf{N} = \begin{pmatrix} -\phi \frac{\partial S_w}{\partial p_c} & \phi \frac{\partial S_w}{\partial p_c} & 0 \\ \phi \frac{\partial S_w}{\partial p_c} & -\phi \frac{\partial S_w}{\partial p_c} & 0 \\ 0 & 0 & \phi \end{pmatrix}, \quad (35a)$$

Table 4
Results of the numerical analysis using the L_1 norm of $E_{h,x}$ and the B&C model.

Id.	Conservative Formulation				Non-Conservative Formulation			
	$D_X = 0 \text{ m}^2/\text{s}$		$D_X = 10^{-5} \text{ m}^2/\text{s}$		$D_X = 0 \text{ m}^2/\text{s}$		$D_X = 10^{-5} \text{ m}^2/\text{s}$	
	$\ E_{h,x}\ _1$	$eOC_{X,1}$	$\ E_{h,x}\ _1$	$eOC_{X,1}$	$\ E_{h,x}\ _1$	$eOC_{X,1}$	$\ E_{h,x}\ _1$	$eOC_{X,1}$
1D ₁	$1.68 \cdot 10^{-2}$	0.94	$3.46 \cdot 10^{-3}$	1.02	$1.69 \cdot 10^{-2}$	0.93	$3.46 \cdot 10^{-3}$	1.02
1D ₂	$8.77 \cdot 10^{-3}$	1.00	$1.70 \cdot 10^{-3}$	1.01	$8.89 \cdot 10^{-3}$	0.98	$1.70 \cdot 10^{-3}$	1.01
1D ₃	$4.38 \cdot 10^{-3}$	1.02	$8.45 \cdot 10^{-4}$	1.00	$4.50 \cdot 10^{-3}$	1.00	$8.45 \cdot 10^{-4}$	1.00
1D ₄	$2.16 \cdot 10^{-3}$	1.02	$4.23 \cdot 10^{-4}$	1.00	$2.25 \cdot 10^{-3}$	1.00	$4.23 \cdot 10^{-4}$	1.00
1D ₅	$1.07 \cdot 10^{-3}$	0.97	$2.12 \cdot 10^{-4}$	1.00	$1.13 \cdot 10^{-3}$	1.00	$2.12 \cdot 10^{-4}$	1.00
1D ₆	$5.45 \cdot 10^{-4}$	0.94	$1.06 \cdot 10^{-4}$	1.00	$5.64 \cdot 10^{-4}$	1.00	$1.06 \cdot 10^{-4}$	1.00
1D ₇	$2.84 \cdot 10^{-4}$		$5.31 \cdot 10^{-5}$		$2.82 \cdot 10^{-4}$		$5.31 \cdot 10^{-5}$	
2D ₁ [□]	$2.59 \cdot 10^{-2}$	1.08	$8.46 \cdot 10^{-3}$	1.01	$2.59 \cdot 10^{-2}$	1.08	$8.46 \cdot 10^{-3}$	1.01
2D ₂ [□]	$1.23 \cdot 10^{-2}$	0.99	$4.19 \cdot 10^{-3}$	0.99	$1.23 \cdot 10^{-2}$	0.99	$4.19 \cdot 10^{-3}$	0.99
2D ₃ [□]	$6.18 \cdot 10^{-3}$	0.97	$2.11 \cdot 10^{-3}$	0.97	$6.18 \cdot 10^{-3}$	0.97	$2.11 \cdot 10^{-3}$	0.97
2D ₄ [□]	$3.16 \cdot 10^{-3}$	0.95	$1.08 \cdot 10^{-3}$	0.94	$3.16 \cdot 10^{-3}$	0.95	$1.08 \cdot 10^{-3}$	0.94
2D ₅ [□]	$1.64 \cdot 10^{-3}$		$5.59 \cdot 10^{-4}$		$1.64 \cdot 10^{-3}$		$5.59 \cdot 10^{-4}$	
2D ₁ [△]	$2.77 \cdot 10^{-2}$	1.09	$8.97 \cdot 10^{-3}$	1.10	$1.83 \cdot 10^{-2}$	1.16	$8.86 \cdot 10^{-3}$	1.09
2D ₂ [△]	$1.36 \cdot 10^{-2}$	0.89	$4.39 \cdot 10^{-3}$	0.92	$8.57 \cdot 10^{-3}$	0.94	$4.36 \cdot 10^{-3}$	0.91
2D ₃ [△]	$6.92 \cdot 10^{-3}$	1.06	$2.19 \cdot 10^{-3}$	1.08	$4.21 \cdot 10^{-3}$	1.10	$2.19 \cdot 10^{-3}$	1.07
2D ₄ [△]	$3.55 \cdot 10^{-3}$		$1.11 \cdot 10^{-3}$		$2.10 \cdot 10^{-3}$		$1.12 \cdot 10^{-3}$	
3D ₁ [□]	$9.35 \cdot 10^{-3}$	1.17	$3.45 \cdot 10^{-3}$	1.00	$9.40 \cdot 10^{-3}$	1.18	$3.45 \cdot 10^{-3}$	1.00
3D ₂ [□]	$4.14 \cdot 10^{-3}$	1.00	$1.72 \cdot 10^{-3}$	0.95	$4.14 \cdot 10^{-3}$	1.00	$1.72 \cdot 10^{-3}$	0.95
3D ₃ [□]	$2.07 \cdot 10^{-3}$		$8.89 \cdot 10^{-4}$		$2.07 \cdot 10^{-3}$		$8.89 \cdot 10^{-4}$	
3D ₁ [△]	$1.40 \cdot 10^{-2}$	0.65	$6.56 \cdot 10^{-3}$	0.78	$9.05 \cdot 10^{-3}$	0.73	$6.36 \cdot 10^{-3}$	0.78
3D ₂ [△]	$1.00 \cdot 10^{-2}$	1.06	$4.36 \cdot 10^{-3}$	1.07	$6.20 \cdot 10^{-3}$	1.10	$4.24 \cdot 10^{-3}$	1.07
3D ₃ [△]	$4.77 \cdot 10^{-3}$	1.23	$2.06 \cdot 10^{-3}$	1.26	$2.88 \cdot 10^{-3}$	1.26	$2.01 \cdot 10^{-3}$	1.20
3D ₄ [△]	$2.30 \cdot 10^{-3}$		$9.77 \cdot 10^{-4}$		$1.36 \cdot 10^{-3}$		$9.83 \cdot 10^{-4}$	

$$\mathbf{u} = \mathbf{0}, \quad \mathbf{u} = \begin{pmatrix} \mathbf{0} & \mathbf{0} & \mathbf{0} \\ \mathbf{0} & \mathbf{0} & \mathbf{0} \\ \mathbf{0} & \mathbf{0} & \mathbf{v}_t \end{pmatrix}, \quad (35b)$$

$$\mathbf{m} = \begin{pmatrix} \lambda_w, \lambda_n \\ \lambda_t, \lambda_t \end{pmatrix}^T, \quad \mathbf{m} = \begin{pmatrix} \lambda_w, \lambda_n \\ \lambda_t, \lambda_t, m_X \end{pmatrix}^T, \quad (35c)$$

$$\mathbf{D} = \begin{pmatrix} \lambda_t \mathbf{K} \mathbf{I} & \mathbf{0} & \mathbf{0} \\ \mathbf{0} & \lambda_t \mathbf{K} \mathbf{I} & \mathbf{0} \\ \mathbf{0} & \mathbf{0} & D_0 \mathbf{I} \end{pmatrix}, \quad \mathbf{D} = \begin{pmatrix} \lambda_t \mathbf{K} \mathbf{I} & \mathbf{0} & \mathbf{0} \\ \mathbf{0} & \lambda_t \mathbf{K} \mathbf{I} & \mathbf{0} \\ \mathbf{0} & \mathbf{0} & D_0 \mathbf{I} \end{pmatrix}, \quad (35d)$$

$$\mathbf{w} = (\lambda_t \rho_w \mathbf{K} \mathbf{g}, \lambda_t \rho_n \mathbf{K} \mathbf{g}, \mathbf{0})^T, \quad \mathbf{w} = (\lambda_t \rho_w \mathbf{K} \mathbf{g}, \lambda_t \rho_n \mathbf{K} \mathbf{g}, \mathbf{0})^T, \quad (35e)$$

$$\mathbf{a} = \begin{pmatrix} \mathbf{0} & \mathbf{0} & \mathbf{0} \\ \mathbf{0} & \mathbf{0} & \mathbf{0} \\ \mathbf{0} & \mathbf{0} & \mathbf{v}_t \end{pmatrix}, \quad \mathbf{a} = \mathbf{0}, \quad (35f)$$

$$\mathbf{r} = \begin{pmatrix} \mathbf{0} & \mathbf{0} & \mathbf{0} \\ \mathbf{0} & \mathbf{0} & \mathbf{0} \\ \mathbf{0} & \mathbf{0} & r_X \end{pmatrix}, \quad \mathbf{r} = \begin{pmatrix} \mathbf{0} & \mathbf{0} & \mathbf{0} \\ \mathbf{0} & \mathbf{0} & \mathbf{0} \\ \mathbf{0} & \mathbf{0} & r_X \end{pmatrix}, \quad (35g)$$

$$\mathbf{f} = \mathbf{0}, \quad \mathbf{f} = \mathbf{0}. \quad (35h)$$

4.3. Numerical analysis

Initial and boundary conditions for the two-phase flow part of the system are the same as in Section 3.1 and except for the choice of time steps τ , we use the same values for the problem parameters. Compared to the numerical analysis in Section 3.1, the time steps τ need to be reduced in order to assure numerical convergence of the transport equation, cf. Table A.6. For the mass fraction X , the initial condition is given by the analytical solution in Eq. (32) evaluated at $t = 0$. We consider Dirichlet boundary conditions given by the analytical solution at Γ_{in} and on the boundaries representing the infinity, i.e., at $x = 1 \text{ m}$ in 1D, on Γ_N and Γ_E in 2D, and on all front faces in 3D, cf. Fig. 1. On the remaining boundaries, zero Neumann boundary conditions are applied. For the numerical

analysis, we set $D_0 = 1 \cdot 10^{-5} \text{ m}^2/\text{s}$, $X_0 = 1$, $A_X = 5 \cdot 10^{-5} \text{ s}^{-1}$, and $B_X = 20 \text{ m}^{-2}$ and we consider $m_X \in \{0, 0.1, 0.01, 1\}$.

In Tables 4 and 5, we show results of the numerical analysis in the L_1 norm for B&C and vG models, respectively, that cover the pure advection case ($D_X = 0$) and diffusion–advection case with the largest diffusion ($D_X = D_0$) considered in this paper. In Section 2 of the supplementary material, we compile tables and figures that cover the results from the whole computational study. In all cases, the computed experimental order of convergences indicate that the numerical scheme is convergent with the first order of accuracy. Although substantially larger norms of $E_{h,x}$ are obtained for the pure advection case compared to the cases with non-zero diffusion D_X , the upwinding strategy defined in Eq. (16) is sufficient to stabilize the numerical scheme for the pure advection problems.

5. Conclusion

Based on the mixed–hybrid finite element method, we have developed a computationally efficient multidimensional numerical scheme for solving a system of n non-stationary partial differential equations with general coefficients that can be parallelized on GPU. The numerical scheme is primarily designed for simulating two-phase compositional flow in porous media and allows for solving problems with degenerate or zero diffusion, or capillary barrier effect in heterogeneous porous materials. We have presented a detailed derivation of the numerical scheme and emphasized the key aspects of its numerical stabilization that is inspired by the upwind technique and our previous work. Furthermore, we have shown how the numerical scheme has to be modified in order to properly simulate the barrier capillary effect that occurs at material discontinuities in heterogeneous porous media.

In order to solve the numerical scheme, a sparse linear system needs to be assembled and solved in each time step. The main advantage of the presented scheme is that the assembly of the linear system as well as the resolution of the linear system can

Table 5
Results of the numerical analysis using the L_1 norm of $E_{h,x}$ and the vG model.

Id.	Conservative Formulation				Non-Conservative Formulation			
	$D_X = 0 \text{ m}^2/\text{s}$		$D_X = 10^{-5} \text{ m}^2/\text{s}$		$D_X = 0 \text{ m}^2/\text{s}$		$D_X = 10^{-5} \text{ m}^2/\text{s}$	
	$\ E_{h,x}\ _1$	$eOC_{X,1}$	$\ E_{h,x}\ _1$	$eOC_{X,1}$	$\ E_{h,x}\ _1$	$eOC_{X,1}$	$\ E_{h,x}\ _1$	$eOC_{X,1}$
1D ₁	$1.78 \cdot 10^{-2}$	1.02	$3.43 \cdot 10^{-3}$	1.02	$1.81 \cdot 10^{-2}$	0.99	$3.43 \cdot 10^{-3}$	1.02
1D ₂	$8.77 \cdot 10^{-3}$	1.03	$1.69 \cdot 10^{-3}$	1.00	$9.08 \cdot 10^{-3}$	0.99	$1.69 \cdot 10^{-3}$	1.00
1D ₃	$4.30 \cdot 10^{-3}$	1.00	$8.43 \cdot 10^{-4}$	1.00	$4.57 \cdot 10^{-3}$	0.99	$8.43 \cdot 10^{-4}$	1.00
1D ₄	$2.16 \cdot 10^{-3}$	0.95	$4.22 \cdot 10^{-4}$	1.00	$2.30 \cdot 10^{-3}$	1.00	$4.22 \cdot 10^{-4}$	1.00
1D ₅	$1.11 \cdot 10^{-3}$	0.92	$2.11 \cdot 10^{-4}$	1.00	$1.15 \cdot 10^{-3}$	1.00	$2.11 \cdot 10^{-4}$	1.00
1D ₆	$5.90 \cdot 10^{-4}$	0.90	$1.06 \cdot 10^{-4}$	1.00	$5.75 \cdot 10^{-4}$	1.00	$1.06 \cdot 10^{-4}$	1.00
1D ₇	$3.16 \cdot 10^{-4}$		$5.29 \cdot 10^{-5}$		$2.88 \cdot 10^{-4}$		$5.29 \cdot 10^{-5}$	
2D ₁ [□]	$2.59 \cdot 10^{-2}$	1.09	$8.45 \cdot 10^{-3}$	1.01	$2.59 \cdot 10^{-2}$	1.09	$8.45 \cdot 10^{-3}$	1.01
2D ₂ [□]	$1.21 \cdot 10^{-2}$	1.00	$4.18 \cdot 10^{-3}$	0.99	$1.21 \cdot 10^{-2}$	1.00	$4.18 \cdot 10^{-3}$	0.99
2D ₃ [□]	$6.05 \cdot 10^{-3}$	0.99	$2.11 \cdot 10^{-3}$	0.97	$6.05 \cdot 10^{-3}$	0.99	$2.11 \cdot 10^{-3}$	0.97
2D ₄ [□]	$3.04 \cdot 10^{-3}$	0.99	$1.07 \cdot 10^{-3}$	0.95	$3.04 \cdot 10^{-3}$	0.99	$1.07 \cdot 10^{-3}$	0.95
2D ₅ [□]	$1.53 \cdot 10^{-3}$		$5.56 \cdot 10^{-4}$		$1.53 \cdot 10^{-3}$		$5.56 \cdot 10^{-4}$	
2D ₁ [△]	$2.88 \cdot 10^{-2}$	1.13	$9.00 \cdot 10^{-3}$	1.10	$1.79 \cdot 10^{-2}$	1.13	$8.84 \cdot 10^{-3}$	1.09
2D ₂ [△]	$1.38 \cdot 10^{-2}$	0.92	$4.40 \cdot 10^{-3}$	0.92	$8.61 \cdot 10^{-3}$	0.91	$4.35 \cdot 10^{-3}$	0.91
2D ₃ [△]	$6.90 \cdot 10^{-3}$	1.09	$2.19 \cdot 10^{-3}$	1.08	$4.32 \cdot 10^{-3}$	1.08	$2.19 \cdot 10^{-3}$	1.06
2D ₄ [△]	$3.47 \cdot 10^{-3}$		$1.11 \cdot 10^{-3}$		$2.18 \cdot 10^{-3}$		$1.12 \cdot 10^{-3}$	
3D ₁ [□]	$9.57 \cdot 10^{-3}$	1.21	$3.45 \cdot 10^{-3}$	1.00	$9.51 \cdot 10^{-3}$	1.20	$3.45 \cdot 10^{-3}$	1.00
3D ₂ [□]	$4.14 \cdot 10^{-3}$	1.00	$1.72 \cdot 10^{-3}$	0.95	$4.14 \cdot 10^{-3}$	1.00	$1.72 \cdot 10^{-3}$	0.95
3D ₃ [□]	$2.07 \cdot 10^{-3}$		$8.89 \cdot 10^{-4}$		$2.07 \cdot 10^{-3}$		$8.89 \cdot 10^{-4}$	
3D ₁ [△]	$1.49 \cdot 10^{-2}$	0.66	$6.64 \cdot 10^{-3}$	0.78	$8.70 \cdot 10^{-3}$	0.72	$6.29 \cdot 10^{-3}$	0.78
3D ₂ [△]	$1.06 \cdot 10^{-2}$	1.09	$4.42 \cdot 10^{-3}$	1.07	$5.98 \cdot 10^{-3}$	1.07	$4.19 \cdot 10^{-3}$	1.07
3D ₃ [△]	$4.93 \cdot 10^{-3}$	1.26	$2.08 \cdot 10^{-3}$	1.28	$2.83 \cdot 10^{-3}$	1.23	$1.99 \cdot 10^{-3}$	1.18
3D ₄ [△]	$2.34 \cdot 10^{-3}$		$9.77 \cdot 10^{-4}$		$1.37 \cdot 10^{-3}$		$9.90 \cdot 10^{-4}$	

Table A.6

Parameters of meshes used in the numerical analyses in Sections 4 and 3.1: identifier (Id.), number of elements N_K , mesh size h , degrees of freedom (=size of the global linear system) N_{dof} , and time steps $\tau_{B\&C}$ and τ_{vG} for the B&C and vG models, respectively. The identifiers describe meshes that consist of segments (1D) rectangles (2D[□]), triangles (2D[△]), cuboids (3D[□]), or tetrahedra (3D[△]), respectively.

Id.	N_K	h [m]	Benchmark in Section 4			Benchmark in Section 5		
			N_{dof}	$\tau_{B\&C}$ [s]	τ_{vG} [s]	N_{dof}	$\tau_{B\&C}$ [s]	τ_{vG} [s]
1D ₁	50	$2.00 \cdot 10^{-2}$	102	60.10	377.00	153	1.78	5.88
1D ₂	100	$1.00 \cdot 10^{-2}$	202	58.50	256.00	303	0.89	2.96
1D ₃	200	$5.00 \cdot 10^{-3}$	402	33.70	132.00	603	0.44	1.48
1D ₄	400	$2.50 \cdot 10^{-3}$	802	15.90	69.00	1203	0.22	0.74
1D ₅	800	$1.25 \cdot 10^{-3}$	1602	5.96	36.60	2403	0.11	0.37
1D ₆	1600	$6.25 \cdot 10^{-4}$	3202	2.55	19.90	4803	0.06	0.19
1D ₇	3200	$3.12 \cdot 10^{-4}$	6402	1.09	11.10	9603	0.03	0.09
2D ₁ [□]	225	$9.43 \cdot 10^{-2}$	960	253.16	317.00	1440	253.16	317.00
2D ₂ [□]	900	$4.71 \cdot 10^{-2}$	3720	90.50	80.00	5580	90.50	80.00
2D ₃ [□]	3600	$2.36 \cdot 10^{-2}$	14640	31.90	19.96	21960	31.90	19.96
2D ₄ [□]	14400	$1.18 \cdot 10^{-2}$	58080	10.62	5.02	87120	10.62	5.02
2D ₅ [□]	57600	$5.89 \cdot 10^{-3}$	231360	3.57	1.26	347040	3.57	1.26
2D ₁ [△]	242	$6.71 \cdot 10^{-2}$	766	454.55	36.36	1149	10.00	5.00
2D ₂ [△]	944	$3.49 \cdot 10^{-2}$	2912	145.99	15.49	4368	4.00	2.00
2D ₃ [△]	3714	$1.64 \cdot 10^{-2}$	11302	44.64	4.64	16953	1.00	0.50
2D ₄ [△]	14788	$8.73 \cdot 10^{-3}$	44684	13.44	1.35	67026	0.25	0.10
2D ₅ [△]	59336	$4.23 \cdot 10^{-3}$	178648	5.00	0.50			
3D ₁ [□]	3375	$1.15 \cdot 10^{-1}$	21600	333.33	235.29	32400	200.00	200.00
3D ₂ [□]	27000	$5.77 \cdot 10^{-2}$	167400	131.58	58.82	251100	12.50	12.50
3D ₃ [□]	216000	$2.89 \cdot 10^{-2}$	1317600	53.48	14.71	1976400	0.78	0.78
3D ₄ [□]	1728000	$1.44 \cdot 10^{-2}$	10454400	22.10	3.68			
3D ₁ [△]	1312	$2.13 \cdot 10^{-1}$	5874	833.33	152.67	8811	10.00	10.00
3D ₂ [△]	3697	$1.27 \cdot 10^{-1}$	15546	571.43	125.79	23319	5.00	5.00
3D ₃ [△]	29673	$6.29 \cdot 10^{-2}$	121678	232.56	60.24	182517	2.50	2.50
3D ₄ [△]	240372	$3.48 \cdot 10^{-2}$	973750	101.01	43.86	1460625	1.00	1.00
3D ₅ [△]	1939413	$1.84 \cdot 10^{-2}$	7807218	25.00	20.00			

be done directly on GPU with the help of the Template numerical library TNL. Therefore, the implementation on GPU can be more than 20× (for rectangles), 14× (for triangles), 24× (for cuboids), or

21× (for tetrahedra) faster than a single-threaded implementation on CPU (with the Intel Turbo Boost Technology disabled), or more than 5× (for rectangles), 4× (for triangles), 7× (for cuboids), or

Table C.7

Fluid properties.		
Symbol	ρ	μ
Units	[kg m ⁻³]	[kg m ⁻¹ s ⁻¹]
Water	1000	0.001
DNAPL ₁ , [35]	1400	0.001
DNAPL ₂ , [37]	1460	0.001

5× (for tetrahedra) faster than a six-threaded implementation on CPU. In the discussion, we compared performance of serial (on CPU), parallel (using OpenMP on CPU), and massive parallel (on GPU) implementations.

The applicability of the numerical scheme has been demonstrated using a series of benchmark problems for two-phase (compositional) flows in (heterogeneous) porous media. We have presented results of a numerical analysis for selected problems of two-phase flow in 1D, 2D, and 3D for which exact (semi-analytical) solutions are known. Then, a series of benchmark problems for two-phase flow in heterogeneous porous media has been presented to illustrate various aspects of numerical approximations of the capillary barrier effect. Additionally, we constructed an analytical solution for a two-phase compositional flow problem and used it in another numerical analysis. In all numerical analyses, we computed the experimental order of convergence using the L_1 and L_2 norms of the numerically approximated solutions and showed that the numerical scheme is convergent with the first order of accuracy.

Acknowledgments

The work was supported by the Czech Science Foundation project no. 17-06759S: *Investigation of shallow subsurface flow with phase transitions* and by project No. 15-27178A of Ministry of Health of the Czech Republic.

Appendix A. Tools for numerical analysis

The L_p norm in $\Omega \subset \mathbb{R}^d$ of some integrable function ψ is defined by

$$\|\psi\|_p = \left(\int_{\Omega} |\psi(\mathbf{x})|^p d\mathbf{x} \right)^{\frac{1}{p}}, \quad (\text{A.1})$$

where we consider $p = 1, 2$ and $d = 1, 2, 3$ in this paper. For a given mesh \mathcal{K}_h , the error $E_{h,g}$ of the numerical solution of some function is defined by

$$E_{h,g} = g_{ex} - g_h, \quad (\text{A.2})$$

where g_{ex} and g_h denote the exact and the numerically approximated function $g = g(t, \mathbf{x})$, respectively.

At a given time $t = T$, we assume the L_p norm of $E_{h,g}$ in the form

$$\|E_{h,g}\|_p = C_{time,g,p} \tau + C_{space,g,p} h^{oc_{g,p}}, \quad (\text{A.3})$$

where h [L] denotes the spatial step, τ [T] denotes the (constant) time step, $C_{time,g,p}$ and $C_{space,g,p}$ are some positive constants, and $oc_{g,p}$ is the order of convergence of the numerical scheme with respect to g in the L_p norm.

We investigate the convergence and accuracy of the numerical scheme using the experimental order of convergence $eoc_{g,p}$ that approximates the order of convergence $oc_{g,p}$ as

$$eoc_{g,p} = \frac{\ln \|E_{h_1,g}\|_p - \ln \|E_{h_2,g}\|_p}{\ln h_1 - \ln h_2}, \quad (\text{A.4})$$

where h_1 and h_2 denote spatial steps of two different meshes \mathcal{K}_{h_1} and \mathcal{K}_{h_2} , respectively.

Appendix B. Transport equation derivation

Following the notation in Section 3, a general compositional continuity equation with a reactive term for a component γ in a phase α is considered in the form

$$\phi \frac{\partial (S_{\alpha} X_{\alpha,\gamma} \rho_{\alpha})}{\partial t} + \nabla \cdot (-\rho_{\alpha} D_{X,\alpha,\gamma} \nabla X_{\alpha,\gamma} + \rho_{\alpha} X_{\alpha,\gamma} \mathbf{v}_{\alpha}) + \rho_{\alpha} r_{\alpha,\gamma} X_{\alpha,\gamma} = 0, \quad (\text{B.1})$$

where $X_{\alpha,\gamma}$ [1] is the mass fraction of the dissolved species γ in the phase α , $\alpha = n, w$. Under the assumption of weak solutions, densities ρ_w and ρ_n can be considered constant in time and space and therefore factored out of Eq. (B.1). Furthermore, we assume local equilibrium partitioning of the component γ between phases for which Henry's law allows to express

$$X_{n,\gamma} = H_{\gamma} X_{w,\gamma}, \quad (\text{B.2})$$

where H_{γ} [1] is the dimensionless Henry's constant. When Eq. (B.2) is substituted into Eq. (B.1), the Henry's constant H_{γ} can be factored out of the resulting equation. As a result, we obtain two equations for $X_{n,\gamma}$ that we sum together to obtain Eq. (31), where we set $X := X_{n,\gamma}$, $D_X := D_{X,w,\gamma} + D_{X,n,\gamma}$, and $r_X := r_{w,\gamma} + r_{n,\gamma}$.

Appendix C. Fluid and material properties

We consider capillary pressure–saturation relationships by (a) Brooks and Corey [28]:

$$S_{w,e}(p_c) = \left(\frac{p_c}{p_{B\&C}} \right)^{-\lambda_{B\&C}} \quad \text{for } p_c \geq p_{B\&C}, \quad (\text{C.1})$$

where $p_{B\&C}$ [ML⁻¹T⁻²] is the entry pressure and $\lambda_{B\&C}$ [1] characterizes the pore distribution of grains in a porous material, or by (b) van Genuchten [29]:

$$S_{w,e}(p_c) = \left[1 + (\alpha_{vG} p_c)^{n_{vG}} \right]^{-1 + \frac{1}{n_{vG}}} \quad \text{for } p_c \geq 0, \quad (\text{C.2})$$

where α_{vG} [M⁻¹L²T²] and n_{vG} [1] are empirical parameters. By $S_{w,e}$, we denote the effective saturation $S_{w,e} = (S_w - S_{w,r}) / (1 - S_{w,r})$, where $S_{w,r}$ [1] is the residual saturation of the wetting phase.

Based on the $p_c \leftrightarrow S_w$ relationships given by (C.1) and (C.2), relative permeability–saturation relationships can be derived as follows from (a) Burdine [26]:

$$k_{r,w}(S_w) = S_{w,e}^{3 + \frac{2}{\lambda_{B\&C}}}, \quad (\text{C.3a})$$

$$k_{r,n}(S_w) = (1 - S_{w,e})^2 \left(1 - S_{w,e}^{1 + \frac{2}{\lambda_{B\&C}}} \right), \quad (\text{C.3b})$$

or (b) Mualem [27]:

$$k_{r,w}(S_w) = S_{w,e}^{\frac{1}{2}} \left(1 - \left(1 - S_{w,e}^{\frac{m_{vG}}{1 - S_{w,e}}} \right)^2 \right), \quad (\text{C.4a})$$

$$k_{r,n}(S_w) = (1 - S_{w,e})^{\frac{1}{3}} \left(1 - S_{w,e}^{\frac{m_{vG}}{1 - S_{w,e}}} \right)^{2m_{vG}}. \quad (\text{C.4b})$$

Appendix D. Illustrative comparison with DuMuX

In Tables D.9 and D.10, we illustrate the computational accuracy and performance of the proposed MHFEM approach in comparison with the fully time-implicit box method implemented using the DuMuX project [34].

Appendix E. Supplementary data

Supplementary material related to this article can be found online at <https://doi.org/10.1016/j.cpc.2018.12.004>.

Table C.8

Material properties.

Symbol	ϕ	K	$\rho_{B\&C}$	$\lambda_{B\&C}$	α_{rG}	n_{rG}	$S_{w,r}$
Units	[1]	$[10^{-12} \text{ m}^2]$	[Pa]	[1]	$[10^{-4} \text{ Pa}^{-1}]$	[1]	[1]
Sand A, [33]	0.343	5.168	4605.80	2.857	1.71	6.64	0.04
Sand B, [35]	0.4	504	370	3.86	22.5	8.06	0.08
Sand C, [35]	0.39	52.6	1324	2.49	5.81	5.34	0.1
Sand D, [37]	0.40	66.4	755	2.7	—	—	0.1
Sand E, [37]	0.39	33.2	1163.5	2.0	—	—	0.12
Sand F, [37]	0.39	33.2	1466.1	2.0	—	—	0.12

Table D.9

Accuracy comparison between the proposed MHFEM approach and the fully time-implicit box method implemented using the DuMu^x project [34] for the 2D test problem discussed in Section 3.1 and with the B&C model used.

Id.	DuMu ^x				NumDwarf			
	$\ E_{h,S_h}\ _1$	$eOC_{S_h,1}$	$\ E_{h,S_h}\ _2$	$eOC_{S_h,2}$	$\ E_{h,S_h}\ _1$	$eOC_{S_h,1}$	$\ E_{h,S_h}\ _2$	$eOC_{S_h,2}$
$2D_1^\Delta$	$2.21 \cdot 10^{-2}$	0.97	$3.74 \cdot 10^{-2}$	0.65	$1.42 \cdot 10^{-2}$	0.98	$2.12 \cdot 10^{-2}$	0.94
$2D_2^\Delta$	$1.13 \cdot 10^{-2}$	0.79	$2.44 \cdot 10^{-2}$	0.53	$7.51 \cdot 10^{-3}$	0.86	$1.15 \cdot 10^{-2}$	0.84
$2D_3^\Delta$	$6.19 \cdot 10^{-3}$	0.98	$1.64 \cdot 10^{-2}$	0.68	$3.93 \cdot 10^{-3}$	1.05	$6.11 \cdot 10^{-3}$	1.03
$2D_4^\Delta$	$3.34 \cdot 10^{-3}$	0.86	$1.07 \cdot 10^{-2}$	0.68	$2.03 \cdot 10^{-3}$	0.90	$3.19 \cdot 10^{-3}$	0.89
$2D_5^\Delta$	$1.79 \cdot 10^{-3}$		$6.78 \cdot 10^{-3}$		$1.06 \cdot 10^{-3}$		$1.68 \cdot 10^{-3}$	

Table D.10

Computational times (in seconds) on Intel Core i7-5820K CPU of the NumDwarf scheme and the fully time-implicit box method implemented using the DuMu^x project [34] for the 2D test problem discussed in Section 3.1 and with the B&C model used.

Id.	DuMu ^x	NumDwarf
$2D_1^\Delta$	9	0.3
$2D_2^\Delta$	120	5
$2D_3^\Delta$	960	98.5
$2D_4^\Delta$	20880	2383
$2D_5^\Delta$	203160	45953

References

[1] M. Blatt, A. Burchardt, A. Dedner, C. Engwer, J. Fahlke, B. Flemisch, C. Gersbacher, C. Gräser, F. Gruber, C. Grüninger, et al., *Arch. Numer. Softw.* 4 (100) (2016) 13–29.

[2] K. Pruess, S. Finsterle, G. Moridis, C. Oldenburg, Y.-S. Wu, *Bull. Geotherm. Res. Council.* 26 (2) (1997) 53–57.

[3] R. Fučík, J. Mikyška, *Proc. Comput. Sci.* 4 (2011) 908–917.

[4] R. Fučík, J. Mikyška, *J. Math-for-Ind.* 3 (2011) 9–19.

[5] H. Hoteit, A. Firoozabadi, *Adv. Water Resour.* 31 (1) (2008) 56–73.

[6] T. Oberhuber, J.V. Vacata, A. Suzuki, *Acta Tech. CSAV* 56 (4) (2011) 447–466.

[7] F. Brezzi, M. Fortin, *Mixed and Hybrid Finite Element Methods*, vol. 15, Springer Science & Business Media, 2012.

[8] P.A. Raviart, J.M. Thomas, *Mathematical Aspects of Finite Element Methods*, Springer, 1977, pp. 292–315.

[9] A. Younes, P. Ackerer, F. Lehmann, *Internat. J. Numer. Methods Engrg.* 67 (1) (2006) 89–107.

[10] R. LeVeque, *Finite Volume Methods for Hyperbolic Problems*, Cambridge University Press, 2002.

[11] E. Anderson, Z. Bai, C. Bischof, S. Blackford, J. Demmel, J. Dongarra, J. DuCroz, A. Greenbaum, S. Hammarling, A. McKenney, et al., *LAPACK Users' Guide*, Soc. for Ind. and App. Math., Philadelphia, PA, 1999.

[12] T.A. Davis, *ACM Trans. Math. Software* 30 (2) (2004) 165–195.

[13] J. Klinkovský, T. Oberhuber, R. Fučík, V. Žabka, *ACM Trans. on Math. Softw.* (2018) in preparation.

[14] C. Cecka, A.J. Lew, E. Darve, *Internat. J. Numer. Methods Engrg.* 85 (5) (2011) 640–669.

[15] J. Chan, Z. Wang, A. Modave, J.F. Remacle, T. Warburton, *J. Comput. Phys.* 318 (2016) 142–168.

[16] A. Logg, K.A. Mardal, G.N. Wells, et al., in: A. Logg, K.A. Mardal, G.N. Wells (Eds.), *Automated Solution of Differential Equations by the Finite Element Method*, Springer, 2012, <http://dx.doi.org/10.1007/978-3-642-23099-8>.

[17] S. Balay, S. Abhyankar, M.F. Adams, J. Brown, P. Brune, K. Buschelman, L. Dalcin, V. Eijkhout, W.D. Gropp, D. Kaushik, M.G. Knepley, L.C. McInnes, K. Rupp, B.F. Smith, S. Zampini, H. Zhang, H. Zhang, *PETSc Users Manual*, Tech. Rep., ANL-95/11 - Revision 3.7, Argonne National Laboratory, 2016, URL <http://www.mcs.anl.gov/petsc>.

[18] A. Monakov, A. Lokhotov, A. Avetisyan, *International Conference on High-Performance Embedded Architectures and Compilers*, Springer, 2010, pp. 111–125.

[19] Y. Saad, M.H. Schultz, *SIAM J. Sci. Stat. Comput.* 7 (3) (1986) 856–869.

[20] Y. Saad, *Iterative Methods for Sparse Linear Systems*, SIAM, 2003.

[21] R. Schreiber, C. Van Loan, *SIAM J. Sci. Stat. Comput.* 10 (1) (1989) 53–57.

[22] H.F. Walker, *SIAM J. Sci. Stat. Comput.* 9 (1) (1988) 152–163.

[23] H. Ishigami, K. Kimura, Y. Nakamura, *Proc. 2011 International Conference on Parallel and Distributed Processing Techniques and Applications, PDPTA2011*, vol. 2, 2011, pp. 775–780.

[24] Y. Yamamoto, Y. Hirota, *JSIAM Lett.* 3 (2011) 89–92.

[25] A.H. Baker, E.R. Jessup, T.V. Kolev, *J. Comput. Appl. Math.* 230 (2) (2009) 751–761.

[26] N.T. Burdine, *Trans. AIME* 198 (1953) 71–78.

[27] Y. Mualem, *Water Resour. Res.* 12 (3) (1975).

[28] R.H. Brooks, A.T. Corey, *Hydrology Papers*, Colorado State University March (1) (1964).

[29] M.T. Van Genuchten, *Soil Sci. Soc. Am. J.* 44 (1980) 892–898.

[30] D.B. McWhorter, D.K. Sunada, *Water Resour. Res.* 26 (3) (1990) 399–413.

[31] R. Fučík, J. Mikyška, M. Beneš, T.H. Illangasekare, *Vadose Zone J.* 6 (1) (2007) 93–104.

[32] R. Fučík, T.H. Illangasekare, M. Beneš, *Adv. Water Resour.* 90 (2016) 51–56.

[33] T. Sakaki, T.H. Illangasekare, *Water Resour. Res.* 43 (12) (2007).

[34] B. Flemisch, M. Darcis, K. Erbertseder, B. Faigle, A. Lauser, K. Mosthaf, S. Müthing, P. Nuske, A. Tatomir, M. Wolff, et al., *Adv. Water Resour.* 34 (9) (2011) 1102–1112.

[35] R. Helmig, *Multiphase Flow and Transport Processes in the Subsurface: A Contribution to the Modeling of Hydrosystems*, Springer Verlag, Berlin, 1997.

[36] C. Van Duijn, J. Molenaar, M. De Neef, *Transp. Porous Media* 21 (1) (1995) 71–93.

[37] P. Bastian, R. Helmig, *Adv. Water Resour.* 23 (3) (1999) 199–216.

Supplementary Material:
Multidimensional Mixed–Hybrid Finite Element Method for
Compositional Two–Phase Flow in Heterogeneous Porous Media and
its Parallel Implementation on GPU

Radek Fučík^a, Jakub Klinkovský^a, Jakub Solovský^a, Tomáš Oberhuber^a, Jiří Mikyška^a

^a*Faculty of Nuclear Sciences and Physical Engineering, Czech Technical University in Prague, Trojanova 13,
120 00 Prague, Czech Republic*

1. Summary

This document contains supplementary information such as figures and tables for the manuscript entitled: *Multidimensional Mixed–Hybrid Finite Element Method for Compositional Two–Phase Flow in Heterogeneous Porous Media and its Parallel Implementation on GPU*.

In Section 2, examples of numerical solutions of the non-wetting phase saturation S_n are presented that correspond to the two-phase flow benchmark problem in \mathbb{R}^d discussed in Section 4.1 of the main manuscript.

Section 3 is devoted to the compositional two-phase flow benchmark problem in \mathbb{R}^d discussed in Section 5 of the main manuscript and contains figures of numerical solutions of the mass fraction X and the numerical error of the solution $E_{h,X}$ for various choices of the diffusion coefficient D_X . Additionally, tables containing L_1 and L_2 norms of the error and experimental orders of convergence are shown in Section 3.6.

2. Numerical Analysis of Two-Phase Flow in Porous Media

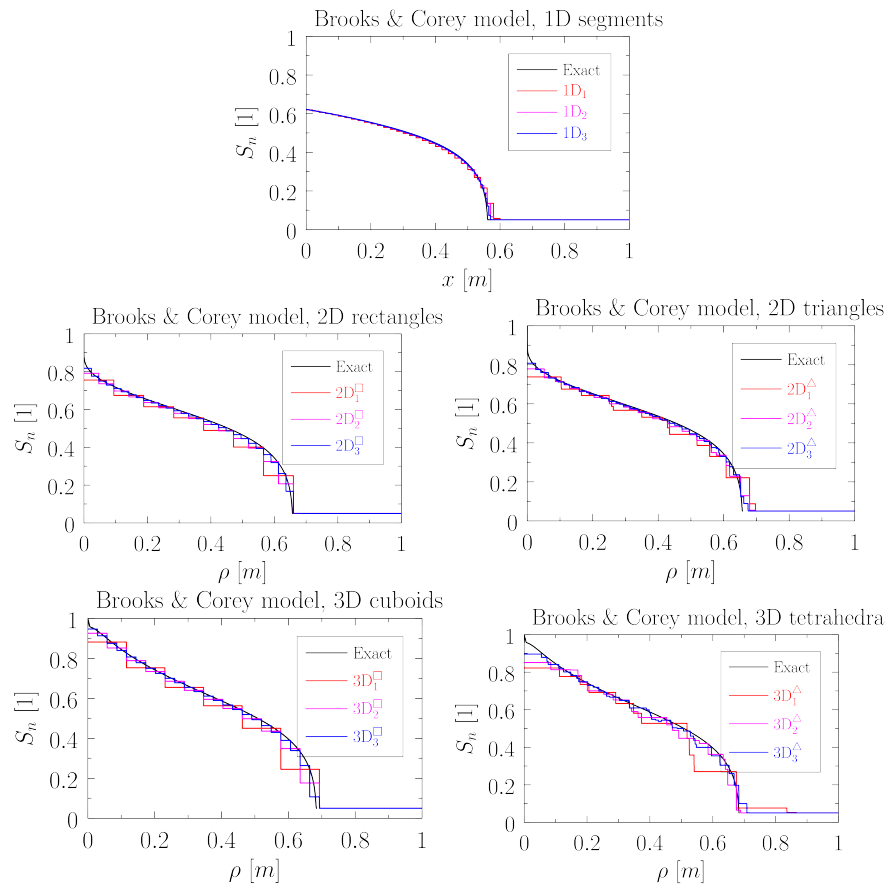


Figure 1: Numerical solutions of the non-wetting saturation profiles at $t = 20000$ s using the Brooks and Corey model.

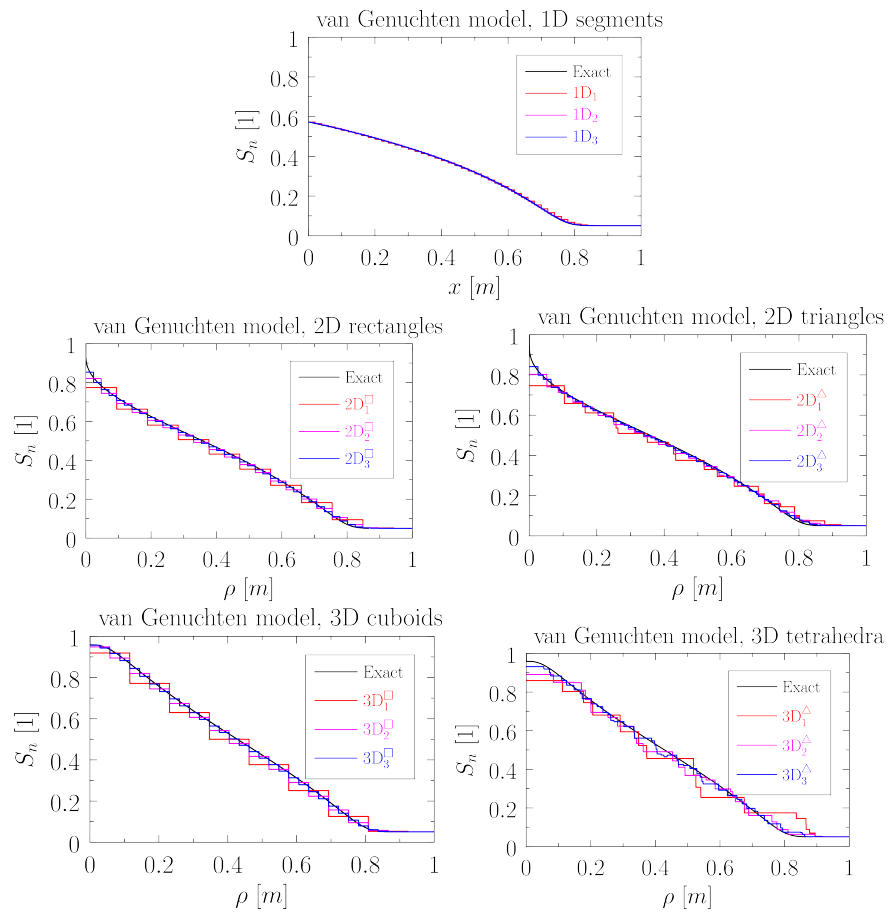


Figure 2: Numerical solutions of the non-wetting saturation profiles at $t = 20000$ s using the van Genuchten model.

3. Numerical Analysis of Compositional Two-Phase Flow in Porous Media

3.1. Results in 1D

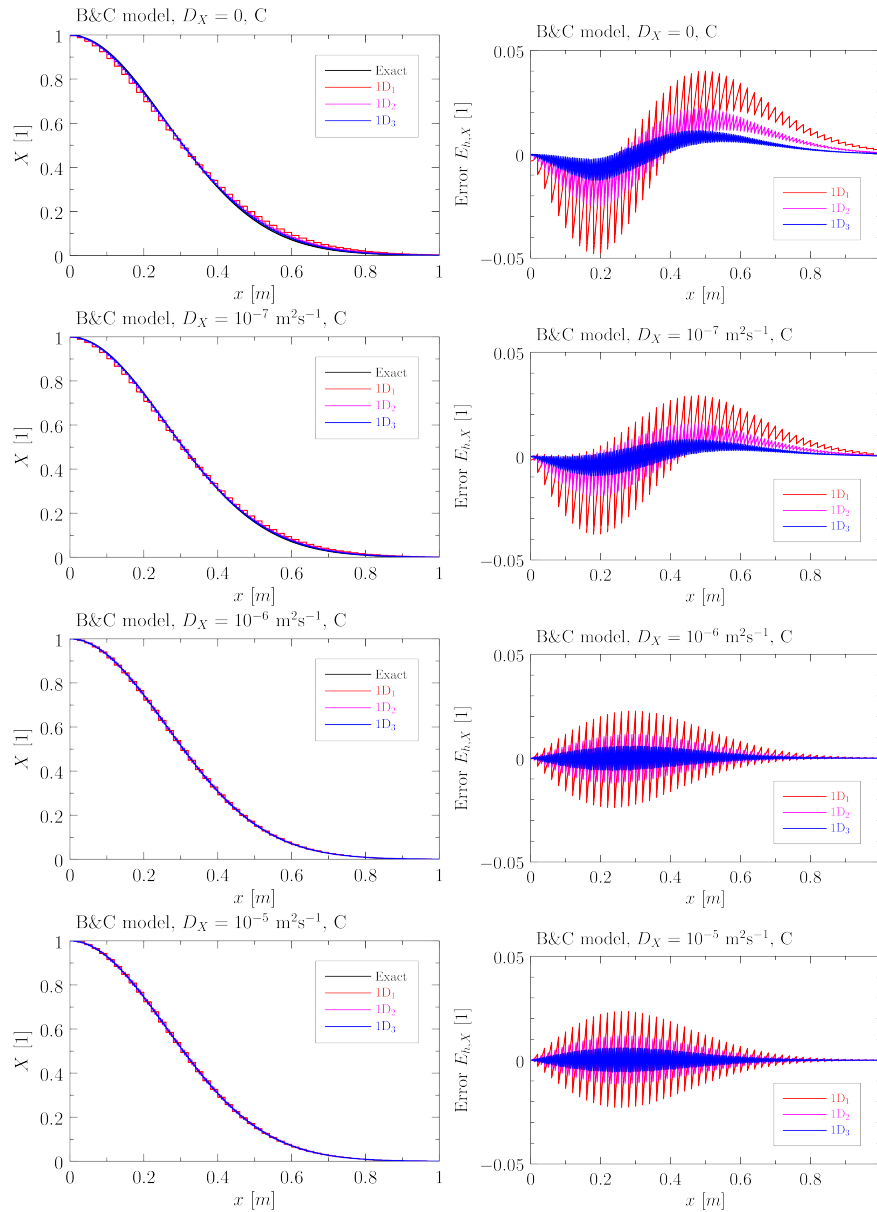


Figure 3: Numerical solutions of the mass fraction profiles X (left column) and plots of the numerical error $E_{h,X}$ (right column) and at $t = 20000$ s using the conservative formulation (C) and the Brooks and Corey model in 1D for various choices of D_X .

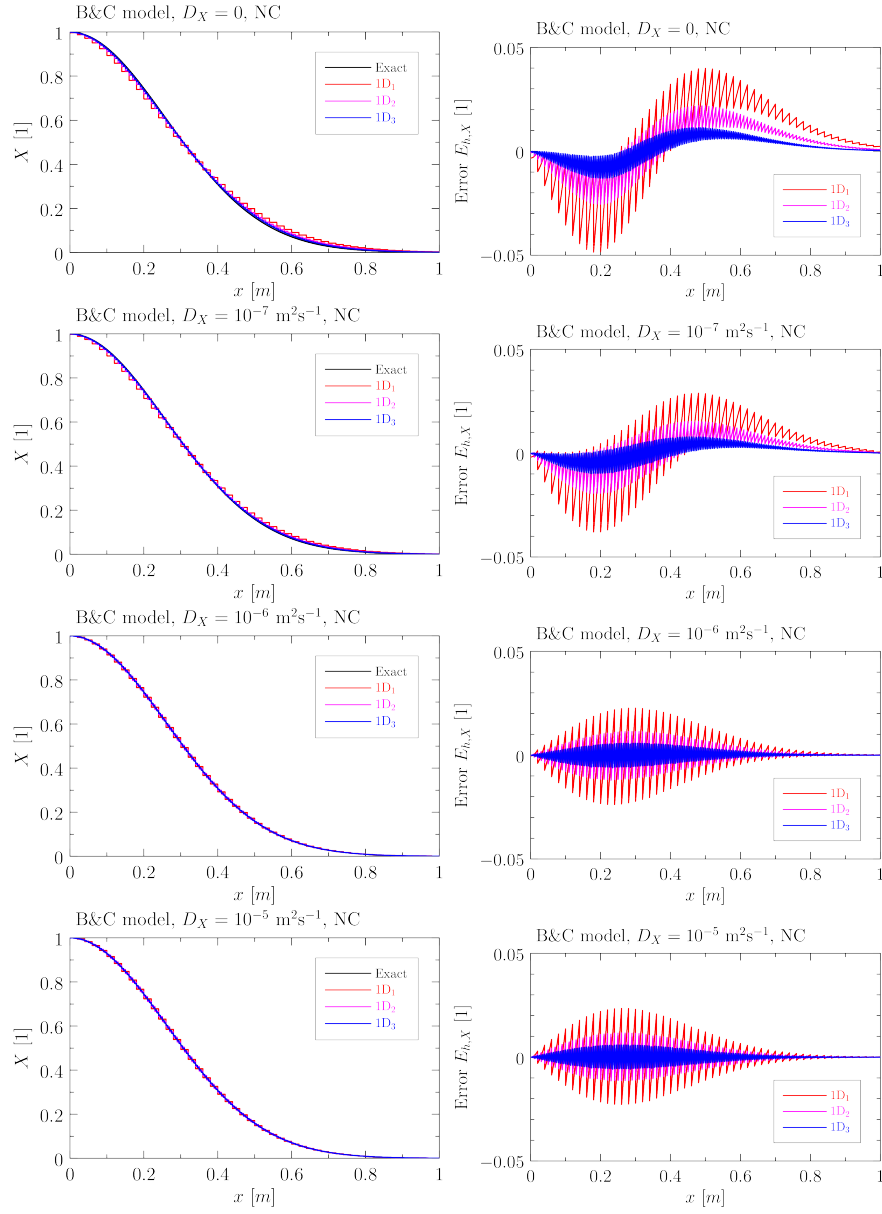


Figure 4: Numerical solutions of the mass fraction profiles X (left column) and plots of the numerical error $E_{h,X}$ (right column) and at $t = 20000$ s using the non-conservative formulation (NC) and the Brooks and Corey model in 1D for various choices of D_X .

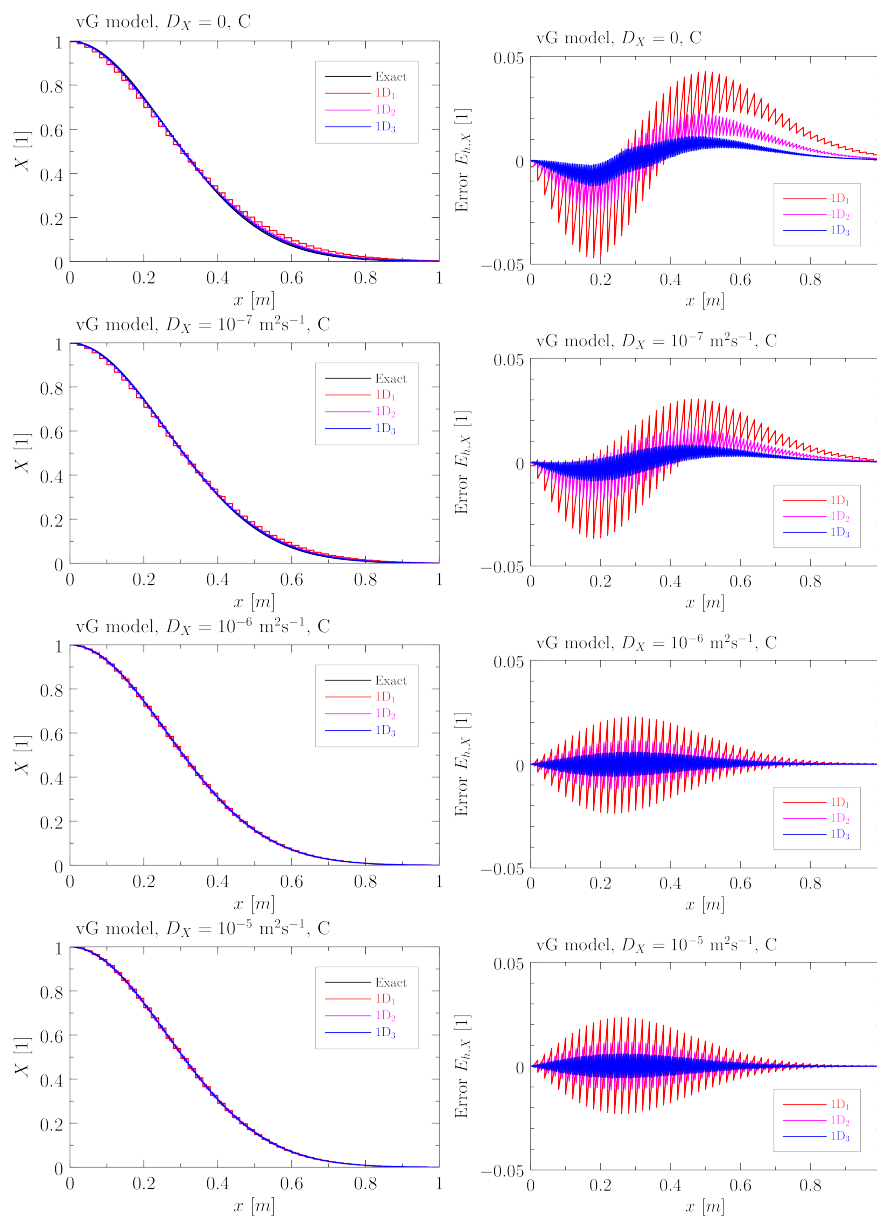


Figure 5: Numerical solutions of the mass fraction profiles X (left column) and plots of the numerical error $E_{h,X}$ (right column) and at $t = 20000$ s using the conservative formulation (C) and the van Genuchten model in 1D for various choices of D_X .

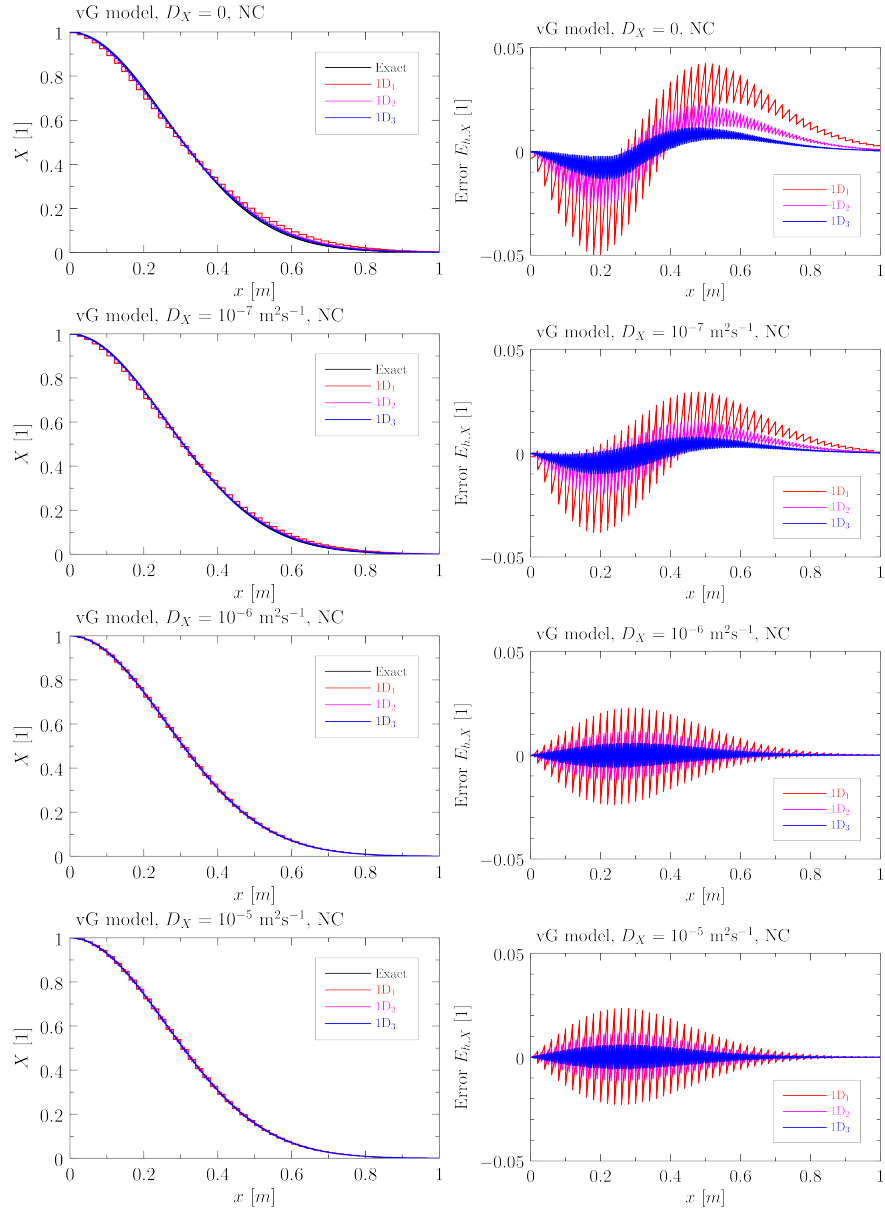


Figure 6: Numerical solutions of the mass fraction profiles X (left column) and plots of the numerical error $E_{h,X}$ (right column) and at $t = 20000$ s using the non-conservative formulation (NC) and the van Genuchten model in 1D for various choices of D_X .

3.2. Results in 2D on rectangles

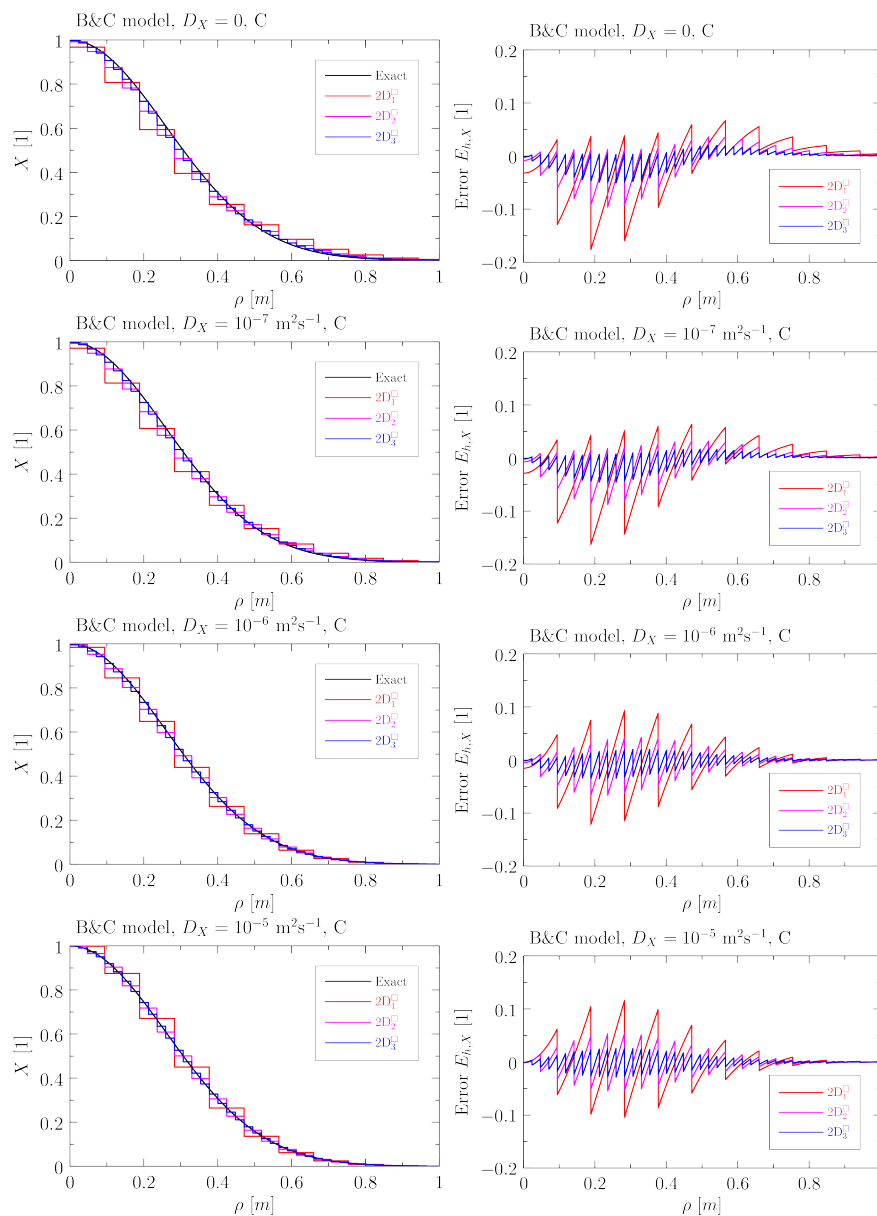


Figure 7: Numerical solutions of the mass fraction profiles X (left column) and plots of the numerical error $E_{h,X}$ (right column) and at $t = 20000$ s using the conservative formulation (C) and the Brooks and Corey model in 2D on rectangles for various choices of D_X .

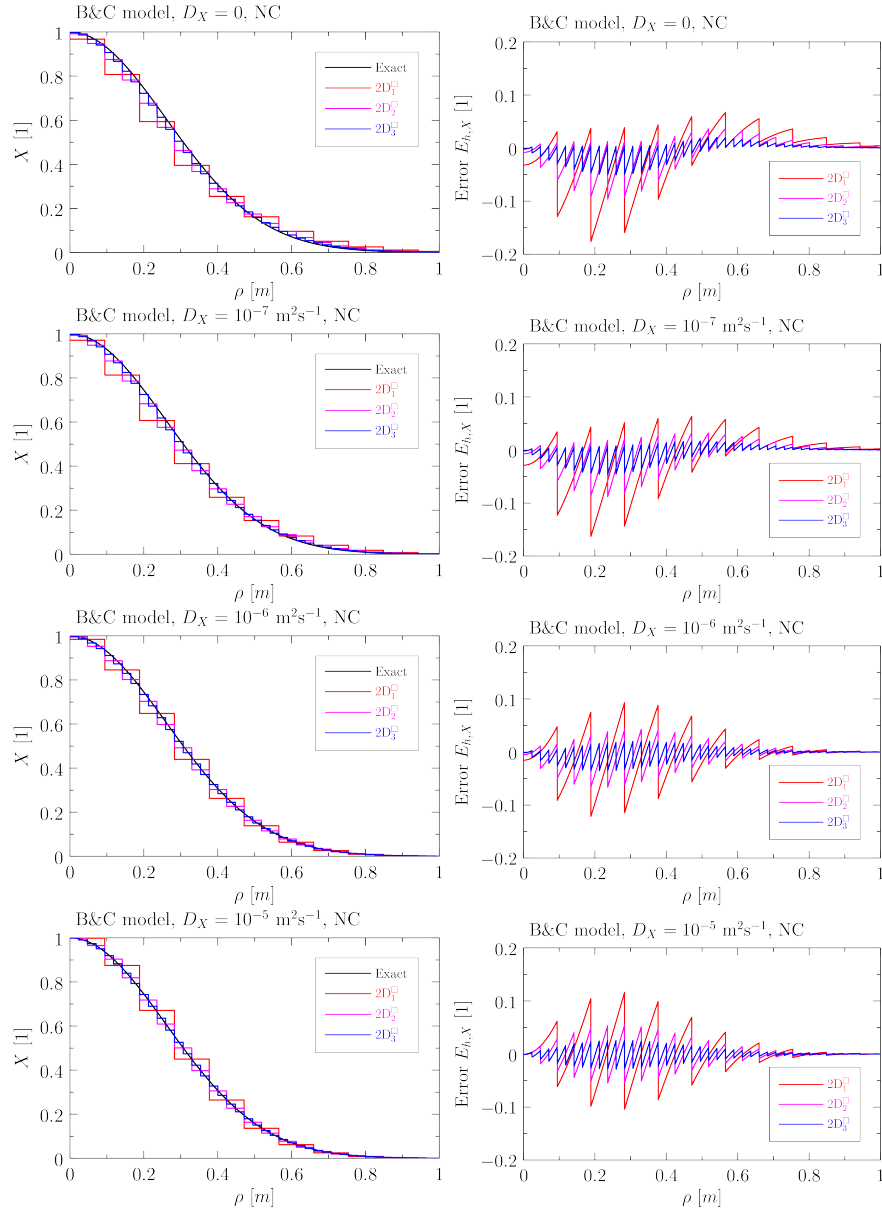


Figure 8: Numerical solutions of the mass fraction profiles X (left column) and plots of the numerical error $E_{h,X}$ (right column) and at $t = 20000 \text{ s}$ using the non-conservative formulation (NC) and the Brooks and Corey model in 2D on rectangles for various choices of D_X .

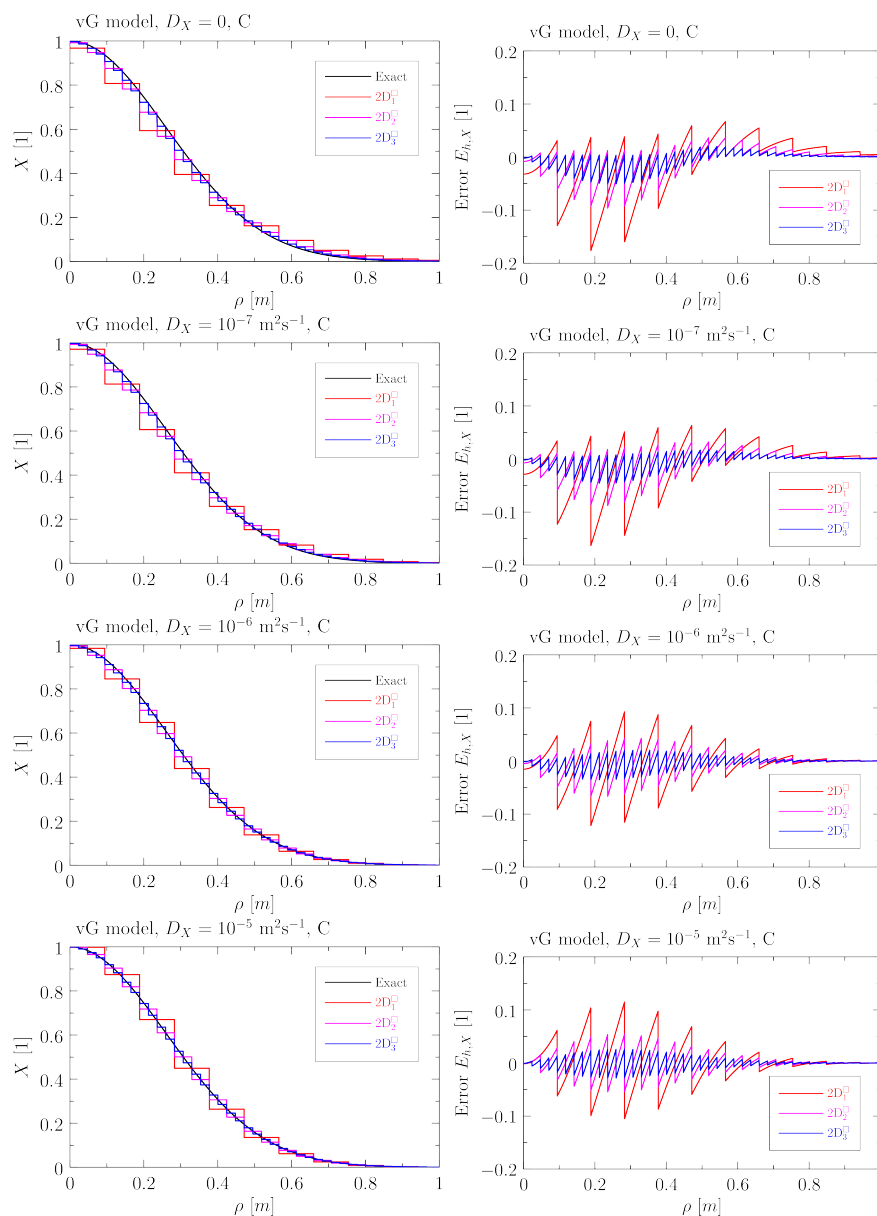


Figure 9: Numerical solutions of the mass fraction profiles X (left column) and plots of the numerical error $E_{h,X}$ (right column) and at $t = 20000 \text{ s}$ using the conservative formulation (C) and the van Genuchten model in 2D on rectangles for various choices of D_X .

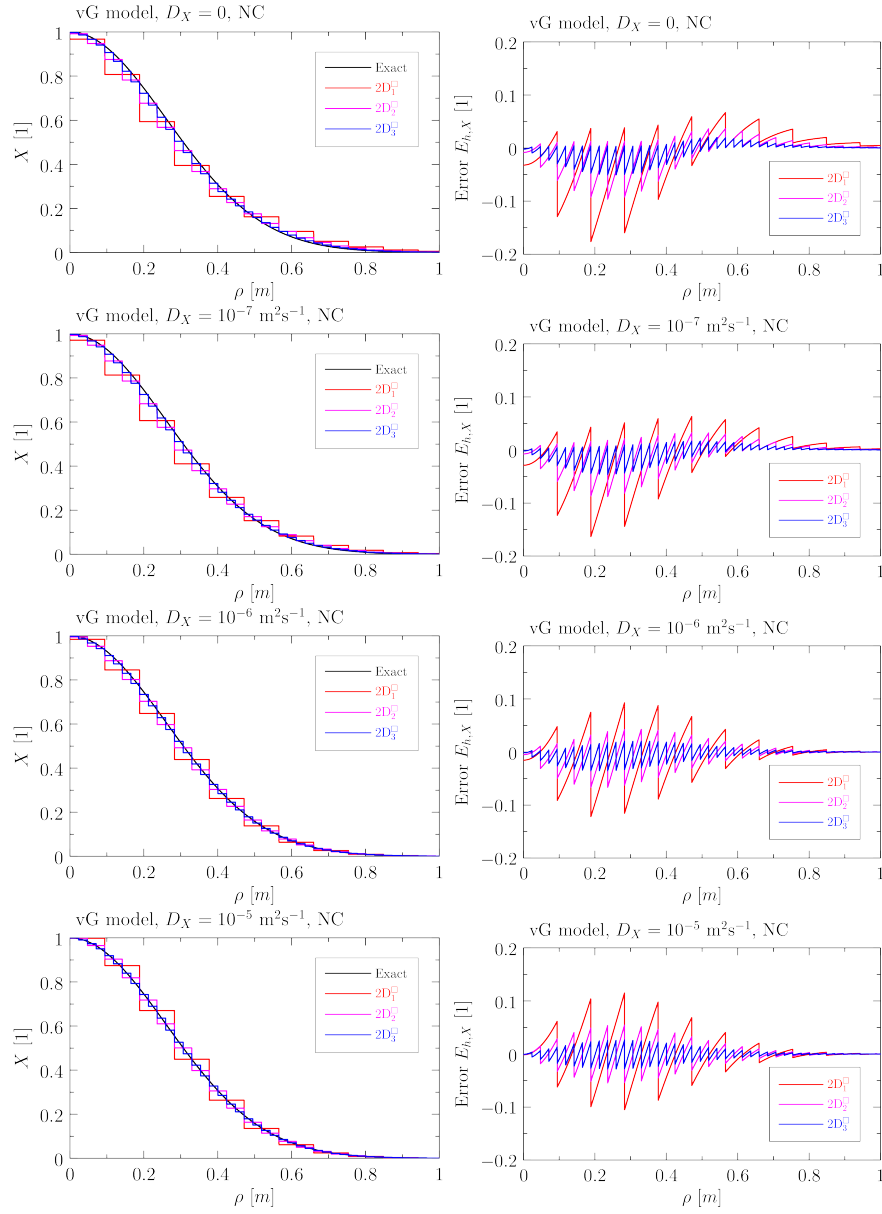


Figure 10: Numerical solutions of the mass fraction profiles X (left column) and plots of the numerical error $E_{h,X}$ (right column) and at $t = 20000$ s using the non-conservative formulation (NC) and the van Genuchten model in 2D on rectangles for various choices of D_X .

3.3. Results in 2D on triangles

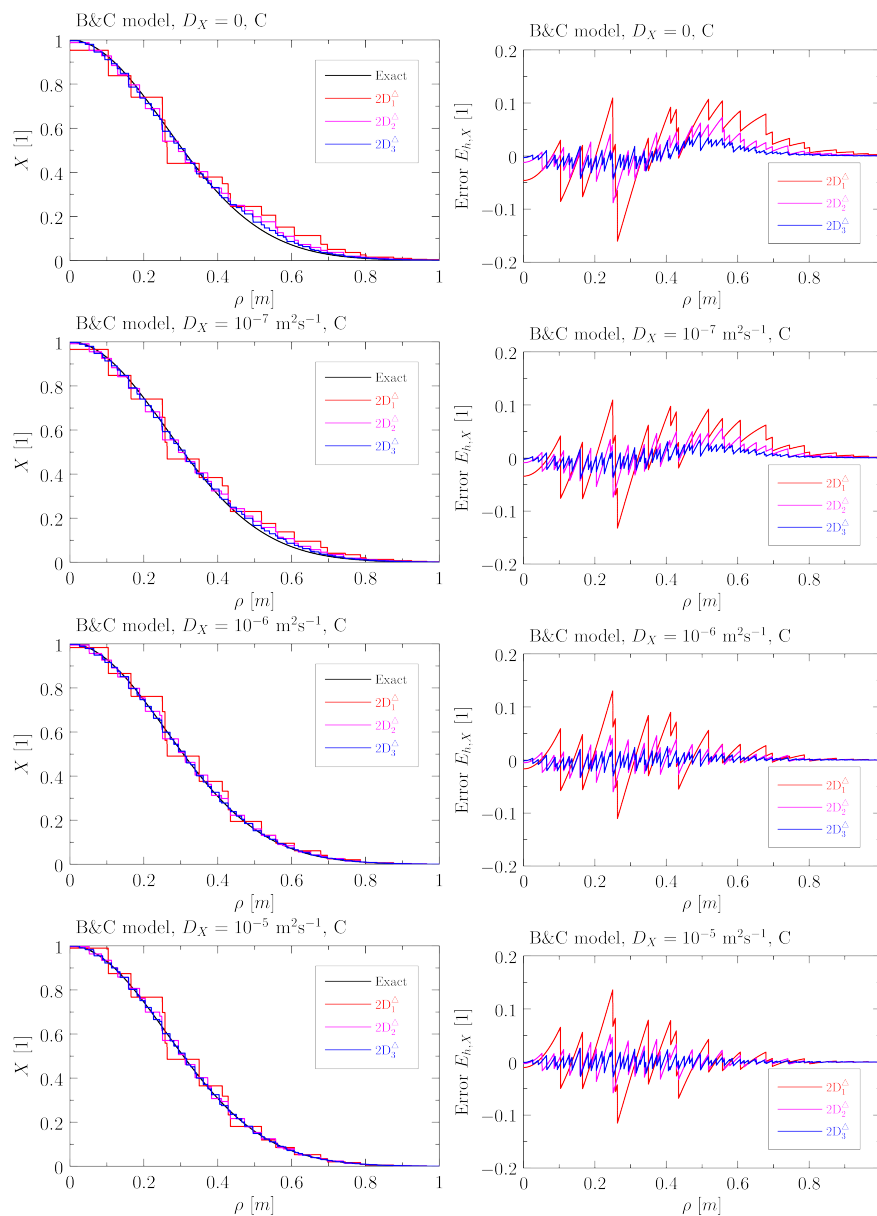


Figure 11: Numerical solutions of the mass fraction profiles X (left column) and plots of the numerical error $E_{h,X}$ (right column) and at $t = 20000$ s using the conservative formulation (C) and the Brooks and Corey model in 2D on triangles for various choices of D_X .

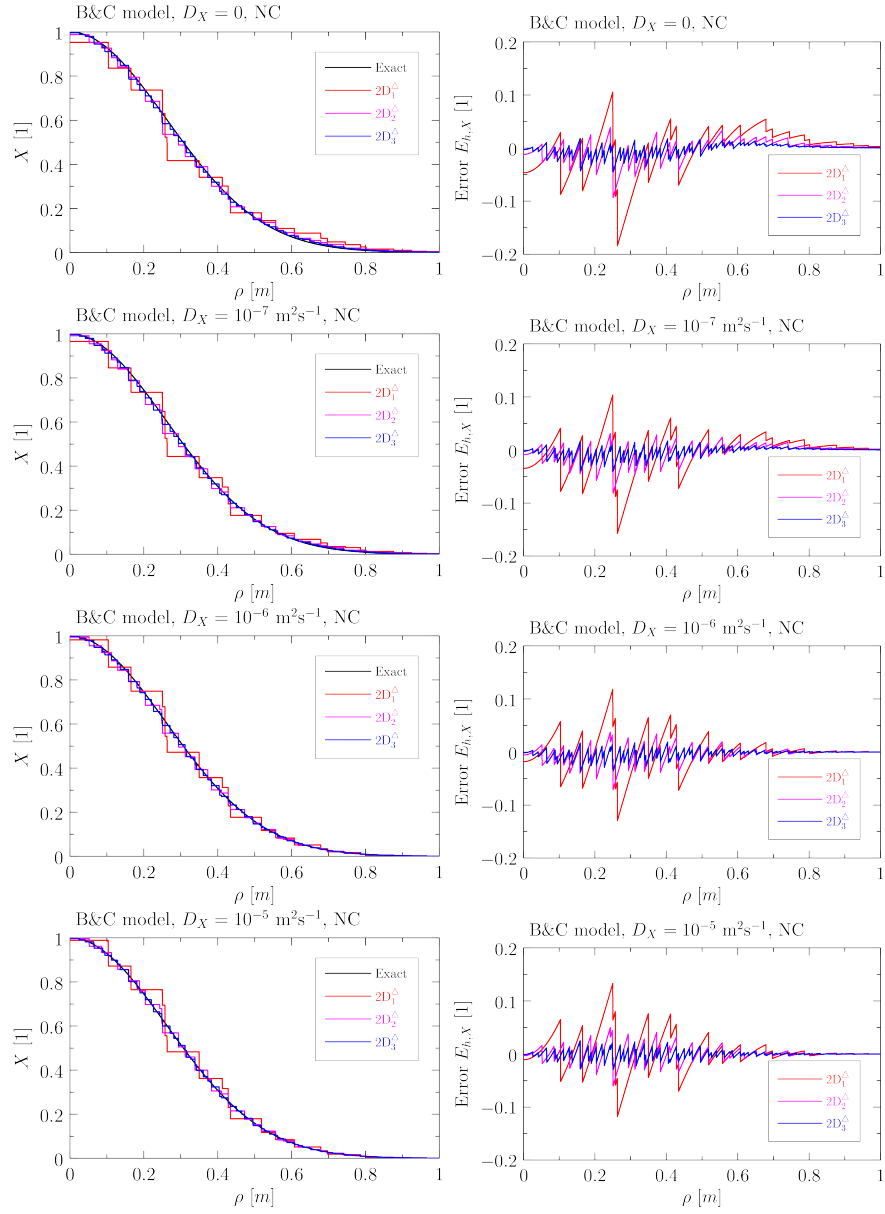


Figure 12: Numerical solutions of the mass fraction profiles X (left column) and plots of the numerical error $E_{h,X}$ (right column) and at $t = 20000$ s using the non-conservative formulation (NC) and the Brooks and Corey model in 2D on triangles for various choices of D_X .

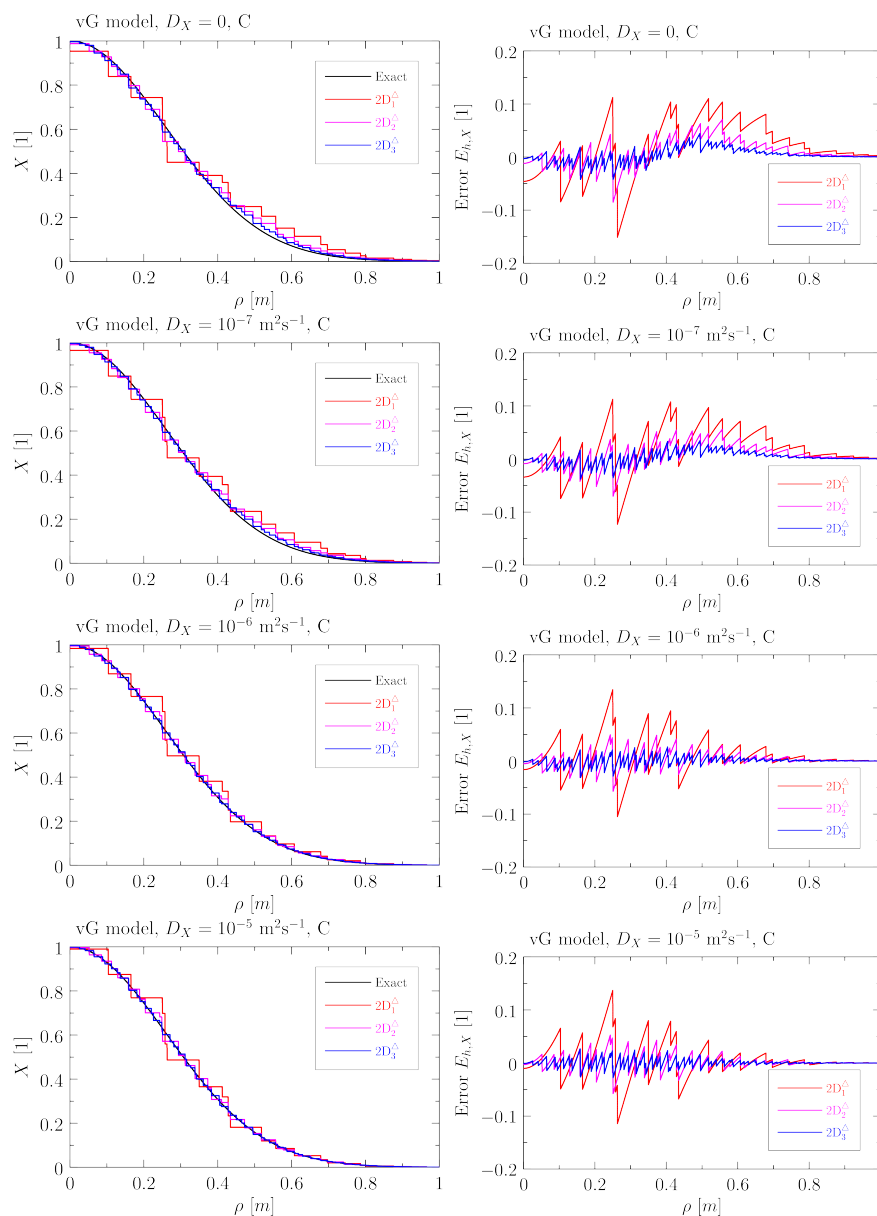


Figure 13: Numerical solutions of the mass fraction profiles X (left column) and plots of the numerical error $E_{h,X}$ (right column) and at $t = 20000$ s using the conservative formulation (C) and the van Genuchten model in 2D on triangles for various choices of D_X .

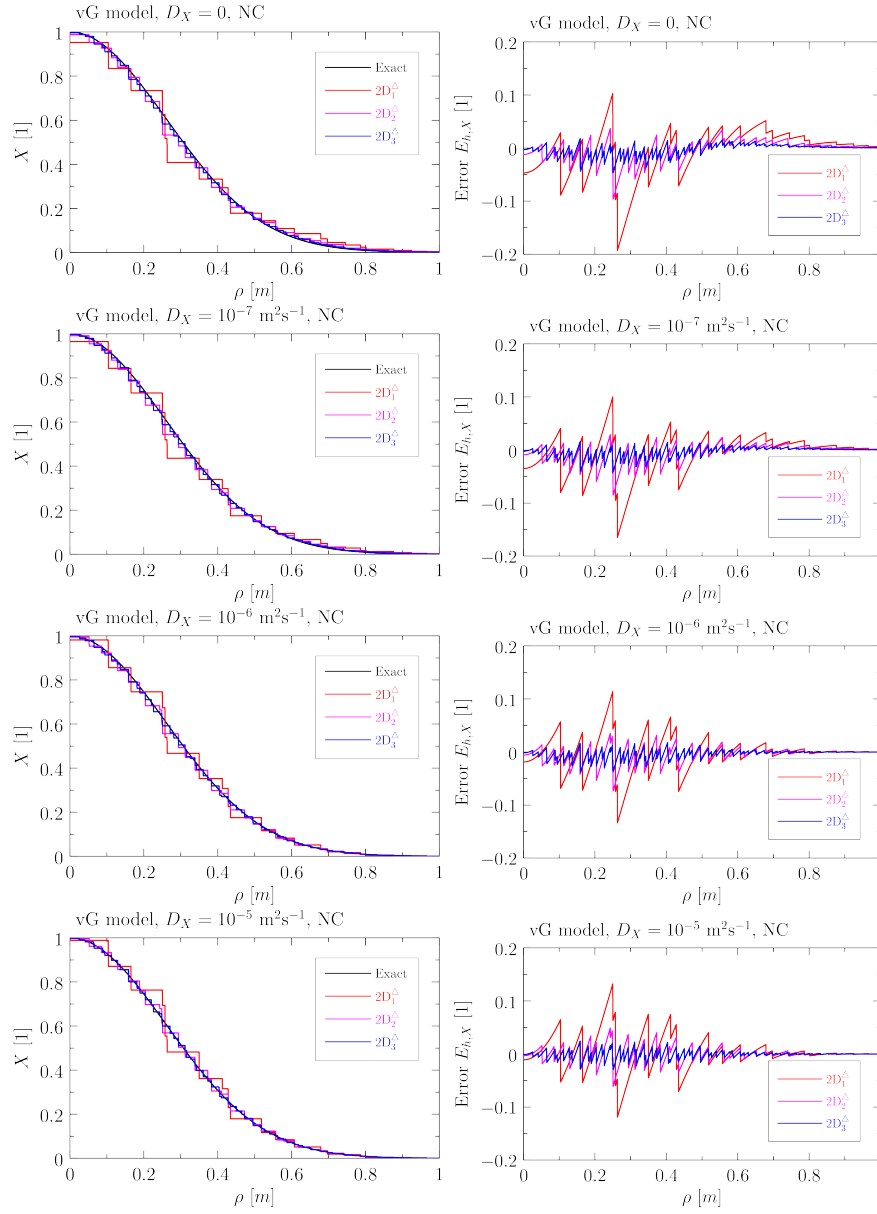


Figure 14: Numerical solutions of the mass fraction profiles X (left column) and plots of the numerical error $E_{h,X}$ (right column) and at $t = 20000$ s using the non-conservative formulation (NC) and the van Genuchten model in 2D on triangles for various choices of D_X .

3.4. Results in 3D on cuboids

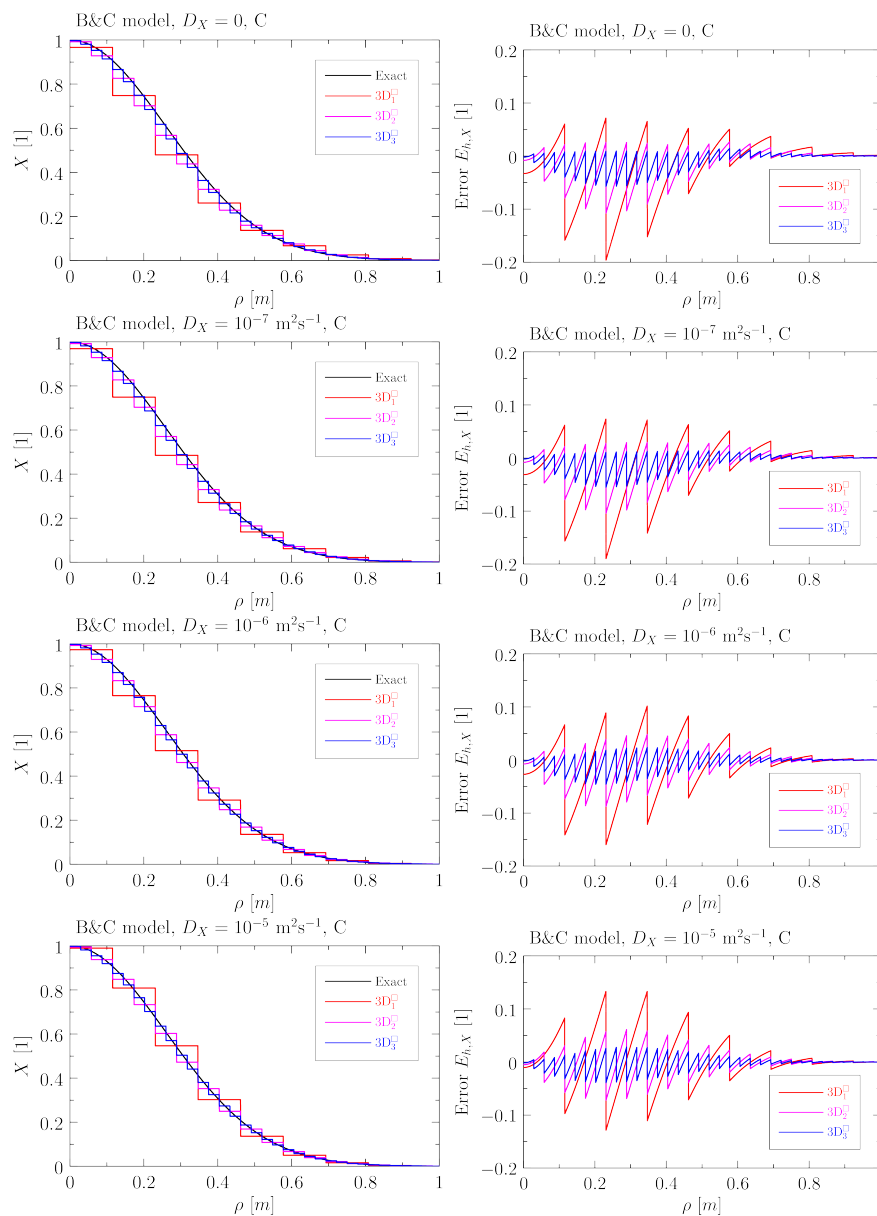


Figure 15: Numerical solutions of the mass fraction profiles X (left column) and plots of the numerical error $E_{h,X}$ (right column) and at $t = 20000$ s using the conservative formulation (C) and the Brooks and Corey model in 3D on cuboids for various choices of D_X .

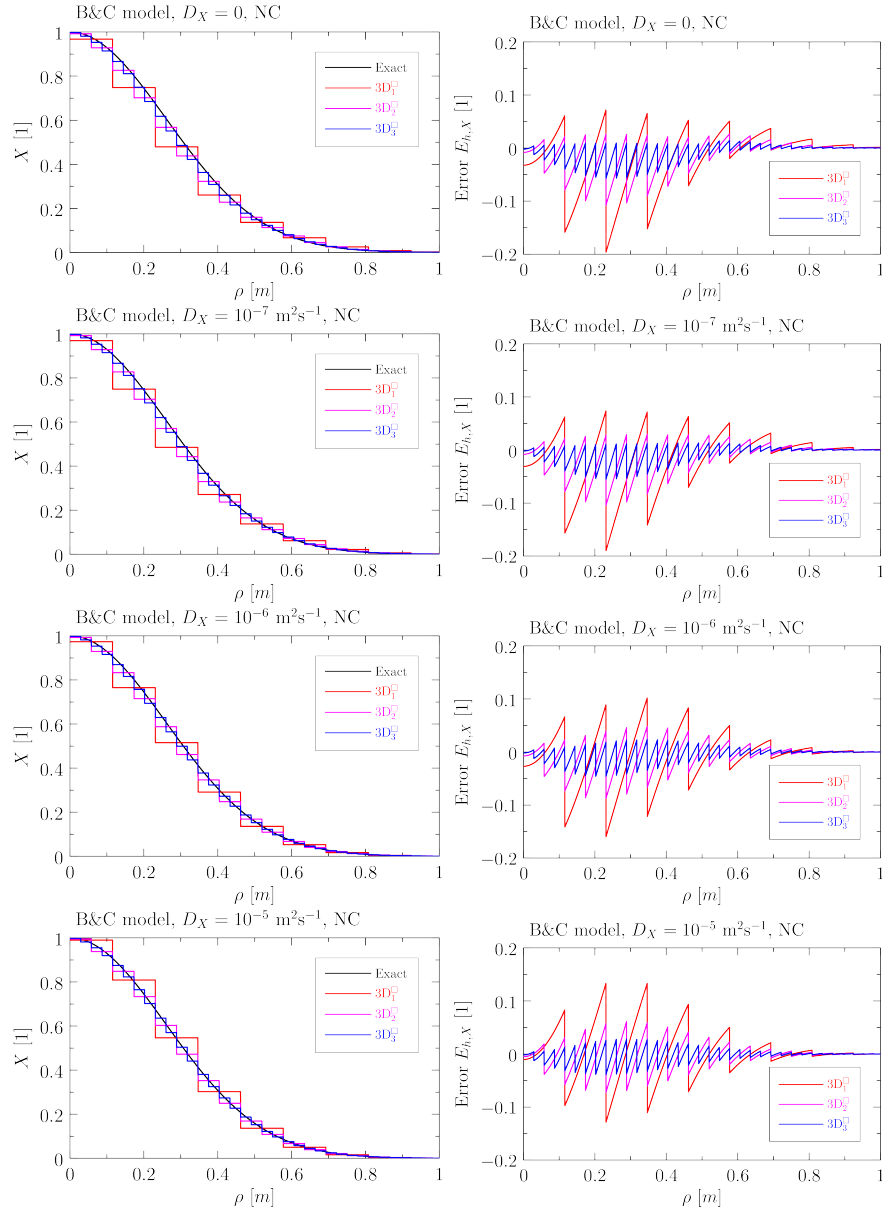


Figure 16: Numerical solutions of the mass fraction profiles X (left column) and plots of the numerical error $E_{h,X}$ (right column) and at $t = 20000$ s using the non-conservative formulation (NC) and the Brooks and Corey model in 3D on cuboids for various choices of D_X .

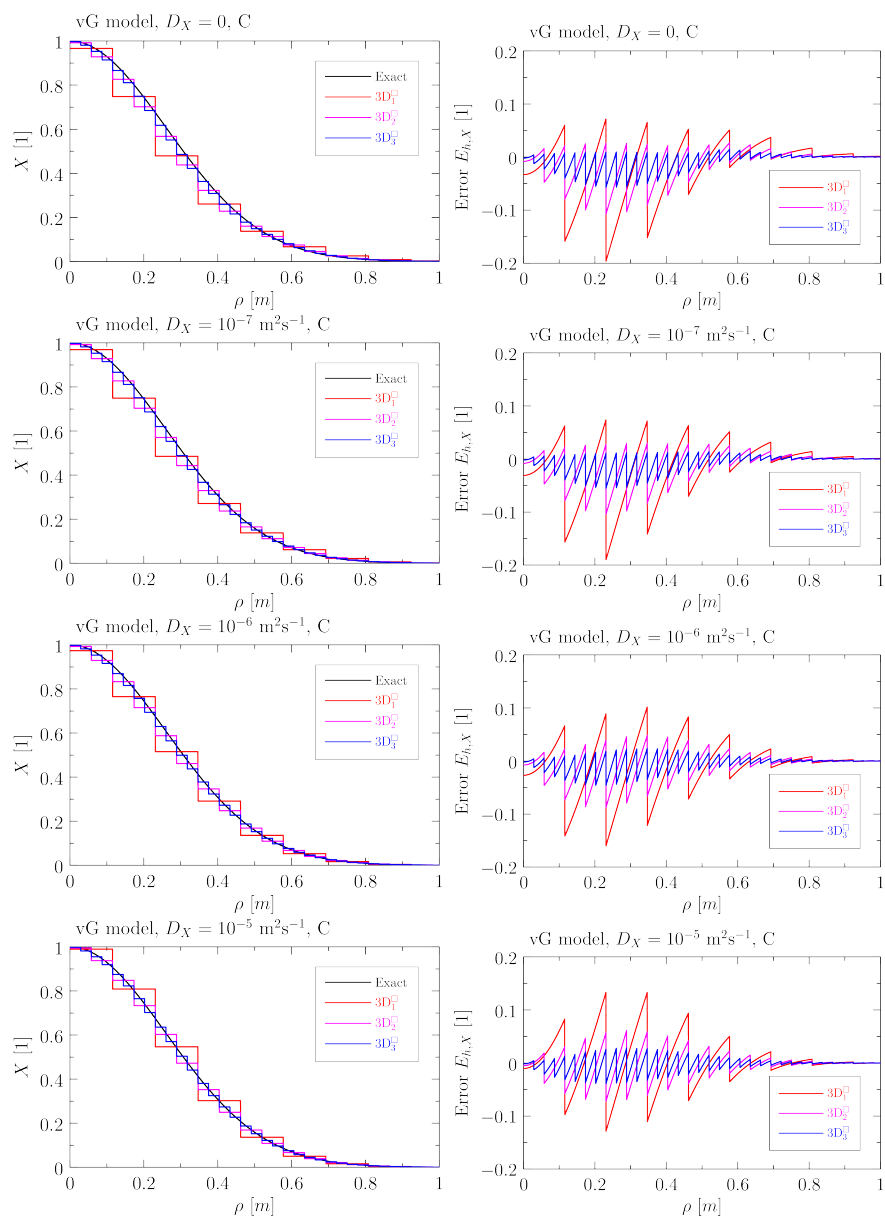


Figure 17: Numerical solutions of the mass fraction profiles X (left column) and plots of the numerical error $E_{h,X}$ (right column) and at $t = 20000$ s using the conservative formulation (C) and the van Genuchten model in 3D on cuboids for various choices of D_X .

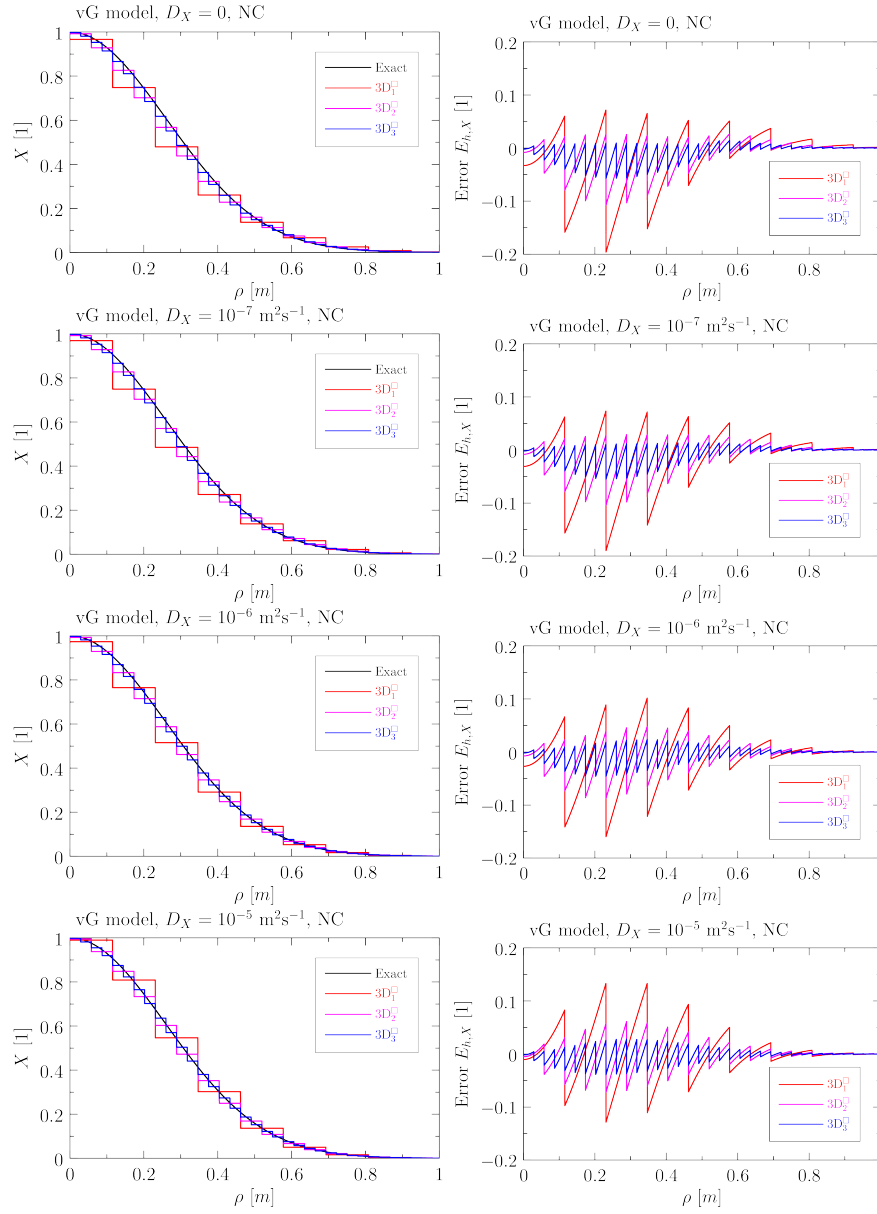


Figure 18: Numerical solutions of the mass fraction profiles X (left column) and plots of the numerical error $E_{h,X}$ (right column) and at $t = 20000\text{s}$ using the non-conservative formulation (NC) and the van Genuchten model in 3D on cuboids for various choices of D_X .

3.5. Results in 3D on tetrahedra

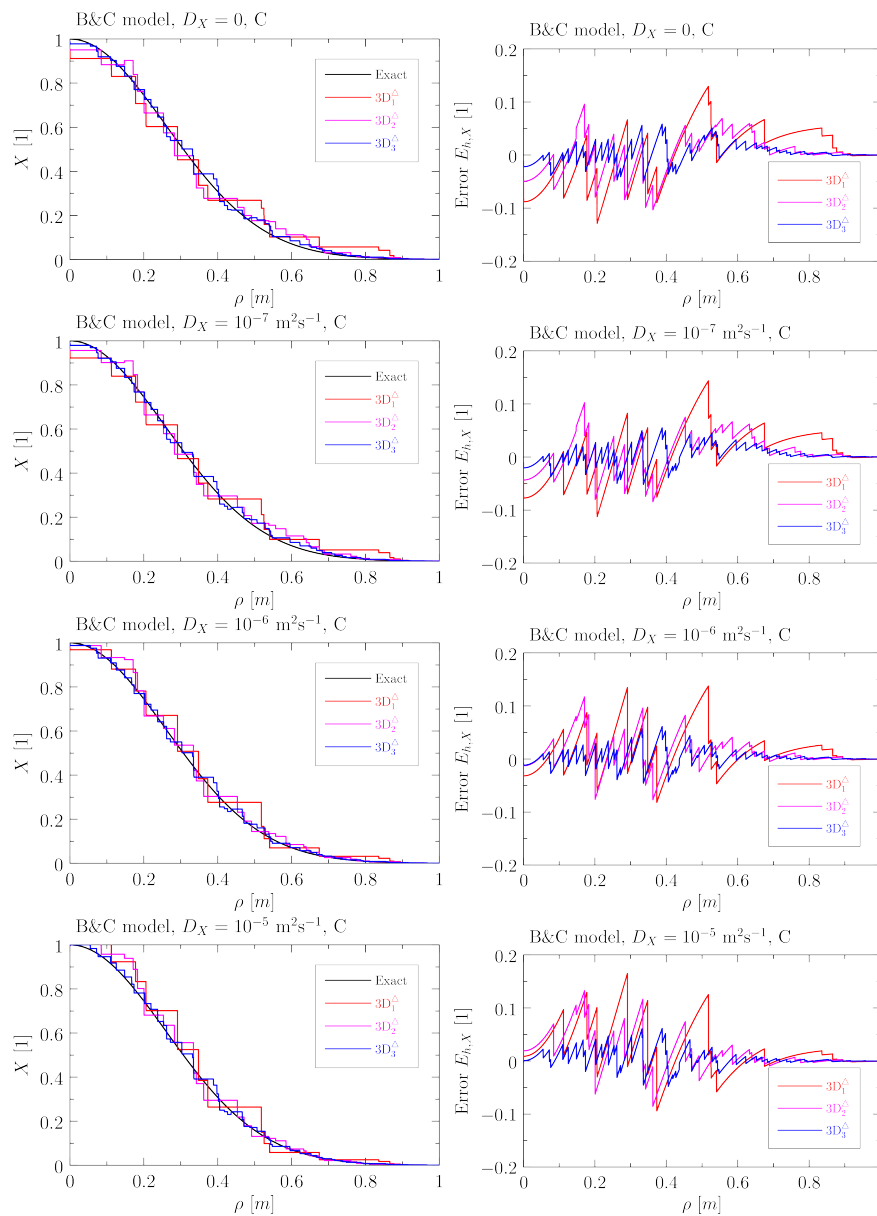


Figure 19: Numerical solutions of the mass fraction profiles X (left column) and plots of the numerical error $E_{h,X}$ (right column) and at $t = 20000$ s using the conservative formulation (C) and the Brooks and Corey model in 3D on tetrahedra for various choices of D_X .

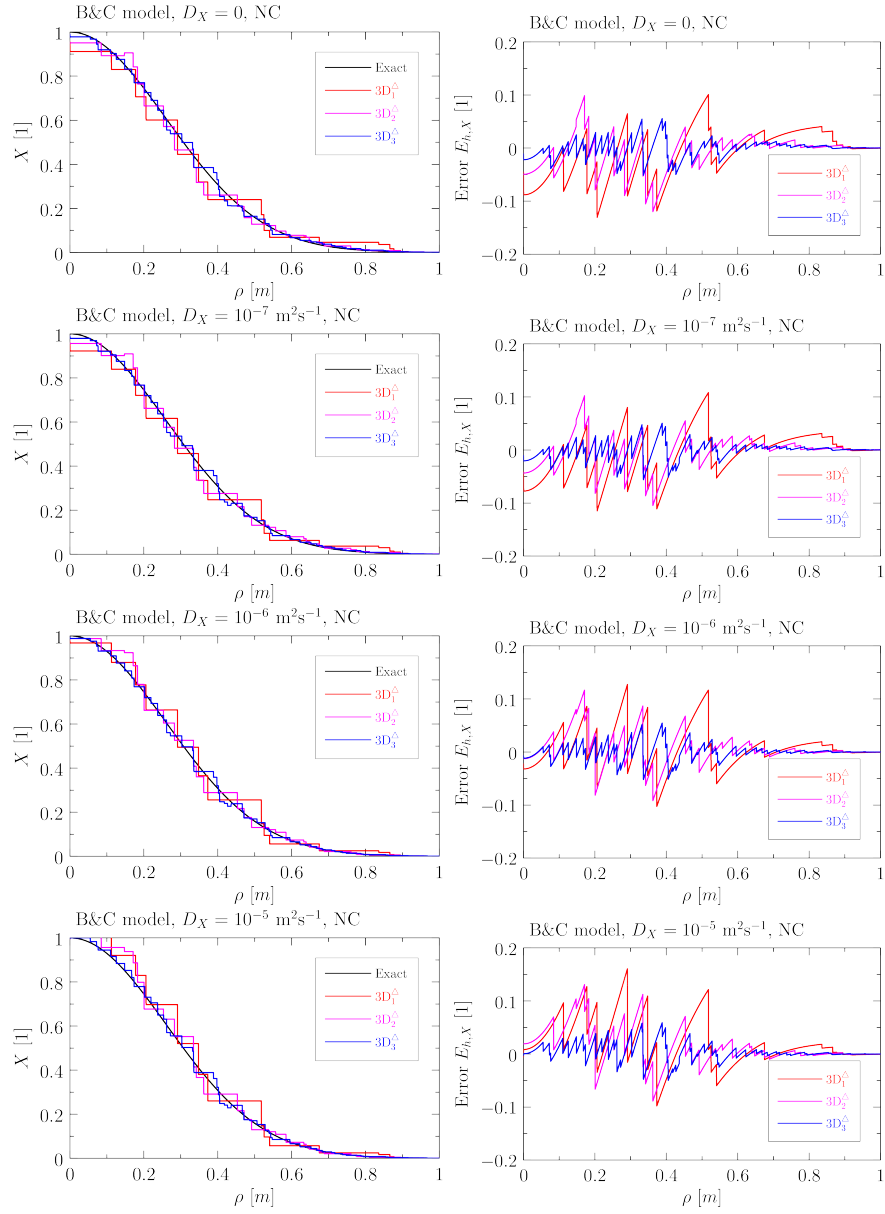


Figure 20: Numerical solutions of the mass fraction profiles X (left column) and plots of the numerical error $E_{h,X}$ (right column) and at $t = 20000$ s using the non-conservative formulation (NC) and the Brooks and Corey model in 3D on tetrahedra for various choices of D_X .

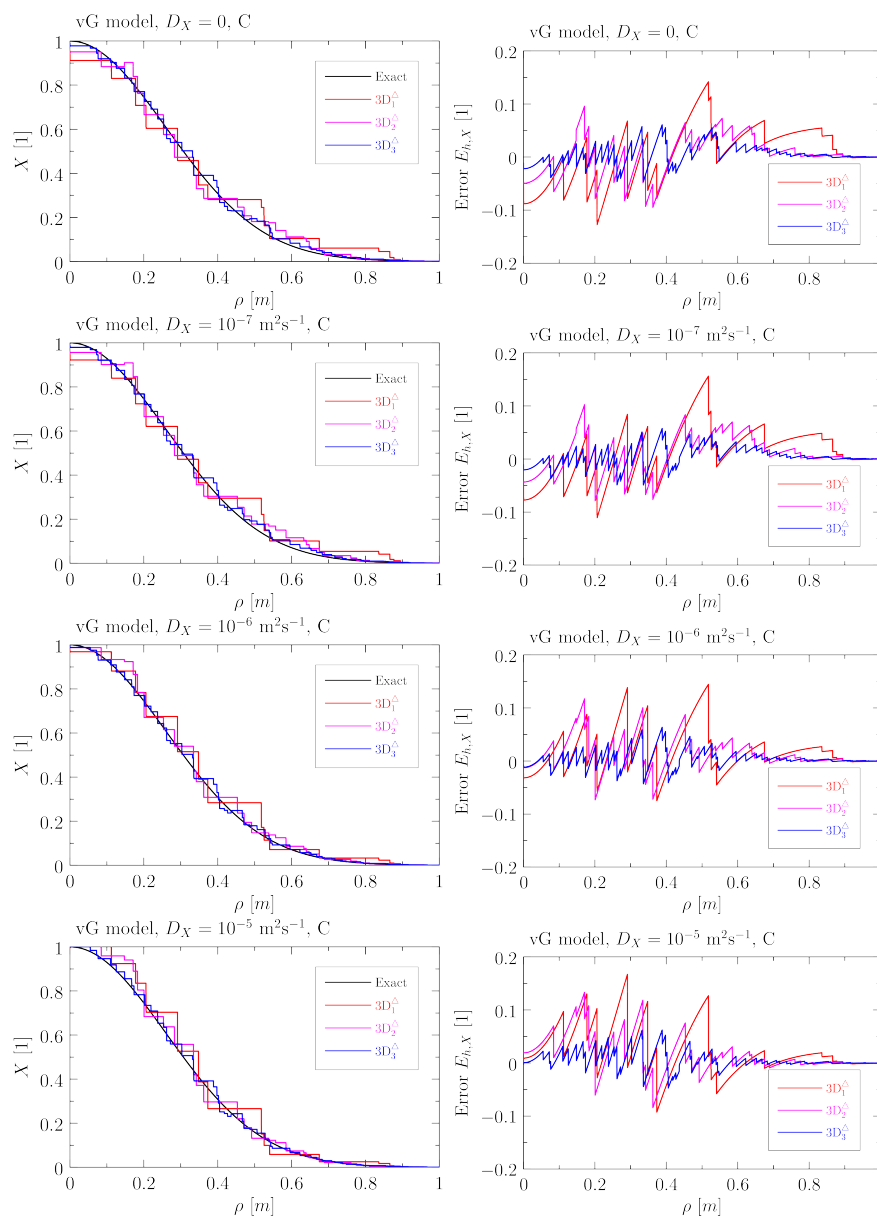


Figure 21: Numerical solutions of the mass fraction profiles X (left column) and plots of the numerical error $E_{h,X}$ (right column) and at $t = 20000$ s using the conservative formulation (C) and the van Genuchten model in 3D on tetrahedra for various choices of D_X .

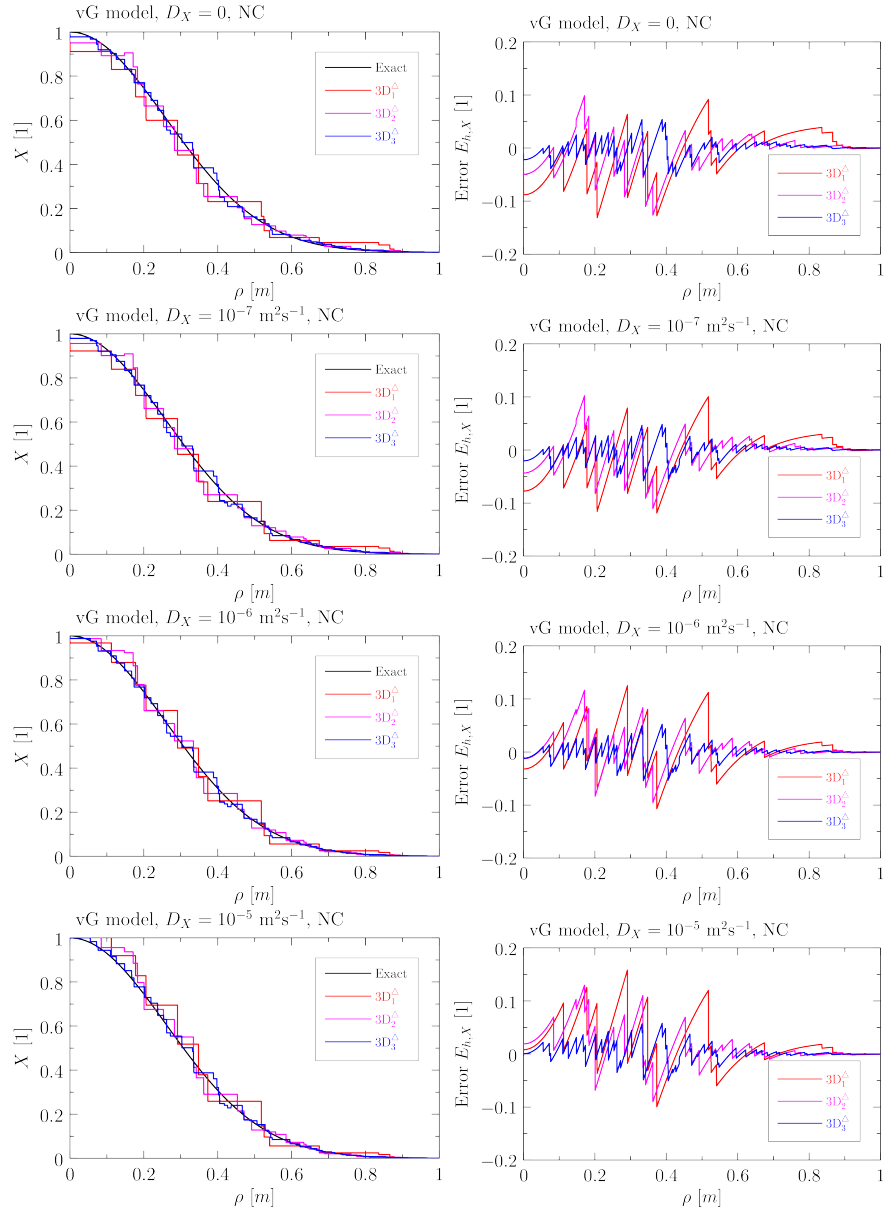


Figure 22: Numerical solutions of the mass fraction profiles X (left column) and plots of the numerical error $E_{h,X}$ (right column) and at $t = 20000$ s using the non-conservative formulation (NC) and the van Genuchten model in 3D on tetrahedra for various choices of D_X .

24

3.6. Experimental orders of convergence

Id.	Conservative Formulation								Non-Conservative Formulation							
	$D_X = 0 \text{ m}^2/\text{s}$		$D_X = 10^{-7} \text{ m}^2/\text{s}$		$D_X = 10^{-6} \text{ m}^2/\text{s}$		$D_X = 10^{-5} \text{ m}^2/\text{s}$		$D_X = 0 \text{ m}^2/\text{s}$		$D_X = 10^{-7} \text{ m}^2/\text{s}$		$D_X = 10^{-6} \text{ m}^2/\text{s}$		$D_X = 10^{-5} \text{ m}^2/\text{s}$	
	$\ E_{h,X}\ _1$	$eoc_{X,1}$	$\ E_{h,X}\ _1$	$eoc_{X,1}$	$\ E_{h,X}\ _1$	$eoc_{X,1}$	$\ E_{h,X}\ _1$	$eoc_{X,1}$	$\ E_{h,X}\ _1$	$eoc_{X,1}$	$\ E_{h,X}\ _1$	$eoc_{X,1}$	$\ E_{h,X}\ _1$	$eoc_{X,1}$	$\ E_{h,X}\ _1$	$eoc_{X,1}$
1D ₁	$1.68 \cdot 10^{-2}$	0.94	$1.09 \cdot 10^{-2}$	0.96	$4.02 \cdot 10^{-3}$	0.99	$3.46 \cdot 10^{-3}$	1.02	$1.69 \cdot 10^{-2}$	0.93	$1.09 \cdot 10^{-2}$	0.96	$4.02 \cdot 10^{-3}$	0.99	$3.46 \cdot 10^{-3}$	1.02
1D ₂	$8.77 \cdot 10^{-3}$	1.00	$5.60 \cdot 10^{-3}$	0.99	$2.02 \cdot 10^{-3}$	0.99	$1.70 \cdot 10^{-3}$	1.01	$8.89 \cdot 10^{-3}$	0.98	$5.62 \cdot 10^{-3}$	0.98	$2.02 \cdot 10^{-3}$	0.99	$1.70 \cdot 10^{-3}$	1.01
1D ₃	$4.38 \cdot 10^{-3}$	1.02	$2.82 \cdot 10^{-3}$	1.00	$1.02 \cdot 10^{-3}$	1.00	$8.45 \cdot 10^{-4}$	1.00	$4.50 \cdot 10^{-3}$	1.00	$2.84 \cdot 10^{-3}$	0.99	$1.02 \cdot 10^{-3}$	1.00	$8.45 \cdot 10^{-4}$	1.00
1D ₄	$2.16 \cdot 10^{-3}$	1.02	$1.41 \cdot 10^{-3}$	1.00	$5.09 \cdot 10^{-4}$	1.00	$4.23 \cdot 10^{-4}$	1.00	$2.25 \cdot 10^{-3}$	1.00	$1.43 \cdot 10^{-3}$	1.00	$5.09 \cdot 10^{-4}$	1.00	$4.23 \cdot 10^{-4}$	1.00
1D ₅	$1.07 \cdot 10^{-3}$	0.97	$7.03 \cdot 10^{-4}$	1.01	$2.55 \cdot 10^{-4}$	1.00	$2.12 \cdot 10^{-4}$	1.00	$1.13 \cdot 10^{-3}$	1.00	$7.17 \cdot 10^{-4}$	1.00	$2.55 \cdot 10^{-4}$	1.00	$2.12 \cdot 10^{-4}$	1.00
1D ₆	$5.45 \cdot 10^{-4}$	0.94	$3.50 \cdot 10^{-4}$	1.01	$1.28 \cdot 10^{-4}$	1.00	$1.06 \cdot 10^{-4}$	1.00	$5.64 \cdot 10^{-4}$	1.00	$3.59 \cdot 10^{-4}$	1.00	$1.28 \cdot 10^{-4}$	1.00	$1.06 \cdot 10^{-4}$	1.00
1D ₇	$2.84 \cdot 10^{-4}$		$1.74 \cdot 10^{-4}$		$6.39 \cdot 10^{-5}$		$5.31 \cdot 10^{-5}$		$2.82 \cdot 10^{-4}$		$1.79 \cdot 10^{-4}$		$6.38 \cdot 10^{-5}$		$5.31 \cdot 10^{-5}$	
2D ₁ ^C	$2.59 \cdot 10^{-2}$	1.08	$1.79 \cdot 10^{-2}$	1.01	$8.56 \cdot 10^{-3}$	0.96	$8.46 \cdot 10^{-3}$	1.01	$2.59 \cdot 10^{-2}$	1.08	$1.79 \cdot 10^{-2}$	1.01	$8.56 \cdot 10^{-3}$	0.96	$8.46 \cdot 10^{-3}$	1.01
2D ₂ ^C	$1.23 \cdot 10^{-2}$	0.99	$8.91 \cdot 10^{-3}$	0.99	$4.40 \cdot 10^{-3}$	0.95	$4.19 \cdot 10^{-3}$	0.99	$1.23 \cdot 10^{-2}$	0.99	$8.91 \cdot 10^{-3}$	0.99	$4.40 \cdot 10^{-3}$	0.95	$4.19 \cdot 10^{-3}$	0.99
2D ₃ ^C	$6.18 \cdot 10^{-3}$	0.97	$4.49 \cdot 10^{-3}$	0.99	$2.29 \cdot 10^{-3}$	0.95	$2.11 \cdot 10^{-3}$	0.97	$6.18 \cdot 10^{-3}$	0.97	$4.49 \cdot 10^{-3}$	0.99	$2.29 \cdot 10^{-3}$	0.95	$2.11 \cdot 10^{-3}$	0.97
2D ₄ ^C	$3.16 \cdot 10^{-3}$	0.95	$2.27 \cdot 10^{-3}$	0.98	$1.18 \cdot 10^{-3}$	0.96	$1.08 \cdot 10^{-3}$	0.94	$3.16 \cdot 10^{-3}$	0.95	$2.27 \cdot 10^{-3}$	0.98	$1.18 \cdot 10^{-3}$	0.96	$1.08 \cdot 10^{-3}$	0.94
2D ₅ ^C	$1.64 \cdot 10^{-3}$		$1.15 \cdot 10^{-3}$		$6.09 \cdot 10^{-4}$		$5.59 \cdot 10^{-4}$		$1.64 \cdot 10^{-3}$		$1.15 \cdot 10^{-3}$		$6.09 \cdot 10^{-4}$		$5.59 \cdot 10^{-4}$	
2D ₁ ^A	$2.77 \cdot 10^{-2}$	1.09	$2.20 \cdot 10^{-2}$	1.06	$1.03 \cdot 10^{-2}$	1.13	$8.97 \cdot 10^{-3}$	1.10	$1.83 \cdot 10^{-2}$	1.16	$1.30 \cdot 10^{-2}$	1.09	$8.73 \cdot 10^{-3}$	1.02	$8.86 \cdot 10^{-3}$	1.09
2D ₂ ^A	$1.36 \cdot 10^{-2}$	0.89	$1.10 \cdot 10^{-2}$	0.88	$4.94 \cdot 10^{-3}$	0.91	$4.39 \cdot 10^{-3}$	0.92	$8.57 \cdot 10^{-3}$	0.94	$6.40 \cdot 10^{-3}$	0.92	$4.50 \cdot 10^{-3}$	0.82	$4.36 \cdot 10^{-3}$	0.91
2D ₃ ^A	$6.92 \cdot 10^{-3}$	1.06	$5.65 \cdot 10^{-3}$	1.06	$2.48 \cdot 10^{-3}$	1.07	$2.19 \cdot 10^{-3}$	1.08	$4.21 \cdot 10^{-3}$	1.10	$3.21 \cdot 10^{-3}$	1.09	$2.42 \cdot 10^{-3}$	1.00	$2.19 \cdot 10^{-3}$	1.07
2D ₄ ^A	$3.55 \cdot 10^{-3}$		$2.89 \cdot 10^{-3}$		$1.26 \cdot 10^{-3}$		$1.11 \cdot 10^{-3}$		$2.10 \cdot 10^{-3}$		$1.61 \cdot 10^{-3}$		$1.29 \cdot 10^{-3}$		$1.12 \cdot 10^{-3}$	
3D ₁ ^C	$9.35 \cdot 10^{-3}$	1.17	$7.44 \cdot 10^{-3}$	1.10	$3.64 \cdot 10^{-3}$	0.96	$3.45 \cdot 10^{-3}$	1.00	$9.40 \cdot 10^{-3}$	1.18	$7.32 \cdot 10^{-3}$	1.08	$3.64 \cdot 10^{-3}$	0.96	$3.45 \cdot 10^{-3}$	1.00
3D ₂ ^C	$4.14 \cdot 10^{-3}$	1.00	$3.47 \cdot 10^{-3}$	1.00	$1.86 \cdot 10^{-3}$	0.98	$1.72 \cdot 10^{-3}$	0.95	$4.14 \cdot 10^{-3}$	1.00	$3.47 \cdot 10^{-3}$	1.00	$1.86 \cdot 10^{-3}$	0.98	$1.72 \cdot 10^{-3}$	0.95
3D ₃ ^C	$2.07 \cdot 10^{-3}$		$1.73 \cdot 10^{-3}$		$9.44 \cdot 10^{-4}$		$8.89 \cdot 10^{-4}$		$2.07 \cdot 10^{-3}$		$1.73 \cdot 10^{-3}$		$9.44 \cdot 10^{-4}$		$8.89 \cdot 10^{-4}$	
3D ₁ ^A	$1.40 \cdot 10^{-2}$	0.65	$1.25 \cdot 10^{-2}$	0.62	$7.64 \cdot 10^{-3}$	0.69	$6.56 \cdot 10^{-3}$	0.78	$9.05 \cdot 10^{-3}$	0.73	$7.50 \cdot 10^{-3}$	0.70	$6.01 \cdot 10^{-3}$	0.72	$6.36 \cdot 10^{-3}$	0.78
3D ₂ ^A	$1.00 \cdot 10^{-2}$	1.06	$9.09 \cdot 10^{-3}$	1.07	$5.34 \cdot 10^{-3}$	1.11	$4.36 \cdot 10^{-3}$	1.07	$6.20 \cdot 10^{-3}$	1.10	$5.22 \cdot 10^{-3}$	1.11	$4.14 \cdot 10^{-3}$	1.06	$4.24 \cdot 10^{-3}$	1.07
3D ₃ ^A	$4.77 \cdot 10^{-3}$	1.23	$4.30 \cdot 10^{-3}$	1.23	$2.45 \cdot 10^{-3}$	1.31	$2.06 \cdot 10^{-3}$	1.26	$2.88 \cdot 10^{-3}$	1.26	$2.41 \cdot 10^{-3}$	1.23	$1.97 \cdot 10^{-3}$	1.14	$2.01 \cdot 10^{-3}$	1.20
3D ₄ ^A	$2.30 \cdot 10^{-3}$		$2.07 \cdot 10^{-3}$		$1.13 \cdot 10^{-3}$		$9.77 \cdot 10^{-4}$		$1.36 \cdot 10^{-3}$		$1.16 \cdot 10^{-3}$		$1.00 \cdot 10^{-3}$		$9.83 \cdot 10^{-4}$	

Table 1: Results of the numerical analysis using the L_1 norm and the Brooks and Corey model.

25

Id.	Conservative Formulation								Non-Conservative Formulation							
	$D_X = 0 \text{ m}^2/\text{s}$		$D_X = 10^{-7} \text{ m}^2/\text{s}$		$D_X = 10^{-6} \text{ m}^2/\text{s}$		$D_X = 10^{-5} \text{ m}^2/\text{s}$		$D_X = 0 \text{ m}^2/\text{s}$		$D_X = 10^{-7} \text{ m}^2/\text{s}$		$D_X = 10^{-6} \text{ m}^2/\text{s}$		$D_X = 10^{-5} \text{ m}^2/\text{s}$	
	$\ E_{h,X}\ _2$	$\text{eoc}_{X,2}$	$\ E_{h,X}\ _2$	$\text{eoc}_{X,2}$	$\ E_{h,X}\ _2$	$\text{eoc}_{X,2}$	$\ E_{h,X}\ _2$	$\text{eoc}_{X,2}$	$\ E_{h,X}\ _2$	$\text{eoc}_{X,2}$	$\ E_{h,X}\ _2$	$\text{eoc}_{X,2}$	$\ E_{h,X}\ _2$	$\text{eoc}_{X,2}$	$\ E_{h,X}\ _2$	$\text{eoc}_{X,2}$
1D ₁	$2.00 \cdot 10^{-2}$	0.92	$1.36 \cdot 10^{-2}$	0.95	$7.61 \cdot 10^{-3}$	1.00	$7.53 \cdot 10^{-3}$	1.00	$2.01 \cdot 10^{-2}$	0.91	$1.36 \cdot 10^{-2}$	0.95	$7.61 \cdot 10^{-3}$	1.00	$7.53 \cdot 10^{-3}$	1.00
1D ₂	$1.06 \cdot 10^{-2}$	0.99	$7.02 \cdot 10^{-3}$	0.98	$3.81 \cdot 10^{-3}$	1.00	$3.76 \cdot 10^{-3}$	1.00	$1.07 \cdot 10^{-2}$	0.97	$7.05 \cdot 10^{-3}$	0.98	$3.81 \cdot 10^{-3}$	1.00	$3.76 \cdot 10^{-3}$	1.00
1D ₃	$5.35 \cdot 10^{-3}$	1.01	$3.55 \cdot 10^{-3}$	1.00	$1.91 \cdot 10^{-3}$	1.00	$1.88 \cdot 10^{-3}$	1.00	$5.47 \cdot 10^{-3}$	0.99	$3.58 \cdot 10^{-3}$	0.99	$1.91 \cdot 10^{-3}$	1.00	$1.88 \cdot 10^{-3}$	1.00
1D ₄	$2.66 \cdot 10^{-3}$	1.00	$1.78 \cdot 10^{-3}$	1.00	$9.55 \cdot 10^{-4}$	1.00	$9.41 \cdot 10^{-4}$	1.00	$2.76 \cdot 10^{-3}$	1.00	$1.81 \cdot 10^{-3}$	0.99	$9.55 \cdot 10^{-4}$	1.00	$9.41 \cdot 10^{-4}$	1.00
1D ₅	$1.33 \cdot 10^{-3}$	0.98	$8.86 \cdot 10^{-4}$	1.01	$4.78 \cdot 10^{-4}$	1.00	$4.70 \cdot 10^{-4}$	1.00	$1.38 \cdot 10^{-3}$	1.00	$9.06 \cdot 10^{-4}$	1.00	$4.78 \cdot 10^{-4}$	1.00	$4.70 \cdot 10^{-4}$	1.00
1D ₆	$6.74 \cdot 10^{-4}$	0.92	$4.41 \cdot 10^{-4}$	1.01	$2.39 \cdot 10^{-4}$	1.00	$2.35 \cdot 10^{-4}$	1.00	$6.93 \cdot 10^{-4}$	1.00	$4.54 \cdot 10^{-4}$	1.00	$2.39 \cdot 10^{-4}$	1.00	$2.35 \cdot 10^{-4}$	1.00
1D ₇	$3.55 \cdot 10^{-4}$		$2.19 \cdot 10^{-4}$		$1.19 \cdot 10^{-4}$		$1.18 \cdot 10^{-4}$		$3.47 \cdot 10^{-4}$		$2.27 \cdot 10^{-4}$		$1.19 \cdot 10^{-4}$		$1.18 \cdot 10^{-4}$	
2D ₁ ^Δ	$3.61 \cdot 10^{-2}$	0.95	$2.69 \cdot 10^{-2}$	0.93	$1.73 \cdot 10^{-2}$	0.93	$1.74 \cdot 10^{-2}$	1.02	$3.61 \cdot 10^{-2}$	0.95	$2.69 \cdot 10^{-2}$	0.93	$1.73 \cdot 10^{-2}$	0.93	$1.74 \cdot 10^{-2}$	1.02
2D ₂ ^Δ	$1.87 \cdot 10^{-2}$	0.94	$1.42 \cdot 10^{-2}$	0.95	$9.10 \cdot 10^{-3}$	0.92	$8.55 \cdot 10^{-3}$	1.00	$1.87 \cdot 10^{-2}$	0.94	$1.42 \cdot 10^{-2}$	0.95	$9.10 \cdot 10^{-3}$	0.92	$8.55 \cdot 10^{-3}$	1.00
2D ₃ ^Δ	$9.75 \cdot 10^{-3}$	0.94	$7.33 \cdot 10^{-3}$	0.97	$4.80 \cdot 10^{-3}$	0.95	$4.29 \cdot 10^{-3}$	0.98	$9.75 \cdot 10^{-3}$	0.94	$7.33 \cdot 10^{-3}$	0.97	$4.80 \cdot 10^{-3}$	0.95	$4.29 \cdot 10^{-3}$	0.98
2D ₄ ^Δ	$5.07 \cdot 10^{-3}$	0.95	$3.74 \cdot 10^{-3}$	0.98	$2.49 \cdot 10^{-3}$	0.97	$2.17 \cdot 10^{-3}$	0.97	$5.07 \cdot 10^{-3}$	0.95	$3.74 \cdot 10^{-3}$	0.98	$2.49 \cdot 10^{-3}$	0.97	$2.17 \cdot 10^{-3}$	0.97
2D ₅ ^Δ	$2.63 \cdot 10^{-3}$		$1.89 \cdot 10^{-3}$		$1.27 \cdot 10^{-3}$		$1.10 \cdot 10^{-3}$		$2.63 \cdot 10^{-3}$		$1.89 \cdot 10^{-3}$		$1.27 \cdot 10^{-3}$		$1.10 \cdot 10^{-3}$	
2D ₁ ^Δ	$4.18 \cdot 10^{-2}$	0.97	$3.36 \cdot 10^{-2}$	0.99	$2.04 \cdot 10^{-2}$	1.12	$1.88 \cdot 10^{-2}$	1.10	$2.71 \cdot 10^{-2}$	1.02	$2.11 \cdot 10^{-2}$	0.96	$1.81 \cdot 10^{-2}$	0.97	$1.85 \cdot 10^{-2}$	1.09
2D ₂ ^Δ	$2.22 \cdot 10^{-2}$	0.84	$1.76 \cdot 10^{-2}$	0.85	$9.79 \cdot 10^{-3}$	0.91	$9.16 \cdot 10^{-3}$	0.93	$1.39 \cdot 10^{-2}$	0.88	$1.13 \cdot 10^{-2}$	0.86	$9.61 \cdot 10^{-3}$	0.81	$9.09 \cdot 10^{-3}$	0.92
2D ₃ ^Δ	$1.17 \cdot 10^{-2}$		$9.23 \cdot 10^{-3}$		$4.92 \cdot 10^{-3}$		$4.54 \cdot 10^{-3}$		$7.12 \cdot 10^{-3}$		$5.89 \cdot 10^{-3}$		$5.22 \cdot 10^{-3}$		$4.55 \cdot 10^{-3}$	
2D ₄ ^Δ	$6.15 \cdot 10^{-3}$	1.02	$4.77 \cdot 10^{-3}$	1.04	$2.49 \cdot 10^{-3}$	1.08	$2.27 \cdot 10^{-3}$	1.10	$3.64 \cdot 10^{-3}$	1.07	$3.03 \cdot 10^{-3}$	1.06	$2.77 \cdot 10^{-3}$	1.00	$2.29 \cdot 10^{-3}$	1.08
3D ₁ ^Δ	$1.84 \cdot 10^{-2}$	0.92	$1.62 \cdot 10^{-2}$	1.00	$1.05 \cdot 10^{-2}$	0.94	$1.02 \cdot 10^{-2}$	1.01	$1.88 \cdot 10^{-2}$	0.95	$1.55 \cdot 10^{-2}$	0.94	$1.05 \cdot 10^{-2}$	0.94	$1.02 \cdot 10^{-2}$	1.01
3D ₂ ^Δ	$9.72 \cdot 10^{-3}$	0.93	$8.12 \cdot 10^{-3}$	0.95	$5.45 \cdot 10^{-3}$	0.96	$5.06 \cdot 10^{-3}$	0.94	$9.72 \cdot 10^{-3}$	0.93	$8.12 \cdot 10^{-3}$	0.95	$5.45 \cdot 10^{-3}$	0.96	$5.06 \cdot 10^{-3}$	0.94
3D ₃ ^Δ	$5.12 \cdot 10^{-3}$		$4.22 \cdot 10^{-3}$		$2.80 \cdot 10^{-3}$		$2.65 \cdot 10^{-3}$		$5.12 \cdot 10^{-3}$		$4.22 \cdot 10^{-3}$		$2.80 \cdot 10^{-3}$		$2.65 \cdot 10^{-3}$	
3D ₁ ^Δ	$3.08 \cdot 10^{-2}$	0.51	$2.71 \cdot 10^{-2}$	0.52	$2.04 \cdot 10^{-2}$	0.63	$1.99 \cdot 10^{-2}$	0.71	$2.04 \cdot 10^{-2}$	0.52	$1.81 \cdot 10^{-2}$	0.52	$1.75 \cdot 10^{-2}$	0.61	$1.93 \cdot 10^{-2}$	0.71
3D ₂ ^Δ	$2.36 \cdot 10^{-2}$	1.00	$2.07 \cdot 10^{-2}$	1.04	$1.47 \cdot 10^{-2}$	1.11	$1.37 \cdot 10^{-2}$	1.11	$1.56 \cdot 10^{-2}$	1.04	$1.38 \cdot 10^{-2}$	1.08	$1.28 \cdot 10^{-2}$	1.08	$1.34 \cdot 10^{-2}$	1.11
3D ₃ ^Δ	$1.17 \cdot 10^{-2}$	1.19	$1.00 \cdot 10^{-2}$	1.21	$6.75 \cdot 10^{-3}$	1.27	$6.35 \cdot 10^{-3}$	1.29	$7.54 \cdot 10^{-3}$	1.21	$6.47 \cdot 10^{-3}$	1.18	$6.01 \cdot 10^{-3}$	1.13	$6.17 \cdot 10^{-3}$	1.22
3D ₄ ^Δ	$5.80 \cdot 10^{-3}$		$4.90 \cdot 10^{-3}$		$3.18 \cdot 10^{-3}$		$2.96 \cdot 10^{-3}$		$3.67 \cdot 10^{-3}$		$3.21 \cdot 10^{-3}$		$3.08 \cdot 10^{-3}$		$2.99 \cdot 10^{-3}$	

Table 2: Results of the numerical analysis using the L_2 norm and the Brooks and Corey model.

Id.	Conservative Formulation								Non-Conservative Formulation							
	$D_X = 0 \text{ m}^2/\text{s}$		$D_X = 10^{-7} \text{ m}^2/\text{s}$		$D_X = 10^{-6} \text{ m}^2/\text{s}$		$D_X = 10^{-5} \text{ m}^2/\text{s}$		$D_X = 0 \text{ m}^2/\text{s}$		$D_X = 10^{-7} \text{ m}^2/\text{s}$		$D_X = 10^{-6} \text{ m}^2/\text{s}$		$D_X = 10^{-5} \text{ m}^2/\text{s}$	
	$\ E_{h,X}\ _1$	$\text{eoc}_{X,1}$	$\ E_{h,X}\ _1$	$\text{eoc}_{X,1}$	$\ E_{h,X}\ _1$	$\text{eoc}_{X,1}$	$\ E_{h,X}\ _1$	$\text{eoc}_{X,1}$	$\ E_{h,X}\ _1$	$\text{eoc}_{X,1}$	$\ E_{h,X}\ _1$	$\text{eoc}_{X,1}$	$\ E_{h,X}\ _1$	$\text{eoc}_{X,1}$	$\ E_{h,X}\ _1$	$\text{eoc}_{X,1}$
1D ₁	$1.78 \cdot 10^{-2}$	1.02	$1.12 \cdot 10^{-2}$	0.99	$3.99 \cdot 10^{-3}$	0.99	$3.43 \cdot 10^{-3}$	1.02	$1.81 \cdot 10^{-2}$	0.99	$1.12 \cdot 10^{-2}$	0.98	$3.99 \cdot 10^{-3}$	0.99	$3.43 \cdot 10^{-3}$	1.02
1D ₂	$8.77 \cdot 10^{-3}$	1.03	$5.62 \cdot 10^{-3}$	1.00	$2.01 \cdot 10^{-3}$	0.99	$1.69 \cdot 10^{-3}$	1.00	$9.08 \cdot 10^{-3}$	0.99	$5.67 \cdot 10^{-3}$	0.98	$2.01 \cdot 10^{-3}$	0.99	$1.69 \cdot 10^{-3}$	1.00
1D ₃	$4.30 \cdot 10^{-3}$	1.00	$2.81 \cdot 10^{-3}$	1.00	$1.01 \cdot 10^{-3}$	0.99	$8.43 \cdot 10^{-4}$	1.00	$4.57 \cdot 10^{-3}$	0.99	$2.87 \cdot 10^{-3}$	0.99	$1.01 \cdot 10^{-3}$	0.99	$8.43 \cdot 10^{-4}$	1.00
1D ₄	$2.16 \cdot 10^{-3}$	0.95	$1.40 \cdot 10^{-3}$	1.00	$5.08 \cdot 10^{-4}$	1.00	$4.22 \cdot 10^{-4}$	1.00	$2.30 \cdot 10^{-3}$	0.99	$1.44 \cdot 10^{-3}$	1.00	$5.07 \cdot 10^{-4}$	1.00	$4.22 \cdot 10^{-4}$	1.00
1D ₅	$1.11 \cdot 10^{-3}$	0.92	$6.99 \cdot 10^{-4}$	1.00	$2.55 \cdot 10^{-4}$	1.00	$2.11 \cdot 10^{-4}$	1.00	$1.15 \cdot 10^{-3}$	1.00	$7.24 \cdot 10^{-4}$	1.00	$2.54 \cdot 10^{-4}$	1.00	$2.11 \cdot 10^{-4}$	1.00
1D ₆	$5.90 \cdot 10^{-4}$	0.90	$3.49 \cdot 10^{-4}$	0.99	$1.28 \cdot 10^{-4}$	1.00	$1.06 \cdot 10^{-4}$	1.00	$5.75 \cdot 10^{-4}$	1.00	$3.63 \cdot 10^{-4}$	1.00	$1.27 \cdot 10^{-4}$	1.00	$1.06 \cdot 10^{-4}$	1.00
1D ₇	$3.16 \cdot 10^{-4}$		$1.75 \cdot 10^{-4}$		$6.39 \cdot 10^{-5}$		$5.29 \cdot 10^{-5}$		$2.88 \cdot 10^{-4}$		$1.81 \cdot 10^{-4}$		$6.36 \cdot 10^{-5}$		$5.29 \cdot 10^{-5}$	
2D ₁ ^Δ	$2.59 \cdot 10^{-2}$	1.09	$1.78 \cdot 10^{-2}$	1.00	$8.54 \cdot 10^{-3}$	0.95	$8.45 \cdot 10^{-3}$	1.01	$2.59 \cdot 10^{-2}$	1.09	$1.78 \cdot 10^{-2}$	1.00	$8.54 \cdot 10^{-3}$	0.95	$8.45 \cdot 10^{-3}$	1.01
2D ₂ ^Δ	$1.21 \cdot 10^{-2}$	1.00	$8.90 \cdot 10^{-3}$	0.99	$4.42 \cdot 10^{-3}$	0.94	$4.18 \cdot 10^{-3}$	0.99	$1.21 \cdot 10^{-2}$	1.00	$8.90 \cdot 10^{-3}$	0.99	$4.42 \cdot 10^{-3}$	0.94	$4.18 \cdot 10^{-3}$	0.99
2D ₃ ^Δ	$6.05 \cdot 10^{-3}$	0.99	$4.49 \cdot 10^{-3}$	0.99	$2.30 \cdot 10^{-3}$	0.95	$2.11 \cdot 10^{-3}$	0.97	$6.05 \cdot 10^{-3}$	0.99	$4.49 \cdot 10^{-3}$	0.99	$2.30 \cdot 10^{-3}$	0.95	$2.11 \cdot 10^{-3}$	0.97
2D ₄ ^Δ	$3.04 \cdot 10^{-3}$	0.99	$2.26 \cdot 10^{-3}$	1.00	$1.19 \cdot 10^{-3}$	0.95	$1.07 \cdot 10^{-3}$	0.95	$3.04 \cdot 10^{-3}$	0.99	$2.26 \cdot 10^{-3}$	1.00	$1.19 \cdot 10^{-3}$	0.95	$1.07 \cdot 10^{-3}$	0.95
2D ₅ ^Δ	$1.53 \cdot 10^{-3}$		$1.13 \cdot 10^{-3}$		$6.18 \cdot 10^{-4}$		$5.56 \cdot 10^{-4}$		$1.53 \cdot 10^{-3}$		$1.13 \cdot 10^{-3}$		$6.18 \cdot 10^{-4}$		$5.56 \cdot 10^{-4}$	
2D ₁ ^Δ	$2.88 \cdot 10^{-2}$	1.13	$2.31 \cdot 10^{-2}$	1.09	$1.08 \cdot 10^{-2}$	1.15	$9.00 \cdot 10^{-3}$	1.10	$1.79 \cdot 10^{-2}$	1.13	$1.27 \cdot 10^{-2}$	1.04	$8.71 \cdot 10^{-3}$	0.97	$8.84 \cdot 10^{-3}$	1.09
2D ₂ ^Δ	$1.38 \cdot 10^{-2}$	0.92	$1.13 \cdot 10^{-2}$	0.91	$5.08 \cdot 10^{-3}$	0.94	$4.40 \cdot 10^{-3}$	0.92	$8.61 \cdot 10^{-3}$	0.91	$6.47 \cdot 10^{-3}$	0.89	$4.62 \cdot 10^{-3}$	0.81	$4.35 \cdot 10^{-3}$	0.91
2D ₃ ^Δ	$6.90 \cdot 10^{-3}$	1.09	$5.68 \cdot 10^{-3}$	1.09	$2.51 \cdot 10^{-3}$	1.09	$2.19 \cdot 10^{-3}$	1.08	$4.32 \cdot 10^{-3}$	1.08	$3.31 \cdot 10^{-3}$	1.08	$2.51 \cdot 10^{-3}$	1.00	$2.19 \cdot 10^{-3}$	1.06
2D ₄ ^Δ	$3.47 \cdot 10^{-3}$		$2.84 \cdot 10^{-3}$		$1.26 \cdot 10^{-3}$		$1.11 \cdot 10^{-3}$		$2.18 \cdot 10^{-3}$		$1.68 \cdot 10^{-3}$		$1.34 \cdot 10^{-3}$		$1.12 \cdot 10^{-3}$	
3D ₁ ^Δ	$9.57 \cdot 10^{-3}$	1.21	$7.32 \cdot 10^{-3}$	1.08	$3.64 \cdot 10^{-3}$	0.96	$3.45 \cdot 10^{-3}$	1.00	$9.51 \cdot 10^{-3}$	1.20	$7.32 \cdot 10^{-3}$	1.08	$3.64 \cdot 10^{-3}$	0.96	$3.45 \cdot 10^{-3}$	1.00
3D ₂ ^Δ	$4.14 \cdot 10^{-3}$	1.00	$3.47 \cdot 10^{-3}$	1.00	$1.86 \cdot 10^{-3}$	0.98	$1.72 \cdot 10^{-3}$	0.95	$4.14 \cdot 10^{-3}$	1.00	$3.47 \cdot 10^{-3}$	1.00	$1.86 \cdot 10^{-3}$	0.98	$1.72 \cdot 10^{-3}$	0.95
3D ₃ ^Δ	$2.07 \cdot 10^{-3}$		$1.73 \cdot 10^{-3}$		$9.44 \cdot 10^{-4}$		$8.89 \cdot 10^{-4}$		$2.07 \cdot 10^{-3}$		$1.73 \cdot 10^{-3}$		$9.44 \cdot 10^{-4}$		$8.89 \cdot 10^{-4}$	
3D ₁ ^Δ	$1.49 \cdot 10^{-2}$	0.66	$1.34 \cdot 10^{-2}$	0.63	$8.09 \cdot 10^{-3}$	0.69	$6.64 \cdot 10^{-3}$	0.78	$8.70 \cdot 10^{-3}$	0.72	$7.21 \cdot 10^{-3}$	0.70	$5.89 \cdot 10^{-3}$	0.72	$6.29 \cdot 10^{-3}$	0.78
3D ₂ ^Δ	$1.06 \cdot 10^{-2}$	1.09	$9.67 \cdot 10^{-3}$	1.10	$5.66 \cdot 10^{-3}$	1.13	$4.42 \cdot 10^{-3}$	1.07	$5.98 \cdot 10^{-3}$	1.07	$5.02 \cdot 10^{-3}$	1.08	$4.06 \cdot 10^{-3}$	1.04	$4.19 \cdot 10^{-3}$	1.07
3D ₃ ^Δ	$4.93 \cdot 10^{-3}$	1.26	$4.49 \cdot 10^{-3}$	1.27	$2.57 \cdot 10^{-3}$	1.34	$2.08 \cdot 10^{-3}$	1.28	$2.83 \cdot 10^{-3}$	1.23	$2.35 \cdot 10^{-3}$	1.19	$1.96 \cdot 10^{-3}$	1.11	$1.99 \cdot 10^{-3}$	1.18
3D ₄ ^Δ	$2.34 \cdot 10^{-3}$		$2.12 \cdot 10^{-3}$		$1.16 \cdot 10^{-3}$		$9.77 \cdot 10^{-4}$		$1.37 \cdot 10^{-3}$		$1.16 \cdot 10^{-3}$		$1.01 \cdot 10^{-3}$		$9.90 \cdot 10^{-4}$	

Table 3: Results of the numerical analysis using the L_1 norm and the van Genuchten model.

27

Id.	Conservative Formulation								Non-Conservative Formulation							
	$D_X = 0 \text{ m}^2/\text{s}$		$D_X = 10^{-7} \text{ m}^2/\text{s}$		$D_X = 10^{-6} \text{ m}^2/\text{s}$		$D_X = 10^{-5} \text{ m}^2/\text{s}$		$D_X = 0 \text{ m}^2/\text{s}$		$D_X = 10^{-7} \text{ m}^2/\text{s}$		$D_X = 10^{-6} \text{ m}^2/\text{s}$		$D_X = 10^{-5} \text{ m}^2/\text{s}$	
	$\ E_{h,X}\ _2$	$\text{eoc}_{X,2}$	$\ E_{h,X}\ _2$	$\text{eoc}_{X,2}$	$\ E_{h,X}\ _2$	$\text{eoc}_{X,2}$	$\ E_{h,X}\ _2$	$\text{eoc}_{X,2}$	$\ E_{h,X}\ _2$	$\text{eoc}_{X,2}$	$\ E_{h,X}\ _2$	$\text{eoc}_{X,2}$	$\ E_{h,X}\ _2$	$\text{eoc}_{X,2}$	$\ E_{h,X}\ _2$	$\text{eoc}_{X,2}$
1D ₁	$2.11 \cdot 10^{-2}$	0.99	$1.38 \cdot 10^{-2}$	0.98	$7.60 \cdot 10^{-3}$	1.00	$7.53 \cdot 10^{-3}$	1.00	$2.14 \cdot 10^{-2}$	0.96	$1.39 \cdot 10^{-2}$	0.96	$7.60 \cdot 10^{-3}$	1.00	$7.53 \cdot 10^{-3}$	1.00
1D ₂	$1.06 \cdot 10^{-2}$	1.01	$7.03 \cdot 10^{-3}$	0.99	$3.81 \cdot 10^{-3}$	1.00	$3.76 \cdot 10^{-3}$	1.00	$1.10 \cdot 10^{-2}$	0.98	$7.11 \cdot 10^{-3}$	0.98	$3.81 \cdot 10^{-3}$	1.00	$3.76 \cdot 10^{-3}$	1.00
1D ₃	$5.27 \cdot 10^{-3}$	0.99	$3.53 \cdot 10^{-3}$	1.00	$1.91 \cdot 10^{-3}$	1.00	$1.88 \cdot 10^{-3}$	1.00	$5.57 \cdot 10^{-3}$	0.98	$3.62 \cdot 10^{-3}$	0.99	$1.91 \cdot 10^{-3}$	1.00	$1.88 \cdot 10^{-3}$	1.00
1D ₄	$2.64 \cdot 10^{-3}$	0.95	$1.77 \cdot 10^{-3}$	1.00	$9.55 \cdot 10^{-4}$	1.00	$9.41 \cdot 10^{-4}$	1.00	$2.81 \cdot 10^{-3}$	0.98	$1.83 \cdot 10^{-3}$	0.99	$9.55 \cdot 10^{-4}$	1.00	$9.41 \cdot 10^{-4}$	1.00
1D ₅	$1.37 \cdot 10^{-3}$	0.86	$8.82 \cdot 10^{-4}$	1.00	$4.78 \cdot 10^{-4}$	1.00	$4.70 \cdot 10^{-4}$	1.00	$1.42 \cdot 10^{-3}$	0.99	$9.18 \cdot 10^{-4}$	1.00	$4.78 \cdot 10^{-4}$	1.00	$4.70 \cdot 10^{-4}$	1.00
1D ₆	$7.55 \cdot 10^{-4}$	0.73	$4.41 \cdot 10^{-4}$	0.99	$2.39 \cdot 10^{-4}$	1.00	$2.35 \cdot 10^{-4}$	1.00	$7.10 \cdot 10^{-4}$	1.00	$4.60 \cdot 10^{-4}$	1.00	$2.39 \cdot 10^{-4}$	1.00	$2.35 \cdot 10^{-4}$	1.00
1D ₇	$4.54 \cdot 10^{-4}$		$2.23 \cdot 10^{-4}$		$1.19 \cdot 10^{-4}$		$1.18 \cdot 10^{-4}$		$3.56 \cdot 10^{-4}$		$2.30 \cdot 10^{-4}$		$1.19 \cdot 10^{-4}$		$1.18 \cdot 10^{-4}$	
2D ₁ ^F	$3.58 \cdot 10^{-2}$	0.95	$2.68 \cdot 10^{-2}$	0.92	$1.73 \cdot 10^{-2}$	0.93	$1.74 \cdot 10^{-2}$	1.02	$3.58 \cdot 10^{-2}$	0.95	$2.68 \cdot 10^{-2}$	0.92	$1.73 \cdot 10^{-2}$	0.93	$1.74 \cdot 10^{-2}$	1.02
2D ₂ ^F	$1.86 \cdot 10^{-2}$	0.94	$1.42 \cdot 10^{-2}$	0.95	$9.12 \cdot 10^{-3}$	0.92	$8.54 \cdot 10^{-3}$	1.00	$1.86 \cdot 10^{-2}$	0.94	$1.42 \cdot 10^{-2}$	0.95	$9.12 \cdot 10^{-3}$	0.92	$8.54 \cdot 10^{-3}$	1.00
2D ₃ ^F	$9.67 \cdot 10^{-3}$	0.96	$7.36 \cdot 10^{-3}$	0.97	$4.82 \cdot 10^{-3}$	0.94	$4.28 \cdot 10^{-3}$	0.99	$9.67 \cdot 10^{-3}$	0.96	$7.36 \cdot 10^{-3}$	0.97	$4.82 \cdot 10^{-3}$	0.94	$4.28 \cdot 10^{-3}$	0.99
2D ₄ ^F	$4.99 \cdot 10^{-3}$	0.97	$3.75 \cdot 10^{-3}$	0.98	$2.51 \cdot 10^{-3}$	0.96	$2.16 \cdot 10^{-3}$	0.98	$4.99 \cdot 10^{-3}$	0.97	$3.75 \cdot 10^{-3}$	0.98	$2.51 \cdot 10^{-3}$	0.96	$2.16 \cdot 10^{-3}$	0.98
2D ₅ ^F	$2.54 \cdot 10^{-3}$	0.97	$1.90 \cdot 10^{-3}$	0.98	$1.29 \cdot 10^{-3}$	0.96	$1.10 \cdot 10^{-3}$	0.98	$2.54 \cdot 10^{-3}$	0.97	$1.90 \cdot 10^{-3}$	0.98	$1.29 \cdot 10^{-3}$	0.96	$1.10 \cdot 10^{-3}$	0.98
2D ₁ ^A	$4.32 \cdot 10^{-2}$	1.01	$3.52 \cdot 10^{-2}$	1.03	$2.12 \cdot 10^{-2}$	1.15	$1.89 \cdot 10^{-2}$	1.10	$2.71 \cdot 10^{-2}$	0.99	$2.15 \cdot 10^{-2}$	0.92	$1.81 \cdot 10^{-2}$	0.92	$1.85 \cdot 10^{-2}$	1.09
2D ₂ ^A	$2.23 \cdot 10^{-2}$	0.87	$1.80 \cdot 10^{-2}$	0.89	$1.01 \cdot 10^{-2}$	0.93	$9.19 \cdot 10^{-3}$	0.93	$1.43 \cdot 10^{-2}$	0.86	$1.19 \cdot 10^{-2}$	0.84	$9.96 \cdot 10^{-3}$	0.79	$9.09 \cdot 10^{-3}$	0.91
2D ₃ ^A	$1.16 \cdot 10^{-2}$	1.06	$9.20 \cdot 10^{-3}$	1.08	$4.97 \cdot 10^{-3}$	1.09	$4.54 \cdot 10^{-3}$	1.10	$7.43 \cdot 10^{-3}$	1.05	$6.26 \cdot 10^{-3}$	1.05	$5.47 \cdot 10^{-3}$	1.00	$4.56 \cdot 10^{-3}$	1.08
2D ₄ ^A	$5.93 \cdot 10^{-3}$		$4.66 \cdot 10^{-3}$		$2.49 \cdot 10^{-3}$		$2.26 \cdot 10^{-3}$		$3.83 \cdot 10^{-3}$		$3.22 \cdot 10^{-3}$		$2.91 \cdot 10^{-3}$		$2.31 \cdot 10^{-3}$	
3D ₁ ^F	$1.99 \cdot 10^{-2}$	1.04	$1.55 \cdot 10^{-2}$	0.94	$1.05 \cdot 10^{-2}$	0.94	$1.02 \cdot 10^{-2}$	1.01	$1.95 \cdot 10^{-2}$	1.00	$1.55 \cdot 10^{-2}$	0.94	$1.05 \cdot 10^{-2}$	0.94	$1.02 \cdot 10^{-2}$	1.01
3D ₂ ^F	$9.71 \cdot 10^{-3}$	0.92	$8.11 \cdot 10^{-3}$	0.95	$5.45 \cdot 10^{-3}$	0.96	$5.06 \cdot 10^{-3}$	0.94	$9.71 \cdot 10^{-3}$	0.92	$8.11 \cdot 10^{-3}$	0.95	$5.45 \cdot 10^{-3}$	0.96	$5.06 \cdot 10^{-3}$	0.94
3D ₃ ^F	$5.11 \cdot 10^{-3}$		$4.21 \cdot 10^{-3}$		$2.80 \cdot 10^{-3}$		$2.65 \cdot 10^{-3}$		$5.11 \cdot 10^{-3}$		$4.21 \cdot 10^{-3}$		$2.80 \cdot 10^{-3}$		$2.65 \cdot 10^{-3}$	
3D ₁ ^A	$3.26 \cdot 10^{-2}$	0.52	$2.89 \cdot 10^{-2}$	0.54	$2.14 \cdot 10^{-2}$	0.64	$2.01 \cdot 10^{-2}$	0.71	$1.99 \cdot 10^{-2}$	0.51	$1.77 \cdot 10^{-2}$	0.52	$1.72 \cdot 10^{-2}$	0.61	$1.91 \cdot 10^{-2}$	0.71
3D ₂ ^A	$2.49 \cdot 10^{-2}$	1.03	$2.19 \cdot 10^{-2}$	1.06	$1.54 \cdot 10^{-2}$	1.12	$1.39 \cdot 10^{-2}$	1.10	$1.53 \cdot 10^{-2}$	1.02	$1.35 \cdot 10^{-2}$	1.06	$1.26 \cdot 10^{-2}$	1.06	$1.32 \cdot 10^{-2}$	1.10
3D ₃ ^A	$1.21 \cdot 10^{-2}$	1.22	$1.04 \cdot 10^{-2}$	1.24	$7.01 \cdot 10^{-3}$	1.30	$6.43 \cdot 10^{-3}$	1.31	$7.48 \cdot 10^{-3}$	1.18	$6.44 \cdot 10^{-3}$	1.15	$6.00 \cdot 10^{-3}$	1.09	$6.11 \cdot 10^{-3}$	1.19
3D ₄ ^A	$5.86 \cdot 10^{-3}$		$5.00 \cdot 10^{-3}$		$3.24 \cdot 10^{-3}$		$2.95 \cdot 10^{-3}$		$3.72 \cdot 10^{-3}$		$3.27 \cdot 10^{-3}$		$3.14 \cdot 10^{-3}$		$3.02 \cdot 10^{-3}$	

Table 4: Results of the numerical analysis using the L_2 norm and the van Genuchten model.

Groundwater

Effect of NAPL Source Morphology on Mass Transfer in the Vadose Zone

by Benjamin G. Petri¹, Radek Fučík², Tissa H. Illangasekare³, Kathleen M. Smits³, John A. Christ⁴, Toshihiro Sakaki³, and Carolyn C. Sauck³

Abstract

The generation of vapor-phase contaminant plumes within the vadose zone is of interest for contaminated site management. Therefore, it is important to understand vapor sources such as non-aqueous-phase liquids (NAPLs) and processes that govern their volatilization. The distribution of NAPL, gas, and water phases within a source zone is expected to influence the rate of volatilization. However, the effect of this distribution morphology on volatilization has not been thoroughly quantified. Because field quantification of NAPL volatilization is often infeasible, a controlled laboratory experiment was conducted in a two-dimensional tank (28 cm × 15.5 cm × 2.5 cm) with water-wet sandy media and an emplaced trichloroethylene (TCE) source. The source was emplaced in two configurations to represent morphologies encountered in field settings: (1) NAPL pools directly exposed to the air phase and (2) NAPLs trapped in water-saturated zones that were occluded from the air phase. Airflow was passed through the tank and effluent concentrations of TCE were quantified. Models were used to analyze results, which indicated that mass transfer from directly exposed NAPL was fast and controlled by advective-dispersive-diffusive transport in the gas phase. However, sources occluded by pore water showed strong rate limitations and slower effective mass transfer. This difference is explained by diffusional resistance within the aqueous phase. Results demonstrate that vapor generation rates from a NAPL source will be influenced by the soil water content distribution within the source. The implications of the NAPL morphology on volatilization in the context of a dynamic water table or climate are discussed.

Introduction

The fate and transport of volatile organic contaminants (VOCs) within the vadose zone has received much attention at contaminated sites due to interest in contaminant attenuation mechanisms, vapor intrusion, and performance of remediation technologies such as soil vapor extraction (Rivett et al. 2011). However, models capable of predicting VOC transport may require knowledge of the rates and mechanisms controlling vapor generation from non-aqueous-phase liquid (NAPL) contaminant sources in the vadose zone. While extensive research has been conducted on NAPL entrapment and mass transfer within the saturated zone (e.g., Schwillie 1988; Miller et al. 1990; Kueper et al. 1993; Saenton

and Illangasekare 2007), knowledge gaps remain in understanding mass transfer (volatilization) from NAPLs in the vadose zone (Rivett et al. 2011).

One area where more knowledge is needed is in determining how the distribution of NAPL within the vadose zone affects mass transfer. NAPL entrapment morphology describes the spatial distribution of the NAPL phase resulting from the infiltration of multiphase fluids in porous media. Within the saturated zone, NAPL entrapment morphologies have been shown to consist of complex distributions of NAPL pools and residual ganglia (Illangasekare et al. 1995; Lemke et al. 2004) that result from NAPL infiltration through heterogeneous porous media (e.g., Kueper et al. 1989; Poulsen and Kueper 1992; Fagerlund et al. 2007). The NAPL entrapment morphology is of particular importance to the mass transfer rate (Lemke et al. 2004; Fure et al. 2006; Page et al. 2007), and quantitative metrics such as the NAPL ganglia-to-pool ratio have been proposed to characterize saturated zone mass transfer behavior (Lemke et al. 2004; Christ et al. 2005; Fure et al. 2006). However, the current literature does not describe such metrics for NAPL mass transfer in the vadose zone, nor has this phenomenon been widely evaluated. This is partly because three-phase air-water-NAPL entrapment morphologies are more complex than two-phase NAPL-water systems. For

¹Corresponding author: Department of Civil and Environmental Engineering, Colorado School of Mines, 1500 Illinois St, Golden, CO 80401; 303-715-8211; fax: 303-273-3413; bpetri@mymail.mines.edu

²Faculty of Nuclear Sciences and Physical Engineering, Czech Technical University in Prague, Prague, Czech Republic.

³Department of Civil and Environmental Engineering, Colorado School of Mines, 1500 Illinois St, Golden, CO 80401.

⁴Department of Civil and Environmental Engineering, U. S. Air Force Academy, Colorado Springs, CO.

Received August 2014, accepted September 2014.

© 2014, National Ground Water Association.

doi: 10.1111/gwat.12284

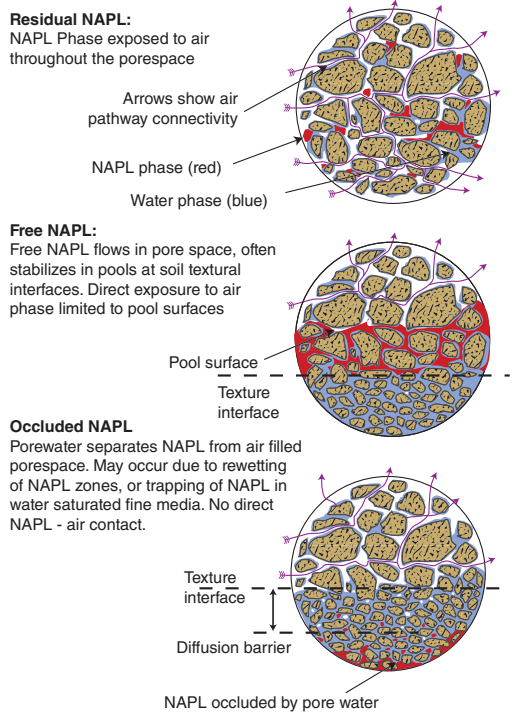


Figure 1. Conceptual model of NAPL configurations within a vadose zone source.

example, constitutive models of three-phase flow conceptualize NAPL as being present in “residual,” “free,” and “occluded” configurations (Figure 1) (Kaluarachchi and Parker 1992; Wipfler and van der Zee 2001; Lenhard et al. 2004; White et al. 2004), whereas two-phase flow systems typically only consider residual and free NAPL. These configurations have important implications for vapor mass transfer.

In the vadose zone, vapor transport is often assumed to be diffusion-dominated (Johnson and Ettinger 1991; Rivett et al. 2011); advection and dispersion within the gas phase are usually included only in the presence of strong barometric effects (Auer et al. 1996; Parker 2003; Tillman et al. 2003; Luo et al. 2009), vapor density effects (Falta et al. 1989; Sleep and Sykes 1989; Lenhard et al. 1995; Jang and Aral 2007), or forced advection such as from soil vapor extraction (SVE). This transport regime affects the assumptions regarding NAPL mass transfer: local equilibrium between NAPL and gas phases is typically assumed under diffusion-dominated conditions (Rivett et al. 2011), while mixing models such as Gilliland-Sherwood correlations are typically used in high advection systems (e.g., Wilkins et al. 1995; Yoon et al. 2002).

However, the current knowledge base does not fully incorporate NAPL entrapment morphologies into either local equilibrium or Gilliland-Sherwood models.

Furthermore, Gilliland-Sherwood correlations are largely unexplored in low advection systems outside SVE (Rivett et al. 2011). Traditional three-phase flow models assume NAPL is an intermediate wetting fluid located at the interface between the air and the water phases (Leverett 1973; Stone 1973; Lenhard and Parker 1987), which has served as a justification for assuming local equilibrium between NAPL and air (Rivett et al. 2011). However, this may not be an appropriate assumption for occluded NAPL. Occluded NAPL may form where NAPL sources are subjected to water imbibition and drainage cycles, such as during water table fluctuations and water infiltration. It is worth noting that occluded NAPL may exist at both the pore scale (e.g., blobs of NAPL isolated from the gas phase by pore water) and the macro scale (e.g., NAPL entrapped in water-saturated fine layers or submerged below the water table). The occluded phase represents a different mass transfer regime than the assumption of direct NAPL-gas contact because the contaminant must first transfer through the aqueous occlusion before it may volatilize within the bulk gas phase (Yoon et al. 2008). Given that typical VOC diffusivities in water are about four orders of magnitude lower than in gases (e.g., the diffusivity for TCE in air is $8.75 \times 10^{-6} \text{ m}^2/\text{s}$ [Lugg 1968] vs. $9.1 \times 10^{-10} \text{ m}^2/\text{s}$ in water [Batterman et al. 1996]), the mass transfer resistance imparted by the aqueous occlusion can be considerable (Yoon et al. 2008).

Studies of bulk volatilization from NAPLs show that mass transfer rates decrease with increasing soil water content (Wilkins et al. 1995; Liang and Udell 1999; Yoon et al. 2002; Yoon et al. 2003; Oostrom et al. 2005) due to a net decrease in the effective diffusivity. However, these studies fail to account for the differing NAPL morphologies that may be present in the subsurface, which lead to large differences among observed mass transfer rates. For example, Yoon et al. (2002) investigated NAPL volatilization in one-dimensional (1D) sand columns ranging from dry to 61% water saturation with a gas-phase Darcy flux of approximately 3 m/h. They report that mass transfer rates decline from equilibrium values when the water saturation exceeded 48% and resulted in tailing of NAPL mass transfer at high water saturations. In contrast, a similar 1D column tested by Liang and Udell (1999) with very high gas velocities ($\sim 115 \text{ m/h}$) observed no effect on volatilization with soil water content (range from dry to 50% water saturation). Note, however, that both experiments were conducted in columns, a design that forces air or vapor flow through the contaminated zone. Field would likely allow the vapor phase to bypass zones of high water or NAPL saturation making it necessary to consider flow in multiple dimensions (2D or 3D). Indeed, a comparison of NAPL dissolution rates in groundwater in 1D vs. 2D and 3D experimental apparatus showed that multidimensional systems had lower mass transfer rates due to flow bypassing (Saba and Illangasekare 2000). Also, in 1D column systems, three-phase flow is often unstable unless two of the phases are reduced to residual (immobile) saturations, which limits the contaminant configurations. For example, Yoon et al. (2002) noted considerable

displacement of the water phase when investigating their highest water saturation systems (61%). Thus, studies in multiple dimensions may be necessary to gain an understanding of mass transfer under field conditions.

Studies in 2D test systems suggest different effective mass transfer behavior than what is observed in the 1D systems. Oostrom et al. (2005) investigated SVE in a variably saturated 2D sand tank contaminated with NAPL. Their experiment found that the removal of NAPL from pools and low permeability regions was only achieved by effectively drying out the porous media, suggesting strong mass transfer limitations even at low water contents—an observation in contrast to the experimental results from the 1D column studies discussed previously. The experiment by Oostrom et al. (2005) contained residual and free NAPL, though it did not explore the role of occluded NAPL.

Saturated zone air sparging studies focusing on NAPL remediation suggest strong mass transfer limitations due to diffusion from the occluded NAPL through the water phase (Braida and Ong 1998; Braida and Ong 2000; Rogers and Ong 2000). However, the three-phase flow regime of these systems differs from typical vadose zone environments because airflow under air sparging is usually restricted to a network of air channels (Clayton 1998). Furthermore, these studies focus on active remediation systems where gas-phase advection is forced at a high rate. For instance, the study by Braida and Ong (1998) explored air channel velocities on the order of 200 to 2000 m/day. SVE experiments by van der Ham and Brouwers (1998) included bulk soil gas flow on the order of 8300 to 38,000 m/day. Thus, to our knowledge, no experimental evidence exists that examines NAPL volatilization at low ranges of advection that may be encountered at sites where active remediation is not present. Conflicting laboratory data and lack of field experimental data, combined with the commonly employed, but untested local equilibrium assumption for NAPL mass transfer illustrates that research is needed to better understand how NAPL morphology affects mass transfer in three-phase systems.

The central challenge in understanding volatilization from NAPL sources lies in incorporating the role of three-phase entrapment morphology into the mass transfer expression. If all three NAPL configurations (shown in Figure 1) are present within the same source, the higher mass transfer contributions from the “residual” and “free” (e.g., pooled) configurations may initially mask smaller contributions from the “occluded” configuration. However, as the source ages, the residual and free fractions will likely be depleted leaving “occluded” NAPL as a long-term source that contributes to significant concentration “tailing.” Because occluded NAPL mass transfer requires diffusion across the aqueous occlusion, it is logical to expect that the thicker the occlusion, the stronger the observed NAPL mass transfer rate limitation. Furthermore, because bulk diffusion and advection transport mass away from the contaminated region, these processes may also affect mass transfer. The objective of this study is to explore mass transfer from

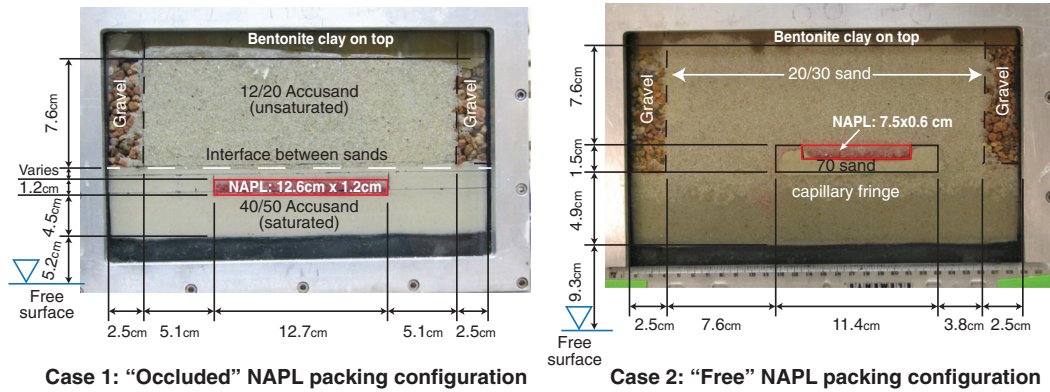
occluded and exposed (i.e., free) NAPL sources under low advection systems to determine the mechanisms and rates of NAPL volatilization. The use of controlled 2D experiments and numerical transport models provides insight into the NAPL mass transfer process and the factors controlling NAPL mass transfer in complex NAPL morphologies commonly found in the vadose zone.

Materials and Methods

Two separate series of experiments were performed for this to meet the stated goals. The first evaluated mass transfer from an “occluded” NAPL source (Case 1, Figure 1) and the second from an “exposed” (free) NAPL source (Case 2). Exploring both NAPL configurations independently enables the comparison of mass transfer characteristics between the two. Both experiments were conducted using the same apparatus, instrumentation and analytical methods, but differed in source creation procedure, sand pack geometry, and experimental procedure (Figure 2). An important procedural difference is that the occluded (Case 1) experiments are run until mass transfer reaches a pseudo steady state because the low mass transfer rates in these systems would require exceptionally long experimental run times (month to years) to completely deplete the NAPL sources. For the exposed (Case 2) NAPL sources, mass transfer is rapid and transient, and therefore these experiments are run until complete NAPL source depletion (within days). An abridged description of the experiment is included here, while a more detailed description is included in the Supporting Information.

Both experiments were conducted in a 2D sand-packed flow tank [internal dimensions: 28 cm × 15.5 cm × 2.5 cm (height × length × depth)] (Figure 2). The rear tank face contained syringe injection ports through which NAPL could be injected to create the desired trapping configuration. Pure trichloroethylene (TCE) was used as the test NAPL, dyed red with 100 mg/L Sudan IV to aid in visualization. The porous media used to pack the tank consisted of well-characterized, uniform, silica sands (Accusand, Unimin Corp., Ottawa, Minnesota) of varied grain size. Selected properties of the test sand are summarized in Table 1. The tank was wet packed with sand and deionized water with different source configurations for Cases 1 and 2 (Figure 2). The tank was subsequently drained to establish an unsaturated zone under hydrostatic conditions. Following drainage, a known mass of NAPL was injected into the source zone.

Immediately after NAPL injection, airflow was introduced into the tank flowing from left to right (Figure 2). Air from a compressed gas cylinder was used as the airflow source and a mass flow controller (Cole Parmer, 16 Series Mass Flow Controller, 0-50 SCCM range) was used to control the airflow. The airflow was bubbled through a water column to humidify the air to prevent evaporative losses and maintain a steady-state water saturation profile throughout each experiment. The flow range tested by this apparatus equates to average pore velocities of around 3 to 145 m/day within the unsaturated zone of the experimental



Case 1: "Occluded" NAPL packing configuration

Case 2: "Free" NAPL packing configuration

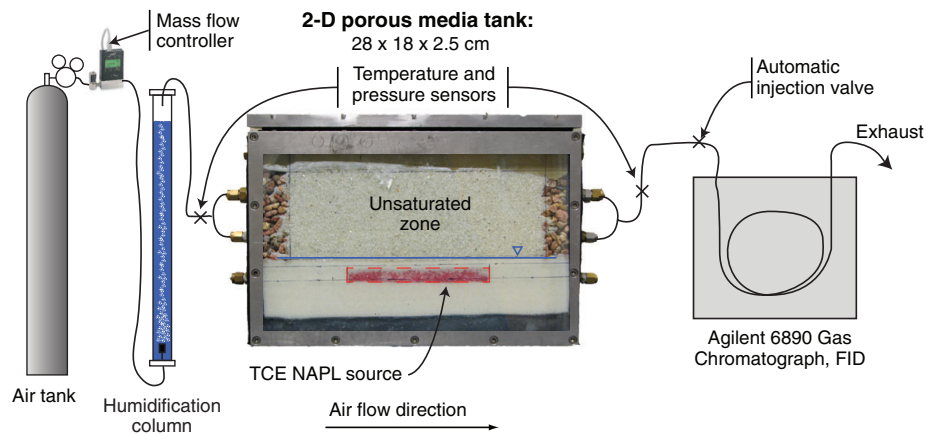


Figure 2. Experimental apparatus and tank packing

Table 1
Selected Properties of Sands

Sand (Tightly Packed)	d_{50}^1 (mm)	Dry Bulk Density (g/cm^3)	Porosity	Residual Water Content ²	Saturated Hydraulic Conductivity (cm/s) ³	van Genuchten α ($1/cm$) ⁴	van Genuchten $n(m = 1 - 1/n)$ ⁴	Source
12/20	1.04	1.82	0.312	0.017	0.376	0.10	9.21	Smits (2010)
20/30	0.75	1.78	0.330	0.027	0.237	0.07	15.68	Smits (2010)
30/40	0.52	1.77	0.334	0.028	0.106	0.06	17.81	Smits (2010)
40/50	0.36	1.74	0.335	0.029	0.052	0.04	10.18	Smits (2010)
70	0.20	1.56	0.413	0.033	0.014	.02	11.53	Smits (2010)
Gravel	~9.5	n/a	0.42	0.01	0.100	0.35	4.30	Retention parameters assumed from Wolf et al. (2007)

¹Estimated from sieve data provided by the manufacturer.

²Measured in a separate 1D long column experiment.

³Measured in a separate hydraulic conductivity test.

⁴Estimated using RETC (van Genuchten et al. 1991).

apparatus. This velocity is considerably lower than velocities previously studied in soil vapor extraction (~100 to 10,000 m/d; Ho and Udell 1992; Wilkins et al. 1995; Yoon et al. 2002; Oostrom et al. 2005) and in air sparging (~100 to 100,000 m/d; Braida and Ong 1998; Braida and Ong 2000; Rogers and Ong 2000) and was intended to represent more passive conditions in the subsurface than have typically been investigated. Temperatures and pressures within the tank were monitored continuously by separate sensors (EC-T, Decagon Devices Inc. and Omega Engineering PX138-001D5V). The average temperature was measured at 22.6 ± 0.7 °C. Absolute pressure within the tank varied with flow rate due to positive pressurization of the apparatus, ranging by 82,090 to 87,171 Pa (note that the atmospheric pressure in Golden Colorado is ~82,000 Pa). The effluent air stream was directed into a gas chromatograph (GC) with a temperature-controlled automated gas sampling valve for continuous measurement of gas-phase TCE concentrations.

Case 1 "Occluded" NAPL Experiments

The objective of the Case 1 experiments was to emplace an occluded NAPL source, with two different occlusion thicknesses, and test their steady-state mass transfer rate under different gas-phase velocities. Different occlusion layer thicknesses are tested because the mass transfer rate from the occluded NAPL is related to the length of the diffusion pathway across the occlusion. The tank was wet-packed with two sands: fine sand (#40/50 sand) in the lower section of the tank and coarse sand (#12/20 sand) in the upper section of the tank (Figure 2). During packing, a coarse sand block (#12/20), 12.7 cm × 1.2 cm, was emplaced within the lower section of fine sand to serve as the NAPL source zone. This packing produces a narrow band of fine sand between the coarse upper tank section and the coarse NAPL source zone (see dimension marked "variable" in Figure 2). This variable dimension is 13.9 mm for the "thick" occlusion layer system and 8.5 mm for the "thin" occlusion layer. Gravel well screens distributed the airflow evenly and the tank top was sealed airtight with bentonite and an aluminum plate.

After packing was complete, the tank was drained by lowering the water table to 5.2 cm below the bottom boundary of the tank using a constant-head device. This creates a suction of approximately 12 cm of water at the interface between the upper coarse sand section and the lower fine sand section. Because of the difference in air entry values for the coarse and fine sands (7.1 and 19.4 cm, respectively), the drainage results in a sharp saturation front at the interface between coarse and fine sand such that the upper coarse sand is drained and the lower fine sand is fully water saturated under tension. Because air entry into the fine sand has not occurred, the coarse sand NAPL source zone also remains fully saturated.

After 24 h of drainage to a hydrostatic condition, the constant head device is isolated via a shutoff valve, and NAPL is injected into the source zone. A known mass of TCE NAPL was slowly injected into the source zone through five injection ports. Injection was performed in

this manner to ensure as high and uniform a NAPL saturation distribution as possible without allowing any NAPL to escape from the source zone. The NAPL is effectively occluded from the gas phase by the water-saturated fine sand that surrounds the source zone. The NAPL injection volumes for the "thick" and "thin" occlusion systems corresponded to 11.3 and 12.3 g, and equate to approximately 52% and 55% NAPL saturation in the source zone, the rest of the pore space being occupied by water. This injection takes approximately 15 min. After injection, airflow is started through the tank and continuous effluent concentration sampling begins. Because mass transfer from NAPLs is affected by the velocity of the mobile phase (Miller et al. 1990; Powers et al. 1994; Saba and Illangasekare 2000), various airflow pore velocities were tested. These alternative velocities were achieved using a step-wise approach that allowed the system to reach steady state (each run was typically 1 to 2 days). An initial velocity was set, and steady state was assumed when the effluent concentration stabilized with minimal variation. Steady state was then maintained for at least 12 h. The velocity was then changed and a new steady state attained. In this manner, six different velocities (Table 2) were tested for both the "thick" and the "thin" occlusion systems while gathering data continuously.

Case 2: "Free" NAPL Experimental Procedure

The objective of the Case 2 experiments was to evaluate mass transfer from an "exposed" NAPL pool representative of the "free" NAPL in Figure 1 and provide a basis for comparison to the Case 1 experiments. For these experiments, the tank was uniformly wet packed with water and medium sand (#20/30 sand), except for a small NAPL source "trough" of very fine sand (#70 sand) in the center of the tank (see Figure 2). This "trough" was aligned with NAPL injection ports and was bounded at its upstream and downstream ends by a 0.6-cm lip to confine the lateral spread of the NAPL. Similar to Case 1, gravel well screens distributed airflow at the left and right boundaries, and bentonite was used to seal the top of the tank. Also similar to Case 1, the tank was drained through suction applied at a known pressure head (9.3-cm water below the tank bottom). However, unlike Case 1 that produces a sharp water saturation front, Case 2 packing produced a capillary fringe in the bottom of the tank. Only the trough remains fully saturated due to the high air-entry pressure of very fine #70 sand (41.2 cm). After drainage is completed, 2.93 g (2.0 mL) of TCE NAPL was slowly injected into the source trough where it settled forming an NAPL pool with approximate dimensions of 7.6 cm × 2.5 cm × 0.6 cm (length × width × depth) and an estimated 50% average saturation of the "trough" pore space. Following NAPL injection, airflow was started in the tank and effluent gas concentrations were monitored as described in Case 1. The experiment was operated until all NAPL was depleted through visual observation from the system and effluent concentrations declined to steady-state values.

Table 2
Summary of Experimental Results

Run	NAPL Configuration	Airflow Rate (Standard cm ³ /min)	Average Pore Velocity (m/d)	Observed Steady-State Concentration (g/m ³) ¹	Mass Flux Rate (mg/min)	Fraction of Saturation Vapor Pressure (%)	Modeled Steady-State Concentration (g/m ³)
1	Case 1: Thick occlusion	50.0	145	0.0401 ± 0.0009	0.002	0.01	0.0971
2	Case 1: Thick occlusion	22.5	67.9	0.1754 ± 0.0001	0.005	0.04	0.2080
3	Case 1: Thick occlusion	10.0	30.2	0.2467 ± 0.0013	0.003	0.06	0.4620
4	Case 1: Thick occlusion	5.00	15.1	0.4999 ± 0.0008	0.003	0.11	0.9185
5	Case 1: Thick occlusion	2.25	6.72	1.5656 ± 0.0024	0.004	0.33	2.0093
6	Case 1: Thick occlusion	1.00	2.88	2.1389 ± 0.0086	0.003	0.48	4.5421
7	Case 1: Thin occlusion	50.0	145	0.1412 ± 0.0003	0.008	0.03	0.1483
8	Case 1: Thin occlusion	22.5	67.4	0.3270 ± 0.0025	0.009	0.08	0.3114
9	Case 1: Thin occlusion	10.0	30.2	0.6542 ± 0.0003	0.008	0.16	0.7088
10	Case 1: Thin occlusion	5.00	15.1	1.2859 ± 0.0012	0.008	0.31	1.4075
11	Case 1: Thin occlusion	2.25	6.72	2.8812 ± 0.0048	0.008	0.68	3.1789
12	Case 1: Thin occlusion	1.00	2.88	5.2813 ± 0.0076	0.006	1.27	6.9203
13	Case 2: Free NAPL (pool)	50.0	138	163.63 ± 5.10	9.442	33	Transient
14	Case 2: Free NAPL (pool)	10.0	29.0	323.78 ± 8.51	3.921	67	Transient
15	Case 2: Free NAPL (pool)	5.00	14.6	426.68 ± 5.30	2.591	87	Transient
16	Case 2: Free NAPL (pool)	1.00	3.84	415.91 ± 3.00	0.484	97	Transient

¹Mean ± 95% confidence interval of the mean.

Model Description

To explore the experimental results using the advection-dispersion-diffusion equation, a numerical model was developed to simulate coupled volatilization and mass transport behavior within the NAPL, gas, and water phases. The model solves for immiscible flow of gas and water phases, nonequilibrium mass transfer of immobile NAPL from the liquid to the gas phase, and mass transport of the volatilized NAPL vapor in the gas phase. The model uses a mixed-hybrid finite element and finite volume numerical method to simulate transient multiphase flow, transport, and mass transfer (see Fučík and Mikyška 2011, 2012 for details). The model formulation and approach is described in detail in the Supporting Information and summarized in brief here with special emphasis on the mass transfer formulation.

The model solves two-phase gas and water flow according to Darcy's law and using the Mualem (1976) and van Genuchten (1980) models for relative permeability and soil water retention functions. Gas-phase density changes due to compressibility and contaminant vapor components are incorporated, and the gas phase is assumed to be at 100% relative humidity. NAPL phase is included, but is assumed immobile. The mass balance equation for the contaminant component is described by an advective-diffusive-dispersive transport Equation 1, which is expressed in terms of the mass fraction of the contaminant in the phase α (Class et al. 2002; Class et al. 2008; Mosthaf et al. 2011):

$$\frac{\partial (\phi S_\alpha X_n^\alpha \rho_\alpha)}{\partial t} + \nabla \cdot (X_n^\alpha \rho_\alpha v_\alpha - D_n^\alpha \nabla X_n^\alpha) = F_{n\alpha}, \quad (1)$$

where $\alpha = g$ represents the gas phase and $\alpha = w$ represents the water phase. For mass transfer between the water and gas phases, the local equilibrium assumption is made via Henry's law,

$$H = \frac{c_n^g}{c_n^w} = \frac{X_n^g \rho_g}{X_n^w \rho_w} \quad (2)$$

where, H , the Henry's constant, is a function of temperature the values of which were provided by Heron et al. (1998). The flux between phases representing mass transfer is commonly described using boundary layer theory, as given by Cussler (2009). For NAPL to gas-phase mass transfer, this flux is represented as a source/sink term, F_{ng} given as

$$F_{ng} = k (c_n^{sat} - X_n^g \rho_g), \quad (3)$$

This formulation solves for a cumulative or lumped mass transfer from the NAPL into the gas phase. The mass transfer rate coefficient k_{ng} is often estimated from empirical Gilliland-Sherwood mixing models (e.g., Wilkins et al. 1995; Braida and Ong 1998; Chao et al. 1998; van der Ham and Brouwers 1998; Yoon et al. 2002; Anwar et al. 2003), which typically follow the form:

$$Sh = Sh_0 (Pe)^\delta (d_0)^\epsilon \left(\frac{S_n}{S_{n,0}} \right)^\beta \quad (4)$$

where Sh is the dimensionless Sherwood number defined as $k_{ng} d_{50}^2 / D_m^g$, d_{50} is the mean soil particle size, Sh_0 is an empirical constant, Pe is the Peclet number defined as $Pe = |v_g| d_{50} / D_m^g \phi$, d_0 is the normalized mean grain size

defined as $d_0 = d_{50}/d_m$, d_m is the mean grain size of sand set as 0.05 cm by the Department of Agriculture (Yoon et al. 2002), $S_{n,0}$ is the initial NAPL saturation, and δ , ε , and β are all empirical exponents of the correlation. The β in particular relates to the decline in mass transfer that occurs as a result in decline in NAPL mass due to decreasing surface area.

The solution approach for the Case 1 and 2 models differed. Because the Case 1 experimental system was operated under a pseudo steady-state condition, a steady-state solution approach was used. For the more transient Case 2 experiments, a transient model was used to estimate mass transfer as these systems were run to full NAPL depletion. In all cases, the TCE NAPL source is assumed to be uniformly distributed at an average initial saturation based on the mass of TCE injected and the source zone porosity. Relative permeability for the gas phase is adjusted to reflect the total liquid saturation (NAPL + water). Mass transfer of TCE into the bulk gas phase (volatilization) is simulated, along with diffusion and advection in the gas phase. Aside from initial drainage to create the gas-water saturation profile, aqueous phase advection was not present in either Case 1 or Case 2 due to the hydrostatic conditions. The atmospheric reference pressure and temperature used for all calculations were based on the measured values from the temperature and pressure sensors.

Case 1 (Occluded NAPL) Simulations

The model simulations were performed stepwise by first solving for drainage in the tank to create the air-water saturation distribution and then simulating the airflow and contaminant transport from the TCE source. Initial drainage was simulated by setting the top tank boundary to atmospheric pressure and the bottom tank boundary to -5.2 cm water pressure, reflecting the drainage pressure in the constant head device. A steady-state solution then derived the hydrostatic gas-water phase distribution for the NAPL volatilization runs. The system is then simulated using the experimental airflow regime. For the advection-dispersion-diffusion equation, given that a negligible mass of the TCE source was volatilized ($<0.8\%$) over the course of the 10-day experiments, the NAPL source in the model was assumed to be constant. Because there is no flow within the source zone, the source was simulated by assigning Dirichlet boundary conditions at the source zone boundaries with the TCE concentration held at this solubility limit (1440 mg/L as measured). The model then simulated the combination of aqueous and gas-phase plumes that emanate from the source to the effluent boundary, where comparisons to the experimental measurements could be made.

Case 2 (Exposed NAPL) Simulations

In Case 2, the rate of mass change in the source zone is very rapid and required solution as a transient problem incorporating the Gilliland-Sherwood mixing model approach (Illangasekare et al. 2010). Again, the initial drainage was modeled as a steady-state process, followed

by transient solution of the mass transfer problem. Model domain dimensions and material parameters were consistent with the experiment as shown in Figure 2. As in Case 1, the initial drainage was solved (for Case 2, the water pressure at the bottom tank boundary was -9.3 cm H_2O). The initial drainage solution was stored for use as the initial condition for the transient NAPL volatilization model, where airflow and volatilization was solved. The initial NAPL saturation S_n^{ini} is assumed to be uniformly distributed within the TCE source trough and is computed from the injected TCE mass (2.93 ± 0.024 g) and the pore volume of the source trough, averaging 53% initial saturation. In this case, a new Gilliland-Sherwood correlation was developed by fitting a select set of parameters (β , Sh_0 , δ) to determine which effluent concentration profile best fits the data from more than 11,000 results obtained using the numerical simulator.

Results and Discussion

Measurements from each experiment include continuous effluent concentration data, as well as temperature, pressure, and airflow rate. The results for the Case 1 and 2 experiments are discussed separately. Modeling results, based on the experiments, are used as a data analysis tool to determine the role of advection-diffusion transport given the two NAPL configurations and to determine how well existing physical transport theory can capture the observed mass transfer behavior. Presented are experimental data followed by comparison to the simulations.

Case 1 "Occluded" NAPL Results

Figure 3a and 3b shows the measured effluent TCE vapor concentration and the gas-phase Darcy flux through the unsaturated portion of the tank for the "thick" and "thin" occlusion experiments. Stepwise changes in the flow rate resulted in step-like behavior in the effluent concentration response, with slower flow rates yielding higher effluent concentrations. The saturation concentration of TCE in the gas phase, estimated from measured temperature data (which fluctuated between $19^\circ C$ and $26^\circ C$) and the TCE saturation vapor pressure curve reported by Boublík et al. (1973), is also given in Figure 3 to show the departure from equilibrium concentrations. Clearly, observed effluent concentrations are lower than the equilibrium saturation concentration, often by two orders of magnitude or more, suggesting significant rate-limited mass transfer across the occlusion layer. Interestingly, effluent concentrations adjusted rapidly to new pseudo steady-state values following decreases in the air-phase flow rate. The measured effluent concentration variations with time are generally well behaved with only minor "blips" in the concentration plot, which correspond to ambient temperature changes in the laboratory. Note that there was an unrecorded no-flow period in the "thick" occlusions system that resulted from a power failure. Though this flow interruption was unplanned, it may present an opportunity for further exploration of transient

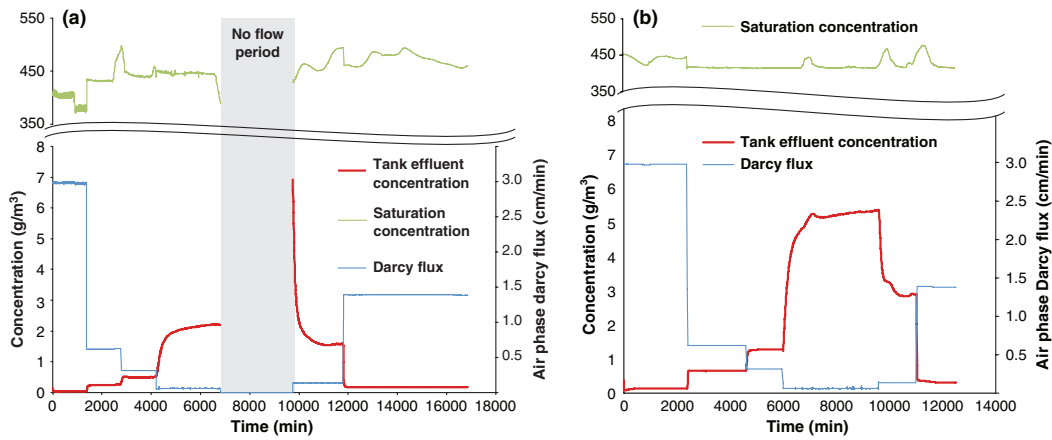


Figure 3. Measured TCE effluent vapor concentration vs. time for (a) the 13.8 mm “thick” occlusion and (b) the 8.5 mm “thin” occlusion. The red line represents the concentration of TCE in the effluent soil gas (g/m^3), green line represents the saturation concentration of TCE estimated from temperature data using values from Boublík et al. (1973) (g/m^3) (note y-axis break), blue line represents the air phase Darcy flux in the unsaturated portion of the tank.

nonequilibrium behavior via the stopped flow method proposed by Brusseau et al. (1989).

Table 2 presents a summary of the experimental results, including the average pseudo steady-state concentration for each flow rate tested in both the “thick” and “thin” occlusion tank experiments, as well as the average TCE mass flux eluting from the tank (product of gas-phase concentration and flow rate).

The rapid response of the system to the air-phase velocity changes may be partly explained by strong rate limitations caused by diffusion across the water-phase occlusion. The data in Table 2 indicate that despite large shifts in air-phase concentrations (range of 0.04 to $2.1 \text{ g}/\text{m}^3$ for the thick occlusion and 0.14 to $5.3 \text{ g}/\text{m}^3$ for the thin occlusion), the average TCE mass flux rate from the occluded sources for all velocities varies over a narrow range (mean, standard deviation of $3.28 \pm 0.89 \mu\text{g}/\text{min}$ for the thick occlusion and $7.74 \pm 0.74 \mu\text{g}/\text{min}$ for the thin occlusion), suggesting that shifts in flow rate largely dilute the relatively constant flux emanating from the occluded source.

The reason the source flux does not respond strongly to changes in airflow can be explained by conventional advection-diffusion theory. Because the “occlusion layer” in this system is stagnant and fully water saturated, it isolates the NAPL source from the flowing air phase in the coarse sand above. To volatilize, the NAPL must first dissolve within the source zone, and then diffuse through the water-phase occlusion to the interface with the gas phase. This diffusive flux is controlled by the concentration gradient across the water occlusion. On the NAPL side of the occlusion, the aqueous TCE concentration is near the solubility limit, whereas at the air-water occlusion interface, the concentration reflects that of the bulk flowing air, which under these experimental conditions are around 1% or less of the gas-phase saturation concentration. Thus,

within this experimental system, the concentration gradient across the occlusion layer is near the maximum value, which results in a source flux that is relatively insensitive to the airflow velocity. This gradient will only reduce significantly if gas-phase TCE concentrations in the bulk gas phase accumulate to significant levels, reducing the net change in concentration across the occlusion. In this event, gas-phase transport processes such as bulk advection and diffusion may begin to affect source flux. Case 1 results are also consistent with what can be explained through theory of diffusion because experimental results demonstrate that the occluded layer thickness affects the source flux, that is, a thicker occlusion has a longer diffusion distance and therefore lower concentration gradient (Table 2).

Comparison of Numerical and Experimental Results for Case 1

The steady-state concentrations predicted by the model for each experimental run are presented in Table 2, while a comparison of model and experimental values for each run is presented in Figure 4. The figure shows that without any fitting or calibration, the model predicts values within the range of the experimental observations, though with a slight positive bias in that the model predicts $144 \pm 29\%$ of the observed steady-state effluent concentrations. However, the fit of the model is considerably better for all of the “thin” occlusion experiments, as well as both “thick” occlusion experiments that occurred after the unexpected flow shutdown, predicting $113 \pm 12\%$ of the experimental value on average. Here, the model prediction nearly brackets the experimental observations. It is important to note that in Case 1 model results, none of the model parameters is fitted through calibration, and only literature values for all basic process parameters are used. This is to ensure that the model yields insight

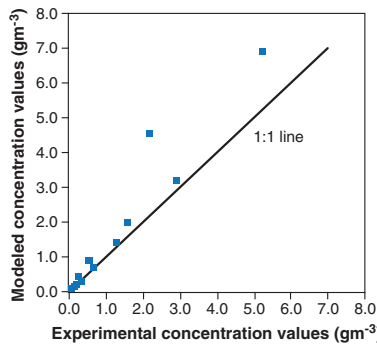


Figure 4. Comparison of steady-state model to steady-state experimental effluent concentration values for Case 1 runs.

into the physical process, rather than just fitting curves to unknown physics.

Overprediction by the model is generally possible due to inaccuracies in the precise representation of source zone geometry and NAPL-phase distribution, which could control the contaminant flux through the occluded layer. In the model, the source is assumed to be at the TCE solubility limit everywhere within the source zone, based on the assumption that the NAPL is uniformly distributed. However, in practice, it is difficult to create uniform saturations in multiphase systems, and in this case, TCE visibly settled toward the bottom of the source zone. Thus, the actual diffusion path in the experimental system might be longer than assumed within the model, leading to overprediction of the simulated mass transfer rate. In the specific case of the “thick” occlusion system where the model overpredicts by a much higher amount, it appears that the no-flow period affected the observed mass transfer behavior. It is possible that before the unexpected no-flow period, the system was not in a fully steady state and that the no-flow period may have given additional time to bring the system up to the steady state. Figure 5 shows a plot of the simulated total TCE concentration (sum of gas and aqueous phases) throughout the tank, as well as the magnitude of the diffusion-dispersion tensor term (e.g., Equation 11). The plot shows that a steep concentration gradient is present within the occlusion layer. Likewise, the dispersion tensor shows a strong discontinuity across the occluding layer. It is this gradient, in combination with the dispersion tensor, that governs mass transfer within the tank. Only a very dilute gas-phase plume (<1% of the saturation) extends downstream from the source, supporting the finding that aqueous-phase diffusion is limiting this mass transfer process.

Case 2, “Exposed” Source Experiments

Results from the exposed source experiments (runs 13 to 16 in Table 1) are presented in Figure 6. The data are normalized by the saturation concentration of TCE to reduce the effect of ambient temperature fluctuations, which caused higher or lower effluent concentrations in

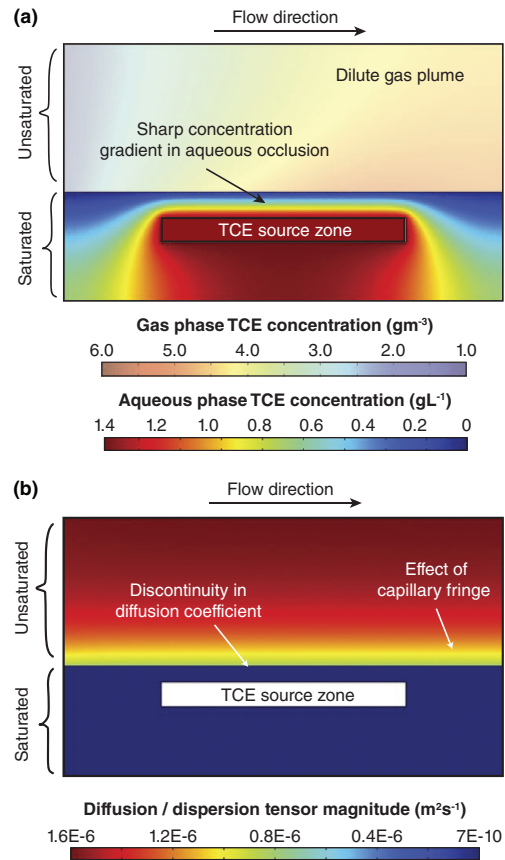


Figure 5. a) Simulated concentration profile: Pastel color scale shows gas phase concentrations, dark scale shows aqueous concentrations. b) Diffusion/Dispersion tensor magnitude profile for run #12, 8.5 mm occlusion run at a pore velocity of 2.88 md⁻¹. TCE source zone is outlined in white.

response to ambient heating and cooling in the laboratory. In contrast to the occluded systems where effluent concentrations never exceeded more than 1% of the saturation concentration, the concentrations in the “exposed” NAPL systems clearly approached the saturation concentration. Upon NAPL injection, the effluent concentration rises quickly and approaches the saturation concentration until the NAPL source is depleted, after which the concentrations diminish. Unlike the occluded systems, the exposed sources were run until depletion of the NAPL was visually confirmed. The overall NAPL recovery mass balance on runs 13 through 16 (conducted sequentially in the same tank) was 97.8%

Compared to the occluded systems, the exposed sources exhibit much higher average mass transfer rates and concentrations (Table 2). This is expected as the absence of an occlusion barrier to mass transport allows the NAPL to diffuse and disperse more rapidly within the

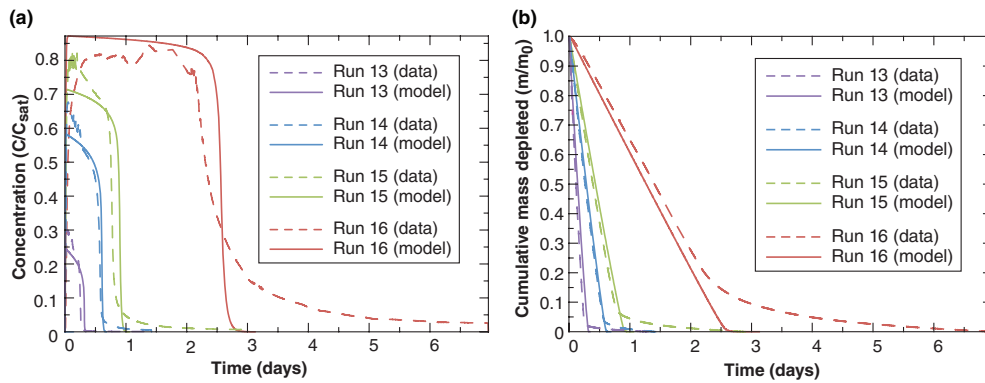


Figure 6. a) Model (solid line) and measured data (dashed) outflow concentration versus time for exposed source NAPL systems, and b) model (solid line) and measured data (dashed) mass depletion curves for exposed source NAPL systems.

soil gas. In addition, the mass flux rate in the NAPL-exposed systems is dependent on the air velocity, which contrasts with the occluded systems that had mass flux rates that were independent of velocity. This suggests that mass transfer in exposed systems is limited by gas-phase advection.

To explore the role of advection in the mass transfer from exposed pools, a transport model was prepared to simulate the mass transfer from the NAPL source. The original intent of running the “exposed” sources was to provide a basis of comparison to the occluded mass transfer systems within a similar porous media. A Gilliland-Sherwood mass transfer expression was tested to determine if such a relation could accurately reproduce the experimental observations. As it was not the original intent of this study to produce a Gilliland-Sherwood mass transfer model, only a narrow range of experiments were run to investigate the mass transfer. However, these experiments do allow the estimation of a simple Gilliland-Sherwood model as a function of the Peclet number, and it is insightful to compare this system to other volatilization mass transfer models in the literature (Table 3).

For the purpose of estimating a Gilliland-Sherwood relationship, the numerical model was used to simulate the tank and the Gilliland-Sherwood parameters were adjusted to best fit the data. Fitted parameters included the regression constant (Sh_0), Peclet number exponent (δ), and the mass tailing parameter (β). The model output was compared to the experimental breakthrough curve. The goal of the fitting procedure was to find a set of fitting parameter values Sh_0 , δ , and β for which the difference between the simulated and the experimental dissolution curves in all four airflow regimes is minimized. The best fit was obtained using a mixture of least squares linear regression, which gave $\beta = 0.2$, $Sh_0 = 1.1 \cdot 10^{-3}$, and $\delta = 0.05$.

In general, when comparing data to the model in Figure 1, the model fits well to the initial mass transfer rate (i.e., the initial peak concentration), as well as the time at which the NAPL mass is depleted (the sharp

drop in concentrations). However, the model does not fit the mass tailing, as it predicts a much more rapid drop in concentrations. This is likely due to the model not properly considering back diffusion from water-saturated areas within the tank. This is particularly apparent in run 16, where considerable mass tailing was observed. Because this was the lowest airflow system, the NAPL was present considerably longer than in the other runs (~ 1.5 days), which would allow considerably more diffusion into the saturated zone at the bottom of the tank. The model did not attempt to capture this behavior, and neglecting this diffusion process may have led to some of the discrepancy between model and data. It is also worth noting that run 16 also had a small amount of NAPL mass escape the source trough and sink into the capillary fringe. This was not considered by the model, but may have affected the experiment.

The best-fit mass transfer correlation described earlier is presented in Table 3, along with other mass transfer correlations that have been used to quantify volatilization in porous media in the literature. Several differences between the proposed and the existing mass transfer correlations are noted: the range of Peclet values (0.003 to 0.15), and the corresponding vapor-phase velocities tested in this system (3 to 145 m/day), is much smaller than those examined in previous studies. Given that equilibrium is expected in a system with no advection, it is logical to conclude that as the velocity decreases, the system approaches equilibrium. This behavior is evident in the much smaller Peclet number exponent in this study (0.05), which is likely at the boundary of applicability for the Gilliland-Sherwood-type model, and approaching a local equilibrium condition. Under local equilibrium, volatilization effectively becomes instantaneous. As a result, the observed NAPL mass flux is a function of the transport of the NAPL vapor away from the NAPL source via diffusion, advection, and dispersion. This contrasts with the occluded NAPL source where the mass flux was insensitive to the bulk diffusion and advection, and controlled instead by diffusion within the occlusion.

Table 3
Volatilization Mass Transfer Correlations

Reference	System Type	Flow Regime	Pore Velocity Range (m/d)	VOC Source Configuration	Source Zone Water Content	Gaseous Dispersion and Dispersion Term	Correlations	Pecllet Range
Wilkins et al. (1995)	ID column	Bulk gas flow	~50 to 1300	Homogeneous NAPL residual	Residual	Neglected	$Sh_0 = 10^{-2.79} Pe^{0.62} d_0^{1.82}$	$0.05 < Pe < 2$
Yoon et al. (2002)	ID column	Bulk gas flow	~50 to 1100	Homogeneous NAPL residual	Residual	Diffusion only	$Sh_0 = 10^{-2.77} Pe^{0.68} d_0^{1.68}$	$0.02 < Pe < 1.5$
van der Ham and Brouwers (1998)	ID column	Bulk gas flow	~8300 to 38,000	Homogeneous NAPL residual	Residual	Neglected	$Sh_0 = 10^{-3.05} Pe^{0.88} d_0^{1.82}$	$5 < Pe < 60$
Anwar et al. (2003)	ID column	Bulk gas flow	~90 to 1700	Homogeneous NAPL residual	None	Diffusion only	$Sh_0 = 10^{-3.30} Pe^{1.15} \theta_n^{-0.30}$	$0.03 < Pe < 3.7$
Chao et al. (1998)	ID column	Air channels	Not reported	Homogeneous aqueous phase	Saturated	Neglected	$Sh_0 = 10^{-4.71} Pe^{0.84} d_0^{1.71} H^{-0.61}$	Not reported
Braida and Ong (1998)	2D cell	Single air channel	~173 to 2160	Homogeneous aqueous phase	Saturated	Neglected	$Sh_0 = 10^{-7.14} Pe^{0.16} d_0^{1.66} H^{-0.83}$ Dam = $10^{-4.81} Pe^{-0.79} H^{-0.83}$	$0.05 < Pe < 1.5$
This study	2D cell	Bulk gas flow	3 to 145	Exposed NAPL pool	Residual	Both included	$Sh_0 = 10^{-2.82} Pe^{0.05}$	$0.003 < Pe < 0.15$

Conclusions and Implications

Experimental results show that vadose zone NAPL morphology strongly controls mass transfer, with occluded NAPL sources emitting considerably lower mass flux than exposed NAPL sources. In practical scenarios, an occluded source may represent NAPL trapped in a fine layer with high water saturation, or NAPL entrapped in or below the capillary fringe. Exposed NAPL may represent pooled or residual NAPL that is in direct contact with bulk air phase. The mass transfer behavior observed from each type of source is adequately explained using traditional advection dispersion diffusion models. Analysis suggests that mass loading from occluded sources is largely dependent on aqueous diffusion through the occlusion. With exposed sources, mass transfer approaches the local equilibrium condition, and thus mass removal becomes sensitive to bulk gas-phase transport processes such as advection and diffusion. Given that such strong differences in behavior are observed between occluded and exposed NAPL, it is logical to assume that improved models of NAPL volatilization will need to carefully include the role of NAPL morphology. In a complex NAPL source zone that includes both exposed and occluded NAPL, mass transfer may initially come overwhelmingly from the exposed portion of the source. However, because of the differences in mass transfer rates, the exposed NAPL may deplete more rapidly as the source ages leaving a longer lived occluded source that may contribute to mass tailing in the field.

The behavior of such a source could be even more complex when the vadose zone is subjected to dynamic hydrologic events affecting the water saturation. If an NAPL is subjected to smearing due to water table fluctuations, or to infiltration from the land surface, these may alter the source morphology, fluctuating between the exposed and the occluded cases. Thus, a source may effectively turn “off” or “on” depending on the water table position, or infiltration from rainfall. This has important implications for management of contaminated sites, such as with the vapor intrusion exposure pathway or operation of remediation systems. Water table fluctuations could be natural, but they can also be caused by anthropogenic operations, such as the operation of pumping wells. Likewise, surface activities might affect infiltration because capping a site with an impermeable barrier may reduce infiltration and expose more sources. Likewise, irrigation may increase infiltration and occlude sources. Incorporating the mass transfer dynamics that may result from such activities may be useful in improving the conceptual model of remediation sites.

This study shows that the NAPL mass transfer behavior can be captured with existing transport theory and modeling approaches under tightly controlled morphologies. However, further work is needed to model NAPL volatilization that considers the full range of three-phase saturation distributions that may occur in the field. An ideal model may be one that could link the soil water retention function to the mass transfer relation, allowing

simulation of mass transfer from complex sources without introducing a large number of new parameters that need to be calibrated. Further study of this problem may require an experimental apparatus capable of controlling and quantifying saturations in a fully three-phase fluid distribution. Ultimately, an improved three-phase mass transfer model may yield a better understanding of how vadose zone NAPL sources behave under dynamic conditions as well as when they age causing changes to morphology.

Nomenclature

Symbol	Units	Meaning
α	—	superscript / subscript denoting phase identity ($g = \text{gas}$, $w = \text{water}$, $n = \text{NAPL}$)
β	—	exponent for NAPL saturation for Gilliland-Sherwood model
c_n^{sat}	kg/m^3	saturated concentration of NAPL vapor in air
c_n^α	kg/m^3	concentration of NAPL in phase α
d_{50}	m	grain size of the porous medium, for which 50% of the entire mass is finer
d_0	m	normalized grain size
d_m	m	reference grain size ($=0.05 \text{ cm}$)
D_m^α	m^2/s	free molecular diffusion of NAPL in phase α
D_n^α	m^2/s	diffusion-dispersion tensor of the NAPL component phase α
δ	—	exponent on Peclet number for Gilliland-Sherwood model
F_α	$\text{kg/m}^3/\text{s}$	specific source/sink term of phase α
F_{ng}	$\text{kg/m}^3/\text{s}$	specific mass transfer term of NAPL into gas phase
H	—	dimensionless Henry's constant
k_{ng}	s^{-1}	mass transfer rate coefficient
Pe	—	Péclet number
ϕ	—	porosity
ρ_α	kg/m^3	density of phase α
S_α	—	volumetric saturation of phase α
$S_{n,0}$	—	initial NAPL saturation of source zone
Sh	—	Sherwood number
Sh_0	—	empirical constant for Gilliland-Sherwood correlation
v_α	m/s	apparent macroscopic velocity of phase α
X_n^α	kg/kg	mass fraction of NAPL component in phase α
t	s	time

Acknowledgments

The authors thank the Strategic Environmental Research and Development Program Grant ER-1687: *Vapor Intrusion from Entrapped NAPL Sources and Groundwater Plumes: Process Understanding and Improved Modeling Tools for Pathway Assessment and Numerical Methods for Multiphase Flow*, and also the

Czech Ministry of Education, Youth and Sports Project KONTAKT II LH14003: *Development and Validation of Porous Media Fluid Dynamics and Phase Transitions Models for Subsurface Environmental Application* for providing funding for this research. The authors also thank Dr. Michal Beneš of Czech Technical University for his gracious review and suggestions on the project.

Supporting Information

Additional Supporting Information may be found in the online version of this article:

Appendix S1. Additional method details and full model description.

References

Anwar, A.H.M.F., T.H. Tien, Y. Inoue, and F. Takagi. 2003. Mass transfer correlation for nonaqueous phase liquid volatilization in porous media. *Environmental Science & Technology* 37: 1277–1283.

Auer, L.H., N.D. Rosenberg, K.H. Birdsell, and E.M. Whitney. 1996. The effects of barometric pumping on contaminant transport. *Journal of Contaminant Hydrology* 24, no. 2: 145.

Batterman, S., I. Padmanabham, and P. Milne. 1996. Effective gas-phase diffusion coefficients in soils at varying water content measured using a one-flow sorbent-based technique. *Environmental Science and Technology* 30: 770–778.

Boublik, T., V. Fried, and E. Hála. 1973. *The Vapour Pressures of Pure Substances: Selected Values of the Temperature Dependence of the Vapour Pressures of Some Pure Substances in the Normal and Low Pressure Region*. New York: Elsevier.

Braida, W., and S.K. Ong. 1998. Air sparging: Air-water mass transfer coefficients. *Water Resources Research* 34, no. 12: 3245–3253.

Braida, W., and S.K. Ong. 2000. Influence of porous media and airflow rate on the fate of NAPLs under air sparging. *Transport in Porous Media* 38, no. 1/2: 29–42.

Brusseau, M.L., P.S.C. Rao, R.E. Jessup, and J.M. Davidson. 1989. Flow interruption: A method for investigating sorption nonequilibrium. *Journal of Contaminant Hydrology* 4: 223–240.

Chao, K.-P., S.K. Ong, and A. Protopapas. 1998. Water-to-air mass transfer of VOCs: Laboratory scale air sparging system. *Journal of Environmental Engineering* 124, no. 11: 1054–1060.

Christ, J.A., L.D. Lemke, and L.M. Abriola. 2005. Comparison of two-dimensional and three-dimensional simulations of dense nonaqueous phase liquids (DNAPLs): Migration and entrapment in a nonuniform permeability field. *Water Resources Research* 41, no. W01007: 12.

Class, H., R. Helmig, and P. Bastian. 2002. Numerical simulation of non-isothermal multiphase multicomponent processes in porous media. 1. An efficient solution technique. *Advances in Water Resources* 25: 533–550.

Class, H., R. Helmig, and I. Neuweiler. 2008. Sequential coupling of models for contaminant spreading in the vadose zone. *Vadose Zone Journal* 7, no. 2: 1–11.

Clayton, W.S. 1998. A field and laboratory investigation of air fingering during air sparging. *Ground Water Monitoring and Remediation* 17, no. 3: 134–145.

Cussler, E.L. 2009. *Diffusion: Mass Transfer in Fluid Systems*. Cambridge, UK: Cambridge University Press.

Fagerlund, F., T.H. Illangasekare, and A. Niemi. 2007. Nonaqueous-phase liquid infiltration and immobilization in

- heterogeneous media: 1. Experimental methods and two-layered reference case. *Vadose Zone Journal* 6, no. 3: 471–482.
- Falta, R.W., I. Javandel, K. Pruess, and P.A. Witherspoon. 1989. Density-driven flow of gas in the unsaturated zone due to the evaporation of volatile organic compounds. *Water Resources Research* 25, no. 10: 2159–2169.
- Fučík, R., and J. Mikyška. 2011. Discontinuous Galerkin and mixed-hybrid finite element approach to two-phase flow in heterogeneous porous media with different capillary pressures. *Procedia Computer Science* 4: 908–917.
- Fučík, R., and J. Mikyška. 2012. Mixed-hybrid finite element method for modelling two-phase flow in porous media. *Journal of Math for Industry* 3: 9–19.
- Fure, A.D., J.W. Jawitz, and M.D. Annable. 2006. DNAPL source depletion: Linking architecture and flux response. *Journal of Contaminant Hydrology* 85: 118–140.
- van Genuchten, M.Th., F.J. Leij, and S.R. Yates. 1991. The RETC code for quantifying the hydraulic functions of unsaturated soils (version 1). Office of Research and Development, U.S. Environmental Protection Agency, EPA/600/2-91/063, 85.
- van Genuchten, M.Th. 1980. A closed-form analytical equation for predicting the hydraulic conductivity of unsaturated soils. *Soil Science Society of America Journal* 44, no. 5: 892–898.
- van der Ham, A.G.J., and H.J.H. Brouwers. 1998. Modeling and experimental investigation of transient, nonequilibrium mass transfer during steam stripping of a nonaqueous phase liquid in unsaturation porous media. *Water Resources Research* 34, no. 1: 47–54.
- Heron, G., T.H. Christensen, and C.G. Enfield. 1998. Henrys law constant for trichloroethylene between 10 and 95 °C. *Environmental Science and Technology* 32: 1433–1437.
- Ho, C.K., and K.K. Udell. 1992. An experimental investigation of air venting of volatile liquid hydrocarbon mixtures from homogeneous and heterogeneous porous media. *Journal of Contaminant Hydrology* 11, no. 3-4: 291.
- Illangasekare, T.H., E.J. Armbruster, and D.N. Yates. 1995. Non-aqueous phase fluids in heterogeneous aquifers: An experimental study. *Journal of Environmental Engineering* 121: 571–579.
- Illangasekare, T.H., C.C. Frippiat, and R. Fučík. 2010. Dispersion and mass transfer in groundwater near-surface geologic formations. In *Handbook of Chemical Mass Transport in the Environment*, ed. Louis J. Thibodeaux and David Mackay, 413–453. Boca Raton, Florida: Taylor and Francis Group.
- Jang, W., and M.M. Aral. 2007. Density-driven transport of volatile organic compounds and its impact on contaminated groundwater plume evolution. *Transport in Porous Media* 67: 353–374.
- Johnson, P.C., and R.A. Ettinger. 1991. Heuristic model for predicting the intrusion rate of contaminant vapors into buildings. *Environmental Science & Technology* 25, no. 8: 1445–1452. DOI:10.1021/es00020a013.
- Kaluarachchi, J.J., and J.C. Parker. 1992. Multiphase flow with a simplified model for oil entrapment. *Transport in Porous Media* 7: 1–14.
- Kueper, B.H., W. Abbott, and G. Farquhar. 1989. Experimental observations of multiphase flow in heterogeneous porous media. *Journal of Contaminant Hydrology* 5, no. 1: 83.
- Kueper, B.H., D. Redman, R.C. Starr, S. Reitsma, and M. Mah. 1993. A field experiment to study the behavior of tetrachloroethylene below the water table: Spatial distribution of residual and pooled DNAPL. *Ground Water* 31: 756–766.
- Lemke, L.D., L.M. Abriola, and J.R. Lang. 2004. Influence of hydraulic property correlation on predicted dense nonaqueous phase liquid source zone architecture, mass recovery and contaminant flux. *Water Resources Research* 40, no. W12417: 18.
- Lenhard, R.J., and J.C. Parker. 1987. Measurement and prediction of saturation-pressure relationships in three-phase porous media systems. *Journal of Contaminant Hydrology* 1: 407–424.
- Lenhard, R.J., M. Oostrom, C.S. Simmons, and M.D. White. 1995. Investigation of density-dependent gas advection of trichloroethylene: Experiment and a model validation exercise. *Journal of Contaminant Hydrology* 19, no. 1: 47.
- Lenhard, R.J., M. Oostrom, and J.H. Dane. 2004. A constitutive model for air-NAPL-water flow in the vadose zone accounting for immobile, non-occluded (residual) NAPL in strongly water-wet porous media. *Journal of Contaminant Hydrology* 71: 261–282.
- Leverett, M.C. 1941. Capillary behavior in porous solids. *Transactions of the American Institute of Mining Engineers* 142, no. 1: 152–169.
- Liang, H.-C., and K.S. Udell. 1999. Experimental and theoretical investigation of vaporization of liquid hydrocarbon mixtures in water-wetted porous media. *Water Resources Research* 35, no. 3: 635–649.
- Lugg, G.A. 1968. Diffusion coefficients of some organic and other vapors in air. *Analytical Chemistry* 40, no. 7: 1072–1077.
- Luo, H., P. Dahlen, P.C. Johnson, T. Peargin, and T. Creamer. 2009. Spatial variability of soil-gas concentrations near and beneath a building overlying shallow petroleum hydrocarbon-impacted soils. *Ground Water Monitoring and Remediation* 29, no. 1: 81–91.
- Miller, C.T., M.M. Poirier-McNeill, and A.S. Mayer. 1990. Dissolution of trapped nonaqueous phase liquids: Mass transfer characteristics. *Water Resources Research* 26, no. 11: 2783–2796.
- Mosthaf, K., K. Baber, B. Flemisch, R. Helmig, A. Leijnse, I. Rybak, and B. Wohlmuth. 2011. A coupling concept for two-phase compositional porous-medium and single-phase free flow. *Water Resources Research* 47, no. 10: 1–19.
- Mualem, Y. 1976. A new model for predicting the hydraulic conductivity of unsaturated porous media. *Water Resources Research* 12, no. 3: 513–522.
- Oostrom, M., J.H. Dane, and T.W. Wietsma. 2005. Removal of carbon tetrachloride from a layered porous medium by means of soil vapor extraction enhanced by desiccation and water table reduction. *Vadose Zone Journal* 4: 1170–1182.
- Page, J.W.E., K. Soga, and T.H. Illangasekare. 2007. The significance of heterogeneity on mass flux from DNAPL source zones: An experimental investigation. *Journal of Contaminant Hydrology* 94: 215–234.
- Parker, J.C. 2003. Physical processes affecting natural depletion of volatile chemicals in soil and groundwater. *Vadose Zone Journal* 2: 222–230.
- Poulsen, M.M., and B.H. Kueper. 1992. A field experiment to study the behavior of tetrachloroethylene in unsaturated porous media. *Environmental Science & Technology* 26, no. 5: 889–895. DOI:10.1021/es00029a003.
- Powers, S.E., L.M. Abriola, J.S. Dunkin, and W.J. Walter Jr.. 1994. Phenomenological models for transient NAPL-water mass-transfer processes. *Journal of Contaminant Hydrology* 16: 1–33.
- Rivett, M.O., G.P. Wealthall, R.A. Dearden, and T.A. McAlary. 2011. Review of unsaturated zone transport and attenuation of volatile organic compound (VOC) plumes leached from shallow source zones. *Journal of Contaminant Hydrology* 123: 130–156.
- Rogers, S.W., and S.K. Ong. 2000. Influence of porous media, airflow rate, and air channel spacing on benzene NAPL removal during air sparging. *Environmental Science & Technology* 34, no. 5: 764–770. DOI:10.1021/es9901112.
- Saba, T., and T.H. Illangasekare. 2000. Effect of groundwater flow dimensionality on mass transfer from entrapped nonaqueous phase liquid contaminants. *Water Resources Research* 36, no. 4: 971–979.

■ P.4 Článek v *Journal of Computational Physics*

Jakub Solovský, Radek Fučík, Michael R Plampin, Tissa H Illangasekare a Jiří Mikyška: *Dimensional effects of inter-phase mass transfer on attenuation of structurally trapped gaseous carbon dioxide in shallow aquifers*, *Journal of Computational Physics*, 405:109178, 2020.

leaked gas [21]. Because water with a higher dissolved CO₂ concentration is heavier than clean water, it will sink and thus reduce potential subsequent release of gas back into the atmosphere [1–3].

During transport into and within the shallow subsurface, changes in pressure, temperature, and surrounding chemical composition induce complex multiphase flow phenomena such as dissolution, exsolution, expansion, and migration of gas phase CO₂ in otherwise water-saturated media. These processes, defined collectively as multiphase CO₂ evolution, have received significant attention in recent years. However, considerable gaps remain in our understanding of these processes, particularly regarding the fundamental interaction between the fluids in the pore space; that is, the mass transfer of CO₂ among aqueous and gaseous phases during flow through porous media. This study aims to help fill that knowledge gap by comparing a model capable of incorporating various conceptualizations of mass transfer with data from highly controlled laboratory experiments.

The goal of the present work is not to validate the numerical model, because kinetic mass transfer models for similar problems have already been validated [8], but rather to demonstrate the conditions under which the kinetic mass transfer affects the multiphase evolution of CO₂ within shallow aquifers. While previous studies have focused primarily on pore- to core-scale interactions between supercritical CO₂ and brine under deep reservoir conditions, we instead analyze intermediate-scale interactions between gas phase CO₂ and freshwater under low temperatures and pressures, so that the associated conclusions may help in the design of monitoring, verification, and risk assessment strategies in the field. We hypothesize that kinetic mass transfer will be important to capture the behavior observed in the experiments under certain flow conditions within shallow aquifers, but that the equilibrium approximation will also be sufficient in some scenarios.

1.1. Overview

In general, there are two principal approaches to modeling inter-phase mass transfer from sources of trapped NAPL (non-aqueous phase liquid) or gas (in this case CO₂): equilibrium and kinetic. The equilibrium approach assumes that the flowing water close to the NAPL/gas source is at the solubility limit with respect to the dissolved phase of the otherwise NAPL-phase constituent. In situations where the groundwater velocities are low, resulting in large residence times for the water to be in contact with the separate phase fluid, the concentrations attain equilibrium almost instantaneously.

While the equilibrium model works well in some situations [22], we demonstrate that for other scenarios, the equilibrium model cannot correctly describe the behavior of the multiphase system, and that a more advanced approach is therefore needed. To address the more complex scenarios, a kinetic mass transfer model is employed in this work, in which the mass transfer rate is defined by rate coefficients. These phenomenological coefficients are defined in terms of correlations containing dimensionless numbers with parameters that are fitted to experimental data (e.g. Gilliland-Sherwood correlations) [14], and can be described in terms of physical processes at the pore scale. However, for practical applications, these coefficients must be determined empirically at the macroscopic scale.

Both the exsolution of previously dissolved gas from an over-saturated solution and the dissolution of trapped separate phase gas into previously under-saturated water are processes of mass transfer between two phases. Both processes are generally assumed to be functions of temperature and several dimensionless quantities. In equilibrium-based models, the rates of exsolution and dissolution are assumed to be equal (both are instantaneous), but in kinetic models, the rates of dissolution and exsolution can be different. Moreover, they can also depend on the geometry of the flow field [23].

The primary goal of this paper is to demonstrate the conditions under which more complex non-equilibrium mass transfer processes occur and also elucidate conditions under which the simplified model is sufficient for the description of the system. The previous works generally isolated various aspects of the system, but did not broadly compare various scenarios against one another to draw more general conclusions about the conditions that lead to the different types of mass transfer processes. Therefore, this work again aims to help fill that knowledge gap.

1.2. Experiments and goals of the study

In this work, we propose a mathematical model that describes two-phase compositional flow including kinetic mass transfer, and investigate how this process affects CO₂ fate and transport in shallow aquifers. This goal was accomplished by comparing results of numerical simulations to laboratory data on exsolution, structural trapping, and dissolution of gaseous CO₂ that was previously generated via intermediate-scale experiments conducted at the Center for Experimental Study of Subsurface Environmental Processes (CESEP) at the Colorado School of Mines. These experiments were unique and valuable in that they were conducted in test systems that were large enough to allow for flow processes similar to those that would occur in the field settings, but within a laboratory environment that allowed for careful control of external conditions and acquisition of data at higher temporal and spatial resolutions than would be possible to obtain in the field. The experiments focused on multiphase CO₂ evolution in shallow aquifers, and were designed to represent hypothetical scenarios related to CO₂ leakage from deep geologic sequestration sites.

The model developed in this study was compared against two different sets of experiments carried out at CESEP: a series of six experiments performed in a quasi-1D “rectangular column” test system, and two experiments conducted in a larger, more complex 2D test system “large tank”. Both systems incorporated layered heterogeneous porous media packing configurations designed to mimic geologic facies transitions in the field. The heterogeneity configuration of the porous media in the experiment was simpler than the one that can usually be expected in the field. However, such a simplified

$$p_c^{B\&C}(S_\ell) = p_d(S_\ell^e)^{-\frac{1}{\lambda}}, \quad (3)$$

where p_d [Pa] is the entry pressure, λ [-] is related to the pore size distribution, and S_α^e denotes the effective saturation defined by

$$S_\alpha^e = \frac{S_\alpha - S_{r\alpha}}{1 - S_{rg} - S_{r\ell}}, \quad (4)$$

where $S_{r\alpha}$ is the residual saturation of phase α .

For the relative permeability functions $k_{r\ell}$ and k_{rg} , the Burdine model [7] with Brooks–Corey parameters is used in the form

$$k_{r\ell}^B(S_\ell) = (S_\ell^e)^{\frac{2+3\lambda}{\lambda}}, \quad (5)$$

$$k_{rg}^B(S_g) = (S_g^e)^2 \left(1 - (1 - S_g^e)^{\frac{2+\lambda}{\lambda}}\right). \quad (6)$$

By definition, the residual saturation $S_{r\alpha}$ describes the fraction of pore volume occupied by phase α that cannot be mechanically displaced. The values of $S_{r\alpha}$ are empirical and are obtained during drainage and imbibition experiments [24]. However, as reported by [22,30], the concept of (mechanically) immobile residual saturation is not sufficient for modeling gas dissolution and exsolution processes, especially in cases, where no gas is initially present in the porous media. Consequently, $S_{rg} = 0$ is used in (4).

On the other hand, experimental evidence [22,30] indicates that a certain threshold of gas saturation has to be reached before the gas phase becomes mobile. Such a value is referred to as the critical gas saturation S_c and the non-wetting phase (gas) relative permeability function k_{rg} is modified as

$$k_{rg}(S_g) = \begin{cases} 0, & \text{if } S_g < S_c, \\ k_{rg}^B\left(\frac{S_g - S_c}{1 - S_c}\right), & \text{otherwise.} \end{cases} \quad (7)$$

2.2. Component transport

In this work, the liquid phase is assumed to be a two component mixture: water and dissolved CO₂ whereas the gas phase as a single component: pure CO₂. Based on [16], the compositional balance equation for CO₂ dissolved in the liquid phase is added to the two phase flow equations (1) and (2) as

$$\frac{\partial(\phi S_\ell \rho_\ell X)}{\partial t} + \nabla \cdot (\rho_\ell \vec{v}_X) = f_X, \quad (8)$$

where X [-] is the mass fraction of CO₂, f_X [kg m⁻³ s⁻¹] is the sink or source term, and \vec{v}_X [m s⁻¹] is the velocity of the CO₂ component given by:

$$\vec{v}_X = X \vec{v}_\ell - \tau_\ell \phi S_\ell D_\ell \nabla X \quad (9)$$

where D_ℓ [m² s⁻¹] is the free molecular diffusion of CO₂ in water, $D_\ell = 1.92 \cdot 10^{-9}$ m² s⁻¹, and τ_ℓ [-] is the tortuosity given by $\tau_\ell = \phi^{1/3} S_\ell^{7/3}$ based on [15].

2.3. Kinetic mass transfer

The mass transfer of CO₂ between both phases (i.e., the dissolution and exsolution processes) is mediated through the sink/source terms f_X in Eq. (8) and f_α in Eq. (1). Based on [17], the kinetic mass transfer model is represented by

$$-f_g = f_\ell = f_X = k(C_s - X \rho_\ell), \quad (10)$$

where C_s [kg m⁻³] is the saturated CO₂ concentration and k [s⁻¹] is the effective (lumped) mass transfer rate coefficient. In general, the effective rate coefficient k is a function of the interfacial area, temperature, properties of porous media, or flow velocity as was discussed in [17], but it is beyond the scope of the present study to address dependency of k on all these quantities since the experiments considered in this work were carried out to address only a few key parameters that affects the multiphase CO₂ evolution. It is further conceptualized that the effective mass transfer coefficient k can be generally different for exsolution and dissolution, and denoted by k_{exs} and k_{dis} , respectively.

The kinetic model on a given element at a certain time allows for only one of the processes (exsolution vs. dissolution) to occur based on the sign of the source term given by Eq. (10) (whether the current concentration is higher or lower than the solubility limit). When the concentration equals the solubility limit, the source term given by Eq. (10) is zero, so the mass transfer also becomes zero and this state is referred to as equilibrium. In the kinetic model, equilibrium is reached

Table 1
Material properties used in the column experiment based on [21,18].

Symbol Units	Identification	ϕ [–]	K [m ²]	p_d [Pa]	λ [–]	$S_{r\ell}$ [–]
	Accusand #20/30	0.32	2.3×10^{-10}	1200	7.33	0.084
	Accusand #50/70	0.34	3.0×10^{-11}	3400	16.9	0.207

Table 2
Settings of the column experiments described in Section 3. The material properties are listed in Table 1. The experiment duration in the last column is selected as the final time t_{fin} of the simulation.

Id.	Overpressure [kPa]	Inflow rate [ml min ⁻¹]	Injection period [h]	Experiment duration [h]
LS	12	4	104.80	150
LF	12	40	10.67	70
MS	20	4	92.62	186
MF	20	40	10.45	73
HS	30	4	98.76	212
HF	30	40	10.20	76

3. Quasi-1D case

First, a quasi-1D column experiment with heterogeneous sand packing is considered with a predominant vertical flow field in which the CO₂ exsolution, trapping, and dissolution processes were investigated.

The computational study presented in this section aims to find the optimal values of the model parameters (critical gas saturation and mass transfer coefficients) that control the multiphase CO₂ evolution in the experimental setup and to use the calibrated numerical model to investigate the spatial and temporal evolution of CO₂ in the column.

3.1. Experimental setup

A series of quasi-1D experiments was carried out in a rectangular column tank packed in a configuration that mimics the apex of an anticlinal geological feature. Fig. 1 shows the column experiment configuration and port positions, where the gas saturation was measured. Properties of the sands used in the experiments are summarized in Table 1.

The packing configuration (sand properties and position of the ports) remained the same for all six column experiments.

Each column experiment consisted of two consecutive injection periods. First, CO₂-saturated water was injected into the column through the injection port located at the bottom of the tank for a given period of time. A portion of the dissolved CO₂ exsolved into the gas phase, migrated upwards, and accumulated under the coarse-fine sand interface. Then, clean de-ionized (DI) water was injected into the column through the same injection port and the gaseous CO₂ dissolved into the clean water and was transported upwards.

The experiments varied in (a) the pressure at which the injected water was saturated by CO₂ (characterized by the overpressure with respect to the atmospheric pressure in the laboratory) and therefore the amount of CO₂ dissolved in water at the inflow, (b) the inflow rate, and (c) the length of the injection period. In Table 2, the settings of the experiments are summarized and the following two-letter notation is introduced. The first letter denotes the overpressure of the injected CO₂: L = low (12 kPa), M = medium (20 kPa), and H = high (30 kPa), whereas the second letter describes the inflow rate: S = slow (4 ml min⁻¹) and F = fast (40 ml min⁻¹).

3.2. Computational study setup

The main goal of the computational study is to determine optimal (best-fitted) values of the unknown model parameters k_{exs} , k_{dis} (the mass transfer coefficients for exsolution and dissolution, respectively), and S_c (the critical gas saturation) based on the experimental data. The experimental procedure previously described in Section 3.1 is for the purposes of the computational study divided into three stages in which 1) exsolution, 2) accumulation, and 3) dissolution were the dominant processes and are therefore investigated consecutively. The division into (almost) isolated stages (the exsolution and accumulation both occurred during the CO₂-saturated water injection) allows us to use each of them to determine the aforementioned unknown parameters separately as will be discussed in the following sections.

The mesh used in the numerical simulations is shown in Fig. 1. The mesh consisted of 2552 elements and was locally refined in the vicinity of the material interfaces. The mesh resolution was sufficient to capture all effects investigated in this work. At the same time, the coarseness of the mesh allowed many computations with various model parameters to be carried out efficiently.

Initially at $t = 0$, the tank contains only pure water with no inflow or outflow: $X = 0$, $p_c = p_d$ (which corresponds to $S_g = 0$), and $p_g = p_c + p_\ell$, where the hydrostatic pressure profile for p_ℓ was prescribed. The final time of each simulation

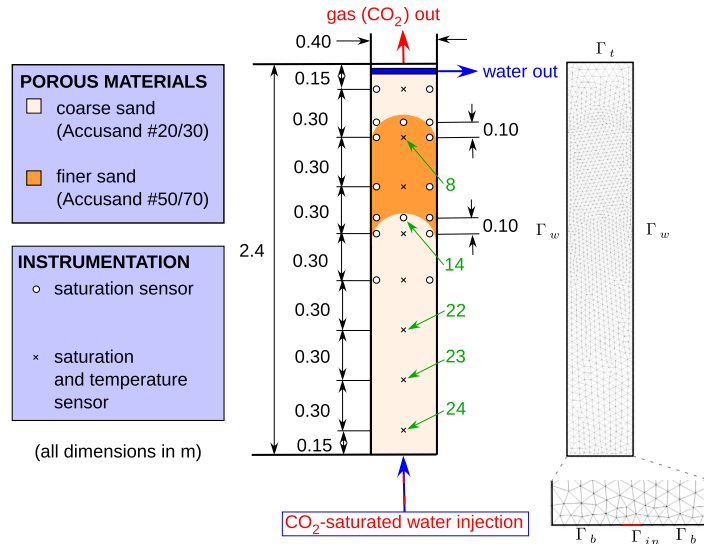


Fig. 1. The column experiment configuration and the triangular mesh of 2552 elements used in the numerical simulations.

t_{fin} is the same as the final time of the corresponding experiment shown in Table 2. Constant time steps of 5 s, 2 s, and 1 s were selected for the low, medium, and high overpressure experiments, respectively.

The boundary conditions are given as follows. At Γ_w and Γ_b , no flow boundary condition is prescribed for both phases as well as for the dissolved CO_2 . At Γ_{in} , no flow boundary condition for the gas phase is prescribed for the whole duration of the experiment. During the injection period, the Neumann boundary condition for the water inflow velocity u_ℓ and the Dirichlet boundary condition for the CO_2 mass fraction X based on the values in Table 2 are prescribed at Γ_{in} . During the rest of each experiment, clean water is injected with a given injection schedule shown in Table 3, i.e., the Dirichlet boundary condition for $X = 0$ and the Neumann boundary condition for u_ℓ are prescribed at Γ_{in} based on the inflow rate given in Table 3. Between the individual injections (rows in Table 3), there is always a one minute break where the injection is stopped that during the experiment allowed for the preparation of the next injection. This break is represented by zero Neumann boundary condition $u_\ell = 0$.

At the upper boundary Γ_t , the Dirichlet boundary conditions $p_c = p_d$, $p_g = p_{ref}$, and $\nabla X = 0$ are prescribed with $p_{ref} = 82$ kPa as the reference atmospheric pressure in the laboratory (at the altitude of approximately 1800 m above sea level). This setting mimics the experimental setup on the upper boundary that allowed for the free outflow of gas and water with dissolved CO_2 .

3.3. Stage 1: exsolution

During the exsolution stage, the CO_2 dissolved in water is injected into the tank and exsolves. For the medium and high overpressure experiments, the gaseous CO_2 is detected in the lower ports (Ports 22 - 24) far from the fine layer barrier.

After the initial growth, the measured gas saturation values lose the underlying growing trend and the oscillations center around a constant value as shown in Fig. 2. In the experiment, the fluctuations are caused by the changes in the gas distribution at the pore scale. For the slow experiment run, there is more time for this diffusive redistribution to occur when the water is not flowing that fast. Therefore, the fluctuations for the slow runs are more significant.

These plateau values represent the fraction of gas phase trapped in the porous medium that remains immobile and can be directly interpreted as the critical saturation S_c .

Combining all four medium and high overpressure experiments, the value of the critical gas saturation is estimated to be $S_c = 0.25$ which is also in agreement with [22].

The dependency of the numerical results on the values of S_c for experiment HS is illustrated in Fig. 3, where the numerical results for the critical gas saturation values 0.05, 0.1, 0.15, 0.2, 0.25, 0.3 are compared. These results indicate that the estimated value $S_c = 0.25$ is a sufficiently good approximation.

Note that no information about S_c can be obtained during this stage for the low overpressure experiments LS and LF because CO_2 does not exsolve before it reaches the middle region of the sand column close to the heterogeneity. Hence, a different mechanism attributed to the capillary barrier of the fine sand is responsible for the detected CO_2 saturation values that are also much higher than those measured in the lower ports for high overpressure experiments.

Table 3
Clean DI water injection schedule for the column experiments.

Id.	LS	LF	MS	MF	HS	HF
duration [h]	12.15	12.44	2.80	14.34	2.87	15.70
inflow rate [ml min ⁻¹]	6	8	32	6	32	6
duration [h]	2.53	2.58	16.83	2.35	14.53	3.03
inflow rate [ml min ⁻¹]	32	32	6	32	8	32
duration [h]	2.80	3.28	2.67	2.62	2.7	2.98
inflow rate [ml min ⁻¹]	32	32	32	32	32	32
duration [h]	3.15	2.25	3.07	2.95	2.67	3.22
inflow rate [ml min ⁻¹]	32	32	32	32	32	32
duration [h]	15.57	14.91	2.3	16.67	2.78	15.67
inflow rate [ml min ⁻¹]	6	6	32	6	32	6
duration [h]	2.98	2.93	15.95	3.17	12.68	2.6
inflow rate [ml min ⁻¹]	32	32	6	32	8	32
duration [h]	5.60	2.45	3.17	3.65	3.93	2.57
inflow rate [ml min ⁻¹]	16	32	32	32	32	32
duration [h]	-	2.92	3.02	16.47	2.73	1.7
inflow rate [ml min ⁻¹]	-	32	32	6	32	32
duration [h]	-	14.6	1.82	-	3.30	2.87
inflow rate [ml min ⁻¹]	-	6	32	-	32	32
duration [h]	-	-	15.28	-	14.733	12.183
inflow rate [ml min ⁻¹]	-	-	6	-	6	8
duration [h]	-	-	3.28	-	4.40	2.05
inflow rate [ml min ⁻¹]	-	-	32	-	16	32
duration [h]	-	-	3.30	-	44.92	-
inflow rate [ml min ⁻¹]	-	-	32	-	2	-
duration [h]	-	-	1.17	-	-	-
inflow rate [ml min ⁻¹]	-	-	32	-	-	-
duration [h]	-	-	17.22	-	-	-
inflow rate [ml min ⁻¹]	-	-	6	-	-	-

3.4. Stage 2: accumulation

During the accumulation stage of the experiment, the injection of water with dissolved CO₂ continues and as more CO₂ exsolves and migrates upwards, the gaseous phase accumulates below the fine layer which, due to a higher entry pressure, acts as a capillary barrier. As a result, the gas saturation below the fine layer reaches up to almost 0.9 as measured in Port 14 placed directly below the heterogeneity. Because of this significant accumulation, this port is selected to demonstrate the dynamics of the mass transfer in this section.

To capture the experimentally observed gas accumulation by the numerical model, enough CO₂ needs to be produced during the exsolution process. For each experimental run, a parameter sensitivity study was carried out in order to determine the optimal value of k_{exs} . Many numerical results were computed for a series of values of k_{exs} with a selected step of 0.01 [s⁻¹].

The optimal values of k_{exs} were subsequently selected among the results of numerically computed S_g values such that they best-fitted the experimentally measured S_g values in all the ports during the accumulation stage. The best fit is considered in terms of the sum of Euclidean norms of difference between the numerical solution and experimental data (L_2 norm over a given time interval) for all the ports.

The numerical results show that substantially large values of k_{exs} have to be considered to produce enough gaseous CO₂ to match the experimental data. Furthermore, a certain threshold $k_{exs}^* = 5 \text{ s}^{-1}$ exists for which the rate of exsolved CO₂ is maximal, i.e., the numerical results are the same for k_{exs}^* and for all $k_{exs} > k_{exs}^*$ as illustrated in Fig. 4 for the HS experiment. Similar dynamics can be observed for all the column experiments and the numerical results show that this threshold value is the same for all the experiments. These findings indicate that a near-equilibrium rather than a rate-limited kinetic mass transfer process is observed during the exsolution stage for all the column experiments.

3.5. Stage 3: dissolution

During the last stage, clean water is injected into the tank and the gaseous CO₂ present in the tank dissolves into the flowing water. The evolution of the experimentally measured gas saturation indicates that similar to the exsolution process, the dissolution is rapid. Parameter sensitivity studies were again carried out for each experimental run to determine the

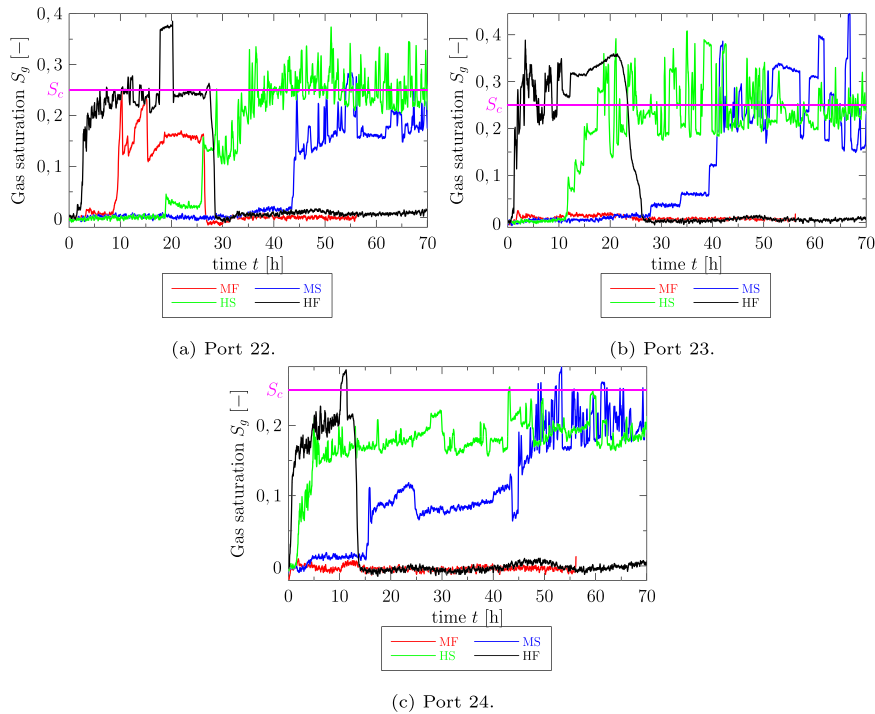


Fig. 2. Medium and high overpressure experiments, measured gas saturation and highlighted value of critical gas saturation $S_c = 0.25$. (For interpretation of the colors in the figure(s), the reader is referred to the web version of this article.)

optimal values of k_{dis} in the same way as in the previous section. The best fit is considered in terms of the sum of Euclidean norms of difference between the numerical solution and experiment for all the ports.

As in the previous section, the results show that a substantially large value of $k_{dis} > k_{dis}^*$ (with $k_{dis}^* = 5 \text{ s}^{-1}$ as the threshold value) is the optimal choice that captures the dissolution process and the threshold value are illustrated in Fig. 5 for Port 14 of the HS experiment. The dissolution rate is represented by the slope of the gas saturation curve. These findings are the same for all the experiments indicating that the CO_2 dissolution can be also interpreted as the near-equilibrium mass transfer process.

3.6. Discussion of results

The division of the experiments into three stages allowed for determination of the optimal values of the model parameters k_{exs} , k_{dis} , and S_c . The influence of the parameter variations was demonstrated for selected experiments and ports. For all computations discussed in this section, the following values of the model parameters, obtained as described above, are used: $S_c = 0.25$, $k_{exs} = k_{dis} = 5 \text{ s}^{-1}$.

Different settings of each experiment such as the overpressure or injection rate summarized in Table 2 allow to observe and explain processes of multiphase CO_2 evolution in porous media using both experimental and numerical data from specific ports as shown in Figs. 6–8, where an overall comparison of the numerical results against the experimental in selected ports is presented for all column experiments.

Once the numerical model is calibrated to fit (in terms of the Euclidean norm) the point-based experimental readings in all the ports, it can be used to recover more details about the spatial and temporal evolution of CO_2 such as the gas formation, migration, accumulation, and dissolution.

First, in Fig. 9, the vertical gas saturation profiles are compared in the middle of the tank at the end of the injection period of each experiment. The gas saturation profiles of the exsolved CO_2 are almost identical for both slow and fast inflow rates implicating that the injected CO_2 overpressure is the main quantity in consideration that affects the depth, where the exsolved CO_2 is first detected.

In Figs. 6, 7, and 8, the accumulation of gaseous CO_2 induced by the heterogeneity is observed at Port 14 (placed directly below the material interface). In this region, the amount of trapped gas is not governed by the value of the critical gas saturation, instead, the difference in porous media entry pressures (i.e., the capillary barrier) plays the key role [19]. On the

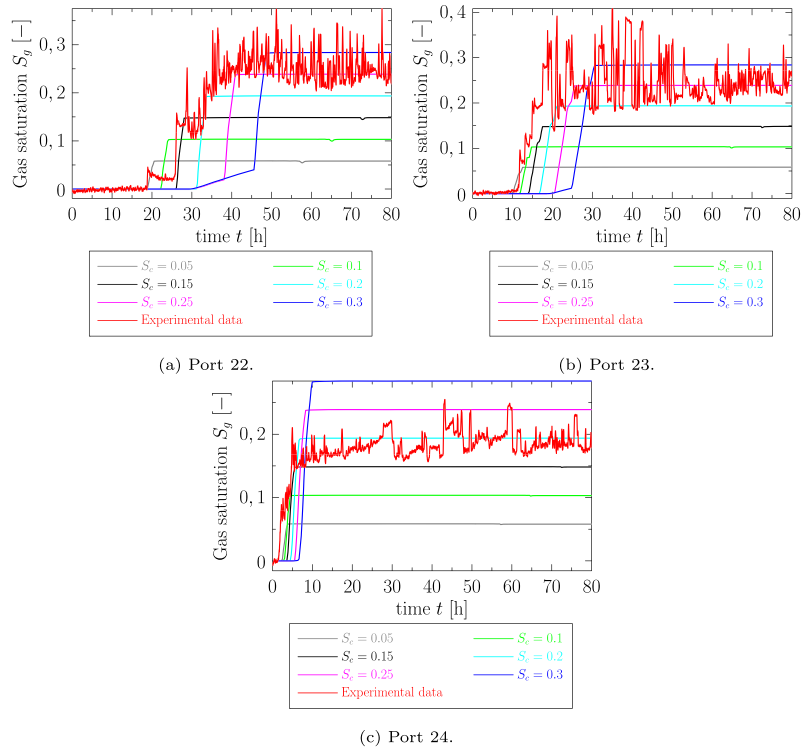


Fig. 3. Experiment HS, gas saturation S_g for various values of critical gas saturation and for large mass transfer rate coefficients $k_{exs} = k_{dis} = 5 \text{ s}^{-1}$.

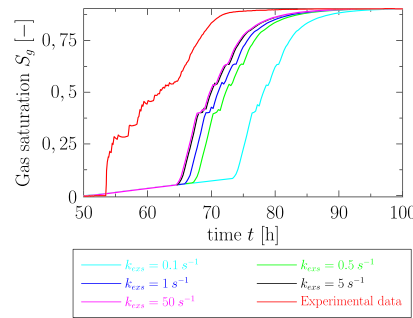


Fig. 4. Experiment HS, gas saturation in Port 14 for various values of mass transfer coefficient for exsolution k_{exs} .

coarse-fine sand interface, the capillary pressure must reach the entry pressure of the fine sand before the gas can penetrate into the fine sand layer [9,13].

At Port 8 located inside the fine layer, the influence of the material interface can be observed in the opposite configuration (coarse sand above the fine one) than before at Port 14. As expected, both numerical results and experimental data in Figs. 6, 7, and 8 indicate that no gas accumulation occurs. Measurements show that the behavior of the system is very similar to the lower ports (Ports 22-24) studied in Stage 1: a plateau gas saturation profile is detected and controlled by the critical gas saturation which seems to have the same value for both coarse and fine sands.

In Fig. 10, the water flow velocities (given by Darcy's law in Eq. (2)) in the middle of the tank are shown. We selected HS and HF experiments to demonstrate the range of velocity observed in the column experiment during both exsolution (CO_2 -saturated water injection) and dissolution (clean water injection) stages for the experiments. The inflow rates of CO_2 -saturated water for the HS and HF experiments are 4 ml min^{-1} and 40 ml min^{-1} respectively (see Table 2). The vertical profiles at the start of the experiment when no gas is presented in the tank are shown in Fig. 10a. The high overpressure

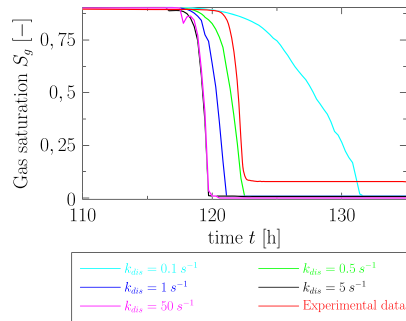


Fig. 5. Experiment HS, gas saturation in Port 14 for various values of mass transfer coefficient for dissolution k_{dis} .

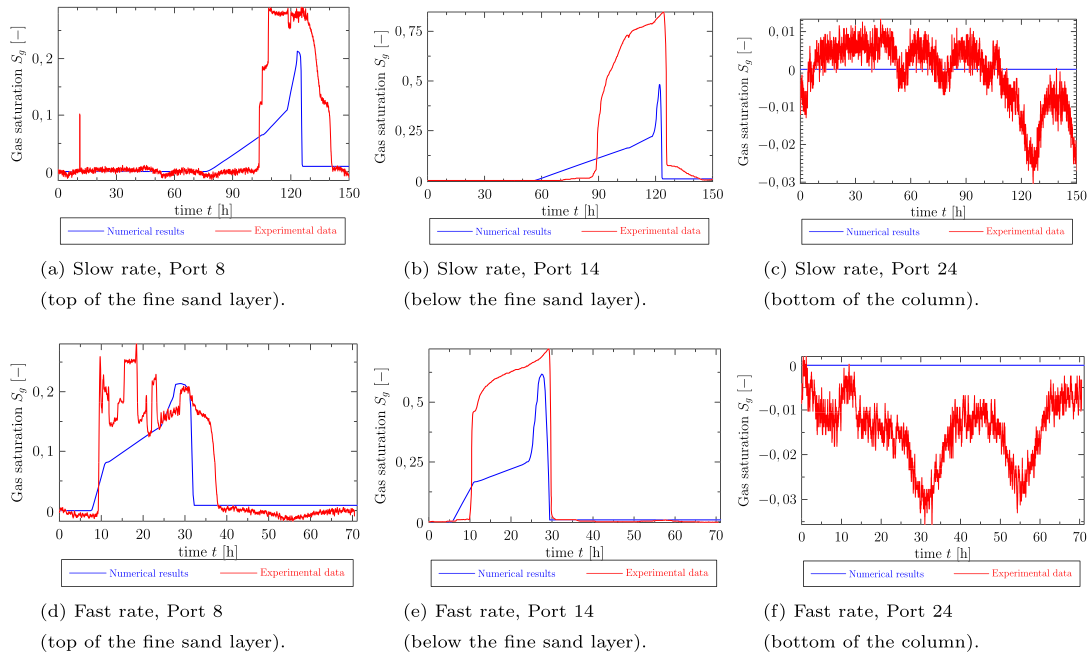


Fig. 6. Low overpressure column experiments LS and LF, gas saturation S_g in selected ports.

experiments are chosen because of the most significant gas accumulation in the tank to demonstrate the impact of the gas phase present in the tank on the velocity as shown in Fig. 10b, where the velocity at the end of the injection period is given. The corresponding gas saturation profiles are shown in Fig. 9. The results show a significant drop in velocity magnitude in the regions of high gas saturation. During the CO₂-saturated water, the injection rate was constant then during the clean water injection, the flow rate varied. The HS and HF experiment allows us to show also the range of the velocity during the dissolution stage, because the flow rates after the CO₂-saturated water injection stopped are 32 ml min⁻¹ and 6 ml min⁻¹ (see Table 3) which gives the lower and upper bound of flow rates for the column experiments during the clean water injection (with the exception of the end of HS experiment, however, there was already almost no gas phase presented during this low flow rate). In Fig. 10c, we show the velocity at the start of the clean water injection. The corresponding gas saturation profiles at this time are identical to those shown in Fig. 9. The x-axis range is chosen with respect to the velocity magnitude in the tank, therefore, the highest velocity magnitude in the vicinity of the injection port is out of the range in Fig. 10, the maximal value of 13.16 m day⁻¹ is reached during the 40 ml min⁻¹ injection rate.

Altogether, the quasi-1D computational study showed that the numerical model is capable to capture the dynamics of the exsolution and dissolution processes observed in the experiments. In the lower region of the column, the critical gas saturation proved to be the best modeling concept that can explain the relatively large values of S_g measured during the injection period of the experiment. The optimal values of k_{exs} and k_{dis} were determined to be the same and equal (or larger)

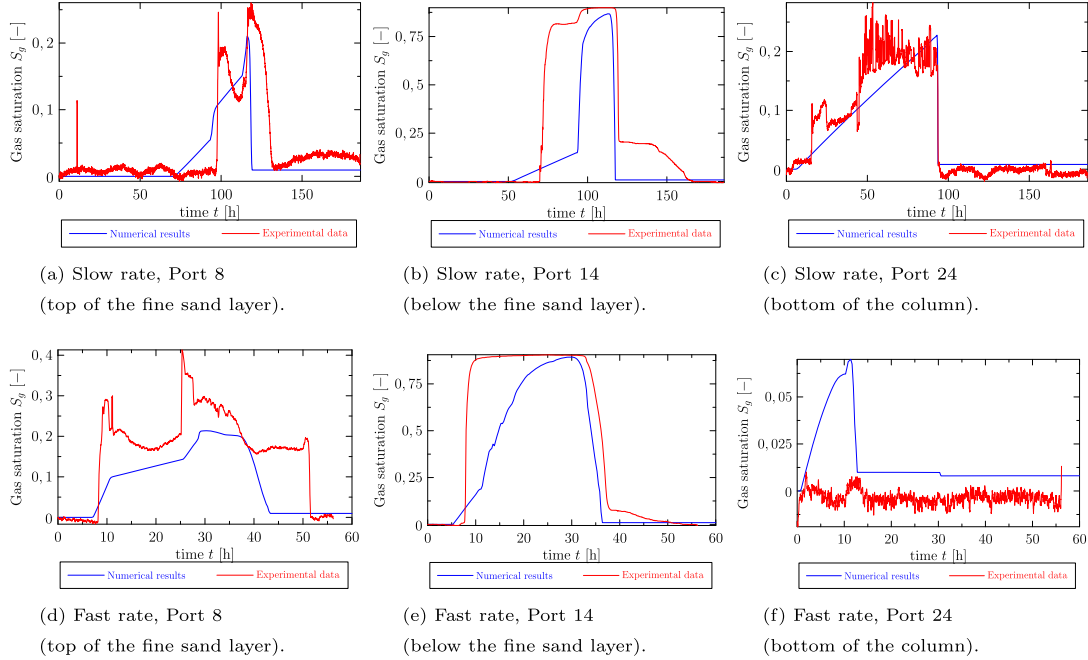


Fig. 7. Medium overpressure column experiments MS and MF, gas saturation S_g in selected ports.

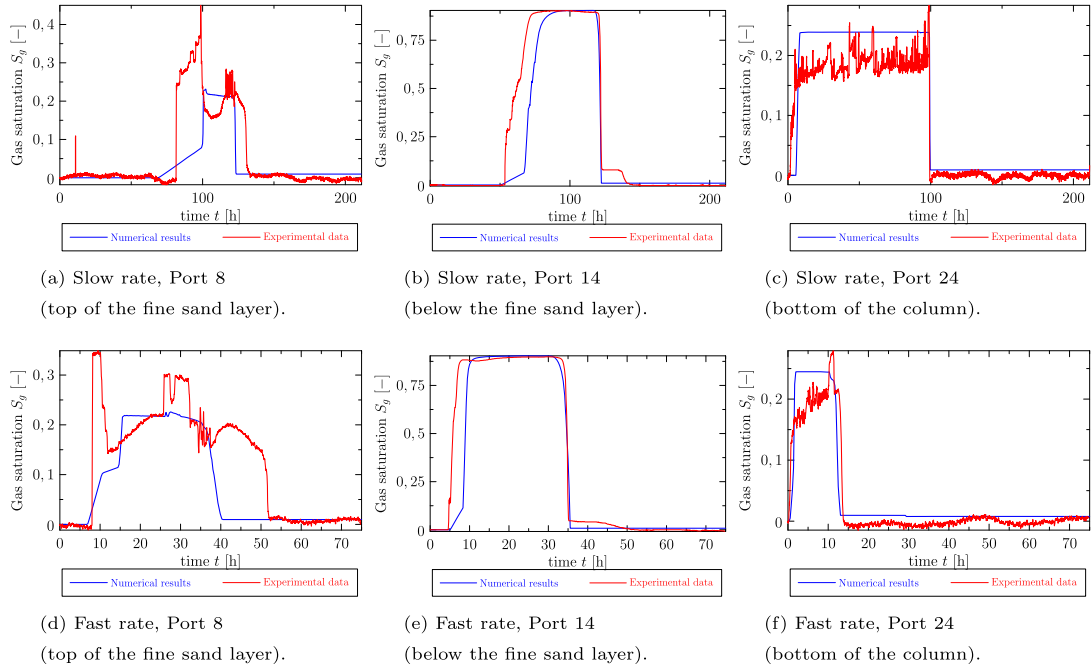


Fig. 8. High overpressure column experiments HS and HF, gas saturation S_g in selected ports.

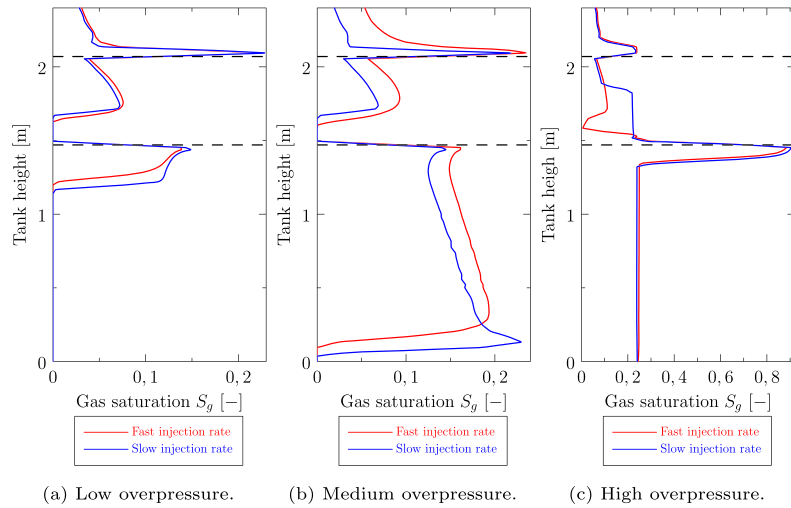


Fig. 9. Gas saturation distribution over the y -axis (tank height) of the tank at the end of the injection period for the column experiments. The material interfaces are depicted using the dashed lines.

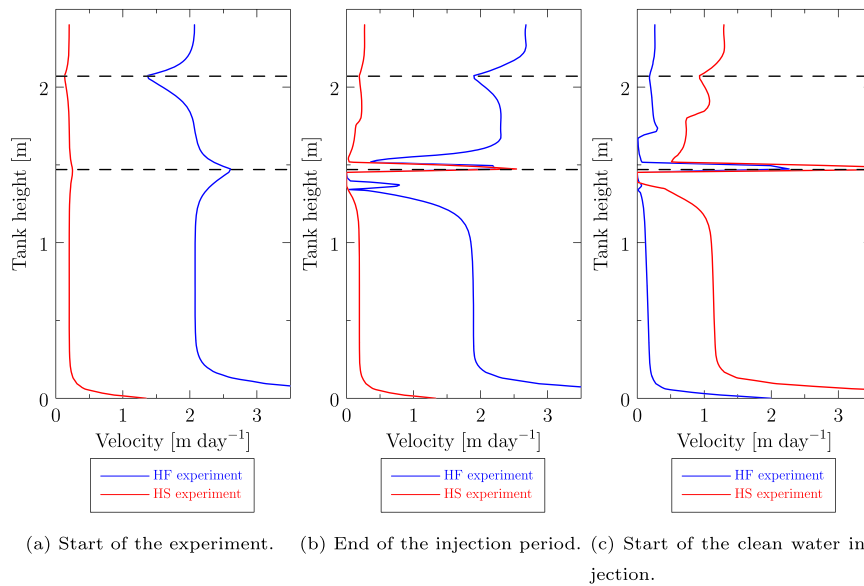


Fig. 10. Water velocity profile over the y -axis (tank height) in the middle of the tank for the HS and HF high overpressure column experiments. The material interfaces are depicted using the dashed lines.

to the threshold rate of 5 s^{-1} , for which further increase of the coefficients has a negligible effect on the numerical results. As a result of this conclusion, any value larger than the threshold can be used to obtain the match with the experimental data. Therefore, the threshold value 5 s^{-1} was chosen, taking into account the computational efficiency and properties of the numerical scheme to avoid enforcing too short of time steps while ensuring stability, thus avoiding unnecessary increase of the computational time. The rapidity of both exsolution and dissolution processes indicate that the kinetic mass transfer model acts as the equilibrium one.

Negative values of the gas saturation were measured during the experiment, however, these values were very small. These negative saturation readings were obtained for all experiments when there is no gas in the vicinity of the port. However, due to various y -axis ranges, they are visible only in the ports, where no gas was detected for the whole duration of

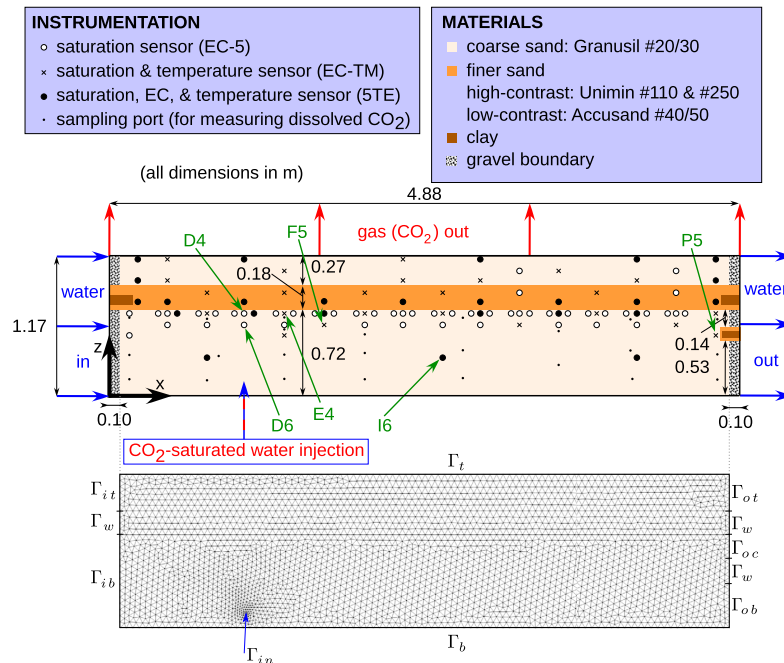


Fig. 11. The large tank experiment configuration adapted from [21] and the triangular mesh of 5638 elements used in numerical simulations. EC stands for the electric conductivity sensor and EC-5, EC-TM, and 5TE denote the specific type of a sensor, for more details, we refer the reader to [21].

the experiment. The negative saturation values are attributed to the post-processing calibration technique with the error of the gas saturation measurements of approximately ± 0.05 . The negative readings reported here are within the measurement error.

4. 2D case

In order to study two dimensional multiphase evolution of CO_2 , two larger laboratory scale tank experiments are considered with a heterogeneous sand packing and a fully developed two dimensional flow field. As in the quasi-1D case, the numerical model is first calibrated using experimental data measured in selected ports and then, the numerical results are used to recover and investigate the spatio-temporal evolution of CO_2 . The main goal of the computational study is to determine whether and how the CO_2 exsolution and dissolution processes differ from the equilibrium ones observed in the quasi-1D column in Section 3. Moreover, the effects of varying temperature are also investigated due to the violation of the isothermal assumption during one of the experiments.

4.1. Experimental setup

Fig. 11 shows the configuration of the large tank experiments including port positions where the gas saturation was measured. The clay and gravel regions shown in Fig. 11 are neglected in the model. In the experiment, the gravel layers are added to uniformly distribute the inflow and outflow boundary conditions. In the model, the boundary conditions are prescribed along the whole corresponding segment of the boundary.

The clay blocks work as impermeable obstacles for the flow and in the model, they are treated as impermeable domains.

At the beginning of each experiment, a lateral flow of DI water through the tank was established by positioning constant head devices on both sides of the tank. Then, the CO_2 saturated water (saturated at 13 kPa overpressure) was injected through the injection port located near the bottom of the tank for a given period of time with the injection rate of 11.2 ml min^{-1} . In the mesh, the injection port is represented by a square with 1 cm long side that are treated as internal mesh boundaries through which the CO_2 -saturated water is injected.

The dissolved CO_2 plume spread in the tank and a portion of CO_2 exsolved, which then migrated through the tank as a gas phase. After the injection was stopped, the experiment continued with the lateral flow of clean DI water only. The dissolved CO_2 plume was transported further to the outflow side of the tank and the gaseous CO_2 dissolved back into the flowing water.

Table 4
Material properties used in the large tank experiment based on [21,18].

Symbol Units	Identification	ϕ [-]	K [m ²]	p_d [Pa]	λ [-]	S_{rel} [-]
	Granusil #20/30	0.41	1.21×10^{-10}	1580	5.79	0.10
	Accusand #40/50	0.42	5.23×10^{-11}	1940	4.09	0.07
	Unimin #110 and #250	0.35	6.39×10^{-14}	8100	5.35	0.17

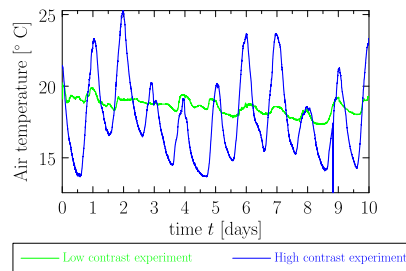


Fig. 12. Air temperature during the high and low contrast experiments.

Two large tank experiments were conducted, which differed in the material of the middle layer and the length of the injection period. In the first large tank experiment (denoted as the high contrast experiment), the layer consisted of a very fine sand Unimin #110 and #250 as shown in Fig. 11. In the second large tank experiment (denoted as the low contrast experiment), the layer consisted of sand Accusand #40/50 that was only slightly finer than the surrounding coarse sand Granusil #20/30. Parameters of these sands are listed in Table 4.

The CO₂-saturated water injection period lasted for 1.88 days in the high contrast experiment and for 2.43 days in the low contrast experiment. In this work, we focus on the first ten days of the experiment. Port positions were the same for both experiments and the lateral water flow rate through the tank was very similar for both runs.

During the low contrast experiment, the temperature was almost constant. The difference between the lowest and highest temperature during the experiment was less than 2 °C as shown in Fig. 12. However, significantly different temperature measurements were obtained for the high contrast experiment. The temperature exhibited fluctuations of more than 10 °C on a daily basis as shown in Fig. 12 which was caused by the problems with the air conditioning in the CESEP experimental facility. Because the large tank experiments were originally not designed to study thermal effects, the tank was not insulated, nor the temperature, heat fluxes, or thermal conductivity of the sands/tanks walls were measured. Hence, due to lack of information concerning initial and boundary conditions, the energy (heat) balance equation is not included in the mathematical model. The thermal effects are at least compensated through C_s which is the only parameter considered as a function of the measured temperature. Such a simplification is justifiable because the tank is narrow (6 cm) compared to its other dimensions (4.88 m in length and 1.17 m in height), so with non-insulated walls, it is safe to assume a uniform temperature distribution within the tank and consider only a temporal violation of the isothermal assumption, not the spatial one.

For more details about the large tank experiments, see [21].

4.2. Computational study setup

The main goal of the computational study in the 2D large tank case is to determine whether the CO₂ exsolution and dissolution occur under equilibrium or kinetic (rate-limited) conditions. As in the quasi-1D case, the first goal of the computational study is to determine the optimal values of k_{exs} , k_{dis} , and S_c compared to the experimental readings from selected ports. Then, the calibrated mathematical model is used to investigate the fundamental differences between the large tank and column experiments and, moreover, the influence of temperature.

Fig. 11 shows the computational domain used in the numerical simulations and the triangular mesh consisting of 5638 elements which is locally refined in the vicinity of the injection port. The mesh resolution is sufficient enough to capture the mass transfer and transport processes of CO₂ and rather coarse at the same time to reduce the computational cost allowing to compute many simulations with variable model parameters. For simplicity, the interior region of the tank without the gravel boundary regions is considered only. Such a simplification is found reasonable since in the experiment, the main role of the gravel is to uniformly distribute the affluent and effluent water along the interior boundaries.

Initially at $t = 0$, the tank contains only pure water: $X = 0$, $p_c = p_d$ (which corresponds to $S_g = 0$, and $p_g = p_c + p_\ell$ where the hydrostatic profile for p_ℓ was prescribed. For both low and high contrast experiments, the final time is $t_{fin} = 10$ days and the time step of 5 s is used.

The boundary conditions are given as follows. No flow boundary condition is prescribed at Γ_w and Γ_b for both phases and for the CO_2 mass fraction. At the injection port Γ_{in} , no flow condition for the gas phase is prescribed for the whole duration of the experiment. During the injection period, the Neumann boundary condition is prescribed for the water inflow velocity u_ℓ and the Dirichlet boundary condition for the CO_2 mass fraction X as described in Section 4.1. For the rest of the experiment, no flow boundary condition is prescribed for water and for the CO_2 mass fraction at Γ_{in} . At Γ_{it} and Γ_{ib} , $X = 0$, $p_c = p_d$, and $p_g = p_c + p_\ell$ where the hydrostatic profile for water pressure p_ℓ corresponding to the constant head device on the left side of the tank are prescribed. At Γ_{ot} , Γ_{oc} , and Γ_{ob} , the Neumann boundary condition for the water velocity u_ℓ is set based on the experimental data, [21], and for the remaining unknowns, $\nabla X = 0$ and the no flow boundary condition for the gas phase are prescribed. This approach allowed for the establishment of lateral flow and accurate reproduction of the water flow field in the tank. At the upper boundary Γ_t , the gas pressure $p_g = p_{ref}$ is kept constant, where $p_{ref} = 82 \text{ kPa}$ is the reference atmospheric pressure in the laboratory, $\nabla X = 0$, and the no flow boundary condition for water are prescribed.

Similar to the column experiment, the experimental procedure described in Section 4.1 can be divided into two stages: 1) exsolution and 2) dissolution. The experiment was designed to (almost) isolate the exsolution and dissolution processes which helps to determine the unknown parameters of the model independently. For this experiment, there is no separate stage to determine the critical gas saturation.

4.3. Critical gas saturation

Unlike in the quasi-1D case, however, the value of the critical saturation S_c cannot be determined directly from the port readings during the exsolution stages. In contrast with the column experiments, there are no gas saturation data ports located close to the injection port. Moreover, the only significant gas phase accumulation was observed directly below the fine sand layer. However, the accumulation in this region is controlled by the capillary barrier of the finer sand and, therefore, gives no information about the critical gas saturation. Likewise, gas saturation readings in the lower homogeneous region of the sand tank are quite low in comparison with the column experiments (approximately of 0.1) which indicates that the role of the critical gas saturation is not as important as in the column experiments. The critical saturation is defined as a threshold at which the gas phase becomes mobile. The gas phase evolution in the ports observed in this experiment is mainly driven by a flow of water with dissolved gas and exsolution rather than by a flow of mobile gas plume. Therefore, the only conclusion that can be drawn about the critical gas saturation from this experiment is that the value is at least 0.1.

4.4. Stage 1: exsolution

During the exsolution stage, the CO_2 dissolved in water is injected into the tank and exsolves in the vicinity of the injection port. The dissolved CO_2 is also transported by the background lateral flow in the downstream direction allowing gas to exsolve further away from the injection port and not only directly above it. As shown in Fig. 13, the gas phase is well detected in Ports D4, D6, E4, F3 (and others).

In this section, we consider the low contrast experiment and the isothermal model is used. First, the model was calibrated with respect to k_{exs} . Many numerical realizations were computed for a series of values of k_{exs} with a selected step of $0.001 \text{ [s}^{-1}\text{]}$. In all the ports, the numerical results of S_g were compared to the experimental data and the difference between them was measured using the Euclidean norm.

For both experiments (with temperature-corrected C_s), the optimal value of $k_{exs} = 0.005 \text{ s}^{-1}$ that minimized the difference was determined. Compared to the column experiments, significantly lower values of the mass transfer coefficients must be used in order to capture the gas evolution properly as illustrated in Fig. 14. For the increasing value of the mass transfer coefficient, the amount of gas detected in the downstream ports (Ports E4 and E5) decreases. For large, near-equilibrium values of k_{exs} comparable to those in the column experiments, CO_2 exsolves rapidly near the injection port and migrates upwards (see Port D4), therefore, less CO_2 remains dissolved in water and little or almost no gas is detected in the downstream ports (Ports E4 and E5) as shown in Fig. 14. This is also demonstrated in Fig. 15, where the comparison between the gas saturation results for the near-equilibrium (with $k_{exs} = 0.1 \text{ s}^{-1}$) and rate limited kinetic (with $k_{exs} = 0.005 \text{ s}^{-1}$) models is shown.

4.5. Thermal effects

In the previous section, we investigated the low contrast experiment and the isothermal model. Without the consideration of thermal effects, however, it is impossible to find a suitable value of k_{exs} to match the high-contrast experimental data. This is illustrated in Figs. 16 and 17, where the gas saturation distributions are compared for constant C_s based on a time-averaged temperature of $19 \text{ }^\circ\text{C}$ and variable temperature-corrected values of C_s . For the constant temperature cases, the gas distribution evolution appears to be the same for both low and high contrast experiments. Since the temperature variations were small during the low contrast experiment, very similar results are also obtained for the variable temperature as shown in Fig. 16. However, the results for the high contrast experiment in Fig. 17 show a substantially different spatial

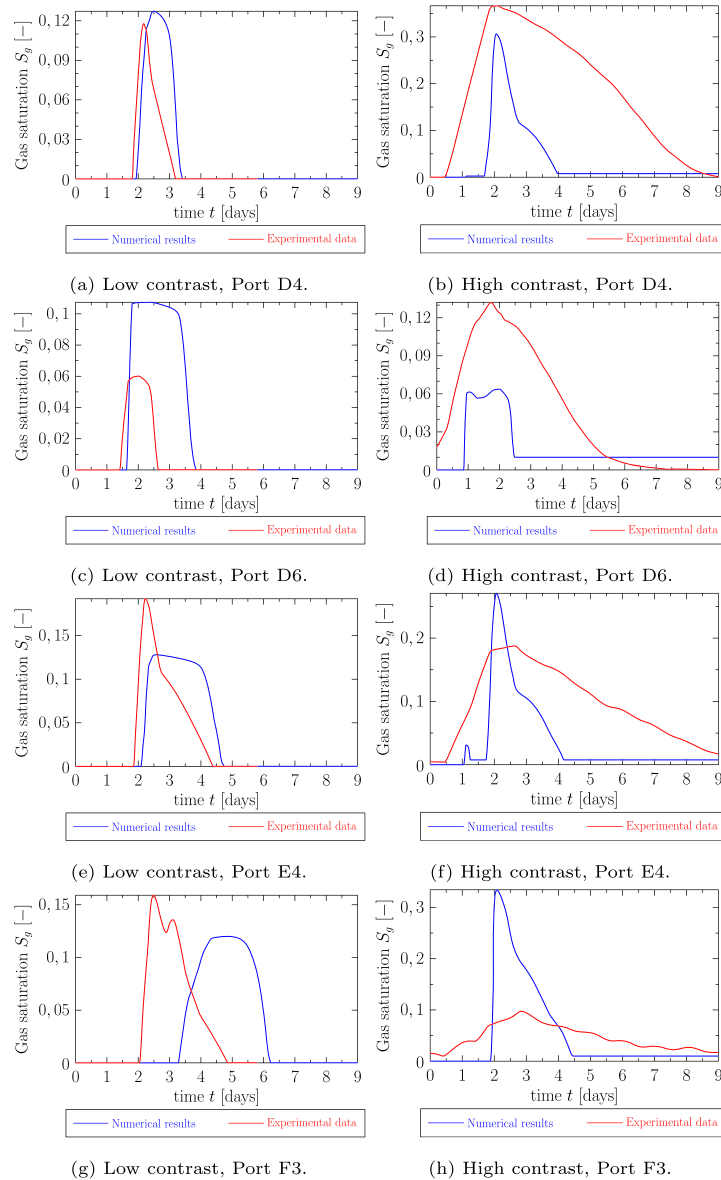


Fig. 13. Large tank experiments, gas saturation S_g , selected ports for the low and high contrast cases.

gas evolution compared to the constant temperature cases that include the barrier effect below the fine layer and larger downstream spreading of the gas phase.

4.6. Stage 2: dissolution

For the dissolution process, an analogous model calibration procedure (with the temperature-corrected C_s) was carried out with the resulting optimal value of $k_{dis} = 0.002 \text{ s}^{-1}$, the same again for both experiments. In Fig. 13, the comparison of the numerical results to the experimental data at selected ports demonstrates that despite of the complexity of the large tank experiments, the numerical model is able to capture the gas saturation evolution sufficiently well.

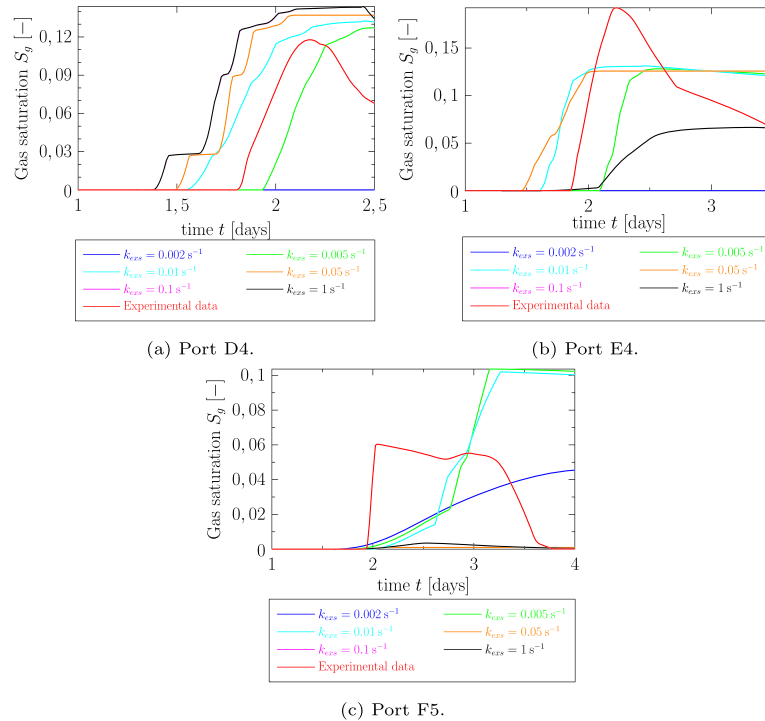


Fig. 14. Gas saturation S_g , various coefficients for exsolution.

4.7. Discussion of results

In Fig. 18, the water flow velocities (given by Darcy's law in Eq. (2)) at the level of the injection port ($y = 0.1$ m) and below the fine sand layer ($y = 0.7$ m) are shown. During the large tank experiments, there are not so significant changes in the flow rate as in the column experiments, therefore, we show the velocity profiles at the start of the experiment and after 48 hours when the gas accumulation is observed below the fine sand layer (although less significant than during the column experiments) for both low and high contrast experiments. There is a difference in the velocity magnitude at the level of the injection port at the later time because at $t = 48$ h in the high contrast experiment, CO_2 -saturated water injection had already ended, while it was still occurring at this time in the low contrast experiment. The corresponding gas saturation distribution is shown in Fig. 15 and Fig. 17 for low contrast and high contrast (non-isothermal model), respectively. The numerical results show that the velocity is similar for both low and high contrast experiments and a decrease in the velocity caused by the accumulated gas can be observed for the high contrast experiment in Fig. 18b. The y-axis range is chosen with respect to the velocity magnitude in the tank, therefore, the maximal value of 2.85 m day^{-1} in the vicinity of the injection port is out of the range in Fig. 18.

The computational study revealed that the equilibrium mass transfer model overpredicts the CO_2 exsolution in the vicinity of the injection port in the large tank experiments, where the two dimensional flow field is present. For specific values of the mass transfer rate coefficients, the kinetic model is able to capture the experimentally observed gas saturation evolution. The optimal values of the mass transfer rate coefficients differ for the exsolution and dissolution processes, indicating that the exsolution is approximately 2.5 times faster than the dissolution. This effect indicates that these processes differ and further emphasizes the necessity of the kinetic mass transfer model that can take this difference into account. In general, the mass transfer rate coefficients k_{exs} and k_{dis} are considered quite low, which means that the mass transfer is rate-limited. However, it is beyond the scope of this paper to rigorously investigate the mass transfer coefficients as a function of flow properties and further research is needed that would extend the understanding of the gas evolution in porous media.

5. Concluding remarks

Potential contamination of shallow freshwater aquifers caused by leakage of CO_2 from deep geologic sequestration sites constitutes a significant risk, the extent and severity of which depend on complex multiphase flow phenomena that control

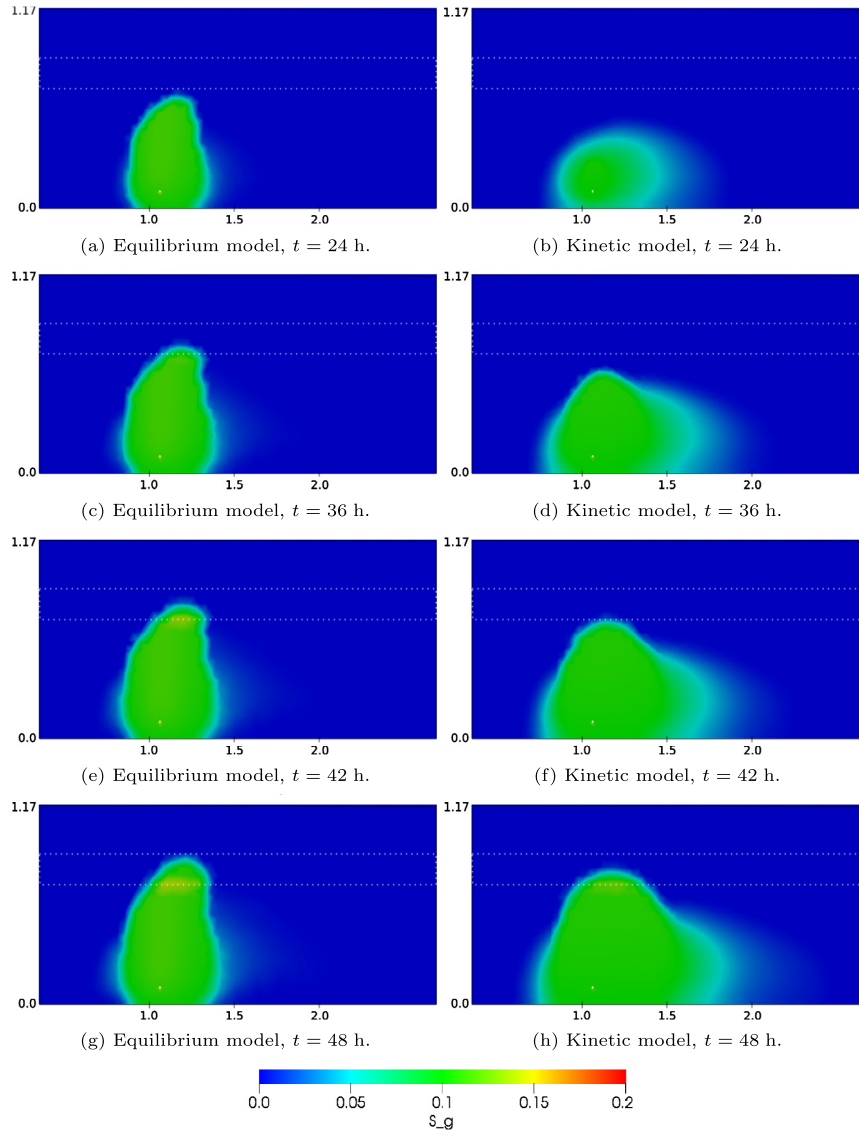


Fig. 15. The gas saturation evolution using the near equilibrium (left) and rate-limited kinetic (right) mass transfer models for the low contrast experiment.

the distribution of CO₂ in the aquifer. One of the least well-understood aspects of the multiphase flow system is the process of CO₂ mass transfer between aqueous and gaseous phases in the presence of flowing groundwater within macroscopic, heterogeneous, porous media systems. Because these processes are exceedingly difficult to observe in the field directly, this study uses experimental data gathered from well-controlled, large-scale laboratory experiments to test the capabilities of an innovative multiphase flow model capable of representing various types of mass transfer processes.

In general, the results indicate that multiphase CO₂ evolution attenuates transport within shallow aquifers, due to dynamic, non-instantaneous exsolution and dissolution processes, and the mathematical model proposed in this work was able to adequately capture the most important processes observed in the experiments. The kinetic mass transfer model was able to reproduce the near-equilibrium mass transfer observed in the quasi-1D column experiments as well as the much slower exsolution and dissolution observed in the 2D large tank experiments. The numerical and experimental results presented here also indicate that in the more complex 2D case, dissolution and exsolution rates differ, and the kinetic model was able

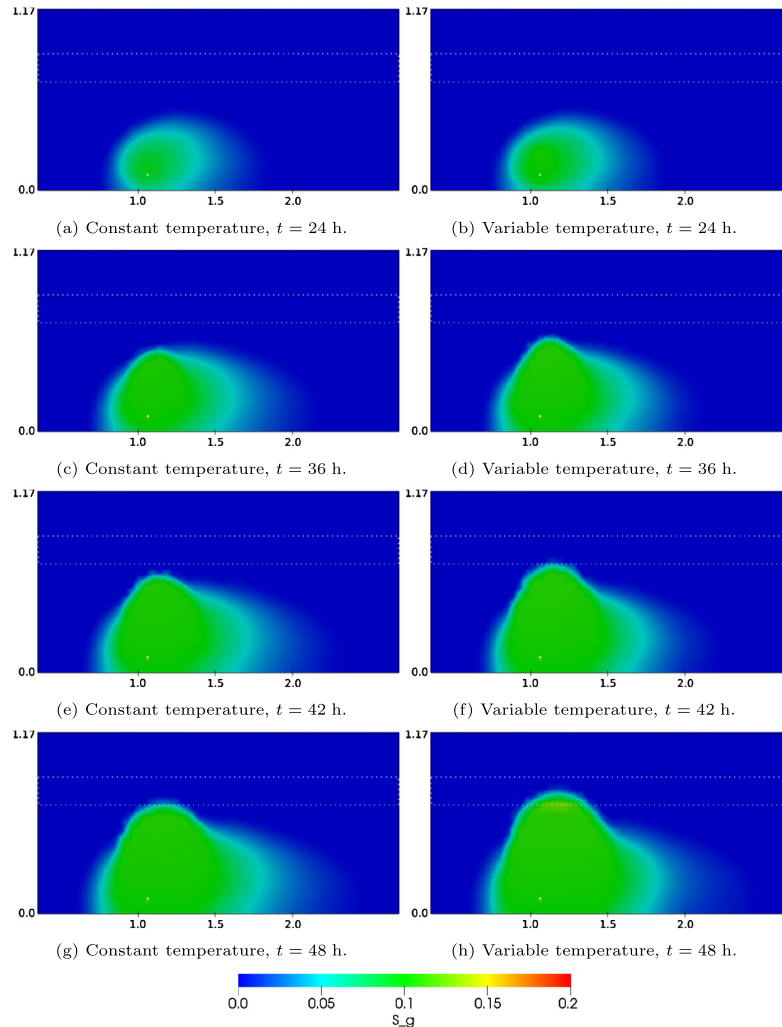


Fig. 16. Gas saturation S_g , comparison of isothermal (left) and non-isothermal (right) models for low contrast experiments.

to quantify this difference. The model was also able to explain significant effects that temperature had on multiphase CO_2 evolution in multi-dimensional porous media systems.

In both experiments, the model captured the effect of heterogeneity on the gas accumulation and confirmed that heterogeneity, even in the simple form presented in the experiment, plays a significant role in the multiphase CO_2 evolution. The nuanced effects of this system component need to be carefully addressed in the future by analyzing more complex heterogeneous scenarios. In both cases studied herein, we decided to use the uniform sampling approach of the mass transfer coefficients values and, therefore, used rather coarse meshes. Such a sensitivity study allowed us to investigate the impact of various mass transfer coefficients on the numerical results.

The difference between the quasi-1D and 2D cases (where the equilibrium and rate-limited approaches, respectively, were found applicable) can possibly be explained by different flow rates of water through the gas-occupied region of the system. However, the velocity profiles shown in Figs. 10 and 18 indicate that the velocity magnitude would not be solely responsible for the fundamentally different results for the quasi-1D and 2D case. The flow velocity magnitude in the 2D case is comparable to the velocity magnitude during the CO_2 -saturated water injection for the slow column experiments. Moreover, during the clean water injection for all column experiments, the flow rate varied and a rather low inflow rate of 6 ml min^{-1} was employed at least once.

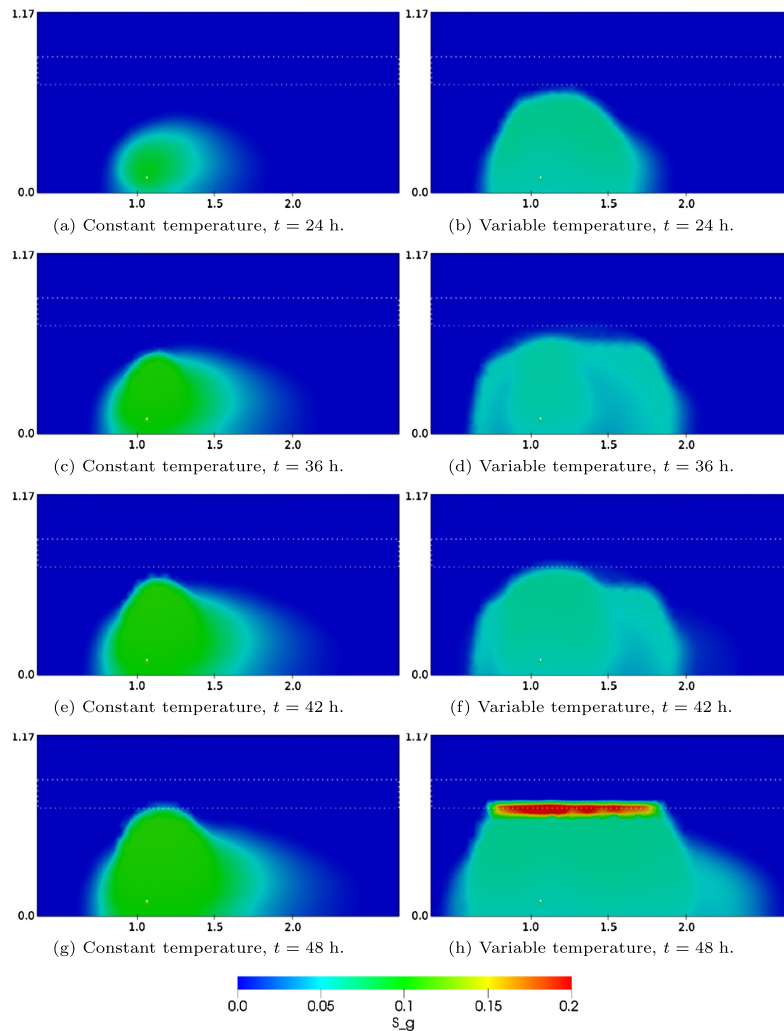


Fig. 17. Gas saturation S_g , comparison of isothermal (left) and non-isothermal (right) models for high contrast experiments.

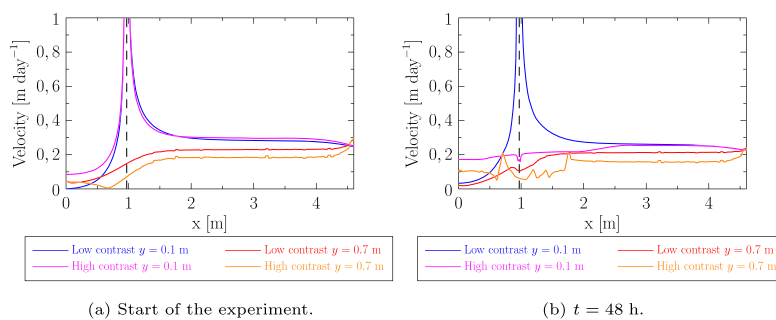


Fig. 18. Water velocity profile over the x -axis at the level of the injection port ($y = 0.1$ m) and below the fine sand layer ($y = 0.7$ m) for large tank experiments. The position of the injection port is depicted using the dashed line.

In the quasi-1D case, water is forced through the gas accumulation, and the dynamic inter-phase contact is therefore likely fast enough that equilibrium mass transfer is applicable. In the 2D case, however, the water flow paths can more easily avoid the gas phase, meaning slower contact with the gas phase, and thus slower dissolution. Further investigation is needed to rigorously test these ideas. The results presented here also demonstrated that multiphase CO₂ evolution is sensitive to temperature changes. We thoroughly investigated the mass transfer process, however, many processes that could affect the mass transport but were not the driving mechanisms for the processes studied here were neglected or simplified in this work. These include the dependence of all quantities on temperature and mechanical dispersion.

In this paper, we discussed the fundamental difference of mass transfer and transport processes between the quasi-1D and 2D cases. Hence, a question arises about the nature of these processes in 3D and their relation to the 2D case. Such a question is beyond the scope of the present study, however, based on the results presented here, such a study seems to be a necessary next step in understanding complex 3D field-scale processes.

Declaration of competing interest

The authors declare that they have no known competing financial interests or personal relationships that could have appeared to influence the work reported in this paper.

Acknowledgements

The work reported in this paper was supported by the Czech Science Foundation under the grant number 17-06759S “Investigation of shallow subsurface flow with phase transitions” and by the Ministry of Education, Youth, and Sports of the Czech Republic under the OP RDE grant number: CZ.02.1.01/0.0/0.0/16-019/0000778 “Centre for Advanced Applied Sciences”. The authors would like to thank the U.S. Department of Energy’s Office of Fossil Energy for providing funding for this research through the National Energy Technology Laboratory’s CO₂ sequestration R&D Program. The support of Dr. Rajesh Pawar of LANL is gratefully acknowledged. National Science Foundation also deserves credit for providing funding for this research through award 1045282. Any use of trade, firm, or product names is for descriptive purposes only and does not imply endorsement by the U.S. Government.

References

- [1] E. Agartan, A. Cihan, T.H. Illangasekare, Q. Zhou, J.T. Birkholzer, Mixing and trapping of dissolved CO₂ in deep geologic formations with shale layers, *Adv. Water Resour.* 105 (2017) 67–81.
- [2] E. Agartan, M. Gaddipati, Y. Yip, B. Savage, C. Ozgen, CO₂ storage in depleted oil and gas fields in the Gulf of Mexico, *Int. J. Greenh. Gas Control* 72 (2018) 38–48.
- [3] E. Agartan, L. Trevisan, A. Cihan, J. Birkholzer, Q. Zhou, T.H. Illangasekare, Experimental study on effects of geologic heterogeneity in enhancing dissolution trapping of supercritical CO₂, *Water Resour. Res.* 51 (3) (2015) 1635–1648.
- [4] P. Bastian, Numerical Computation of Multiphase Flows in Porous Media, Habilitation thesis, Kiel University, 2000.
- [5] J. Bear, A. Verruijt, *Modeling Groundwater Flow and Pollution: with Computer Programs for Sample Cases*, Springer, 1987.
- [6] R. Brooks, A. Corey, Hydraulic Properties of Porous Media, Colorado State University, Hydrology Paper, vol. 3, 1964, p. 27.
- [7] N. Burdine, Relative permeability calculations from pore size distribution data, *J. Pet. Technol.* 5 (1953) 71–78.
- [8] C. Chang, Q. Zhou, J. Guo, Q. Yu, Supercritical CO₂ dissolution and mass transfer in low-permeability sandstone: effect of concentration difference in water-flood experiments, *Int. J. Greenh. Gas Control* 28 (2014) 328–342.
- [9] A. Ern, I. Mozolevski, L. Schuh, Discontinuous galerkin approximation of two-phase flows in heterogeneous porous media with discontinuous capillary pressures, *Comput. Methods Appl. Mech. Eng.* 199 (23) (2010) 1491–1501.
- [10] R. Fučík, J. Mikyška, J. Solovský, J. Klinkovský, T. Oberhuber, Multidimensional mixed-hybrid finite element method for compositional two-phase flow in heterogeneous porous media and its massively parallel implementation on GPU, *Comput. Phys. Commun.* (2018).
- [11] R. Helmig, *Multiphase Flow and Transport Processes in the Subsurface, a Contribution to the Modelling of Hydrosystems*, Springer, 1997.
- [12] M. Hesse, A. Woods, Buoyant dispersal of CO₂ during geological storage, *Geophys. Res. Lett.* 37 (1) (2010).
- [13] H. Hoteit, A. Firoozabadi, Numerical modeling of two-phase flow in heterogeneous permeable media with different capillarity pressures, *Adv. Water Resour.* 31 (1) (2008) 56–73.
- [14] T.H. Illangasekare, C.C. Fripriat, R. Fučík, L. Thibodeaux, D. Mackay, *Dispersion and Mass Transfer Coefficients in Groundwater of Near-Surface Geologic Formations*, CRC Press, Boca Raton, FL, USA, 2010.
- [15] R.J. Millington, J.P. Quirk, Permeability of porous solids, *Trans. Faraday Soc.* 57 (1961) 1200–1207.
- [16] K. Mosthaf, K. Baber, B. Flemisch, R. Helmig, A. Leijnse, I. Rybak, B. Wohlmuth, A coupling concept for two-phase compositional porous-medium and single-phase compositional free flow, *Water Resour. Res.* 47 (10) (2011).
- [17] J. Niessner, S.M. Hassanzadeh, Modeling kinetic interphase mass transfer for two-phase flow in porous media including fluid-fluid interfacial area, *Transp. Porous Media* 80 (2009) 329–344.
- [18] M. Plampin, T. Illangasekare, T. Sakaki, R. Pawar, Experimental study of gas evolution in heterogeneous shallow subsurface formations during leakage of stored CO₂, *Int. J. Greenh. Gas Control* 22 (2014) 47–62.
- [19] M.R. Plampin, R.N. Lassen, T. Sakaki, M.L. Porter, R.J. Pawar, K.H. Jensen, T.H. Illangasekare, Heterogeneity-enhanced gas phase formation in shallow aquifers during leakage of CO₂-saturated water from geologic sequestration sites, *Water Resour. Res.* 50 (12) (2014) 9251–9266.
- [20] M.R. Plampin, M.L. Porter, R.J. Pawar, T.H. Illangasekare, Multi-scale experimentation and numerical modeling for process understanding of CO₂ attenuation in the shallow subsurface, *Energy Proc.* 63 (2014) 4824–4833.
- [21] M.R. Plampin, M.L. Porter, R.J. Pawar, T.H. Illangasekare, Intermediate-scale experimental study to improve fundamental understanding of attenuation capacity for leaking CO₂ in heterogeneous shallow aquifers, *Water Resour. Res.* 53 (12) (2017) 10121–10138.
- [22] M.L. Porter, M. Plampin, R. Pawar, T. Illangasekare, CO₂ leakage in shallow aquifers: a benchmark modeling study of CO₂ gas evolution in heterogeneous porous media, *Int. J. Greenh. Gas Control* 39 (2015) 51–61.

■ P.5 Článek v *International Journal of Heat and Mass Transfer*

Tomáš Smejkal, Jiří Mikyška a Radek Fučík: Numerical modelling of adsorption and desorption of water vapor in zeolite 13X using a two-temperature model and mixed-hybrid finite element method numerical solver. *International Journal of Heat and Mass Transfer*, 148:119050, 2020.



Contents lists available at ScienceDirect

International Journal of Heat and Mass Transfer

journal homepage: www.elsevier.com/locate/hmt

Numerical modelling of adsorption and desorption of water vapor in zeolite 13X using a two-temperature model and mixed-hybrid finite element method numerical solver



Tomáš Smejkal, Jiří Mikyška*, Radek Fučík

Faculty of Nuclear Sciences and Physical Engineering, Department of Mathematics, Czech Technical University in Prague, Trojanova 13, 120 00 Prague 2, Czech Republic

ARTICLE INFO

Article history:

Received 24 August 2019

Revised 8 November 2019

Accepted 12 November 2019

Available online 21 November 2019

Keywords:

Zeolite 13X

Adsorption

Desorption

LDF Model

Thermo-chemical energy storage

MHFEM

Langmuir-Freundlich isotherms

Operator splitting

ABSTRACT

In this paper, we present a new two-temperature mathematical model for a thermo-chemical energy storage based on the adsorption and desorption of the water vapor in zeolite 13X. The adsorption process is modelled using the Linear Driving Force (LDF) model and the Langmuir-Freundlich isotherms. A numerical solver based on the mixed-hybrid finite element method and operator splitting technique is proposed. Furthermore, we present a computational study of the charging and discharging processes of the thermo-chemical energy storage emphasising the behaviour of the two temperatures: fluid temperature and zeolite temperature.

© 2019 Elsevier Ltd. All rights reserved.

1. Introduction

The transition from fossil fuels to cleaner and renewable energy sources is currently one of the highest world priorities. According to the International Energy Association (IEA), buildings consume 35% of the world energy and cause approximately 33% of global CO₂ emissions [1]. Solar energy is one of the most suitable choices for replacing fossil fuels. However, to use solar energy to its maximum potential, proper heat energy storage has to be designed.

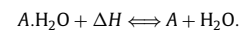
In recent years, various approaches for the heat energy storage have been proposed and studied. These approaches can be divided into three categories based on how the heat is stored: latent, sensible, or thermo-chemical. The first one uses Phase Change Materials (PCMs), where the latent heat is released when the phase change occurs. Review of these materials and their usage in the heating of buildings are presented, e.g., in [2–4]. In the sensible TES (Thermal Energy Storage) system, the energy is stored or released by increasing or decreasing the temperature of the storage medium. A one or two-tank molten salt are examples of such materials [5,6]. The state of the art of this approach can be found in, e.g., [7]. The last category is the thermo-chemical energy storage,

where the heat ΔH is released due to a chemical reaction



for some materials A and B , where the symbol. represents a chemical bond. The modelling and the numerical simulation of these energy storages are our main subjects of focus. There exist many concepts and materials which can be used for energy storage. Hydrogen systems with metallic hydrides for storing hydrogen were one of the first concepts in the 90s for the hydrogen engines. Later, a concept for thermal energy storage was proposed in [8]. Other possibilities include carbonate systems with CO₂ [9] or calcination with CaO [10]. A review on high-temperature thermo-chemical heat energy storage can be found in [11].

In this work, we are interested in the modelling of the thermo-chemical heat energy storage using the zeolite, which is a crystalline aluminosilicate with a specific structure and a large internal surface area. A specific zeolite (e.g., 13X) can adsorb water and release heat. Such process can be described as



The properties of the zeolite 13X have been studied experimentally and also theoretically [12–14]. Furthermore, a variety of numerical models has been proposed. In [15,16], a numerical model with only one temperature has been presented. The model includes a heat

* Corresponding author.

E-mail address: jiri.mikyska@jfifi.cvut.cz (J. Mikyška).

loss due to the reactor wall. The numerical model is solved using COMSOL Multiphysics software [17], but no additional information about the numerical solver is given. Another one-temperature model has been presented in [13] where the momentum conservation is calculated with the extended Brinkman equation [18,19] and again, no information about the numerical solution is provided. In [20], a two-dimensional and a two-temperature model is presented and solved using the Gear's method [21] in Matlab software package [22]. In [23], a particle simulation in a rotating drum was performed to survey particle mixing. The adsorption was implemented in a CFD discrete particle solver for thermodynamic studies. Simulations were performed using the Navier-Stokes Solver ANSYS FLUENT [24]. In [25], a two-temperature model is developed, and a finite volume approach for the discretization is used. The resulting differential equations are solved again using the Gear's method.

In this work, we use a different approach from those published previously. In our model, we employ a two-temperature approach. One temperature (T_f) is assigned to the fluid, the other one (T_s) to the zeolite (solid matrix). Therefore, we do not assume a local thermal equilibrium and study the behaviour of individual temperatures before, during, and after adsorption or desorption process. In Section 4, we will show that with an appropriate parameter adaptation, the temperature difference can be significant. Therefore, the assumption of the local thermal equilibrium is not possible, and the two-temperature model is necessary for precise simulation. One another feature arises from this two-temperature approach. In this approach, numerical constants such as the heat capacities are easily computable for both systems, and no averaging between them or other procedure has to be performed. Another difference from most published papers is our numerical solver, which is based on the mixed-hybrid finite element method (MHFEM) with a semi-implicit approach for the time discretization [26]. MHFEM is superior to the methods described above in that it approximates scalar variables and their gradients with the same order of accuracy. In the previous approaches, which are based on finite difference, finite volume or classical finite element methods, the gradients of scalar variables are evaluated by performing numerical differentiation, which leads to the loss of accuracy. As these gradients are needed to evaluate transport velocities, the accurate approximation of these gradients is important for the accuracy of the whole transport simulation. Another unique feature of our approach is the use of the operator splitting approach. This approach enables to decouple computation of the transport from the computation of the adsorption. It is therefore possible to use different time steps for the computation of transport of heat and mass between the cells and for the processes occurring within a cell (adsorption). As the speeds of both processes can be very different, the splitting technique make it possible to use smaller time steps for adsorption without the need for unnecessarily small time steps for the transport simulation. This results in much more efficient computation compared to the case when all these processes are treated using the same time stepping scheme.

The structure of this paper is as follows. In Section 2, the mathematical model is presented. In Section 3, a description of the numerical solution is provided. In Section 4, computational studies for the charging and discharging processes of the thermo-chemical energy storage are presented. In Section 5, the results are discussed and some conclusions are drawn.

2. Physical and mathematical model

In this paper, the studied system is a fixed packed bed filled with zeolite 13X beads. Dry (humid) air is supplied to the bed, and the desorption (adsorption) process of the water vapor in the zeolite takes place. During the desorption (adsorption) process, the ze-

olite beads do not change position in the bed and create a porous medium with a fixed solid matrix.

Our mathematical model consists of four balance equations representing the balance of mass, the water mass fraction, the energy of the fluid, and the energy of the solid matrix:

$$\phi \frac{\partial \rho_f}{\partial t} + \nabla \cdot (\rho_f \mathbf{v}) = 0, \quad (1)$$

$$\phi \rho_f \frac{\partial w_w}{\partial t} + \rho_f \mathbf{v} \cdot \nabla w_w + \nabla \cdot (-\rho_f D_{pm} \nabla w_w) = -(1 - \phi) \rho_s \frac{\partial q}{\partial t} M_w, \quad (2)$$

$$\phi \rho_f c_v \frac{\partial T_f}{\partial t} + \nabla \cdot (\rho_f c_v T_f \mathbf{v} - k_f \nabla T_f) - T_f \nabla \cdot (\rho_f c_v \mathbf{v}) - \phi \frac{\partial P}{\partial t} - \beta (T_s - T_f) = 0, \quad (3)$$

$$(1 - \phi) \rho_s c_s \frac{\partial T_s}{\partial t} - \nabla \cdot (k_s \nabla T_s) - \beta (T_f - T_s) = (1 - \phi) \rho_s \frac{\partial q}{\partial t} \Delta H, \quad (4)$$

respectively, where ϕ [-] is the porosity, ρ_f [kg m⁻³] is the fluid mass density, \mathbf{v} [m s⁻¹] is the velocity of the fluid, w_w [-] is the water mass fraction, D_{pm} [m² s⁻¹] is the diffusive coefficient, ρ_s [kg m⁻³] is the density of the zeolite particle, q [mol kg⁻¹] is the adsorbed water vapor in the zeolite, M_w [kg mol⁻¹] is the molar mass of water, c_v [J kg⁻¹ K⁻¹] is the specific heat of fluid at constant volume, T_f [K] is the temperature of the fluid, k_f [W m⁻¹ K⁻¹] is the thermal conductivity of the fluid, P [Pa] is the pressure, β [W K⁻¹] is the heat transfer coefficient between the fluid and the solid matrix (zeolite), T_s [K] is the temperature of the solid matrix, c_s [J kg⁻¹ K⁻¹] is the specific heat of solid matrix, k_s [W m⁻¹ K⁻¹] is the thermal conductivity of the solid matrix, and ΔH [J mol⁻¹] is the isosteric heat of the adsorption.

The velocity \mathbf{v} of the fluid is given by the Darcy's law

$$\mathbf{v} = -\frac{K}{\mu} (\nabla P - \rho_f \mathbf{g}), \quad (5)$$

where K [m²] is the intrinsic permeability, μ [Pa s] is the dynamic viscosity, and \mathbf{g} [m s⁻²] is the gravity vector. In our model, the gravity is neglected, i.e., $\mathbf{g} = \mathbf{0}$. The diffusive coefficient D_{pm} is calculated using [27]

$$D_{pm} = \phi \tau D_m, \quad (6)$$

where τ is the tortuosity and D_m is the molecular diffusion. The tortuosity is calculated using Millington-Quirk model [28]

$$\tau = \phi^{\frac{1}{2}}. \quad (7)$$

The system of the balance laws is supplemented by the equation of state of the ideal gas [29]

$$P(T, \rho_f, w_w) = \left(\frac{(1 - w_w) \rho_f}{M_a} + \frac{w_w \rho_f}{M_w} \right) RT, \quad (8)$$

where M_a is the molar mass of air and R is the universal gas constant. The heat transfer coefficient β is modelled [24] using

$$\beta = 6 \frac{k_f (1 - \phi) \phi Nu}{d_s^2}, \quad (9)$$

where d_s is the diameter of the zeolite particle and the Nusselt number Nu expresses an increase in the heat flux by convection compared to the case when there is only conduction and no convection. The Nusselt number is calculated using correlation by Gunn [30]

$$Nu = (7 - 10\phi + 5\phi^2) \left(1 + 0.7 Re^{0.2} Pr^{\frac{1}{3}} \right) + (1.33 - 2.4\phi + 1.2\phi^2) Re^{0.7} Pr^{\frac{1}{3}}, \quad (10)$$

where the Reynolds number Re and the Prandtl number Pr are calculated using

$$Pr = \frac{c_p \mu}{k_f}, \quad (11)$$

$$Re = \frac{\rho_f d_s}{\mu} |\mathbf{v}|. \quad (12)$$

The specific heats c_v and c_p are calculated using

$$c_v(W_w) = w_w c_{v,w} + (1 - w_w) c_{v,a}, \quad (13)$$

$$c_p(W_w) = w_w c_{p,w} + (1 - w_w) c_{p,a}, \quad (14)$$

where c_{ij} for $i \in \{v, p\}$ and $j \in \{w, a\}$ are the specific heats at constant pressure (subscript p) or volume (subscript v) of the water vapor and air, respectively.

The adsorbed water vapor $q = q(t, \mathbf{x})$ in the zeolite is modelled using the kinetic model. We choose the Linear Driving Force (LDF) model which is frequently used for the adsorption and desorption of the water vapor in the zeolite (e.g., [15,16,25]). This model can be formulated as

$$\frac{\partial q}{\partial t} = k_{LDF}^* (q^* - q), \quad (15)$$

where $k_{LDF}^* > 0$ is the rate of the adsorption and q^* is the equilibrium state. The rate of the adsorption is calculated using the relation [31]

$$k_{LDF}^* = \frac{k^*}{\rho_s RT_s \frac{\partial q}{\partial p_w}}, \quad (16)$$

where k^* is an empirical numerical constant. The equilibrium state q^* is model using the Langmuir-Freundlich isotherms

$$q^* = \frac{q_{max} (bP_w)^{1/n}}{1 + (bP_w)^{1/n}}, \quad (17)$$

where q_{max} is the maximum amount of the adsorbed water vapor in the zeolite and P_w is the partial pressure of the water vapor. In the previous equation, b and n are parameters of the kinetic model, which can be calculated using [32]

$$b = b_0 \exp\left(\frac{\Delta E}{RT_0} \left(\frac{T_0}{T} - 1\right)\right), \quad (18)$$

$$\frac{1}{n} = \frac{1}{n_0} + \alpha \left(1 - \frac{T_0}{T}\right), \quad (19)$$

where n_0 , ΔE , α , and q_{max} are empirical constants. The temperature T_0 is set to $T_0 = 293.15$ K. The isosteric heat of the adsorption ΔH is obtained using [32]

$$\Delta H = \Delta E - \alpha RT_0 n^2 \ln\left(\frac{q}{q_{max} - q}\right). \quad (20)$$

In summary, our mathematical model consists of five equations: four balance Eqs. (1)–(4) and one kinetic Eq. (15). To complete the mathematical model, the equations have to be equipped with initial conditions and an appropriate set of boundary conditions. The initial conditions read as

$$P(0, \mathbf{x}) = P^{(ini)}, \quad \forall \mathbf{x} \in \Omega, \quad (21)$$

$$w_w(0, \mathbf{x}) = w_w^{(ini)}, \quad \forall \mathbf{x} \in \Omega, \quad (22)$$

$$T_f(0, \mathbf{x}) = T_f^{(ini)}, \quad \forall \mathbf{x} \in \Omega, \quad (23)$$

$$T_s(0, \mathbf{x}) = T_s^{(ini)}, \quad \forall \mathbf{x} \in \Omega, \quad (24)$$

$$q(0, \mathbf{x}) = q^{(ini)}, \quad \forall \mathbf{x} \in \Omega. \quad (25)$$

In order to describe the boundary conditions, we define $\partial\Omega$ as the boundary of Ω and for each variable $\varphi \in \{P, w_w, T_f, T_s\}$ denote Γ_φ and $\Gamma_{\mathbf{q}_\varphi}$ the Dirichlet and the Neumann part of the boundary, respectively. These parts of the boundary have to satisfy

$$\Gamma_\varphi \cup \Gamma_{\mathbf{q}_\varphi} = \partial\Omega, \quad (26)$$

$$\Gamma_\varphi \cap \Gamma_{\mathbf{q}_\varphi} = \emptyset, \quad (27)$$

for $\varphi \in \{P, w_w, T_f, T_s\}$. Then, an appropriate set of boundary conditions for all $t \in (0, t_{final})$ reads as

$$P(t, \mathbf{x}) = P^{(D)}, \quad \forall \mathbf{x} \in \Gamma_P, \quad \mathbf{q}_P(t, \mathbf{x}) \cdot \mathbf{n} = q_P^{(N)}, \quad \forall \mathbf{x} \in \Gamma_{\mathbf{q}_P}, \quad (28)$$

$$w_w(t, \mathbf{x}) = w_w^{(D)}, \quad \forall \mathbf{x} \in \Gamma_{w_w}, \quad \mathbf{q}_{w_w}(t, \mathbf{x}) \cdot \mathbf{n} = q_{w_w}^{(N)}, \quad \forall \mathbf{x} \in \Gamma_{\mathbf{q}_{w_w}}, \quad (29)$$

$$T_f(t, \mathbf{x}) = T_f^{(D)}, \quad \forall \mathbf{x} \in \Gamma_{T_f}, \quad \mathbf{q}_{T_f}(t, \mathbf{x}) \cdot \mathbf{n} = q_{T_f}^{(N)}, \quad \forall \mathbf{x} \in \Gamma_{\mathbf{q}_{T_f}}, \quad (30)$$

$$T_s(t, \mathbf{x}) = T_s^{(D)}, \quad \forall \mathbf{x} \in \Gamma_{T_s}, \quad \mathbf{q}_{T_s}(t, \mathbf{x}) \cdot \mathbf{n} = q_{T_s}^{(N)}, \quad \forall \mathbf{x} \in \Gamma_{\mathbf{q}_{T_s}}, \quad (31)$$

where \mathbf{n} is the outward normal vector to the $\partial\Omega$ and \mathbf{q}_φ for $\varphi \in \{P, w_w, T_f, T_s\}$ is the conservative flux.

3. Numerical solution

In this section, we describe the numerical algorithm for solving the mathematical model. By Δt , we denote the time step and define the time level t_n by

$$t_n = n\Delta t, \quad n \in \mathbb{N}_0. \quad (32)$$

The system of Eqs. (1)–(4), (15) from the time level t_n to the new time level t_{n+1} is solved in two steps using the operator splitting technique [33]. First, the system (1)–(4) is solved with time step Δt and zero right-hand-sides, i.e. without the adsorption. Secondly, the following system of equations

$$\frac{\partial q}{\partial t} = k_{LDF}^* (q^* - q), \quad (33)$$

$$\phi \rho_f \frac{\partial w_w}{\partial t} = -(1 - \phi) \rho_s \frac{\partial q}{\partial t} M_w, \quad (34)$$

$$(1 - \phi) \rho_s c_s \frac{\partial T_s}{\partial t} = (1 - \phi) \rho_s \frac{\partial q}{\partial t} \Delta H, \quad (35)$$

is solved with the time step Δt and with initial values being the solution of the first step. After these two steps, one computational time step Δt is completed. This splitting technique is needed because the adsorption is a very rapid process compared to the convection and diffusion. Since the adsorption process is rapid, the choice of the computation step Δt is restricted. When the computation step Δt is too large, the simulated mass of water vapor adsorbed in the zeolite can exceed the total mass currently present in a given cell, thus resulting in negative w_w and a failure of the computation. This problem occurs, for example, when $w_w = 0.01131$, $T_s = 294.15$ K, $q = 5$ mol kg^{-1} , $\Delta t = 0.1$ s, $\mathbf{v} = 0$ m s^{-1} , and with parameters from Table 2. After a single time step Δt using the forward Euler method, the values will be $q = 5.00213$ mol kg^{-1} , $w_w = -0.0583083$, and the simulation will fail. With the strategy presented in Section 3.2, the computational steps can be adapted and the situation when $w_w < 0$ is avoided. In the next sections, we will describe both steps of this algorithm in details.

3.1. Numerical solution of Eqs. (1)–(4) with zero right-hand-sides

The first step is solved using the mixed-hybrid finite element method implemented in a numerical library NumDwarf [26] which is designed to solve a system of n partial differential equation in the form

$$\sum_{j=1}^n N_{i,j} \frac{\partial Z_j}{\partial t} + \sum_{j=1}^n \mathbf{u}_{i,j} \cdot \nabla Z_j + \nabla \cdot \left[m_i \left(- \sum_{j=1}^n \mathbf{D}_{i,j} \nabla Z_j + \mathbf{w}_i \right) + \sum_{j=1}^n Z_j \mathbf{a}_{i,j} \right] + \sum_{j=1}^n r_{i,j} Z_j = f_i \tag{36}$$

for $i = 1, \dots, n$, where $Z_j = Z_j(t, \mathbf{x})$ are the unknown functions, $N_{i,j}$, $r_{i,j}$, and m_i are scalar coefficients, $\mathbf{u}_{i,j}$, \mathbf{w}_i , and $\mathbf{a}_{i,j}$ are vector coefficients, $\mathbf{D}_{i,j}$ are matrix coefficients, $t > 0$ is time, and $\mathbf{x} \in \mathbb{R}^d$ is the spatial variable, where d is the dimension. The solver implemented in the NumDwarf library can solve the system (36) for an arbitrary dimension. The system (36) is supplemented by an initial condition

$$Z_j(0, \mathbf{x}) = Z_j^{(ini)}, \quad \forall \mathbf{x} \in \Omega, j = 1, \dots, n, \tag{37}$$

and boundary conditions for all $t \in (0, t_{final})$,

$$Z_j(t, \mathbf{x}) = Z_j^{(D)}, \quad \forall \mathbf{x} \in \Gamma_{Z_j} \subset \partial\Omega, j = 1, \dots, n, \tag{38}$$

$$\mathbf{q}_i(t, \mathbf{x}) \cdot \mathbf{n} = q_i^{(N)}, \quad \forall \mathbf{x} \in \Gamma_{\mathbf{q}_i} \subset \partial\Omega, i = 1, \dots, n, \tag{39}$$

where \mathbf{q}_i is the conservative flux

$$\mathbf{q}_i = m_i \left(- \sum_{j=1}^n \mathbf{D}_{i,j} \nabla Z_j + \mathbf{w}_i \right). \tag{40}$$

The NumDwarf solver is based on the mixed-hybrid finite element method with the semi-implicit approach for the time discretization. The main advantage of the mixed-hybrid finite element method is that the scalar unknowns $Z_j(t, \mathbf{x})$ and their fluxes \mathbf{q}_i are approximated with the same order of accuracy [34]. This property is not present in the finite volume methods where the approximation of the fluxes is less accurate [35]. In the derivation of the NumDwarf solver, the authors assumed that the scalar unknowns $Z_j(t, \mathbf{x})$ are continuously differentiable with respect to time t , weakly differentiable with respect to spatial vector \mathbf{x} , and fluxes \mathbf{q}_i belong to the function space $\mathbf{H}(\text{div}, \Omega)$ [36]. Let \mathcal{K}_h is the spatial discretization of the computational domain Ω . On each element $K \in \mathcal{K}_h$, the solver approximates \mathbf{q}_i in the lowest order Raviart-Thomas-Nédélec space $\mathbf{RTN}_0(K)$ [34,37]. Furthermore, the i th equation of (36) is discretized using a finite volume approach to obtain the averages of Z_j over $K \in \mathcal{K}_h$

$$Z_{j,K}(t) = \frac{1}{|K|} \int_K Z_j(t, \mathbf{x}) d\mathbf{x}, \tag{41}$$

where $|K|$ is the measure of element K . The resulting system of ODEs is discretized in time using the finite differences

$$\frac{dZ_{j,K}}{dt} \approx \frac{Z_{j,K}(t_{k+1}) - Z_{j,K}(t_k)}{\Delta t}, \tag{42}$$

for $j = 1, \dots, n$. A semi-implicit approach for the time discretization is adopted. In the time step from level t_k to t_{k+1} , the unknowns Z_j in $\mathbf{r}_{i,j}$ are evaluated from level t_{k+1} , in $\mathbf{a}_{i,j}$ from time level t_k . In each time step, a single sparse system of linear equations is obtained and solved using a suitable direct or iterative solver. Here, the UMFPACK solver [38] is used. For more details the reader is referred to [26].

As the primary unknowns, we choose

$$Z_1 = P, Z_2 = w_w, Z_3 = T_f, Z_4 = T_s, \tag{43}$$

i.e., the pressure, the mass fraction of the water vapor, the temperature of the fluid, and the temperature of the zeolite, respectively. With these primary variables, the system of Eqs. (1)–(4) can be written in the form of Eq. (36), if the non-zero coefficients in (36) are chosen as

$$\mathbb{N} = \begin{pmatrix} \phi \frac{\partial \rho_f}{\partial P} & \Phi \frac{\partial \rho_f}{\partial w_w} & \Phi \frac{\partial \rho_f}{\partial T_f} & 0 \\ 0 & \phi \rho_f & 0 & 0 \\ 0 & 0 & \phi \rho_f c_v & 0 \\ 0 & 0 & 0 & (1 - \Phi) \rho_s c_s \end{pmatrix}, \tag{44}$$

$$\mathbf{u} = \begin{pmatrix} 0 & 0 & 0 & 0 \\ 0 & \rho_f \mathbf{v} & 0 & 0 \\ 0 & 0 & c_v \mathbf{v} \rho_f & 0 \\ 0 & 0 & 0 & 0 \end{pmatrix}, \quad m = \begin{pmatrix} \rho_f \\ \rho_f \\ 1 \\ 1 \end{pmatrix}, \tag{45}$$

$$D = \begin{pmatrix} \frac{\kappa}{\mu} & 0 & 0 & 0 \\ 0 & D_{pm} & 0 & 0 \\ 0 & 0 & k_f & 0 \\ 0 & 0 & 0 & k_s \end{pmatrix}, \quad r = \begin{pmatrix} 0 & 0 & 0 & 0 \\ 0 & 0 & 0 & 0 \\ 0 & 0 & \beta & -\beta \\ 0 & 0 & -\beta & \beta \end{pmatrix}. \tag{46}$$

3.2. Numerical solution with the source/sink terms

In the second step of our numerical method, Eqs. (33)–(35) are solved in time interval $[t_n, t_{n+1}]$ using the fourth order Runge-Kutta method [39]. With time step η , the method iterates the solution using

$$q(t + \eta, \mathbf{x}) = q(t, \mathbf{x}) + \frac{\eta}{6} (k_1^{(1)} + 2k_2^{(1)} + 2k_3^{(1)} + k_4^{(1)}), \tag{47}$$

$$w_w(t + \eta, \mathbf{x}) = w_w(t, \mathbf{x}) + \frac{\eta}{6} (k_1^{(2)} + 2k_2^{(2)} + 2k_3^{(2)} + k_4^{(2)}), \tag{48}$$

$$T_s(t + \eta, \mathbf{x}) = T_s(t, \mathbf{x}) + \frac{\eta}{6} (k_1^{(3)} + 2k_2^{(3)} + 2k_3^{(3)} + k_4^{(3)}). \tag{49}$$

Denoting the right-hand-side of the Eqs. (15), (2), and (4) by

$$f^{(1)}(q, w_w, T_s) = k_{LDf}^* (q^* - q), \tag{50}$$

$$f^{(2)}(q, w_w, T_s) = - \frac{(1 - \phi) \rho_s k_{LDf}^* (q^* - q) M_w}{\phi \rho_f}, \tag{51}$$

$$f^{(3)}(q, w_w, T_s) = \frac{(1 - \phi) k_{LDf}^* (q^* - q) \Delta H}{c_s}, \tag{52}$$

respectively, the coefficients $k_j^{(i)}$ are calculated using

$$k_1^{(i)} = f^{(i)}(q, w_w, T_s), \tag{53}$$

$$k_2^{(i)} = f^{(i)}(q + \eta k_1^{(1)}/2, w_w + \eta k_1^{(2)}/2, T_s + \eta k_1^{(3)}/2), \tag{54}$$

$$k_3^{(i)} = f^{(i)}(q + \eta k_2^{(1)}/2, w_w + \eta k_2^{(2)}/2, T_s + \eta k_2^{(3)}/2), \tag{55}$$

$$k_4^{(i)} = f^{(i)}(q + \eta k_3^{(1)}, w_w + \eta k_3^{(2)}, T_s + \eta k_3^{(3)}), \tag{56}$$

for $i = 1, 2, 3$. We start our computation with step size $\eta = \Delta t$. If $w_w(t + \eta, \mathbf{x}) < 0$, the computation step is discarded and the step size is adapted using

$$\eta = -w_w \frac{6}{k_1^{(2)} + 2k_2^{(2)} + 2k_3^{(2)} + k_4^{(2)}}. \tag{57}$$

The computation continues until $t = t_{n+1}$.

Table 1
Parameters in the balance equations.

parameter	value
ϕ [-]	0.35
D_m [m ² s ⁻¹]	$1.9 \cdot 10^{-9}$
K [m ²]	10^{-10}
μ [Pa s]	$1.8205 \cdot 10^{-5}$
R [J mol ⁻¹ K ⁻¹]	8.3144621
M_o [kg mol ⁻¹]	0.02897
M_w [kg mol ⁻¹]	0.018
$c_{v,a}$ [J kg ⁻¹ K ⁻¹]	718
$c_{v,w}$ [J kg ⁻¹ K ⁻¹]	1460
$c_{p,a}$ [J kg ⁻¹ K ⁻¹]	1005
$c_{p,w}$ [J kg ⁻¹ K ⁻¹]	1870
c_s [J kg ⁻¹ K ⁻¹]	880
k_f [W m ⁻¹ K ⁻¹]	$30 \cdot 10^{-3}$
k_s [W m ⁻¹ K ⁻¹]	0.4
d_s [m]	$2 \cdot 10^{-3}$
ρ_s [kg m ⁻³]	1152
g [m s ⁻²]	0

Table 2
Parameters of the kinetic model for the zeolite 13X. Data taken from Gaeini et al. [16].

parameter	value
q_{max} [mol kg ⁻¹]	19
b_0 [Pa ⁻¹]	4.002
ΔE [J mol ⁻¹]	65 572
n_0 [-]	2.976
α [-]	0.377
k^* [s ⁻¹]	7

3.3. The full algorithm

In this section, we summarize the essential steps of our numerical method:

0. Let a final time t_{final} , time step Δt , and initial and boundary conditions be given. Set the iteration counter $n = 0$.
1. Solve system (1)–(4) from time level t_n to time level t_{n+1} using the numerical procedure defined in Section 3.1.
2. Solve system (33)–(35) from time level t_n to time level t_{n+1} using the numerical procedure defined in Section 3.2. Set the initial conditions to the previously calculated values on time level t_{n+1} .
3. If $t_{n+1} = t_{final}$, terminate algorithm. Otherwise, set $n = n + 1$ and go to Step 1.

4. Results

In this section, we present simulated results using the model described in Section 3. The numerical values for the coefficients used in Eqs. (1)–(4) are presented in Table 1. The numerical values needed for the kinetic model are provided in Table 2. These values are used for both adsorption and desorption processes.

In our numerical study, the axial flow is neglected, therefore, a 1D model is satisfactory and the computation set Ω is an interval $\Omega = (0, L)$. In the examples below, we use $L = 0.5$ m. A graphical schematic drawing is depicted in Fig. 1. Two processes will be studied: the charging and the discharging process. During the charging process, hot air is drying the zeolite and the water vapor adsorbed in the zeolite is being desorbed. During the discharging process, humid air is supplied, the water vapor is being adsorbed in the zeolite, and the heat is released. In both cases, a computational study is performed. Four different meshes and corresponding time steps are used. The individual time steps and meshes are presented in Table 3. The errors of the numerical solution $s^{(j)}$ (su-

Table 3
Meshes and corresponding time steps used in the computation study.

ID	number of elements	Δt [s]
1	25	$4 \cdot 10^{-3}$
2	50	$2 \cdot 10^{-3}$
3	100	$1 \cdot 10^{-3}$
4	200	$5 \cdot 10^{-4}$

perscript indicates which mesh was used) are measured in L_1 and L_2 norms which are defined as

$$error_{L_1}^{(j)} = \sup_{t \in [0, t_{final}]} \int_{\Omega} |s^{(j)}(t, \mathbf{x}) - s^{(exact)}(t, \mathbf{x})| dx, \quad (58)$$

$$error_{L_2}^{(j)} = \sup_{t \in [0, t_{final}]} \left(\int_{\Omega} |s^{(j)}(t, \mathbf{x}) - s^{(exact)}(t, \mathbf{x})|^2 dx \right)^{\frac{1}{2}}, \quad (59)$$

where $s^{(exact)}$ is the exact solution. As this solution is not available, the solution on the finest mesh is used as the reference solution. Having the errors measured, the experimental order of convergence EOC can be determined as

$$EOC_j^{(i)} = \frac{\ln error_{L_i}^{(j-1)} - \ln error_{L_i}^{(j)}}{\ln 2}. \quad (60)$$

List of symbols

Latin:	
b	parameter of the kinetic model
c_v	specific heat of fluid at constant volume
c_p	specific heat of fluid at constant pressure
c_s	specific heat of solid
D_{pm}	diffusive coefficient
d_s	diameter of zeolite particle
EOC	experimental order of convergence
ΔH	isosteric heat of adsorption
k_{LDF}	rate of adsorption
k_f	thermal conductivity of fluid
k_s	thermal conductivity of solid
L	length of computation set
M_w	molar mass of water vapor
n	parameter of kinetic model
Nu	Nusselt number
P	pressure
Pr	Prandtl number
q	water vapor adsorbed in zeolite
q^*	equilibrium state
q_{max}	maximum amount of water vapor adsorbed in zeolite
Re	Reynolds number
t	time
t_{final}	final time of simulation
T_f	temperature of fluid
T_s	temperature of solid
\mathbf{v}	velocity
w_w	water mass fraction
Greek:	
α	parameter of kinetic model
β	heat transfer coefficient
$\partial\Omega$	boundary of Ω
ϕ	porosity
ρ_f	density of fluid
ρ_s	density of zeolite
τ	tortuosity
η	time step
Ω	computation domain
Subscripts:	
f	fluid
s	solid
w	water
a	air

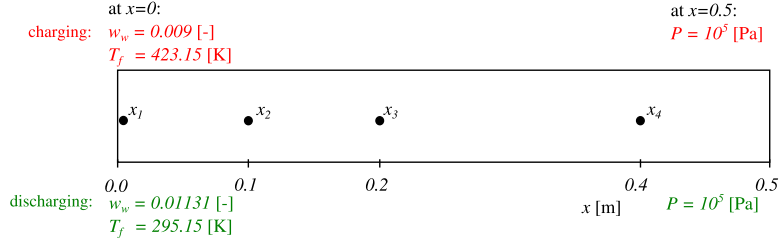


Fig. 1. A schematic drawing of the thermo-chemical battery with the Dirichlet boundary conditions during the charging process (red color) and during the discharging process (green color). (For interpretation of the references to colour in this figure legend, the reader is referred to the web version of this article.)

4.1. Charging process

In the first part of the computation study, the charging of a hypothetical thermo-chemical battery is modelled. The charging process is carried out by drying the zeolite with hot air. In our simulation, the temperature of the air is 423.15 K (150 °C). Since we do not have any experimental data, the results from this example will be used as the initial condition for the modelling of the discharging process. The initial conditions are set to

$$p^{(ini)} = 10^5 \text{ Pa}, \tag{61}$$

$$w_w^{(ini)} = 0.00468, \tag{62}$$

$$T_f^{(ini)} = 294.65 \text{ K}, \tag{63}$$

$$T_s^{(ini)} = 294.65 \text{ K}, \tag{64}$$

$$q^{(ini)} = 17.5 \text{ mol kg}^{-1}. \tag{65}$$

The boundary $\partial\Omega$ consists of two points $x = 0$ and $x = L$. The Dirichlet boundary conditions are

$$p^{(D)} = 10^5 \text{ Pa, for } x = L, \tag{66}$$

$$w_w^{(D)} = 0.009, \text{ for } x = 0, \tag{67}$$

$$T_f^{(D)} = 423.15 \text{ K, for } x = 0. \tag{68}$$

The Dirichlet boundary conditions are also depicted in Fig. 1. The value of the water vapor represents a relative humidity of approximately 52% at 20 degrees Celsius. At $P(t, 0)$, we prescribe Neumann boundary condition for the flux

$$\mathbf{q}_p \cdot \mathbf{n} = v^{(inflow)} \rho_f^{(inflow)} = 0.311814 \text{ kg s}^{-1} \text{ m}^{-3}, \tag{69}$$

where \mathbf{n} is the outward normal with respect to the corresponding part of the $\partial\Omega$. This flux numerically represents the airflow rate of 1 liter per second in a tube with a diameter of 0.07 m. In all other cases we prescribe zero Neumann boundary condition. The computation time is set to $t_{final} = 12$ h. During the charging process, the amount of water vapor in the zeolite is decreasing and after approximately 11 h the system is in equilibrium. The resulting water vapor q adsorbed in the zeolite profile after 12 h is given in Fig. 2. Furthermore, the time developments of the water vapor adsorbed in the zeolite q , the water fraction w_w , and the temperatures T_f, T_s at chosen points are depicted in Fig. 3a–d, respectively. The chosen points are $x_1 = 0.01$ m, $x_2 = 0.11$ m, $x_3 = 0.21$ m, and $x_4 = 0.41$ m. The temperature steadily rises in all points as the hotter air is being pushed inside the tube. From the time development of the mass fraction of the water (Fig. 3b), one can observe the

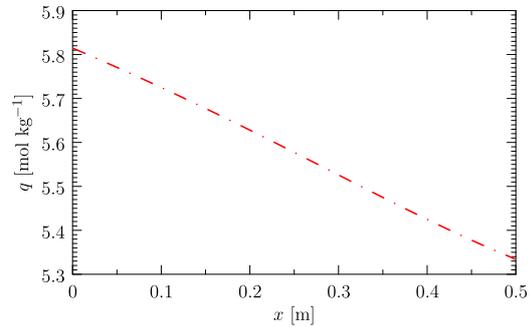


Fig. 2. Water vapor q in the zeolite after the charging (drying) process at the final time $t = 12$ h.

Table 4
Errors and experimental order of convergence of chosen variables during the charging (drying) process. The errors and experimental orders of convergence (EOC) are defined by Eqs. (58)–(60).

T_f :				
mesh ID	error L_1	error L_2	EOC ¹	EOC ²
1	$8.49 \cdot 10^2$	$4.90 \cdot 10^1$		
2	$3.82 \cdot 10^2$	$2.21 \cdot 10^1$	1.15	1.15
3	$1.30 \cdot 10^2$	7.54	1.55	1.55
T_s :				
mesh ID	error L_1	error L_2	EOC ¹	EOC ²
1	$8.35 \cdot 10^2$	$4.82 \cdot 10^1$		
2	$3.72 \cdot 10^2$	$2.15 \cdot 10^1$	1.17	1.17
3	$1.25 \cdot 10^2$	7.24	1.57	1.57
q :				
mesh ID	error L_1	error L_2	EOC ¹	EOC ²
1	$3.54 \cdot 10^1$	2.05		
2	$1.54 \cdot 10^1$	$8.89 \cdot 10^{-1}$	1.20	1.20
3	5.11	$2.95 \cdot 10^{-1}$	1.59	1.59
w_w :				
mesh ID	error L_1	error L_2	EOC ¹	EOC ²
1	$2.63 \cdot 10^{-1}$	$1.52 \cdot 10^{-2}$		
2	$1.25 \cdot 10^{-1}$	$7.20 \cdot 10^{-3}$	1.08	1.08
3	$4.42 \cdot 10^{-2}$	$2.55 \cdot 10^{-3}$	1.50	1.50

strong increase of the water vapor in the first hours of the process. This increase is caused by the drying process when the water vapor is being desorbed from the zeolite and transported in the fluid. The most interesting is the time development of the water vapor adsorbed in the zeolite. In the first point $x_1 = 0.01$ m, the zeolite is dry in about 3 h. In other points the process is slower. In the last point $x_4 = 0.41$ m, the drying process is finished after approximately 11 h. The convergence test, which was described at the beginning of this section, is presented in Table 4 where the errors of numerical solutions and experimental orders of convergence are

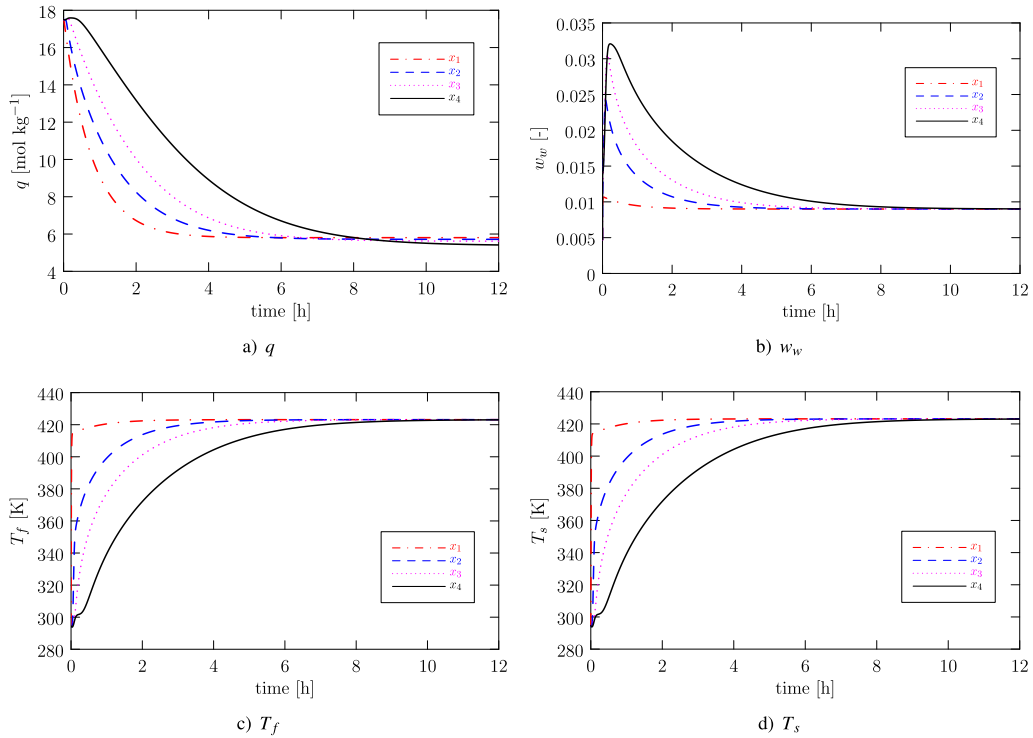


Fig. 3. Time development of the given primary variables at chosen points during the charging (drying) process using the finest mesh (mesh 4).

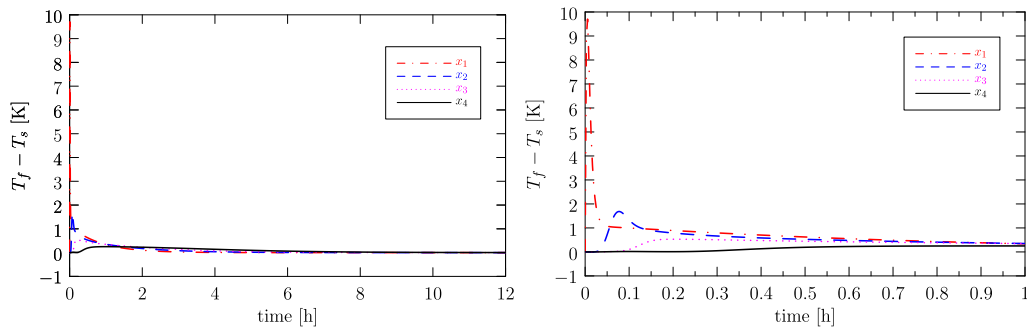


Fig. 4. Time development of the difference in temperatures $T_f - T_s$ at chosen points during the charging (drying) process using the finest mesh (mesh 4) (left). The magnification of the first hour of the process (right).

calculated. In all cases, the experimental order of convergence is more than one. Therefore, the convergence of our method is verified. In Fig. 5, the comparison of the solutions on different meshes is presented. The time developments of the fluid temperatures T_f at different points are depicted. One can observe that the most significant changes are in the first point $x = 0.01$ m. In other cases, the time developments are almost identical. However, in all cases, the numerical solutions on the coarse mesh are underestimated.

As we are using a two-temperature model, we can study a temperature difference between the fluid and zeolite temperatures. In Fig. 4, the time development of the difference $T_f - T_s$ of chosen points is depicted. One can observe that the difference is always

non-negative, therefore, the fluid temperature is always higher than the temperature of the zeolite. The most significant difference is at the left boundary (point $x_1 = 0.010$ m) where the value is up to 9.5 K. This is mainly caused by the boundary condition $T_f(t, 0) = 423.15$ K which forced the temperature of the fluid to remain at this value at the left boundary. In the other chosen points, the difference is also positive with a higher difference in the first hour of the drying process. The difference at the beginning is caused by the desorption of the water vapor in the zeolite when the zeolite is cooled down. After approximately six hours, the difference in temperatures is negligible because the desorption process is almost finished. This is in agreement with Fig. 3a

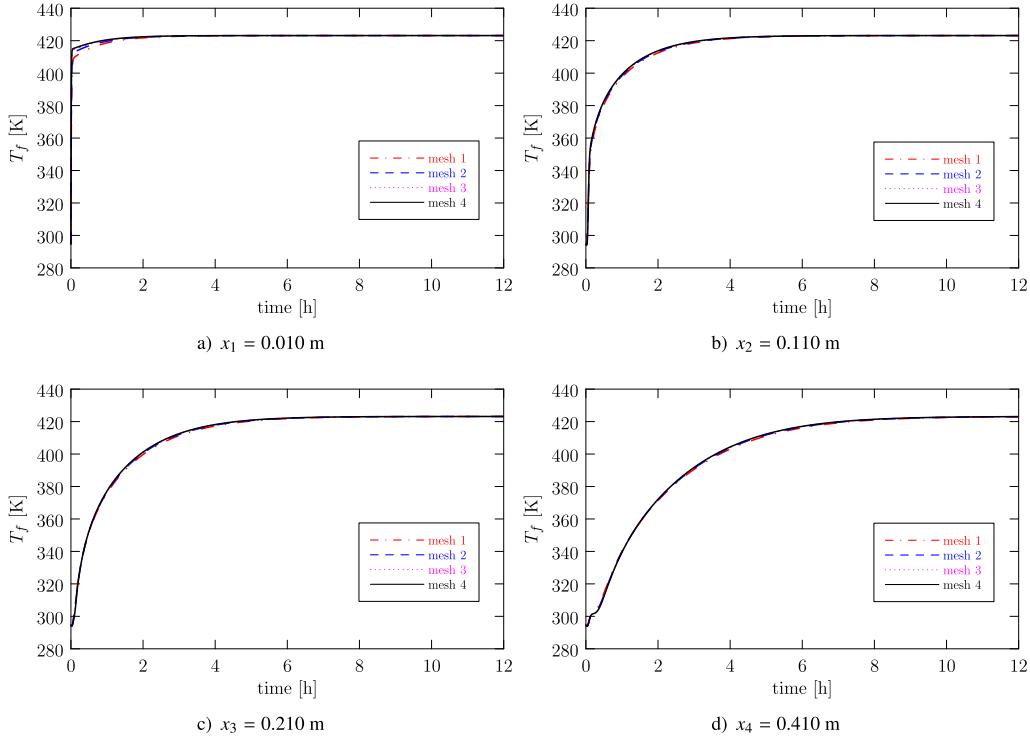


Fig. 5. Comparison of the numerical solutions T_f during the charging process on different meshes.

where the amount of adsorbed water vapor q in the zeolite is depicted.

4.2. Discharging process

The second part of our numerical study is the discharging process when the zeolite adsorbs water vapor and its temperature rises. This is caused by the relatively wet air which is brought into contact with the zeolite. The discharging process will be studied in two cases. First, with the diameter of the zeolite particles $d_s = 0.002$ m. Second, we increase the diameter to $d_s = 0.01$ m.

As an initial condition for the water vapor adsorbed in the zeolite q , the resulting state after the charging process is taken, see Fig. 2. Other initial conditions are set to

$$p^{(ini)} = 10^5 \text{ Pa}, \quad (70)$$

$$w_w^{(ini)} = 0.00468, \quad (71)$$

$$T_f^{(ini)} = 294.65 \text{ K}, \quad (72)$$

$$T_s^{(ini)} = 294.65 \text{ K}. \quad (73)$$

The boundary conditions have identical form as in the charging process, only the numerical values for the temperature and water mass fraction are different:

$$w_w^{(D)} = 0.01131, \text{ for } x = 0, \quad (74)$$

$$T_f^{(D)} = 295.15 \text{ K, for } x = 0. \quad (75)$$

The mass water fraction represents the relative humidity of approximately 65% at 20 degrees Celsius. At $P(t, 0)$, we prescribe same Neumann boundary condition as in the charging process. The flux is set to

$$\mathbf{q}_p \cdot \mathbf{n} = \nu^{(inflow)} \rho_f^{(inflow)} = 0.311814 \text{ kg s}^{-1} \text{ m}^{-3}, \quad (76)$$

The computation time is set to $t_{final} = 8$ h. First, we present computation results with diameter $d_s = 0.002$. Similarly to the charging process, Figs. 6a–d show the time developments of the water vapor adsorbed in the zeolite, the water mass fraction, the fluid temperature, and the zeolite temperature, respectively at chosen points. As the water vapor is being adsorbed, the temperature of the zeolite and consequently the temperature of the fluid steady rise and approach toward the maximum, which is approximately 350 K. After the adsorption is finished, the system is in the equilibrium, and the temperatures start to decrease. In the case of point $x_2 = 0.11$ m, the temperature returns to its initial value in approximately two hours. These time developments of the temperatures are in agreement with the time development of the water vapor q in the zeolite (see Fig. 6a). At all points the water vapor adsorbed in the zeolite increases to its equilibrium value $16.81 \text{ mol kg}^{-1}$ and remains on this level until the end of the computation. In Fig. 6b, the time development of the water mass fraction is depicted, showing that for almost 5 h, the air leaving the area is completely dry since all water vapor is adsorbed in the zeolite. Only after 4 h the adsorption on the right side of the computation domain is completed and the leaving air starts having a higher mass water fraction. In Table 5, the errors and the experimental orders of convergence are presented. It can be observed that all orders of convergence are

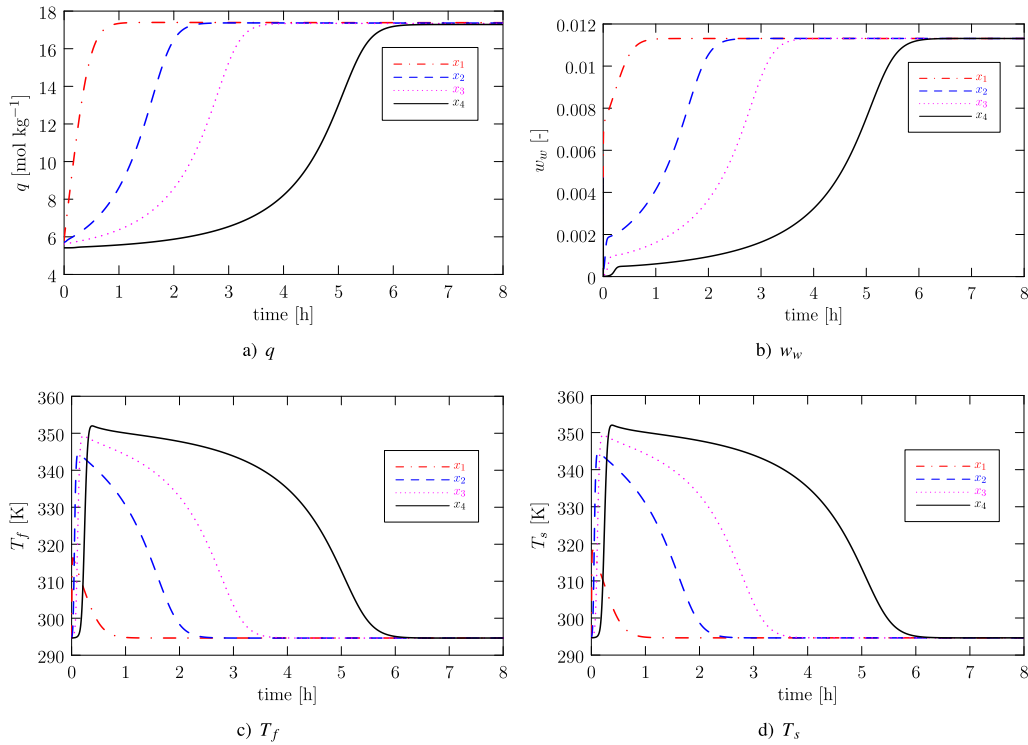


Fig. 6. Time development of the given primary variables at chosen points during the discharging (wetting) process with $d_s = 0.002$ m using the finest mesh (mesh 4).

Table 5

Errors and experimental order of convergence of chosen variables during the discharging (wetting) process with $d_s = 0.002$ m. The errors and experimental orders of convergence (EOC) are defined by Eqs. (58)–(60).

T_f :				
mesh ID	error L_1	error L_2	EOC ¹	EOC ²
1	$2.12 \cdot 10^3$	$1.22 \cdot 10^2$		
2	$1.15 \cdot 10^3$	$6.63 \cdot 10^1$	0.89	0.88
3	$4.48 \cdot 10^2$	$2.59 \cdot 10^1$	1.36	1.36
T_s :				
mesh ID	error L_1	error L_2	EOC ¹	EOC ²
1	$2.10 \cdot 10^3$	$1.21 \cdot 10^2$		
2	$1.13 \cdot 10^3$	$6.52 \cdot 10^1$	0.89	0.89
3	$4.36 \cdot 10^2$	$2.52 \cdot 10^1$	1.37	1.37
q :				
mesh ID	error L_1	error L_2	EOC ¹	EOC ²
1	$1.40 \cdot 10^2$	8.10		
2	$6.23 \cdot 10^1$	3.60	1.17	1.17
3	$2.11 \cdot 10^1$	1.22	1.56	1.56
w_w :				
mesh ID	error L_1	error L_2	EOC ¹	EOC ²
1	$2.04 \cdot 10^{-1}$	$1.18 \cdot 10^{-2}$		
2	$9.65 \cdot 10^{-2}$	$5.57 \cdot 10^{-3}$	1.08	1.08
3	$3.40 \cdot 10^{-2}$	$1.96 \cdot 10^{-3}$	1.51	1.51

around one. In the worst case 0.89, in the best case 1.56. The convergence is also illustrated in Fig. 7, where the time development of the fluid temperature at different points is depicted. It can be observed that the use of a coarse mesh leads to an overestimation of the solution. This property can be observed in all time develop-

ments. The most visible case is at the point $x_1 = 0.01$ m. This overestimation is more significant than the underestimation observed during the charging process (see Fig. 5). Moreover, the errors during the discharging process are higher in comparison to the errors during the charging process.

In Fig. 8, the time development of the difference between the fluid and zeolite temperature during the discharging process is depicted. Two phenomena can be observed. The first one is the positive difference ($T_f > T_s$) in the first hour of the process. This is caused by the rapid adsorption of the initial water vapor. A closer examination of the data reveals that the initial water vapor $w_w = 0.00468$ immediately decreases everywhere to an approximate value $w_w = 10^{-5}$. The released heat is then transported by convection and creates this difference. The other one is the negative difference ($T_f < T_s$), which happened at each point in a different time. These are caused by the adsorption from the humid air which is prescribed by the boundary condition. Similarly to the charging process, the difference is the highest (2 K) at the left boundary where the boundary condition $T_f(t, \mathbf{x}) = 295.15$ K fixes the fluid temperature. The temperature difference at the other points is at the maximum after approximately 1.5, 3, and 5 h, respectively. This time scale is in agreement with the adsorption time development. From the time development of the water vapor adsorbed in the zeolite (Fig. 6a) one can observe that the process at the chosen points is the fastest during the negative peaks in Fig. 8. When the adsorption is not in progress, the difference of the temperatures is negligible and a local thermal equilibrium can be assumed.

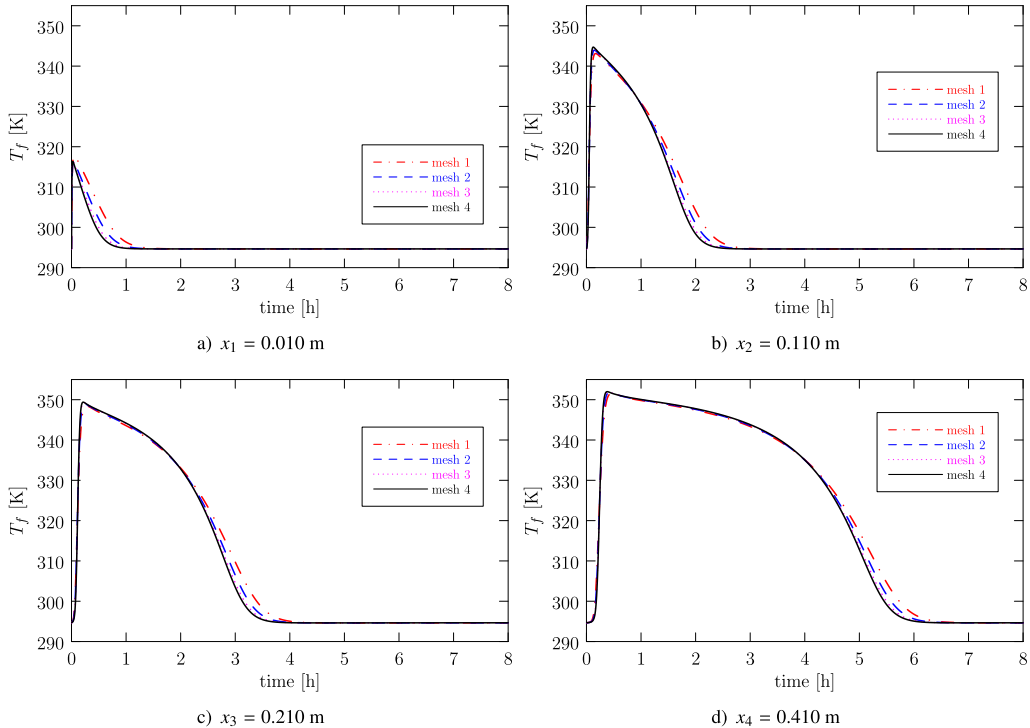


Fig. 7. Comparison of the numerical solutions T_f during the discharging (wetting) process with $d_s = 0.002$ m on different meshes.

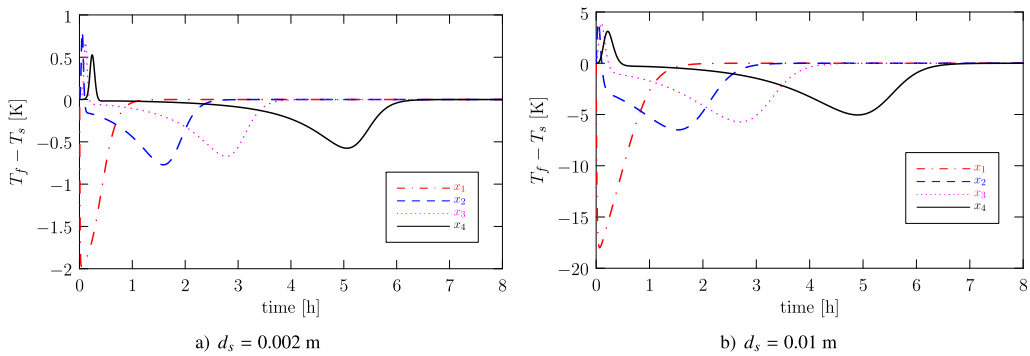


Fig. 8. Time development of the difference in temperatures $T_f - T_s$ at chosen points during the discharging (wetting) process using the finest mesh (mesh 4).

Second, we present the results computed using the diameter of the zeolite $d_s = 0.01$ m. In Figs. 9a–d, the time developments of the water vapor adsorbed in the zeolite, the water mass fraction, the fluid temperature, and the zeolite temperature, respectively, are depicted. In comparison to the time developments with a smaller diameter, no significant changes are observed. In Table 6, the errors and the experimental orders of convergence are presented. In comparison to the values with smaller diameters, the errors are lower and the experimental orders of convergence are always higher. The minimum value of EOC is 0.99, the maximum is 1.59, indicating that that numerical scheme is convergent. In

Fig. 10, the time developments of the temperature of the fluid T_f at different points are presented. Similarly to the discharging process with $d_s = 0.002$ m, in all time developments, an overestimation of the solution on the coarse mesh can be observed. In Fig. 8, the difference of temperatures at chosen points on the finest mesh is depicted. The development has a similar progress. At the beginning, the positive differences ($T_f > T_s$) are observed. Then, the negative differences ($T_f < T_s$) during the adsorption process are detected. At the end of the simulation, when the adsorption process is finished, the difference of the temperature is negligible. However, in comparison with the setting of $d_s = 0.002$ m, one can observe more

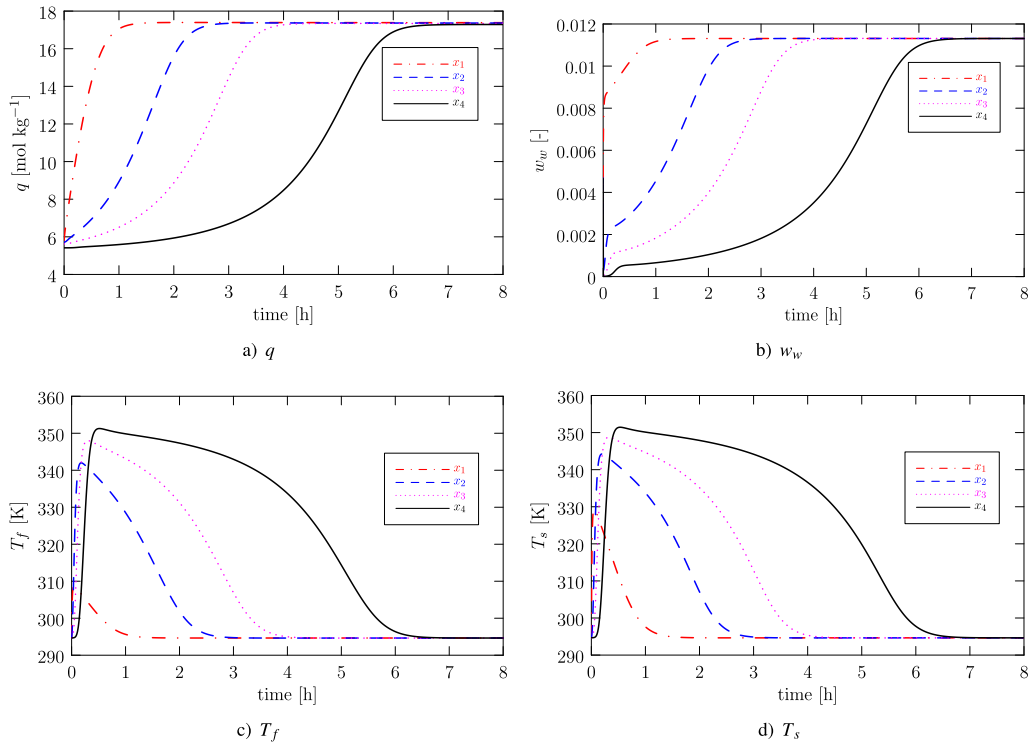


Fig. 9. Time development of the given primary variables at chosen points during the discharging (wetting) process with $d_s = 0.01$ m using the finest mesh (mesh 4).

Table 6
Errors and experimental order of convergence of chosen variables during the discharging (wetting) process with $d_s = 0.01$ m. The errors and experimental orders of convergence (EOC) are defined by Eqs. (58)–(60).

T_f :				
mesh ID	error L_1	error L_2	EOC ¹	EOC ²
1	$8.44 \cdot 10^2$	$4.87 \cdot 10^1$		
2	$3.97 \cdot 10^2$	$2.29 \cdot 10^1$	1.09	1.09
3	$1.39 \cdot 10^2$	8.05	1.51	1.51
T_s :				
mesh ID	error L_1	error L_2	EOC ¹	EOC ²
1	$8.68 \cdot 10^2$	$5.01 \cdot 10^1$		
2	$4.37 \cdot 10^2$	$2.52 \cdot 10^1$	0.99	0.99
3	$1.63 \cdot 10^2$	9.40	1.42	1.42
q :				
mesh ID	error L_1	error L_2	EOC ¹	EOC ²
1	$1.17 \cdot 10^2$	6.74		
2	$5.05 \cdot 10^1$	2.92	1.21	1.21
3	$1.68 \cdot 10^1$	$9.71 \cdot 10^{-1}$	1.59	1.59
w_w :				
mesh ID	error L_1	error L_2	EOC ¹	EOC ²
1	$1.50 \cdot 10^{-1}$	$8.66 \cdot 10^{-3}$		
2	$6.91 \cdot 10^{-2}$	$3.99 \cdot 10^{-3}$	1.12	1.12
3	$2.40 \cdot 10^{-2}$	$1.38 \cdot 10^{-3}$	1.53	1.53

significant differences. With a larger diameter of the particles, the heat transfer coefficient has a lower value, and the difference between the temperatures is, therefore, larger (approximately by the order of ten). The most significant difference is again in the vicinity

of the left boundary, where the temperature difference is greater than 15 K.

5. Conclusion

In this work, we presented a two-temperature mathematical model of adsorption and desorption of water vapor in the zeolite 13X. The mathematical model consisted of four balance equations and one kinetic equation based on the Linear Driving Force model and Langmuir-Freundlich isotherms. As we used the two-temperature model, the local thermal equilibrium was not assumed. The mathematical model was solved using the mixed-hybrid finite element method implemented in a numerical library NumDwarf. To handle the source/sink terms, the operator splitting technique was adopted. The computational study verified convergence in both charging and discharging processes. The experimental orders of convergence were between 1 and 1.5.

In the computational study, we investigated the behaviour of individual temperatures. During the charging process, when hot air was brought into contact with moist zeolite, the difference was only observed in the first hour of the process. During the discharging process, when humid air was brought into contact with dry zeolite, higher differences between the temperatures were observed. When the adsorption process was the most rapid, the maximum difference was approximately 2 K and was observed in the vicinity of the boundary. This high value was caused by the Dirichlet boundary condition. At other points, the difference was at maximum approximately 0.7 K. However, with a parameter adaptation, the difference between the temperatures can be more significant.

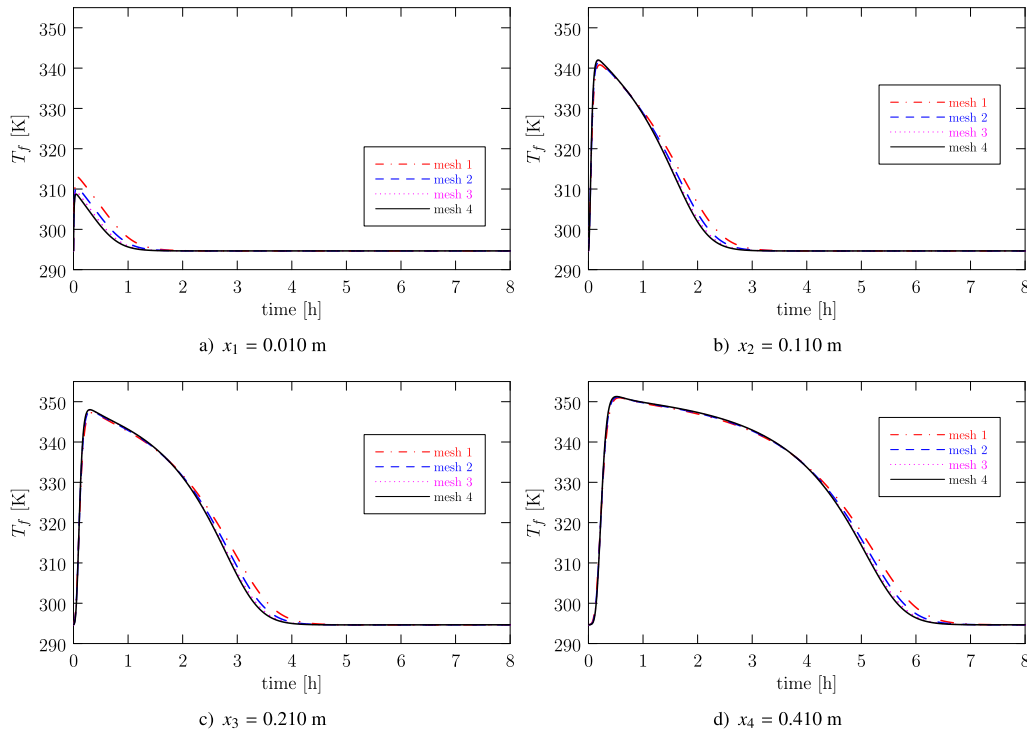


Fig. 10. Comparison of the numerical solutions T_f during the discharging (wetting) process with $d_s = 0.01$ m on different meshes.

We showed a computation study of the discharging process with an increased value of the diameter of zeolite $d_s = 0.01$ m (the original value was $d_s = 0.002$ m). The resulting temperature difference was approximately ten times larger. The maximum (approximately 20 K) was observed in the vicinity of the left boundary, where the Dirichlet boundary condition was prescribed.

Declaration of Competing Interest

None.

Acknowledgments

The work was supported by the project Thermal energy storage materials: thermophysical characteristics for the design of thermal batteries, project no. 17-08218S of the Czech Science Foundation, 2017-2019 and the project Application of advanced supercomputing methods in mathematical modeling of natural processes, project no. SGS17/194/OHK4/3T/14 of the Student Grant Agency of the Czech Technical University in Prague, 2017-2019.

Supplementary material

Supplementary material associated with this article can be found, in the online version, at [10.1016/j.ijheatmasstransfer.2019.119050](https://doi.org/10.1016/j.ijheatmasstransfer.2019.119050).

References

[1] International Energy Agency, Transition to sustainable buildings: strategies and opportunities to 2050, 2013, doi:10.1787/9789264202955-en.

[2] A. Sharma, V. Tyagi, C. Chen, D. Buddhi, Review on thermal energy storage with phase change materials and applications, *Renewable Sustainable Energy Rev.* 13 (2) (2009) 318–345, doi:10.1016/j.rser.2007.10.005.

[3] K. Pielichowska, K. Pielichowski, Phase change materials for thermal energy storage, *Prog. Mater. Sci.* 65 (2014) 67–123, doi:10.1016/j.pmatsci.2014.03.005.

[4] S.A. Mohamed, F.A. Al-Sulaiman, N.I. Ibrahim, M.H. Zahir, A. Al-Ahmed, R. Saidur, B.S. Yilbas, A.Z. Sahin, A review on current status and challenges of inorganic phase change materials for thermal energy storage systems, *Renewable Sustainable Energy Rev.* 70 (2017) 1072–1089, doi:10.1016/j.rser.2016.12.012.

[5] D. Kearney, U. Herrmann, P. Nava, B. Kelly, R. Mahoney, J. Pacheco, R. Cable, N. Potrovitz, D. Blake, H. Price, Assessment of a molten salt heat transfer fluid in a parabolic trough solar field, *J. Sol. Energy Eng.* 125 (2) (2003) 170–176.

[6] D. Brosseau, J.W. Kelton, D. Ray, M. Edgar, K. Chisman, B. Emms, Testing of thermocline filler materials and molten-salt heat transfer fluids for thermal energy storage systems in parabolic trough power plants, *J. Sol. Energy Eng.* 127 (1) (2005) 109–116.

[7] M. Liu, N.S. Tay, S. Bell, M. Belusko, R. Jacob, G. Will, W. Saman, F. Bruno, Review on concentrating solar power plants and new developments in high temperature thermal energy storage technologies, *Renewable Sustainable Energy Rev.* 53 (2016) 1411–1432, doi:10.1016/j.rser.2015.09.026.

[8] D.N. Harries, M. Paskevicius, D.A. Sheppard, T.E.C. Price, C.E. Buckley, Concentrating solar thermal heat storage using metal hydrides, *Proc. IEEE* 100 (2) (2012) 539–549, doi:10.1109/JPROC.2011.2158509.

[9] B. Stanmore, P. Gilot, Review- calcination and carbonation of limestone during thermal cycling for CO2 sequestration, *Fuel Process. Technol.* 86 (16) (2005) 1707–1743, doi:10.1016/j.fuproc.2005.01.023.

[10] K. Kyaw, M. Kanamori, H. Matsuda, M. Hasatani, Study of carbonation reactions of Ca-Mg oxides for high temperature energy storage and heat transformation, *J. Chem. Eng. Jpn.* 29 (1) (1996) 112–118, doi:10.1252/jcej.29.112.

[11] P. Pardo, A. Deydier, Z. Anxionnaz-Minvielle, S. Rougé, M. Cabassud, P. Cognet, A review on high temperature thermochemical heat energy storage, *Renewable Sustainable Energy Rev.* 32 (2014) 591–610, doi:10.1016/j.rser.2013.12.014.

[12] H. Zondag, B. Kikkert, S. Smeding, R. de Boer, M. Bakker, Prototype thermochemical heat storage with open reactor system, *Appl. Energy* 109 (2013) 360–365, doi:10.1016/j.apenergy.2013.01.082.

[13] B. Mette, H. Kerskes, H. Drück, H. Müller-Steinhagen, Experimental and numerical investigations on the water vapor adsorption isotherms and kinet-

- ics of binderless zeolite 13X, *Int. J. Heat Mass Transf.* 71 (2014) 555–561, doi:10.1016/j.ijheatmasstransfer.2013.12.061.
- [14] K. Johannes, F. Kuznik, J.-L. Hubert, F. Durier, C. Obrecht, Design and characterisation of a high powered energy dense zeolite thermal energy storage system for buildings, *Appl. Energy* 159 (2015) 80–86, doi:10.1016/j.apenergy.2015.08.109.
- [15] M. Gaeini, H. Zondag, C. Rindt, Non-isothermal kinetics of zeolite water vapor adsorption into a packed bed lab scale thermochemical reactor, in: 15th International Heat Transfer Conference, 2014.
- [16] M. Gaeini, H. Zondag, C. Rindt, Effect of kinetics on the thermal performance of a sorption heat storage reactor, *Appl. Therm. Eng.* 102 (2016) 520–531.
- [17] COMSOL, COMSOL Multiphysics User's Guide, Comsol, 2006.
- [18] O. Bey, G. Eigenberger, Gas flow and heat transfer through catalyst filled tubes, *Int. J. Therm. Sci.* 40 (2) (2001) 152–164, doi:10.1016/S1290-0729(00)01204-7.
- [19] M. Winterberg, E. Tsotsas, Correlations for effective heat transport coefficients in beds packed with cylindrical particles, *Chem. Eng. Sci.* 55 (23) (2000) 5937–5943, doi:10.1016/S0009-2509(00)00198-6.
- [20] M. Duquesne, J. Toutain, A. Sempay, S. Ginetet, E.P. del Barrio, Modeling of a nonlinear thermochemical energy storage by adsorption on zeolites, *Appl. Therm. Eng.* 71 (1) (2014) 469–480, doi:10.1016/j.applthermaleng.2014.07.002.
- [21] C.W. Gear, L.R. Petzold, ODE methods for the solution of differential/algebraic systems, *SIAM J. Numer. Anal.* 21 (4) (1984) 716–728.
- [22] L.F. Shampine, M.W. Reichelt, J.A. Kierzenka, Solving index-1 DAEs in MATLAB and simulink, *SIAM Rev.* 41 (3) (1999) 538–552.
- [23] C. Reichl, D. Lager, G. Englmair, B. Zettl, M. Popovac, Fluid dynamics simulations for an open-sorption heat storage drum reactor based on thermophysical kinetics and experimental observations, *Appl. Therm. Eng.* 107 (2016) 994–1007, doi:10.1016/j.applthermaleng.2016.06.119.
- [24] ANSYS, ANSYS Fluent, Release 15.0, ANSYS, Inc. Southpointe, 275 Technology Drive, Canonsburg, PA 15317, USA, 2013.
- [25] F. Kuznik, D. Gondre, K. Johannes, C. Obrecht, D. David, Numerical modelling and investigations on a full-scale zeolite 13X open heat storage for buildings, *Renew. Energy* 132 (2019) 761–772, doi:10.1016/j.renene.2018.07.118.
- [26] R. Fučík, J. Klínek, J. Solovský, T. Oberhuber, J. Mikyška, Multidimensional mixed-hybrid finite element method for compositional two-phase flow in heterogeneous porous media and its parallel implementation on GPU, *Comput. Phys. Commun.* 238 (2019) 165–180.
- [27] R. Helmig, *Multiphase Flow and Transport Processes in the Subsurface: A Contribution to the Modeling of Hydrosystems*, Environmental Engineering, Springer, 1997.
- [28] R.J. Millington, J.P. Quirk, Permeability of porous solids, *Trans. Faraday Soc.* 57 (1961) 1200–1207, doi:10.1039/TF9615701200.
- [29] A. Firoozabadi, *Thermodynamics and Applications of Hydrocarbons Energy Production*, McGraw-Hill, 2015.
- [30] D.J. Gunn, Transfer of heat or mass to particles in fixed and fluidized beds, *Int. J. Heat Mass Transf.* 21 (1978) 467–476.
- [31] D.M. Ruthven, *Principles of Adsorption and Adsorption Processes*, Wiley-Interscience, 1984.
- [32] D.D. Do, *Adsorption Analysis: Equilibria and Kinetics*, Imperial College Press, 1998.
- [33] R.J. Leveque, *Finite Volume Methods for Hyperbolic Problems*, Cambridge University Press, 2004.
- [34] F. Brezzi, M. Fortin, *Mixed and hybrid finite element methods*, vol. 15, Springer Science & Business Media, 2012.
- [35] J.H. Ferziger, M. Perić, *Computational Methods for Fluid Dynamics*, Springer Berlin Heidelberg, 2001.
- [36] A. Kufner, O. John, S. Fučík, *Function Spaces, Mechanics: Analysis*, Springer Netherlands, 1977.
- [37] P.-A. Raviart, J. Thomas, *Mathematical Aspects of Finite Element Methods*, Springer, 1977.
- [38] T.A. Davis, A column pre-ordering strategy for the unsymmetric-pattern multirontal method, *ACM Trans. Math. Softw.* 30 (2) (2004) 165–195, doi:10.1145/992200.992205.
- [39] J.C. Butcher, *Numerical Methods for Ordinary Differential Equations*, second ed., John Wiley & Sons, 2008.

■ P.6 Článek v *Mathematical Problems in Engineering*

Michal Beneš, Radek Fučík, Vladimír Havlena, Vladimír Klement, Miroslav Kolář, Ondřej Polívka, Jakub Solovský a Pavel Strachota: *An Efficient and Robust Numerical Solution of the Full-Order Multiscale Model of Lithium-Ion Battery*, *Mathematical Problems in Engineering*, ID3530975, 2018.

Research Article

An Efficient and Robust Numerical Solution of the Full-Order Multiscale Model of Lithium-Ion Battery

Michal Beneš,¹ Radek Fučík,¹ Vladimír Havlena,² Vladimír Klement,¹ Miroslav Kolář,¹ Ondřej Polívka,¹ Jakub Solovský,¹ and Pavel Strachota¹

¹Department of Mathematics, Faculty of Nuclear Sciences and Physical Engineering, Czech Technical University in Prague, Trojanova 13, 120 00 Praha 2, Czech Republic

²Honeywell Prague Laboratory, V Parku 2326/18, 148 00 Praha 4, Czech Republic

Correspondence should be addressed to Pavel Strachota; pavel.strachota@jfifi.cvut.cz

Received 31 August 2017; Revised 5 December 2017; Accepted 8 January 2018; Published 7 February 2018

Academic Editor: Michele Brun

Copyright © 2018 Michal Beneš et al. This is an open access article distributed under the Creative Commons Attribution License, which permits unrestricted use, distribution, and reproduction in any medium, provided the original work is properly cited.

We propose a novel and efficient numerical approach for solving the pseudo two-dimensional multiscale model of the Li-ion cell dynamics based on first principles, describing the ion diffusion through the electrolyte and the porous electrodes, electric potential distribution, and Butler-Volmer kinetics. The numerical solution is obtained by the finite difference discretization of the diffusion equations combined with an original iterative scheme for solving the integral formulation of the laws of electrochemical interactions. We demonstrate that our implementation is fast and stable over the expected lifetime of the cell. In contrast to some simplified models, it provides physically consistent results for a wide range of applied currents including high loads. The algorithm forms a solid basis for simulations of cells and battery packs in hybrid electric vehicles, with possible straightforward extensions by aging and heat effects.

1. Introduction

Modern Li-ion batteries possess advantages making them a popular choice in many different applications. Their light weight, low self-discharge rate, and performance especially matter for power storage in hybrid electric vehicles (HEV). There are ongoing efforts to optimize the control strategy of the HEV powertrain in order to improve not only the range of the vehicle, but also the total useful battery capacity during its lifetime. Mathematical models of Li-ion cells based on first principles provide insight into the dynamics of the battery cycling and the information from the computational simulations can be used during the design of the control algorithms.

The basic reference for simulating Li-ion cell dynamics is the isothermal model proposed by Newman and Tiedemann [1] and Doyle et al. [2]. For the model with thermal effects included, we refer the reader, for example, to Cai and White [3], Kumaresan et al. [4], or Gu and Wang [5]. The aging effects of Li-ion batteries are discussed, for example, by Ramadass et al. [6, 7] or Ning et al. [8, 9].

Recently, several approximate techniques were successfully applied to reduce the computational complexity of these models. In [10, 11], Subramanian et al. used perturbation techniques. Model reduction and Chebyshev polynomial methods were used by Bhikkaji and Söderström in [12]. In Smith et al. [13], the residue grouping method was used. Cai and White [14] developed a reduced-order model by means of orthogonal decomposition.

In our work, we strive to create a robust yet computationally efficient algorithm for predicting the state of Li-ion batteries subject to intense and variable loading over extended time periods. We adopt the full-order pseudo two-dimensional model of Li-ion cell dynamics describing ion diffusion through the electrolyte, charge flow, and the Butler-Volmer kinetics, as summarized in [15]. We propose a novel approach to the solution of electrochemical interactions by means of integral reformulation of the governing equations and an iterative scheme for their solution. As a result, our algorithm remains stable for a wide range of applied currents. The simulations are fast enough to cover the

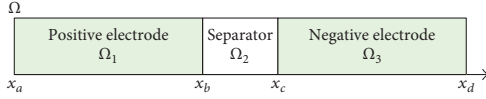


FIGURE 1: One-dimensional representation of the lithium-ion cell.

long term behavior of the battery while still resolving both the macroscale diffusion processes across the cell as well as position-dependent microscale dynamics in the porous material of the electrodes (in contrast to the single-particle models; see, e.g., [16, 17]).

The paper is structured as follows. In Section 2, we present the summary of the mathematical model. Section 3 is dedicated to the derivation of the integral solution of electrochemical interactions, leading to the formulation of an iterative algorithm. In Section 4, we shortly comment on the implementation of the algorithm so as to be able to explain some further ideas. In Section 5, we first use our model to replicate the study by Subramanian et al. [18] and Dao et al. [15] and discuss the obtained outcomes. Further on, we proceed with the analysis of the effect of the numerical algorithm parameters. We draw conclusions about the applicability of the proposed approach for long term simulations.

2. Summary of the Mathematical Model

2.1. Geometrical Setting. As shown in Figure 1, the one-dimensional representation of the lithium-ion cell computational domain $\Omega = [x_a, x_d]$ is divided into three parts such that $\Omega = \Omega_1 \cup \Omega_2 \cup \Omega_3$, where $\Omega_1 = [x_a, x_b]$ is the positive electrode, $\Omega_2 = [x_b, x_c]$ is the separator, and $\Omega_3 = [x_c, x_d]$ is the negative electrode. Any single point $x_0 \in \Omega$ corresponds to a cross section through the real three-dimensional cell by the plane $x = x_0$. Neither the area nor the shape of this cross section are known or needed in the 1D model. All respective quantities such as the applied current density I_{app} and the mass fluxes are calculated per unit cross section area.

In the following text, the quantities corresponding to the solid electrodes and electrolyte are indexed by s and e , respectively, and the quantities defined in Ω_k are enumerated by the appropriate subdomain index $k \in \{1, 2, 3\}$. The values of all quantities depend on time t which lies within the interval $\mathcal{J} = (0, t_{\text{final}})$.

2.2. Diffusion of Li^+ in the Electrolyte. Depending on the mode of operation (charge/discharge), the lithium ions are extracted (*deintercalated*) from the porous material of one electrode, transferred through the electrolyte across the separator by diffusion, and finally intercalated into the porous material of the other electrode. Based on [15], the governing equations for diffusion read

$$\epsilon_k \frac{\partial c_{e,k}}{\partial t} = \frac{\partial}{\partial x} \left(D_e \tau_k \frac{\partial c_{e,k}}{\partial x} \right) + (1 - t_+^0) a_k j_k \quad \text{in } \Omega_k \times \mathcal{J} \quad (1)$$

for each $k \in \{1, 2, 3\}$. The meanings of the symbols in (1) are as follows.

$c_{e,k}$ [mol m^{-3}] denotes the concentration of Li^+ in the electrolyte.

ϵ_k [1] is the material porosity (void fraction).

D_e [$\text{m}^2 \text{s}^{-1}$] is the diffusion coefficient of Li^+ in the electrolyte.

τ_k [1] is the tortuosity factor of the porous medium given by the Bruggeman relationship [19] $\tau_k = \epsilon_k^{\text{brugg}_k}$, where ϵ_k [1] is the porosity of the medium and brugg_k [1] is the Bruggeman coefficient.

t_+^0 [1] is the transference number of Li^+ in the electrolyte.

j_k [$\text{mol m}^{-2} \text{s}^{-1}$] denotes the (de)intercalation flux of Li^+ from the internal surface of the porous material into the electrolyte per unit surface area ($j_2 = 0$ as no lithium ions are stored in the material of the separator).

a_k [m^{-1}] is the internal surface area of the porous material per unit volume.

Equation (1) is accompanied by a number of boundary conditions. First, the lithium ions cannot leave the outer boundary of the cell which implies

$$\frac{\partial c_{e,1}}{\partial x} \Big|_{x=x_a} = \frac{\partial c_{e,3}}{\partial x} \Big|_{x=x_d} = 0. \quad (2)$$

The other boundary conditions ensure continuity of the concentration in the electrolyte at the interdomain boundaries

$$\begin{aligned} c_{e,2} \Big|_{x=x_b} &= c_{e,1} \Big|_{x=x_b}, \\ c_{e,3} \Big|_{x=x_c} &= c_{e,2} \Big|_{x=x_c}, \end{aligned} \quad (3)$$

as well as the continuity of the interdomain concentration fluxes

$$\begin{aligned} D_e \tau_2 \frac{\partial c_{e,2}}{\partial x} \Big|_{x=x_b^+} &= D_e \tau_1 \frac{\partial c_{e,1}}{\partial x} \Big|_{x=x_b^-}, \\ D_e \tau_3 \frac{\partial c_{e,3}}{\partial x} \Big|_{x=x_c^+} &= D_e \tau_2 \frac{\partial c_{e,2}}{\partial x} \Big|_{x=x_c^-}. \end{aligned} \quad (4)$$

The initial conditions are given by

$$c_{e,k} \Big|_{t=0} = c_{e,k}^0, \quad \text{in } \Omega_k, \quad \forall k \in \{1, 2, 3\}. \quad (5)$$

2.3. Diffusion inside the Porous Electrodes. The electrodes are made of porous material, that is, a mixture of void space (filled with electrolyte) and a solid continuum. At the microscopic level, the solid matrix is modeled in the form of small spherical particles releasing (deintercalating) or absorbing (intercalating) lithium ions through their surface. Lithium then diffuses through each particle in the radial direction according to the current concentration distribution.

The material balance for lithium in a single active solid material particle in the positive or negative electrode is governed by Fick's second law in spherical coordinates [3, 15]:

$$\frac{\partial c_{s,k}}{\partial t} = \frac{D_s}{r^2} \frac{\partial}{\partial r} \left(r^2 \frac{\partial c_{s,k}}{\partial r} \right) \quad \text{in } \Omega_{\text{part},k} \times \Omega_k \times \mathcal{J} \quad (6)$$

for each $k \in \{1, 3\}$. The distance from the center of the spherical particle r lies in the interval $\Omega_{\text{part},k} = (0, R_{s,k})$.

$R_{s,k}$ is the radius of the solid particles in the electrode Ω_k .

$c_{s,k}$ [mol m⁻³] is the concentration of lithium in the particle.

D_s [m²s⁻¹] is the diffusion coefficient of lithium in the particle.

The initial concentration distribution in a particle is given by

$$c_{s,k}|_{t=0} = c_{s,k}^0 \quad \text{in } \Omega_{\text{part},k} \times \Omega_k. \quad (7)$$

At the center of the particle, the boundary condition

$$-D_s \left. \frac{\partial c_{s,k}}{\partial r} \right|_{r=0} = 0 \quad (8)$$

imposes zero flux of lithium. On the particle surface, the flux is equal to the consumption/production rate of Li⁺ due to the electrochemical reaction occurring at the solid/liquid interface; that is,

$$-D_s \left. \frac{\partial c_{s,k}}{\partial r} \right|_{r=R_{s,k}} = j_k. \quad (9)$$

2.3.1. Scale Coupling. For each $x \in \Omega_k$, the number of spherical particles per unit cross section area and in the range $(x, x + dx)$ is

$$dn_k = \frac{1 - \epsilon_k - \epsilon_{f,k}}{(4/3)\pi R_{s,k}^3} dx. \quad (10)$$

The solid matrix occupies a volume fraction $1 - \epsilon_k - \epsilon_{f,k}$, because apart from electrolyte, there can be some amount of inert material (*filler*) with the volume fraction $\epsilon_{f,k}$ [15]. According to (10), the number of spherical particles per unit volume at $x \in \Omega_k$ is

$$n_k = \frac{1 - \epsilon_k - \epsilon_{f,k}}{(4/3)\pi R_{s,k}^3}. \quad (11)$$

All such particles are assumed to have the same radial distribution of concentration $c_{s,k}$. In particular, we denote the concentration at the particle surface as

$$c_{s,\text{surf},k}(x, t) = c_{s,k}(R_{s,k}, x, t). \quad (12)$$

The total surface area of these particles per unit volume

$$a_k = n_k 4\pi R_{s,k}^2 = \frac{3(1 - \epsilon_k - \epsilon_{f,k})}{R_{s,k}} \quad (13)$$

is a material property. Its values for some porous materials can be found in literature [20], allowing the calculation of the radius of the respective spherical particles $R_{s,k}$ from (13).

2.4. Electrochemical Interactions. Equations (1) and (6) determine the chemical state of the cell provided that the fluxes j_1 and j_3 are given. The connection between the concentrations of lithium ions and the respective mass fluxes comes from the modeling of the electrochemical interactions in the cell which also allows the calculations of other quantities such as the cell voltage. Whereas the diffusion equations in Sections 2.2 and 2.3 are readily prepared for numerical solution by standard tools (e.g., the method of finite differences), the equations summarized below require nontrivial treatment.

By the end of Section 2.4, the equations do not contain partial derivatives with respect to t and r . For any function $f : \Omega_k \times \mathcal{F} \rightarrow \mathbb{R}$, $k \in \{1, 2, 3\}$, we therefore simplify the notation $\partial f / \partial x$ to f' .

2.4.1. Electrical Potential in the Porous Electrodes. The charge continuity equations in the solid electrodes placed at Ω_1 and Ω_3 are given by Ohm's law [15] as

$$\sigma_k^{\text{eff}} \phi_{s,k}'' = a_k F j_k \quad \text{in } \Omega_k \times \mathcal{F}, \quad k \in \{1, 3\} \quad (14a)$$

with the boundary conditions

$$-\sigma_1^{\text{eff}} \phi_{s,1}'(x_a) = I_{\text{app}}, \quad (14b)$$

$$-\sigma_1^{\text{eff}} \phi_{s,1}'(x_b) = 0, \quad (14c)$$

$$-\sigma_3^{\text{eff}} \phi_{s,3}'(x_c) = 0, \quad (14d)$$

$$-\sigma_3^{\text{eff}} \phi_{s,3}'(x_d) = I_{\text{app}}, \quad (14e)$$

$$\phi_{s,3}(x_d) = 0, \quad (14f)$$

where

$\phi_{s,k}$ [V] is the solid phase electrical potential,

F [C mol⁻¹] is Faraday's constant,

I_{app} [A m⁻²] is the current density applied to the electrode ($I_{\text{app}} > 0$ corresponds to charging and $I_{\text{app}} < 0$ to discharging),

Fj_k [A m⁻²] denotes the charge flux in terms of Li⁺ ions from the internal surface of the porous material into the electrolyte per unit surface area,

σ_k^{eff} [S m⁻¹] is the effective electronic conductivity defined as

$$\sigma_k^{\text{eff}} = (1 - \epsilon_k - \epsilon_{f,k}) \sigma_k, \quad (15)$$

σ_k [S m⁻¹] is the electronic conductivity.

2.4.2. Electrical Potential in the Electrolyte. Based on [15], the charge continuity equation in the electrolyte is given by

$$\left(\kappa_k^{\text{eff}} \phi_{e,k}' \right)' = -a_k F j_k + \frac{2RT}{F} (1 - t_+) \left(\kappa_k^{\text{eff}} \frac{c'_{e,k}}{c_{e,k}} \right)' \quad (16a)$$

$$\text{in } \Omega_k \times \mathcal{F}, \quad k \in \{1, 2, 3\}$$

with the boundary conditions

$$-\kappa_1^{\text{eff}} \phi'_{e,1}(x_a) = 0, \quad (16b)$$

$$-\kappa_1^{\text{eff}} \phi'_{e,1}(x_b) = -\kappa_2^{\text{eff}} \phi'_{e,2}(x_b) = I_{\text{app}}, \quad (16c)$$

$$-\kappa_2^{\text{eff}} \phi'_{e,2}(x_c) = -\kappa_3^{\text{eff}} \phi'_{e,3}(x_c) = I_{\text{app}}, \quad (16d)$$

$$-\kappa_3^{\text{eff}} \phi'_{e,3}(x_d) = 0, \quad (16e)$$

$$\phi_{e,1}(x_b) = \phi_{e,2}(x_b), \quad (16f)$$

$$\phi_{e,2}(x_c) = \phi_{e,3}(x_c), \quad (16g)$$

where

$\phi_{e,k}$ [V] is the electrical potential in the electrolyte,
 R [J mol⁻¹K⁻¹] is the universal gas constant,
 T [K] is the temperature,
 κ_k^{eff} [S m⁻¹] is the effective ionic conductivity of the electrolyte given by $\kappa_k^{\text{eff}} = \tau_k \kappa_k$ that accounts for the tortuous path of the porous medium, where κ_k [S m⁻¹].

For the reference ionic conductivity κ_k , we use the empirical correlation reported in [15]:

$$\begin{aligned} \kappa_k &= 4.1253 \cdot 10^{-2} + 5.007 \cdot 10^{-4} c_{e,k} - 4.7212 \\ &\cdot 10^{-7} c_{e,k}^2 + 1.5094 \cdot 10^{-10} c_{e,k}^3 - 1.6018 \\ &\cdot 10^{-14} c_{e,k}^4, \quad k \in \{1, 2, 3\}. \end{aligned} \quad (17)$$

2.4.3. Butler-Volmer Reaction Kinetics. Lithium is conserved and its fluxes from the solid particles and into the electrolyte are both equal to j_k . The charge transfer Fj_k is proportional to the mass transfer and is subject to Butler-Volmer reaction kinetics [6, 7, 15, 21] in the form

$$j_k = \delta_k \left[\exp\left(\frac{\alpha_{a,k} F}{RT} \eta_k\right) - \exp\left(-\frac{\alpha_{c,k} F}{RT} \eta_k\right) \right], \quad (18a)$$

$$k = 1, 3,$$

with

$$\delta_k = K_k (c_{s,\text{max},k} - c_{s,\text{surf},k})^{1/2} c_{s,\text{surf},k}^{1/2} c_{e,k}^{1/2}. \quad (18b)$$

The meanings of the symbols in (18a) and (18b) are the following:

K_k [mol^{-1/2}m^{5/2}s⁻¹] is the reaction rate coefficient,
 $\alpha_{a,k}$ and $\alpha_{c,k}$ [1] are the anodic and cathodic transfer coefficients of electrochemical reaction,
 $c_{s,\text{max},k}$ [mol m⁻³] is the saturated concentration of Li⁺ ions in the solid phase,
 η_k [V] is the intercalation overpotential described as

$$\eta_k = \phi_{s,k} - \phi_{e,k} - U_k. \quad (19)$$

In (19), U_k [V] is the open circuit potential determined by the following empirical correlations:

$$U_1 = \frac{-4.875 + 5.839\theta_1 - 1.507\theta_1^3 + 0.531\theta_1^5}{\theta_1 - 1.005}, \quad (20)$$

$$U_3 = 0.15 - 0.10\theta_3 + \frac{0.00778}{\theta_3},$$

where $\theta_k = c_{s,\text{surf},k}/c_{s,\text{max},k}$, $k = 1, 3$.

3. Integral Solution of Electrochemical Interactions

For a given time t , the flux j_k , $k \in \{1, 3\}$, can be calculated by the solution of the system of two differential equations (14a) and (16a) and the algebraic equation (18a) for the unknowns $\phi_{e,k}$, $\phi_{s,k}$, η_k , and j_k , together with the respective boundary conditions (see Section 2.4). It turns out that this set of equations can be transformed into a system of two ordinary differential equations (ODEs) for η_k and J_k , where by J_k we denote the integrated mass transfer function defined by

$$J_k(x) = \int_{x_{\ell,k}}^x j_k(\xi) d\xi, \quad \forall x \in [x_{\ell,k}, x_{r,k}], \quad k \in \{1, 3\}, \quad (21)$$

and $x_{\ell,k}$, $x_{r,k}$ represent the left and right boundary coordinates of Ω_k , respectively.

3.1. Derivation of the Differential Equations. In order to derive the ODE for η_k , we first integrate (14a) with respect to x over the interval $(x_{\ell,k}, x) \subset \Omega_k$, $k \in \{1, 3\}$. Using the boundary conditions (14b) and (14d), we obtain

$$\phi'_{s,1} = \frac{a_1 F}{\sigma_1^{\text{eff}}} J_1 - \frac{I_{\text{app}}}{\sigma_1^{\text{eff}}}, \quad \forall x \in \Omega_1, \quad (22a)$$

$$\phi'_{s,3} = \frac{a_3 F}{\sigma_3^{\text{eff}}} J_3, \quad \forall x \in \Omega_3. \quad (22b)$$

Similarly, by integrating (16a) for $k \in \{1, 2, 3\}$ and using the boundary conditions (16b), (16c), and (16d), we arrive at

$$\phi'_{e,1} = -\frac{a_1 F}{\kappa_1^{\text{eff}}} J_1 + \frac{2RT}{F} (1 - t_+^0) \frac{c'_{e,1}}{c_{e,1}}, \quad \forall x \in \Omega_1, \quad (22c)$$

$$\phi'_{e,2} = \frac{2RT}{F} (1 - t_+^0) \frac{c'_{e,2}}{c_{e,2}} - \frac{I_{\text{app}}}{\kappa_2^{\text{eff}}}, \quad \forall x \in \Omega_2, \quad (22d)$$

$$\phi'_{e,3} = -\frac{a_3 F}{\kappa_3^{\text{eff}}} J_3 + \frac{2RT}{F} (1 - t_+^0) \frac{c'_{e,3}}{c_{e,3}} - \frac{I_{\text{app}}}{\kappa_3^{\text{eff}}}, \quad (22e)$$

$\forall x \in \Omega_3$.

Subtractions of (22c) from (22a) and (22e) from (22b) allow expressing the derivative of η_k defined by (19) as

$$\eta'_1 = a_1 F J_1 \frac{\sigma_1^{\text{eff}} + \kappa_1^{\text{eff}}}{\sigma_1^{\text{eff}} \kappa_1^{\text{eff}}} - \frac{I_{\text{app}}}{\sigma_1^{\text{eff}}} - \frac{2RT}{F} (1 - t_+^0) \frac{c'_{e,1}}{c_{e,1}} - U'_1, \quad (23a)$$

$$\eta'_3 = a_3 F J_3 \frac{\sigma_3^{\text{eff}} + \kappa_3^{\text{eff}}}{\sigma_3^{\text{eff}} \kappa_3^{\text{eff}}} + \frac{I_{\text{app}}}{\kappa_3^{\text{eff}}} - \frac{2RT}{F} (1 - t_+^0) \frac{c'_{e,3}}{c_{e,3}} - U'_3. \quad (23b)$$

The ODE for J_k is given directly by the Butler-Volmer reaction kinetics (18a) in the form

$$J'_k = \delta_k \left[\exp\left(\frac{\alpha_{a,k} F}{RT} \eta_k\right) - \exp\left(-\frac{\alpha_{c,k} F}{RT} \eta_k\right) \right], \quad (24)$$

$k = 1, 3.$

Differentiating (24) with respect to x and plugging in η_k from (23a) and (23b), respectively, lead to a single second-order ODE for J_k . The corresponding boundary conditions follow from the definition of J_k given by (21) and evaluation of (22a), (22b) at $x = x_b$ and $x = x_c$ together with the boundary conditions given by (14c) and (14e). They read

$$J_1(x_a) = 0, \quad (25a)$$

$$J_1(x_b) = \frac{I_{\text{app}}}{a_1 F},$$

$$J_3(x_c) = 0, \quad (25b)$$

$$J_3(x_d) = -\frac{I_{\text{app}}}{a_3 F},$$

and they complete two well posed problems for the unknowns J_1 and J_3 .

However, in the following, we use (23a) and (23b), (24), and (25a) and (25b) and transform them into integral equations that can be solved iteratively by means of numerical integration.

3.2. ODE System in General Form. Assume a general coefficient form of ODEs ((23a) and (23b)) and (24) in the following compact form:

$$\eta'(x) = \alpha(x) J(x) + \beta(x), \quad (26a)$$

$$J'(x) = \mathfrak{B}(\eta(x), x), \quad (26b)$$

where

$$\mathfrak{B}(\eta(x), x) = \delta(x) \cdot (\exp(\alpha_a \gamma(x) \eta(x)) - \exp(-\alpha_c \gamma(x) \eta(x))), \quad (26c)$$

for all $x \in (x_l, x_r)$ with the following boundary conditions:

$$J(x_l) = 0, \quad (26d)$$

$$J(x_r) = \varepsilon, \quad (26e)$$

where $x_l = x_{l,k}$, $x_r = x_{r,k}$, $\alpha_a = \alpha_{a,k}$, $\alpha_c = \alpha_{c,k}$, the coefficients $\delta = \delta_k$ are given by (18b), and $\alpha = \alpha_k$, $\beta = \beta_k$, and $\varepsilon = \varepsilon_k$ correspond to the following domain-defined coefficients (denoted by the indices $k = 1$ and $k = 3$):

$$\alpha_1 = a_1 F \frac{\sigma_1 + \kappa_1^{\text{eff}}}{\sigma_1 \kappa_1^{\text{eff}}},$$

$$\alpha_3 = a_3 F \frac{\sigma_3 + \kappa_3^{\text{eff}}}{\sigma_3 \kappa_3^{\text{eff}}},$$

$$\beta_1 = -\frac{I_{\text{app}}}{\sigma_1} - \frac{2RT}{F} (1 - t_+^0) \frac{c'_{e,1}}{c_{e,1}} - U'_1,$$

$$\beta_3 = \frac{I_{\text{app}}}{\kappa_3^{\text{eff}}} - \frac{2RT}{F} (1 - t_+^0) \frac{c'_{e,3}}{c_{e,3}} - U'_3, \quad (27)$$

$$\gamma_1 = \frac{F}{RT},$$

$$\gamma_3 = \frac{F}{RT},$$

$$\varepsilon_1 = \frac{I_{\text{app}}}{a_1 F},$$

$$\varepsilon_3 = -\frac{I_{\text{app}}}{a_3 F}.$$

3.3. Derivation of the Integral Equation. Integrating (26a), (26b), (26c), (26d), and (26e) from x_l to $x \in [x_l, x_r]$, we obtain

$$\eta(x) = \lambda + \int_{x_l}^x \alpha(\zeta) J(\zeta) + \beta(\zeta) d\zeta, \quad (28a)$$

$$J(x) = \int_{x_l}^x \mathfrak{B}(\eta(\zeta), \zeta) d\zeta, \quad (28b)$$

where, in (28a), $\lambda = \eta(x_l)$ is the unknown integration constant and in (28b) the boundary condition given by (26d) was already employed.

Equations (28a) and (28b) can be combined into a single integral equation in two different ways:

$$\eta(x) = \lambda + \int_{x_l}^x \alpha(\zeta) \int_{x_l}^{\zeta} \mathfrak{B}(\eta(\xi), \xi) d\xi + \beta(\zeta) d\zeta, \quad (29)$$

or

$$J(x) = \int_{x_l}^x \mathfrak{B} \left(\lambda + \int_{x_l}^{\zeta} \alpha(\xi) J(\xi) + \beta(\xi) d\xi, \zeta \right) d\zeta. \quad (30)$$

3.4. Equation for λ . The integral equation given by (30) allows determining the value of the unknown integration constant λ since the remaining boundary condition given by (26e) implies

$$\varepsilon = \int_{x_l}^{x_r} \mathfrak{B} \left(\lambda + \int_{x_l}^{\zeta} \alpha(\xi) J(\xi) + \beta(\xi) d\xi, \zeta \right) d\zeta. \quad (31)$$

Under the assumption of constant temperature T , γ becomes constant in (26c). As a result, (26c) and (31) can be combined to obtain

$$\varepsilon = \Lambda^{\alpha_a} I_a - \Lambda^{-\alpha_c} I_c, \quad (32)$$

where $\Lambda = \exp(\gamma\lambda)$ denotes the term with the unknown parameter λ and the coefficients I_a and I_c read as

$$I_a = \int_{x_l}^{x_r} \delta(\zeta) \exp\left(\alpha_a \gamma \int_{x_l}^{\zeta} \alpha(\xi) J(\xi) + \beta(\xi) d\xi\right) d\zeta, \quad (33a)$$

$$I_c = \int_{x_l}^{x_r} \delta(\zeta) \exp\left(-\alpha_c \gamma \int_{x_l}^{\zeta} \alpha(\xi) J(\xi) + \beta(\xi) d\xi\right) d\zeta. \quad (33b)$$

If $\alpha_a = \alpha_c$, (32) is easily resolved by

$$\Lambda^{\alpha_a} = \Lambda^{\alpha_c} = \frac{\varepsilon + \sqrt{\varepsilon^2 + 4I_a I_c}}{2I_a}; \quad (34a)$$

that is,

$$\lambda = \frac{1}{\gamma} \ln\left(\frac{\varepsilon + \sqrt{\varepsilon^2 + 4I_a I_c}}{2I_a}\right). \quad (34b)$$

In general, (32) is a highly nonlinear equation that needs to be solved numerically.

3.5. Iterative Scheme for Solving the Integral Equation. We propose the following iterative scheme for solving the integral equation given by (30):

$$\begin{aligned} \tilde{J}_{n+1}(x) &= \int_{x_l}^x \mathfrak{B}\left(\lambda_n + \int_{x_l}^{\zeta} \alpha(\xi) J_n(\xi) + \beta(\xi) d\xi, \zeta\right) d\zeta, \end{aligned} \quad (35)$$

$$J_{n+1}(x) = (1 - \omega) J_n(x) + \omega \tilde{J}_{n+1}(x), \quad (36)$$

where λ_n is the solution of (32) which has to be updated at every iteration step for given J_n , $n = 0, 1, 2, \dots$, and $\omega \in (0, 1]$ is a relaxation coefficient that serves as a tuning parameter allowing control of the convergence of the iteration scheme. Note that, with values of ω close to 1, the iterative scheme given by (35) diverges rapidly because of the exponential functions in (26c). As the initial guess in (35), we choose $J_0 \equiv 0$ in the first call to the iterative solver and the previously calculated value of J in the subsequent calls. The iterative process is terminated when the norm of \tilde{J}_{n+1} is below a given threshold ϑ . The values of ω and ϑ are discussed further in Section 5.2.

3.6. Computational Algorithm for Solving the System of ODEs. Let us summarize the algorithm that allows computing the electrolyte and the solid phase electrical potentials and the respective charge fluxes. The steps of the computational algorithm are as follows:

- (1) In the given time step, use the prescribed profiles of $c_{e,k}$ and $c_{s,surf,k}$ and the value of I_{app} to solve (26a), (26b), (26c), (26d), and (26e) using the iteration scheme given by (35) to obtain the integrated charge fluxes J_1 and J_3 .
- (2) Compute the intercalation overpotentials η_1 and η_3 using (28a).
- (3) Compute the fluxes $j_1 = J_1'$ and $j_3 = J_3'$ from (26b); that is, $j_1(x) = \mathfrak{B}(\eta_1(x), x)$, and $j_3(x) = \mathfrak{B}(\eta_3(x), x)$, respectively.
- (4) Compute $\phi_{s,3}$ by integrating (22b) and using the boundary condition given by (14f).
- (5) Compute $\phi_{e,3}$ by integrating (22e) and using the boundary condition that follows from (19) as

$$\phi_{e,3}(x_c) = \phi_{s,3}(x_c) - \eta_3(x_c) - U_3(x_c). \quad (37)$$
- (6) Compute $\phi_{e,2}$ by integrating (22d) and using the boundary condition given by (16g).
- (7) Compute $\phi_{e,1}$ by integrating (22c) and using the boundary condition given by (16f).
- (8) Compute $\phi_{s,1}$ by integrating (22a) and using the boundary condition that follows from (19) as

$$\phi_{s,1}(x_b) = \phi_{e,1}(x_b) - \eta_1(x_b) - U_1(x_b). \quad (38)$$
- (9) The value of $\phi_{s,1}(x_a)$ represents the external apparent voltage of the cell.

4. Implementation of the Numerical Algorithm

There are two diffusion processes on different time and spatial scales in the model. They are both solved by the implicit Euler scheme of the finite difference method [22] with generally different time steps. In Ω , (1) is solved on a grid of N uniformly spaced nodes x_0, \dots, x_{N-1} and the positions of the individual grid nodes determine their correspondence to the domains Ω_k , $k \in \{1, 2, 3\}$. This grid is also used for numerical integration in the algorithm described in Section 3. For each node $x_i \in \Omega_k$, $k \in \{1, 3\}$, another mesh of M nodes exists that discretizes the interval $[0, R_{s,k}]$, where (6) is solved. The algorithm uses multiple time scales to update the individual quantities. It carries out the diffusion in the solid particles for each x_i with a constant time step Δt . After a given number of time steps, the integral solver is called, which updates the values of j_k for each x_i . For the time period between the updates of j_k , the macroscopic diffusion in the electrolyte governed by (1) and the microscopic diffusion in the spherical particles governed by (6) are completely independent. This allows a suitable multiple of Δt to be used as the time step for the diffusion in the electrolyte.

5. Simulation Results

In this section, we demonstrate the capabilities of our algorithm and investigate its behavior depending on the settings

TABLE I: Model parameters based on literature values [15, 18].

(a) Global parameters				
Parameter	Unit	Value		
t_+^0	[1]	0.363		
F	[C mol ⁻¹]	96487		
T	[K]	298.15		
x_a	[μm]	0		
x_b	[μm]	80		
x_c	[μm]	105		
x_d	[μm]	193		
D_e	[m ² s ⁻¹]	7.5×10^{-10}		
(b) Domain-specific parameters				
Parameter	Unit	Positive electrode Ω_1	Separator Ω_2	Negative electrode Ω_3
k		1	2	3
σ_k	[S m ⁻¹]	100		100
$\epsilon_{f,k}$	[1]	0.025		0.0326
ϵ_k	[1]	0.385	0.724	0.485
brugg _k	[1]	4	4	4
$\alpha_{a,k}$	[1]	0.5		0.5
$\alpha_{c,k}$	[1]	0.5		0.5
$c_{s,max,k}$	[kmol m ⁻³]	51.554		30.555
$R_{s,k}$	[μm]	2		2
K_k	[mol ^{-0.5} m ^{2.5} s ⁻¹]	2.3444×10^{-11}		5.0307×10^{-11}
$D_{s,k}$	[m ² s ⁻¹]	1×10^{-14}		3.9×10^{-14}
$c_{s,k}^0$	[kmol m ⁻³]	$0.4955 \cdot c_{s,max,1}$		$0.8551 \cdot c_{s,max,3}$
$c_{e,k}^0$	[kmol m ⁻³]	1	1	1

of the numerical solver parameters. For all simulations, we use the model parameters taken from [15, 18], as summarized in Table I.

5.1. Single Discharge Cycle. We compare the results of our algorithm to those described in [15, 18]. In Figure 2(a), the evolution of cell voltage during one discharge cycle with low discharge currents (0.5C, 1C) is shown. Our results coincide almost completely with the simulations using the full-order finite difference model by Subramanian et al. [18]. There is also a fair agreement with the results of the simplified and reduced model proposed by Dao et al. [15]. The notable exception is the initial part of the evolution where Dao et al. observe no voltage drop because of loading.

The situation changes for higher discharge currents (2C, 3C, and 4C), as plotted in Figure 2(b). In this case, the results of the simplified model are completely different from ours. Again, the simplified model does not account for immediate voltage drop due to an increased load. On the other hand, the voltage readings at $t = 0$ based on our model form an almost perfectly linear dependence on the applied current, as can be seen in Figure 3. This is in correspondence with the usual representation of battery cells in DC electrical circuits where a constant internal resistance is considered.

The above arguments indicate that the reduced model ceases to be valid for higher currents while our proposed

model continues to provide expected and consistent results (see also the model comparison in [17]). Unfortunately, the results of the full-order model from [18] are not available for currents above 1C, although the authors state that they are able to simulate such situations. The insufficient information contained in the reduced model can also be demonstrated on Li⁺ concentration profiles in the electrolyte. Significant differences occur even for low currents, as can be seen in Figure 4. In Figure 5, the concentration profile comparison with another implementation of the full-order model [3] is provided. Qualitatively, the agreement is satisfactory. However, complete match of the curves could not be achieved due to the lack of information about the model parameters in [3].

5.2. Properties of the Numerical Solver. We are interested in the influence of the numerical solver parameters on the accuracy and speed of the simulation. Several tests were performed, involving the parameters explained in Section 4. As the test vehicle, the voltage curve of a single discharge cycle with various values of the applied current was used.

- (i) We tested several grid resolutions in the spatial domain Ω , ranging from $N = 20$ to $N = 800$. For each value of N , uniform grids from $M = 20$ to $M = 400$ were utilized for diffusion inside the spherical particles. For the 1C applied current and M fixed, the solution is almost independent of the value

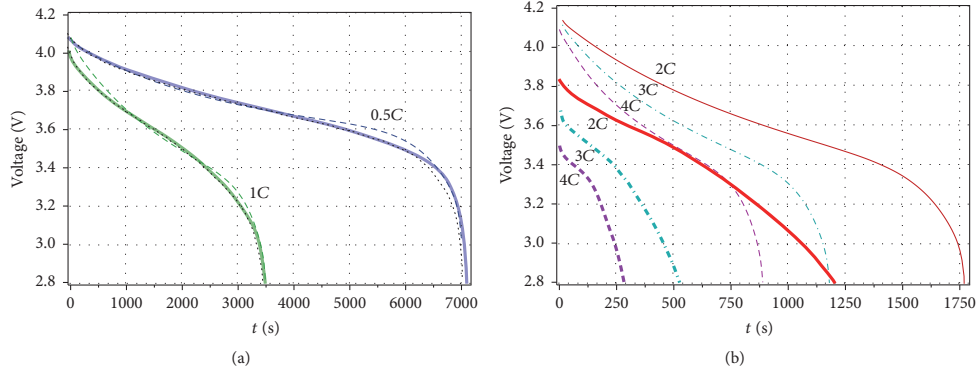


FIGURE 2: Cell voltage evolution during one deep discharge cycle. (a) Discharge currents 0.5C and 1C; comparison of our results (thick solid lines in the background) with Dao et al. ([15], dashed lines) and Subramanian et al. ([18], dotted lines). (b) Discharge currents 2C, 3C, and 4C; comparison of our results (thick lines) with Dao et al. ([15], thin lines). The same line styles correspond to the same discharge current.

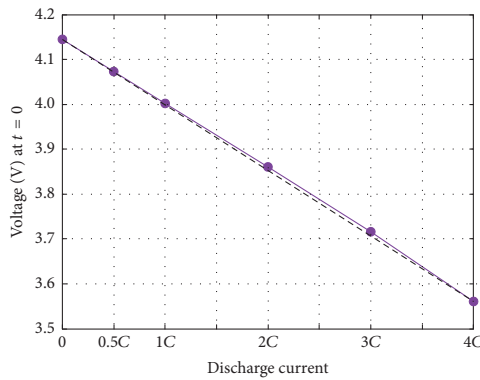


FIGURE 3: The almost perfectly linear dependence of the cell voltage on the applied current. The solid line connects the subsequent data points; the dashed line connects the first and the last point.

of N provided that $N \geq 50$. For different values of M , there are slight differences mostly in the final part of the voltage curve, as demonstrated in Figure 6. As M increases, the differences between the subsequent cases become smaller, which suggests convergence of the numerical method. No rigorous convergence tests (such as measuring the experimental order of convergence [23]) were performed, though. With higher applied currents, the value of N also affects the shape of the voltage curve. For the 2C applied current, the differences in the results become negligible for any combination of M and N satisfying $M > 200$, $N > 200$.

The simulation of the whole 1C discharge cycle with $M = N = 100$, $\Delta t = 10^{-1}$ s, $\omega = 0.05$, and $\vartheta = 10^{-13}$ can be performed in less than 10 seconds on a single core of an Intel i7-6700K @ 4 GHz CPU, which is 350x

faster than the real discharge process on average. Our computational tests indicate that decreasing M and N below approximately 50 nodes (and losing accuracy as seen in Figure 6) is not necessarily beneficial for the computational time.

(ii) As explained in Section 4, the integral solver need not be called in every time step. We performed some computations with a fixed (and unnecessarily small) time step $\Delta t = 10^{-3}$ s. The integral solver was set to be called in the intervals $m \cdot \Delta t$, for several different values of $m \in \mathbb{N}$. In addition, the diffusion in electrolyte was also solved using the time step $m \cdot \Delta t$. All the results were virtually identical. The numbers of iterations of the integral solver for all these cases are summarized in Figure 7. As expected, the number of iterations in both Ω_1 and Ω_3 is higher when the solver is called less frequently because the previous solution is used as the

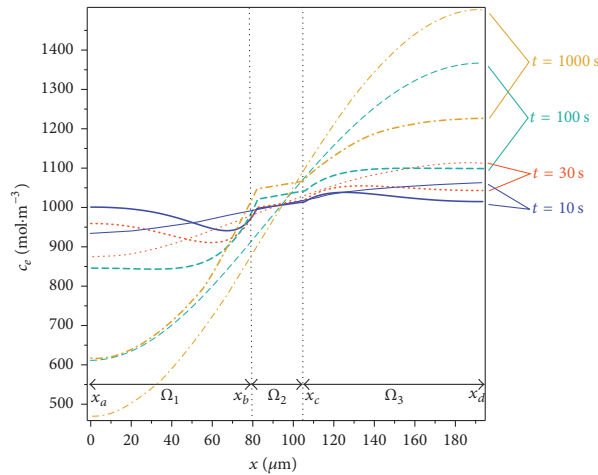


FIGURE 4: Comparison of the spatial profiles of c_e at selected time levels. Thick lines represent our results, thin lines are the results from [15]. The same line styles correspond to the same time t . Discharge current 1C.

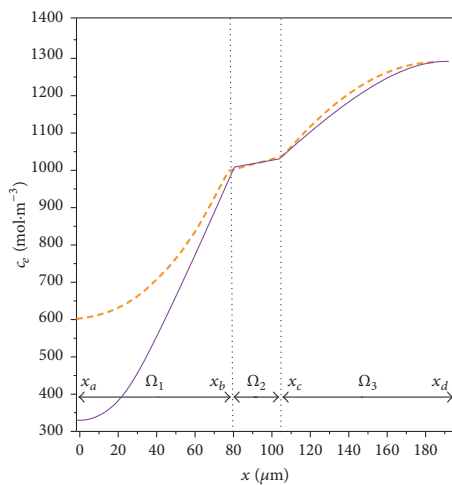


FIGURE 5: Comparison of the spatial profiles of c_e at the end of 1C discharge cycle ($t = 3500$ s). The solid line represents our results; the thick dashed line is the result from [3].

initial guess for the next iteration. In fact, calling the solver in long time steps brings little computational time savings, as demonstrated in Figure 8.

- (iii) Next, the influence of the relaxation parameter ω was investigated. The maximum value of ω sufficient for the convergence of the integral solver depends on the applied current and other settings (e.g., the approximate bounds are $\omega < 10^{-1}$ for 1C discharge

and $\omega < 2 \times 10^{-3}$ for 4C discharge). However, once such value is found, it is undesirable to further decrease ω as it only leads to prolonged computational times. Provided that the integral solver converges, its accuracy is only controlled by the value of ϑ and is independent of the setting of ω .

For long term simulations with other included effects such as battery aging, the basic version of the algorithm has to be stable over extended time periods. We performed a stability test by simulating over 1000 constant current charge/discharge cycles in the prescribed voltage range. The results in Figure 9 testify that the algorithm not only exhibits excellent stability, but also allows long simulations as its computational time is many hundreds of times shorter than the real duration of the simulated processes.

6. Conclusion

We have developed an efficient numerical algorithm for the solution of the full-order version of the well known model of Li-ion cell dynamics, as used by [15, 18]. For low to moderate applied currents, the obtained simulation results are in good agreement with the studies performed in both [15, 18]. For higher discharge rates, our algorithm proves to maintain physically consistent behavior in contrast to the simplified model by [15]. Moreover, its implementation is fast and stable enough to enable cycling simulations over the expected lifetime of the cell. These properties justify the choice of the full-order model for our ongoing efforts to simulate the behavior of both individual cells and battery packs installed in hybrid electric vehicles. The proposed numerical algorithm is a convenient basis for such efforts, as it allows straightforward generalizations in order to incorporate heat effects and aging

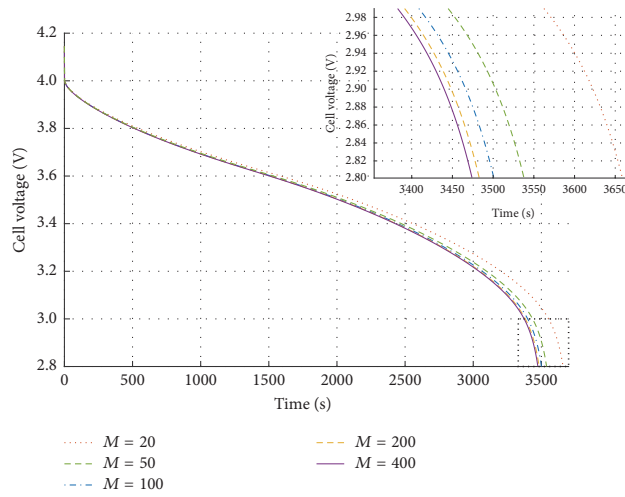


FIGURE 6: The voltage curves for one IC discharge cycle in simulations using different mesh resolutions for the discretization of the spherical particles. The marked region of the plot is zoomed in to better illustrate the differences. $N = 100$, $\Delta t = 10^{-1}$ s, $\omega = 0.05$, and $\vartheta = 10^{-13}$. Integral solver called in every time step.

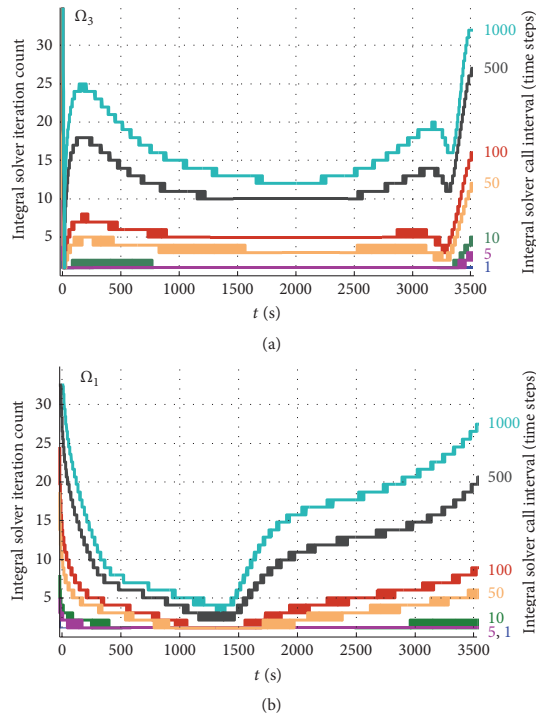


FIGURE 7: The number of iterations of the integral solver depending on the frequency of its calls. Discharge current IC: $N = 100$, $M = 50$, $\Delta t = 10^{-3}$ s, $\omega = 0.05$, and $\vartheta = 10^{-13}$.

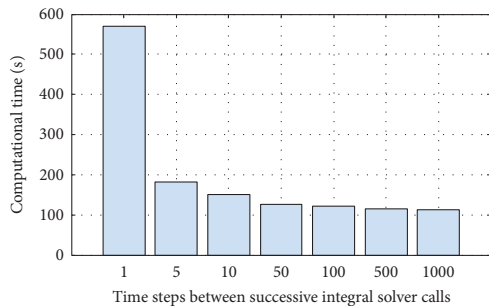


FIGURE 8: Computational times of one discharge cycle depending on the frequency of the calls of the integral solver. Discharge current 1C; time step $\Delta t = 10^{-3}$ s. Computed on an Intel i5-2500 @ 3.3 GHz CPU.

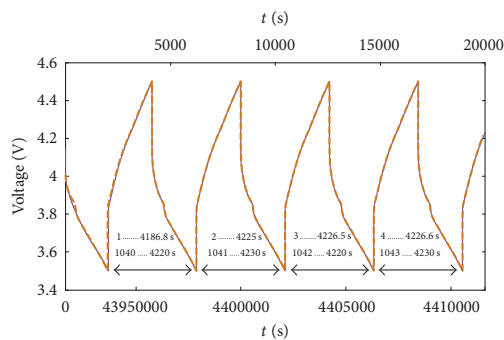


FIGURE 9: Algorithm stability test during 1C constant current discharge/charge cycling within the voltage range from 3.4 V to 4.5 V. A total of 1043 cycles in the physical time period of 4.41×10^6 s (51 days) have been simulated. The voltage curve is plotted by the solid line for the first four cycles and by the thick dashed line for the last four cycles. In addition, the cycle numbers and cycle durations are indicated. Numerical parameters: $N = 100$, $M = 50$, $\Delta t = 10^{-1}$ s, $\omega = 0.05$, and $\vartheta = 10^{-14}$. The integral solver was called in every time step. The computation took less than 3 hours on a single core of an Intel i7-6700K @ 4 GHz CPU.

phenomena in the scope of the models found, for example, in [3, 6–9].

Conflicts of Interest

The authors declare that there are no conflicts of interest regarding the publication of this manuscript.

Acknowledgments

This work has been supported by the Technological Agency of the Czech Republic, *Dynamic Lithium-Ion Battery Management for Hybrid Electric Vehicles*, Project no. TA04021244.

References

- [1] J. Newman and W. Tiedemann, "Porous-electrode theory with battery applications," *AIChE Journal*, vol. 21, no. 1, pp. 25–41, 1975.
- [2] M. Doyle, T. Fuller, and J. Newman, "Modeling of galvanostatic charge and discharge of the lithium/ polymer/insertion cell," *Journal of The Electrochemical Society*, vol. 140, no. 6, pp. 1526–1533, 1993.
- [3] L. Cai and R. E. White, "Mathematical modeling of a lithium ion battery with thermal effects in COMSOL Inc. Multiphysics (MP) software," *Journal of Power Sources*, vol. 196, no. 14, pp. 5985–5989, 2011.
- [4] K. Kumaresan, G. Sikha, and R. E. White, "Thermal model for a Li-ion cell," *Journal of The Electrochemical Society*, vol. 155, no. 2, pp. A164–A171, 2008.
- [5] W. B. Gu and C. Y. Wang, "Thermal-electrochemical modeling of battery systems," *Journal of The Electrochemical Society*, vol. 147, no. 8, pp. 2910–2922, 2000.
- [6] P. Ramadass, B. Haran, P. M. Gomadam, R. White, and B. N. Popov, "Development of first principles capacity fade model for Li-ion cells," *Journal of The Electrochemical Society*, vol. 151, no. 2, pp. A196–A203, 2004.
- [7] P. Ramadass, B. Haran, R. White, and B. N. Popov, "Mathematical modeling of the capacity fade of Li-ion cells," *Journal of Power Sources*, vol. 123, no. 2, pp. 230–240, 2003.
- [8] G. Ning and B. N. Popov, "Cycle life modeling of lithium-ion batteries," *Journal of The Electrochemical Society*, vol. 151, no. 10, pp. A1584–A1591, 2004.
- [9] G. Ning, R. E. White, and B. N. Popov, "A generalized cycle life model of rechargeable Li-ion batteries," *Electrochimica Acta*, vol. 51, no. 10, pp. 2012–2022, 2006.
- [10] V. R. Subramanian, V. D. Diwakar, and D. Tapriyal, "Efficient macro-micro scale coupled modeling of batteries," *Journal of The Electrochemical Society*, vol. 152, no. 10, pp. A2002–A2008, 2005.
- [11] V. R. Subramanian, V. Boovaragavan, and V. D. Diwakar, "Toward real-time simulation of physics based lithium-ion battery models," *Electrochemical and Solid-State Letters*, vol. 10, no. 11, pp. 255–260, 2007.
- [12] B. Bhikkaji and T. Söderström, "Reduced order models for diffusion systems using singular perturbations," *Energy and Buildings*, vol. 33, no. 8, pp. 769–781, 2001.
- [13] K. A. Smith, C. D. Rahn, and C.-Y. Wang, "Model-based electrochemical estimation and constraint management for pulse operation of lithium ion batteries," *IEEE Transactions on Control Systems Technology*, vol. 18, no. 3, pp. 654–663, 2010.
- [14] L. Cai and R. E. White, "Reduction of model order based on proper orthogonal decomposition for lithium-ion battery simulations," *Journal of The Electrochemical Society*, vol. 156, no. 3, pp. A154–A161, 2009.
- [15] T.-S. Dao, C. P. Vyasarayani, and J. McPhee, "Simplification and order reduction of lithium-ion battery model based on porous-electrode theory," *Journal of Power Sources*, vol. 198, pp. 329–337, 2012.
- [16] M. Guo, G. Sikha, and R. E. White, "Single-particle model for a lithium-ion cell: Thermal behavior," *Journal of The Electrochemical Society*, vol. 158, no. 2, pp. A122–A132, 2011.
- [17] S. Santhanagopalan, Q. Guo, P. Ramadass, and R. E. White, "Review of models for predicting the cycling performance of lithium ion batteries," *Journal of Power Sources*, vol. 156, no. 2, pp. 620–628, 2006.

- [18] V. R. Subramanian, V. Boovaragavan, V. Ramadesigan, and M. Arabandi, "Mathematical model reformulation for lithium-ion battery simulations: Galvanostatic boundary conditions," *Journal of The Electrochemical Society*, vol. 156, no. 4, pp. A260–A271, 2009.
- [19] D.-W. Chung, M. Ebner, D. R. Ely, V. Wood, and R. Edwin García, "Validity of the Bruggeman relation for porous electrodes," *Modelling and Simulation in Materials Science and Engineering*, vol. 21, no. 7, Article ID 074009, 2013.
- [20] P. W. C. Northrop, V. Ramadesigan, S. De, and V. R. Subramanian, "Coordinate transformation, orthogonal collocation, model reformulation and simulation of electrochemical-thermal behavior of lithium-ion battery stacks," *Journal of The Electrochemical Society*, vol. 158, no. 12, pp. A1461–A1477, 2011.
- [21] J. Newman and K. E. Thomas-Alyea, *Electrochemical Systems*, Wiley Interscience, 2004.
- [22] V. Thomée, "Finite difference methods for linear parabolic equations," *Handbook of Numerical Analysis*, vol. 1, pp. 5–196, 1990.
- [23] J. R. Rice and M. Mu, "An experimental performance analysis for the rate of convergence of 5-point star on general domains," Tech. Rep., Department of Computer Sciences, Purdue University, 1988.

■ P.7 Kapitola v Handbook of Chemical Mass Transport in the Environment

Tissa H. Illangasekare, Christophe C. Fripiat a Radek Fučík: *Dispersion and mass transfer coefficients in groundwater of near-surface geologic formations*, kapitola v: *Handbook of Chemical Mass Transport in the Environment*, strany 418–456. CRC Press, 2010.

15 Dispersion and Mass Transfer Coefficients in Groundwater of Near-Surface Geologic Formations

Tissa H. Illangasekare, Christophe C. Fripiat, and Radek Fučík

CONTENTS

Part 1	Dispersivity in Soil and the Up-Most Groundwater of Geologic Formations	
15.1	Introduction	414
15.2	Transport Process: Differential Advection	415
15.3	Transport Theory	416
15.3.1	Hydrodynamic Dispersion at the Microscopic Pore Scale	416
15.3.2	Governing Equations	418
15.3.3	Hydrodynamic Dispersion at the Macroscale	419
15.3.4	Upscaling Models for Dispersion Coefficients	420
15.4	Estimation of Transport Parameters	421
15.4.1	Regression Laws to Estimate Dispersivity Coefficients	422
15.4.2	Laboratory Methods for the Determination of Dispersivity	425
15.4.2.1	Methods for Column Tests	425
15.4.2.2	Device for Transverse Dispersivity	426
15.4.3	Field Methods for the Determination of Dispersivity Coefficients	427
15.4.3.1	Natural Gradient Tests	427
15.4.3.2	Forced Gradient Test	428
15.5	Example Calculations	429
15.5.1	Laboratory Estimation of α_L for an Unsaturated Medium Sand	429
15.5.2	Analysis of Single-Well Withdrawal Tests in a 2D Heterogeneous Medium	431
	Literature Cited	433

413

space and the scale of the measurement. Hence, the dispersivity is considered to be scale-dependent.

The outline of the material to be presented is as follows. The physical process that contributes to hydrodynamic dispersion and how the process is parameterized at the macroscopic scale is reviewed. A summary of existing knowledge on the scale dependence of dispersivity is presented. This will be followed by a discussion on how the parameter is estimated in the field using various field testing methods. Finally, two example applications will be presented to demonstrate how this process is modeled.

15.2 TRANSPORT PROCESS: DIFFERENTIAL ADVECTION

Consider two fluids of equal viscosity and equal density. One of the fluids is displacing the other one from a porous medium. Initially, also assume that the flow is one-dimensional. The mean position of the front of the second fluid will evolve according to the mean advective velocity. However, as the displacement progresses, both fluids will mix due to diffusion and mechanical dispersion.

Mechanical dispersion is the tendency for fluids to spread out from the flow lines that they would be expected to follow according to the advective hydraulics of the flow system. This spreading process results from microscopic velocity variations, causing fluid particles to move at various velocities through the tortuous paths of the medium. There are three basic mechanisms producing these pore-scale velocity variations: (1) the variability in pore lengths, which causes fluid elements starting at a given distance from each other and proceeding at the same velocity not to remain the same distance apart, (2) friction along soil grains and viscous shear forces, yielding a smaller velocity at the border of a pore, and a maximum velocity at its center, and (3) the variability in pore sizes, which results in a variability of pore-scale velocity. Mechanical dispersion is a nonsteady and irreversible process, as initial fluid distributions cannot be recovered by reversing the flow direction.

Figure 15.1 describes the classical laboratory column experiment used to determine mechanical dispersion. Steady-state flow is established in a column packed with a homogeneous granular medium. A nonreactive tracer at concentration C_0 [ML^{-3}] is continuously introduced at the upstream end of the column from time t_0 [T]. If the column is initially solute-free, the tracer input can be represented as a step-function (Figure 15.1b). The relative concentration C/C_0 [–] of the column outflow is plotted as a function of time (Figure 15.1c). This type of curve is called a *breakthrough curve*. If there is no mixing of any sort, the plot of C/C_0 is a step change from 0 to 1 at $t = t_m$, where t_m corresponds to advective transport through the column. If the only mixing process taking place is molecular diffusion, sharp concentration gradients will be smoothed out and the plot of C/C_0 will slightly spread. In real situations, mechanical mixing will cause a significantly larger spreading of concentration distributions. An early breakthrough will be observed for $t \ll t_m$ as a result of microscopic velocities larger than the mean velocity. Reciprocally, the concentration distribution will also exhibit a long tail for $t \gg t_m$ due to fluid particles moving along slow-velocity flow lines. When diffusion can be neglected, the plot of C/C_0 is therefore a representation of the pore-scale velocity distribution.

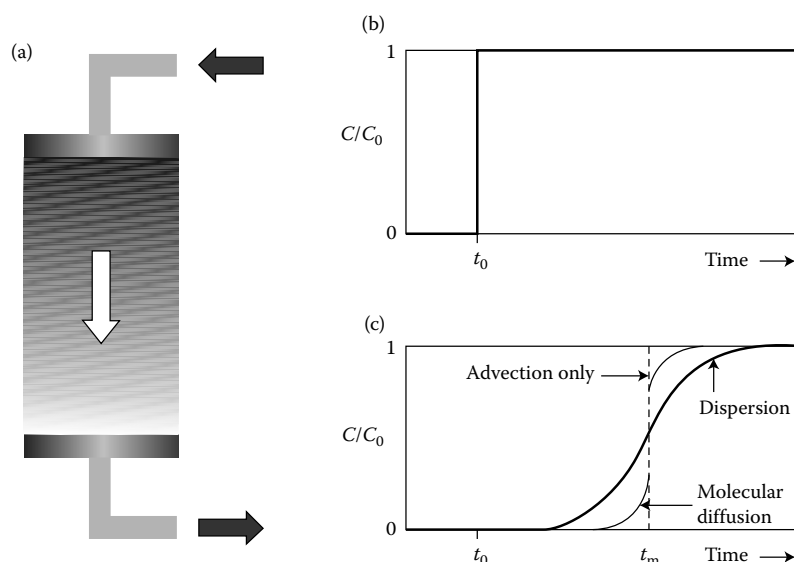


FIGURE 15.1 One-dimensional column experiment: (a) Sketch of the column device; (b) step-function input of tracer; and (c) Relative tracer concentration at column outlet and the effect of advection, diffusion, and dispersion. (After Freeze, A.R. and Cherry, J.A. 1979. *Groundwater*, Upper Saddle River, Prentice Hall, NJ.)

When the transport problem is multidimensional, even if the flow system remains one-dimensional, a solute plume originating from a point source will disperse both longitudinally and transversely to mean flow direction. Transverse dispersion is caused by the fact that the flow paths can split and branch out to the side to bypass soil grains as a fluid flows through a porous medium. This will occur even in the laminar flow conditions that are prevalent in groundwater flow.

15.3 TRANSPORT THEORY

15.3.1 HYDRODYNAMIC DISPERSION AT THE MICROSCOPIC PORE SCALE

As the effect of dispersion is similar to that of diffusion, the dispersive solute flux is classically represented using a diffusion-like or Fickian law:

$$J_m = -\theta D_m \nabla C, \quad (15.1)$$

where J_m [$\text{ML}^{-2}\text{T}^{-1}$] is the dispersive solute mass flux in direction, θ [-] is the volumetric water content, and D_m [L^2T^{-1}] is a fictitious diffusion coefficient called mechanical dispersion. As mechanical dispersion is mathematically analogous to diffusion at the microscopic scale and as both processes cannot be separated from each other in flowing groundwater, they are usually combined into a single parameter called

hydrodynamic dispersion coefficient:

$$D = D_m + D_d, \quad (15.2)$$

where D_d [L^2T^{-1}] an effective diffusion coefficient. In a three-dimensional system, the hydrodynamic dispersion coefficient is a second-order tensor that takes the form

$$D = \begin{bmatrix} D_{xx} & D_{yx} & D_{zx} \\ D_{xy} & D_{yy} & D_{zy} \\ D_{xz} & D_{yz} & D_{zz} \end{bmatrix}, \quad (15.3)$$

In a uniform flow field, if the principal directions of the dispersion tensor are aligned with the principal directions of the velocity flow field, the dispersion coefficient tensor can be reduced to

$$D = \begin{bmatrix} D_L & 0 & 0 \\ 0 & D_{TH} & 0 \\ 0 & 0 & D_{TV} \end{bmatrix}. \quad (15.4)$$

where D_L [L^2T^{-1}] is a longitudinal hydrodynamic dispersion coefficient, and D_{TH} and D_{TV} [L^2T^{-1}] are horizontal and vertical transverse hydrodynamic dispersion coefficients, respectively. When horizontal and vertical transverse dispersion coefficients are equal, one defines $D_T = D_{TH} = D_{TV}$.

The relative contribution of mechanical dispersion and diffusion to solute transport is evaluated using Peclet numbers. A Peclet number is a dimensionless number that relates the effectiveness of mass transport by advection to the effectiveness of mass transport by diffusion or dispersion. Peclet numbers have the general form

$$Pe = \frac{vd}{D_d} \quad \text{or} \quad Pe = \frac{vL}{D_L}.$$

$v = q/\theta$ [LT^{-1}] is the average pore-water velocity and q [LT^{-1}] is the specific discharge of water through the porous medium, or the Darcy velocity. d [L] is a characteristic grain size and L [L] is a characteristic transport distance. For low Peclet numbers, D_L and D_T are both equal to the effective diffusion coefficient. At larger Peclet numbers, longitudinal and transverse coefficients of hydrodynamic dispersion are found to depend strongly on the average pore-scale water velocity. The exact relationship between pore-scale dispersion and velocity can be obtained from theoretical considerations for simple or hypothetical pore systems (Saffman, 1959). Except in the case of very simple conceptual models, one can generally find that the coefficients of hydrodynamic dispersion are linearly related to velocity

$$D_L = D_d + \alpha_L v, \quad (15.5a)$$

$$D_{TH} = D_d + \alpha_{TH} v, \quad (15.5b)$$

$$D_{TV} = D_d + \alpha_{TV} v, \quad (15.5c)$$

where α_L , α_{TH} , and α_{TV} [L] are characteristic lengths called longitudinal dispersivity, horizontal transverse dispersivity, and vertical transverse dispersivity, respectively. Since dispersivities quantify mechanical dispersion resulting from pore-scale velocity variations, they are characteristic properties of a medium. Field-studies have shown that Equations 15.5a through 15.5c are also valid at large scale, for typical groundwater flow conditions. For example, Klotz et al. (1980) investigated a more general relation $D_L = Av^B + D_d$ and found that exponent B should be close to 1. They also showed the dependence of dispersivity to soil sedimentological properties.

Equations 15.5a through 15.5c have been shown to accurately model dispersion in saturated porous media and for a stationary flow in unsaturated media. In transient conditions, however, the relationship between hydrodynamic dispersion coefficients and velocity becomes more complicated. In unsaturated media, the water content of the soil changes with the water flux. Hence, the structure of the water-filled pore space also changes with the water flux. The flow field, and therefore the distribution of pore velocities, depends on the saturation of the medium (Flury et al., 1994). As a consequence, dispersivity coefficients are strongly impacted by the volumetric water content. Usually, dispersivity is found to increase when the water content decreases as a result of the larger tortuosity of solute trajectories and a disconnection of continuous flow paths (Vanclouster et al., 2006). In some cases, especially when the activation of macropores significantly enhances pore-water variability, dispersivity is found to increase with volumetric water content. Currently, there is no unique validated theoretical model available for dispersivity in transient unsaturated flow.

15.3.2 GOVERNING EQUATIONS

Combining advective flux and Fickian hydrodynamic dispersive flux, and applying the principle of mass conservation over a representative elementary volume of soil yields

$$\frac{\partial \theta C}{\partial t} = \nabla \cdot (\theta D \cdot \nabla C - C \cdot q(\theta)), \quad (15.6)$$

where the specific discharge of water through the porous medium depends on the volumetric water content of the medium. Equation 15.6 is the governing equation for solute transport in unsaturated porous media. It is usually referred to as the *advection–dispersion equation* (ADE) or the *convection–dispersion equation*. The initial and boundary value problem obtained by combining the above second-order PDE with the initial concentration distribution in the medium and appropriate boundary conditions is solved to obtain space–time distributions of solute concentrations. It must be noted that specific discharge and volumetric water content to be used in Equation 15.6 must be obtained by separately solving the unsaturated flow equation.

In unsaturated medium, especially at low water content, the liquid phase is not fully connected, and therefore not fully participating to the flow. In such a situation, Equation 15.6 must be augmented by a sink term that accounts for mass exchange by diffusion toward stagnant zones. This type of model is usually referred to as a *mobile–immobile model*, or a *two-region model* (Coats and Smith, 1964; van Genuchten and

Wierenga, 1978).

$$\frac{\partial \theta_m C_m}{\partial t} + \frac{\partial \theta_{im} C_{im}}{\partial t} = \nabla \cdot (\theta_m D \cdot \nabla C_m - C_m \cdot q(\theta_m)), \quad (15.7)$$

where θ_m [–] and θ_{im} [–] are the volumetric fraction of mobile and immobile water, respectively. C_m [ML⁻³] and C_{im} [ML⁻³] are solute concentrations in the mobile and immobile zone respectively. In this case, D refers to hydrodynamic dispersion in the mobile zone. As an additional unknown appears in Equation 15.7, an additional relationship is required to solve the problem. Usually, it comes from the assumption of linear nonequilibrium or rate-limited mass transfer (Coats and Smith, 1964)

$$\frac{\partial C_{im}}{\partial t} = \omega(C_m - C_{im}), \quad (15.8)$$

where ω [T⁻¹] is a mass transfer rate coefficient (see Part 2). A one-dimensional diffusion model can also be used (Rao et al., 1980). Breakthrough curves computed from Equation 15.7 are characterized by a significant tailing and longer times to reach a unit relative concentration as a result of slow diffusion exchange of solutes between the mobile and the immobile zone.

15.3.3 HYDRODYNAMIC DISPERSION AT THE MACROSCALE

The traditional approach to modeling transport in natural formations is to assume that the advection–dispersion equation also holds at large scale. However, field investigations show in a consistent manner that the values of dispersion coefficients derived under laboratory conditions do not apply to large scale transport. Whereas typical values of dispersivity from column experiments range between 0.01 and 0.1 m, values of macroscopic dispersivity (or macrodispersivity) are in general three to four orders of magnitude larger (Gelhar et al., 1992; Lallemand-Barres and Peaudecerf, 1978). It has also been widely observed that field-scale dispersion coefficients increase with distance and with time (Sauty, 1980).

The main key to understanding this scale effects is heterogeneity. Dispersion is an advective process, as it is caused by variations in fluid velocity. However, variations in fluid velocity do not only take place at the pore scale, but also occurs at larger scales, ranging from macroscopic to megascopic. At the field scale, commonly encountered geological structures influence contaminant transport drastically, leading to velocity variations over several orders of magnitude. This includes the effects of stratification and the presence of lenses with higher or lower permeability. At the megascopic scale, differences between geologic formations also cause nonideality in solute transport. As the flow path increases in length, a solute plume can encounter greater and greater variations in the aquifer, causing the variability of the velocity field to increase. Because dispersivity is related to the variability of the velocity, neglecting or ignoring the true velocity distribution (i.e., by replacing the heterogeneous medium by an equivalent homogeneous one) must be compensated for by a corresponding higher apparent (or effective) dispersivity, leading to what is commonly called the scale effect of dispersion.

15.3.4 UPSCALING MODELS FOR DISPERSION COEFFICIENTS

During the past three decades, a number of theoretical studies have been carried out to describe field-scale dispersive mixing as a function of soil heterogeneity and develop upscaling methods for the estimation of macrodispersivities. These upscaling methods can usually be categorized into deterministic or stochastic methods.

Deterministic upscaling methods require the spatial variability of the hydraulic conductivity of the soil to be fully characterized. Flow and transport are solved for a given set of initial and boundary conditions, either using analytical or numerical methods. Macroscopic mixing properties of the heterogeneous medium are then obtained by assuming that the solute plume is migrating in an equivalent homogeneous medium. Historically, deterministic upscaling models turned out to be mostly applied to compute macrodispersion coefficients of perfectly stratified aquifers (Berentsen, 2005, 2007; Guven et al., 1984; Marle et al., 1967; Mercado, 1967).

The idea behind stochastic models is that soil properties cannot be practically fully characterized. To a certain extent, the hydraulic conductivity exhibits random patterns, which result in a statistical uncertainty of concentration distributions. Stochastic analysis enables the variability in flow and transport to be related to the variability and the spatial structure associated to hydraulic properties of the heterogeneous medium considered. Let us define Y as the natural logarithm of the hydraulic conductivity K , and assume that Y is normally distributed. This assumption accommodates the large hydraulic variations that can be found in the field and excludes negative values, which is consistent with the physical requirement that permeability is positive. The distribution of Y is fully characterized by its mean and its covariance function. The covariance function describes the variability of Y , based on two parameters: The variance σ_Y^2 [–] and the correlation length λ [m]. The variance is a measure of the degree of variability of Y , whereas λ quantifies its spatial variability. A large value of λ indicates that Y values are correlated over large distances. On the contrary, a small value of λ indicates that there is no particular spatial structure for Y . λ can therefore be understood as a characteristic length of heterogeneity.

Stochastic upscaling theories are found to be attractive since they allow the estimation of macrodispersion coefficients based on a statistical description of soil heterogeneity. They also allow the demonstration of the scale-dependence of macrodispersion coefficients. For large scale, stochastic theories usually predict the convergence of macrodispersion coefficients toward constant asymptotic values. For example, the asymptotic value of longitudinal macrodispersivity α_L^* for a saturated isotropic medium with $\alpha_L \ll \lambda$ is given by (Dagan, 1984; Gelhar and Axness, 1983)

$$\alpha_L^*(\infty) = \sigma_Y^2 \frac{\lambda}{\gamma^2}, \quad (15.9)$$

where γ [–] is a flow factor accounting for the dependency of effective permeability on dimensionality. In two-dimensional situations, $\gamma = 1$, whereas in three-dimensional situations, $\gamma = \exp(\sigma_Y^2/6)$. It must be noted that Dagan (1984) states that γ should be kept equal to 1 in all situations. Equation 15.9 shows that macrodispersivity is directly linked to the structure of the log-hydraulic conductivity field, and increases when the variability of Y increases. Similar analytical expressions can be obtained

for transverse macrodispersivity α_T^*

$$\alpha_T^*(\infty) = \sigma_Y^2 \frac{\alpha_L + 3\alpha_T}{8} \quad (2D), \quad (15.10a)$$

$$\alpha_T^*(\infty) = \sigma_Y^2 \frac{\alpha_L + 4\alpha_T}{15\gamma^2} \quad (3D), \quad (15.10b)$$

where Equations 15.10a and 15.10b are applicable to two-dimensional (2D) and three-dimensional (3D) plumes, respectively. As for longitudinal macrodispersivity, transverse macrodispersivity is thus found to depend on the dimensionality of the problem considered. Equations 15.10a and 15.10b also show that when local mixing can be neglected, heterogeneity does not produce any macroscale transverse spreading. Gelhar and Axness (1983) have computed exact expressions for α_L^* and α_T^* under various conditions. Time-dependent analytical solutions of α_L^* in two- and three-dimensional isotropic media are given by Dagan (1988). Other authors have derived analytical expressions in other specific cases (see the reviews by Dagan, 1989; Gelhar, 1993; Rubin, 2003). Stochastic theories are typically limited to $\sigma_Y^2 \ll 1$ and to situations where λ is much smaller than the scale of the problem.

The authors have also applied stochastic methods to situations where hydraulic conductivity is not log-normally distributed. Rubin (1995) and Stauffer and Rauber (1998) propose analytical expressions for macrodispersion coefficients in aquifers made of two materials of different hydraulic conductivity. Stochastic methods have also been applied to situations where heterogeneity cannot be characterized using a single finite correlation scale (Di Federico and Neuman, 1998; Rajaram and Gelhar, 1995; Zhan and Wheatcraft, 1996).

Most of the results presented above are related to solute transport in saturated heterogeneous media. In the vadose zone, the variability in water saturation usually contributes to enhance the variability in water velocity, and therefore solute spreading (Russo, 1998). However, it has been shown that macrodispersion coefficients for solute transport in unsaturated soils characterized by strong stratification are usually smaller than saturated values, especially at low water content (Harter and Zhang, 1999).

15.4 ESTIMATION OF TRANSPORT PARAMETERS

Although the theoretical studies reported in previous section have generated some important answers to key questions regarding scale effects, the estimation of dispersivities from the practitioner's point of view still faces a lot of difficulties. Stochastic upscaling methods for dispersivities require a significant amount of data to determine the statistical characteristics of hydraulic conductivity variations for a given site. Considering the costs of field investigation, it is generally rare to find a site that has enough data points for this kind of statistical evaluation.

Currently, the only practically viable method to obtain a priori estimates of dispersivities is by means of empirical approaches, which are based on regression curves fitted on dispersivity data. In this section, major compilations of existing data on

[mm] or coefficient of uniformity $C_u = d_{60}/d_{10}$ [–]. Mean grain size and uniformity of grain size are usually considered as the two most important factors affecting grain size. For relatively uniform materials, dispersivity is directly proportional to median grain size. For less uniform materials, the shape of the particle size distribution is the dominant factor for dispersivity and α_L is directly proportional to the coefficient of uniformity. Dispersivity is also found to be inversely proportional to porosity.

In unsaturated media, the estimation of pore-scale dispersivity is complicated by its additional dependence on the saturation degree S_w [–]. The saturation degree is the volume of water per unit pore volume of the medium. It is usually related to the capillary pressure. In an isolated unsaturated soil pore, a curved interface appears between air and water phases and a pressure difference exists across the interface. This pressure difference depends on the interfacial forces between air and water and on the radius of the pore. Following standard conventions, the capillary pressure is defined as the difference between the pressure in the air phase and in the water phase. At the continuum scale, there exists a relationship between capillary pressure and the saturation of the porous medium. A porous medium consists of a distribution of pores with different radii. If an increasing macroscopic capillary pressure is applied to a porous media, the air phase would invade the larger pores and the water phase would be present in smaller pores. The larger sized pores could not support the capillary pressure and would release water. Thus, the larger the capillary pressure, the smaller amount of water will be present in the porous medium. The relationship between capillary pressure and the water phase content is referred to as the capillary pressure curve or the retention function, which is an intrinsic property of a porous medium. A well-known model for the retention function of a porous medium is the model of van Genuchten (van Genuchten, 1980, 1991). It is characterized by two parameters a^* [cm^{-1}] and n^* [–]. a^* is related to the threshold capillary pressure required to start draining the porous medium. Hence, it is also related to the smallest pore size of the medium. n^* is related to the distribution of pore size. A small value of n^* reflects a large distribution of pore size, while a small value of n^* would apply to a relatively uniform porous medium (Lu and Likos, 2004). In the model of Sato et al. (2003), the pore-scale dispersivity is expressed as a function of the van Genuchten parameters and as a function of effective saturation degree (see Table 15.1). The effective saturation degree S_{we} [–] links with the saturation degree using $S_{we} = (S_w - S_{wr}) / (1 - S_{wr})$, where S_{wr} [–] is the residual saturation degree. The longitudinal dispersivity tends to increase when the saturation of the medium decreases. For example, the equations provided by Haga et al. (1999) reported in Table 15.1 predict that dispersivity is 1.8 times larger at a saturation degree of 80% as compared to full saturation, 4.3 times larger at a saturation degree of 60%, and 15.2 times larger at a saturation degree of 40%.

Figure 15.2 shows one of the most recent compilations of longitudinal dispersivity values in field-scale saturated-flow situations. The trend for α_L to increase with scale L is relatively clear. Field data typically range between 0.01 m and 5500 m at scales of 0.75 m to 100 km. Also, the values for porous (unconsolidated) and fractured (consolidated rock) media tend to scatter over a similar range. At a given scale, the longitudinal dispersivity typically ranges over 2–3 orders of magnitude. This degree of variation can be explained in terms of stochastic macrodispersion theories presented in Section 15.3.3. When the reliability of the data is accounted for, the scale dependence

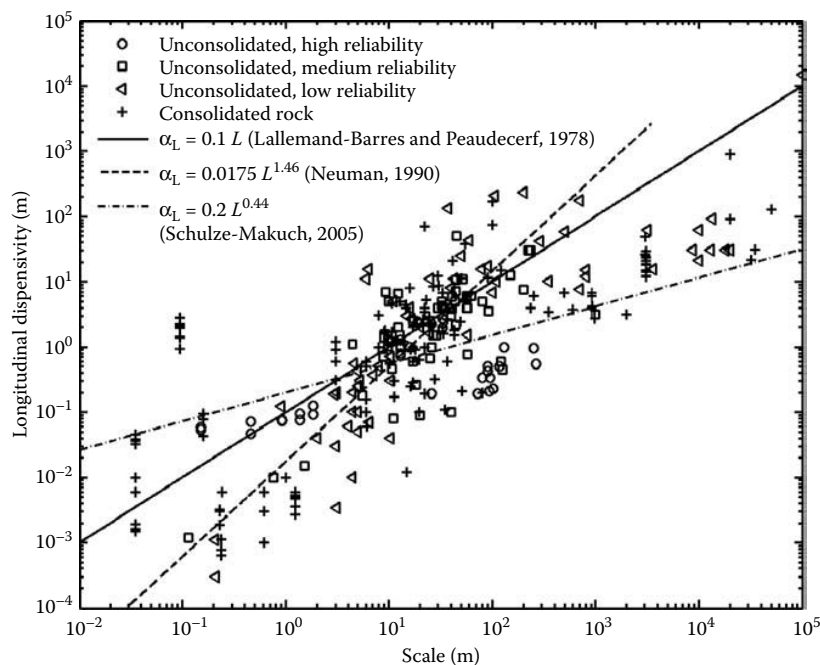


FIGURE 15.2 Field-scale longitudinal dispersivity coefficients as a function of scale. [Adapted from Schulze-Makuch, D. 2005. Longitudinal dispersivity data and implications for scaling behavior. *Ground Water* 43(3): 443–456.]

of longitudinal dispersivity is less obvious: There are no high-reliability points at scales larger than 300 m. This reflects the fact that large-scale α_L values are almost exclusively obtained from contamination plume simulations or environmental tracer studies. As large-scale controlled tracer experiments require a very long period of time, such experiments have not been conducted.

Scaling relationships for longitudinal dispersivities are usually described using power laws of the form

$$\alpha_L = cL^d, \quad (15.11)$$

where c [L^{1-d}] is a characteristic property of the medium and d [–] a scaling exponent. Early attempts to fit a regression law on compiled field data yielded a simple rule $\alpha_L = L/10$ (Lallemand-Barres and Peaudecerf, 1978). Later, Neuman (1990) found $\alpha_L = 0.175 L^{1.46}$, valid for $L < 3500$ m. He also fitted two separate regression lines for $L < 100$ m and $L > 100$ m. He found $\alpha_L = 0.0169 L^{1.53}$ for $L < 100$ m and $\alpha_L = 0.32 L^{1.83}$ for $L > 100$ m. Recently, Schulze-Makuch (2005) performed regressions on field data accounting for their reliability. He found $\alpha_L = 0.2 L^{0.44}$

using high-reliability dispersivity data only for unconsolidated sands. He also established regression laws for consolidated rocks of various types. Other authors have also provided other regression laws (Arya, 1986; Xu and Eckstein, 1995).

Gelhar et al. (1992) caution users routinely adopting α_L values from Figure 15.2 or from a linear representation of the data. Instead, users should favor the use of dispersivity values in the lower half of the range at any given scale. If values in the upper part of the range are adopted, excessively large dilution may be predicted and the environmental consequences misrepresented.

Field data on transverse dispersivity are relatively scarce, and available data are generally of a lower reliability compared to longitudinal dispersivity. Only Gelhar et al. (1992) provide a compilation of α_{TH} and α_{TV} values, but they do not provide regression laws. Typically, values of α_{TH} are found to be about one order of magnitude smaller than α_L , while values of α_{TV} are about two orders of magnitude smaller than α_L . The smaller values of α_{TV} reflect the roughly horizontal stratification of hydraulic conductivity in permeable sedimentary materials. Small α_{TV} values also imply that contaminant plumes will potentially show very limited vertical mixing with high concentrations at given horizons. The trend for transverse dispersivity coefficients to increase with scale is usually less clear due to the low reliability of larger-scale data, generally based on contaminant events, for which sources are ill-defined.

15.4.2 LABORATORY METHODS FOR THE DETERMINATION OF DISPERSIVITY

15.4.2.1 Methods for Column Tests

Pore-scale longitudinal dispersivity can be determined in the laboratory using columns packed with the porous media under investigation. The device is similar to that depicted in Figure 15.1 for saturated flow experiments. Under unsaturated flow conditions, flow boundary conditions must be adapted. Usually, the column is placed vertically, with an irrigation system on top, imposing a constant discharge. One appropriate analytical solution to the advection-equation is (Kreft and Zuber, 1978)

$$\frac{C}{C_0} = \frac{1}{2} \operatorname{erfc} \left(\frac{L - vt}{2\sqrt{D_L t}} \right) + \frac{1}{2} \exp \left(\frac{vL}{D_L} \right) \operatorname{erfc} \left(\frac{L + vt}{2\sqrt{D_L t}} \right), \quad (15.12)$$

where, in unsaturated conditions, $v = v(\theta)$ and $D_L = D_L(\theta)$. erfc is the complementary error function. It assumes as initial condition $C(x, 0) = 0$, and as boundary conditions $C(0, t) = C_0$ and $C(\infty, t) = 0$. Fitting of this solution (e.g., using a least-square criterion) onto observed breakthrough curves allows the simultaneous determination of D_L and v .

For high Peclet numbers, the second term in Equation 15.12 can be neglected. Rewriting this equation for saturated conditions using the number of pore volumes $U = vt/L$ [–] as temporal variable yields

$$\frac{C}{C_0} = \frac{1}{2} \operatorname{erfc} \left(\frac{1 - U}{2\sqrt{\frac{U D_L}{vL}}} \right). \quad (15.13)$$

This equation has several properties that render the estimation of v and D_L easier: The plot of the outlet concentration curve as a function of $J = (U - 1)/\sqrt{U}$ corresponds to a normal probability distribution with a mean $\mu_J = 0$ and a standard deviation $\sigma_J = \sqrt{2D_L/vL}$. The plot C/C_0 versus J on normal probability paper should therefore be linear. The mean pore velocity is estimated using $v = L/t_m$, t_m corresponding to $C/C_0 = 0.5$. The value of D_L is found from

$$D_L = \frac{vL}{8}(J_{0.84} - J_{0.16})^2, \quad (15.14)$$

where $J_{0.16}$ and $J_{0.84}$ are the values of J corresponding to 16% and 84% of relative concentration, respectively.

This method is typically valid when effluent concentrations are measured. When using a measurement device that allows the measurement of pore-water concentrations, other boundary conditions apply to the advection equation and Equation 15.12 is not valid anymore (Kreft and Zuber, 1978; van Genuchten and Parker, 1984). Attention must also be paid to experimental artifacts arising from specific laboratory devices. For example, if injection is performed in a volume of water outside of the column (like a device to maintain the piezometric head), the actual injection condition is not an instantaneous step variation. Due to mixing with the volume of water, the injection is actually exponential. Not accounting for such effects can result in a serious bias in the estimated values of dispersivity (Novakowski, 1992).

15.4.2.2 Device for Transverse Dispersivity

Existing methods to estimate transverse dispersion are usually based either on tracer tests or on dissolution tests. Dissolution tests generally imply groundwater flow along a stagnant zone containing constant concentration gas (Klenk and Grathwohl, 2002; McCarthy and Johnson, 1993), NAPL (Oostrom et al., 1999a; 1999b; Pearce et al., 1994) or solid (Delgado and Guedes de Carvalho, 2001; Guedes de Carvalho and Delgado, 1999; 2000). Transverse dispersivity can then be inferred from the rate of dissolution of the third phase that is obtained through solute breakthrough curve measurements at the laboratory model outlet.

Most of laboratory tracer tests designed to determine transverse dispersion coefficients are performed in a uniform flow at constant mean velocity. Blackwell (1962), Hassinger and von Rosenberg (1968), and recently Frippiat et al. (2008) used the so-called “annulus-and-core” approach, in which the inlet and the outlet cross-sections of a column are divided into two concentric zones. The concentration of the solution flowing in the inner inlet zone (the core) is rapidly increased, while the solution in the outer inlet zone (the annulus) is kept solute-free. Transverse dispersivity is computed by comparing steady-state concentration of effluent solutions in the outlet annulus and core zones. Divided inlets were also adopted in several other column studies involving intrusive local concentration measurements (Bruch, 1970; Grane and Gardner, 1960; Han et al., 1985; Harleman and Rumer, 1963; Perkins and Johnston, 1963; Zhang et al., 2006). Other authors preferred point injection (Pisani and Tosi, 1994; Robbins, 1989). A few specific devices imply nonuniform flow: Cirpka and Kitanidis (2001) and Benekos et al. (2006) investigate flow and transport in a helix and in a cochlea

to determine transverse dispersivity. Kim et al. (2004) determined local longitudinal and transverse dispersivities in a laboratory aquifer model with a local recharge zone.

15.4.3 FIELD METHODS FOR THE DETERMINATION OF DISPERSIVITY COEFFICIENTS

In theory, velocity and dispersivities can be estimated from virtually any test where tracer is added in a controlled way to the groundwater. However, a few standard tests are generally preferred because simple procedures are available to interpret the results. The choice of which test configuration to adopt then results from practical or economical constraints, from the duration of test, to the number of observation wells, to the spatial scale to investigate.

Standard tracer tests are typically used at relatively small field scales. Estimates of dispersivity at scales larger than several hundred of meters usually rely on different methods, either using historical contamination data or exploiting natural variations in the chemistry of natural recharge of the aquifer. However, estimates of advection and dispersion based on data from contaminant plumes or environmental tracer measurements are less reliable than field tracer tests, since there is a larger uncertainty in the location and the intensity of source zone. Often, there is also an inadequate number of sampling points.

15.4.3.1 Natural Gradient Tests

The natural gradient test involves monitoring a small volume of tracer as it moves down the flow system. The resulting concentration distributions provide the data necessary to determine advective velocities, dispersivities, but also chemical parameters. This type of test is usually considered to be of a high reliability. When the test is performed in a supposedly homogeneous formation using a fully penetrating well, a two-dimensional analytical solution of the advection–dispersion equation can be used (Domenico and Schwartz, 1997):

$$\frac{C}{C_0} = \frac{V/b}{4\pi t \sqrt{D_L D_T}} \exp\left(-\frac{(x-vt)^2}{4D_L t} - \frac{y^2}{4D_T t}\right), \quad (15.15)$$

in which it is assumed that the injection well is located at the origin of the coordinate system and that velocity is constant and aligned with the x -axis. V [L^3] is the volume of tracer solution injected and b [L] is the thickness of the aquifer. When the injection well is screened on a very small portion of its length, the three-dimensional solution of the advection–dispersion equation must be used (Domenico and Schwartz, 1997):

$$\frac{C}{C_0} = \frac{V}{8(\pi t)^{3/2} \sqrt{D_L D_{TH} D_{TV}}} \exp\left(-\frac{(x-vt)^2}{4D_L t} - \frac{y^2}{4D_{TH} t} - \frac{z^2}{4D_{TV} t}\right). \quad (15.16)$$

Dispersivity coefficients can be estimated by fitting Equation 15.15 or 15.16 on concentration data monitored in observation wells. Other analytical solutions are also available when the lateral extent of the source cannot be neglected or for sorbing or decaying tracer species (see, e.g., Domenico and Schwartz, 1997).

15.4.3.2 Forced Gradient Test

Forced gradient tests are conducted using injection and/or pumping wells, locally increasing hydraulic gradients at levels significantly larger than those naturally occurring in aquifers. The advantage is that test duration is greatly diminished. Compared to a natural gradient test of the same duration, the tested volume of the aquifer is also usually larger. As a result, due to the unavoidable heterogeneity of the soil, dispersivities obtained from forced-gradient tests are also usually larger than the values obtained from natural gradient tests performed in the same aquifer (Fernandez-Garcia et al., 2005; Tiedeman and Hsieh, 2004).

15.4.3.2.1 Single-Well Injection or Withdrawal Test

The single-well injection test involves pumping at a constant rate. In case an observation well is located close to the injection well, observed concentrations during the injection phase can be fitted using (Gelhar and Collins, 1971)

$$\frac{C}{C_0} = \frac{1}{2} \operatorname{erfc} \left(\frac{r^2 - R^{*2}}{\left(\frac{16}{3} \alpha_L (R^{*3} - r_w^3) \right)^{1/2}} \right), \quad (15.17)$$

R^* [L] being the mean radial position of the tracer front

$$R^* = \sqrt{\frac{Qt}{\pi b \theta}}, \quad (15.18)$$

and r [L] is the radial position from the injection well, r_w [L] is the radius of the well, Q [L^3T^{-1}] is the injection rate and b [L] the thickness of the aquifer. Values of longitudinal dispersivity determined using this type of test are usually considered to be relatively reliable (Gelhar et al., 1992).

In the single-well withdrawal test, a radially converging steady-state flow field is established by pumping at a constant rate in a well. A fixed amount of tracer is injected in a second well. A solute plume develops and starts to migrate toward the pumping well. Analytical solutions for concentration in the pumping well under such conditions are not straightforward to evaluate and often imply semianalytical expressions with power series (Chen, 1999; Moench, 1989). Simplified solutions are given by Sauty (1980), and Welty and Gelhar (1994). One of the advantages of the single-well withdrawal test is that it allows the simultaneous estimation of longitudinal and transverse dispersivities. However, since the converging flow field tends to counteract spreading due to longitudinal dispersion, α_L estimates are thought to be of a lower reliability.

15.4.3.2.2 Single-Well Push–Pull Test

This type of test involves two distinct flow phases. First, tracer is injected in a well at a constant flow rate. The tracer is moving radially from the well. After a certain period of injection, flow is reversed and the tracer is pumped out of the soil at the same

rate. The tracer is moving radially toward the pumping well. The single-well push-pull test does not require any observation well: Concentrations are monitored at the well during the recovery phase. Measured data can be analyzed using the analytical solution developed by Gelhar and Collins (1971):

$$\frac{C}{C_0} = \frac{1}{2} \operatorname{erfc} \left(\frac{\frac{V_p}{V_i} - 1}{\left(\frac{16}{3} \frac{\alpha_L}{R^*} \left[2 - \left(1 - \frac{V_p}{V_i} \right)^{3/2} \right] \right)^{1/2}} \right). \quad (15.19)$$

where V_i [L^3] is the total volume of water injected in the aquifer during the first phase, and $V_p = V_p(t)$ [L^3] is the volume of water withdrawn from the aquifer at time t of phase 2.

The single-well push-pull test is a small-scale test and is generally found to have a limited applicability in estimating macrodispersivities. The dispersion process in a single-well push-pull test is significantly different from that of unidirectional flow: Macrodispersion near the injection well results from differential advection caused by vertical variations in hydraulic conductivity. As a result, the tracer travels at different velocities as it radiates outwards. But it will also travel with the same velocity pattern as it goes back to the production well. This means that the mixing process is partially reversible and that the dispersivity might be underestimated compared to that of unidirectional flow.

15.4.3.2.3 Two-Well Tracer Test

In the two-well test, water is pumped from one well and injected into the other at the same rate to create a steady-state flow regime. The tracer is added in the injection well and monitored in the withdrawal well. Also, dispersivity estimates can be improved by adding more observation wells between the pumping-injection doublets. In general, these tests can be performed over several hundreds of meters in sandy formations. Analytical solutions are provided by Grove and Beetem (1970) and Maloof and Protopoulos (2001).

Dirac input should be preferred rather than step input. A potential problem with the step input test configuration is that the breakthrough curve is not strongly influenced by dispersion except in the early stages, when concentrations are low. For this reason, tests based on this approach are generally considered to produce low-reliability dispersivity data.

15.5 EXAMPLE CALCULATIONS

15.5.1 LABORATORY ESTIMATION OF α_L FOR AN UNSATURATED MEDIUM SAND

Problem description: Figure 15.3 shows the results of two one-dimensional laboratory test performed by Sato et al. (2003). The porous medium consists of a

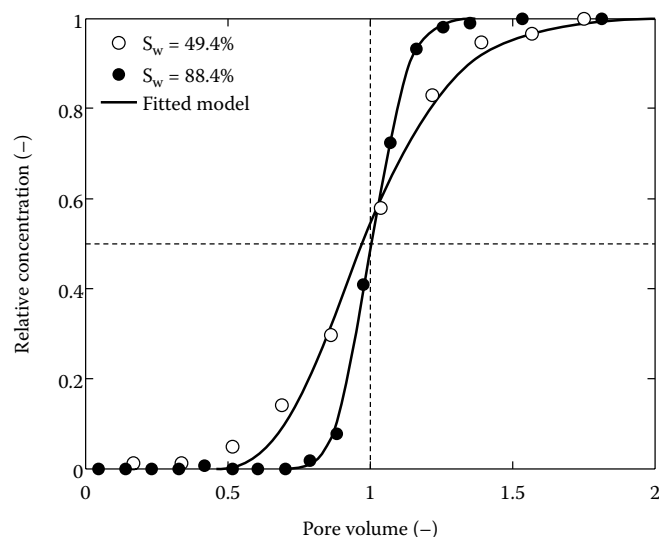


FIGURE 15.3 Experimental breakthrough curves for Toyoura sand and fitted solutions of the advection–dispersion equation. (After Sato, T., Tanahashi, H. and Loaiciga, H.A. 2003. Solute dispersion in a variably saturated sand. *Water Resources Research* **39**: doi: 10.1029/2002WR001649.)

repacked sample of Toyoura sand, a medium sand characterized by a median grain size $d_{50} = 180 \mu\text{m}$ and van Genuchten parameters $a^* = 0.036 \text{ cm}^{-1}$ and $n^* = 4.2$. The column has an internal diameter of 5 cm and a length of 12 cm. Steady-state unsaturated flow was established by injecting water at the top of the column at a constant rate and draining water at the bottom of the column. Controlled air suction was applied at the bottom of the column to suppress boundary effects and establish a constant vertical profile of water content through the column. Two tests are reported: Test 1 was performed at a saturation of $S_w = 49.4\%$, and Test 2 was performed at a saturation of $S_w = 88.4\%$. A pore-water velocity of 0.5 cm/min was used for each test.

Question: Determine experimental values of longitudinal dispersivity from the time series of concentration recorded during each column test.

Solution: For a homogeneous medium with a constant saturation degree, Equation 15.12 can be used to analyze the experimental data. Fitting of this equation to the data (e.g., by minimizing the sum of the squared residuals between the equation and the data) yields experimental dispersivity values of $\alpha_L = 0.4 \text{ cm}$ and $\alpha_L = 0.06 \text{ cm}$ for Test 1 and Test 2, respectively. The corresponding column Peclet numbers are $Pe = 30$ and $Pe = 195$ for Test 1 and Test 2, respectively. These values are large, so the use of Equation 15.13 instead of Equation 15.12 yields relatively similar results. Using the van Genuchten parameters of the saturation curve, the value of parameter a was used in the empirical law established by Sato et al. (2003) is $a = 0.066$ (see Table 15.1). The empirical values of longitudinal dispersivity are then 0.27 cm

and 0.08 cm for Test 1 and Test 2 respectively, which is reasonably close to actual values.

15.5.2 ANALYSIS OF SINGLE-WELL WITHDRAWAL TESTS IN A 2D HETEROGENEOUS MEDIUM

Problem description: Chao et al. (2000) carried out intermediate-scale tracer experiments in a two-dimensional horizontal laboratory tank (244 cm × 122 cm × 6.35 cm). The tank was packed with five different sands, in order to create a heterogeneous medium with well-defined statistical properties. The sands used were crushed silica sands. The heterogeneous packing was designed to simulate a lognormal distribution of saturated hydraulic conductivity (K) using five different sands. The resulting $\ln K$ distribution had a mean value of 4.75, a variance of 1.81, and an isotropic correlation length of 10 cm (Figure 15.4). Convergent tracer tests were performed, using potassium bromide as a conservative tracer. A total of 36 tracer tests were carried out, in order to investigate the effect of (1) pumping rate; (2) distance between injection well and pumping well; and (3) direction between injection well and pumping well.

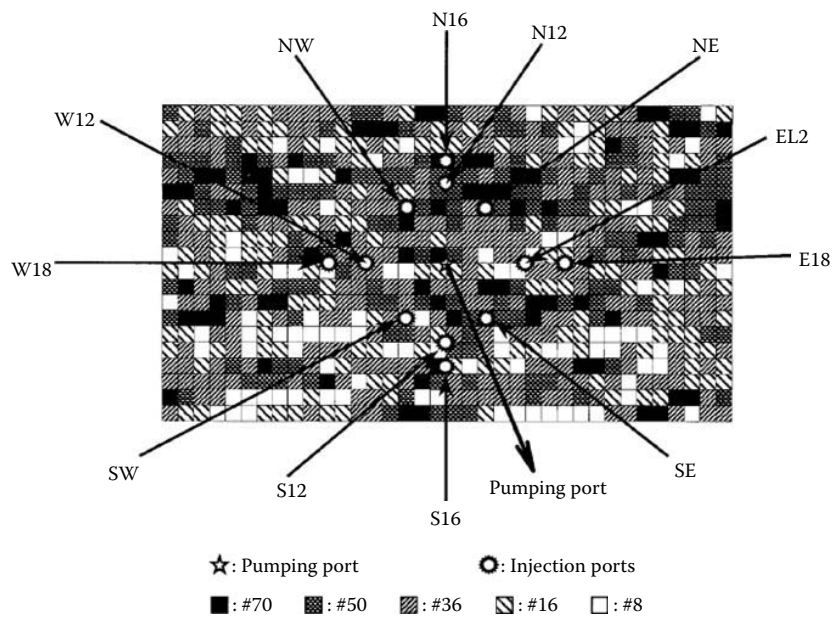


FIGURE 15.4 Experimental representation of the two-dimensional laboratory tank, showing the heterogeneous pattern of the hydraulic conductivity field and the locations of injection and pumping ports. Each block has dimensions of 6.1 × 6.1 cm. The sands are referred to using their respective sieve size. (From Chao, H.-C., Rajaram, H., and Illangasekare, T.H. 2000. *Water Resources Research* 36(10): 2869–2884. With permission.)

Question: Determine experimental values of longitudinal dispersivity from the time series of concentration recorded during each tracer test.

Solution: The breakthrough curves from the tracer tests were analyzed using a two-dimensional analytical solution provided by Welty and Gelhar (1994):

$$\frac{C}{C_0} = \frac{V}{2\pi\theta bR^2 \sqrt{\frac{16\pi\alpha_L}{3R} \left(1 - \left|1 - \frac{t}{t^*}\right|^{3/2}\right)}} \exp\left(\frac{-\left(1 - \frac{t}{t^*}\right)^2}{\frac{16\alpha_L}{3R} \left(1 - \left|1 - \frac{t}{t^*}\right|^{3/2}\right)}\right) \quad (15.20)$$

where R [L] is the radial distance between the injection well and the pumping well. The mean transit time t^* [T] can be computed using Equation 15.18. A least-square criterion was adopted to determine α_L by fitting Equation 15.20 onto experimental data. As summarized in Table 15.2, the dispersivity estimates ranged from 0.065 to 0.953 cm. The high variability of α_L reflects the variability of the hydraulic conductivity field. Even at the same scale, different tracer tests in the same heterogeneous medium yield widely different estimates of transport parameters. The estimated dispersivities at the same scale varied by a factor of 2–6.

Chao et al. (2000) also performed a one-dimensional tracer test in their tank. They obtained a longitudinal dispersivity of 12.0 cm. The theoretical value computed using Equation 15.9 is 18.1 cm. Several factors account for this discrepancy:

TABLE 15.2
Dispersivity (cm) Estimates from Radial Flow
Tracer Experiments

Injection Port	Radius (cm)	$Q = 25$ mL/min	$Q = 50$ mL/min	$Q = 75$ mL/min
NE	25.4	0.207	0.201	0.140
NW	25.4	0.182	0.245	0.146
SE	25.4	0.116	0.109	0.065
SW	25.4	0.329	0.370	0.399
E12	30.4	0.362	0.363	0.485
W12	30.4	0.439	0.333	0.225
S12	30.4	0.392	0.465	0.369
N12	30.4	^a	0.482	0.499
E18	45.7	0.741	0.567	0.395
W18	45.7	0.658	0.777	0.953
S16	40.6	^a	^a	^a
N16	40.6	0.368	0.439	0.303

Source: From Chao, H.-C., Rajaram, H., and T.H. Illangasekare. 2000. *Water Resources Research* 36(10): 2869–2884. With permission.

^a Unreliable data.

- Dispersivity is actually scale-dependent, and the theoretical value computed using Equation 15.9 is a large-scale asymptotic value, whereas the experimental value corresponds to a finite displacement of about 22 correlation lengths.
- The presence of lateral no-flow boundaries tends to decrease the overall variability of flow, and therefore the macroscale value of dispersivity.
- The tracer test was carried out in a single realization of the heterogeneous hydraulic conductivity field. There are number of other realizations satisfying the same statistical properties, each potentially yielding different α_L values. Since Equation 15.9 yields a theoretical value that represents the average over all possible realizations of the K field, one could expect the value of a single realization to be different.

The main reason for the discrepancy between the one-dimensional tracer test and the radial tracer test lies in the dimension of the source zone. One-dimensional tracer tests are characterized by a large source zone (i.e., the full cross-section of the medium), whereas convergent tracer tests have a point source. In the latter case, solute plumes do not sample the full variability of aquifer properties, and therefore undergo smaller dispersion processes. This mostly highlights that, even if theories are available to predict macroscale dispersion coefficients, they are bounded to certain limitations which could make them unsuited to given situations.

LITERATURE CITED

- Arya, A. 1986. Dispersion and reservoir heterogeneity. PhD dissertation. University of Texas at Austin.
- Benekos, I.D., Cirpka, O.A. and P.K. Kitanidis. 2006. Experimental determination of transverse dispersivity in a helix and a cochlea. *Water Resources Research* 42: W07406, doi:10.1029/2005/WR004712.
- Berentsen, C.W.J., Verlaan, M.L. and C.P.J.W. van Kruijsdijk. 2005. Upscaling and reversibility of Taylor dispersion in heterogeneous porous media. *Physical Review E* 71: doi: 10.1103/PhysRevE.71.046308.
- Berentsen, C.W.J., van Kruijsdijk, C.P.J.W. and M.L. Verlaan. 2007. Upscaling, relaxation and reversibility of dispersive flow in stratified porous media. *Transport in Porous Media* 68: 187–218.
- Blackwell, R.J. 1962. Laboratory studies of microscopic dispersion phenomena. *Society of Petroleum Engineers Journal* 2(1): 1–8.
- Bromly, M., Hinz, C., and L.A.G. Aylmore. 2007. Relation of dispersivity to properties of homogeneous saturated repacked soil columns. *European Journal of Soil Science* 58: 293–301.
- Bruch, J.C. 1970. Two-dimensional dispersion experiments in a porous medium. *Water Resources Research* 6(3): 791–800.
- Chen, J.-S., Liu, C.-W. and C.-M. Liao. A novel analytical power series solution for solute transport in a radially convergent flow field. *Journal of Hydrology* 266: 120–138.
- Chao, H.-C., Rajaram, H. and T.H. Illangasekare. 2000. Intermediate-scale experiments and numerical simulations of transport under radial flow in a two-dimensional heterogeneous porous medium. *Water Resources Research* 36(10): 2869–2884.

- Cirpka, O.A. and P.K. Kitanidis. 2001. Theoretical basis for the measurement of local transverse dispersion in isotropic porous media. *Water Resources Research* 37(2): 243–252.
- Coats, K.H. and B.D. Smith. 1964. Dead-end pore volume and dispersion in porous media. *Society of Petroleum Engineers Journal* 4: 73–84.
- Dagan, G. 1984. Solute transport in heterogeneous formations. *Journal of Fluid Mechanics* 145: 151–177.
- Dagan, G. 1988. Time-dependent macrodispersion for solute transport in anisotropic heterogeneous aquifers. *Water Resources Research* 24(9): 1491–1500.
- Dagan, G. 1989. *Flow and Transport in Porous Formations*. Berlin: Springer-Verlag.
- Delgado, J.M.P.Q. and J.R.F. Guedes de Carvalho. 2001. Measurement of the coefficient of transverse dispersion in flow through packed beds for a wide range of values of the Schmidt number. *Transport in Porous Media* 44: 165–180.
- Di Federico, V. and S.P. Neuman. 1998. Transport in multiscale log conductivity fields with truncated power variograms. *Water Resources Research* 34(5): 963–973.
- Domenico, P.A. and F.W. Schwartz. 1997. *Physical and Chemical Hydrogeology*, 2nd ed. New York: Wiley.
- Fernandez-Garcia, D., Illangasekare, T.H. and H. Rajaram. 2005. Differences in the scale-dependence of dispersivity and retardation factors estimated from forced-gradient and uniform flow tracer tests in three-dimensional physically and chemically heterogeneous porous media. *Water Resources Research* 41: doi:10.1029/2004WR003125.
- Flury, M., Fluhler, H., Jury, W.A. and J. Leueberger. 1994. Susceptibility of soils to preferential flow of water: A field study. *Water Resources Research* 31: 2443–2452.
- Freeze, A.R. and J.A. Cherry. 1979. *Groundwater*. Upper Saddle River, NJ: Prentice-Hall.
- Frippiat, C.C., Conde Pérez, P. and A.E. Holeyman. 2008. Estimation of laboratory-scale dispersivities using an annulus-and-core device. *Journal of Hydrology* 362: 57–68, doi: 10.1016/j.jhydrol.2008.08.007.
- Gelhar, L.W. 1993. *Stochastic Subsurface Hydrology*. Englewood Cliffs, NJ: Prentice-Hall.
- Gelhar, L.W. and M.A. Collins. 1971. General analysis of longitudinal dispersion in nonuniform flow. *Water Resources Research* 7(6): 1511–1521.
- Gelhar, L.W. and C.L. Axness. 1983. Three-dimensional stochastic analysis of macrodispersion in aquifers. *Water Resources Research* 19(1): 161–180.
- Gelhar, L.W., Welty, C. and K.R. Rehfeldt. 1992. A critical review of data on field-scale dispersion in aquifers. *Water Resources Research* 28(7): 1955–1974.
- Grane, F.E. and G.H.F. Gardner. 1961. Measurement of transverse dispersion in granular media. *Journal of Chemical and Engineering Data* 6(2): 283–287.
- Grove, D.B. and W.A. Beetem. 1971. Porosity and dispersion constant calculations for a fractured carbonated aquifer using the two well tracer test method. *Water Resources Research* 7(1): 128–134.
- Guedes de Carvalho, J.R.F. and J.M.P.Q. Delgado. 1999. Mass transfer from a large sphere buried in a packed bed along which liquid flows. *Chemical Engineering Science* 54: 1121–1129.
- Guedes de Carvalho, J.R.F. and J.M.P.Q. Delgado. 2000. Lateral dispersion in liquid flow through packed beds at $P_{em} < 1400$. *AIChE Journal* 46(5): 1089–1095.
- Guen, O., Molz, F.J. and J.G. Melville. 1984. An analysis of dispersion in a stratified aquifer. *Water Resources Research* 20(10): 1337–1354.
- Haga, D., Niibori, Y. and T. Chida. 1999. Hydrodynamic dispersion and mass transfer in unsaturated flow. *Water Resources Research* 35(4): 1065–1077.
- Han, N.-W., Bhakta, J. and R.G. Carbonell. 1985. Longitudinal and lateral dispersion in packed beds: effect of column length and particle size distribution. *AIChE Journal* 31(2): 277–288.

- Harleman, D.R.F. and R.R. Rumer. 1963. Longitudinal and lateral dispersion in an isotropic porous medium. *Journal of Fluid Mechanics* 16: 385–394.
- Harter, T. and D. Zhang. 1999. Water flow and solute spreading in heterogeneous soils with spatially variable water content. *Water Resources Research* 35(2): 415–426.
- Hassinger, R.C. and von Rosenberg, D.U. 1968. A mathematical and experimental investigation of transverse dispersion coefficients. *Society of Petroleum Engineers Journal* 8(2): 195–204.
- Kim, S.-B., Jo, K.-H., Kim, D.-J. and W.A. Jury. 2004. Determination of two-dimensional laboratory-scale dispersivities. *Hydrological Processes* 18: 2475–2483.
- Klenk, I.D. and P. Grathwohl. 2002. Transverse vertical dispersion in groundwater and the capillary fringe. *Journal of Contaminant Hydrology* 58: 111–128.
- Klotz, D., Seiler, K.-P., Moser, H. and F. Neumaier. 1980. Dispersivity and velocity relationship from laboratory and field experiments. *Journal of Hydrology* 45: 169–184.
- Kreft, A. and A. Zuber. 1978. On the physical meaning of the dispersion equation and its solutions for different initial and boundary conditions. *Chemical Engineering Science* 33: 1471–1480.
- Lallemand-Barres, A. and P. Peaudecerf. 1978. Recherche des relations entre la valeur de la dispersivité macroscopique d'un milieu aquifère, ses autres caractéristiques, et les conditions de mesure. Etude bibliographique. *Bulletin du BRGM 2e série, section III*, 4: 277–284.
- Lu, N. and W.J. Likos. 2004. *Unsaturated Soil Mechanics*. Hoboken, NJ: John Wiley and Sons.
- Maloof, S. and A.L. Protopapas. 2001. New parameters for solution of two-well dispersion problem. *Journal of Hydrologic Engineering* 6(2): 167–171.
- Marle, C.M., Simandoux, P., Parcsirszky, J. and C. Gaulier. 1967. Etude du déplacement de fluides miscibles en milieu poreux stratifié. *Revue de l'Institut Français du Pétrole* 22: 272–294.
- McCarthy, K. and R.L. Johnson. 1993. Transport of volatile compounds across the capillary fringe. *Water Resources Research* 29(6): 1675–1683.
- Mercado, A. 1967. The spreading pattern of injected waters in a permeability stratified aquifer. *Artificial Recharge of Aquifers and Management of Aquifers* 72: 23–36.
- Moench, A.F. 1989. Convergent radial dispersion: A Laplace transform solution for aquifer tracer testing. *Water Resources Research* 25(3): 439–447.
- Neuman, S.P. 1990. Universal scaling of hydraulic conductivities and dispersivities in geologic media. *Water Resources Research* 26(8): 1749–1758.
- Novakowski, K.S. 1992. An evaluation of boundary conditions for one-dimensional solute transport. 2. Column experiments. *Water Resources Research* 28(9): 2411–2423.
- Oostrom, M., Hofstee, C., Walker, R.C. and J.H. Dane. 1999a. Movement and remediation of trichloroethylene in a saturated homogeneous porous medium. 1. Spill behavior and initial dissolution. *Journal of Contaminant Hydrology* 37: 159–178.
- Oostrom, M., Hofstee, C., Walker, R.C. and J.H. Dane. 1999b. Movement and remediation of trichloroethylene in a saturated homogeneous porous medium. 2. Pump-and-treat and surfactant flushing. *Journal of Contaminant Hydrology* 37: 179–197.
- Pearce, A.E., Voudrias, E.A. and M.P. Whelan. 1994. Dissolution of TCE and TCA pools in saturated subsurface systems. *Journal of Environmental Engineering* 120(5): 1191–1206.
- Perkins, T.K. and O.C. Johnston. 1963. A review of diffusion and dispersion in porous media. *Society of Petroleum Engineers Journal* 3(1): 70–84.
- Pisani, S. and N. Tosi. 1994. Two methods for the laboratory identification of transversal dispersivity. *Ground Water* 32(3): 431–438.

- Rajaram, H. and L. W. Gelhar. 1995. Plume-scale dependent dispersion in aquifers with a wide range of scales of heterogeneity. *Water Resources Research* 31(10): 2469–2482.
- Rao, P.S., Rolston, D.E., Jessup, R.E. and Davidson, J.M. Solute transport in aggregated porous media: Theoretical and experimental evaluation. *Soil Science Society of America Journal* 44: 1139–1146.
- Robbins, G.A. 1989. Methods for determining transverse dispersion coefficients of porous media in laboratory column experiments. *Water Resources Research* 25(6): 1249–1258.
- Rubin, Y. 1995. Flow and transport in bimodal heterogeneous formations. *Water Resources Research* 31(10): 2461–2468.
- Rubin, Y. 2003. *Applied Stochastic Hydrogeology*. Oxford: Oxford University Press.
- Russo, D. 1998. Stochastic analysis of flow and transport in unsaturated heterogeneous porous formation: Effects of variability in water saturation. *Water Resources Research* 34(4): 569–581.
- Saffman, P.G. 1959. A theory of dispersion in a porous medium. *Journal of Fluid Mechanics* 6: 312–349.
- Sato, T., Tanahashi, H. and H.A. Loaiciga. 2003. Solute dispersion in a variably saturated sand. *Water Resources Research* 39: doi: 10.1029/2002WR001649.
- Sauty, J. 1980. An analysis of hydrodispersive transfer in aquifers. *Water Resources Research* 16(1): 145–158.
- Schulze-Makuch, D. 2005. Longitudinal dispersivity data and implications for scaling behavior. *Ground Water* 43(3): 443–456.
- Stauffer, F. and M. Rauber. 1998. Stochastic macrodispersion model for gravel aquifers. *Journal of Hydraulic Research* 36(6): 885–896.
- Tiedeman, C.R. and P.A. Hsieh. 2004. Evaluation of longitudinal dispersivity estimates from simulated forced- and natural-gradient tracer tests in heterogeneous aquifers. *Water Resources Research* 40: doi:10.1029/2003WR002401.
- Vanclooster, M., Javaux, M. and J. Vanderborght. 2005. Solute transport in soil at the core and field scale. *Encyclopedia of Hydrological Science, Part 6: Soils*, doi: 10.1002/0470848944.hsa073.
- van Genuchten, M.T. and P.J. Wierenga. 1976. Mass transfer studies in sorbing porous media. I. Analytical solutions. *Soil Science Society of America Journal* 40: 473–480.
- van Genuchten, M.T. 1980. A closed-form equation for predicting the hydraulic conductivity of unsaturated soils. *Soil Science Society of America Journal* 44: 892–898.
- van Genuchten, M.T. and J.C. Parker. 1984. Boundary conditions for displacement experiments through short laboratory soil columns. *Soil Science Society of America Journal* 48: 703–708.
- van Genuchten, M.T., Leij, F.J. and S.R. Yates. 1991. *The RETC Code for Quantifying the Hydraulic Functions of Unsaturated Soils*, version 1.0. EPA/600/2-91/065. U.S. Salinity Laboratory, Riverside, CA.
- Welty, C. and L.W. Gelhar. 1994. Evaluation of longitudinal dispersivity from nonuniform flow tracer tests. *Journal of Hydrology* 153: 71–102.
- Xu, M. and Y. Eckstein. 1995. Use of weighted least-squares method in evaluation of the relationship between dispersivity and field scale. *Ground Water* 33(6): 905–908.
- Xu, M. and Y. Eckstein. 1997. Statistical analysis of the relationships between dispersivity and other physical properties of porous media. *Hydrogeology Journal* 5(4): 4–20.
- Zhan, H. and S.W. Wheatcraft. 1996. Macrodispersivity tensor for nonreactive solute transport in isotropic and anisotropic fractal porous media: Analytical solutions. *Water Resources Research* 32(12): 3461–3474.

Dispersion and Mass Transfer Coefficients in Groundwater

437

Zhang, X., Qi, X., Zhou, X. and H. Pang. 2006. An *in situ* method to measure the longitudinal and transverse dispersion coefficients of solute transport in soil. *Journal of Hydrology* 328: 614–619.

ADDITIONAL READING

- Aris, R. 1956. On the dispersion of a solute in a fluid flowing through a tube. *Proc. Royal Soc. London A* 235: 67–77.
- Batu, V. 2006. *Applied Flow and Solute Transport Modeling in Aquifers. Fundamental Principles and Analytical and Numerical Methods*. Boca Raton, FL: CRC Press.
- Bear, J. 1972. *Dynamics of Fluids in Porous Media*. New York: American Elsevier Publishing Company.
- Bedient, P.B., Rifai, H.S. and C.J. Newell. 1999. *Ground Water Contamination: Transport and Remediation*. Upper Saddle River, NJ: Prentice-Hall.
- Berkowitz, B., Cortis, A., Dentz, M. and H. Scher. 2006. Modeling nonFickian transport in geological formations as a continuous time random walk. *Reviews of Geophysics* 44: doi: 10.1029/2005RG000178.
- de Marsily, G. 1986. *Quantitative Hydrogeology—Groundwater Hydrology for Engineers*. New York: Academic Press.
- Davis, S.N., Campbell, D.J., H.W. Bentley and T.J. Flynn. 1985. *Ground Water Tracers*. Wothington: National Water Well Association.
- Elfeki, A.M.M., Uffink, G.J.M. and F.B.J. Barends. 1997. *Groundwater Contaminant Transport: Impact of Heterogeneous Characterization*. Rotterdam: Balkema.
- Fetter, C.W. 1999. *Contaminant Hydrogeology*, 2nd ed. Upper Saddle River, NJ: Prentice-Hall.
- Fried, J.J. 1975. *Groundwater Pollution*. Amsterdam: Elsevier.
- Frippiat, C.C. and A.E. Holeyman. 2008. A comparative review of upscaling methods for solute transport in heterogeneous porous media. *Journal of Hydrology* 362: 150–176, doi: 10.1016/j.jhydrol.2008.08.015
- Gaspar, E. 1987. *Modern Trends in Tracer Hydrology*. Vol. I. Boca Raton, FL: CRC Press.
- Gaspar, E. 1987. *Modern Trends in Tracer Hydrology*. Vol. II. Boca Raton, FL: CRC Press.
- Greenkorn, R.A. 1983. *Flow Phenomena in Porous Media*. New York: Marcel Dekker.
- Javaux, M. and M. Vanclooster. 2003. Scale- and rate-dependent solute transport within an unsaturated sandy monolith. *Soil Science Society of America Journal* 67(5): 1334–1343.
- Kass, W. 1998. *Tracer Techniques in Geohydrology*. Rotterdam: Balkema.
- Matheron, G. and G. De Marsily. 1980. Is transport in porous media always diffusive? A counterexample. *Water Resources Research* 16(5): 901–917.
- Ptak, T., Piepenbrink, M. and Martac, E. 2004. Tracer tests for the investigation of heterogeneous porous media and stochastic modeling of flow and transport—a review of some recent developments. *Journal of Hydrology* 294: 122–163.
- Scheidegger, A.E. 1960. *The Physics of Flow through Porous Media*. New York: Macmillan.
- Taylor, G.I. 1953. Dispersion of soluble matter in solvent flowing slowly through a tube. *Proceedings of the Royal Society of London A* 219: 186–203.
- Taylor, G.I. 1954. Conditions under which dispersion of a solute in a stream of solvent can be used to measure molecular diffusion. *Proceedings of the Royal Society of London A* 225: 473–477.
- Tindal, J.A. and J.R. Kunkel. 1999. *Unsaturated Zone Hydrology for Scientists and Engineers*. Upper Saddle River, NJ: Prentice-Hall.
- Wheatcraft, S.W. and S.W. Tyler. 1988. An explanation of scale-dependent dispersivity using concepts of fractal geometry. *Water Resources Research* 24(4): 566–578.

PART 2 MASS TRANSFER COEFFICIENTS IN PORE-WATER ADJACENT TO NONAQUEOUS LIQUIDS AND PARTICLES

15.6 INTRODUCTION

Organic chemicals and hydrocarbons with very low aqueous solubility remain a separate phase or as nonaqueous phase liquids (NAPLs) for long periods of time in the subsurface contributing to soil and groundwater contamination. At a very fundamental level, the mass transfer occurs at the NAPL–water interfaces within the pores. However, when the NAPLs enter the soil, they produce complex entrapment morphologies and architecture that makes the mass transfer process complex. The morphologies of entrapment at the pore scale and the spatial distribution that defines the architecture are controlled by many factors that include the spill configuration, type, and physical and chemical properties of NAPL and the subsurface heterogeneity. Uncertainty associated with all these controlling factors contributes to the prediction uncertainty of how much dissolved mass flux is generated from source zones of NAPL-contaminated sites. The focus of this section is to discuss and present modeling methods that are used to predict mass transfer from entrapped NAPL sources taking into consideration the various entrapment morphologies and architecture that occur at naturally heterogeneous field sites. To be of practical value, methods have to be developed to up-scale this mass transfer process from smaller measurement scales (laboratory) to the field.

The outline of the presented material is as follows. The mass transfer that occurs at the NAPL–water interfaces at the pore scale is generally approximated using a linear model based on film theory. In extending this formulation to the representative elemental volume (REV) scale in porous media, it is necessary to define an overall mass transfer rate coefficient. The theoretical development of phenomenological models that are used to estimate these overall mass transfer coefficients is presented. Methods to up-scale these REV scale models to field scale are presented. A set of examples based on intermediate-scale laboratory tests is presented to demonstrate the use of these methods.

15.7 DISTRIBUTION AND MORPHOLOGY OF NAPLs IN POROUS MEDIA

Nonaqueous phase liquids are classified into two groups depending on their specific gravity. Hydrocarbons and petroleum products that are less dense than water are referred to as light nonaqueous phase liquids (LNAPLs). Solvents, cold tar, wood preservatives that are heavier than water are referred to as dense nonaqueous phase liquids (DNAPLs). They are classified as nonaqueous phase liquids because of their very low solubility. They stay as a separate fluid phase when in contact with water for a very long period of time. When introduced on to the ground surface because of accidental spills, improper disposal or leaking from storage systems, NAPLs migrate through the unsaturated zone of the subsurface where the wetting water phase partially occupies the pore space. Because of surface tension, the water pressure stays at less than atmospheric (capillary suction). During migration, the NAPL that behaves as a nonwetting fluid in the presence of water displaces the nonwetting air phase. After the

NAPL front has propagated, a fraction of the NAPL remains entrapped within the soil pores. Before reaching the water table (where the water pressure is at atmospheric), the NAPL front will penetrate the zone that is referred to as the capillary fringe where the pore water is close to saturation but is under less than atmospheric pressure. The NAPL front will penetrate the capillary fringe and reaches the water table. After reaching the water table, the behavior of NAPL depends on the relative density compared to water. Lighter than water LNAPLs tend to float on the water table and the dense DNAPLs will penetrate the water table and enters the saturated zone of the aquifer where the water pressures are higher than atmospheric. Depending on the conditions as determined by the spill volume, rate, fluid, and porous media properties, the DNAPL behaves unstably and will migrate preferentially as fingers (Held and Illangasekare, 1995). Laboratory and theoretical studies suggest that, even in the most homogeneous of porous media, the infiltration and dissolution of dense NAPL solvents into the saturated zone will tend to occur as a number of scattered fingers and not along one uniform plug or front. Once a sufficient amount of NAPL accumulates and the NAPL solvent enters the porous medium, downward movement will continue until all of the NAPL solvent is present as suspended fingers, ganglia, and/or as pools of NAPL accumulated on lower-permeable layers. Because fingers tend to have small dimensions in the saturated zone (usually occupying single pore throat), significant fraction of NAPL mass in the saturated zone may be present as NAPL pools (Anderson et al., 1992). However, deep penetration of downward moving fingers and subsequent formation of new pools of NAPL flowing through the finger result in a complex spill morphology and thus the prediction of finger penetration into the porous medium is also important (Illangasekare et al., 1995).

The entrapped NAPL, both in the unsaturated and saturated zones produce fluid–fluid interfaces through which mass transfer occurs. The unsaturated zone NAPLs produce NAPL–water and NAPL–air interfaces. Water infiltrating through the unsaturated zone picks up the dissolved mass and transports the solute to the saturated zone. The mass transfer that occurs through the NAPL–air interface contributes to the vapor migration through the air phase. In the following sections, we will only focus on the mass transfer that occurs at NAPL–water interfaces, thus focusing only on the problem of groundwater contamination by NAPLs.

15.8 CONCEPTUAL MODELS OF MASS TRANSFER

A variety of models exist to describe mass transfer phenomena among phases in a multiphase system. Here, an overview from simple dispersion model (Johnson and Pankow, 1992) to solute mass flux models (Miller et al., 1990; Powers et al., 1992; Geller and Hunt, 1993; Imhoff et al., 1993), including various models for Sherwood transfer rate number is presented in this section.

15.8.1 ONE-DIMENSIONAL VERTICAL DISPERSION MODEL

Johnson and Pankow (1992) presented a simple analytical model for dissolution of pools of a NAPL by treating the mass transfer to be a vertical transport process. The general two-dimensional mass transport equation can be simplified by assuming:

(1) the time required for total pool dissolution is exceedingly longer in comparison with the contact time between the pool and the flowing groundwater, therefore, a steady-state form of the advection–dispersion equation can be used, (2) sorption is not important at steady state, and (3) groundwater flows with the velocity v in the horizontal direction. Thus, a two-dimensional steady-state equation can be used. The governing equation is given by

$$v \frac{\partial C}{\partial x} = D_T \frac{\partial^2 C}{\partial z^2}, \quad (15.21)$$

where C [ML^{-3}] is the concentration of NAPL, v [LT^{-1}] is the groundwater velocity in the horizontal direction, z [L] is the vertical distance above the pool and x [L] is the horizontal distance along the length of the pool with the origin at the beginning of the pool. The vertical dispersion coefficient D_T [L^2T^{-1}] is given either by Equation 15.5b or Equation 15.5c.

Hunt et al. (1988) presented the analytical solution of Equation 15.21 with the boundary conditions $C(x, +\infty) = 0$ and $C(x, 0) = C_s$ for all $x \in (0, L_p)$ and $C(0, z) = 0$ for all $z \in (0, L_p)$, where L_p is the length of the pool. Based on this solution, the vertical concentration profile at the downgradient edge of the pool ($x = L_p$) is given by

$$C(L_p, z) = C_s \operatorname{erfc} \left(\frac{z\sqrt{v}}{2\sqrt{D_v L_p}} \right), \quad (15.22)$$

where C_s [ML^{-3}] is the solubility limit of the dissolving NAPL component. Based on the above solution, the time for complete dissolution of the pool can be estimated. If a pool consists of constant thickness with a thickness/length ratio r , then the time to complete dissolution τ_p will be given by

$$\tau_p = \frac{r\rho L_p^{3/2} \sqrt{\pi}}{C_s \sqrt{4D_v v}}, \quad (15.23)$$

where ρ [ML^{-3}] is the density of the NAPL. The above derivation assumes a surface area averaged mass transfer across the pool length.

15.8.2 LINEAR DRIVING MODEL FOR INTERPHASE MASS TRANSFER

A common concept implicit in many mass transfer theories is to describe the mass transfer across two phase boundaries through a mass transfer rate coefficient. The driving force in this case is determined by the difference in the concentration at the phase boundary (e.g., NAPL surface) and the bulk phase (e.g., water or air). This linear relationship is given by

$$J = k_l(C_s - C), \quad (15.24)$$

where J [$\text{ML}^{-2}\text{T}^{-1}$] is the mass flux rate from the NAPL, k_l [LT^{-1}] is the mass transfer rate coefficient, C_s [ML^{-3}] is the aqueous phase concentration under conditions

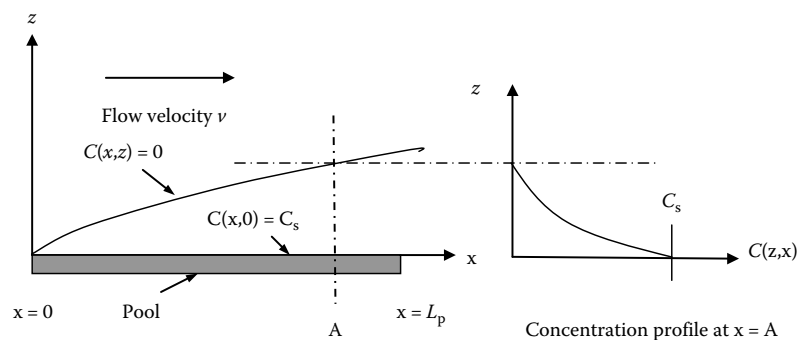


FIGURE 15.5 Dissolution of a NAPL pool.

when the NAPL is in thermodynamic equilibrium with the solute in the aqueous phase (solubility limit of NAPL in water) and C [ML^{-3}] is the aqueous phase solute concentration in the bulk solution. The subscript l denotes that the driving force acts along the longitudinal direction normal to the direction of flux. Note that this model does not assume the presence of a porous medium.

15.8.3 STAGNANT FILM MODEL

A conceptual model that describes mass transfer across two phases is assumed to occur through a stagnant aqueous film adjacent to the interface has been adopted for porous media applications. A schematic illustration of the process that occurs is shown in Figure 15.6.

As there is no mass storage within the film, the concentration gradient has to be linear. Applying Fick's law, an expression for steady mass flux J [$\text{ML}^{-2}\text{T}^{-1}$] is obtained as

$$J = -D_l \frac{dC}{dl} = \frac{D_l}{\delta} (C_s - C), \quad (15.25)$$

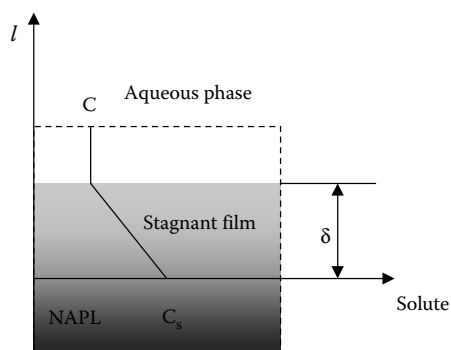


FIGURE 15.6 Stagnant film model.

where D_l [L^2T^{-1}] is the diffusion coefficient in free liquid and δ [L] is the thickness of the assumed stagnant film. By introducing a mass transfer coefficient $k_l = D_l/\delta$ [LT^{-1}] an equation similar to the linear driving model can be written as

$$J = k_l(C_s - C). \quad (15.26)$$

The macroscopic groundwater flow equations are written at the representative elemental volume (REV) scale. As (Δ) is defined as the pore scale (NAPL–water interface within a pore) and cannot be measured, a lumped mass transfer coefficient defined at the REV scale is used (Pankow and Cherry, 1995). Hence, a linear driving force model similar to Equation 15.24 can be used to describe mass flux from entrapped NAPL sources in porous media. This is accomplished by introducing a lumped mass transfer rate coefficient K_c [T^{-1}] (Miller et al., 1990). The mass rate equation for mass rate J' [$ML^{-3}T^{-1}$] then takes the form

$$J' = K_c(C_s - C). \quad (15.27)$$

The pore-scale mass transfer coefficient k_l and the lumped mass transfer coefficient K_c are related by

$$K_c = k_l \frac{A_n}{V}, \quad (15.28)$$

where A_n [L^2] is the total NAPL–water surface area within the REV of volume V [L^3]. As A_n cannot be measured or estimated in practical situations in involving ground water contamination, K_c is treated as an empirically determined parameter.

15.9 EMPIRICAL MASS TRANSFER RATE COEFFICIENTS

As was explained in the previous section, the lumped mass transfer rate coefficient needs to be empirically determined because the basic parameters that describe the mass transfer process cannot be measured for porous media systems. However, an insight to the processes that contribute to mass transfer can be obtained by studying simple settings, where the governing equations can be solved to obtain closed form analytical solutions. Chemical engineering literature provides number of examples of such closed form solutions (e.g., Bird et al., 1961). By identifying the driving forces and mechanisms that contribute to mass transfer, the terms that appear in these closed form solutions can be arranged into dimensionless groups. One example has relevance to understanding dissolution from a pool and entrapped NAPLs, it is the case of the dissolution of the wall when the water flows through a tube of length L and internal radius R (Figure 15.7). The flow through the tube is assumed to be laminar.

The closed-form solution for the advection–dispersion equation expressed in dimensionless group that is referred to as the Graetz–Nusselt problem solution is given as

$$Sh = \left(\frac{2}{3\Gamma(4/3)} \right) Re^{1/3} Sc^{1/3} \left(\frac{L}{R} \right) \quad (15.29)$$

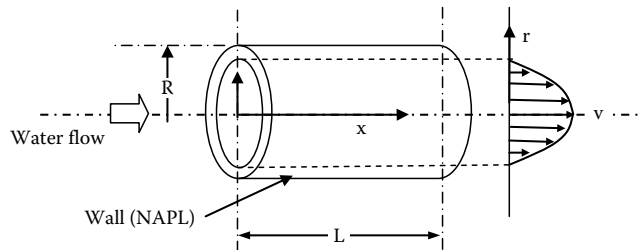


FIGURE 15.7 Dissolution of wall during laminar flow.

where Γ is the gamma function, Re [–] is the Reynolds number, and Sc [–] is the Schmidt number. The dimensionless Sherwood number Sh [–] is related to the mass transfer coefficient k_l as $Sh = k_l d_p / D_l$, where d_p [L] is the geometric mean particle diameter. The relationships such as the one given by Equation 15.29 are referred to as Gilliland–Sherwood models.

Saba and Illangasekare (2000) proposed a model for two-dimensional flow conditions. This model introduced a dissolution length along the flow path. Also, the appearance of a tube radius allows for the introduction of the volumetric NAPL content into the phenomenological model. Conceptually, as the NAPL gets depleted, the effective radius of the flow tube changes. The Gilliland–Sherwood model that was proposed by Saba and Illangasekare (2000) is of the form

$$Sh' = a Re^\beta Sc^\alpha \left(\frac{\theta_n d_{50}}{\tau L} \right)^\eta, \quad (15.30)$$

where Sh' [–] is a modified form of Sherwood number used for porous media applications defined as

$$Sh' = \frac{K d_p^2}{D_l}. \quad (15.31)$$

The terms a , β , α , and n are empirical coefficients [–], τ [–] is the tortuosity factor of the flow path, L [L] is the dissolution length, d_{50} [L] is the mean grain size, and θ_n [–] is the volumetric NAPL content. The mass transfer coefficient K [T^{-1}] that appears in Equation 15.31 is the lumped mass transfer coefficient and it contains the NAPL/water interface area as introduced in Equation 15.28.

The correlation based on Equation 15.30 that was fitted to NAPL dissolution data obtained in a two-dimensional dissolution cell by Saba and Illangasekare (2000) is

$$Sh' = 11.34 Re^{0.28} Sc^{0.33} \left(\frac{\theta_n d_{50}}{\tau L} \right)^{1.037}. \quad (15.32)$$

Gilliland–Sherwood correlations were developed for a number of test systems and configurations by a number of investigators. These correlations are listed in Table 15.3.

TABLE 15.3
Gilland–Sherwood Correlations Reported by Different Investigators

Reference	Correlation	Valid Range
Estimated from Geller and Hunt (1993) in Imhoff et al. (1993)	$Sh' = 70.5 Re^{1/3} \theta_n^{4/9} S_{ni}^{1/9} \varphi^{-2/3} \left(\frac{d_p}{d_{ni}} \right)^{5/3}$	$\theta_n \in (0, 0.056)$ $Re \in (0, 0.014)$
Miller et al. (1990)	$Sh' = 12(\varphi - \theta_n) Re^{0.75} \theta_n^{0.60} Sc^{0.5}$	$\theta_n \in (0.016, 0.07)$ $Re \in (0.00015, 0.1)$
Est. from Parker et al. (1991) in Imhoff et al. (1993)	$Sh' = 1240(\varphi - \theta_n) Re^{0.75} \theta_n^{0.60}$	$\theta_n \in (0.02, 0.03)$ $Re \in (0.1, 0.2)$
Powers et al. (1992)	$Sh' = 57.7(\varphi - \theta_n)^{0.61} Re^{0.61} d_{50}^{0.64} U_i^{0.41}$	$Re \in (0.012, 0.21)$
Imhoff et al. (1993)	$Sh' = 340 Re^{0.71} \theta_n^{0.87} \left(\frac{x}{d_p} \right)^{-0.31}$	$\theta_n \in (0, 0.04)$ $(\varphi - \theta_n) Re \in (0.0012, 0.021)$ $x/d_{50} \in (1.4, 180)$
Powers et al. (1994)	$Sh' = 4.13 Re^{0.598} \left(\frac{d_{50}}{d_p} \right)^{0.673} U_i^{0.369} \left(\frac{\theta_n}{\theta_{ni}} \right)^\beta$ $\beta = 0.518 + 0.114 \left(\frac{d_{50}}{d_p} \right) + 0.1 U_i$	$Re \in (0.015, 0.023)$

Note: θ_n [–] is the NAPL content, φ [–] is the porosity, S_{ni} [–] is the initial NAPL saturation, d_p [L] is the diameter of the porous media mean particle, d_{ni} [L] is the mean value of the initial NAPL ganglia, d_{50} [L] is the particle diameter such that 50% of the porous media are finer by weight (median particle size), U_i [–] is the uniformity index, and x/d_p [–] is the dimensionless distance into the region of residual NAPL.

The correlation by Geller and Hunt (1993) was developed for variable volumetric content, that is, S_n or n are not constant. The phenomenological model for mass transfer was based on the correlation developed by Wilson and Geankoplis reported by Imhoff et al. (1993) with an assumed spherical shape of NAPL ganglia. In that case, it was necessary to choose the initial NAPL saturation S_{ni} and the initial NAPL ganglia diameter d_{ni} , which are not needed in other models, since a shrinking NAPL ganglia was examined in this study. In the development of the correlation by Miller et al. (1990) the residual NAPL within the porous medium was established by mechanical stirring glass beads, water, and NAPL. The laboratory created NAPL ganglia were more spherical and smaller in size than that obtained by the displacement mechanism as in the correlation by Powers et al. (1992), who explain that dissolution is fast in the work of Miller et al. (1990) because these relatively small spherical NAPL ganglia have larger interfacial contact area for an equivalent NAPL volumetric content. A constant volumetric NAPL content and a steady state dissolution experimental data were correlated. In a study by Parker et al. (1991) the residual NAPL distribution was

created by mechanical mixing of sand and NAPL. This technique results in a similar residual NAPL morphology as in the previous case, that is, likely small spherical NAPL ganglia with different structure than in the case of natural NAPL displacement mechanism. As in the case of (Miller et al., 1990), a constant volumetric NAPL content and steady-state dissolution were considered. To develop the correlation by Powers et al. (1992), the residual NAPL distribution was achieved by an immiscible displacement process: NAPL first flooded a water saturated medium and then it was followed by water flush to displace the mobile NAPL. This process creates NAPL ganglia in a similar way they are created under natural conditions, that is, the ganglia are nonuniformly displaced and variously shaped. Imhoff et al. (1993) used a different regression techniques based on the Gauss–Newton nonlinear least-squares algorithm and linear least-squares regression. The authors conclude that the simplest model which adequately described TCE dissolution for the porous medium is that obtained by nonlinear regression of power law, where the exponential variation of Sh with x/d_p was suggested. The major difference between this and other models (see Table 15.3) lies in the inclusion of the x/d_p coefficient in the correlation of the mass transfer rate. The correlation by Powers et al. (1994) included the uniformity index U_i . Since the shrinking of the NAPL blobs is considered in this model, the modified Sherwood number correlation includes the initial volumetric NAPL content θ_{ni} .

Saba and Illangasekare (2000) compared some of the models listed in Table 15.3 based on one-dimensional testing systems and demonstrated that the correlation based on two-dimensional data result in significant errors. This finding suggested that the flow dimensionality has to be taken into consideration when upscaling the models based on one-dimensional systems to multidimensional flow systems in the field.

Saenton and Illangasekare (2007) proposed a method to upscale the mass transfer rate coefficient for numerical simulation of mass transfer in heterogeneous source zones where NAPLs are entrapped. The basic approach involves the use of geo-statistical parameters of the heterogeneity and the statistics that describes how the NAPL saturation is distributed in the source zone. Through numerical experiments the authors demonstrated that the mass transfer is most sensitive to the vertical smearing of the NAPL that is represented by the second moment of the saturation distribution. The upscaled mass transfer correlation is given by

$$\overline{Sh} = Sh_0(1 + \sigma_Y^2)^{\varphi_1} \left(1 + \frac{\Delta z}{\lambda_z}\right)^{\varphi_3} \left(\frac{\hat{M}_{II,z}}{\hat{M}_{II,z}^*}\right)^{\varphi_5}, \quad (15.33)$$

where \overline{Sh} is the up-scaled Sherwood number containing the effective mass transfer rate coefficient, σ_Y^2 is the variance of the $\ln K$ field, Δz is the vertical dimensions of the simulation grid, λ_z is the vertical correlation length and the last set of terms is the dimensionless second moment of the vertical saturation distribution. This method of upscaling was validated using data from an intermediate scale tank experiment.

15.10 EXAMPLE PROBLEMS

A cleanup of a contaminated porous medium by complete dissolution is one of the many applications of the presented models. Based on different geometrical entrapment

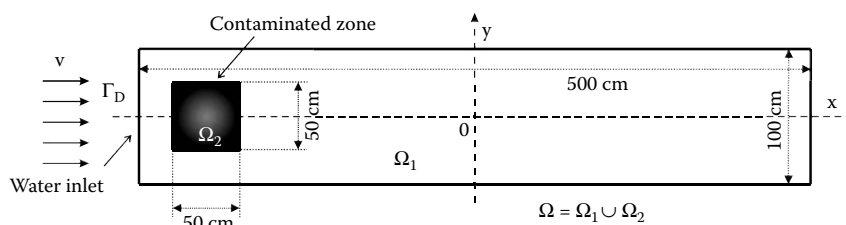


FIGURE 15.8 Illustration of two-dimensional complete dissolution problem.

of the NAPL, the Graetz–Nusselt model given by Equation 15.29 or the Powers et al. (1994) model (see Table 15.3) for the Sherwood number Sh is used.

The contaminated sand is initially assumed to contain NAPL at its residual saturation, that is, $S_{ni} = S_{nr}$, and thus it cannot be cleaned otherwise than by dissolution. Hence, the contaminated sand is put into a horizontally placed tube that contains clean sand of the same properties as it is shown in Figure 15.8. Constant flux of water v_x is introduced to the inlet and only laminar Darcian flow is considered.

The dissolution of the entrapped NAPL system is modeled by the following two-dimensional transport equation:

$$\frac{\partial \theta_w C}{\partial t} + \nabla(D \nabla C) - v \nabla C + J = 0, \quad (15.34)$$

where C [ML^{-3}] is the solute concentration in water, θ_w [–] is the volumetric water content given as $\theta_w \phi S_w$, ϕ is the porosity, and S_w [–] is the water saturation related to the NAPL saturation as $S_w + S_n = 1$. D [L^2T^{-1}] is the hydrodynamic dispersion tensor given as

$$D = \begin{bmatrix} D_m + v_x \alpha_L & 0 \\ 0 & D_m \end{bmatrix}, \quad (15.35)$$

where v [LT^{-1}] is the velocity of the horizontal flow of water, that is, $v = (v_x, 0)$, D_m [L^2T^{-1}] is the mechanical dispersion introduced in Equation 15.1, α [L] the longitudinal dispersivity introduced in Equation 15.5, and J [$ML^{-2}T^{-1}$] is the dispersive solute mass flux given by Equation 15.24.

Since the saturation of NAPL changes during the dissolution process, the mass conservation equation is added in the form

$$\rho_n \frac{\partial S_w}{\partial t} = S_w J, \quad (15.36)$$

where ρ_n [ML^{-3}] is the NAPL density.

Equations 15.34 and 15.36 are supplemented by initial and boundary conditions. Initially, the saturation of water and the concentration of NAPL are given as

$$S_w = \begin{cases} 1 & \text{in } \Omega_1 \\ 1 - S_{ni} & \text{in } \Omega_2 \end{cases}, \quad C = 0 \quad \text{in } \Omega. \quad (15.37ic)$$

The boundary conditions are given as

$$S_w = 1 \quad \text{on } \partial\Omega \quad (15.37.bc1)$$

$$\nabla_n C = 0 \quad \text{on } \partial\Omega/\Gamma_D, \quad (15.37.bc2)$$

$$C = 0 \quad \text{on } \Gamma_D, \quad (15.37.bc3)$$

where $\nabla_n C$ denotes the derivative of C in the direction of the outer normal of the boundary.

15.10.1 DISSOLUTION USING SPHERICAL BLOBS MODEL

Powers et al. (1994) considered a spherical TCE entrapment in a porous medium and the respective model for the modified Sherwood number is shown in Table 15.3. In order to correctly illustrate the dissolution process, dissolution of TCE in the Ottawa sand used by Powers et al. (1994) is discussed in this section (refer to Table 15.4 for fluid and sand properties).

15.10.2 DISSOLUTION USING TUBULAR MODEL

As introduced in Equation 15.29, the Graetz–Nusselt closed-form solution for the Sherwood number models dissolving walls of a single tubular TCE entrapment. In

TABLE 15.4
Ottawa Sand and TCE Fluid Properties

	Symbol	Units (SI)	Value
<i>Property of Ottawa Sand</i>			
Porosity	ϕ	–	0.37
Median particle size	D_{50}	m	7.1×10^{-4}
Medium particle size	d_p	m	2×10^{-4}
Darcian velocity	V	m s^{-1}	9.796×10^{-5}
Initial NAPL saturation	S_{ni}	–	0.01
Uniformity index	U_i	–	1.21
<i>Property of TCE</i>			
Density	ρ_n	kg m^{-3}	1470
Solubility limit in water	C_s	kg m^{-3}	1.27
Molecular diffusivity	D_m	$\text{m}^2 \text{s}^{-1}$	8.8×10^{-10}
Longitudinal dispersion	α_L	m	1
Dynamic viscosity	μ_n	$\text{kg m}^{-1} \text{s}^{-1}$	5.9×10^{-4}
<i>Property of Water</i>			
Density	ρ_w	kg m^{-3}	1000
Dynamic viscosity	μ_w	$\text{kg m}^{-1} \text{s}^{-1}$	0.001

Source: Based on Powers, S.E., Abriola, L.M. and W.J. Weber Jr. 1994. *Water Resources Research* 30: 321–332.

order to extend the use of such a model to the macroscopic scale, mean tube length L [L], outer radius R_{out} [L], and initial radius R_{ini} [L] have to be chosen such that NAPL can be assumed to be uniformly redistributed in these tubes. If the number of the tubes, mean length L and mean outer radius R_{out} remain constant during the dissolution, the following upscaled formula for the Graetz–Nusselt model can be used:

$$\text{Sh} = \left(\frac{2}{3\Gamma(4/3)} \right) \text{Re}^{1/3} \text{Sc}^{1/3} L^{1/3} \left(R_{\text{out}}^2 - \frac{S_n}{S_{n,\text{ini}}} (R_{\text{out}}^2 - R_{\text{ini}}^2) \right)^{-1/6}. \quad (15.38)$$

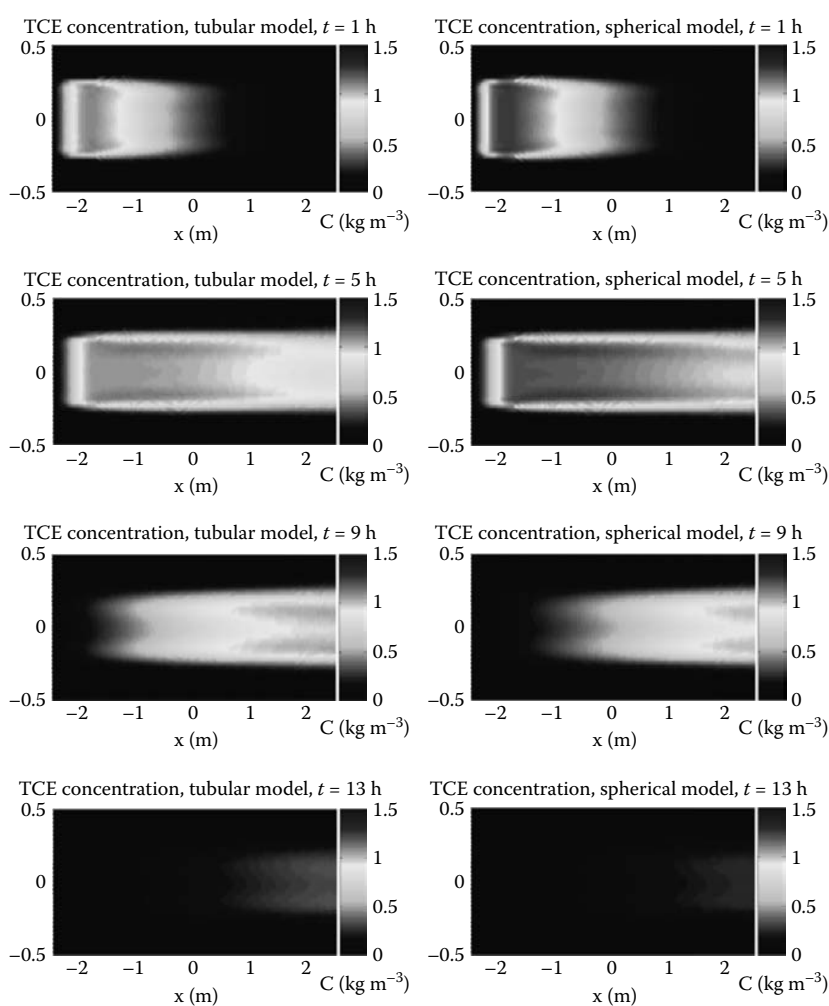


FIGURE 15.9 Concentration distribution in the domain after 1, 5, 9, and 13 h obtained by tubular (left side) and spherical (right side) models for the Sherwood number Sh .

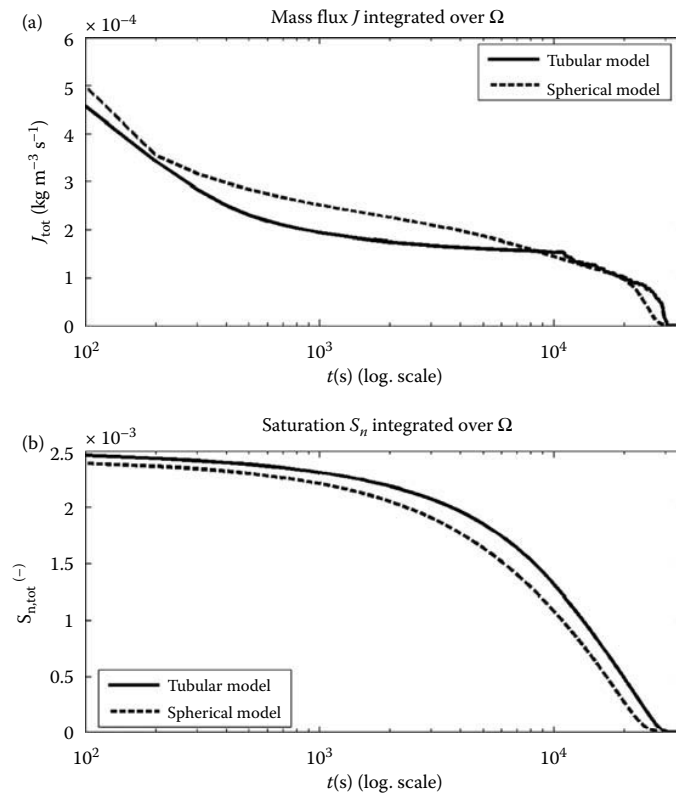


FIGURE 15.10 Time evolution of the total integrated mass flux J (a) and total integrated TCE saturation S_n (b).

Trivial algebraic manipulations in Equation 15.38 reveal that only values of L/R_{out} and $R_{\text{ini}}/R_{\text{out}}$ have to be known and, consequently, there are only two degrees of freedom to determine. In the numerical simulations, the mean length of a tube is given as $L = d_p/100$ and the last parameter R_{out} is chosen such that the Sherwood number has the same value as in the case of the spherical blobs model by Powers et al. (1994) in the previous section.

15.10.3 NUMERICAL EXPERIMENTS

The problem defined by Equations 15.34 and 15.36 together with the initial and boundary conditions (15.37) is solved by the finite element method.

The concentration distribution for the spherical and tubular model are shown in Figure 15.9. The evolution of the total saturation $S_{n,\text{tot}}$ and the total mass flux J_{tot} of the TCE is shown in Figure 15.10. The total saturation or the total mass flux is given by the integration of S_n or J over the domain Ω , respectively.

As a consequence of the calibration of the Graetz–Nusselt problem to give exactly the same value of the initial Sherwood number, both models behave in a similar way. There is a slight difference in the dynamics of the dissolution as the spherical blobs model by Powers et al. (1994) gives stronger TCE flux than the Graetz–Nusselt model. However, the complete dissolution time of the residual TCE content is the same for both models as it is shown in Figure 15.10.

LITERATURE CITED

- Anderson, M.R., Johnson, R.J. and J.F. Pankow. 1992. Dissolution of dense chlorinated solvents into groundwater. *Environmental Sciences and Technology* 30: 250–256.
- Bird, R.B., Stewart, W.E. and N. Lightfoot. 1961. Transport Phenomena. *Journal of the Electrochemical Society* 108(3): 78C–79C.
- Geller, J.T. and J.R. Hunt. 1993. Mass transfer from nonaqueous phase organic liquids in water saturated porous media. *Water Resources Research* 28: 833–846.
- Held, R.J. and T.H. Illangasekare. 1995. Fingering of dense nonaqueous phase liquids in porous media. 1. Experimental investigation. *Water Resources Research* 31(5): 1213–1222.
- Hunt, J.R., Sitar, N. and K.S. Udell. 1988. Nonaqueous phase liquid transport and cleanup. 1. Analysis and mechanisms. *Water Resources Research* 24: 1247–1258.
- Illangasekare, T.H., Ramsey, J.L., Jensen, K.H. and M.B. Butts. 1995. Experimental study of movement and distribution of dense organic contaminants in heterogeneous aquifers. *Journal of Contaminant Hydrology* 20(1–2): 1–25.
- Imhoff, P.T., Jaffe, P.R. and G.F. Pinder. 1993. An experimental study of complete dissolution of nonaqueous phase liquids in saturated media. *Water Resources Research* 30(2): 307–320.
- Johnson, R.J. and J.F. Pankow. 1992. Dissolution of dense chlorinated solvents into groundwater. 2. Source functions for pools of solvent. *Environmental Sciences and Technology* 26: 896–901.
- Miller, T.C., Poirier-McNeill, M.M. and A.S. Mayer. 1990. Dissolution of trapped NAPLs: Mass transfer characteristics. *Water Resources Research* 26(11): 2783–2796.
- Pankow, J.F. and J.A. Cherry. 1996. *Dense Chlorinated Solvents and Other DNAPLs in Groundwater*. Waterloo Educational Services, Rockwood, Ontario, Canada.
- Parker, J.C., Katyal, A.K., Kaluarachchi, J.J., Lenhard, R.J., Johnson T.J., Jayaraman, K., Unlu, K. and Zhu, J.L. 1991. *Modeling Multiphase Organic Chemical Transport in Soils and Ground Water*. U.S. Environ. Protection Agency, Washington, DC, Rep. EPA/600/2-91/042.
- Powers, S.E., Abriola, L.M. and W.J. Weber Jr. 1992. An experimental investigation nonaqueous phase liquid dissolution in saturated systems: Steady state mass transfer rates. *Water Resources Research* 28: 2691–2705.
- Powers, S.E., Abriola, L.M. and W.J. Weber Jr. 1994. An experimental investigation of nonaqueous phase liquids dissolution in subsurface systems: Transient mass transfer rates. *Water Resources Research* 30: 321–332.
- Saba, T. and T.H. Illangasekare. 2000. Effect of groundwater flow dimensionality on mass transfer from entrapped nonaqueous phase liquids. *Water Resources Research* 36(4): 971–979.
- Saenton, S. and T.H. Illangasekare. 2007. Upscaling of mass transfer rate coefficient for the numerical simulation of dense nonaqueous phase liquid dissolution in heterogeneous aquifers. *Water Resources Research* 43: W02428, doi:10.1029/2005WR004274.

ADDITIONAL READING

- Glover, K., Munakata-Marr, J. and T.H. Illangasekare, 2007. Biologically-enhanced mass transfer of tetrachloroethene from DNAPL in source zones: Experimental evaluation and influence of pool morphology, *Environmental Science and Technology* 41(4): 1384–1389.
- Illangasekare, T.H., Munakata-Marr, J.J., Siegrist, R.L., Soga, K., Glover, K.C., Moreno-Barbero, E., Heiderscheidt, J.L. et al., 2007. *Mass Transfer from Entrapped DNAPL Sources Undergoing Remediation: Characterization Methods and Prediction Tools*. SERDP Project CU-1294, Final Report, 435pp.
- Kaplan, A.R., Munakata-Marr, J. and T.H. Illangasekare. 2008. Biodegradation of residual dense nonaqueous-phase liquid tetrachloroethene: Effects on mass transfer. *Bioremediation Journal* 12(1): 23–33.
- Oostrom, M., Dane, J.H. and T. W. Wietsma. 2006. A review of multidimensional, multi-fluid intermediate-scale experiments: Nonaqueous phase liquid dissolution and enhanced remediation. *Vadose Zone Journal* 5: 570–598.

geologic parameters of field systems can be used to obtain effective field scale parameterizations.

A second example on soil water evaporation and gas flow is used to highlight and discuss some challenges in upscaling processes controlled by land/atmospheric interaction.

This section includes four other companion chapters focusing on a number of aspects of hydrogeological processes that are of central importance in geosciences and engineering. A summary of these chapters is provided here.

Chapter 11. *Pore-Scale Chemical Reactions in Diffusion-Limited Environments at the Pore Scale (D. Benson)*. This chapter addresses an issue related to mixing at the pore scale and its contribution to chemical reactions. This is of importance in many problems in the subsurface that involve fluid flow and chemical reactions. Two examples that are of current interest are groundwater contamination and mineralization of dissolved CO₂ in geologic formations. The classical differential equations of chemical reactions assume perfect mixing among reactants. This chapter presents a method to rectify the problem associated with the well mixed assumption in both theoretical and applied settings.

Chapter 12. *Porosity in reactive geochemical systems (A. Navarre-Sitchler, G. Rother, & J. Kaszuba)*. This chapter addresses the fundamental issue of reactive fluids in pore spaces; reactive fluids can create a dynamic system that affects the network of pores and hence the flow through the system. The author makes the argument that many fundamental geologic processes, the physical characteristics of pore networks in rocks in geologic materials are not well understood due to their dynamic nature and features at different length scales. Rock weathering and saprolite formation and geochemical reactions within CO₂ geologic sequestration are used as two examples to demonstrate how geochemical reactions affect porosity. Both of these examples have important implications for Earth Science.

Chapter 13. *Quantifying the heterogeneity of hydrologic properties of rocks in core floods (R. Pini & S. Benson)*. This chapter discusses the effect of sub-core scale heterogeneities on multiphase flow by considering both experimental and modeling studies. Novel experimental methods that allow non-destructive measurements of core- and sub-core-scale hydrogeological properties during conventional core-flooding tests are presented. These methods allow for the measurement of porosity, permeability and capillary pressure vs saturation relationships needed in multiphase flow modeling. This approach represents a significant improvement from conventional core

standing of the behavior of non-aqueous phase liquid (NAPL) in subsurface formations, it can be conceptualized that in heterogeneous systems, the ScrCO_2 will preferentially migrate into higher permeability zones and pool under the interface of the confining low permeability layers due to capillary barrier effects (very high entry pressure needed for the non-wetting fluid to displace the wetting fluid) [2–4]. The formation brine with dissolved CO_2 is heavier and will tend to migrate downwards resulting in unstable finger development contributing to convective mixing [5]. This dissolution process in the long-term is expected to contribute to permanent trapping as a fraction of the dissolved CO_2 mineralizes.

A related problem associated with geologic CO_2 sequestration where gas dissolution is of interest is when the CO_2 leaks from the deep formation either through caprock fractures, faults or defective casings in abandoned wells. If the liquid ScrCO_2 leaks, it will be carried upwards in the overlying formation until it encounters another confining layer. Again, the possibility exists for the liquid to encounter other leakage points and flow to shallow formations where the ScrCO_2 passes its critical point and becomes a gas or dissolves into the formation water due to its high solubility. It has been shown in laboratory studies that when the water with dissolved CO_2 encounters texture transitions in the overlying formations, the gas exsolves and accumulates below low permeability layers in the shallow subsurface [6]. Gas bubbles tend to form due to accumulation of gas molecules in the pores of the rock or rough surfaces of the solid grains where nucleation of the bubbles mostly occurs [7]. Nucleation rate is a function of solubility and cavity size distribution that controls the sizes of forming bubbles. Once the gas phase is formed, it migrates upward due to buoyancy and expands due to decreasing pressure until it encounters an impermeable layer. Accumulated gas can then migrate laterally until it finds a preferential pathway and continues to migrate upward reaching the shallow subsurface, thus potentially affecting large areas of the aquifer and eventually the land surface. When fresh water passes through these gas-entrapped zones, mass transfer occurs across the gas/water interfaces contributing to CO_2 gas dissolution. The combined effects of gas trapping and dissolution help to attenuate the leaking CO_2 thus potentially reducing atmospheric loading. All processes that are relevant to trapping, dissolution and gas migration occur at the pore-scale and assessment of trapping efficiency and leakage risks in the field require upscaling.

interface can result in advective flux much larger than diffusive flux (e.g. atmospheric pumping).

Poulsen and Møldrup [10] evaluated the effects of wind-induced pressure fluctuations on CO₂ migration and emissions at a landfill site. They analyzed the impact of wind induced gas emission as a function of the standard deviation in pressure variations. They found that the soil-air permeability and the pressure fluctuation amplitude significantly affected gas emission and that 40% of the total gas emissions flux came from wind turbulence-induced gas transport. Maier et al. [11] also found that turbulence induced pressure pumping reached up to 60% of the diffusive flux rates.

The upscaling related challenges of this problem come from first determining what pore-scale processes are important in coupling multi-phase flow in the subsurface with the free flow in the atmosphere. Second, how these processes are properly upscaled when the soil conditions change both laterally and vertically. The effects of topography of the land surface and vegetation also have to be factored in.

10.2.3. Vapor Intrusion

Chlorinated solvents that are in the form of NAPLs when introduced to the subsurface through accidental spills or improper disposal are prevalent at industrial waste sites. These chemicals that are suspected or known carcinogens if ingested through contaminated water or inhaled as vapor results in major health risks. After a spill, NAPL can persist as a separate phase in the vadose zone and in the saturated zone below the water table entrapped within the soil pores. The gas phase NAPL in the vadose zone can readily disperse into air, into the air spaces within soil or underneath a structure, leading to vapor intrusion, or the entry of a volatile chemical to indoor air from underlying contamination in soil and groundwater [12]. It has been reported that the average American spends more than 21 hours per day indoors and roughly 18 hours indoors for every hour spent outdoors [13]. Although it is not conclusively known whether vapor intrusion is a widespread problem with respect to long-term exposure at the very low levels expected in enclosed spaces such as in buildings and basements, several cases have received national attention. In a U.S. Environmental Protection Agency (EPA) review article [14] state, due to difficulty in conclusively identifying the soil-to-indoor pathway via indoor sampling, researchers have suggested moving the focus of vapor intrusion investigations outside the home. The processes that govern the vapor transport in the heterogeneous subsurface

the presence of the mine. Because landmine sensors (e.g. ground penetrating radar and thermal imagery) exploit soil and environmental conditions to discern between mines and other objects, all current mine detection technologies require that the spatial and temporal variability of key environmental conditions such as climate, vegetation, soil type, depth of ground water table, and topography be understood. If these factors and the ability to model them in a variety of domains become well defined, then sensor and algorithm simulations can more realistically be tailored to particular operational scenarios and technologies [18]. However, research efforts on mine detection are generally geared toward sensor development and sensor fusion while very little effort has been made to evaluate the environmental conditions that affect sensor performance [19–21]. Although many numerical and experimental investigations have been performed, they focus on the response/effectiveness of the technology or neglect important parameters like soil heterogeneity, and the temporal and spatial variability of the soil moisture and/or thermal properties. Thus, there is a knowledge gap between the signal processing technique and fundamental processes that occur in shallow subsurface zones as affected by near surface boundary conditions. Increasing our knowledge of the effects of geohydrologic/thermal properties and behaviors on the landmine signature is needed to fill the knowledge gap in order to better understand, model/simulate, and predict the environmental conditions that are most dynamic to mine detection performance. The shallow subsurface soil moisture processes as controlled by the mass and heat flux boundary conditions at the land–atmospheric interface are central to the problem of detection of land mines using sensing technologies. Hence, in developing models for signal interpretation in the field, the issues of multiphase flow parameter up–scaling in the shallow subsurface becomes centrally relevant.

10.3. Multiphase Flow

Fundamental to the behavior of water, supercritical CO₂, NAPLs and gases in the systems that are of relevance to the problems introduced in the previous section is the processes that govern multiphase flow in porous media. In this section, the role of heterogeneity, continuum representation and the governing equations of multiphase flow are first presented. This is followed by the introduction of a commonly used constitutive model and a brief review of upscaling theories as applied to constitutive models.

where $\chi(\mathbf{x}) [-]$ is the void space indicator function and the volume $V_r [L^3]$ is a sphere of radius $r [L]$ centered around the spatial point $\mathbf{x}_0 [L]^3$. The REV is such volume V_r for which exist radii r_{micro} and r_{macro} such that the porosity given by Eq. (10.1) is independent of the radius r within the range as shown in Fig. 10.2. The microscale description ($r < r_{micro}$) focuses on the behavior of a large number of molecules of the present phases (e.g., liquid and gas phases through the soil solid matrix). The equations describing their flow are those of the continuum mechanics within the pores (e.g. direct numerical simulations). The continuum (Fig. 10.2) or REV scale is defined as the scale in which the mean is a constant deterministic quantity and the variance approaches zero [22]. At this scale, individual pores or phase interfaces are no longer noticeable. It is at this scale that is referred to as macroscopic scale the Darcy equation is applicable. At this macroscopic scale, the description of the flow of phases introduces new equations which are the transposition of the mass balance, momentum and energy microscale balances. For example, the equation of Darcy is the momentum balance at the macroscopic scale which can be deduced from Navier–Stokes equations. In these macroscopic equations appear effective properties, as the permeability in Darcy’s law, the relative permeability and capillary pressure in the multiphase case, etc. These effective properties can be theoretically obtained from microscopic properties using upscaling techniques.

The field scale (Figs. 10.1 and 10.2) is defined as the spatial dimension where the soil properties become nonstationary [23]. Natural field scale media are in fact generally heterogeneous and contributes to both spatially and temporally non-linear multiphase flow behavior. At this scale, the soil properties are rarely the same at every point of the medium. When solving the governing equations of flow or transport using numerical schemes, where the domain is discretized into computational blocks or grids, it is possible to take into account the effect of these heterogeneities using block sizes smaller than the characteristic size of the heterogeneities. As this may not be feasible due to high computational demands, a second upscaling stage is needed to describe the field scale properties from the macroscale description.

10.3.2. Processes and Constitutive Models

Multi-phase porous media systems consist of fluids that exist in separate phases in the inter-granular pore spaces. Figure (10.3) schematically

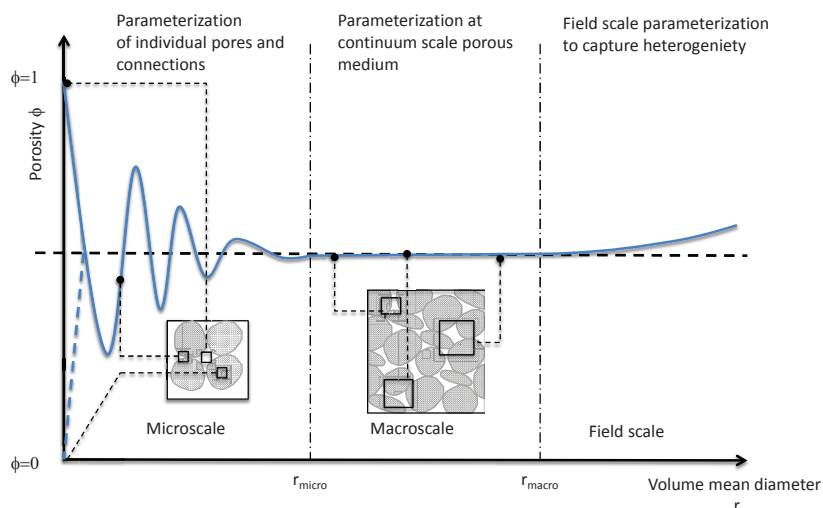


Fig. 10.2. Porosity as a function of the volume mean radius r . Heterogeneity and scale. Here the averaging of porosity over the different length scales from pore, homogeneous continuum scale to heterogeneous field scale is shown.

shows such systems encountered in hydrogeological applications. Two-phase problems of water flow in the unsaturated zone above the water table associated with rainfall infiltration, aquifer recharge and irrigation involve water and air as the wetting and non-wetting fluids, respectively. Below the water table, the soil pores are fully saturated with water, thus describing the flow as a single-phase problem. In industry, related problems involving accidental releases of partially immiscible fluids (NAPLs) such as industrial solvents, wood treating agents and petroleum products, the fluid displaces some of the non-wetting air phase resulting in a three-phase system. When NAPLs that are heavier than water penetrate the water table, the non-wetting phase displaces some of the pore-water resulting in a two-phase system. Interfacial tension at wetting/non-wetting fluid interfaces within pores introduces additional force of capillarity that is not present in saturated single-phase flow systems.

Each fluid in a multiphase system is characterized by its own pressure state. The differences in pressure arise from imbalances of molecular forces at fluid interfaces [24]. In a two-phase system, the capillary pressure $p_c [ML^{-1}T^{-2}]$ that depends on the wetting phase saturation $S_w [-]$ is defined as the pressure difference between wetting and non-wetting phases

$$p_c(S_w) = p_{nw} - p_w, \quad (10.2)$$

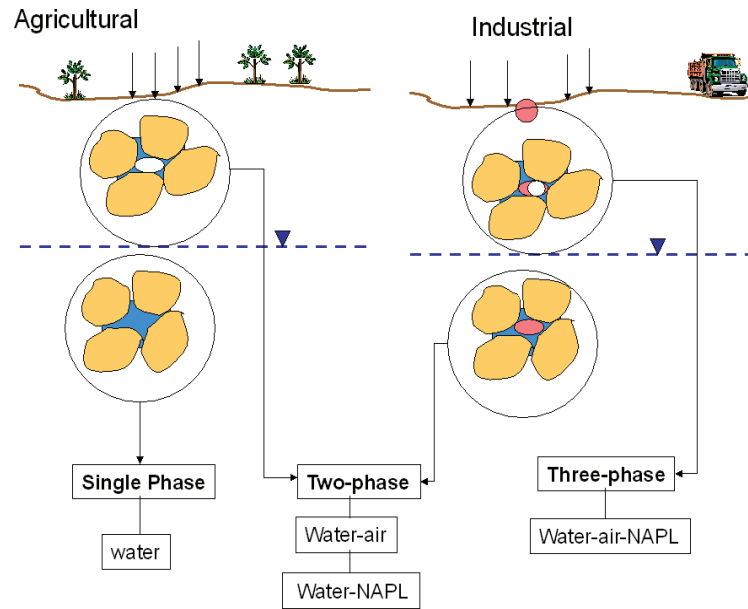


Fig. 10.3. Multi-phase porous media systems in hydrogeology.

where p_{nw} [$ML^{-1}T^{-2}$] is the non-wetting phase pressure and p_w [$ML^{-1}T^{-2}$] is the wetting phase pressure. The relationship of capillary pressure and fluid content is referred to as the capillary pressure function (that is referred to as the retention function in unsaturated flow systems). As given in Eq. (10.2), capillary pressure is usually expressed as a function of the saturation of the wetting fluid. This relationship is an intrinsic property of a given porous medium and the two-fluid system. Data on capillary pressure as a function of saturation are obtained experimentally and fitted with mathematical functions to obtain constitutive models for multiphase flow. Two commonly used constitutive models for capillary pressure in soil physics and geohydrologic applications are presented by Brooks and Corey [25] and van Genuchten [26]. The Brooks-Corey model for the retention function is,

$$p_c(S_w) = p_d S_e^{\frac{1}{\lambda}}, \quad \text{for } p_c \geq p_d, \quad (10.3)$$

where λ [-] is a fitting parameter, and p_d [$ML^{-1}T^{-2}$] is the pressure at which the non-wetting fluid first enters the pores when the non-wetting phase builds up and is called *displacement* or *entry* pressure. The effective

saturation S_e is defined as,

$$S_e = \frac{S_w - S_{r,w}}{1 - S_{r,w} - S_{r,nw}}, \quad (10.4)$$

where $S_{r,w}$ [–] and $S_{r,nw}$ [–] are the residual or minimum saturation wetting and non-wetting fluid, respectively.

When multiple fluid phases are present within the pore space, the ability of the medium to conduct a given fluid within a pore will not depend on the geometry of the pore space only, but also on fluid properties, geometry of the fluid-filled part of the pore space and phases volume fraction. Darcy's law that was originally developed and applied for single phase flow is adopted for multiphase flow through the use of the concept of relative permeability [27] as,

$$\mathbf{q}_\alpha = -\frac{k_{r,\alpha}(S_\alpha)}{\mu_\alpha} \mathbf{K}_i (\nabla p_\alpha - \rho_\alpha \mathbf{g}), \quad \text{for } \alpha = w, nw, \quad (10.5)$$

where \mathbf{q}_α [LT^{-1}]³ is the apparent macroscopic velocity of the phase α , μ_α [$ML^{-1}T^{-1}$] is the dynamic viscosity of the phase α , \mathbf{K}_i [L^2]^{3×3} is the intrinsic permeability tensor, $k_{r,\alpha}$ [–] is the α -phase relative permeability function, ρ_α [ML^{-3}] is the density of the phase α , and \mathbf{g} [LT^{-2}]³ is the gravitational acceleration vector. The relative permeability $k_{r,\alpha}$ of fluid phase α ranges between zero and one and depends on the fluid saturation S_α .

By extension, the hydraulic conductivity tensor \mathbf{K} [LT^{-1}]^{3×3} also becomes a function of saturation of the phase α ,

$$\mathbf{K} = \mathbf{K}(S_\alpha) = \frac{k_{r,\alpha}(S_\alpha)\rho_\alpha g}{\mu_\alpha} \mathbf{K}_i, \quad (10.6)$$

where g [LT^{-2}] is the scalar gravitational acceleration constant.

The Brooks–Corey constitutive model for the relative permeabilities of the wetting and the non-wetting phases are

$$k_{r,w} = S_e^{-\frac{2+3\lambda}{\lambda}}, \quad (10.7a)$$

$$k_{r,nw} = (1 - S_e)^2 \left(1 - S_e^{-\frac{2+\lambda}{\lambda}}\right). \quad (10.7b)$$

Darcy's law for multiphase flow (Eq. (10.5)) and the mass balance for each phase are combined to derive the governing equations for multiphase flow in two-phase system as,

$$\phi \frac{\partial(\rho_\alpha S_\alpha)}{\partial t} - \nabla \cdot \left(\frac{\rho_\alpha k_{r,\alpha}}{\mu_\alpha} \mathbf{K}_i (\nabla p_\alpha - \rho_\alpha \mathbf{g}) \right) = F_\alpha, \quad (10.8)$$

where F_α [$ML^{-3}T^{-1}$] is the source/sink term and fluid phase $\alpha = w, nw$. Equation (10.8) written for each phase in the multiphase flow system, in combination with the constitutive models for capillary pressures (Eq. (10.3)) and relative permeabilities (Eq. (10.7)) provide the full formulation of the mathematical model to solve for the phase pressures and saturations for given initial and boundary conditions and source terms. These governing equations are derived for the continuum macro-scale (or Darcy scale). The parameters that appear in these equations have to be upscaled to computational grid scale when used in simulations. The upscaling of constitutive models of capillary pressure and relative permeability are discussed in the next section.

10.3.3. Upscaling Constitutive Parameters

It is well supported in literature that the highly non-linear distribution of hydrologic processes often limits the ability to track interactions from scale-to-scale and across space and time. The primary question driving the upscaling problem is: can laboratory scale measurements successfully be applied to properly describe larger scale flow and transport behavior? We know that one can directly apply laboratory measured soil hydraulic properties as inputs for lab scale studies and simulation models. However, in developing upscaling methods, it is necessary to recognize that it is not practical to take measurements at all points in the subsurface system to determine the needed parameters. Hence, the development of theoretical foundations for any upscaling method leads to a practical question: how can soil hydraulic parameters determined for homogeneous samples collected at a limited number of locations or the laboratory scale be used to determine the parameters of the discretized grid blocks of models (grid-block scale) that simulate the field scale behavior? One option is to spatially distribute laboratory scale soil hydraulic properties across larger scales. Alternatively, the lab or discrete in-situ scale properties can be used as initial estimates and improved upon by using inverse modeling or during model calibration. Inverse modeling attempts to minimize differences between observation and simulation using analytical or numerical solutions that include constitutive relationships that contain estimated parameters [28].

The texture variability that contributes to changes in porosity with scale also affects the parameters that depend on the pore sizes and pore size distribution. These include permeability and hydraulic conductivity in saturated groundwater flow, soil-water retention and relative permeability

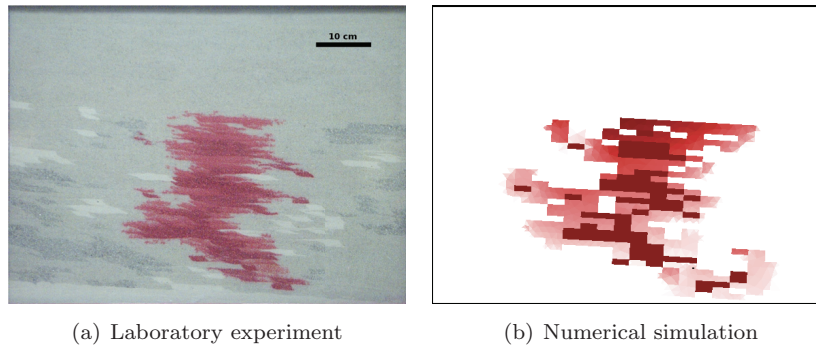


Fig. 10.4. Laboratory simulation of multiphase flow in a heterogeneous porous medium (a) and numerical simulation using the upscaled parameters (b). The numerical solution was obtained using the mixed hybrid finite element method described in Refs. [33, 34].

estimated upscaled parameters in Fig. 10.4.

At the REV scale, the multiphase system is characterized by the constitutive relationships that include capillary pressure and relative permeability as functions of saturation (Eqs. (10.3) and (10.7)). The issue of upscaling these constitutive models is common to the types of problems in multiphase flow that were presented in Section 10.2. Parameter upscaling has been extensively studied by petroleum engineering as applied to hydrocarbon reservoirs, soil physicists in irrigation water management and geo-hydrologist for applications in subsurface remediation involving solvents and petroleum wastes. Constitutive models are developed from measurements made in the laboratory using small samples whose sizes correspond to size of cores extracted during field investigations. The basic way these parameters are upscaled in multiphase systems is very different from single-phase flow, because in addition to the subsurface heterogeneity, the non-linearities of the basic processes play a critical role [36]. These non-linearities also contribute to different fluid retention behavior at different length scales.

Early work on upscaling in unsaturated flow systems (water as wetting and air as non-wetting fluids) based on small perturbations (e.g. [37]) is not generally applicable when the size of the field domain is small compared to the length scales of the heterogeneity. In the development of upscaling for two-phase flow, some researchers adopted percolation network models used in pore-scale investigations to upscale constitutive relationships at the macro-scale [38–40]. In small samples that are used to get the retention function in the laboratory, the water content that corresponds to a

The upscaled hydraulic conductivity was given as

$$K(p_c) = \frac{1}{V} \int_V k(p_c)^\omega dV, \quad (10.10)$$

where, $K [LT^{-1}]$ and $k [LT^{-1}]$ are the upscaled and sample scale hydraulic conductivities, respectively, and $\omega [-]$ is a constant scalar parameter. This expression assumes that even though the sample scale relative permeability primarily depends on the pore-size distribution, the upscaled conductivity does not. This approach, even though practical, is limited to steady-state unsaturated flow in porous media with large air entry values. In petroleum engineering, the problem of upscaling constitutive models was posed in the context of managing the computing efficiency by using large grid blocks. The upscaling methods used pseudo-functions [44] that accounts for the heterogeneity within the large grid-block to replace the multiphase effective permeabilities and capillary pressures [45]. The goal was to use large grid dimensions to utilize available computing power manageable levels and with minimum loss of accuracy due to simplified representation of the heterogeneity. Use of this method still requires fine-grid simulations of a representative reservoir section to determine the appropriate pseudo-functions for the selected parameters. Even though some computing efficiencies have been achieved, these methods were considered to be without strong theoretical foundation [42].

Other techniques have been proposed and used for upscaling two-phase flow. In homogenization [46, 47], stochastic representation of conservation laws in porous medium are used to get non-linear effective equations that are considered to govern the flow behavior of the homogenized equivalent of the randomly heterogeneous porous medium. Another method referred to as the large-scale volume averaging (e.g. [48]), the flow equations and the properties at a larger scale are calculated by averaging from a lower scale. This method has been demonstrated to be more efficient than methods based on pseudo-functions that require full simulations using fine-grid model [45]. The volume averaging technique has been extensively used to predict the macro-scale transport properties for many processes including transport in heterogeneous porous media [49], two-phase flow [50], two-phase inertial flow [51], reactive media [45, 52], solute transport with adsorption [53] multi-component mixtures [54], and coupled heat and mass transfer with Soret effect [55, 56].

The question of using a one- or two-equation model is raised when modeling two phase (or region when working at the Darcy's scale) flow in

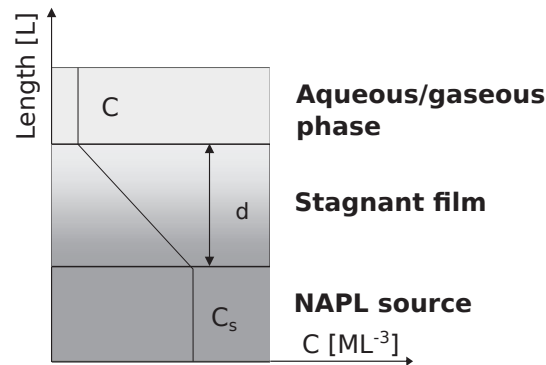


Fig. 10.5. Stagnant layer model with linear concentration profile between the NAPL source concentration C_s and the concentration C the in the bulk phase.

all mass transfer rate coefficient. By extending the single film theory, a linear driving force model similar to Eq. (10.11) can be used to describe mass flux from entrapped non-wetting phase (NAPL, ScrCO_2 or CO_2 gas plume) sources in porous media. This is accomplished by introducing a lumped mass transfer rate coefficient K_c [T^{-1}] [60]. The interface mass rate J' [$ML^{-3}T^{-1}$] in porous medium takes the form

$$J' = K_c(C_s - C). \quad (10.12)$$

The pore-scale mass transfer coefficient k_ℓ and the lumped mass transfer coefficient K_c are related by

$$K_c = k_\ell \frac{A_{nw}}{V} \quad (10.13)$$

where A_{nw} [L^2] is the total NAPL–water surface area within the REV of volume V [L^3]. As A_{nw} cannot be directly measured, in practical applications in porous media, K_c is treated as an empirically determined parameter for a specific multiphase system.

10.4.2. Gilliland–Sherwood models

Phenomenological models that are used to predict the mass transfer rate coefficient k_ℓ or the lumped mass transfer coefficient K_c are referred to as Gilliland–Sherwood models and are represented by dimensionless Sherwood number Sh and modified Sherwood number Sh' . The Sherwood number Sh is related to the mass transfer rate coefficient k_ℓ as

$$Sh = k_\ell \frac{d_p}{D_\ell}, \quad (10.14)$$

where d_p [L] is the geometric mean of particle diameter and D_ℓ [L^2T^{-1}] is the diffusion coefficient in the free liquid. The modified Sherwood number Sh' that involves the lumped mass transfer rate K_c and is suitable for use in porous media applications is defined as

$$Sh' = K_c \frac{d_p^2}{D_\ell}. \quad (10.15)$$

Therefore instead of K_c , the dimensionless Sherwood number Sh' is determined empirically in order to describe the mass transfer process under various physical and chemical conditions in the porous media.

Building on the concept of upscalable Gilliland-Sherwood model for porous media, an empirical model for REV scale mass transfer was proposed by Ref. [61] in a general form

$$Sh' = \alpha Re^\beta Sc^\gamma \left(\frac{\theta_n d_{50}}{\tau L} \right)^\delta, \quad (10.16)$$

that involves four dimensionless fitting parameters α , β , γ , and δ , dimensionless Reynolds and Schmidt numbers Re [–] and Sc [–], respectively, dissolving NAPL content θ_n [–], d_{50} [L] is the particle diameter such that 50% of the porous media are finer by weight (median particle size), τ [–] is the tortuosity factor of the flow path, and L [L] is the dissolution length. The corresponding model that was fitted by Saba and Illangasekare [61] to dissolution data obtained in a two-dimensional flow configuration in a small scale test tank is $\alpha = 11.34$, $\beta = 0.28$, $\gamma = 0.33$, $\delta = 1.037$. Saba and Illangasekare [61] compared other Gilliland-Sherwood models that have appeared in literature and showed that the dimensionality of water flow has to be taken into consideration when upscaling the models based on one-dimensional systems to multi-dimensional flow systems in the field. An overview of other Gilliland-Sherwood models for the modified Sherwood number Sh' applicable for various dissolution configurations within the porous medium is given in [62]. Liu et al. [63] developed a Gilliland-Sherwood model for a synthetic porous medium consisting of random-size spheres and solving the groundwater flow and mass transfer at the pore-scale using a multi-physics simulator COMSOL Multiphysics[®]. This model is given as

$$Sh = 3.81 Re^{0.57} Sc^{0.33}. \quad (10.17)$$

As the flow is laminar and the kinematic viscosity is constant and the mass transfer is dependent on advection and diffusion, [63] was able to represent

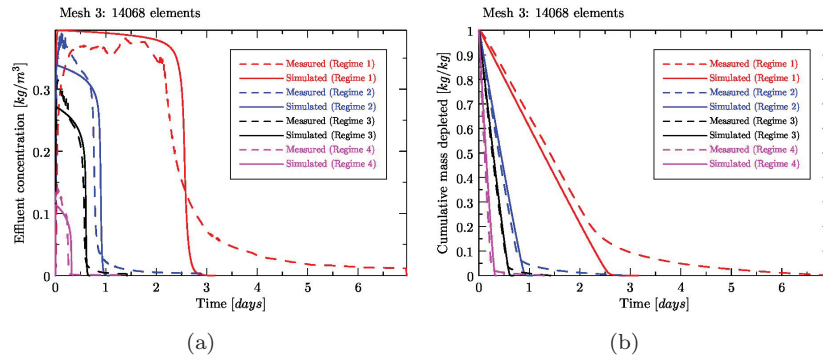


Fig. 10.6. TCE concentration (a) and cumulative TCE content depletion (b) temporal profiles compared to laboratory measured data (dotted lines), [64].

the Sh number as only a function of the Péclet number Pe as

$$Sh = 0.094Pe^{0.56}. \quad (10.18)$$

Petri et al. [64] investigated a complete volatilization of a volatile organic compound (VOC) pool in the context of generation of contaminant vapor plumes in heterogeneous porous medium. In the experiment, an immobile NAPL pool of trichlorethylene (TCE) was created in the source zone placed inside a small tank. In one of the scenarios, the pool was exposed to the flowing 100% humidified air under four different velocities studied. A numerical model was developed and used to determine the Gilliland–Sherwood model hypothesized in the general form proposed by [61] in the form

$$Sh' = 0.0011Pe^{0.05} \left(\frac{\theta_n}{\theta_n^{ini}} \right)^{0.2} d_0^{1.68}, \quad (10.19)$$

where θ_n^{ini} [–] is the initial NAPL content in the source zone. The small exponent of the Péclet number suggests that the velocity of the flowing air has a negligible effect on the rate of volatilization. In Fig. 10.6, the experimentally measured effluent concentration and the cumulative TCE content depletion are compared to the results of the mathematical model.

10.4.3. Upscaling of Mass Transfer Rate Coefficients

The upscaling of dissolution of trapped non–aqueous phase (NAPLs) has been studied for applications in remediation of sites contaminated with solvents and petroleum waste [62, 65].

The goal of upscaling dissolution is to determine what parameters of the field systems have to be included to determine the effective mass transfer rate coefficient. Saenton and Illangasekare [66] hypothesized that as the mass loading to the flowing water occurs at the pores where NAPL is entrapped, the total mass loading at the grid-scale will depend on the saturation distribution of the NAPL. They quantified the distribution (or spread) through a dimensionless second moment $M_{II,z}$ [–]. The mass that gets loaded is transported within the grid block by the flowing water and the net mass generation is a result of mixing within the block. This velocity driven mixing was captured through the use of geostatistical parameters of the heterogeneity field and the size of the grid block. Using synthetic data from numerical simulations where various NAPL entrapment architecture were created in correlated random fields, Saenton and Illangasekare [66] obtained an expression for the upscaled mass transfer correlation as

$$\overline{\text{Sh}} = \text{Sh}_0(1 + \sigma_Y^2)^{\varphi_1} \left(1 + \frac{\Delta z}{\lambda_z}\right)^{\varphi_2} \left(\frac{\hat{M}_{II,z}}{\hat{M}_{II,z}^*}\right)^{\varphi_3} \quad (10.20)$$

where $\overline{\text{Sh}}$ [–] is the upscaled Sherwood number containing the effective mass transfer rate coefficient, σ_Y^2 is the variance of the log K field, Δz [L] is the vertical dimensions of the simulation grid, λ_z [L] is the vertical correlation length and the last set of terms is the dimensionless second moment of the vertical saturation distribution. This method of upscaling was validated using data from an intermediate scale tank experiment [62] shown in Fig. 10.7.

The example of upscaling of a mass transfer that occurs at the pore-scale to grid scale provides the framework for developing upscaling methods for problems in carbon sequestration. The method was developed for a two-dimensional flow case and validated in a two-dimensional test system. As was discussed earlier, heterogeneity and flow dimensionality will play a critical role in the upscaling process. Hence, further study is needed to evaluate the effects of the third spatial dimensions and use of other parameters of the geologic formations when the assumption of stationarity that is built into the geostatistical parametrization is not valid. Also, the issue of how the dissolved mass diffuses into low permeability formations and how the process gets upscaled needs further study and development [67].

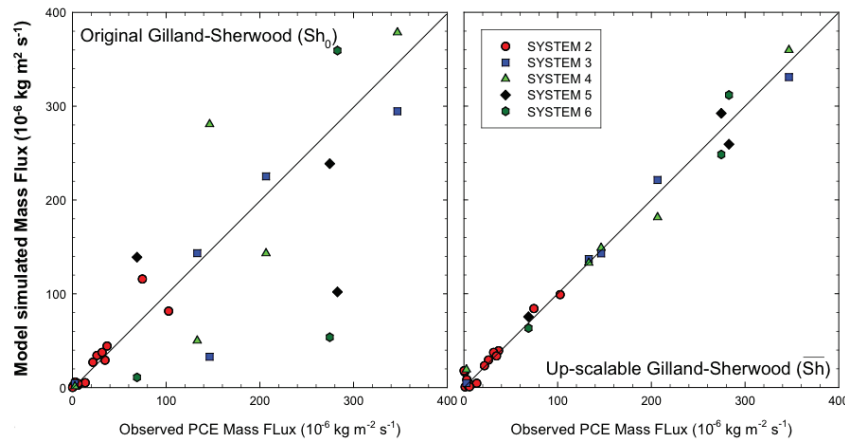


Fig. 10.7. Upscaling of NAPL dissolution: (a) Comparison of observed mass flux and mass flux estimated using the small-scale dissolution model, (b) comparison of observed mass flux and mass flux estimated using the upscaled dissolution model (system 2–5 refer to different grid sizes used in the simulations) [62].

10.5. Land/atmospheric Interactions

A variety of coupled processes and feedbacks between thermal, hydrological, geochemical and biological processes occur at the land-atmospheric interface. These coupled processes and feedbacks significantly influence the energy and mass balances and hence environmental conditions. Understanding heat, mass and momentum fluxes at the land surface at all relevant scales remains a major scientific challenge. Understanding mass and heat fluxes across the land surface at all relevant scales from laboratory to field remains a major scientific challenge. One such exchange process is evaporation, an important process that affects the water and energy balance in the soil and atmosphere, and consequently changes the local and global climatic behavior. In this section a review of the efforts to understand and upscale the processes associated with evaporation are presented.

10.5.1. Processes and Modeling

As conceptually shown in Fig. 10.8, the rate of soil evaporation is affected by atmospheric conditions (e.g. humidity, temperature, thermal radiation, wind velocity and turbulent flow regime), and thermal, and hydraulic properties of soil (thermal and hydraulic conductivity, porosity), all of which are strongly coupled. This strong coupling between processes leads to highly

Traditionally, the influences of atmospheric conditions are applied at the soil surface and aerodynamic resistance is applied on the border between the air flow and permeable media (e.g. [69, 71–73]). In these cases, evaporation rate E [$ML^{-2}T^{-1}$] can be given as

$$E = \frac{1}{r_s + r_v} ((\rho_v)_{pm} - (\rho_v)_{ff}), \quad (10.21)$$

where r_s [$L^{-1}T$] is the soil surface resistance for water vapor transport, r_v [$L^{-1}T$] is the aerodynamic resistance for water vapor, $(\rho_v)_{pm}$ [ML^{-3}] is the vapor density immediately below the soil surface (in porous medium) and $(\rho_v)_{ff}$ [ML^{-3}] is the vapor density immediately above the soil surface (in free medium). The vapor density above the soil surface is calculated from measurement of relative humidity on the boundary of the porous medium domain in the free flow medium.

In Eq. (10.21), the aerodynamic resistance for vapor transport depends on surface roughness properties and wind speed [69, 74]. The soil surface resistance depends on soil surface water content. The relationship between aerodynamic resistance to vapor transport and soil water content is typically expressed in an exponential form; there are many exponential empirical functions used to describe this relationship [71, 73]. Although this approach is widely used, modeling comparison studies have shown significant variation between model parameterizations and evaporative fluxes [75–78]. Recently, with the goal of addressing the issue of coupling the land to the atmosphere, [77] evaluated three different modeling approaches of bare soil evaporation formulated with different land surface boundary conditions and compared modeling results to laboratory generated experimental data. Results demonstrated that no one approach could be deemed most appropriate for every situation, demonstrating that further work focusing on the land/atmospheric interface, properly incorporating the complex interactions between the land and the atmospheric boundary layer is needed to increase the understanding of the processes that control shallow subsurface soil moisture flow that controls bare soil evaporation.

The modeling of non-isothermal single-phase (two-component) transfer in the atmosphere and two-phase (two-component) transfer in porous media have been separately investigated by many authors (e.g. [79–81]). Recently, numerical advances have been made in the coupling of free flow (Navier–Stokes) with porous media flow (Darcy flow) [82–87], however, these models were not adequately validated with experimental data. Mosthaf et al. [85] extended the classical single-phase coupling to two-phase

the land and atmosphere during the process of evapotranspiration, assessing groundwater recharge rates, and optimizing water management for agricultural purposes. Despite the importance of these predictions, standard models have limited capabilities to predict water or gas fluxes, flow pathways and water distribution. Even common practices such as understanding evaporation dynamics from homogeneous soils or water distribution after a heavy rainfall has proven to be difficult with standard models (e.g. [77, 93–96]). This can be partially attributed to models not capturing the physical behavior through proper system description/parameterization. As our computational capabilities continue to improve, our ability to describe the added complexity of physical systems should also improve rather than continuing to rely on the standard methods. By understanding the relative contribution of processes at various scales and how the processes can best be implemented at different scales to more accurately predict environmental behaviors remains a challenge. The challenges associated with upscaling mass transport through soil pores close to the land surface comes from the need to parametrize processes that couple Darcian flow in the soil to Stokes flow in the atmosphere. Practical and theoretical limitations of modeling efforts are often magnified at the land–atmosphere interface, where water and energy fluxes are highly dynamic and dramatically influenced by changes in thermal and moisture gradients and direction of flows [97]. However, for most conventional models and practical applications involving vadose zone, the strong coupling between the land and the atmosphere is rarely considered. This is due to the complexity of the problem in field scenarios and the scarcity of field or laboratory data capable of testing and refining energy and mass transfer theories. For most subsurface models, the soil surface serves as the upper boundary to the porous medium domain and is characterized using prescribed flux terms that serve as sources or sinks. Similarly, in most atmospheric models, the vadose zone serves as a lower boundary with prescribed fluxes. Such an approach is a simplification of the interaction processes above and below the soil surface. Although widely used due to its simplicity and ease of use, such an approach has been shown by both atmospheric and hydrogeological scientists to misrepresent flux conditions, resulting in model prediction errors [98]. When considering heterogeneous soils, this is particularly relevant. Heterogeneous soils result in complex flux conditions due to water fluxes from coarse to fine textured soils [94, 99]. This is not captured when prescribing a constant flux over the entire soil surface boundary. In addition, variations in soil surface conditions (e.g. soil type, texture, vegetation) can

scaling in multiphase flow are the relationships between capillary pressure vs saturation and relative permeability vs saturation. The parameter up-scaling methods for these are fundamentally different from that of single phase flow because of the non-linearity of these multiphase parameters. Techniques based on percolation network models, stochastic homogenization, large-scale volume averaging and methods based on pseudo-functions had limited success and the need exist for the development of more generalized approaches that can be applicable to both two-phase and three-phase systems.

The problem of dissolution of trapped non-aqueous liquids (NAPLs) has received recent attention in relation to dissolution trapping of stored supercritical CO₂ in deep geologic formations. Methods have been developed to up-scale the mass transfer rate coefficients to simulate field scale behavior by treating the effective dissolution as a mixing process controlled by the architecture of the NAPL entrapment and geostatistical parameters of the permeability field. This method provides a possible framework to develop dissolution upscaling for supercritical CO₂. However, whether rate limited conditions exist in field settings requires additional evaluation prior to developing such methods. The net mass loading from supercritical CO₂ trapped zones will not only be controlled by dissolution, but also back diffusion from low permeability zones in the heterogeneous formation. Methods are needed to obtain effective parameters that capture both these processes to predict long-term effectiveness of dissolution trapping.

Parameterization of processes that control land-atmospheric interactions is at its early stages of development. The knowledge gaps in the understanding of these processes from pore scale to larger scales, have resulted in models that rarely consider the strong coupling between the land and the atmosphere. Until these knowledge gaps are filled through experimental studies conducted at multiple scales, any validation of such up-scaling theories and methods are not possible.

Field data for validation of upscaling methods are often incomplete and costly to obtain. In field settings, the degree of control that is needed to obtain such data is not adequate. The intermediate laboratory scale offers the ability to study, under controlled conditions, complicated processes in the heterogeneous subsurface in multiple dimensions at different scales.

A conclusion can be made that scaling issues can only be resolved through the integration of theory with experiments, requiring innovative, multidisciplinary research efforts aimed at overcoming our current limited understanding of the influence of small scale processes on larger scale flow behavior.

Greek symbols

Notation	Units	Description	Page
θ_n	[-]	NAPL volumetric content	184
λ	[-]	Brooks and Corey fitting parameter	175
λ_z	[L] Vertical correlation length	186	
μ_α	[$ML^{-1}T^{-1}$]	Dynamic viscosity of phase α	176
ρ_α	[ML^{-3}]	Density of phase α	176
τ	[-]	Torosity factor	184
Φ	[-]	Porosity	172
χ	[-]	Void space indicator function	172

References

- [1] L. W. Gelhar, Stochastic subsurface hydrology from theory to applications, *Water Resour. Res.* **22**(9S), 135S–145S (1986).
- [2] T. H. Illangasekare, J. L. Ramsey Jr, K. H. Jensen, and M. B. Butts, Experimental study of movement and distribution of dense organic contaminants in heterogeneous aquifers, *J. Contam. Hydrol.* **20**(1), 1–25 (1995).
- [3] F. Fagerlund, T. H. Illangasekare, and A. Niemi, Nonaqueous-phase liquid infiltration and immobilization in heterogeneous media: 1. experimental methods and two-layered reference case, *Vadose Zone J.* **6**(3), 471–482 (2007).
- [4] F. Fagerlund, T. H. Illangasekare, and A. Niemi, Nonaqueous-phase liquid infiltration and immobilization in heterogeneous media: 2. application to stochastically heterogeneous formations, *Vadose Zone J.* **6**(3), 483–495 (2007).
- [5] E. Agartan, L. Trevisan, A. Cihan, J. Birkholzer, Q. Zhou, and T. Illangasekare, Experimental Study on Effects of Geologic Heterogeneity in Enhancing Dissolution Trapping of Supercritical CO₂, in review in, *Water Resour. Res.* (2014).
- [6] M. Plampin, T. Illangasekare, T. Sakaki, and R. Pawar, Experimental study of gas evolution in heterogeneous shallow subsurface formations during leakage of stored CO₂, *Int. J. Greenh. Gas Cont.* **22**, 47–62 (2014).
- [7] I. N. Tsimpanogiannis and Y. C. Yortsos, Model for the gas evolution in a porous medium driven by solute diffusion, *AIChE Journal.* **48**(11), 2690–2710 (2002).
- [8] L. Bernstein, P. Bosch, O. Canziani, Z. Chen, R. Christ, O. Davidson, W. Hare, S. Huq, D. Karoly, V. Kattsov, et al., IPCC, 2007: climate change 2007: synthesis report. Contribution of working groups I, II, and III to the Fourth Assessment Report of the Intergovernmental Panel on Climate Change, *Intergovernmental Panel on Climate Change, Geneva* (2007).
- [9] US EPA. Inventory of US greenhouse gas emissions and sinks: 1990–2009. Technical report, US Environmental Protection Agency (2011).
- [10] T. G. Poulsen and P. Møldrup, Evaluating effects of wind-induced pressure fluctuations on soil-atmosphere gas exchange at a landfill using stochastic modelling, *Waste Manage. Res.* **24**(5), 473–481 (2006).

- Geophysical Union (2005).
- [28] Y.-K. Zhang and K. Schilling, Temporal scaling of hydraulic head and river base flow and its implication for groundwater recharge, *Water Resour. Res.* **40**(3) (2004).
- [29] G. Dagan et al., *Flow and Transport in Porous Formations*. Springer-Verlag GmbH & Co. KG. (1989).
- [30] L. W. Gelhar, *Stochastic Subsurface Hydrology*. Prentice-Hall (1993).
- [31] Y. Zhang, C. W. Gable, and M. Person, Equivalent hydraulic conductivity of an experimental stratigraphy: Implications for basin-scale flow simulations, *Water Resour. Res.* **42**(5) (2006).
- [32] P. Renard and G. De Marsily, Calculating equivalent permeability: A review, *Adv. Water Resour.* **20**(5), 253–278 (1997).
- [33] R. Fučík and J. Mikyška, Discontinuous Galerkin and Mixed–Hybrid Finite Element Approach to Two–Phase Flow in Heterogeneous Porous Media with Different Capillary Pressures, *Procedia Computer Science.* **4**, 908–917 (2011).
- [34] R. Fučík and J. Mikyška, Mixed-hybrid finite element method for modelling two-phase flow in porous media, *Journal of Math-for-Industry.* **3**, 9–19 (2011).
- [35] F. Fagerlund and G. Heinson, Detecting subsurface groundwater flow in fractured rock using self-potential (sp) methods, *Environmental Geology.* **43**(7), 782–794 (2003).
- [36] B. Ataie-Ashtiani, S. Hassanizadeh, M. Celia, M. Oostrom, and M. D. White. Effective two-phase flow parameters for heterogeneous porous media. Technical report, Pacific Northwest National Laboratory (PNNL), Richland, WA (US) (2000).
- [37] A. Montoglou and L. Gelhar, Effective hydraulic conductivities of transient unsaturated flow in stratified aquifer, *Water Resour. Res.* **23**(1), 57–67 (1987).
- [38] I. Chatzis and F. Dullien, Modelling Pore Structure By 2-D And 3-D Networks With Application to Sandstones, *J. Can. Petrol. Technol.* **16**(1) (1977).
- [39] B. H. Kueper and D. B. McWhorter, The use of macroscopic percolation theory to construct large-scale capillary pressure curves, *Water Resour. Res.* **28**(9), 2425–2436 (1992).
- [40] H. Rajaram, L. A. Ferrand, and M. A. Celia, Prediction of relative permeabilities for unconsolidated soils using pore-scale network models, *Water Resour. Res.* **33**(1), 43–52 (1997).
- [41] A. Desbarats, Upscaling capillary pressure-saturation curves in heterogeneous porous media, *Water Resour. Res.* **31**(2), 281–288 (1995).
- [42] A. Desbarats, Scaling of constitutive relationships in unsaturated heterogeneous media: A numerical investigation, *Water Resour. Res.* **34**(6), 1427–1435 (1998).
- [43] H. Liu, G. Bodvarsson, and G. Zhang, Scale dependency of the effective matrix diffusion coefficient, *Vadose Zone J.* **3**(1), 312–315 (2004).
- [44] T. Lasseter, J. Waggoner, and L. Lake, Reservoir heterogeneities and their

- on mass transfer from entrapped nonaqueous phase liquid contaminants, *Water Resour. Res.* **36**(4), 971–979 (2000).
- [62] T. Illangasekare and C. Frippiat. Miscible and immiscible pollutants in subsurface systems. In ed. H. Fernando, *Handbook Of Environmental Fluid Dynamics*. Taylor and Francis Group (2010).
- [63] Y. Liu, T. H. Illangasekare, and P. K. Kitanidis, Long-Term Mass Transfer and Mixing-Controlled Reactions of A DNAPL Plume from Persistent Residuals, *J. Contam. Hydrol.* **157**, 11–24 (2014).
- [64] B. Petri, R. Fučík, T. H. Illangasekare, K. M. Smits, J. A. Christ, T. Sakaki, and C. C. Sauck, Effect of nonaqueous phase liquid source morphology on mass transfer in the vadose zone: Experimental and modeling study, to appear in *Groundwater J.* (2014).
- [65] T. Illangasekare, C. Frippiat, and R. Fučík. Dispersion and mass transfer coefficients in groundwater of near-surface geologic formations. In eds. L. J. Thibodeaux and D. Mackay, *Handbook of Estimation Methods: Environmental Mass Transport Coefficients, Dispersion and Mass Transfer Coefficients*, pp. 413–452. CRC Press (2010).
- [66] S. Saenton and T. H. Illangasekare, Upscaling of mass transfer rate coefficient for the numerical simulation of dense nonaqueous phase liquid dissolution in heterogeneous aquifers, *Water Resour. Res.* **43**(2) (2007).
- [67] B. T. Wilking, D. R. Rodriguez, and T. H. Illangasekare, Experimental Study of the Effects of DNAPL Distribution on Mass Rebound, *Groundwater J.* **51**(2), 229–236 (2013).
- [68] M. Sakai, S. B. Jones, and M. Tuller, Numerical evaluation of subsurface soil water evaporation derived from sensible heat balance, *Water Resour. Res.* **47**(2) (2011).
- [69] M. Bittelli, F. Ventura, G. S. Campbell, R. L. Snyder, F. Gallegati, and P. R. Pisa, Coupling of heat, water vapor, and liquid water fluxes to compute evaporation in bare soils, *J. Hydrol.* **362**(3), 191–205 (2008).
- [70] R. S. Jassal, T. A. Black, M. D. Novak, D. Gaumont-Guay, and Z. Nesic, Effect of soil water stress on soil respiration and its temperature sensitivity in an 18-year-old temperate douglas-fir stand, *Glob. Change Biol.* **14**(6), 1305–1318 (2008).
- [71] P. Camillo and R. Gurney, A resistance parameter for bare-soil evaporation models, *Soil Sci.* **141**(2), 95–105 (1986).
- [72] M. D. Novak, Dynamics of the near-surface evaporation zone and corresponding effects on the surface energy balance of a drying bare soil, *Agri. For. Meteorol.* **150**(10), 1358–1365 (2010).
- [73] A. A. van de Griend and M. Owe, Bare soil surface resistance to evaporation by vapor diffusion under semiarid conditions, *Water Resour. Res.* **30**(2), 181–188 (1994).
- [74] G. S. Campbell and J. M. Norman, *An Introduction to Environmental Biophysics*. Springer (1998).
- [75] C. Desborough, A. Pitman, and P. Iranneiad, Analysis of the relationship between bare soil evaporation and soil moisture simulated by 13 land surface schemes for a simple non-vegetated site, *Global Planet. Change.* **13**(1),

- draulic properties and soil water flow processes in heterogeneous soils, *Vadose Zone J.* **6**(1), 1–28 (2007).
- [93] Z. Wang, A. Tuli, and W. A. Jury, Unstable flow during redistribution in homogeneous soil, *Vadose Zone J.* **2**(1), 52–60 (2003).
- [94] P. Lehmann and D. Or, Evaporation and capillary coupling across vertical textural contrasts in porous media, *Phys. Rev. E.* **80**(4), 046318 (2009).
- [95] N. Shokri, P. Lehmann, and D. Or, Characteristics of evaporation from partially wettable porous media, *Water Resour. Res.* **45**(2) (2009).
- [96] K. M. Smits, A. Cihan, T. Sakaki, and T. H. Illangasekare, Evaporation from soils under thermal boundary conditions: Experimental and modeling investigation to compare equilibrium-and nonequilibrium-based approaches, *Water Resour. Res.* **47**(5) (2011).
- [97] P. Lehmann, I. Neuweiler, J. Vanderborght, and H.-J. Vogel, Dynamics of fluid interfaces and flow and transport across material interfaces in porous media modeling and observations, *Vadose Zone J.* **11**(3) (2012).
- [98] R. Seager, M. Ting, I. Held, Y. Kushnir, J. Lu, G. Vecchi, H.-P. Huang, N. Harnik, A. Leetmaa, and N.-C. Lau, Model projections of an imminent transition to a more arid climate in southwestern North America, *Science.* **316**(5828), 1181–1184 (2007).
- [99] U. Nachshon, A. Ireson, G. van der Kamp, and H. Wheeler, Sulfate salt dynamics in the glaciated plains of north america, *J. Hydrol.* **499**, 188–199 (2013).
- [100] K. Kondo, M. Tsuchiya, and S. Sanada, Evaluation of effect of microtopography on design wind velocity, *J. Wind Eng. Ind. Aerodyn.* **90**(12), 1707–1718 (2002).
- [101] J. Li and S. Islam, On the estimation of soil moisture profile and surface fluxes partitioning from sequential assimilation of surface layer soil moisture, *J. Hydrol.* **220**(1), 86–103 (1999).
- [102] J. D. Bolten, V. Lakshmi, and E. G. Njoku, Soil moisture retrieval using the passive/active l-and s-band radar/radiometer, *(IEEE) Trans. Geosci. Remote Sensing.* **41**(12), 2792–2801 (2003).
- [103] W. F. Krajewski, M. C. Anderson, W. E. Eichinger, D. Entekhabi, B. K. Hornbuckle, P. R. Houser, G. G. Katul, W. P. Kustas, J. M. Norman, C. Peters-Lidard, et al., A remote sensing observatory for hydrologic sciences: A genesis for scaling to continental hydrology, *Water Resour. Res.* **42**(7) (2006).
- [104] D. K. Nykanen and E. Foufoula-Georgiou, Soil moisture variability and scale-dependency of nonlinear parameterizations in coupled land-atmosphere models, *Adv. Water Resour.* **24**(9), 1143–1157 (2001).
- [105] W. T. Crow and E. F. Wood, Multi-scale dynamics of soil moisture variability observed during SGP97, *Geophys. Res. Lett.* **26**(23), 3485–3488 (1999).
- [106] P. R. Houser, W. J. Shuttleworth, J. S. Famiglietti, H. V. Gupta, K. H. Syed, and D. C. Goodrich, Integration of soil moisture remote sensing and hydrologic modeling using data assimilation, *Water Resour. Res.* **34**(12), 3405–3420 (1998).
- [107] W. T. Crow and E. F. Wood, The assimilation of remotely sensed soil

